UNIVERSITAT POLITÈCNICA DE VALÈNCIA

Department of Cartographic Engineering Geodesy and Photogrammetry

Establishing a Real-time Precise Point Positioning Early Warning System

Author: Mutaz Wajeh Abdlmajid Qafisheh

Thesis Advisors:

Ángel Esteban Martín

Raquel M. Capilla Romà

Valencia, Date

27/06/2024

Abstract

Real-Time Early Warning Systems are a critical approach implemented for monitoring geo-hazard disasters such as earthquakes, tsunamis, volcanic activities, and land subsidence. The Earth's population has experienced a substantial increasement, consequently exposing a growing number of people to the effects of various geo-hazard disasters. These influences could impact citizens and countries at different severity levels, reaching high costs in terms of human beings and economic losses. However, the early warning system's ability to initiate proper and reliable warnings significantly impacts in disaster cost reductions in terms of saving lives, reducing home and infrastructure damages, and mitigating economic losses.

Real-Time Precise Point Positioning (RT-PPP) plays a significant role as part of the Early Warning Systems, due to its potential to provide real-time tracking and global coverage and its reliance on precise real-time measurements acquired from only one receiver. However, the RT-PPP approach applies State Space Representation (SSR) products that are highly sensitive to several GNSS error sources. As a result, the warning system's availability and reliability are negatively impacted. It may even be triggered to issue false warnings by factors such as long initialization times, convergence losses, due to poor quality of orbital and clock corrections, ambiguity resolutions, or/and multipath error. Furthermore, poor satellite geometry and the latency of SSR products severely affect the performance of real-time PPP positioning.

In this research, we investigated the effect and mitigation of latency on real-time correction products. The International GNSS Services (IGS) provides official real-time products for RT-PPP; these products contain clock and orbit corrections, among others, and they are the main research concerns as the combination process increases the latency impact on both RT-PPP results and influences the early warning systems performance based on this positioning technique. In this research, investigations into the potentiality of using machine learning approaches to overcome latency problems were carried out. The research examines the Support Vector Regression (SVR) and Autoregressive Integrated Moving Average (ARIMA) machine learning models to predict the corrections broadcasted in SSR products that have a big capability in order to be used instead of the corrections impacted with latency.

The prediction process requires the implementation of rolling sliding windows for training and parametrization of the research machine learning models. Next, the research has investigated the establishment of RT-PPP early warning systems with the aid of machine learning. The deformation simulation engine was created during the research, which was then utilized through a series of experiments to obtain an adequate RT-PPP scenario for research database creation. The created database is consequently used to train and test several machine learning models and their influences on the early warning system performance.

The research results regarding latency showed that the SVR and ARIMA models could mitigate the latency influences for the primary navigation satellite systems GPS and GLONASS by around twenty percent. The SVR model showed a tendency to predict outliers; however, the execution time for the SVR is significantly faster than the ARIMA model processing time.

Regarding the performance of the RT-PPP early warning system, the research statistically evaluates several machine learning models, including decision tree, random forest, support vector classifier, K nearest neighbors, logistic regression, and extreme gradient boosting models as machine learning approaches for establishing an early warning system. The extreme gradient boosting and random forest models were more accurate than the other utilized models, with 97 and 99 percent overall accuracy. At the same time, the extreme gradient boosting showed less tendency to initiate false alarms, with 2.48 percent compared to 16.28 percent for the random forest model.

From the research findings, we derived a set of statistical assessments to evaluate the performance of the established early warning systems. These statistical assessments can evaluate the ability of the utilized machine learning models regarding deformation detections and the model's tendency to initiate false warnings. The study's results confirmed that extreme gradient boosting is the most effective machine learning technique for creating an early warning system. The research contributions can benefit citizens, businesses, stakeholders, and government agencies.

Landslides, land uplifting, volcanic activity, earthquakes, and tsunamis are only some of the geo-natural hazards where the aid of the RT-PPP early warning system can be established. This thesis' findings can also aid emergency planners and managers by providing them with more accurate descriptions of real-time warnings, enhancing the understanding of the likely extent of deformations extents and their impacts.

Resumen

Los sistemas de alerta temprana en tiempo real son instrumentos claves para vigilar posibles desastres geológicos como terremotos, tsunamis, actividades volcánicas, hundimiento del terreno o deslizamientos de ladera. Durante las últimas décadas, el número de personas afectadas por los diversos desastres geológicos ha aumentado de forma sustancial. Las consecuencias negativas de estos desastres afectan a la población y a las infraestructuras con diferentes niveles de gravedad, pudiendo llegar a tener un impacto elevado en pérdidas humanas y económicas. Sin embargo, los sistemas de alerta temprana tienen la capacidad de proporcionar avisos adecuados y confiables, lo que puede llevar a minimizar las pérdidas humanas y económicas.

El método de Posicionamiento Puntual Preciso en tiempo real (RT-PPP) desempeña un papel importante como parte de los sistemas de alerta temprana; debido a su capacidad para proporcionar seguimiento en tiempo real, cobertura global y su capacidad de obtención de mediciones precisas en tiempo real adquiridas por un solo receptor. A pesar de esto, el método (RT-PPP) utiliza productos para la corrección de la órbita y los relojes de los satélites (productos SSR) que son sensibles de los errores de la tecnología GNSS. Como consecuencia, estos errores pueden afectar la disponibilidad y fiabilidad de los sistemas de alerta temprana basados en la técnica RT-PPP. Debido a estos errores, se pueden llegar a generar avisos falsos, algunos de estos errores son: largos tiempos de inicialización, falta de continuidad y exactitud en los resultados, mala calidad de corrección de órbita y reloj de los satélites, mala resolución de la ambigüedad, etc. Además, la mala geometría de los satélites y la latencia de los productos SSR afectan gravemente el rendimiento del posicionamiento PPP en tiempo real.

Este trabajo de investigación, se enfoca, en una primera parte, en el análisis de los efectos y los métodos de mitigación de la latencia de los productos de corrección en tiempo real. El International GNSS Service (IGS) proporciona productos oficiales para materializar la técnica de PPP en tiempo real, estos productos contienen correcciones para las órbitas y los relojes de los satélites que se generan como combinación de los calculados en los diferentes centros de cálculo repartidos por el mundo. Este proceso de combinación aumenta la latencia y, por tanto, su impacto en la solución RT-PPP, afectando el desempeño de cualquier sistema de alerta temprana basada en RT-PPP. Así, en esta tesis, se usará el enfoque de Aprendizaje Automático para resolver el problema

de la latencia, intentando predecir los valores de las correcciones en los productos SSR para el tiempo de la latencia. Se han utilizado los modelos de Support Vector Regression (SVR) y de media móvil integrada autorregresiva (ARIMA) para la predicción, necesitando, en el proceso, la implantación de ventanas deslizantes para entrenar y parametrizar los modelos de aprendizaje automático.

En segundo lugar, la investigación se enfoca en el desarrollo de un sistema de alerta temprana que combina el método RT-PPP con los modelos de aprendizaje automático. Para ello, se ha desarrollado un motor de simulación de deformación que se ha utilizado, mediante una serie de experimentos, para obtener el escenario RT-PPP más coherente con el objetivo de generar una base de datos. Más tarde, se utiliza la base de datos para entrenar y verificar diferentes modelos de aprendizaje automático y su influencia en el desempeño de los sistemas de alerta temprana.

Los resultados de la investigación de la parte de la latencia han indicado que los modelos SVR y ARIMA podrán mitigar la influencia de la latencia para los principales sistemas de navegación por satélite (GPS y GLONASS) en alrededor de un veinte por ciento. El modelo SVR mostró una tendencia a predecir valores atípicos; sin embargo, el tiempo de ejecución del SVR es significativamente menor que el tiempo de procesamiento del modelo ARIMA.

En cuanto al desempeño del sistema RT-PPP de alerta temprana, este trabajo de investigación ha evaluado, estadísticamente, varios modelos de aprendizaje automático, entre ellos los métodos de Árbol de decisión, Random Forest, Máquina de vectores de soporte (SVM), K vecinos más cercanos, Regresión logística, y el modelo de boosting extremo por gradientes (XGB). El análisis de los resultados indica que los modelo de XGB y Random Forest muestran los resultados más coherentes y precisos con 97 y 99 porciento de precisión. Asimismo, el modelo XGB muestra menos tendencia a iniciar falsas alarmas con un 2,48 por ciento en comparación con el 16,28 por ciento del modelo Random Forest.

A partir de los resultados de la investigación, se derivan un conjunto de pruebas estadísticas para evaluar el desempeño de los sistemas de alerta temprana establecidos. Estas pruebas estadísticas pueden evaluar la capacidad de los modelos de aprendizaje automático utilizados con respecto a la detección de deformaciones y la tendencia del modelo a iniciar falsos avisos. Los resultados confirman que el modelo de XGB es la técnica de aprendizaje automático más eficaz para crear un

sistema de alerta temprana en estas condiciones. Los resultados de esta investigación pueden beneficiar a ciudadanos, empresas y agencias gubernamentales.

Deslizamientos de tierra, levantamientos de tierras, actividad volcánica, terremotos y tsunamis son algunos de los peligros geológicos en los que se puede necesitar la ayuda de sistema de alerta temprana basado en la técnica RT-PPP. Los resultados de esta tesis pueden también ayudar a los planificadores y gestores de emergencias proporcionándoles descripciones más precisas de las advertencias en tiempo real, mejorando la comprensión de los posibles alcances de la deformación y sus impactos.

Resum

Els sistemes d'alerta primerenca en temps real són instruments claus per vigilar possibles desastres geològics com ara terratrèmols, tsunamis, activitats volcàniques, enfonsament del terreny o lliscaments de vessant. Durant les darreres dècades, el nombre de persones afectades pels diversos desastres geològics ha augmentat de manera substancial. Les conseqüències negatives d'aquests desastres afecten la població i les infraestructures amb diferents nivells de gravetat i poden arribar a tenir un impacte elevat en pèrdues humanes i econòmiques. Tot i això, els sistemes d'alerta primerenca tenen la capacitat de proporcionar avisos adequats i fiables, la qual cosa pot portar a minimitzar les pèrdues humanes i econòmiques.

El mètode de Posicionament Puntual Precís en temps real (RT-PPP) té un paper important com a part dels sistemes d'alerta primerenca; a causa de la seva capacitat per proporcionar seguiment en temps real, cobertura global i la seva capacitat d'obtenció de mesuraments precisos en temps real adquirits per un sol receptor. Tot i això, el mètode RT-PPP utilitza productes per a la correcció de l'òrbita i els rellotges dels satèl·lits (productes SSR) que són sensibles als errors de la tecnologia GNSS. Com a conseqüència, aquests errors poden afectar la disponibilitat i la fiabilitat dels sistemes d'alerta primerenca basats en la tècnica RT-PPP. A causa d'aquests errors, es poden arribar a generar avisos falsos, alguns d'aquests errors són: llargs temps d'inicialització, manca de continuïtat i exactitud als resultats, mala qualitat de correcció d'òrbita i rellotge dels satèl·lits, mala resolució de l'ambigüitat, etc. A més, la mala geometria dels satèl·lits i la latència dels productes SSR afecten greument el rendiment del posicionament PPP en temps real.

Aquest treball de recerca s'enfoca, en una primera part, a l'anàlisi dels efectes i els mètodes de mitigació de la latència dels productes de correcció en temps real. L'International GNSS Service (IGS) proporciona productes oficials per materialitzar la tècnica de PPP en temps real, aquests productes contenen correccions per a les òrbites i els rellotges dels satèl·lits que es generen com a combinació dels calculats als diferents centres de càlcul repartits pel món. Aquest procés de combinació augmenta la latència i, per tant, el seu impacte en la solució RT-PPP, afectant l'exercici de qualsevol sistema d'alerta primerenca basada en RT-PPP. Així, en aquesta tesi, s'usarà l'enfocament d'aprenentatge automàtic (*Machine Learning*) per resoldre el problema de la latència, intentant predir els valors de les correccions en els productes SSR per al temps de la latència. S'han

utilitzat els models de Support Vector Regression (SVR) i de mitjana mòbil integrada autoregressiva (ARIMA) per a la predicció, necessitant, en el procés, la implantació de finestres lliscants per entrenar i parametritzar els models d'aprenentatge automàtic.

En segon lloc, la recerca s'enfoca en el desenvolupament d'un primer sistema d'alerta que combina el mètode RT-PPP amb els models d'aprenentatge automàtic. Per fer-ho, s'ha desenvolupat un motor de simulació de deformació que s'ha utilitzat mitjançant una sèrie d'experiments per obtenir l'escenari RT-PPP més coherent amb l'objectiu de generar una base de dades. Més tard, s'utilitza la base de dades per entrenar i verificar diferents models d'aprenentatge automàtic i la seva influència en l'exercici dels primers sistemes d'alerta.

Els resultats de la investigació de la part de la latència han indicat que els models SVR i ARIMA podran mitigar la influència de la latència per als principals sistemes de navegació per satèl·lit (GPS i GLONASS) al voltant d'un vint per cent. El model SVR va mostrar una lleugera tendència a predir valors atípics; tot i això, el temps d'execució del SVR és significativament menor que el temps de processament del model ARIMA.

Pel que fa a desenvolupament del sistema RT-PPP d'alerta primerenca, aquest treball de recerca ha avaluat, estadísticament, diversos models d'aprenentatge automàtic, entre ells els mètodes d'Arbre de Decisió, *Random Forest*, Màquina de Vectors de Suport (SVM), K veïns més propers, Regressió Logística, i el model de *Boosting Extrem* per gradients (XGB). L'anàlisi dels resultats indica que els models de XGB i *Random Forest* mostren els resultats més coherents i precisos amb 97 i 99 porcent de precisió respectivament. Així mateix, el model XGB mostra menys tendència a iniciar falses alarmes amb un 2,48% en comparació del 16,28% del model *Random Forest*.

A partir dels resultats de la recerca, es deriven un conjunt de proves estadístiques per avaluar l'exercici dels sistemes d'alerta primerenca establerts. Aquestes proves estadístiques poden avaluar la capacitat dels models d'aprenentatge automàtic utilitzats pel que fa a la detecció de deformacions i la tendència del model a iniciar falsos avisos. Els resultats confirmen que el model XGB és la tècnica d'aprenentatge automàtic més eficaç per crear un primer sistema d'alerta en aquestes condicions. Els resultats d'aquesta recerca poden beneficiar ciutadans, empreses i agències governamentals.

Lliscaments de terra, aixecaments de terres, activitat volcànica, terratrèmols i tsunamis són alguns dels perills geològics en els quals es pot necessitar l'ajuda de sistema d'alerta primerenca basat en la tècnica RT-PPP. Els resultats d'aquesta tesi també poden ajudar els planificadors i els gestors d'emergències proporcionant-los descripcions més precises de les advertències en temps real, millorant la comprensió dels possibles abasts de la deformació i els seus impactes.

Acknowledgments

I would like to express my heartfelt gratitude to the individuals and organizations involved in successfully completing my Ph.D. thesis. First and foremost, I am very thankful to my outstanding Thesis Advisors, Ángel Esteban Martín, and Raquel M. Capilla Romà, for their exceptional leadership and unflinching support. Their guidance and skills were critical in shaping the outcome of this study.

To my beloved father, thank you for being my constant pillar of strength, inspiring me to achieve my best, and always believing in my capabilities. I am forever indebted to my late mother, whose love, sacrifices, and blessings continue to guide me even in her absence. This thesis is dedicated to her soul.

I am eternally grateful to my wife and kids, Maryam, Aya, and Sara, for their unending love, understanding, and encouragement. Your constant support has been instrumental in overcoming obstacles and attaining academic greatness. I would like to convey my heartfelt gratitude to Universitat Politècnica de València for providing the essential resources, facilities, and academic environment to help me complete this thesis. Likewise, I am delighted to honour the excellent education and information I received from Palestine Polytechnic University.

I also want to thank everyone who helped with this thesis's production through motivating talks, critical comments, or practical aid. Your contributions have been quite beneficial.

Please accept my heartfelt gratitude to those whose names are not expressly stated here but have had a beneficial impact.

Finally, I want to thank my family, friends, and colleagues for their unfailing support and encouragement. Your faith in my ability was a driving element behind this tremendous accomplishment.

Table of Content

List of Figures

List of Tables

Abbreviations

ACI	American Concrete Institute
ACS	Analysis Centers
AI	Artificial Intelligence
AIUB	Astronomical Institute at the University of Bern
AltBOC	Alternate Binary Offset Carrier
ANL	Actual Negative Label
APC	Antenna Phase Center
API	Application Programming Interface
APL	Actual Positive Label
APREF	Asia-Pacific Reference Frame
AR	Ambiguity Resolutions
ARIMA	Autoregressive Integrated Moving Average
ARP	Antenna Reference Point
AUC	Area Under Curve
AUSPOS	Geoscience Australia Online Position User Services
BDS	BeiDou Navigation Satellite System
BETN	BeiDou Experimental Tracking Network
BIH	International Time Bureau
BKG	Bundesamt für Kartographie und Geodäsie
BNC	BKG Ntrip Client
BOC	Binary Offset Carrier
CAS	Commercial Authentication Services
CBOC	Composite Binary Offset Carrier
CCRS	Conventional Celestial Reference System
CDDIS	Crustal Dynamics Data Information System
CDMA	Code Division Multiple Access
CGCS	China Geodetic Coordinate System
CLS	Collecte Localisation Satellites
CNC	Computer Numerical Control
CNES	Centre National d'Etudes Spatiales
CNN	Convolution Neural Network
CODE	Center for Orbit Determination in Europe
CORS	Continuously Operating Reference Stations
COV	Confounding Variables
CTRS	Conventional Terrestrial Reference System
CV	Control Variables
DART	Deep Ocean Assessment and Reporting Tsunami
DBSCAN	Density-Based Spatial Clustering of Applications with Noise
DGNSS	Differential GNSS
DGPS	Differential GPS

DL	Deep Learning
DORIS	Doppler Orbitography, and Radio Positioning Integrated by Satellite
DT	Decision Tree
DV	Dependent Variables
ECEF	Earth Center Earth Fixed
EGEP	European GNSS Evolution program
EGNOS	European Geostationary Navigation Overlay Service
EM-DAT	The International Disaster Database
EPN	EUREF Permanent Network
EPOS	European Plate Observing System
EQC	Earthquake Commission
ESA	European Space Agency
ESOC	European Space Operations Center
ETRF	European Terrestrial Reference Frame
EUREF	Regional Reference Frame Sub-Commission for Europe
EV	Extraneous Variables
EWRICA	Early-Warning and Rapid Impact Assessment with real-time GNSS in the Mediterranean
EWS	Early Warning System
FAGS	Federation of Astronomical and Geophysical Data Analysis Services
FCB	Fractional Cycle Bias
FDMA	Frequency Division Multiple Access
FN	False Negative
FNE	False Neutral Events
FOC	Full Operational Capability
FP	False Positive
FTP	File Transfer Protocol
GADER	GPS Aided and DART Ensured Real-Time
GAGAN	GPS-Aided GEO Augmented Navigation
GBAS	Ground-Based Augmentation Systems
GBM	Gradient Boosting Machine
GDP	Gross Domestic Product
GEO	Geostationary Orbit
GFZ	German Research Centre for Geosciences
GGSP	Galileo Geodetic Service Provider
GIFRES	GNSS IF Recording Station
GIM	Global Ionospheric Map
GITEWS	German Indonesian Tsunami Early Warning System
GLONASS	GLObalnaya NAvigatsionnaya Sputnikovaya Sistema
GNS	Geological and Nuclear Sciences
GNSS	Global Navigation Satellite System
GOCA	GNSS/LPS/LS-based Online Control and Alarm System
GOP	Geodetic Observatory Pecny

GPR	Gaussian Process Regressions
GPS	Global Positioning System
GRAS	Ground-Based Regional Augmentation System
GRC	GNSS Research Center
GREAT	GPS-aided Real-Time Earthquake and Tsunami Alert System
G-SEIS	GPS-SurfacE Deformations within Seconds
GSRM	Global Strain Rate Map
GSS	Galileo Sensor Stations
GSSC	GNSS Science Support Center
GTEP	GSSC Thematic Exploitation Platform
GTRF	Galileo Terrestrial Reference Frame
GUARDIAN	GNSS-based Upper Atmospheric RT Disaster Information and Alert Network
HAS	High Accuracy Service
HDOP	Horizontal Dilution of Precision
HTDP	Horizontal Time-dependent positioning
HTTP	Hypertext Transfer Protocol
IAF	Institute of Applied Research
ICRS	International Celestial Reference System
IERS	International Earth Rotation and Reference Systems Service
IGEO	Inclined Geostationary Orbit
IGEX	International GLONASS Experiment
IGM	IGS Messages
IGN	Instituto Geográfico Nacional
IGS	International GNSS Service
ILRS	International Laser Ranging Service
INS	Inertial Navigation Systems
IP	Internet Protocol
IRC	Integer Recovery Clock
ITRF	International Terrestrial Reference Frame
ITRS	International Terrestrial Reference System
ITU	International Telecommunication Union
IV	Independent Variables
IWV	Integrated Water Vapor
JPL	Jet Propulsion Laboratory
KN	K Nearest
KNN	K Nearest Neighbors
KPSS	Kwiatkowski–Phillips–Schmidt–Shin
LAAS	Local-Area Augmentation System
LINZ	Land Information New Zealand
LPS	Local Positioning systems
LR	Logistic Regression
LRA	Laser Reflectors Array

LS	Local Sensors
LSTM	Long Short-Term Memory
LVZ	low-velocity zone
MAC	Master Auxiliary Concept
MAS	Master Control Stations
MAE	Mean absolute error
MC	Mass Center
MEO	Medium Earth Orbital
MGEX	Multi-GNSS Experiment
MHEWS	Multi-Hazard Early Warning Systems
MIT	Massachusetts Institute of Technology
ML	Machine Learning
MPM	Minimax Probability Machines
MRS	Multi Reference Station
MSAS	Multi-functional Satellite Augmentation System
NASA	National Aeronautics and Space Administration
NAVIC	Navigation with Indian Constellation
NAVISP	Navigation-Related Research and Technology Initiatives
NAVSTAR	Navigation Signal Timing and Ranging
NGL	Nevada Geodetic Laboratory
NGS	National Geodetic Survey
NMA	Norwegian Mapping Authority
NMEA	National Marine Electronics Association
NML	Negative Model Label
NN	Nearest Neighbours
NOAA	National Oceanic and Atmospheric Administration
NRC	National Research Canada
NRTK	Network RTK
NTRIP	Networked Transport of RTCM over Internet Protocol
OPUS	Online Position User Services
OS	Open Service
OSNMA	Open Service Navigation Message Authentication
PCA	Principal Component Analysis
PDOP	Position Dilution of Precision
PGA	Peak Ground Acceleration
PGD	Peak Ground Displacements
PGV	Peak Ground Velocity
PML	Positive Model Label
POFMD	Probability Of False Motion Detection
POFNMD	Probability Of False Non-Motion Detection
POFOSD	Probability Of False Out of Service Detection
POIFC	Probability Of Initiating False Classifications

POTMD	Probability Of True Motion Detection
POTNMD	Probability Of Truly Non-Motion Detection
POTOSD	Probability Of Truly Out of Service Detection
PPP	Precise Point Positioning
PPS	Precise Positioning Services
PRN	Pseudo-Random Codes
PRS	Public Regulated Services
PSD	Post Seismic Deformation
PTWC	Pacific Tsunami Warning Center's
PTWS	Pacific Tsunami Warning and Mitigation System
PZ	Parametry Zemli 1990 goda
QZSS	Quasi-Zenith Satellite System
RBF	Radial Basis Function
RF	Random Forest
RINEX	Receiver Independent Exchange Format
RMSE	Root Mean Squared Error
RNSS	Regional Navigation Satellites Systems
ROC	Receiver Operating Characteristics
RS	Restricted Service
RSW	Rolling Sliding Window
RT	Real-Time
RT-PPP	Real-Time Precise Point Positioning
RT-PPP EWS	Real-Time Precise Point Positioning Early Warning System
RTCM	Radio Technical Commission Maritime Service
RTK	Real-Time Kinematic
RTS	Real-Time Service
RTX	Trimble Range Point
SAR	Satellite Rader interferometry
SBAS	Satellite-Based Augmentation Service
SDCM	System for Differential Correction and Monitoring
SLR	Satellite Laser Ranging
SMCS	Short Message Communication Service
SNAS	System of Differential Correction and Monitoring
SOPAC	Scripps Institution of Oceanography's Orbit and Permanent Array Center
SPP	Single Point Positioning
SPS	Standard Positioning Services
SSR	State Space Representation
SSRA	State Space Representation APC
SSRC	State Space Representation CoM
STD	Slant Tropospheric Delay
STDL	Latency Standard Deviation
STDP	Predictions Standard Deviation

SVC	Support Vector Classifier
SVD	Singular Value Decomposition with Truncation
SVM	Support Vector Machine
SVR	Support Vector Regression
TAI	International Atomic Time
TBC	Trimble Business Center
TCP	Transmission Control Protocol
TEC	Total Electron Content
TEVC	Total Electron Vertical Content
TFM	Time-Frequency Mask Convolution Neural Network
TN	True Negative
TNE	True Neutral Events
TP	True Positive
TRANSIT	Navy Navigation Satellite System
TRF	Terrestrial Reference Frame
UAV	Unmanned Aerial Vehicle
UN	United Nations
UN-SPIDER	United Nations Platform for Space-based Information for Disaster Management
UNAVCO	University NAVSTAR
UNDRR	United Nations Office for Disaster Risk Reduction
UNESCO	United Nations Educational, Scientific and Cultural Organization
UPC	Universitat Politècnica de Catalunya
URA	User Range Accuracy
US	United States
USA	United States of America
USGS	United States Geological Survey
USNO	United States Naval Observatory
UTC	Coordinated Universal Time
VLBI	Very Large Baseline Interferometry
VRS	Virtual Reference Station
VTEC	Vertical Total Electron Content
WASS	Wide Area Augmentation System
WGS	World Geodetic System
WHU	Wuhan University
XGB	Extreme Gradient Boosting
ZHD	Zenith Hydrostatic Delay
ZPD	Zenith Path Delay
ZTD	Zenith Total Delay
ZWD	Zenith Wet Delay

Chapter 1 Thesis Introduction

1.1 Introduction

The global population surge has led to unregulated urbanization, resulting in slum growth and inadequate urban planning, particularly in developing nations, causing disorderly clustering of individuals in makeshift dwellings.

Moreover, this expansion of unregulated urbanization brings forth the potential for individuals to settle in nearby regions that are susceptible to geo-hazards, such as earthquakes, tsunamis, landslides, or volcanic eruptions. The absence of proper planning and regulations further exacerbates the vulnerability of these areas to geological and natural calamities.

As urban populations grow, the demand for massive structures increases, necessitating resilient infrastructure like dams, bridges, tunnels, and transportation networks to support these urban centers. Moreover, there has been a significant rise in the demand for various forms of power generation; this includes expanding nuclear power plants, electrical power infrastructure, water treatment and water supply units, and offshore energy projects.

Global warming and climate change pose significant challenges to metropolitan areas, including increased sea levels, heavy rainfall, and unmanaged groundwater extraction, exposing them to geo-hazards. Slum areas, residential structures, and associated infrastructures are vulnerable to various environmental conditions such as wind loads, landslides, ground subsidence, earthquakes, and tsunamis (Capilla, Berné, Martín, & Rodrigo, 2016; Cina & Piras, 2015; Şanlıoğlu, Zeybek, & Özer Yiğit, 2016). These hazards can cause extensive destruction, leading to structural failures, loss of life, injuries, and significant infrastructure damage. For the mitigation of these risks, it is crucial to prioritize measures that enhance the constructions and associated infrastructures, such as implementing robust construction practices, improving structural integrity, and establishing early warning systems and evacuation plans (Beskhyroun, Wegner, & Sparling, 2011; Hristopulos, Mertikas, Arhontakis, & Brownjohn, 2007; Kaloop, Elbeltagi, Hu, & Elrefai, 2017; Khoo, Tor, & Ong, 2010; Rizos & Cranenbroeck, 2010).

The International Emergency Events Database (EM-DAT) is considered a global disaster database. The database contains information regarding disaster events, including the impact of a disaster in social and economic terms, geo-locations, number of affected people, and total deaths, among others. The database categorized the disasters into two main categories: natural and technological groups. The natural class contains several subclasses of geophysical phenomena (earthquakes, volcanic, and dry mass movements), and the meteorological subclass contains disasters such as (storms, heat and cold waves, or other severe weather conditions). In addition, floods and landslides belong to the hydrological subclass. The remaining sub-classes are climatological, biological, and extra-terrestrial (The International Disaster Database, 2022).

The United Nations for Disaster Risk Reduction (UNDRR) reported the human cost of disasters, including an overview of the disaster's impact between 1980-2019. The report revealed that natural hazards cost around one million and a quarter of deaths and nearly three trillion US dollars in economic losses between 2000-2019. Additionally, the report compared the number of natural hazard occurrences between 1980-2019 (Yaghmaei, 2020). Accordingly, a remarkable increase in the related meteorological hazards, including extreme temperature, floods, storms, and landslide events, was found. The research summarizes the natural hazards related to geo-hazards. Consequently, Figure 1.1 compares the number of geo-hazards between 1980-2019 in terms of the number of occurrences with respect to several geo-hazard types, such as earthquakes, landslides, mass movements, and volcanic activities. The investigations show that earthquake events increased by around 21 percent in 2000-2019 compared to 1980-2000. However, the number of landslide events increased by 48 percent during the same period (Reduction, 1901; Vereinte Nationen Office for Disaster Risk Reduction,2022.; Yaghmaei, 2020a, 2020b).

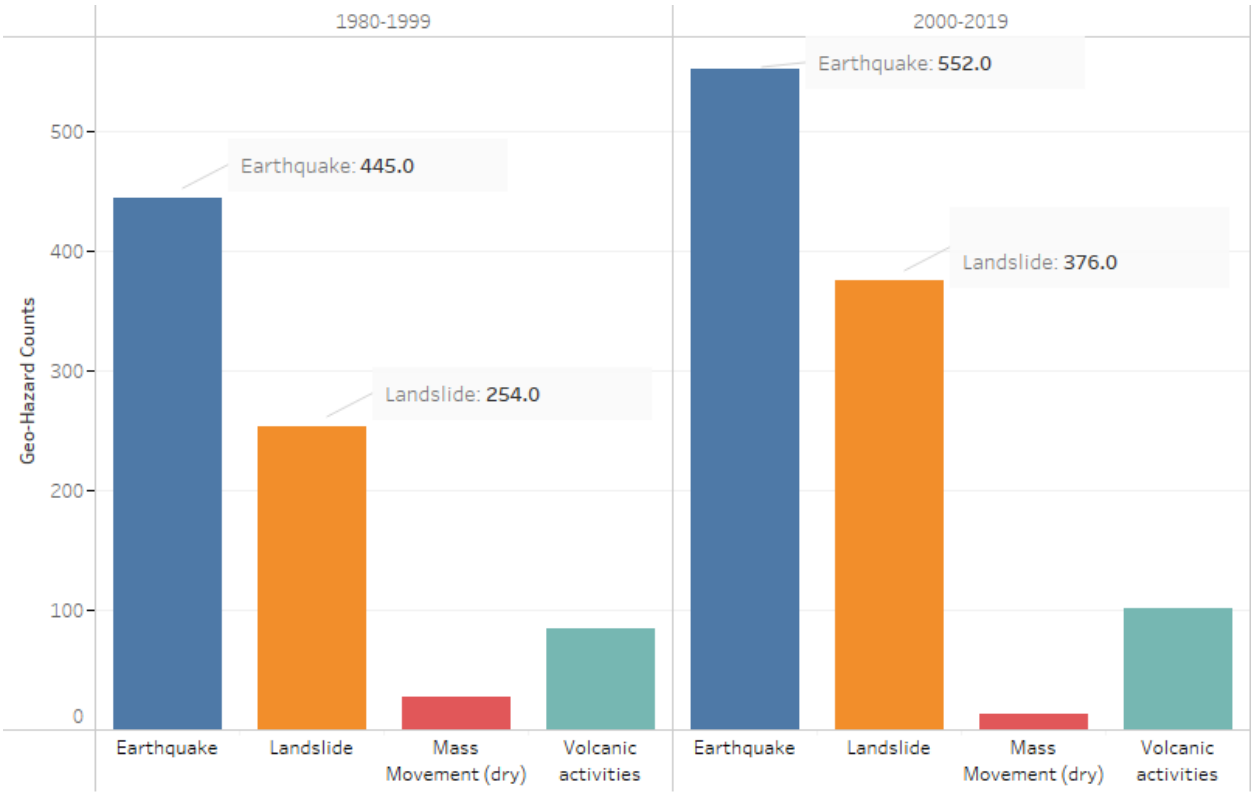

Figure 1.1 Geo-hazard events occurrences comparison between 1980-1999 and 200-2019.

(Prepared by the author).

In order to investigate the impact of natural geo-hazard disasters, the research explored the EM-DAT between 2000 and the nineteenth of July 2023 and filtered the database regarding the research-related disasters, including earthquakes, tsunamis, landslides, dry mass movements, and volcanic activities. The investigation was carried out to demonstrate the number of recorded disasters and the impact of disasters at a national scale with respect to total deaths, the number of affected people, and economic losses. EM-DAT recorded around thirty-five thousand two hundred ninety-five geo-hazard events globally during this period. Figure 1.2 shows the distribution of the recorded geo-hazard events. The figure shows that countries like Japan, India, Pakistan, Iran, Mexico, And Peru have more than twenty recorded geo-hazard events in the last twenty-three years. For instance, China and Indonesia recorded 168 and 154 geo-hazard events, respectively. It could be justified that the pre-mentioning countries located within the zone have high seismic activities.

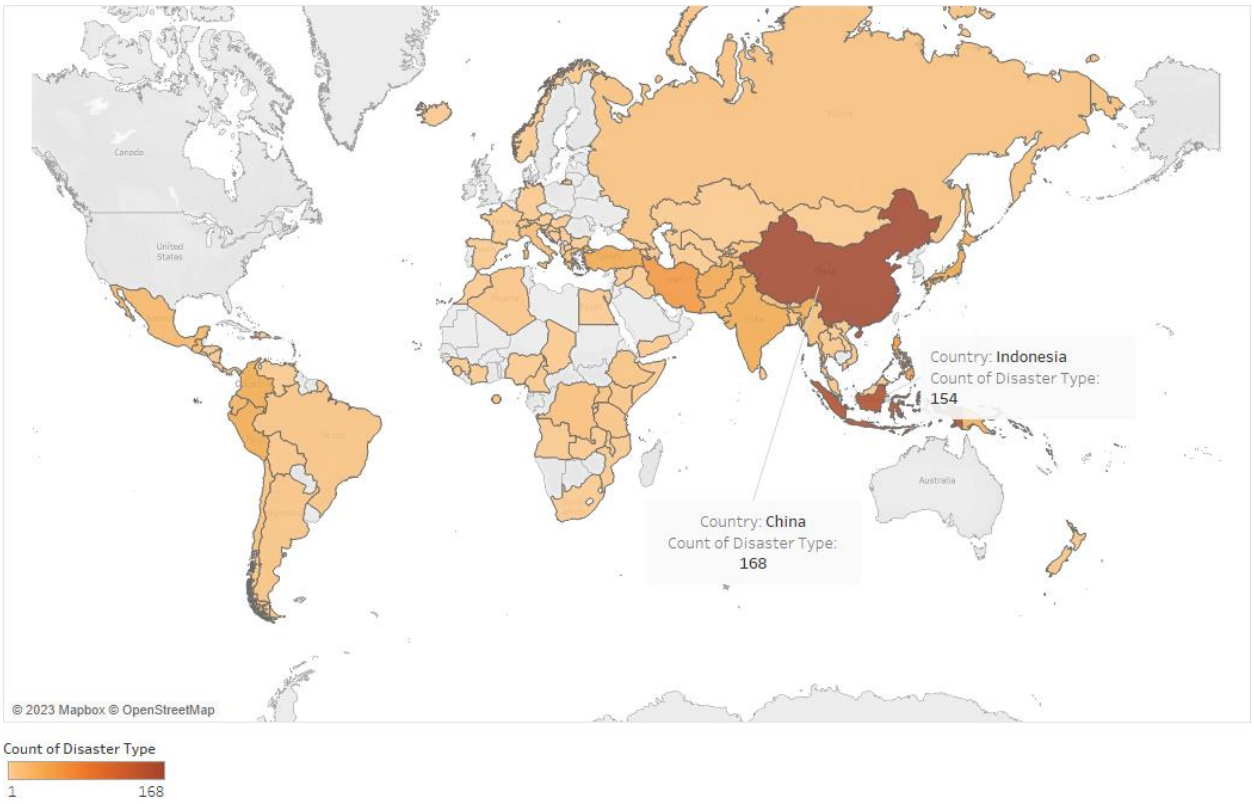

Figure 1.2 Geo-hazard events distribution.

(Prepared by the author).

In terms of the research investigation regarding human losses, the thirty-five thousand two hundred ninety-five geo-hazard events claim more than eight hundred thousand death tolls. Figure 1.3 shows that countries Pakistan, China, and Indonesia recorded around 75, 96, and 183 thousand death tolls in the last twenty-three years. Earthquakes and tsunamis are considered the most important causes of death due to geo-hazard disasters.

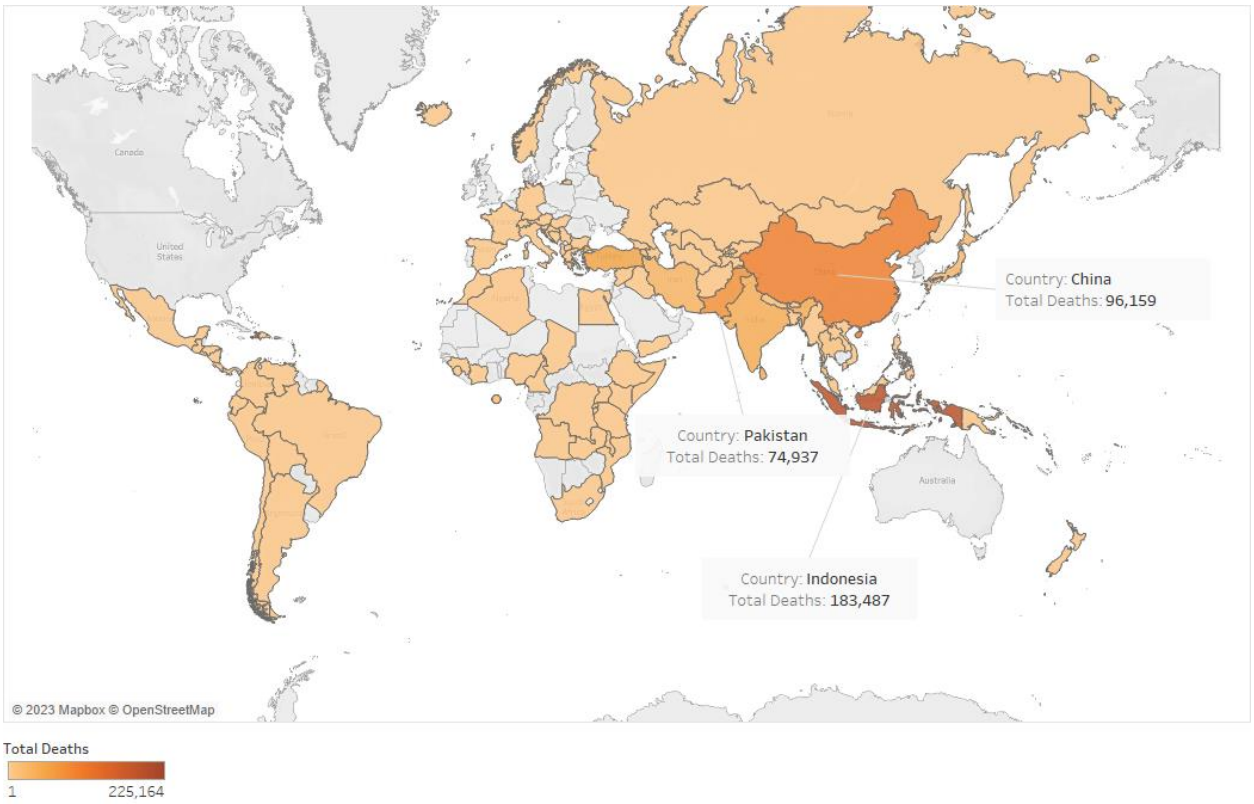

Figure 1.3 Geo-hazard events human cost.

(Prepared by the author).

In the context of the research inquiry about the quantification of affected individuals, it was observed that 35,295 geo-hazard disasters substantially impacted a global scale, affecting a staggering populace exceeding one hundred forty-two million. Figure 1.4 denotes the count of individuals affected by various factors, including structural damage to residences, displacement from disaster-stricken areas, and the deficiency of essential utilities such as electricity and water supplies. Figure 1.4 also shows that countries Turkey, China, and Indonesia recorded around 17, 66, and 14 million impacted persons in the last twenty-three years.

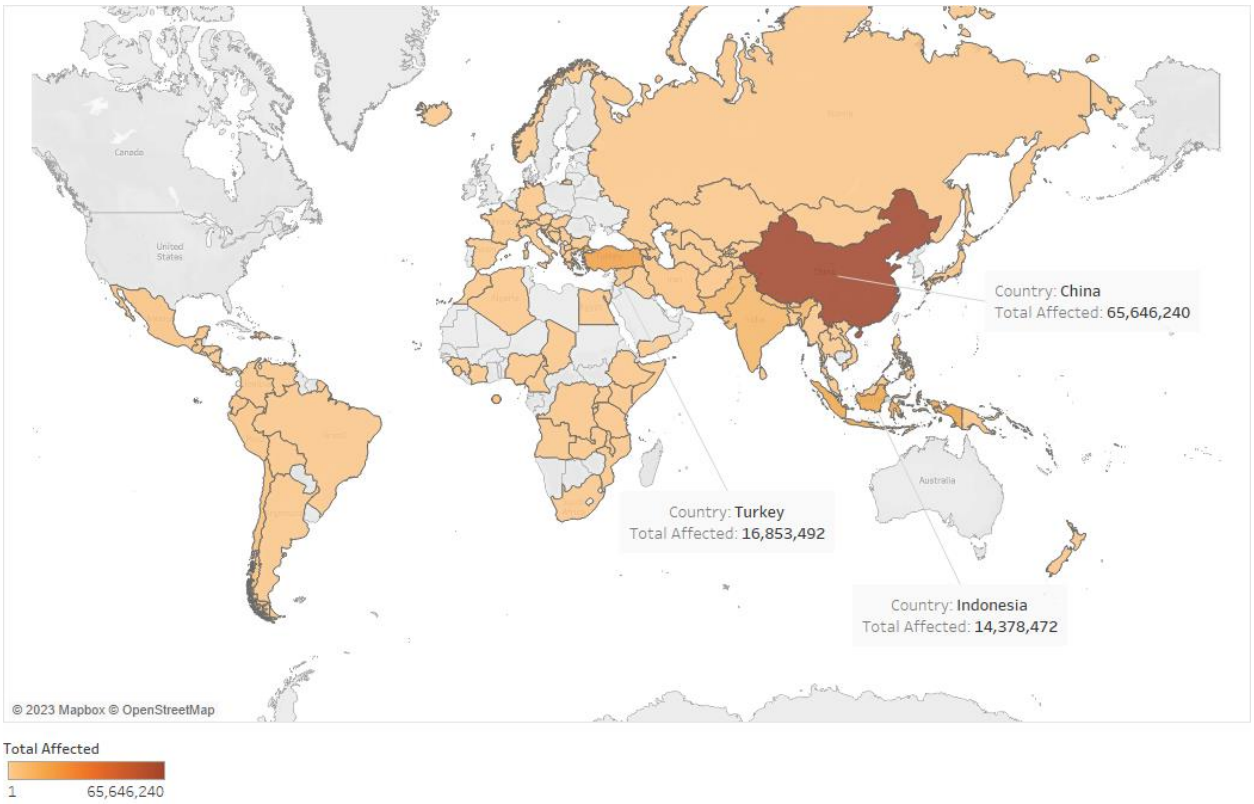

Figure 1.4 The impact of Geo-Hazards disasters at the human scale.

(Prepared by the author).

In the context of the research inquiry about the quantification of economic losses, it was observed that the economic losses due to geo-hazard disasters cost more than eight hundred twenty-six million United States (US) dollars in the past twenty-three years. Figure 1.5 shows the impact of Geo-Hazards disasters at the national economic scale. For example, countries like Japan recorded around 434 million US dollars during the last twenty-three years. At the same time, around 147 million US dollars have been recorded in China.

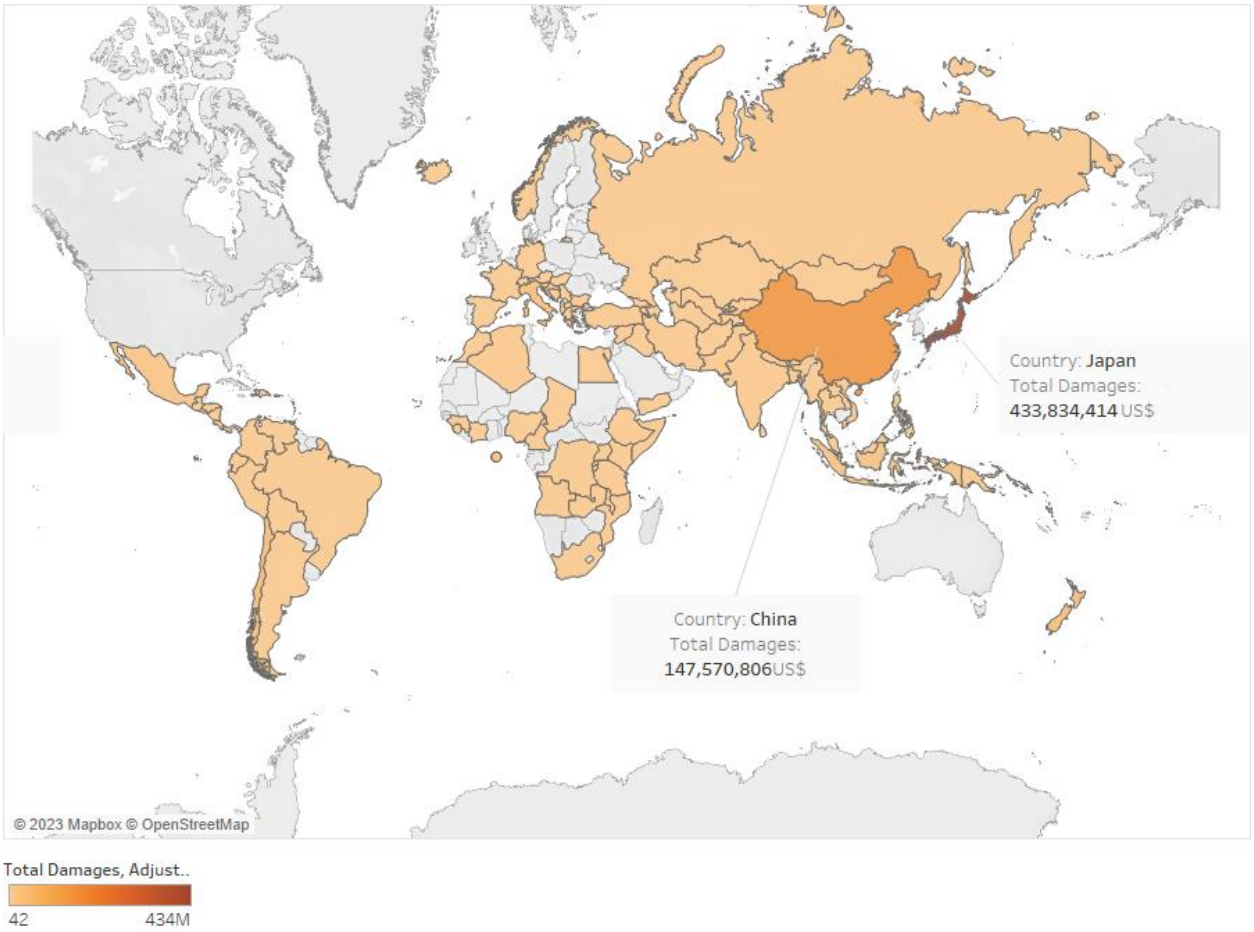

Figure 1.5 The impact of Geo-Hazards disasters at the economic scale.

(Prepared by the author).

The UNDRR prominently distributed and transmitted authoritative, timely, accurate, and actionable warnings during the second International Early Warning Conference 2003. The likelihood and severity of potential threats can be better understood with the help of these alerts. A key takeaway from the meeting was the need for widespread preparation in response to the warnings.

UNDRR has grouped early warning systems targeting distinct types of natural disasters. These systems include hydrology threats, biological and health hazards, crop and livestock illnesses, and geological hazards like tsunamis, earthquakes, volcanic eruptions, and landslides.

On the contrary, the multi-hazard early warning systems have recently received increasing attention on a global scale. These systems are designed to deal with the difficulties posed by a wide variety of hazards and the effects they can have, whether they happen singly, together, in a chain reaction, or gradually over time. They are aware of the potential ties and interdependencies between various hazards and the combined consequences of these hazards.

Early Warning Systems (EWSs) are specialized and established to accommodate a single geo-natural hazard type, such as earthquakes, tsunamis, volcanic, and landslide risks. Accordingly, various tools and methods are integrated into establishing accommodated EWS. Consequently, the distinguishing characteristics of these EWSs could be addressed as implementing complex systems, high establishing costs, various response times regarding warning dissemination, and limitations in converging areas.

Alternatively, establishing a Real-Time Precise Point Positioning Early Warning System (RT-PPP EWS), based on RT-PPP measurements has the capability to reduce the EWS establishing costs as a consequence of using a single Global Navigation Satellite System (GNSS) receiver operating with the aid of a global GNSS network of permanent stations. In addition, the solution provided by this method overcomes coverage area limitations issues that could arise if the EWS relies on traditional GNSS solutions. Another concerning issue regarding utilizing a traditional GNSS is the impact on deformation results as both GNSS receivers, even the whole GNSS network, are all subjected to deformations during natural hazard events; this resulted in the widespread use of Precise Point Positioning (PPP) in many areas and applications. Several studies have examined the appropriateness of the Precise Point Positioning (PPP) approach for remote areas with inadequate infrastructure. This approach can overcome the coverage constraints of adjacent base GNSS stations or the expensive implementation and maintenance of GNSS network solutions. Barker et al. (2002) and Bezicoglue et al. (2019) explored the potential of this approach in offshore, antarctic, and marine environments.

Multiple government-level international documents stress the significance of early warning systems. The Sendai Framework for Catastrophe Risk Reduction, adopted by the United Nations in 2015, recognizes early warning systems as essential for reducing and preventing disaster risk. This framework also emphasizes the importance of early warning systems, which must be significantly improved by 2030 to contribute to better Disaster Risk Reduction. The Hyogo Framework for Action (2005-2015): Developing the Resilience of Nations and Communities to Disasters also emphasized early warnings, ranking it as the second of five priorities for action. In recent years, there has been a massive influx of people into geo-natural hazards in metropolitan regions. The ability to take preventative measures on time before the onset of disasters is a crucial feature of early warning systems. These solutions could save many lives by minimizing the likelihood of accidents and property loss and reinforcing public and private sector business continuity efforts.

Therefore, this thesis has the potential for substantial societal, economic, and knowledge contributions.

Concerning the impact on society, the results of this thesis may be helpful for local communities, stakeholders, and the public sector. The developed RT-PPP EWS can aid in improving emergency preparedness towards geo-natural hazards such as landslides, land uplifting, volcanic, earthquakes, and tsunami land deformations. Findings from this thesis can also provide emergency planners or managers with better capability and insight for planning emergency rescue actions based on reliably described real-time scenarios and expected damages.

Regarding the impact on the economy, findings from the thesis provide opportunities for companies, the public, and the private sector to design and implement business continuity of an EWS, as well as engineering applications of RT-PPP EWS. As the system can initiate early warnings of the expected deformations at a given location, in-advance planning can be developed to produce decision models for actions to take during warnings, with the primary goal of reducing geo-natural hazard consequences. However, utilizing the RT-PPP EWS could be an affordable solution, especially for developing countries (slum areas) or remote places were establishing traditional EWS could not be economically feasible.

The following could be considered regarding the knowledge contributions:

- Confirming the impact of latency on the RT-PPP performance and coordinates accuracy and precision.
- Improving the RT-PPP solutions using machine learning models to overcome the latency impact. Latency is treated as a time series variable so that ML models can be used for prediction.
- Establishing a global and affordable EWS as a monitoring solution, especially for remote and vulnerable regions.
- Confirming the correlation between the research features, such as error sources, with the RT-PPP EWS performance.
- Establishing RT-PPP EWS with prior known probabilities regards the ability of initiation true /false /out-of-service early warnings.
- Presenting a new approach with the ability to accommodate the establishment of the RT-PPP EWS concerning various deformation types.
- Creating and designing the deformation simulation engine as a data generation tool to train the RT-PPP EWS machine learning models.
- The ability to establish an integrated RT-PPP EWS with other complementary data, such as geotechnical methods, remote sensing data, geophones, seismometers, and metrological means this could be utilized by expanding feature space and re-training the machine learning models.

1.2 Research aim, objectives, and research hypothesis

This dissertation aims to develop a reliable, integrated, and precise RT-PPP EWS by integrating machine-learning classification models with RT-PPP measurements. For the sake of achieving the dissertation aim, the following objectives have been created:

1. **Literature review:** To ensure the innovation and foundation of the research, a literature review was conducted, identifying and analysing existing studies on machine learning approaches, early warning systems, and precise point positioning relevant to deformation monitoring.
2. **Latency reduction:** Examine how Real-Time State Space Representation (RT-SSR) products in the RT-PPP EWS can affect latency and how machine learning methods can be used to predict and possibly mitigate this impact.
3. **Data Preparation and Analysis:**
    a. Collect relevant RT-PPP positional information.
    b. Pre-process the data to ensure its consistency, accuracy, and compatibility with machine learning algorithms.
    c. Analyze the relationship between various research variables and RT-PPP coordinate accuracy.
4. **Establishing the RT-PPP EWS machine learning model development:**
    a. Identify and select informative features from the pre-processed data that can improve the accuracy and robustness of the RT-PPP EWS.
    b. Develop and train machine learning models using the research experiments and chosen features, and create and train machine learning models emphasizing methods like support vector machines, decision trees, logistic regression, extreme gradient boosting, nearest neighbouring, and random forests.
5. **System integration and evaluation:**
    a. Integrate the trained machine learning models into the RT-PPP EWS framework. This will enable real-time processing and evaluation of positioning data.

b. Evaluate the performance of the proposed system in terms of accuracy, precision, robustness, and timeliness. Consider various scenarios and the probabilities of correctly detecting or not detecting true motions and potential errors.

The following hypotheses were formulated and tested to facilitate the investigation of the objective as mentioned above.

A. The latency value in International GNSS Service (IGS) clock correction products may impact the RT-PPP results.
B. The machine learning models, for instance, the Support Vector Regression (SVR) and Autoregressive Integrated Moving Average (ARIMA), can overcome the latency problem; those methods are selected because GNSS clock corrections can be considered stationary time series signals that have no trends, seasonality or cyclical patterns.
C. There is an improvement in the obtained RT-PPP results using the Machine Learning (ML) models.
D. In the context of RT-PPP EWs research, the investigations propose the existence of relationships among the research variables, displacement values, deformation types, correction stream selection, orbital and clock corrections, quality indicators, and east, north, and up displacements. Furthermore, it is hypothesized that these relationships extended to RT-PPP results and RT-PPP EWS performance.
E. Machine learning models and the variables used during the training phase impact the RT-PPP Early Warning System (EWS) performance.
F. Different RT-PPP Early Warning Systems (EWS) can be established to accommodate various deformation types.
G. The performance of RT-PPP EWS is influenced by using the machine learning models.

1.3 Thesis organization

This section provides a complete overview of the thesis dissertation organization. The dissertation is composed of eight chapters and three Appendices.

Chapter 1 introduces the thesis aim and the primary objectives. The thesis organization part also provides an overview of the study motivations.

Chapter 2 includes an overview of the satellite navigation systems, their signal spectrum, reference systems, and terrestrial reference frames. This chapter contains the primary error sources in GNSS that generally affect the GNSS measurements. Additionally, Chapter Two covers different GNSS organizations and analysis centers that focus on the dissemination of GNSS data, services, and correction products.

Chapter 3 includes an overview of the PPP from different perspectives, such as the PPP scientific notation and background, the main advantages and the disadvantages of the technique, the State Space presentation (SSR), products to perform in RT-PPP, different SSR products, and a summary of the current products provided by the IGS and other ACs. Additionally, Chapter Three covers different software tools used in the field of RT-PPP.

Chapter 4 includes a review of the Early Warning Systems (EWSs), their necessity, and a brief background in natural hazards related to earth crust deformations such as earthquakes, tsunamis, volcanic activities, and landslides. In addition, some examples of uses are DGNSS, PPP, and RT-PPP-based EWS projects and studies.

Chapter 5 briefly reviews Machine Learning (ML), including classification and regression algorithms. The chapter includes ML performance evaluation through different assessment matrices. Eventually, the chapter concluded with some GNSS and ML applications.

Chapter 6 of this thesis expounds upon the research methodology, consisting of two primary components. The first component elucidates the research methodology adopted to enhance the RT-PPP quality via a comprehensive investigation of various ML algorithms in order to reduce the latency. The research predominantly centers on the application of SSR products that contain corrections such as satellite clock and orbital corrections, code, and phase biases, among others explained in the previous chapter. All of them are particularly susceptible to latency effects. The second component of this chapter entails the illustrations of the ML algorithms utilized to build the early warning system provided with the proposed methodology investigation results. The chapter also contains a detailed account of the proposed engine designed to simulate earth deformation events, including the experiments' parameters and the system's limitations.

Chapter 7 describes the research findings, which are discussed in detail in Chapter 7. The first section of this chapter clarifies the studies' findings with respect to the prediction of RT-PPP corrections to eliminate the latency effect. Latency affects RT-PPP performance; thus, they are particularly interested in this study's focus area: clock and orbit corrections and the rest of the components of the SSR products. In addition, it affects the performance of EWS. The following sections of this chapter focus on the foundational and central research results carried out to launch the RT-PPP early warning system, with illustrations that summarize the ML techniques' results for tracking deformation in multiple directions.

Chapter 8 concludes the research findings regarding the RT-PPP EWS, study challenges, future works, and the research recommendations. It also concludes the research's preliminary results concerning latency and RT-PPP EWS.

Appendix A contains the main Ph.D. activities.

Appendix B contains the research's comprehensive findings regarding the latency investigations. This section provides the rest of the figures and table regarding the range and standard deviation comparison to the research study year 2021.

Appendix C holds the preliminary research results with respect to the establishment of RT-PPP EWS. The section includes the 48 research experiments' results, such as the scatter plots and the Horizontal Dilution of Precision (HDOP).

Chapter 2 GNSS Background

2.1 Satellite navigation systems and signal spectrum

2.1.1 Global Positioning System

The Navy Navigation Satellite System, known as TRANSIT, is the original satellite navigation system. However, the initial system was replaced with the Global Positioning System (GPS) due to long periods of unavailability and low accuracy (Hofmann-Wellenhof et al., 2012).

The first GPS satellites were launched in 1978. Those satellites were deployed for system validation and testing (National Aeronautics and Space Administration, 2022).

Since 1978, the GPS has evolved with different satellites that have been launched in several satellite blocks. The number of operational GPS satellites is nearly 31, distributed in different blocks. Block I, Blocks II and IIA, Block III, Block IIR, Block IIR-M, Block IIF, and Block IIIF. Table 2.1 shows that the number of operational satellites is 6, 7, 12, and 6 in Blocks IIR, IIR-M, IIF, and III, respectively (National Coordination Office for Space-Based Positioning, 2021). The GPS constellation status mentioned above corresponds to the last update on July 14, 2023. Figure 2.1 shows GPS satellites in different blocks.

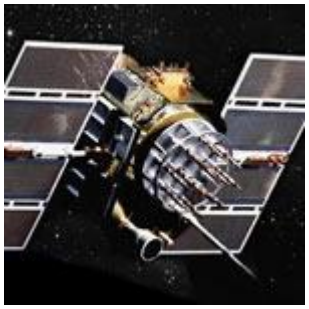

Block IIA

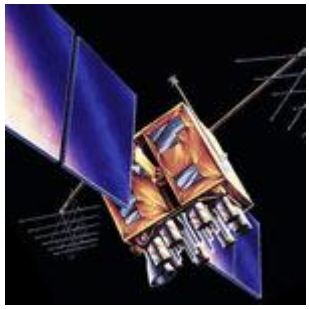

Block IIR

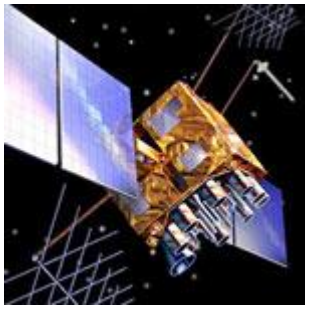

Block IIR-M

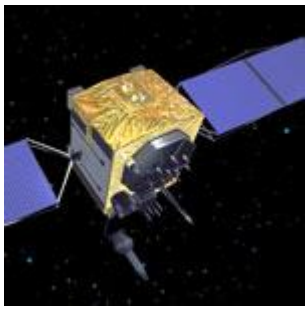

Block IIF

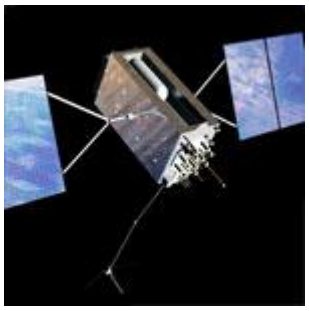

Block III/IIIF

Figure 2.1 GPS satellite blocks.

(Source: www.gps.gov).

It took the United States of America (USA) Department of Defence around 14 years to reach the full operation level (Hein, 2020). Unlike other navigation satellite systems, GPS satellites are distributed among six orbital plans tilted with an angle equal to 55 degrees concerning the equator plan (Hofmann-Wellenhof et al., 2012). The GPS was designed to provide the availability of using five to eight satellites globally. Three GPS signal carriers, L1, L2, and L5, are deployed, with 1575.42 MHz, 1227.60 MHz, and 1176.45 MHz frequencies. Accordingly, the number of available GPS satellites and their signals are sufficient for positioning determination. Discrimination for different satellites, those signals are transmitted with Code Division Multiple Access (CDMA) with different Pseudo-Random Codes (PRNs). The GPS receiver on the earth's surface or onboard low-orbit satellites generates local replicas with different PRNs to distinguish and track different GPS satellites. Those signals are mainly dedicated to military usage through the Precise Positioning Services (PPS); however, the Standard Positioning Services (SPS) could be used by both civilian and authorized users. Nevertheless, the GPS modernization program currently

focuses on deploying the third civilian signals, L2C, L5, and L1C; those signals will be mainly used for civilian commercial and safety of life applications (Hein, 2020; National Coordination Office for Space-Based Positioning, 2020).

Improved compatibility with Galileo E signals is a goal of the new generation of Block III satellites; Block III satellites can transmit the new (L1C) civil signals. The current satellites are deployed with a Laser Reflectors Array (LRA) and Search and Rescue (SAR) payload (National Coordination Office for Space-Based Positioning, 2020).

It was scheduled to start the launch of the Block III satellites in 2016; this date was delayed two years. From 2018 till the time of writing this thesis, Block III contained four satellites, and this number is projected to increase to ten satellites by the end of 2023. This number of satellites in the current block will improve compatibility and civil applications. Table 2.1 shows the GPS constellation status through different years and the signal segment characteristics for different blocks.

Table 2.1 GPS constellation space and signal block characteristics (source: www.gps.gov).

Block	Lunch period	Number of launched satellites	L1	L2	L2C	L5	L1C
I	1978-1985	11	×	×			
II	1989-1990	9	×	×			
IIA	1990-1997	19	×	×			
IIR	1997-2004	13	×	×			
IIR-M	2005-2009	8	×	×	×		
IIF	2010-2016	12	×	×	×	×	
III	2018- 2023	10	×	×	×	×	×

In many scientific applications, the GPS has been involved, such as earth dynamics (Hu et al., 2018; Mével et al., 2015; Miura et al., 2004), landslides monitoring (Calcaterra et al., 2012; Komac et al., 2015), deformation monitoring (Hristopulos et al., 2007; Khoo et al., 2010; Tang et al., 2017) the realization of International Terrestrial Reference Frame (ITRF) (Collilieux et al., 2011), Very Large Baseline Interferometry (VLBI) (Balidakis et al., 2018), soil moisture estimation and remote sensing (Martín, Ibáñez, et al., 2020; Martín, Luján, et al., 2020), radio occultation, and self-driving vehicles (Li et al., 2017; Wickert et al., 2001).

2.1.2 GLONASS

The GLONASS navigation system was created in the Soviet Union in the early 1970s (GLObalnaya NAvigatsionnaya Sputnikovaya Sistema). Since the collapse of the Soviet Union, the Russian Federation has been responsible for maintaining and developing the system.

The first GLONASS satellites were launched in the early 1980s. The number of GLONASS satellites dropped during the Soviet Union collapse period. The GLONASS satellites are distributed in different blocks. Block I, Block IIa, and Block IIb, Blocks IIV, Block III, Block M, Block K. Currently, the number of operational satellites is 22 in Block M and 2 in Block K (Zaminpardaz et al., 2021). Table 2.2 shows the GLONASS constellation evolution; the table also includes the distribution of the GLONASS signal among different blocks. Figure 2.2 shows GLONASS satellites in both blocks (Anatoly Zak, 2021).

GLONASS M GLONASS K

Figure 2.2 GLONASS satellites blocks.

(Source: www. RussianSpaceWeb.com).

The GLONASS satellites were distributed among 3 Medium Earth Orbital (MEO) plans with a nominal altitude reaching 19100 km. The inclination angle concerning the equator plan is around 65 degrees (Hofmann-Wellenhof et al., 2012). The GLONASS was designed to provide availability, especially at higher altitudes regions (Weber & Springer, 2001). The system currently

contains nearly 24 satellites in full operational mode; however, due to its short lifespan, this number has fluctuated since the 1890s.

GLONASS broadcasts two levels of service: high and standard precision carried on GLONASS signals. GLONASS central frequencies are 1602 MHz and 1246 MHz. The system implemented the Frequency Division Multiple Access (FDMA) in order to distinguish GLONASS signals, allowing the system to transmit signals with central frequency shifted with small offsets. Equations 2.1 and 2.2 represent the frequency distribution in the L1 and L2 bands, respectively.

$$f1(n) = 1602 + 0.5625 \times n \quad (2.1)$$

$$f2(n) = 1246 + 0.4375 \times n \quad (2.2)$$

Where:

$f1$ and $f2$: carrier frequencies in MHz.

n: channel numbers whose integer value varies between -7 to 6.

The FDMA allows GLONASS satellites to share frequencies with GLONASS antipodal satellites. The modernization program includes deploying more stable clocks onboard satellites. The current and future GLONASS Block K satellites are capable of broadcasting both FDMA and CDMA (Прикладной потребительский центр Госкорпорации “Роскосмос,” 2020) (Hein, 2020; Zaminpardaz et al., 2021). The GLONASS modernization includes improving the lifespan and implementing the SAR payload (Anatoly Zak, 2021; Urlichich et al., 2011; Zaminpardaz et al., 2021). The last two GLONASS satellites were launched in October and November 2022. Using GPS/GLONASS enhances positioning determination's quality, integrity, and availability. Both systems have been used in several scientific applications (Afraimovich et al., 2013; Milyukov et al., 2010; Scaioni et al., 2018; Tronin, 2010).

Table 2.2 GLONASS constellation space and signal block characteristics (source: https://www.glonass-iac.ru/en/sostavOG/).

Block	Lunch period	Number of launched satellites	FDMA				CDMA
			L1		L2		L3
			L1OF	L1SF	L2SF	L2OF	L3OC
Block I	1982-1985	10	×	×	×		
Block IIA	1985-1989	9	×	×	×		
Block IIb	1987-1988	12	×	×	×		
Block IIV	1988-2005	56	×	×	×		
Block III	2001	1	×	×	×		
Block M	2003-2020	50	×	×	×	×	
Block K	2011- 2023	8	×	×	×	×	×

2.1.3 Galileo

Galileo, the first European navigation satellite system, was born in the 1990s due to cooperation between the European Space Agency (ESA) and the European Commission (Steigenberger & Montenbruck, 2017). The first two Galileo satellites were launched in the period between 2005 to 2008. They were named GIOVE-A and GIOVE-B; both satellites were launched to preserve the allocated frequency for the Galileo system by the International Telecommunication Union (ITU) (Gao et al., 2008; Taylor et al., 2007). Consequently, both involve orbital validation, system verifications, and signal testing. The Galileo satellites are distributed among different blocks. Block GIOVE contains two retired satellites, Block IOV contains four satellites, and it will have 22 satellites. It is projected that the Galileo system will reach Full Operational Capability (FOC) by 2025 (NovAtel Inc, 2015; Sanz Subirana, 2013). Figure 2.3 shows Galileo satellites in IOV, FOC, and GIOVE blocks. Table 2.3 shows the evolution of the Galileo constellation; the table also includes the distribution of the Galileo signal amongst different blocks.

Galileo IOV

Galileo GIOVE B

Galileo GIOVE A

Galileo FOC

Figure 2.3 Galileo satellite blocks.

(Source: www.space.skyrocket.de).

Currently, the system has nearly 23 operational satellites and five auxiliary satellites for orbital replacements. Those satellites are distributed in three equally spaced MEO plans with altitudes around 23 222 km. The MEO plans are inclined concerning the equator plan with a 56-degree angle (European Union Agency for Space Program, 2022).

The system broadcasts signals through different L bands, specifically E1, E6, and E5. The higher bandwidth and the implementations of Alternate Binary Offset Carrier (AltBOC), Composite Binary Offset Carrier (CBOC), and Binary Offset Carrier (BOC) allow for avoiding radio jamming and interference, enhancing the signal-to-noise ratio, degrading the multipath effect and most importantly, increasing the interoperability with another GNSS system (Banville et al., 2008; Sanz Subirana, 2013).

Galileo implements various services carrying transmitted signals. Those services are divided into three categories: free-of-charge services such as Open Service (OS) and Open Service Navigation Message Authentication (OSNMA), which contains information that allows GNSS receivers to

guarantee that the receiver received correct navigation messages. Furthermore, High Accuracy Service (HAS) achieves a sub-meter accuracy level. The HAS is considered an open high-accuracy service based on broadcasting PPP corrections utilizing the Galileo E6 signals. This level of accuracy could be beneficial for several types of applications, including surveying, mapping, precision agriculture, and scientific communities (Hernandez et al., 2018). This second category contains paid services or required authentications like Public Regulated Services (PRS) and Commercial Authentication Services (CAS). The third service is dedicated to safety and life applications, called SAR (European Union Agency for Space Program, 2022).

Table 2.3 Galileo constellation space and signal characteristics (source: https://www.gsc-europa.eu/system-service-status/constellation-information)

phases	Lunch period	Number of launched satellites	E5		E6	E1	E5
			E5a	E5b			
GIOVE	2005-2008	2	×	×			
IOV	2011-2012	4	×	×	×	×	×
FOC	2014-2024	22	×	×	×	×	×

The Galileo navigation system has been involved in many scientific activities and attracted scholars' attention, including the Multi-GNSS Experiment (MGEX) (Afraimovich et al., 2013; Hadas & Hobiger, 2021; Paziewski et al., 2020; The Multi-GNSS Experiment and Pilot Project (MGEX), 2016; Zedek et al., 2021; European Parliamentary Research Service, 2018).

2.1.4 BeiDou Navigation Satellite System

The 1980s of the previous century saw the conception of the Chinese navigation system. The navigation system is named BeiDou, which means the great Bear stars constellations as both satellites and stars constellations used for navigation (Test and Assessment Research Center of China Satellite Navigation Office, 2022b).

The first BeiDou satellite was launched in 2000 and was of the type BeiDou-1. Over time, new types emerged, such as BeiDou-2 and BeiDou-3. The BeiDou satellites are distributed in three distinct types of orbital plans: Geostationary (GEO), Inclined Geostationary (IGEO), and MEO (NovAtel Inc, 2015). The first FOC level of service consists of 30 satellites. It comprises six satellites distributed equally among GEO and IGEO, and the rest in MEO (Test and Assessment

Research Center of China Satellite Navigation Office, 2022b). According to (Suya et al., 2022), the constellation composites of 15 BeiDou-2 satellites and 29 of the type BeiDou-3. More information regards the updated constellation status can be found on the official website of the Test and Assessment Research Center of China Satellite Navigation Office (Test and Assessment Research Center of China Satellite Navigation Office, 2022a). Figure 2.4 shows BeiDou satellites in Blocks 1, 2, and 3. Table 2.4 shows the BeiDou constellation development; the table also includes the spreading of the BeiDou signals amongst different blocks.

BeiDou GEO

BeiDou MEO

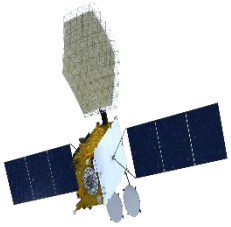

BeiDou IGSO

Figure 2.4 BeiDou satellite blocks.

(Source: http://www.csno-tarc.cn/en/system/introduction).

The Chinese system offers several services, including Short Message Communication Service (SMCS), Satellite-Based Augmentation Service (SBAS), OS, SAR, and Precise Point Positioning (PPP) service. The middle band frequencies are 1176.45, 1207.14, 1268.52, 1561.098, and 1575.42 MHz; those services are transmitted on various L band signals B2a and B2b, B3l, B1l, and B1C (Chong, 2009; Suya et al., 2022). As a result, the BeiDou data is considered in numerous scientific applications, such as the research of the International GNSS Monitoring and Assessment System,

China Aerospace (China Aerospace Corporation, 2018), and the MGEX project (The Multi-GNSS Experiment and Pilot Project (MGEX)), particularly in the Asia and China Regions. However, BeiDou faces numerous difficulties with satellite stability and low-performance precision, particularly at higher latitudes (Chong, 2009; Suya et al., 2022).

Table 2.4 BeiDou constellation space and signals characteristics (source: http://www.csno-tarc.cn/en/system/constellation).

Block	Lunch period	Number of launched satellites	B1	B2	B3
Block BDS-1	2000-2006	4	×	×	
Block BDS-2	2007-2019	20	×	×	×
Block BDS-3	2015-2022	35	×	×	×

2.1.5 Regional Navigation Satellites Systems (RNSS)

Besides the primary global navigation satellite system, new navigation systems were set up. However, those regional navigation systems mainly incorporate global navigation satellite systems. The RNSS's most beneficial is that it can assist GNSS observations regarding continuity, integrity, accuracy, and availability.

2.1.5.1 Navigation with Indian Constellation (NavIC)

NavIC just took the place of the previous term, the Indian Regional Navigation Satellite System. The primary goal of establishing NavIC is to offer navigation services to the Indian part of the Asia continent. SPS and Restricted Service (RS) are two services that NavIC offers. Currently, eight active satellites are divided among the system's GEO and IGSO orbits. Those satellites transmit their signals through 1176.45 MHz in the L band and 2492.02 MHz in the S-band (Department of Space, 2022; Hein, 2020).

2.1.5.2 Quasi-Zenith Satellite System (QZSS)

QZSS is integral to GPS for positioning enhancement. However, this system was planned to assist only navigation users over the Japanese islands. The first QZSS satellite was launched in 2010. The system contains four operational satellites that transmit GPS-like signals, and three more satellites will launch sooner; the QZSS plan will include nearly eleven operational satellites. The primary benefit of employing QZSS is to improve positioning quality in contemporary cities and

urban canyons. To some extent, the satellites maintain to stay above the sky of the GNSS users (Cabinet Office, 2022; Hein, 2020; Kogure et al., 2006).

2.1.6 Augmentation system

Besides various navigation systems, augmentation systems are vital, especially in safety and life applications. Flight operations include landing, taking off, flight manoeuvres, and maritime operations like harbour traffic management. Consequently, the augmentation systems capabilities extended to deliver improved positioning performance. Enhancing navigation regarding achieved accuracy, availability, reliability, and integrity (Bernhard Hofmann-Wellenhof, 2008).

It is possible to think of an augmentation system in the same way as a differential system but with the added ability to offer integrity information. From the GNSS user's side, is it possible to deliver that information using SBAS or Ground-Based Augmentation Systems (GBAS). Both systems track GNSS measurements to analyse and generate corrections, then disseminate them to the desired users. Different systems work under SBAS, such as Wide Area Augmentation System (WASS), European Geostationary Navigation Overlay Service (EGNOS), Multi-functional Satellite Augmentation System (MSAS), GPS Aided GEO Augmented Navigation (GAGAN), (System of Differential Correction and Monitoring) (SNAS), and System for Differential Correction and Monitoring (SDCM). The broadcasted information from the above system is transmitted through the geostationary satellites system, which makes them available specifically for a wide area. Figure 2.5 shows the SBAS system coverage regions (Bernhard Hofmann-Wellenhof, 2008; Grewal et al., 2020).

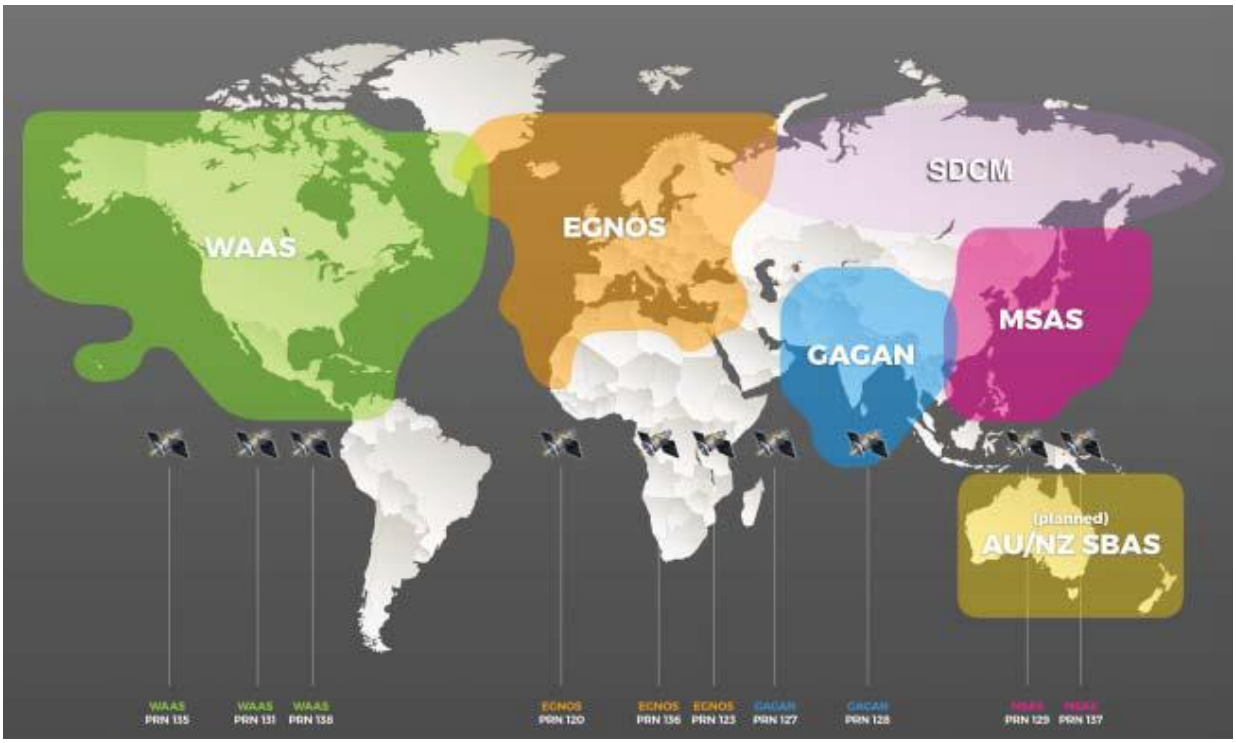

Figure 2.5 SBAS coverage area.

(Source: (Grewal et al., 2020)).

Similarly to the SBAS system, the GBAS meets more restrictions requirements, especially for aviation. The GBAS broadcasted information could be transmitted to nearby users through ground communications. GBAS can be categorized as a Ground-Based Regional Augmentation System (GRAS), Local-Area Augmentation System (LAAS), and Pseudolites (Grewal et al., 2020).

2.1.7 Summary of GNSS systems

The number of navigational satellites has been increasing recently. Currently, more than 150 satellites are orbiting the Earth and providing various navigation signals. Those signals are distributed in L and S bands. The ability of the new satellite's family, besides SBAS and GBAS, to transmit multiple singles across multiple frequency bands will allow researchers in this field to test out novel concepts like Real-Time Precise Point Positioning (RT-PPP) applications (Teunissen & Khodabandeh, 2015) auto vehicles (Darwish & Abu Bakar, 2018), and Unmanned Aerial Vehicles (UAVs) (Grayson et al., 2018). More than 17 signals provide OS for GNSS users; however, this number increases notably for Authentication users (Bernhard Hofmann-Wellenhof, 2008; El-Rabbany, 2002; Kubo, 2008; Sanz Subirana, 2013). GNSS is encountering several challenges, such as improving the compatibility between different systems and reducing the frequency interferences; presently, L-band and S-band are saturated with different GNSS signals from various systems. Therefore, it is required to implement new technologies and novel ideas to implement a new generation of navigation signals, such as CBOC and AltBOC (Banville et al., 2008). Accordingly, as many modern civilian applications rely on navigation signals, a complete agreement is necessary to safeguard all GNSS civilians against interferences, particularly during times of war. The distribution of GNSS satellites among various systems is depicted in Figure 2.6. The Y-axis displays the number of active satellites, and the X-axis displays the name of the active system.

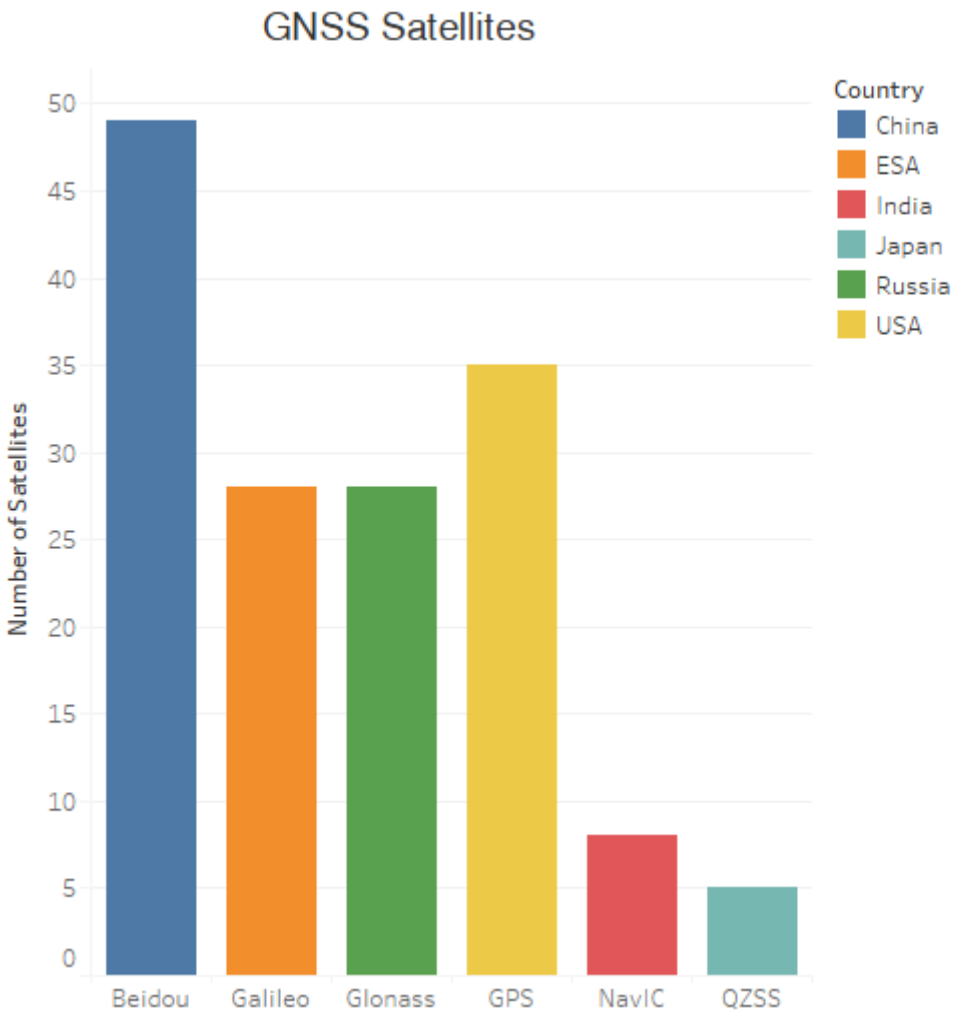

Figure 2.6 Number of GNSS constellations operational satellites.

(Prepared by the author).

The distribution of the GNSS and RNSS signal spectra in the L and S bands is depicted in Figure 2.7. The central frequency, the names of the signals, the type of modulation, and the signal's frequency domain spectrum are all included in the figure.

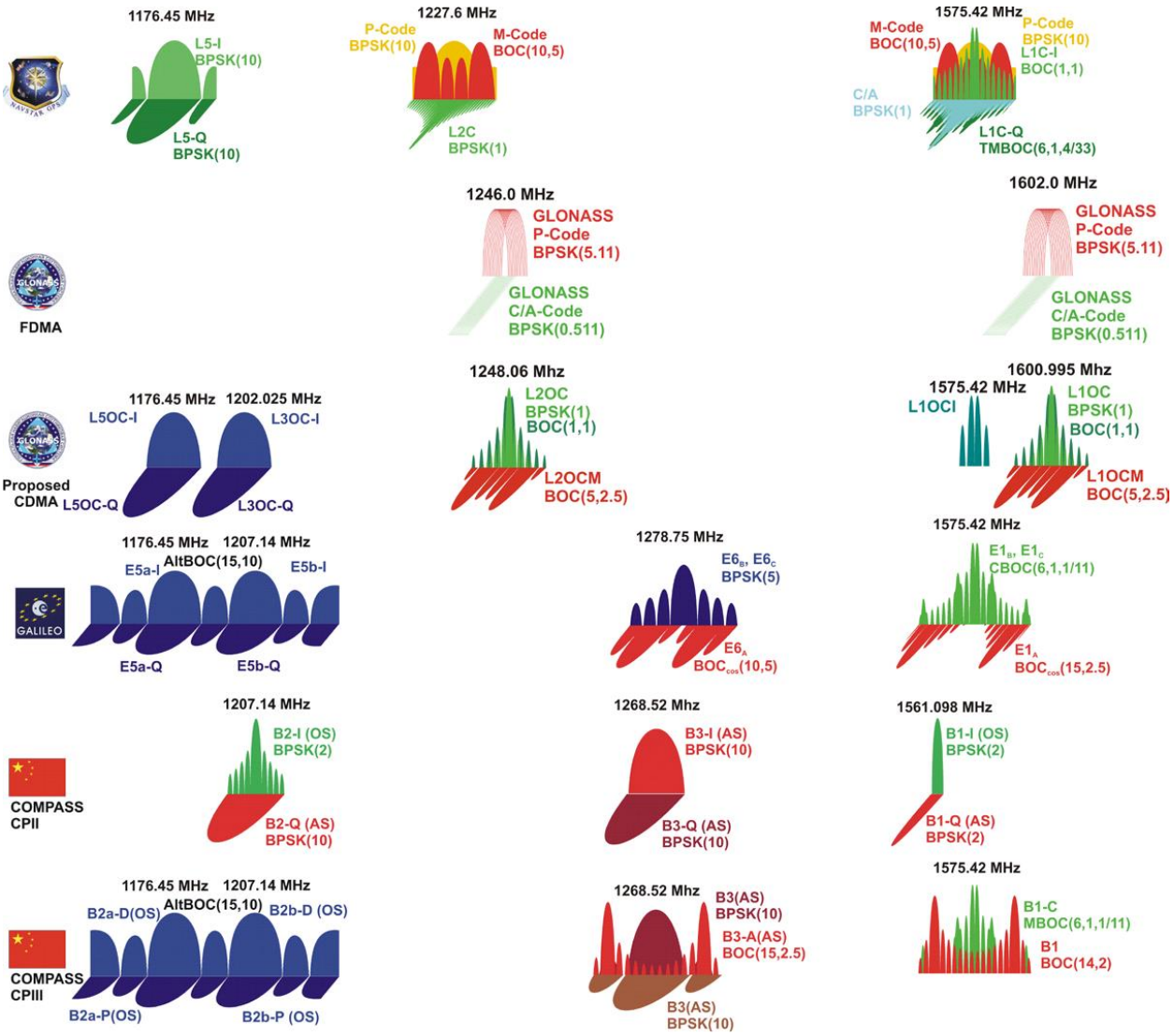

Figure 2.7 GNSS signals spectrum.

(Source: https://gssc.esa.int/navipedia/images/c/cf/GNSS_All_Signals.png).

2.2 Geodetic reference systems and frames

Using GNSS without geodesy and specifying the geodetic systems and frames is impossible (Deng, 2015). Consequently, it is crucial to understand the background and the characteristics of the different geodetic systems as the consequence of using different reference frames in the GNSS systems. According to the way of defining the reference system parameters, such as the directions of the axes, the system origin, whether or not it corresponds to the earth's center of mass, or whether the predefined axes are fixed or rotate with the earth. Accordingly, two of the primary reference systems have been used in navigation. The Conventional Celestial Reference System (CCRS) (Capitaine et al., 2000) and The Conventional Terrestrial Reference System (CTRS) (Sillard & Boucher, 2001). Noting that the reference system and frame are distinct. The conventional reference system defines the three orthogonal axes in terms of the center of the system and axis direction and contains mathematical models and standards. In contrast, the frame implements that theoretical concept through observations and establishes the reference coordinates of reference points, which materialize the conventional reference system (SanzSubirana, 2013).

2.2.1 Conventional celestial reference system

The geo-mass and the system’s genesis are the same in this right-handed system. The Y-axis is established orthogonally to define the right-handed system, and the Z-axis is orthogonal to the equatorial plane. The X-axis points towards the Vernal equinox, and the Z-axis to the Celestial Pole (ICRS pole considering precession and nutation movements). CCRS is an inertial reference system that does not rotate with the Earth. (Bernhard Hofmann-Wellenhof, 2008; Sanz Subirana, 2013).

2.2.2 International earth rotation and reference systems service

The Federation of Astronomical and Geophysical Data Analysis Services (FAGS) was created in 1987 by the International Astronomical Union and the International Union of Geodesy and Geophysics.

IERS (International Earth Rotation and Reference Systems Service), is the organization in charge of upholding international time and reference frame guidelines. Its main office is in Paris, (France);

several IERS components are spread across the US, Europe, and Australia. IERS aims to maintain and realize the international celestial reference system and frame and the international terrestrial reference system and frame, update earth orientation parameters, and interpret time and space variations for both systems (Federal Agency for Cartography and Geodesy, 2013).

2.2.3 Conventional terrestrial reference system

Earth Center Earth Fixed is the name of this system (ECEF). The X-axis points in the direction needed to produce a 90° angle concerning the Z-direction and connect with the earth's equatorial plane. The X-axis is directed towards the Greenwich zero meridian. The Z-axis aligns with the center of the polar motion circles of the Earth's rotation. Additionally, the Z and X directions are orthogonal to the Y axis. The practical implementation of CTRS is called the Terrestrial Reference Frame (TRF). IERS publishes International TRF under the name ITRFyy, where yy represents the year of publishing the ITRF. However, the main GNSS system implements a different TRF, which is aligned with the correct ITRFyy frame computing the transformation through selected station coordinates. Consequently, it is required to convert the measured observations from each scheme to the desired TRF, getting the coordinates instantaneously in any of the TRF systems or events in the local or country coordinate system (Bernhard Hofmann-Wellenhof, 2008; Sanz Subirana, 2013).

2.2.4 Reference system and international terrestrial reference frame

The earth's crust has continuously formed and deformed for millions of years. Diverse phenomena shaping our planet's surfaces result in a relative displacement of points on the earth's crust. These phenomena include changes in ice cap coverage, earth fluids, earthquake activity, and plate tectonics movement (Altamimi et al., 2016). The plate tectonics theory was formalized in the 1960s. The earth's rigid rocks exist in the crust and lithospheric layers. Those two layers float above the soft substratum where movements occur (Falvey, 1974). Millions of years ago, all current continents were tied together and formed Pangea. Due to the earth's crust motions, the number of tectonic plates and their margin vary over time. Based on the above clarifications, realizing different reference frames adopting the earth's crust variations is mandatory. The International Terrestrial Reference System (ITRS) defines the procedures required for reference

frame creation. These procedures determine the coordinates and velocities of a series of stations distributed worldwide. Therefore, the obtained observations define the TRFyy (Altamimi et al., 2002). GNSS, VLBI, Satellite Laser Ranging (SLR), Doppler Orbitography, and Radio Positioning Integrated by Satellite (DORIS) are the observation methods used to implement the ITRF (International Terrestrial Frame, 2020a). Realization of the ITRF is a composite of different tasks that increase the frame complexity. When merging the measurements from the previous observation methods, it is also necessary to consider the terrestrial tide, atmospheric and oceanic stresses, plate tectonics, and other seismic movements. The non-linear model was employed in the ITRF 2014 generation (Altamimi et al., 2016). However, the ITRF 2020 is an augmented parametric frame.

The number of stations used for ITRF realization has increased, and this includes also performing TRF realization with more advanced technologies, leading to an increase in the ITRF's accuracies. Around 1,200 sites operating with different positioning techniques are involved in the ITRF 2020 realization. The available ITRF solution includes input data, computation approach, and frame definitions, which are available on the ITRF solutions web page (International Terrestrial Frame, 2020).

ITRF 2020 is currently under development. More than 1200 stations are involved in Frame generation. The accuracy of the 2020 frame is projected to be an improvement of the previous 2014 frame. The number of co-location stations where the observation methods are combined is increased. Thanks to IGS products, which led to the densification of the ITRF stations. Three innovations in current realization: firstly, time series analysis of the co-location stations; secondly, yearly and half-yearly estimation for co-location station; and finally, fitting the GNSS observation in the Post Seismic Deformation (PSD) model. Equation 2.3 describes the PSD model. Figure 2.8 shows the station networks involved in the last ITRF realization (ITRF 2020).

$$X(t) = X(t_0) + \dot{X}(t - t_0) + \delta\dot{X}_{PSD}(t) + \delta X_f(t) \quad (2.3)$$

Where:

$X(t)$: denotes the station position at epoch equal t.

$X(t_0)$: represents the station position at epoch equal to t0.

$\dot{X}(t - t_0)$: denotes the station velocity vector.

$\delta X_{PSD}(t)$: represents the whole sum of the post-seismic distortion modifications at the t epoch.

$\delta X_f(t)$: denotes the annual and semi-annual frequencies.

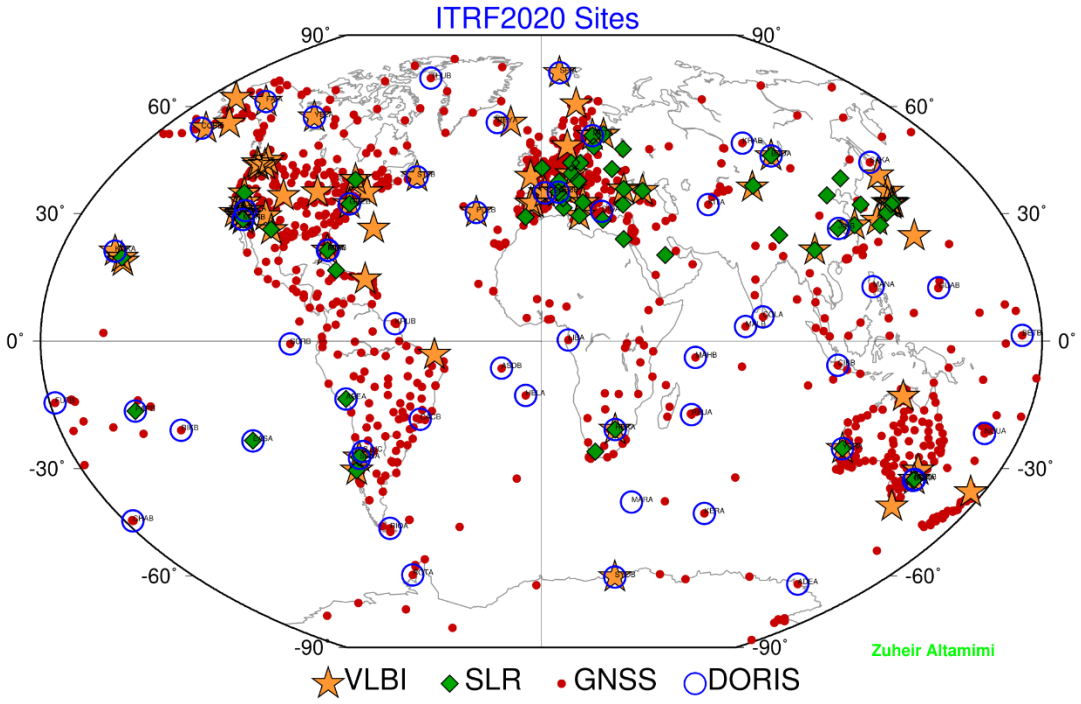

Figure 2.8 ITRF 2020 network.

(Source: Zuheir Altamimi).

2.3 GNSS Reference Frames

2.3.1 GPS Reference Frame WGS-84

The GPS used the World Geodetic System 1984 (WGS-84). The USA Department of Defence is responsible for establishing and then updating the reference frame for both the USA and globally. Previous references were WGS-60, WGS-66, and WGS72. The last updated version, WGS-84, was agreed to ITRF2000, thanks to Horizontal Time-Dependent Positioning (HTDP) measuring the shifting between ITRF 2000 and current measurements. Consequently, the GPS satellites broadcast their location in WGS-84. Subsequently, the GPS users reveal their coordinates in the same reference frame (Bernhard Hofmann-Wellenhof, 2008; KUMAR, 1988; Sanz Subirana, 2013).

GPS users express their coordinate location in X, Y, and Z Cartesian coordinate systems. If geodetic coordinates are needed in terms of latitude, longitude, and height above a reference ellipsoid, the GRS80 (Geodetic Reference System) ellipsoid can be used. These coordinates are taken from a predetermined ellipsoid that originates in the Geo-mass and has semi-major axes of a=6,378,137 m and b=6,356,752.3. However, the ellipsoidal heights could be converted to orthometric heights utilizing the Earth Gravitational Model 2008 or 2020 (EGM08, EGM20) (Nikolaos et al., 2015; Barnes and Daniel, 2019).

2.3.2 GLONASS Reference Frame PZ-90

The GLONASS satellites transmit their locations in Parametry Zemli-90 (PZ-90). This geocentric system was realized by specifying the Z-axis direction concerning the north pole. The X-axis is formed by the union of the equatorial plane and the prime meridian, while the Y-axis is orthogonal to both X and Z. The directions depend on the IERS and the International Time Bureau (BIH). The reference frame was established from different observations, including gravitational measurements, Doppler, laser ranging, and altimetry, and those measurements are coincidental with the ITRF2000. The International GLONASS Experiment (IGEX-98) defined the conversion parameters between WGS-84 and PZ-90. Consequently, GNSS users can use GPS and GLONASS in either WGS-84 or PZ-90 frames(Bazlov et al., 1999; Bernhard Hofmann-Wellenhof, 2008; Boucher & Altamimi, 2001; Sanz Subirana, 2013).

2.3.3 Galileo Reference Frame (GTRF)

The Galileo Geodetic Service Provider (GGSP) has been responsible for establishing and updating the GTRF. Unlike the GPS and GLONASS, the GGSP decided to keep the GTRF within 3 centimetres of consistency, so it was required from the GGSP side to continuously maintain the GTRF with the last ITRF-released version. Maintaining such accuracy is essential to increasing the density of Galileo Sensor Stations (GSS) (Bernhard Hofmann-Wellenhof, 2008; Sanz Subirana, 2013; Team et al., 2011).

2.3.4 BeiDou reference frame

The China Geodetic Coordinate System 2000 (CGCS2000) is associated with global ellipsoids and has the subsequent attributes of a semi-major axis a=6378137.0 m and semi-minor axis b= 6356752.31414. The CGCS was established as a replacement for the old Beijing and Xi'an geodetic coordinate systems to establish a robust conversion. A dense network has been used consisting of 2000 stations. The CGCS2000 refers to the ITRF97 (Bernhard Hofmann-Wellenhof, 2008; Prepared et al., 2009; Sanz Subirana, 2013).

2.4 GNSS error sources

The GNSS measurements are affected by many types of errors that mislead the ranging values between satellites and the GNSS receiver; those errors are caused mainly by atmospheric propagation delays, including the Ionospheric and tropospheric layers. Biases, clock stability, among others, and the environmental site conditions with the multipath, and interferences cause other error sources.

2.4.1 Satellite clock errors

The positioning solution mainly depends on the ranges of the distances between GNSS satellites and GNSS receivers. Both satellites and the receivers stamp the coming and transmitted signals and the locally generated signals with transmitting and receiving time. Therefore, small biases in calculating travelling time can lead to a remarkable amount; for example, ten nanoseconds of differences result in a ranging error with an amount of around three meters (El-Rabbany, 2002). Numerous clocks, mostly rubidium atomic oscillators, Cesium, and passive hydrogen maser

clocks, are installed onboard GNSS satellites. Frequent drift and offsets affect these clock oscillators (Wells, 1999). The GNSS satellite owns its time reference called satellite time; However, it requires the receiver side to measure the time concerning more common times to establish a position solution. The ground Master Control Stations (MCSs) are responsible for disseminating GNSS common time by calculating the satellite's clock perturbations concerning the common reference time for instant GPS time (Kaplan & Hegra, 2006). Next, it is required to upload these corrections to satellites and transmit them to the GNSS users. The polynomial equation 2.4 shows corrections applied to the satellite's clocks (Grewal et al., 2020).

$$\Delta t_{sv}^{i} = a_{f0} + a_{f1}\left(t_{sv}^{i} - t_{oc}^{i}\right) + a_{f2}\left(t_{sv}^{i} - t_{oc}^{i}\right)^{2} + \Delta t_{r}^{i} \quad (2.4)$$

Where:

a_s: are the clock corrections coefficients.

t_{sv}^{i}: is the corresponding time to the i^{th} satellite.

Δt_{r}^{i}: relativistic clock correction corresponding to the i^{th}.

t_{oc}^{i}: the clock data reference time.

2.4.2 Receiver clock errors

Unlike clocks deployed onboard GNSS satellites, the quartz crystal oscillators inside the receiver clocks are less accurate than rubidium, Cesium, and Hydrogen maser. In addition, from a mathematical perspective, the position solution unknowns include the receiver clock biases concerning the GNSS reference common time. This bias contains corrections for frequency drift and shifts inside the GNSS receiver clocks. From an economic point of view, deploying very expensive clocks for GNSS receivers is not feasible.

2.4.3 Satellites orbital errors

This type of error can be illustrated by the differences between the broadcast and the actual satellite's locations. The GNSS MCS_s are in charge of determining and predicting the satellite's locations from the series of ground control points and antennas. Nevertheless, the higher

atmospheric conditions, solar wind, and variation in the gravitational field for the moon, sun, earth, and other celestial objects lead to differences between the predicted location and actual locations of the GNSS satellites; these differences classify into the three main categories:

Class 1: Satellites radial errors.

Class 2: Satellites along-track errors.

Class 3: Satellites cross-track errors.

These three error classes are corrected in terms of components and correction rates. Figure 2.9 shows the direction of the orbital error components.

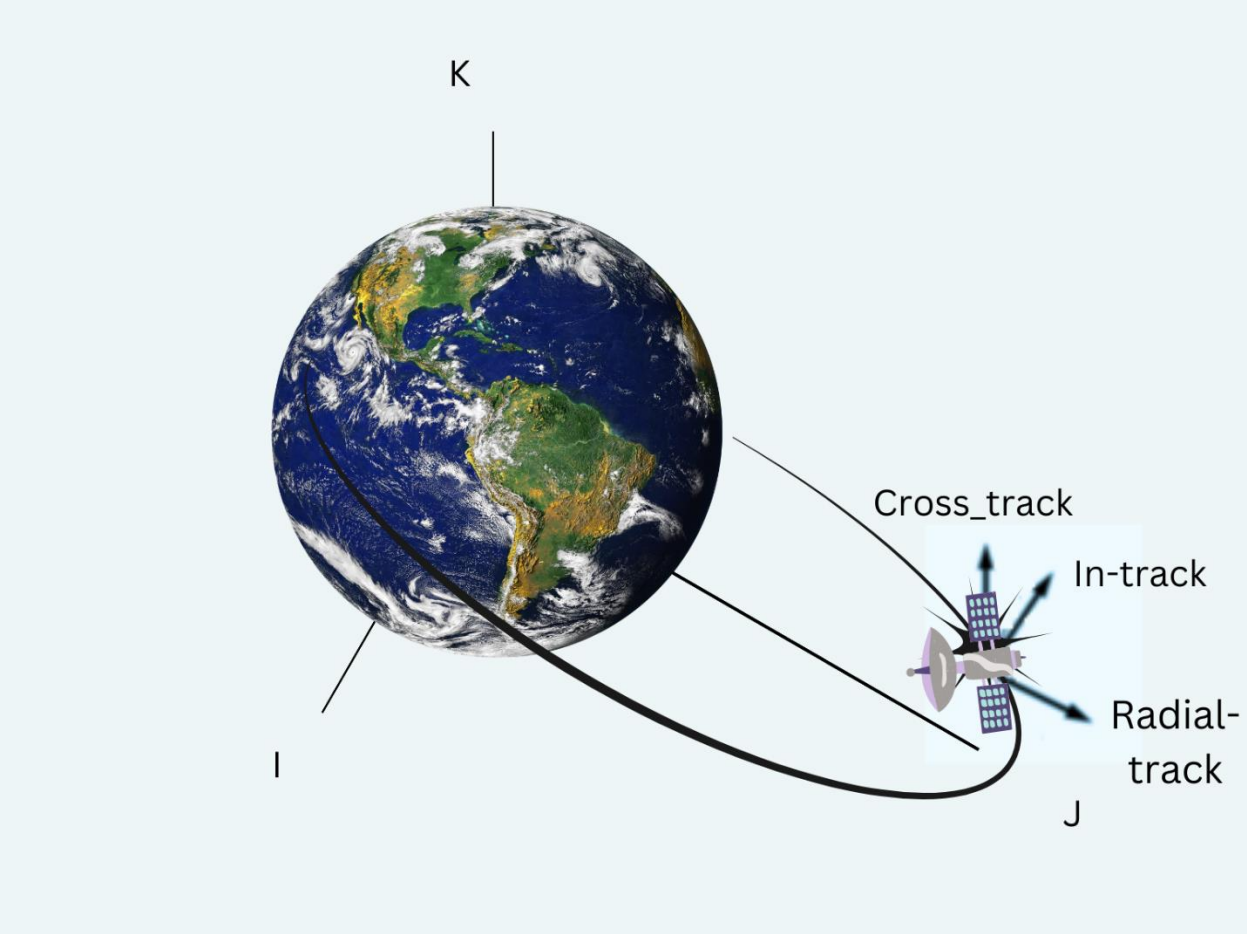

Figure 2.9 Satellite orbital error components.

(Prepared by the author).

2.4.4 Satellites wind-up error

This type of error affects the phase measurements. The GNSS satellites must maintain their solar panels toward the sun's direction. Consequently, the GNSS MCSs exerted small manoeuvrers to preserve the satellite's directions. Therefore, the magnitude of counting wave cycles could be affected. Various GNSS methods and software can deal with wind-up (Kouba & Héroux, 2001; Wu et al., 1992). Wind-up mitigation is highly recommended for accurate applications (Sanz Subirana, 2013).

2.4.5 Satellites antenna phase center error

The mitigation of this type of error is required for precise applications. This mitigation is not required for the GNSS users who rely on the satellite's ephemeris data. The satellite coordinates in the navigation message itself, referring to the Antenna Phase Center (APC) for ECEF. The precise orbital corrections are produced through different analysis centers as well from the IGS organization (Sanz Subirana, 2013; The International GNSS Service, 2022). Concerning the Satellite Mass Center (MC), these corrections are computed. Accordingly, the offset between the APC and MC is required (Kouba & Héroux, 2001). Figure 2.10 illustrates the offsets between the APC and MC.

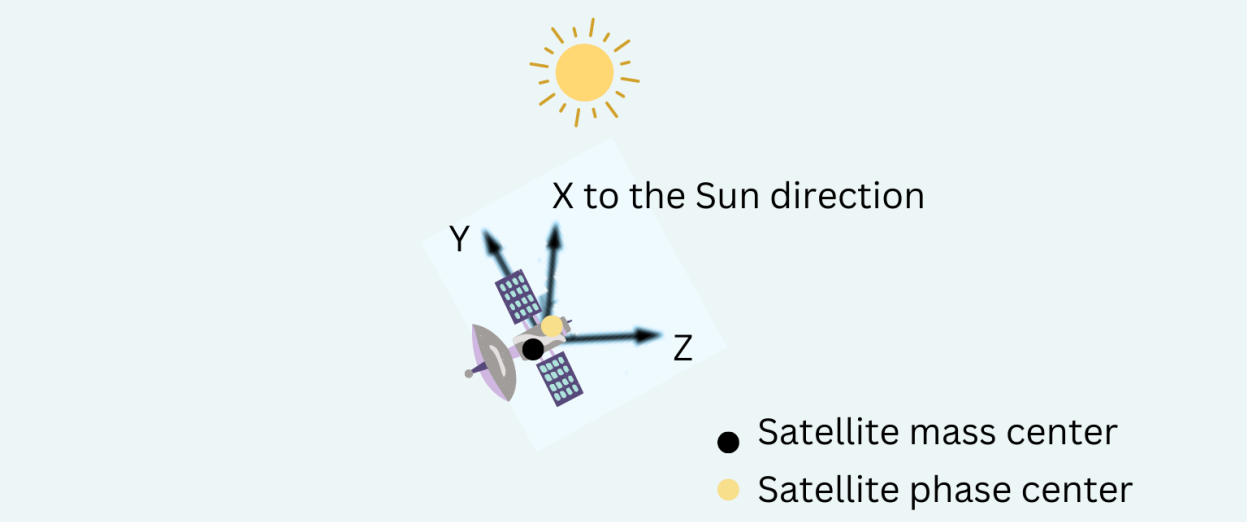

Figure 2.10 Satellite mass and phase center.

(Prepared by the author).

The variation between the APC and MC are provided through ANTEX files. Consequently, the different GNSS software, such as RKLIP and BKG Ntrip Client (BNC) software, uses a range of these offset values in order to approximately correct the GNSS satellite's location with respect to the MC (Georg Weber, Leoš Mervart, Andrea Stürze, Axel Rülke & Stöcker, 2016; Takasu, 2009).

2.4.6 Receiver antenna phase center error

GNSS receivers, during the positioning period, track different incoming signals. The points where the incoming signals have been received are known as the receiver antenna phase center. Due to the variations in the GNSS signal strength, satellite elevation angles, and antenna types, this center does not agree with the geometrical center. In the same way, most of the GNSS receiver's providers indicate these offsets in the ANTEX files (Schmid et al., 2007). Alternatively, this error could be mitigated using the differential GNSS method, especially for short baselines. Figure 2.11, which depicts the configuration of the wide-use Dorne Margolin T GNSS ring antenna. L2 and L1 APCs are used to denote the antenna phase center for the GPS L1 and L2 signals. However, the ARP indicates the actual antenna reference point (Sanz Subirana, 2013).

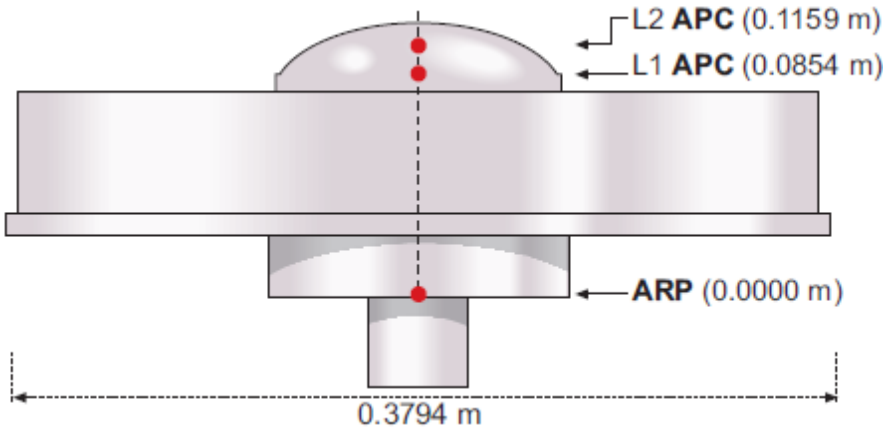

Figure 2.11 Dorne Margolin T GNSS receiver Antenna.

(Source: (Sanz Subirana, 2013)).

2.4.7 Multipath error

The ranging measurements must rely on the time difference between the transmitting signals from GNSS satellites and the receiving time measured by the GNSS receiver. That means the measurements must be carried from point to point or, in other words, from satellites to the receiver; however, it is possible that some signals could be reflected mainly from reflective surfaces such as water bodies, skyscrapers, or any glassy objects. The multipath error severely influences the GNSS measurements and could reach a level of 450 m (Sanz Subirana, 2013). Unlike other GNSS error sources, this type of error cannot be mitigated using differential GNSS methods, and even more, it is difficult to model (Grewal et al., 2020). This error source could be reduced in different ways, for instance, by careful site selection for the GNSS receiver station's location and by increasing the receiver antenna height over the ground level. Other methods could be employed, including time domain processing, the directed antenna array, long-term signal monitoring, and correlator technology (Grewal et al., 2020). For high-precision GNSS receivers, the GNSS manufacturing companies add protective layers that enhance the multipath mitigations. Figure 2.12 shows the two paths of the incoming GNSS signal.

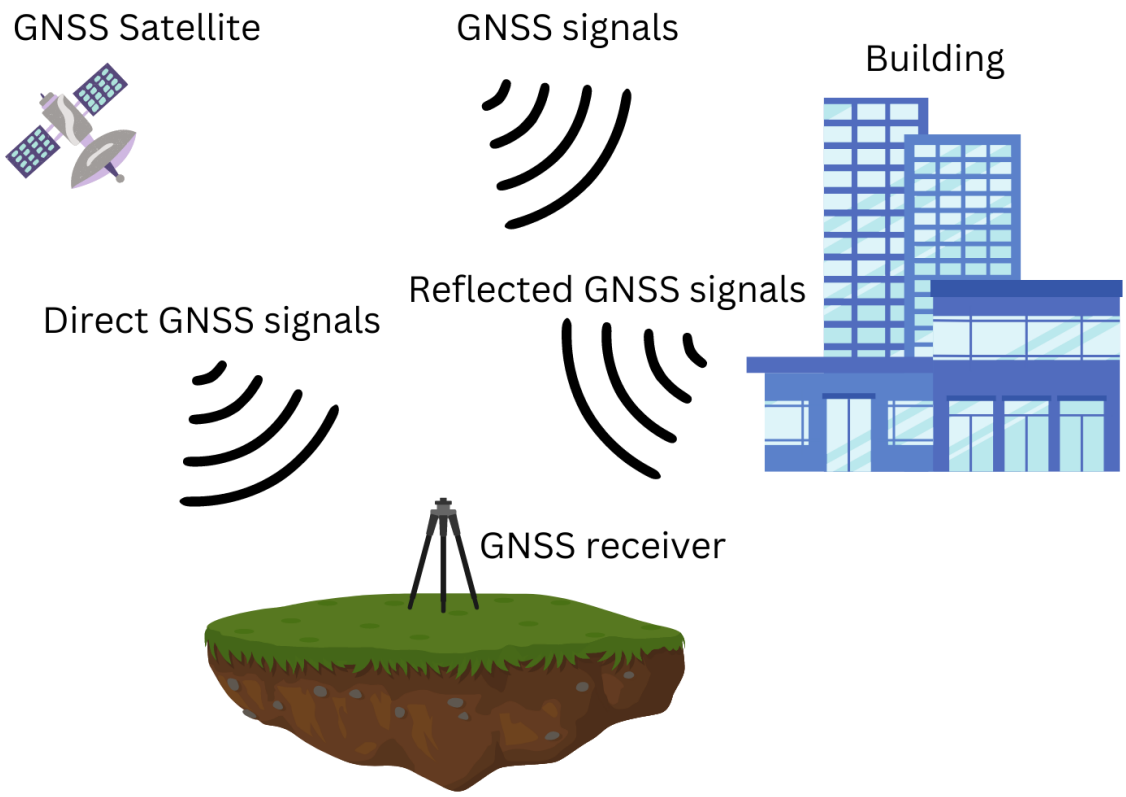

Figure 2.12 Multi-path error.

(Prepared by the author).

2.4.8 Atmospheric delay

The incoming GNSS satellite signals interact with the atmosphere. The atmosphere itself is composed of different layers. Those layers contain different gases and vary with temperature; the borders between layers are constructed according to the temperature variation (Noël, 2012). The GNSS signals consequently react differently as they pass through several levels. The signal travelling speed and the bending of the signal path are considered significant effects of the atmosphere (Dodson, 1986; Sanz Subirana, 2013). The tropospheric and ionospheric layers remarkably impact the measured ranges (Grewal et al., 2020).

The Atmosphere affects the satellite signals by fluctuating signal speeds and directions. The refractive index investigates the atmospheric effect on signal propagation (Enge, 1994). Equation 2.5 shows that the medium with a refractive index of more than one means the signal experiences

a delay in that medium; on the contrary, if the n value is less than one, this medium speeds-up the upcoming signals.

$$n = c/v \tag{2.5}$$

n: refractive index.

c: signal speed in a vacuum.

v: denotes the speed of the signals in the travelling medium.

Based on the relationship between the frequencies of the signals and the refractive index. The medium can be dispersive if the n value depends on the frequency values. Alternatively, it cannot be a dispersive medium if the n values are free of the dependency of signal frequencies (Bernhard Hofmann-Wellenhof, 2008). To correct the GNSS data, the atmospheric inaccuracies are broken down into tropospheric and ionospheric errors.

2.4.8.1 Tropospheric delay

The tropospheric layer is close to the surface of the earth. Both the troposphere and stratosphere layers affect the GNSS signals. Those layers cover an altitude of around 50 Km above ground level (El-Rabbany, 2002). The GNSS signal traveling through the tropospheric layer encounters delay; accordingly, the range measurements will be longer than the actual geometric ranges. The tropospheric layer is a non-dispersive medium at the level of L band frequencies (Sanz Subirana, 2013).

Consequently, the troposphere disturbs code and phase observations with different frequencies with the same amount of propagation delay. The tropospheric error has two components: dry and wet. The dry components occur due to Nitrogen and Oxygen, while water vapor, rain, and ice droplets may be responsible for the wet component (Enge & Misra, 2011). The wet and dry components cause the GNSS ranging measurements to have an extra time delay; consequently, the ranging measurement encounters 2-2.5 meters additional length with respect to the actual geometrical distance between GNSS satellites and GNSS users (Enge & Misra, 2011; Sanz Subirana, 2013). This error can be mitigated using differential GNSS methods, especially for short baselines where the climatological conditions are more or less the same between the GNSS pair

receivers (RTCM Special Committee, 2016). The stand-alone GNSS users can use different models to correct atmospheric errors. Most models have required the satellite's elevation angles, the user's geographical location, and the altitude above the mean sea level.

Equation 2.6 shows the tropospheric estimation in meters (Grewal et al., 2020).

$$\Delta^{Tr} = 10^{-6} \int_a^b N \, ds \tag{2.6}$$

Where:

Δ^{Tr} : the estimated tropospheric delay in meters.

ds: denotes the GNSS signal path between the GNSS user and satellites.

a, b: The integral limits representing the upper and lower tropospheric boundaries.

N: The atmospheric refractivity, including the wet and dry elements.

The 90% of the delay is attributable mainly to the dry component, which is also known as the Zenith Hydrostatic Delay (ZHD). The dry tropospheric gases, in particular Oxygen and Nitrogen, are a significant factor in the ZHD. On the other hand, the wet tropospheric delay is caused mainly by the presence of water vapor, rain, and humidity, which is also known as the Zenith Wet Delay (ZWD). Comparatively speaking, it is easier to anticipate the dry tropospheric delay. However, the complex modelling needed for the tropospheric wet components makes it impossible to estimate the wet tropospheric delay with high accuracy.

$$N = N_d + N_w \tag{2.7}$$

Equation 2.7 shows the atmospheric refractivity, including the two parts. Misra and Enge (2012) provide a mathematical approach to estimating the atmospheric refractivity parts.

$$N_d = 77.64 \, \frac{P}{T} \tag{2.8}$$

$$N_w = 3.73 \, X \, 10^5 \, \frac{e}{T^2} \tag{2.9}$$

P and e in Equations 2.8 and 2.9 signify the total pressure and water vapor in millibars, respectively, and T denotes the temperature in Kelvin.

It is worth highlighting several terms utilized to describe the tropospheric delay, including the Zenith Total Delay (ZTD). It is the total amount of time that the troposphere adds to a GNSS signal as it travels from the GNSS satellites to the users as it is projected in the zenith direction. Usually, the tropospheric delay is estimated utilizing the Zenith Path Delay (ZPD) and mapping function. Additionally, the ZPD is the total amount of time the troposphere adds to a GNSS signal as it travels from the GNSS satellites to the users. Equations 2.10 and 2.11 show simple mathematical formulas utilizing satellite elevation angles to extract the dray and wet delays (Enge & Misra, 2011).

$$m_d(\mathrm{el}) = \frac{1}{\sin(el) + \frac{0.00143}{\tan(el) + 0.0445}} \tag{2.10}$$

$$m_d(\mathrm{el}) = \frac{1}{\sin(el) + \frac{0.00143}{\tan(el) + 0.0445}} \tag{2.11}$$

However, several models implement different mathematical approaches for determining both atmospheric components. Mapping of Niell, Saastamoinen, and Hopfield examples of models for reducing tropospheric error (Hofmann-Wellenhof et al., 2012; Niell, 1996; Sanz Subirana, 2013). Modelling tropospheric error attracts the attention of many scholars (Balidakis et al., 2018; Dong et al., 2018; Yao et al., 2017).

2.4.8.2 Ionosphere delay

The ionosphere layer formulates due to the interactions between the X-ray and ultraviolet energy with gas particles and atoms; consequently, these interactions lead to gas ionization (El-Rabbany, 2002). The ionospheric layer stretches and covers 1000 km above the troposphere (Grewal et al., 2020). The influence of the ionization reaction releases free electrons. Total Electron Content (TEC) is the sum of total free electron charges between the GNSS satellites and the GNSS receiver

(Hofmann-Wellenhof et al., 2012). Equation 2.12 shows the formula used to calculate the TEC for a particular GNSS satellite (Enge & Misra, 2011).

$$TEC = \int_{sat}^{Res} n_e(l)dl \quad (2.12)$$

Where:

TEC: is the total electron content.

$n_e(l)$: signifies the electron density from the satellites to the receiver.

GNSS signal suffers a slowing down in its propagation rate and a deviation in its direction of travel. Unlike the troposphere, the ionosphere is a dispersive medium. Accordingly, the phase refractive and group indices in meter values depend on the frequency of incoming signals. Equations 2.13 and 2.14 show the indices calculations (Enge & Misra, 2011).

$$n_{ph} = 1 - \frac{40.3}{f^2} * \text{Ne} \quad (2.13)$$

$$n_{gr} = 1 + \frac{40.3}{f^2} * \text{Ne} \quad (2.14)$$

Ne signifies the density of electrons, and f represents the frequency of the satellite's signals.

The ionospheric delay is a dominating error source in GNSS measurements, and its value could vary from several meters to hundreds of meters in ranging measurements (Wells, 1999). The receiver's geographic location is one of several ionospheric delay magnitude variables. Polar and equatorial regions are experiencing more ionospheric activities rather than mid-altitude. Satellite elevation angle and measurement time also affect the GNSS measurements; day measurements practice more ionospheric delay than night measurements. Solar storms also severely influence the GNSS measurements (NovAtel Inc, 2015).

Differential GNSS (the recommended baseline length does not exceed 20 km) (El-Rabbany, 2002). Nevertheless, the single-frequency stand-alone GNSS receiver could benefit from predefined models such as Klobucher and NeQuik (ESA, 2017; Klobuchar, 1987).

$$\varphi_{Iono-free} = \frac{f1^2 * \varphi_1 - f2^2 * \varphi_2}{f1^2 - f2^2} \quad (2.15)$$

$$R_{Iono-free} = \frac{f1^2 * R_1 - f2^2 * R_2}{f1^2 - f2^2} \quad (2.16)$$

Where $\varphi_{Iono-free}$ signifies the phase measurements free from the ionospheric delay, while R represents the measurements of code free from the ionosphere's effect, and f represents the GNSS signal frequency.

This dominant error can be mitigated in different ways. Firstly, a stand-alone GNSS receiver capable of tracking multifrequency signals can use the Ione-free model shown in equations 2.15 and 2.16 (Wells, 1999). However, for the same GNSS revivers operating in differential mode, when two receivers operate simultaneously in the same area, the inaccuracy can be removed using differential GNSS (the recommended baseline length does not exceed 20 km) (El-Rabbany, 2002). Nevertheless, the single-frequency stand-alone GNSS receiver could benefit from predefined models such as Klobucher and NeQuik(ESA, 2017; Klobuchar, 1987).

The fluctuation in the GNSS signal route is minimal for satellites with an elevation angle of at least five degrees (El-Rabbany, 2002). However, it is necessary to consider the Vertical Total Electron Vertical Content (VTEC). The mapping function between the ionospheric delay related to VTEC and zenith angle z is shown in equation 2.17. (Hoffmann-Wellenhof & H. Lichtenegg, 2001).

$$\Delta^{Iono} = \pm \frac{1}{\cos(z)} \frac{40.3}{f^2} * TEVC \quad (2.17)$$

Numerous studies are being developed regarding ionospheric delay estimation and modelling, particularly in ionospheric scintillation. This phenomenon refers to TEC's sudden and unexpected values(Crane, 1977; Kintner et al., 2007, 2009).

2.4.9 Cycle slip

The incidence of cycle slip is one of the flaws in phase carrier measurement. The GNSS receiver must continue to count the proportion of the carrier cycle during the tracking time. One cycle will be added to the starting cycle counts if the fractional phase changes from 360 to 0 degrees (Hoffmann-Wellenhof & Lichtenegg, 2001; Grewal et al., 2020). (NovAtel, 2015) define a cycle slip as "a jump in the number of integer cycles," These jumps may happen depending on the local

environment, such as nearby structures, power lines, and tree leaves. Cycle slip could be caused by receiver hardware manufacturing quality as well as software capabilities (Hoffmann-Wellenhof & Lichtenegg, 2001; Grewal et al., 2020).

2.4.10 Relativistic effect

The relativistic effect may only be necessary for precise positioning. The overall impact range calculation is less than 2 cm; therefore, it may be disregarded for most applications. The relativistic error was mainly caused by the gravitational field variation, which is known as general relativity, and special relativity related to the satellite velocity fluctuations, both causing satellite clock drifting.

The influence of general relativity causes clocks onboard satellites to run quicker as the satellites' altitude rises. The total impact reaches about 45 microseconds each day. Conversely, special relativity specifies that satellite clocks operate slower when the satellites travel with higher velocities and will operate faster while the satellites travel with slower velocities. This effect required additional correction of around 7 microseconds each day. The satellite's clocks are attuned to a slightly transmitted lower frequency of nominal frequencies on the ground before launching the satellites to ensure the satellite-transmitted nominal frequencies. It is important to note that the influence of relativistic effect varies slightly among different satellites, as it accounts for minor changes in the clock's rate with respect to changes in orbital eccentricity value.

This phenomenon is not only impacting the onboard satellite clock, but it is also affecting the GNSS signals. At the same time, it interacts with the earth's gravitational field, leading to a propagation delay known as the Shapiro signal delay, which signifies the amount of delay that electromagnetic signals experience as they pass through the earth’s gravitational fields. Accordingly, the relativistic corrections of the geometric range can be applied to the distorted Euclidean distance range caused by the gravitational field effects on space-time (Ashby, 2003).

2.4.11 Instrumental delay

The instrumental delays are caused by the GNSS signals generation process inside the satellites and simultaneously at the receiver side during tracking and receiving the signals. The GNSS signals pass through several devices, such as antennas, filters, frequency amplifiers, and cables.

It is worth highlighting that the receiver's instrumental delay is included in the receiver clock estimate. On the other hand, the satellite instrumental delay can be cancelled by utilizing the Iono-free combination or mitigated by using the related information in the broadcasted navigation message (Enge & Misra, 2011; Sanz Subirana, 2013).

2.4.12 Receiver clock jumps

Unlike expensive and accurate clocks used onboard GNSS satellites, the inexpensive clock is deployed in GNSS receivers. In order to mitigate the substantial clock, offset drifts encountered in GNSS receivers, a common strategy employed involves the periodic introduction of clock jumps. These clock adjustments manifest as integral multiples of milliseconds and uniformly impact all observable data. Consequently, they remain unnoticeable through the examination of geometry-free linear combinations. However, they are evident as visible cycle slips within carrier observations. In positioning methodologies reliant on undifferenced data, the impacts of receiver clock offsets do not cancel out, necessitating the obligatory correction of all clock events (Kim & Lee, 2012).

2.4.13 Satellites eclipse periods

In order to operate the GNSS satellites effectively, the orientation of satellite solar panels must remain perpendicular to the sun's direction to receive the required operational energy. At the same time, the satellite antenna must be directed toward the earth’s center mass. However, the GNSS satellites encounter eclipse periods when the earth, sun, and the satellite are at the same line. Accordingly, during this period, the earth's shadow impacted the satellite, leading to the orientation problem of both satellites’ solar panels and antennae. However, after the eclipse, the satellite implements small manoeuvres to well-orient solar panels and satellite antenna.

Consequently, a sudden variation of wind-up occurs. The eclipse duration and the amount of the phase wind-up error are varied and related to the satellite's orbital characteristics. For instance, GPS block II/IIA encountering eclipse period lasts 45-30 minutes, resulting in a 10 cm phase wind-up. High-accurate GNSS positioning approaches must be omitted from positioning calculations (Kuba, 2009). Figure 2.13 illustrates the satellite eclipse period.

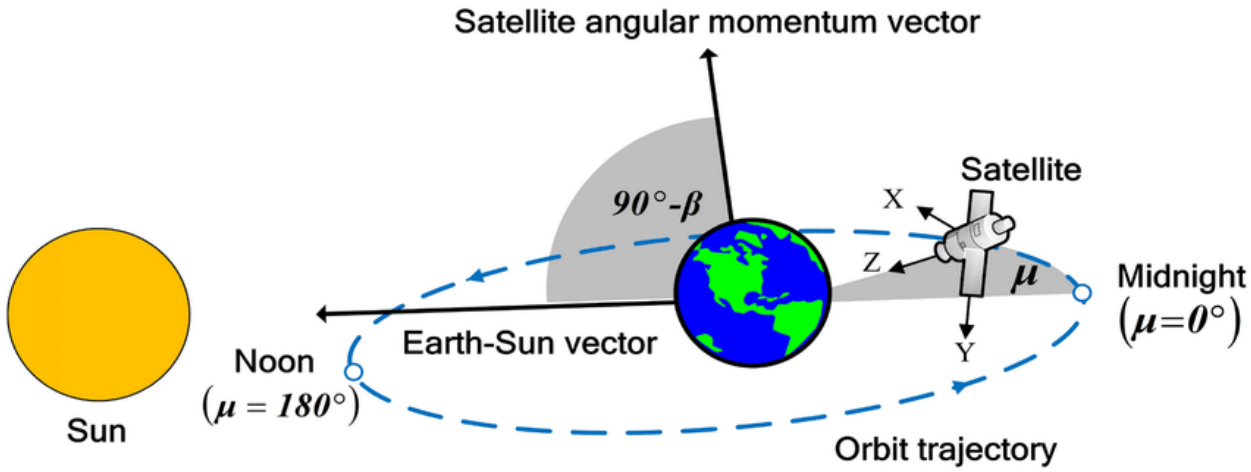

Figure 2.13 Satellite eclipse periods.

(Source: Liu et al., 2022).

2.4.14 Satellite problems

The GNSS broadcasting navigation messages contain satellite health indicators, which are used to eliminate unhealthy satellites from positioning calculations. Rarely few GNSS satellites encounter unrecorded manoeuvring or failure problems, which is not indicated in the navigation message. Consequently, the Center for Orbit Determination in Europe (CODE) is updated daily on the SAT_yyyy.CRX files recorded unusual satellite behaviours (Dach et al., 2015).

2.4.15 Additional GNSS error sources

The pre-mentioned GNSS error sources impact the GNSS positioning accuracy; this impact could vary from several centimetres up to tenths of meters during pseudorange and carrier range calculations. In addition to section two, error sources, it is worth highlighting that GNSS signals encountering additional errors such as radio interference, selective availability, signal spoofing,

and hacking could also be considered intentional error sources that impact the GNSS system's performance. Eventually, Table 2.5 summarizes the magnitude of several GNSS error sources.

Table 2.5 Magnitude of the different errors on GNSS ranges.

Error source	Magnitude (meter)
Orbit eccentricity	About 15
Space curvature	Less than 0.018
Shapiro delay	Less than 0.02
Phase wind-up	Less than 0.12
Ionospheric delay	Less than 100
Tropospheric delay	About 2.23
Troposphere curvature	Less than 0.03
GNSS satellite phase center offset	Less than 2.7
GNSS satellite phase center variation	Less than 0.01
GNSS receiver phase center offset	Less than 0.12
GNSS receiver phase center variation	Less than 0.02
GNSS satellite differential code bias	Less than 14
GNSS receiver differential code bias	Less than 2

2.5 International GNSS Services (IGS)

In 1992, the International GPS Services IGS began with a trial run. It officially started in 1994 (Beutler et al., 1999). In 2005, the IGS was renamed International GNSS Services. The IGS comprises around 512 GNSS stations and 350 worldwide agencies such as institutes, universities, and research centers from 118 different regions and countries. Figure 2.14 shows a map that describes how the IGS stations are distributed globally.

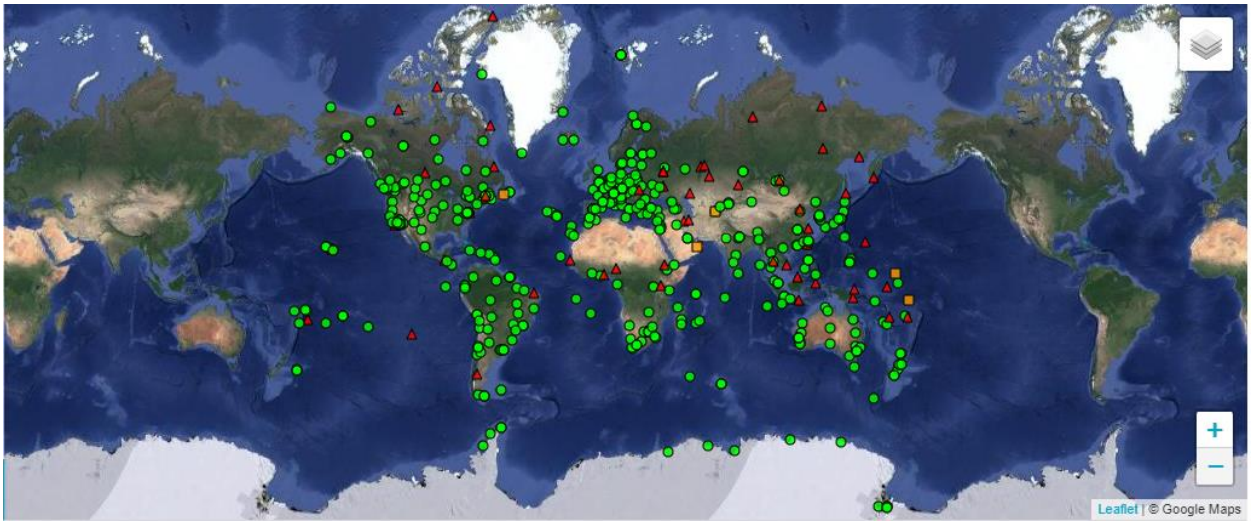

Figure 2.14 IGS Networks 2023 stations in 2023.

(Source: https://igs.org/network/#station-map-list).

IGS is in charge of offering top-notch GNSS information, products, and facilities, mainly to academic and non-commercial users. It provides different products for the navigation community, for instance, GNSS orbital and clock corrections, earth rotation corrections, and atmospheric data. Those products are vital for monitoring earthquakes and volcanic and crustal deformations. The organization is also involved with tropospheric and ionospheric mapping activities. The IGS, with predicted and final products and services, aids the realizations and the extensions of the International Terrestrial Frames (ITRFs).

The international service consists of different components: associate members, a governing board, a central bureau, data centers, analysis centers, an analysis center coordinator, associate analysis centers, working groups, an infrastructure committee, station-operating agencies, and contributing organizations. Figure 2.15 shows the structures of the IGS entities.

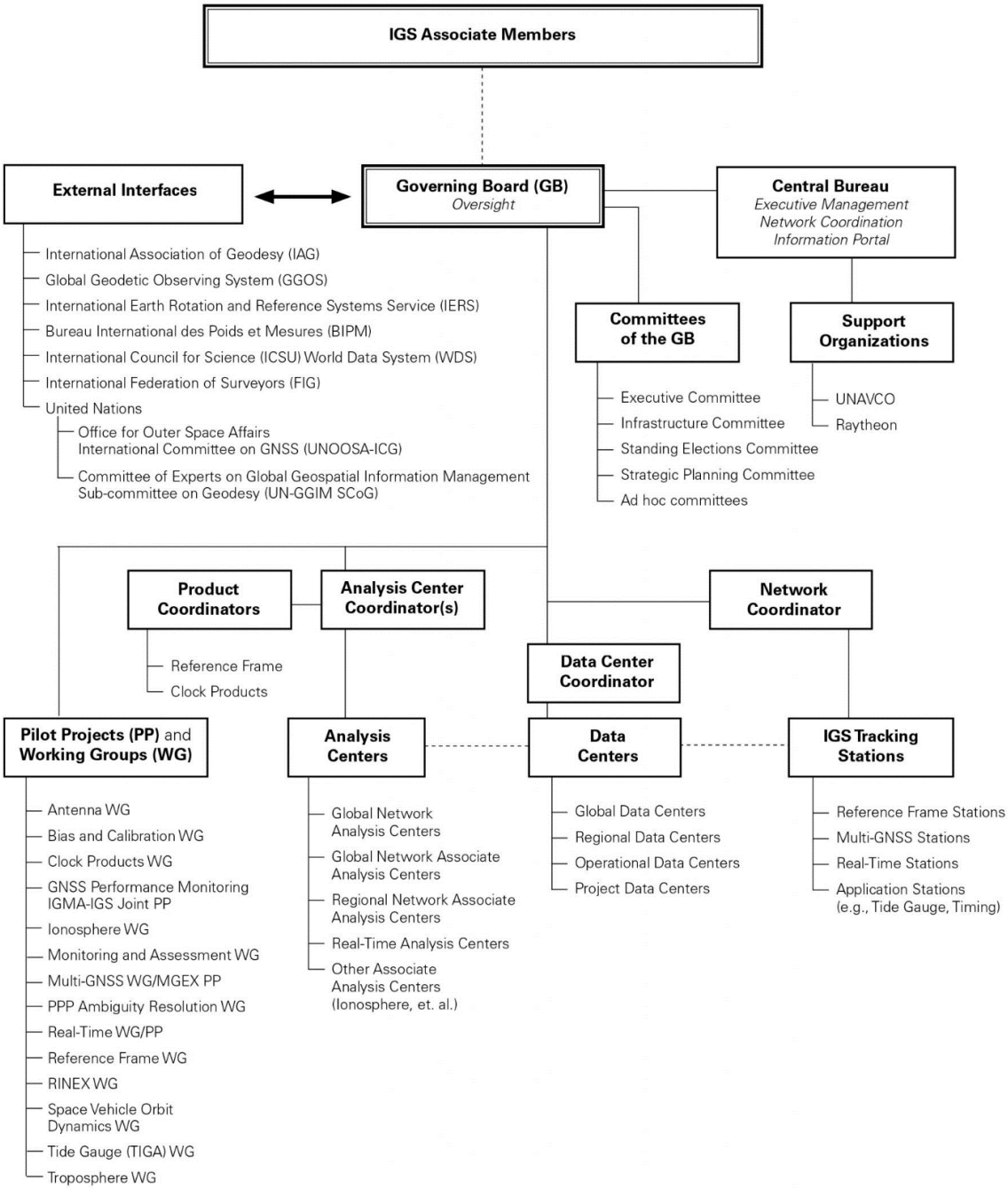

Figure 2.15 IGS structures.

(Source: https://igs.org/organization).

File access services allow users to download different navigation, observations, corrections, and precise satellite coordinates. The Real-Time Service (RTS) was officially launched in 2013; the RTS's main target is maintaining the global navigation GNSS permanent stations and disseminating real-time products (Caissy & Agrotis, 2011). Currently, various Analysis centers are involved in RTS (IGS, 2020). IGS provides various products like real-time clock products, orbital bias corrections, and ionospheric and tropospheric corrections in various latency periods. The main clock products that are offered on the IGS platform are shown in Table 2.6.

Table 2.6 Products from IGS Clock (IGS, 2020b).

Type	Accuracy(nanoseconds)	Latency	Updates	Sample Interval
Broadcast	~5 RMS ~2.5 SDev	real-time	--	Daily
Ultra-Rapid (predicted half)	~3 RMS ~1.5 SDev	real-time	at 03, 09, 15, 21 UTC	15 min
Ultra-Rapid (observed half)	~150 ps RMS ~50 ps SDev	3 - 9 hours	at 03, 09, 15, 21 UTC	15 min
Rapid	~75 ps RMS ~25 ps SDev	17 - 41 hours	at 17 UTC daily	5 min
Final	~75 ps RMS ~20 ps SDev	12 - 18 days	every Thursday	15 min Sat.: 30s Stn.: 5 min

The IGS provides orbital products as radial, cross, and long-track correction parameters. IGS also provides these products with the same latencies as clock products. Table 2.7 demonstrates those products regarding accuracy, latency, updating rates, and sampling intervals.

Table 2.7 IGS Orbit products (IGS, 2020b).

Type	Accuracy (cm)	Product Latency	Updating Time	Sample Interval (min)
Broadcast	Around 100	real-time	--	Daily
Ultra-Rapid (predicted half)	Around 5	real-time	03, 09, 15, 21 UTC	15
Ultra-Rapid (observed half)	Around 3	3 - 9 hours	03, 09, 15, 21 UTC	15
Rapid	Around 2.5	17 - 41 hours	17 UTC daily	15
Final	Around 2.5	12 - 18 days	every Thursday	15

IGS broadcasts real-time products over the Internet using Networked Transport of RTCM via Internet Protocol (NTRIP). The IGS analysis center combines corrections from diverse analysis centers. These products are disseminated using different streams. Currently, the IGS is replacing the old stream names. Table 2.8 shows the names of the current and previous streams. Additionally, the IGS broadcasts a real-time Global Ionospheric model through the IONO00IGS1 stream.

Table 2.8 IGS streams (The International GNSS Service, 2022).

Old stream name	Current stream name
IGS01/IGC01	SSRA01IGS1/SSRC01IGS1
IGS02/IGC02	SSRA02IGS1/SSRC02IGS1
IGS03/IGC03	SSRA03IGS1/SSRC03IGS1

2.5.1 IGS working groups

IGS has initiated several working groups to manage and complete its mission. These groups work in GNSS antennas, biases, GNSS receivers, satellite calibration, clock products improvement, ionospheric and tropospheric mitigations, GNSS monitoring, multi-GNSS experiments, PPP, reference frames, Rinex, vehicle orbit dynamic, and the tide gauge (IGS, 2022).

2.5.2 Main international GNSS Services analysis centers

2.5.2.1 IGS data center Wuhan University

The GNSS Research Center (GRC), founded in January 1998 at Wuhan University, is dedicated to a vital satellite location and navigating studies, cutting-edge technical applications, and further development. In order to address the demand for the establishment and applications of the BeiDou system, the benefits of well-built GNSS disciplines, personnel development, and international partnership at Wuhan University (WHU) present a substantial chance for GRC growth. Meanwhile, GRC will serve as a platform for examining and evolving novel GNSS system knowledge, practices, applications, and training capable individuals in this area. The goal of GRC is to become a pioneer center for GNSS research and innovation. Various centers, including the National Engineering Research Center for Satellite Navigation and Positioning, the Satellite

Navigation and Positioning Laboratory, the Lab for Navigation and Location-based Services, the Research Center for BeiDou, the Research Center for General Technology, the Center for Crust Movement Observation, and the analysis center of the IGS, are currently associates with GRC (Guo et al., 2016; Wuhan University, 2015).

2.5.2.2 Geodetic Observatory Pecny (GOP)

In the fields of earth's gravity observation, modelling, theoretical research, mathematical formulation of prospective theories, satellite altimetry, DORIS analyses (Štěpánek et al., 2017), GNSS observation, data administration, and analysis, GOP is an active IGS contributor supports several worldwide scientific services. These services include gravity and the international center of earth tides. It also participates in many national and international projects (Research Institute of Geodesy, 2012b).

GOP contributes to a range of GNSS in several fields, gathering and distributing accurate stations with high-accuracy GNSS data, creating plans and tools for accurate GNSS assessments, and creating software instruments for accurate GNSS data processing, quality control, and distribution (Dousa, 2010; Research Institute of Geodesy, 2012a).

2.5.2.3 Centre National d’Etudes Spatiales center

CNES/CLS are the abbreviations of Centre National d’Etudes Spatiales (CNES) and Collecte Localisation Satellites (CLS). In 2007, CNES/CLS began operating as a GNSS analysis center. Since then, groups from CNES and CLS have routinely processed GPS and GNSS data from a network of stations worldwide (Centre National d'Etudes Spatiales, 2017).

They calculate accurate GNSS orbits at the sub-centimeter level along with Earth rotation parameters and station locations. By May 20, 2010, CNES was formally admitted to the Europe's space agency. This is for the sake of expanding the influence of Europe's space abilities and guaranteeing that space investments continue to benefit both global and European populations. As a result, this technique raises the quality of CNES products (Centre National d’Etudes Spatiales, 2017; Katsigianni et al., 2019; Loyer et al., 2012).

2.5.2.4 European space agency

ESA was established as the European intergovernmental organization in 1975 with the signing of the ESA Accord. It had ten original member states. These ratified the ESA Convention by depositing their ratification instruments by 1980 after signing it in 1975. In 1975, ESA launched Cos-B, a space probe designed to track cosmic emissions (ESA, 1975)

ESA's goal is to influence the growth of Europe's space capabilities and ensure that the mass of European citizens continues to have an advantage from investments in space, in addition to developing several spatial projects for Europe. Currently, ESA has 22 members not only from Europe, but it also has cooperation agreements with other countries (Bonnet & Manno, 1994).

The European Space Operations Center (ESOC) is one of the most significant departments within the ESA, and it is situated in the German city of Darmstadt. ESOC handles activities involving satellites. European satellites are launched, tracked, communicated with, and maneuverer, among other things.

The ESA runs numerous European activities in satellite navigation, earth observation, telecommunication, space science, and transportation. ESA leads numerous European navigation programs. The European GNSS Evolution Program (EGEP), the European Geostationary Navigation Overlay Service (EGNOS), Galileo, and ESA's Navigation Innovation and Support Program are all Navigation-Related Research and Technology Initiatives (NAVISP) (Sanchez et al., 2008).

2.5.2.5 GNSS Science Support Centre (GSSC)

The GNSS Science Support Center aims to make the GNSS research activities available in Europe to improve GNSS implementations in the European infrastructure.

The main activities of the GSSC focus on the GNSS datasets and improve the scientific application by implementing the GNSS with Machine Learning, Big Data, and the Internet-of-thing (Navarro et al., 2019).GSSC is considered a pioneer center by establishing the ongoing GNSS IF Recording Station (GIFRES), which provides one petabyte daily for the GIFRES stations. Such a considerable amount of data could be considered a robust floor for establishing many Artificial Intelligence (AI)

and ML applications. In addition, GSSC is involved with many scientific domain disciplines such as earth science, Space science, Physics, and Metrology (ESA, 2022). GSSC cooperates with many organizations, including European Space Agency (ESA), International GNSS Service (IGS), Instituto Geográfico Nacional (IGN), Bundesamt für Kartographie und Geodäsie (BKG), International Laser Ranging Service (ILRS), Norwegian Mapping Authority (NMA), and Crustal Dynamics Data Information System (CDDIS). GSSC Thematic Exploitation Platform (GTEP) is considered one of the essential pillar services the GSSC provides. GTEP delivers online services, analysis, GNSS data uploading, and downloading.

2.5.2.6 German Research Centre for Geosciences (GFZ)

The Prussian Academy of Sciences was the source of inspiration for creating the National Research Institute for Earth Sciences (GFZ). The current GFZ form was introduced around the start of the 1990s in the previous Century. The research efforts of the GFZ are supported by the German Ministries of Education and Sciences (German Research Centre for Geosciences, 2020a).

In addition to the engineering sciences disciplines of rock mechanics, engineering hydrology, and seismology, which are closely coordinated within the center, GFZ is involved in numerous research scientific fields such as physics, mathematics, chemistry, and biology (German Research Centre for Geosciences, 2020a).

For example, Geodesy, Geophysics, Geochemistry, Geosystems, and Geoinformation all have numerous geo-departments inside GFZ. The GFZ goal title, "The future can only be guaranteed by people who comprehend the System Earth and its interactions with Man," inspired the establishment of all the departments above (German Research Centre for Geosciences, 2020b).

Due to its strong computing capabilities and high-quality output, the GFZ is regarded as one of the most significant IGS centers from the perspective of space navigation (Männel et al., 2020a, 2020b; Springer & Hugentobler, 2001). Similar to CNES, multiple ambiguity-fixing techniques are applied during the computational process (Uhlemann et al., 2010).

2.5.2.7 Center for Orbit Determination in Europe

The scientific faculty have created numerous research institutions at Bern University in Switzerland. By 1992, the Bern Astronomical Institute established the Center for Orbit Determination in Europe (CODE). The CODE was founded as a collaboration between the BKG, the Munich Institute of Astronomy and Geodesy, and the Swiss Federal Office of Topography (University of Bern, 2022).

CODE involves many research activities such as IGS MGEX, Regional Reference Frame Sub-Commission for Europe (EUREF) (Prange et al., 2015; Springer et al., 1997), permeant network, and data monitoring. In addition, CODE performs comparative analysis for GNSS and SLR data (Springer et al., 1997; Urschl et al., 2005).

Like other analysis centers, CODE offers and supports a variety of GNSS solutions. With the following topic in mind, many other products are produced on a regular basis, including orbits, earth rotation parameters, satellite and receiver clock corrections, station coordinates, troposphere, and ionosphere models. Like other analysis centers, CODE offers and supports a variety of GNSS solutions. With the following topic in mind, a variety of different products, including earth and orbital parameters, are regularly produced (Schaer, 1997; Schaer et al., 1996).

2.5.2.8 Jet propulsion laboratory

The Jet Propulsion Laboratory (JPL), National Aeronautics and Space Administration (NASA) field center, and research and development facility supported by the federal government is located in California, USA. JPL was established in the 1930s and is owned by NASA and run by the adjacent California Institute of Technology (Westwick, 2008). Although it also performs astronomy and Earth-orbit missions, the laboratory's primary duties are developing and managing planetary spacecraft. Moreover, it manages the Deep Space Network (Conway, 2015; Jet Propulsion Laboratory, 2020).

In addition, JPL conducts numerous earth science-related studies, including those on the atmosphere, the biosphere, wildfires, and natural disasters. JPL is also in charge of much research related to planetary sciences (Edberg et al., 2016; Jet Propulsion Laboratory, 2020).

2.5.2.9 Massachusetts institute of technology

The Department of Earth, Atmospheric, and Planetary Sciences at the Massachusetts Institute of Technology (MIT) supports researchers. Efforts include improving the capability, reliability, and programs for analysing GPS measurements primarily to study crustal deformation. MIT is currently constructing an IGS analysis center (Massachusetts Institute of Technology, 2022). More information regarding MIT IGS activities can be found on the website http://geoweb.mit.edu.

2.5.2.10 NOAA/National Geodetic Survey

The National Geodetic Survey (NGS) was established as the Survey of the Coast in 1807. NGS is part of the National Oceanic and Atmospheric Administration (NOAA).

In order to provide a uniform coordinate system that defines definitions of USA areas, NGS maintains and provides access to national reference systems. NGS is committed to working on various earth science-related topics, such as GNSS, geodesy, datum and transformation, remote sensing, and land surveying. Through Online Position User Services (OPUS), NGS enables highly accurate GNSS services (US Department of Commerce, 2022). In addition, it is involved in antenna calibration and Continuously Operating Reference Stations (CORS) (US Department of Commerce, 2019).

The CORS network, which NOAA runs, provides GNSS data to assist geophysical, meteorological, and three-dimensional locating applications nationwide.

The CORS network unites the efforts of hundreds of governmental, academic, and corporate institutions in a multi-purpose, multi-agency cooperative project. The radio stations are privately owned and run. Each agency provides NGS with its GNSS/GPS carrier phase, code range, and station metadata, which are examined and freely available.

NGS offers a variety of solutions to help various GNSS users and industries, including horizontal and vertical coordinate conversion (U.S. National Geodetic Survey, 2022), geodetic and GPS plugins and software distribution, level correction services, and horizontal time-dependent positioning (Roman et al., 2010).

2.5.2.11 Scripps Institution of Oceanography's Orbit and Permanent Array Center (SOPAC)

Since its inception in 1991, Services from SOPAC have been made available to a large client base, focusing on the analysis and archiving of precise GPS data/metadata and data products. The term SOPAC is now used to describe our research group, which employs geodetic and seismic data for various engineering, surveying, geodesy, and geophysics projects (Scripps Orbit and Permanent Array Center / California Spatial Reference Center, 2019).

In order to support ongoing research issues, SOPAC concentrates on evaluating high-accuracy GNSS, geodetic, and seismic observations. Monitoring crustal deformation, structural monitoring, and developing early warning systems for earthquake and tsunami events are the core study areas of SOPAC (Bock & Wdowinski, 2020; Golriz et al., 2021; Ruhl et al., 2019; Scripps Orbit and Permanent Array Center / California Spatial Reference Center; Watanabe et al., 2018).

Like NGS, SOPAC provides GNSS users with different service options such as coordinate transformation, GNSS standards, and monitoring tools like daily and weekly displacement time series analysis.

2.5.2.12 United States Naval Observatory (USNO)

USNO is considered one of the oldest scientific and military agencies in the US; its establishment goes back to 1830. UNSO produces many products related to the earth, astronomy, and timing. USNO, the prediction center, through rapid services, produces daily and weekly earth orientation parameters (United States Naval Observatory, 2020). In addition, USNO is responsible for announcing and introducing the leap second and Delta T. Accordingly; it maintains International Atomic Time (TAI) and Coordinated Universal Time (UTC) (Dick, 2011; Nelson et al., 2001).

2.5.2.13 Nevada Geodetic Laboratory (NGL)

NGL is a space geodesy research organization that uses GNSS to monitor Nevada's tectonic and geothermal activities, study global surface mass loading patterns, and address scientific concerns (The Nevada Geodetic Laboratory, 2022).

NGL is responsible for maintaining and producing GNSS products through the MAGNET GNSS Network. NGL supports different research areas in many fields, and from a geoscience point of view, they focus on land subsidence and uplifting, reference frames, and tectonic displacements (Kreemer et al., 2014; Overacker et al., 2022).

NGL initiates the mission of the Global Strain Rate Map (GSRM) project, which is to determine a globally self-consistent strain rate and velocity field model. This model provides essential input for seismic hazards at a global and regional scale (Nevada Geodetic Laboratory, 2017).

2.5.2.14 The Crustal Dynamics Data Information System (CDDIS)

Initially, CDDIS was intended to act as a central data archive for NASA's program. As a component of the larger NASA earth science creativity projects and for the space geodesy developments, its function has grown to provide continuous support to the community of space geodesy and geodynamics. With its foundation in 1982, It became a specialized data repository created exclusively for preserving and sharing datasets essential to space geodesy.

The CDDIS now primarily stores and shares data relating to GNSS systems, including GPS and GLONASS and other navigation systems, laser ranging, very long baseline interferometry and Doppler orbitography, and radio-positioning integrated by satellite (Noll, 2010).

2.5.3 The Multi-GNSS Experiment (MGEX)

IGS created MGEX to track, compile, and examine GNSS signals. BeiDou, Galileo, QZSS, and Navigation with Indian Constellation (NAVIC) are involved in MGEX activities besides adapting the GPS and GLONASS modernization. Analysis centers describe new satellites and signals, evaluate the efficiency of various pieces of equipment, and create GNSS processing software (International GNSS Services, 2022; Montenbruck et al., 2014). IGS will keep adding exact ephemeris data and biased information for all constellations. A global network of multi-GNSS stations was built and connected with pre-established reference stations operating on GPS and GLONASS systems. Orbit and clock products for most new constellations are routinely generated. MGEX networks are involved in many activities and improving the correction products; consequently, the network is involved in determining earth rotation and orbital parameters for

instance. Additionally, the MGEX network provides real-time/ post-processed products used in PPP (Guo et al., 2017; Lou et al., 2014; Xue et al., 2021).

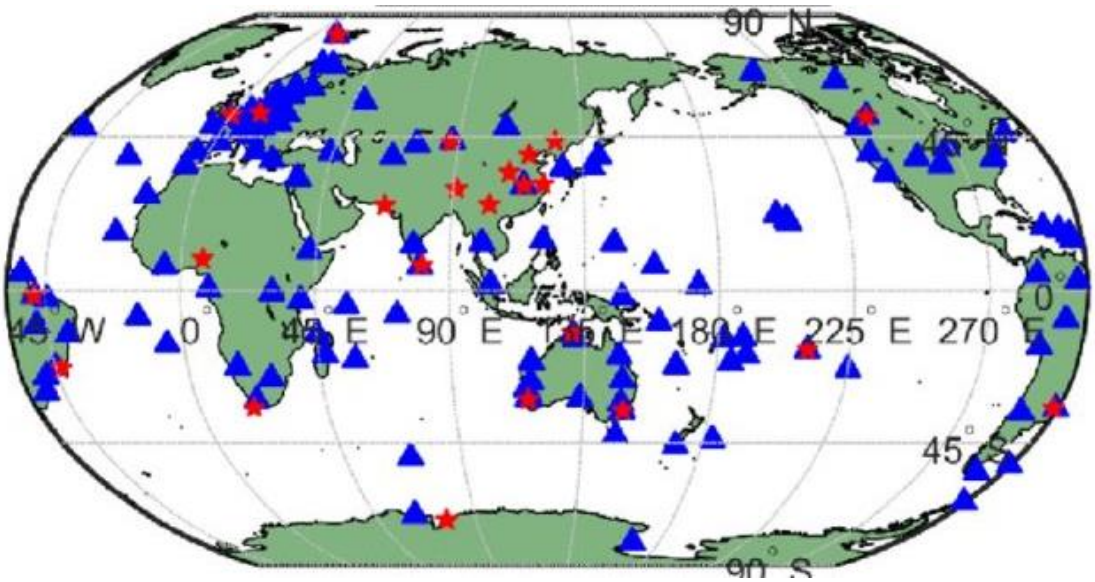

Figure 2.16 MGEX stations.

(Source:(Xue et al., 2021)).

2.6 Other regional and continental projects

2.6.1 The EUREF

The EUREF Permanent Network (EPN) is a continuously operating GNSS network in Europe. The EPN performs the daily EPN coordination to estimate positions and velocities for the GNSS stations. The alignment between the ETRF and ITRF is required to maintain the mm level of accuracy (Kenyeres et al., 2019) and to correct the definition of both regional and international frames. More information related to the ETRF and ITRF can be found in Chapter 2.2, Geodetic Reference Systems and Frames.

The EPN contains permanent GNSS stations working in different GNSS systems. EPN Data section and analysis center provides access to and analysis of the GNSS data. It provides post-processed and real-time GNSS products, products, and services related to the reference frame

(Royal Observatory of Belgium, 2021). Figure 2.17 shows the distribution of EPN; it is worth mentioning that some stations are located outside Europe.

Figure 2.17 EUREF stations.

(Source:(Bruyninx et al., 2019)).

2.6.2 European Plate Observing System (EPOS)

The EPOS is a diverse, dispersed research structure that allows the coordinated use of data, data tools, and facilities contributed by members of Europe's solid Earth science community. In order to develop new concepts and tools for precise, long-lasting, and sustainable answers to societal questions about geo-hazards and those geodynamic phenomena (including geo-resources) relevant to the environment and human welfare, EPOS brings together Earth researchers, national research infrastructures, technology experts, decision-makers, and the public. EPOS is involved in many research projects, especially for geo-hazard and earth source management. EPOS provides comprehensive services like seismology, GNSS services, geological modelling, and monitoring volcanic and Tsunami activities (European Plate Observing System, 2021).

2.6.3 Sirgas

The geodetic reference system for the Americas is called SIRGAS. Its realization in the Americas involves regional densification of the ITRF. In addition to the geometrical reference system, SIRGAS defines and implements a vertical reference system based on the geopotential field.

All scientific and practical efforts linked to accurate geo-referencing and navigation, Earth sciences studies, and multidisciplinary applications have been developed and combined with the appropriate backing from SIRGAS. In particular, SIRGAS provides the region's geospatial data infrastructure with its essential layer.

2.6.4 Asia-Pacific Reference Frame (APREF)

In sectors including mining, agriculture, and building, positioning technologies are being used more and more frequently. Additionally, there has been significant potential from asset managers, hazard modelers, and emergency services recently. These users' applications call for centimeter-level or superior geodetic infrastructure. The Asia-Pacific area needs a constant, continuously improved, and freely obtainable reference frame to deliver this. APREF provides many GNSS services like Australia Geoscience Online GNSS Processing Service (AUSPOS) with analyses of around 596 stations from different contributors. It is also involved in the geoscience antenna calibration group. Different agencies contribute to the APREF (Asia-Pacific Reference Frame, 2021).

2.6.5 The African Geodetic Reference Frame (AGRF)

The AGRF has been developed to offer accurate and reliable geospatial reference data for the African continent. It is a reference system for various geodetic and cartographic applications, such as land surveying, mapping, and navigation. The AGRF seeks to further knowledge of the morphology of the Earth, exact coordinate determination, and observation of continental crust motion and tectonic activity in Africa. A shared reference frame facilitates cross-national and intranational coordination of planning and development initiatives. The creation of the African Geodetic Reference Frame represents a substantial advancement in the precision and dependability of geospatial data throughout Africa. It is essential for advancing scientific research, infrastructural planning, and sustainable development on the African continent. It also improves Africa's capacity to participate in international geospatial projects and partnerships (Combrinck, 2008, 2010).

2.6.6 The North American Reference Frame (NAREF)

A geocentric reference system anchored to the stable region of the North American tectonic plate. Its main goal is to estimate positional coordinates and motion vectors for places located within the boundaries of the North American continent. Many applications, including geodesy, topographic surveying, navigational systems, and cartography, find widespread use for NAREF.

The public can freely use NAREF's dynamic solution through the IGS Service. NAREF is used by various organizations, including governmental organizations, academic institutions, and private businesses, to meet their unique geographic demands.

NAREF has essential improvements over earlier reference frames, particularly NAD83. Precision, stability, and broader worldwide applicability are areas where NAREF has advantages. Additionally, because the public has open access to data from Continuously Operating Reference Stations (CORS) within the framework, NAREF stands out as a more inclusive and accessible resource (Craymer et al., 2007; North American Reference Frame Densification, 2021).

2.6.7 Japanese Geodetic Datum 2011 (JGD2011)

The Japanese Geodetic Datum 2011 is Japan's current geodetic reference system. This geocentric reference system is aligned to the International Terrestrial Reference Frame. The crucial task of defining the positional coordinates and dynamic velocities of geographic points distributed across the breadth of the Japanese archipelago is taken up by JGD 2011. Its uses include geodesy, topographic surveying, navigational systems, and cartography, among many other disciplines.

The Geographical Survey Institute of Japan (GSI) is responsible for the creation of JGD2011, which was inspired by the seismic events of the 2011 Pacific Coast Tohoku Earthquake, which caused significant crustal deformation in Japan. JGD2011 was carefully developed to exceed the stability and accuracy standards set by Japan's previous geodetic reference systems. It was also planned to harmonize with other international reference frames (Geospatial Information Authority of Japan, 2021).

.

A comprehensive network of strategically placed CORS is essential to the operational definition of JGD2011. These stations' data are processed methodically to produce weekly coordinate solutions combined into a single JGD2011 solution.

Weekly changes are made to the JGD2011 framework, which is easily accessible to the general public on the GSI website. It is helpful for various businesses, including public and private sector firms and academic and research institutes.

Compared to earlier geodetic reference systems in Japan, such as the Tokyo Datum, JGD2011 has several benefits, including precision, stability, and seamless integration with international reference frames. Additionally, JGD2011 is a more inclusive resource due to the public's generous access to data from CORS stations (Geospatial Information Authority of Japan, 2021).

Chapter 3 Precise Point Positioning Technique

3.1 Introduction

Several ways of positioning and time synchronization have been used in GNSS positioning. Those methods vary in cost, complexity, and coverage area to provide accurate results both in post-process or RT solutions. Measurements can diverge with respect to achieved accuracy, integrity, continuity, and availability. Achieving affordable worldwide coverage and accurate RT positioning is a continuously demandable goal.

Single Point Positioning (SPP) is the autonomous GNSS positioning method. Due to the low accuracy of the broadcasted navigation information with respect to satellite ephemerids, satellite clock offsets, and other essential bias corrections, the accuracy achieved with SPP positioning is insufficient. In addition, utilizing the broadcasted ionospheric model is insufficient to mitigate the ionospheric error. Accordingly, SPP measurements could reach five meters as an accuracy level if the code has been used or around one meter if the carrier and/or pseudo-distance measurements are utilized (Pan et al., 2019). Such a level of accuracy could not meet the desired specifications for aviation, geodetics, or other high-accurate applications. Using a couple or a network of high-cost GNSS receivers in the relative positioning method could be a solution to reach a centimeter level of accuracy or more. Relative positioning could be implemented in several ways (Waldhauser & Ellsworth, 2000; Zhao et al., 2015; Zhong et al., 2010). Firstly, single differences where both carrier measurements from GNSS pairs are differentiated, resulting in eliminating satellite clocks biases and mitigating the rest of the common errors. Secondly, with the double differencing techniques, the clock bias for both receivers is eliminated, and mitigation for the rest of the errors. Finally, performing the triple differences requires observations from two different epochs, which means this technique cannot work in RT. The main advantage of triple differences is its ability to remove ambiguities; conversely, the main disadvantages are not RT and its sufferers from highly noisy correlated measurements (Zhao et al., 2015).

Three relative positioning methods are the most commonly used: RT positioning, Differential GNSS (DGNSS), Real-Time Kinematic (RTK), and Network RTK. DGNSS operates one of the couple receivers over a well-known (master) coordinates station. Consequently, the GNSS receiver

computes the biases and offsets which affect the master receiver. Those biases and offset corrections can drive the measurements at the rover side and correct its location.

These corrections can be used in different latency modes: the post-processing mode, where the measurements are stored and processed, or in RT, where the corrections are transmitted through Radio Technical Commission Maritime Service (RTCM) format to the rover through a radio link or over the mobile network. This last one is the RT Kinematic operational mode. The main weakness of using RTK is that positioning quality could be degraded remarkably if both receivers need to be operated within 20 km or more. Consequently, deploying more receivers is necessary to maintain a good quality of the corrections. Subsequently, covering vast areas required establishing a Network RTK (NRTK) of GNSS reference stations. NRTK can be implemented through many concepts such as Virtual Reference Station (VRS), Multi Reference Station (MRS), and Master Auxiliary Concept (MAC) (Brown et al., 2005; Fotopoulos & Cannon, 2001; Landau et al., 2002). More information regarding the concepts and the main differences between the aforementioned concepts can be found in (Janssen, 2009).

DGNSS dominated positioning until the late 1990s when NASA's JPL showed that PPP's precision might be similar to relative positioning (Zumberge et al., 1997) with the advantage that no reference stations at the user side are needed. Eventually, improving PPP could lead to considering it as an optimal positioning approach.

3.2 Precise point positioning

The PPP concept was presented by Zumberge et al. (1997), followed by Kouba and Héroux, (2001b), with a proposal of utilizing both IGS products and the undifferenced coding or pseudo distances and carrier phase measurements from dual frequency GNSS receivers. PPP uses external correction products and models for the error sources rather than relying on relative measurements between receivers.

Several considerations must be taken into account while using the PPP approach. The GNSS users must receive high-quality orbital and clock corrections products. Different ACs and IGS monitor and track a vast network of globally distributed GNSS receivers located on permanent stations to produce such products. Global GNSS networks use Networked Transport of RTCM through

Internet Protocol to calculate and distribute those adjustments (Weber et al., 2005). The first part of atmospheric error, which is a tropospheric error, could be mitigated using server models, for instance, the Mapping of Niell, Saastamoinen, and Hopfield (Niell, 1996; Sanz Subirana, 2013). Using ionosphere-free linear combinations of the code and phase observables is sufficient to eliminate 99% of the ionospheric error and to get a centimetre's level of accuracy (Zumberge et al., 1997). Corrections such as solid earth tides, satellite phase wind-up, GNSS receiver antenna center variation and offset polar motion, ocean and atmospheric loads are needed to improve PPP accuracy (Stürze et al.,2012 and 2016)

The real benefit of the PPP approach is that it does not require a local reference receiver or network of connected receivers. The PPP allows users to position themselves with a centimeter to decimetre accuracy in places impractical to utilize standard RTK and NRTK methods. The PPP method is independent of GNSS master or network stations; therefore, it can be considered an absolute positioning approach that can determine precise positioning and navigation in the ITRF, which makes it an ideal technique for deformation monitoring and EWS.

As part of an analysis of the current state of PPP accuracy, Gao and Shen, (2002), utilized GPS-PPP in kinematic mode, reaching a decimetre level of accuracy within two hours of convergence time. Similarly, Chen et al., (2004), showed that it was possible to determine the position of Bouy with a decimetre accuracy level. Bisnat, (2004), showed that GPS-PPP could enhance location determinations with a decimetre accuracy, aiding precise orbit determination operations. Jiang et al. (2015) proposed a simulated process for carrier phase observations to avoid cycle slip; the research showed that the accuracy of the GPS-PPP coordinates could achieve a centimeter accuracy level. Similarly, accurate results were achieved by the research done by Almeida et al., (2016). and Odijk et al., (2015), indicated that a few decimetres of coordinate accuracy are achievable after one hour. The same authors' work investigated the GPS-PPP performance in the Asian Pacific region (Bisnath, 2004; Chen et al., 2004; de Almeida et al., 2016; Jiang et al., 2015; Odijk et al., 2015; Shen & Gao, 2002).

A suggestion of adding more measurements and improving the positioning accuracy and convergence time of the PPP technique could be possible by merging various navigation systems (Bisnath & Gao, 2009a). Many GNSS approaches rely on GPS first positioning determination, and

the observations matrix can be improved by adding observations from other navigation systems. Accordingly, the research conducted by Nik and Petovello, (2010), demonstrates that the GLONASS constellation can be utilized as an augmented system to GPS in order to produce navigational solutions that are more dependable and accurate. Jokinen et al., (2011), showed that using GLONASS and GPS improves the station coordinates accuracy; a different study showed GLONASS with GPS decreased 3D errors by around 11% (Jokinen et al., 2013). Another study indicated that using multiple constellations is preferable in terms of improving the positioning performance and reducing the solution converging time rather than using a single constellation containing the same number of satellites (Miaoyan et al., 2008).

Compared to results produced using PPP GPS or GLONASS, Cai and Gao, (2013b), claimed that PPP GLONASS and GPS would greatly reduce the station coordinate error in each of the three components. The smaller number of GLONASS satellites, the poorer satellite geometry, the lower accuracy of GLONASS precise products, and the difficulty of resolving GLONASS ambiguities are cited as why the station coordinates error using PPP GLONASS is greater than the error using PPP GPS. The use of PPP GLONASS was also tested on 15 globally dispersed stations over the first three days in November 2011; Cai and Gao, (2013a), study revealed that PPP GLONASS could achieve an average accuracy of around 0.05 m in all coordinate components. However, their findings can be deemed inaccurate for PPP GPS and PPP GLONASS since they assumed that the receiver clock offset differed between GPS and GLONASS when it should have the same variation for the same receiver but with an offset concerning both constellations. Different studies showed that GLONASS would improve the geometry of the satellites above the GNSS user's sky. Jokinen et al. (2013) showed that GLONASS and GPS PPP combinations achieved a 32% average error reduction. So, combining GPS and GLONASS improved the station's accuracy (Anquela Julián et al., 2013; Cai et al., 2013).

Anquela Julián et al., (2013), asset combining GPS and GLONASS PPP observations with ESA orbital and clock products. They concluded that the accuracy of 3 mm, 5 mm, and 14 mm for the east, north, and up repetitively are available with 24-hour static positioning. However, a decimetre accuracy could be reachable after 1 hour. More fine accuracy resolution is achieved after 2 hours to reach 5 cm accuracy. These results are done for 2D positioning; for 3D positioning, the

convergence time reaches five hours to get a 5 cm accuracy. Zheng et al., (2022), Comparing GLONASS and GPS's performance, the GLONASS system shows good accuracy in higher latitude regions. The study provides this value because the GLONASS has a higher orbital inclination angle (Cai & Gao, 2013a; Zheng et al., 2022).

In 2012, it was a challenge to evaluate the GALILEO positioning performance with the availability limitations of the presence of 4 GALILEO satellites above the user sky. However, Langley et al. (2012) demonstrated that it is possible to achieve several decimetres of accuracy using PPP-GALILEO (Langley et al., 2012). A study of the availability to use RT-PPP with only the GALILEO system can be found (Tobías & Navarro, 2015). The study presented a 50 cm difference between computed and calibrated receiver positions (Tobías & Navarro, 2015).

PPP-GALILEO can reach a centimeter to decimetre accuracy level after the convergence period; the contribution of GALILEO can improve the average positioning accuracy by 27.70% for GPS+ GALILEO kinematic PPP compared with the GPS-only solution. 10.90% in all components for GPS + GLONASS + GALILEO PPP compared to GPS + GLONASS PPP. Adding GALILEO observations shortens the average convergence time for Multi-GNSS PPP solutions. (Xia et al., 2019).

The current number of GALILEO satellites is around 24, and the system is near reaching full operational capability (European Space Agency, 2022); around 5 to 6 are available for most locations covering the globe. It makes global positioning and time determination accurate (Kiliszek & Kroszczyński, 2020).

Lizhong et al., (2013), results showed that BeiDou static and kinematic PPP have centimeter-level precision. In static mode, BeiDou accuracy is greater than 1 cm horizontally and 3 cm vertically; in kinematic mode, it is 1 to 2 cm horizontally and 4–7 cm vertically. PPP BeiDou kinematics is better than PPP GPS for the chosen location (Zhao et al., 2013). Additionally, they found that PPP GPS and BeiDou have RMS values smaller than 1 cm horizontally and 3 to 4 cm vertically. Odijk et al., (2015), showed that PPP- BeiDou reached a few decimetres of coordinate accuracy after more than an hour; Odijk justified this long initialization time due to the poor geometry of BeiDou satellites in the study area. However, the study mentioned that reduced the initialization time to a half hour if both GPS and BeiDou are utilized in PPP acquisition (Odijk et al., 2015). Cheng et al.

(2020) investigated the BeiDou-PPP services in China, where the PPP- BeiDou reached 15 and 30 centimetric levels of accuracy with around 13 minutes of converging time. However, the study lacked a proper investigation or comparison regarding the initialization time improvement.

Regarding BeiDou-PPP, Luo et al., (2018), demonstrated that the accuracy of BeiDou-PPP under high ionospheric irregulating could reach around 1.80 meters. However, during normal ionospheric conditions, the study result showed that the BeiDou-PPP could reach around 15 centimetres (Luo et al., 2018). Similar findings were reported by the BeiDou performance comparison study among BeiDou-PPP, BeiDou-RTK, and with/without the aid of an inertial navigation system (Gao et al., 2017). A recent study investigated the performance of BeiDou-PPP with the advent of the third BeiDou satellite generation (Xu et al., 2022). Xu et al., (2022), demonstrate that the arrival of new BeiDou signals allows the implementation of PPP with triple and quadratic ionospheric combinations. Consequently, Xu et al., (2022), demonstrated that BeiDou's innovative combination accuracy outperforms regards the conventional Iono-free combination by 25% when applying the quadratic ionospheric combination, in addition to a 7% enhancement of accuracy performance when the triple ionospheric combination is utilized.

Initially, Tegedor et al., (2014), conducted a comprehensive PPP study and used MGEX data sets to analyse the accuracy and availability of quadratic constellations PPP solutions. They discovered that using GALILEO, GLONASS, BeiDou, and GPS satellite systems simultaneously improves the accuracy of PPP kinematic results. Under open sky situations, the accuracy improvement is relatively small compared to the PPP GLONASS and GPS; however, the benefit only became more noticeable under circumstances of reduced sky visibility. However, this study did not include any investigations regarding initialization time improvements utilizing quadratic constellations PPP solutions.

Li et al., (2015), analysed Multi-GNSS PPP improvements in satellite visibility, satellite geometry, position dilution of precision, converging time, accuracy, continuity, and dependability in restricted situations using 100 days of MGEX and BeiDou Experimental Tracking Network data (BETN). PPP GPS can approach millimetre precision after many hours of convergence, whereas PPP GLONASS is inferior, notably in the Up component. PPP GLONASS, GALILEO, GPS, and BeiDou improve station coordinates with average accuracy by roughly 31% compared to PPP GPS.

The same study employed similar PPP combination experiments, but this time in RT mode. They analysed around 120 stations using PPP GLONASS, GALILEO, GPS, and BeiDou and observed a 25% enhancement in station coordinate accuracy compared to PPP GPS. Wang et al., (2018), validated one month of Multi-GNSS RT-PPP data and concluded that the achieved 3D accuracy was 5 to 7 cm.

Liu et al., (2017), proposed a combined inter-system bias and GLONASS code inter-frequency biases model for Multi-GNSS PPP. A total of 32 stations of data from a single month in April 2015 were utilized to validate the combined proposed model.

Based on data from 90 MGEX tracking stations, we can determine how elevation masks affect the performance of Multi-GNSS kinematic PPP. Increasing the horizontal and vertical components' position accuracy during the first 10 minutes has little impact when the elevation mask is below 25 degrees. Nevertheless, after 15 minutes, the impact on the vertical component is visible. When the elevation mask is lower than 25 degrees, the PPP float solution can approach 5 cm and 10 cm for the horizontal or vertical components after convergence. The outcomes demonstrate that the Position Dilution of Precision (PDOP) rises as the elevation mask rises. In general, if the mask elevation for the PPP float solution is increased, the positioning accuracy and convergence speed will decrease (Wu et al., 2021).

According to Alcay and Turgut., (2021), evaluation of the RT-PPP method, the accuracy is better than 5 cm and 10 cm in both the horizontal and vertical directions. The reference coordinates acquired from 24 hours of static PPPs were compared with the calculated RT-PPP coordinates as an accuracy reference. A decimetre accuracy was achievable within a few minutes if the Multi-GNSS PPP is utilized with the aid of corrected Global Ionospheric Maps (GIMS) and tropospheric zenith delay information (Aggrey & Bisnath, 2019a). Li et al., (2021), have looked at the accuracy and convergence period of PPP. They discovered that the positioning accuracy for the horizontal and vertical components could exceed 20 cm after 30 min of convergence. Be more accurate than 10 cm for the horizontal component and 15 cm for the vertical component after 60 minutes, respectively Li et al. (2021).

With respect to achieved accuracy, Zhang et al., (2018a), obtained RMSE results of orbits for various RTS products, with a range variation from 3.8 cm to 7.5 cm. Clocks' average STDEs range

from 1.9 cm to 5.6 cm. It is worth mentioning that the pre-mentioned study did not investigate the nine RT streams concerning the Multi-GNSS. It focuses on GPS as not all streams support Multi-GNSS RT. Ogutcu et al., (2021), concluded that using the full operational capability of the BeiDou system enhanced the Multi-GNSS positioning with around 10% as an average for all coordinates components. Lv et al., (2022), investigated the RT-PPP accuracy level utilizing different frequencies and combinations from different BeiDou generations with the aid of GPS signals. The study findings demonstrated that a decimetre-level accuracy is achievable from different combinations; however, the best accuracy results were obtained with the third BeiDou satellite generation (Lv et al., 2022).

3.2.1 RT double differences approach versus RT-PPP approach

Bisnath and Gao., (2009), study is one of the first studies investigating the PPP techniques as an alternative to relative positioning through double differences. The study showed that both techniques could achieve decimetre accuracy in RT applications, where the accuracy of re-processed measurements could achieve a centimeter level or more (Bisnath & Gao, 2009b). The main advantage of double differences is that the prementioned accuracy can be achieved instantly when the ambiguity is resolved. However, fast converging time and maintaining accuracy are spatially correlated with the distance between the rover and the base receiver. Consequently, to maintain the double differences measurements and quality, operating in areas within 10-20 Km from the base or establishing GNSS networks is required. Accordingly, it raises both operational and establishment costs.

Tang et al., (2017), used a monitoring application's RT-PPP and double differences methods. According to the study's findings, frequency domain analysis for RT-PPP time series and double differences all showed similar results. The investigation revealed that for the RT-PPP and double differences coordinates evaluations, the RMS reached approximately 8 centimetres within five hours of observations (Tang et al., 2017).

Theoretically, PPP solutions could eliminate measurement biases and errors without differences in the measurements as they rely on precise correction products. This allows the use of the PPP

approach worldwide with the same accuracy as the double differences. However, the main disadvantages and limitations of PPP are described in section 3.5.

3.2.2 Linear observation model and mathematical model for precise point positioning

The dual frequency pseudo-range and carrier-phase observables are essential for this approach. The PPP model is a point positioning technique that needs precise satellite products and atmospheric models, among others.

PPP aims to determine the exact receiver coordinates (or as exact as possible), receiver clock, ZTD, and initial phase ambiguities for each GNSS satellite.

One of the most crucial elements determining the effectiveness of the PPP algorithm is the precision of the satellite clocks and orbits. The quantity and qualities of the measurements are another essential part that influences PPP outcomes.

The PPP linear observation relies on both code (or pseudoranges) and carrier observations, and it is required to construct the ionosphere-free combination for both measurements. Consequently, the ionospheric delay is mitigated. Equation 3.1 and 3.2 represents the carrier and code combinations (Gao et al., 2019; Liu et al., 2012; Wang & Rothacher, 2013).

$$\mathcal{P}_R^S = \rho_R^S + c * (dt_R - dt^S) + Tropo_R^S + \mathcal{M}_{Pc} + \varepsilon_{Pc} \quad (3.1)$$

$$\varphi_R^S = \rho_R^S + c * (dt_R - dt^S) + Tropo_R^S + \lambda_N * \omega_R^S + B_R^S + m_{\varphi c} + \varepsilon_{\varphi c} \quad (3.2)$$

Where:

$\mathcal{P}_R^S$: Indicates the combined unsmoothed code measurement between the GNSS satellite and receiver.

φ_R^S: Denotes the combined unsmoothed carrier measurement between the GNSS satellite and receiver.

ρ_{Rec}^{Sat}: Indicates the geometrical distance between the satellite antenna phase center and the GNSS receiver.

c: represents the speed of light.

$dt_R \; and \; dt^S$: Denote the receiver and satellite clock offsets to the standard GNSS time.

$Tropo_R^S$: Is the tropospheric delay caused by passing the GNSS signal through tropospheric layers.

$\mathcal{M}_{Pc}$: Represents the multipath error that affects the code measurements.

$m_{\varphi c}$: Is the multipath error affecting the carrier measurements.

$\lambda_N * \omega_R^S$: represents the wind-up effect of circular polarization of the GNSS signals. The relative orientation of the satellite and reception antennas, as well as the orientation of the line of sight, determine the Wind-up impact on phase measurements.

B_R^S: is the floated ionospheric-free ambiguity.

$\varepsilon_{Pc} \; and \; \varepsilon_{\varphi c}$: represent the remaining error involving the combined ionospheric combinations for code and carrier measurements.

Solving the previous equations is possible through linearization of them for the initial receiver location $(x_{R,intial}, y_{R,intial}, z_{R,intial})$

$$\mathcal{P}_R^S = \rho_R^S + \frac{x_{R,i}-x_S}{\rho_R^S} * \Delta x_R + \frac{y_{R,i}-y_S}{\rho_R^S} * \Delta y_R + \frac{z_{R,i}-z_S}{\rho_R^S} * \Delta z_R + c * (dt_R - dt^S) + Tropo_R^S + \mathcal{M}_{Pc} + \varepsilon_{Pc} \quad (3.3)$$

Where $\Delta x_R, \Delta y_R, \Delta z_R$ Represent the differences between the receiver's initial and actual locations. Additionally, $Tropo_R^S$ can be splitted in:

$$Tropo_R^S = Tropo_{R,i}^S + M_{Wet,R*}^S \Delta Tr_{Z,wet} \quad (3.4)$$

Where:

$Tropo_{R,i}^S$: is the troposphere nominal term containing dry and wet tropospheric components.

$M_{Wet,R}^S$: is the tropospheric mapping factor.

$\Delta Tr_{Z,wet}$: is a component parameter vector of the wet component.

The tropospheric effect is divided into dry and wet components, and several mapping functions are utilized to determine both magnitudes. However, the dry component can be well defined

theoretically, contrary to the wet components, where several parameters are utilized to determine its magnitude.

$$\mathcal{P}_R^S - \rho_R^S + cdt^S - Tropo_{R,i}^S = \frac{x_{R,i}-x_S}{\rho_R^S} * \Delta x_R + \frac{y_{R,i}-y_S}{\rho_R^S} * \Delta y_{Rec} + \frac{z_{R,i}-z_S}{\rho_R^S} * \Delta z_R + cdt_R + M_{Wet,R}^S \Delta Tr_{Z,wet} \quad (3.5)$$

The last equation can be constructed for the carrier measurements similarly. Additionally, the terms before on the right side of the equation are called Prefit-residuals. Accordingly, the Prefit-residuals equations can be constructed for all the tracked GNSS satellites as follows:

$$\mathcal{P}_R^{S_1} - \rho_R^{S_1} + cdt^{S_1} - Tropo_{R,i}^{S_1} = \frac{x_{R,i}-xx_{S1}}{\rho_R^{S1}} * \Delta x_{Rec} + \frac{y_{R,i}-y_{S_1}}{\rho_R^{S_1}} * \Delta y_R + \frac{z_{R,i}-z_{S_1}}{\rho_R^{S1}} * \Delta z_{R+} cdt_R + M_{Wet,Rec}^{S1} \Delta Tr_{Z,wet} \quad (3.6)$$

$$\varphi_R^{S1} - \rho_R^{S_1} + cdt^{S_1} - Tropo_{R,i}^{S_1} - \lambda_N \omega_R^{S_1} = \frac{x_{Rec,i}-x_{S_1}}{\rho_R^{S_1}} * \Delta x_R + \frac{y_{R,i}-y_{S_1}}{\rho_R^{S_1}} * \Delta y_R + \frac{z_{Ri}-z_{S_1}}{\rho_R^{S_1}} * \Delta z_{R+} cdt_R + M_{Wet,R}^{S_1} \Delta Tr_{Z,wet} + B_R^{S_1} \quad (3.7)$$

Suppose 1 to k satellites above the sky of the GNSS user for one epoch. Then, the representation of the design matrix is defined in this way:

$$\begin{vmatrix} Prefit(\mathcal{P}^{S1}) \\ Prefit(\varphi^{S1}) \\ \vdots \\ \vdots \\ \vdots \\ \vdots \\ \vdots \\ \vdots \\ Prefit(\mathcal{P}^{Sk}) \\ Prefit(\varphi^{Sk}) \end{vmatrix} = \begin{vmatrix} \frac{x_{R,i}-x_{S1}}{\rho_R^{S1}} & \frac{y_{R,i}-y_{S1}}{\rho_R^{S1}} & \frac{z_{R,i}-z_{S1}}{\rho_R^{S1}} & 1 & M_{Wet,R}^{S1} & 0 & \dots & 0 \\ \frac{x_{R,i}-x_{S1}}{\rho_R^{S1}} & \frac{y_{R,i}-y_{S1}}{\rho_R^{S1}} & \frac{z_{R,i}-z_{S1}}{\rho_R^{S1}} & 1 & M_{Wet,R}^{S1} & 1 & \dots & 0 \\ \vdots & \dots & \dots & \dots & \dots & \dots & \cdots & \vdots \\ \vdots & \dots & \dots & \dots & \dots & \dots & \cdots & \vdots \\ \frac{x_{R,i}-x_{Sk}}{\rho_R^{Sk}} & \frac{y_{R,i}-y_{Sk}}{\rho_R^{Sk}} & \frac{y_{R,i}-y_{Sk}}{\rho_R^{Sk}} & 1 & M_{Wet,R}^{Sk} & 0 & \dots & 0 \\ \frac{x_{R,i}-x_{Sk}}{\rho_R^{Sk}} & \frac{y_{R,i}-y_{Sk}}{\rho_R^{Sk}} & \frac{z_{R,i}-z_{Sk}}{\rho_R^{Sk}} & 1 & M_{Wet,R}^{Sk} & 0 & \dots & 1 \end{vmatrix} \begin{vmatrix} \Delta x_R \\ \Delta y_R \\ \Delta z_R \\ cdt_R \\ \Delta Tr_{Z,wet} \\ \vdots \\ \vdots \\ B_R^{S1} \\ \vdots \\ B_R^{Sk} \end{vmatrix}$$

The last unknowns in the above matrices can be solved using least squares techniques. Consequently, the initial approximations of the GNSS receiver location can be improved through multiple iterations until sufficient accuracy is reached. The following equation describes how the GNSS location state can improve.

$$(x_R, y_R, z_R) = \left(x_{R,intial}, y_{R,intial}, z_{R,intial}\right) + (\Delta x_R, \Delta y_R, \Delta z_R) \quad (3.8)$$

The Kalman filter resolves the PPP linear model (Sanz Subirana, 2013). The following consideration must be taken into account by utilizing the Kalman filter:

- When a cycle slips, **carrier phase ambiguities (BC)** are treated as fixed throughout continuous phase arcs and as white noise.
- **Wet tropospheric delay** (*Trz; wet*) is assumed to be a random walk process.
- **The receiver clock** (*cdt*) is considered to be a white-noise method.
- GNSS receiver coordinates

❖ The coordinates values are treated as constants for static measuring.

❖ The coordinates values are taken as white noise or a random walk process for kinematic measuring.

Like any other GNSS positioning method, satellite visibility has a vital constraint impact on PPP performance. Even the most accurate orbit and timing data are meaningless if the user cannot track satellite signals. The bias estimations of the floated ionospheric-free ambiguity $\widehat{\dot{B}_C}$ needs a transition period to fix the ambiguity; this is influenced by the satellite's geometry, model quality, and data noise until it reaches a converging solution. Using the comprehensive set of satellites from all the various systems will provide the greatest service possible. Accordingly, using the Multi-GNSS PPP will yield the best results.

The written linear equations for the PPP models in this section are well described in Kouba & Héroux, (2001b), Sanz Subirana, (2013), and Wang et al., (2018), for example.

3.2.3 Precise point positioning modelling components

In order to achieve sufficient PPP accuracy, it is required to improve the pre-mentioned linear model with extra modelling parameters, including parameters required to correct the satellite antenna phase center; similar parameters need correct the GNSS receiver with respect to the antenna reference point, phase wind-up, atmospheric parameters, and earth deformation effects.

3.2.3.1 Satellite antenna phase center

The broadcasted ephemeris information disseminated by the GNSS satellites refers to the APC; however, the precise orbit information transmitted through IGS and some ACs referred to the satellite MC. Consequently, the conversion between APC and MC is required. Subsequently, the eccentricity vector is used in the conversion process. The values of these vectors vary for satellite types and blocks. The IGS ANTEX files contain eccentricity vectors needed to perform such corrections. More illustrations regarding this type of error can be found in section 2.4.5 (Enge, 1994; Hofmann-Wellenhof et al., 2012; Kouba & Héroux, 2001b).

3.2.3.2 Receiver antenna phase center

This type of error is described in section 2.4.6. The GNSS receiver manufacturing provides users with precise values needed to correct the receiver APC. The APC varies with different frequency values; additionally, the satellite elevation angle plays a role in this variation. Consequently, the receiver's manufacturing industries and IGS ANTEX files offer different values to different GNSS signals (Enge, 1994; Hofmann-Wellenhof et al., 2012; Kouba & Héroux, 2001b).

3.2.3.3 Satellites wind-up effect

For accurate positioning, the wind-up error needed to be mitigated; this error is caused by satellite manoeuvrers that are performed to keep the solar panel in the direction of the sun—accordingly, this affects the carrier phase measurements. The wind-up affects all coordinate components (Enge, 1994; Hofmann-Wellenhof et al., 2012; Kouba & Héroux, 2001b).

3.2.3.4 Satellites and receiver delay

Such as several electronic devices, the GNSS receivers, and satellites showed instrumental delay. Antennas, cables, as well as the various implemented filters used in GNSS receivers or satellites are potential reasons for these delays. These lags also impact code and carrier observations. The receiver delay is absorbed with receiver clock bias; however, the PPP measurements implemented with an Iono-free combination eliminate the effect of the satellite delay. On the contrary, for a single-frequency receiver, the broadcasted navigation message contains the value of the total group delay (Subirana et al., 2011).

3.2.3.5 Cycle slip

The incidence of cycle slip is one of the faults in phase carrier measurement. The GNSS receiver must continue to count the proportion of the carrier cycle during the tracking time. When the fractional phase changes between 360 and 0 degrees, one cycle will be added to the initial cycle counts on each occasion (Wellenhof & Lichtenegg, 2001). The definition of a cycle slip is "a jump in the number of integer cycles" (NovAtel Inc, 2015).

These changes may happen depending on the local surroundings, such as nearby structures, electric lines, and leaves and branches. Cycle slip could be influenced by the receiver's physical manufacturing quality and software design (Wellenhof & Lichtenegg, 2001). If a satellite's cycle slip is detected in PPP observations, it is not resolved during computation; instead, a new column for this satellite is added to the system equations.

3.2.3.6 Earth deformation effects

Solid tides are caused by the shifting of the earth's surface and, as a result, by changes in the location of the coordinates brought on by the gravitational pull of other bodies, primarily the Sun and Moon. The spherical harmonics expansion can be used to express 2D displacements that are produced by solid tides (Krásná et al., 2013). The ocean loading and pole tides are two additional tides that might impact GNSS measurements; however, their negligible effect might be disregarded (Kouba & Héroux, 2001b).

3.3 Real-time precise satellite clock and orbital products and formats

3.3.1 Real-time precise satellite orbits and clocks

The orbital and clocks corrections are divided into three categories—the first concerns the number of radial, along-track, and cross-track corrections for the satellite's locations. The second correction category concerns the rate of correction for radial, along-track, and cross-track. The last category is used to solve the satellite clock biases. Those corrections can be expressed in the RTCM-SSR format as:

$$\Delta_{SSR}(t_0, IODE) = \left(\delta\mathcal{O}_r, \delta\mathcal{O}_a, \delta\mathcal{O}_c, \delta\dot{\mathcal{O}}_r, \delta\dot{\mathcal{O}}_a, \delta\dot{\mathcal{O}}_c, \mathcal{C}_0, \mathcal{C}_1, \mathcal{C}_2\right) \quad (3.9)$$

Where:

Δ_{SSR}: represents the state space representation for correcting the orbital positions of satellites and clocks.

$(t_0, IODE)$: indicate the relevant broadcast ephemeris that was used to determine the current orbital and clock corrections, which is, t_0. However, the IODE signifies the issue of data ephemeris.

$(\delta\mathcal{O}_r, \delta\mathcal{O}_a, \delta\mathcal{O}_c)$: are the radial, along-track, and cross-track adjustment components.

$(\delta\dot{\mathcal{O}}_r, \delta\dot{\mathcal{O}}_a, \delta\dot{\mathcal{O}}_c)$: are the radial, along-track, and cross-track correction rates.

$(\mathcal{C}_0, \mathcal{C}_1, \mathcal{C}_2)$: are the coefficients terms of the RT satellite clock adjustments.

The first step is to combine radial, along-track, and cross-track adjustment and rate components with respect to t.

$$\delta\mathcal{O}_t = \begin{vmatrix} \delta\mathcal{O}_r \\ \delta\mathcal{O}_a \\ \delta\mathcal{O}_c \end{vmatrix}_t = \begin{vmatrix} \delta\mathcal{O}_r \\ \delta\mathcal{O}_a \\ \delta\mathcal{O}_c \end{vmatrix}_{t_0} + \begin{bmatrix} \delta\dot{\mathcal{O}}_r \\ \delta\dot{\mathcal{O}}_a \\ \delta\dot{\mathcal{O}}_c \end{bmatrix}(t - t_0) \tag{3.10}$$

The second required step is to use the R matrix to compute the satellite's location corrections.

$$\delta Xt \equiv \begin{vmatrix} \delta x \\ \delta y \\ \delta z \end{vmatrix} = R \cdot \begin{vmatrix} \delta Or \\ \delta Oa \\ \delta Oc \end{vmatrix} \tag{3.11}$$

Where the R=[e_{radial} e_{along} e_{cross}], the orbital corrections by:

$e_{radial} = \frac{\dot{r}}{|\dot{r}|}$,$e_{along} = \frac{r \times \dot{r}}{|r \times \dot{r}|}$, and $e_{cross} = e_{radial} \times e_{along}$.

Where:

e_i: represents the radial, longitudinal, and cross components.

r: is the position vector as determined by the satellite's broadcast parameters.

$\dot{r}$: is derived from the broadcast satellite's characteristics as the velocity vector.

RTCM Committee, (2016), provides the transformation matrix R required to transform the pre-mentioned corrections to ECEF format.

The third required step is to adjust the broadcasted satellite locations as mentioned below:

$$\begin{bmatrix} X_P \\ Y_P \\ Z_P \end{bmatrix}_t = \begin{vmatrix} X_b \\ Y_b \\ Z_b \end{vmatrix}_t - \begin{vmatrix} \delta x \\ \delta y \\ \delta z \end{vmatrix}_t \tag{3.12}$$

Where: (X_P, Y_P, Z_P) indicates the precise corrected satellite coordinates, (X_b, Y_b, Z_b) represents the broadcasted satellite locations and $(\delta x, \delta y, \delta z)$ denotes the ECEF corrections.

The fourth step is a concern to correct the onboard satellite clock. Equation number 3.13 shows the required steps to implement the SSR corrections.

$$\delta \mathcal{C} = \mathcal{C}_0 + \mathcal{C}_1(t - t_0) + \mathcal{C}_2(t - t_0)^2 \tag{3.13}$$

$$t_p^{Sat} = t_b^{Sat} + \frac{\delta \mathcal{C}}{c} \tag{3.14}$$

The $(\mathcal{C}_0, \mathcal{C}_1, \mathcal{C}_2)$ coefficients terms are transmitted with SSR messages for each satellite, t_p^{Sat} indicates the precise corrected time, and t_b^{Sat} is the satellite broadcast time.

3.3.2 State Space Representation (SSR)

The Radio Technical Commission for Maritime Services (RTCM) Special Committee (SC) is a worldwide non-profit organization dedicated to science, profession, and education.

The SSR represents the GNSS error as a state vector. The main aim of the SSR is to develop an applicable format to transform the GNSS corrections and products for GNSS precise point positioning. Three milestones have been constructed, including developing the orbital and clock satellites' error and code biases, secondly, including the vertical ionospheric parameters, and the adaptation of the satellite's phase biases. Thirdly, it can provide tropospheric and slant ionospheric information (Wübbena, 2012). Both vertical ionospheric and phase biases are not included in the initial SSR messages.

Since 1994, IGS has ensured that high-quality, accessible GNSS data solutions are always available. These technologies enable applications in science, education, and the marketplace to use

them in a global reference frame. The IGS expands its capacity to provide a service for applications needing RT access to IGS solutions through RTS (IGS, 2020a).

Multi-GNSS items have been included since 1994; IGS has worked to ensure that there is always access to GNSS data products of the highest accessing rate. The IGS actually manages the Real-Time Service (RTS) as a public utility. Users are provided with complimentary or open access through membership.

Initially, the RTCM specification for RTCM-SSR was used to construct RTS correction streams (IGS, 2020b; Wübbena, 2012). The items are now made accessible in the IGS-SSR format regarding long lags in establishing this standard to meet the requirements beyond GPS and GLONASS. The items are distributed using the NTRIP protocol. RTS-corrected orbits are expressed in the ITRF 2014 reference frame. The most recent standards include quality indicators, correction messages for clocks, biases for transmitted code and phase, multi-GNSS orbits, and global ionospheric information. Soon, extensions will be planned to include satellite attitudes, phase center deviations, and shifts. Additionally, it is projected to enhance the current ionospheric models (IGS, 2020c, 2020b).

The last IGS SSR V1.0 format was released in October 2020 and is designed to support Multi-GNSS RT positioning. The primary message's ID is 4076, which includes several sub-messages. The table below shows the most recent sub-message version (Federal Agency for Cartography and Geodesy, 2022; IGS, 2020b).

Table 3.1 RT sub-messages including 4076 primary messages (Source: (IGS, 2020b)).

Sub Messages	GNSS	IGM Type Name
IM021	GPS	Orbit Correction
IM022	GPS	Clock Correction
IM023	GPS	Combined Orbit and Clock Correction
IM024	GPS	High-Rate Clock Correction
IM025	GPS	Code Bias
IM026	GPS	Phase Bias
IM027	GPS	URA
IM041	GLONASS	Orbit Correction
IM042	GLONASS	Clock Correction
IM043	GLONASS	Combined Orbit and Clock Correction
IM044	GLONASS	High-Rate Clock Correction

IM045	GLONASS	Code Bias
IM046	GLONASS	Phase Bias
IM047	GLONASS	URA
IM061	GALILEO	Orbit Correction
IM062	GALILEO	Clock Correction
IM063	GALILEO	Combined Orbit and Clock Correction
IM064	GALILEO	High-Rate Clock Correction
IM065	GALILEO	Code Bias
IM066	GALILEO	Phase Bias
IM067	GALILEO	URA
IM081	QZSS	Orbit Correction
IM082	QZSS	Clock Correction
IM083	QZSS	Combined Orbit and Clock Correction
IM084	QZSS	High-Rate Clock Correction
IM085	QZSS	Code Bias
IM086	QZSS	Phase Bias
IM087	QZSS	URA
IM101	BDS	Orbit Correction
IM102	BDS	Clock Correction
IM103	BDS	Combined Orbit and Clock Correction
IM104	BDS	High-Rate Clock Correction
IM105	BDS	Code Bias
IM106	BDS	Phase Bias
IM107	BDS	URA
IM121	SBAS	Orbit Correction
IM122	SBAS	Clock Correction
IM123	SBAS	Combined Orbit and Clock Correction
IM124	SBAS	High-Rate Clock Correction
IM125	SBAS	Code Bias
IM126	SBAS	Phase Bias
IM127	SBAS	URA
IM201	GNSS	SSR Ionosphere VTEC Spherical Harmonics

Note: The URA indicates the User Range Accuracy.

3.3.3 Current real-time state space representation products at IGS and analysis centers

Different SSR streams are produced by IGS and other Analysis Centers (ACs); the following table, (as of October 2023), shows some RT streams (Federal Agency for Cartography and Geodesy, 2022; IGS, 2020b).

Table 3.2 SSR streams

SSR Stream	Identifier	Supported System	Format	Software generator
BCEP00BKG0	Assisted-GNSS	GPS+GLO+GAL+BDS+ QZS+SBAS	RTCM 3.3	BNC
BCEP00GMV0	Assisted-GNSS	GPS+GLO+GAL+BDS+ QZS	RTCM 3.3	magicGNSS
BCEP01BKG0	Assisted-GNSS	GPS	RTCM 3.1	BNC
BCEP02BKG0	Assisted-GNSS	GLO	RTCM 3.1	BNC
BCEP03BKG0	Assisted-GNSS	GAL	RTCM 3.3	BNC
BCEP04BKG0	Assisted-GNSS	SBAS	RTCM 0.0	BNC
BCEP05BKG0	Assisted-GNSS	SBAS	RTCM 0.0	BNC
BCEP06BKG0	Assisted-GNSS	IRS	RTCM 0.0	BNC
BCEP07BKG0	Assisted-GNSS	SBAS	RTCM 0.0	BNC
IGC01	RTCM-SSR CoM	GPS	RTCM 3.1	RETINA
IGS01	RTCM-SSR APC	GPS	RTCM 3.1	RETINA
IGS02	BRDC_APC_ITRF	GPS+GLO+GAL	RTCM 3.1	BNC
IGS03	BRDC_APC_ITRF	GPS+GLO+GAL+BDS	RTCM 3.1	BNC
IONO00CAS1	IGS-SSR	GPS+GLO+GAL+BDS	RTCM 3.3	GPSNet
IONO00CNE1	IGS-SSR	GPS+GLO+GAL+BDS	RTCM 3.3	PPP-WIZARD
IONO00IGS1	IGS-SSR		RTCM 3.1	UPC-Software
IONO00UPC1	IGS-SSR		RTCM 3.1	UPC-Software
IONO01IGS0	RTCM-SSR		RTCM 0.0	BDSMART-IONO
IONO01IGS1	IGS-SSR		RTCM 3.1	BDSMART-IONO
OSBC00WHU0	RTCM-SSR CoM	GPS+GLO+GAL+BDS	RTCM 3.1	PANDA
OSBC00WHU1	IGS-SSR CoM	GPS+GAL+BDS	RTCM 3.1	PANDA

SIRGAS200001	RTCM-SSR APC SIRGAS2000	GPS+GLO+GAL	RTCM 3.1	BNC
SIRGAS200002	RTCM-SSR APC SIRGAS2000	GPS+GLO+GAL+BDS	RTCM 3.1	BNC
SSRA00BKG0	RTCM-SSR APC	GPS+GLO+GAL	RTCM 3.1	RETICLE
SSRA00BKG1	IGS-SSR APC	GPS+GLO+GAL	RTCM 3.1	RETICLE
SSRA00BKG1_DREF91	BRDC_APC_ITRF	GPS+GLO+GAL	RTCM 3.1	RETICLE
SSRA00CAS0	RTCM-SSR APC	GPS+GLO+GAL+BDS	RTCM 3.1	GPSNet
SSRA00CAS1	IGS-SSR APC	GPS+GLO+GAL+BDS+ QZS	RTCM 3.1	GPSNet
SSRA00CNE0	RTCM-SSR APC	GPS+GLO+GAL+BDS	RTCM 3.1	PPP-WIZARD
SSRA00CNE1	IGS-SSR APC	GPS+GLO+GAL+BDS	RTCM 3.1	PPP-WIZARD
SSRA00ESA0	RTCM-SSR APC	GPS	RTCM 3.1	RETINA
SSRA00ESA1	IGS-SSR APC	GPS	RTCM 3.1	RETINA
SSRA00GFZ0	RTCM-SSR APC	GPS+GLO+GAL+BDS	RTCM 3.1	EPOS-RT
SSRA00GFZ1	IGS-SSR APC	GPS+GLO+GAL+BDS	RTCM 3.1	EPOS-RT
SSRA00GMV0	RTCM-SSR APC	GPS+GLO+GAL+BDS	RTCM 3.1	magicGNSS
SSRA00GMV1	IGS-SSR APC	GPS+GLO+GAL+BDS	RTCM 3.1	magicGNSS
SSRA00NRC0	RTCM-SSR APC	GPS	RTCM 3.1	HPGNSSC
SSRA00SHA1	IGS-SSR APC	GPS+GLO+GAL	RTCM 3.1	none
SSRA00WHU0	RTCM-SSR APC	GPS+GLO+GAL+BDS	RTCM 3.1	PANDA
SSRA00WHU1	IGS-SSR APC	GPS+GLO+GAL+BDS	RTCM 3.1	PANDA
SSRA01CNE0	RTCM-SSR APC	GPS+GLO+GAL+BDS	RTCM 3.1	PPP-WIZARD
SSRA01ESA0	RTCM-SSR APC	GPS	RTCM 3.1	RETINA
SSRA01ESA1	IGS-SSR APC	GPS	RTCM 3.1	RETINA
SSRA01GFZ0	RTCM-SSR APC	GPS+GLO+GAL+BDS	RTCM 3.1	EPOS-RT
SSRA01GFZ1	IGS-SSR APC	GPS+GLO+GAL+BDS	RTCM 3.1	EPOS-RT

SSRA01IGS0	RTCM-SSR APC	GPS	RTCM 3.1	RETINA
SSRA01IGS1	IGS-SSR APC	GPS	RTCM 3.1	RETINA
SSRA02IGS0	RTCM-SSR APC	GPS+GLO+GAL	RTCM 3.1	BNC
SSRA02IGS1	IGS-SSR APC	GPS+GLO+GAL	RTCM 3.1	BNC
SSRA03IGS0	RTCM-SSR APC	GPS+GLO+GAL+BDS	RTCM 3.1	BNC
SSRA03IGS1	IGS-SSR APC	GPS+GLO+GAL+BDS	RTCM 3.1	BNC
SSRA11IGS0	RTCM-SSR APC	GPS	RTCM 3.1	RETINA
SSRA21IGS0	RTCM-SSR APC	GPS	RTCM 3.1	RETINA
SSRC00BKG0	RTCM-SSR CoM	GPS+GLO+GAL	RTCM 3.1	RETICLE
SSRC00BKG1	IGS-SSR CoM	GPS+GLO+GAL	RTCM 3.1	RETICLE
SSRC00CAS0	RTCM-SSR CoM	GPS+GLO+GAL+BDS+ QZS	RTCM 3.1	GPSNet
SSRC00CAS1	IGS-SSR CoM	GPS+GLO+GAL+BDS+ QZS	RTCM 3.1	GPSNet
SSRC00CNE0	RTCM-SSR CoM	GPS+GLO+GAL+BDS	RTCM 3.1	PPP-WIZARD
SSRC00CNE1	IGS-SSR CoM	GPS+GLO+GAL+BDS	RTCM 3.1	PPP-WIZARD
SSRC00ESA0	RTCM-SSR CoM	GPS	RTCM 3.1	RETINA
SSRC00ESA1	IGS-SSR CoM	GPS	RTCM 3.1	RETINA
SSRC00GFZ0	RTCM-SSR CoM	GPS+GLO+GAL+BDS	RTCM 3.1	EPOS-RT
SSRC00GFZ1	IGS-SSR CoM	GPS+GLO+GAL+BDS	RTCM 3.1	EPOS-RT
SSRC00GMV0	RTCM-SSR CoM	GPS+GLO+GAL+BDS	RTCM 3.1	magicGNSS
SSRC00GMV1	IGS-SSR CoM	GPS+GLO+GAL+BDS	RTCM 3.1	magicGNSS
SSRC00SHA1	IGS-SSR CoM	GPS+GLO+GAL	RTCM 3.1	none
SSRC00WHU0	RTCM-SSR CoM	GPS+GLO+GAL+BDS	RTCM 3.1	PANDA
SSRC00WHU1	IGS-SSR CoM	GPS+GLO+GAL+BDS	RTCM 3.1	PANDA
SSRC00WHU2	IGS-SSR CoM	GPS+GLO+GAL+BDS	RTCM 3.1	PANDA
SSRC01CNE0	RTCM-SSR CoM	GPS+GLO+GAL+BDS	RTCM 3.1	PPP-WIZARD
SSRC01ESA0	RTCM-SSR CoM	GPS	RTCM 3.1	RETINA
SSRC01ESA1	IGS-SSR CoM	GPS	RTCM 3.1	RETINA

SSRC01GFZ0	RTCM-SSR CoM	GPS+GLO+GAL+BDS	RTCM 3.1	EPOS-RT
SSRC01GFZ1	IGS-SSR CoM	GPS+GLO+GAL+BDS	RTCM 3.1	EPOS-RT
SSRC01IGS0	RTCM-SSR CoM	GPS	RTCM 3.1	RETINA
SSRC01IGS1	IGS-SSR CoM	GPS	RTCM 3.1	RETINA
SSRC01WHU0	RTCM-SSR CoM	GPS	RTCM 3.1	PANDA
SSRC02IGS0	RTCM-SSR CoM	GPS+GLO+GAL	RTCM 3.1	BNC
SSRC02IGS1	IGS-SSR CoM	GPS+GLO+GAL	RTCM 3.1	BNC
SSRC03IGS0	RTCM-SSR CoM	GPS+GLO+GAL+BDS	RTCM 3.1	BNC
SSRC03IGS1	IGS-SSR CoM	GPS+GLO+GAL+BDS	RTCM 3.1	BNC
SSRC11IGS0	RTCM-SSR CoM	GPS	RTCM 3.1	RETINA
SSRC21IGS0	RTCM-SSR CoM	GPS	RTCM 3.1	RETINA

All SSR streams have the prefix SSRC or SSRA for CoM orbits and APC orbits, respectively. The GPS, GLO, GAL, BDS, and QZS denote the Global Positioning System, GLONASS, GALILEO, BeiDou, and Quasi-Zenith Satellite System.

Several academic universities and centers are involved as stream producers, such as Shanghai Astronomical Observatory (SHAO), Bundesamt für Kartographie und Geodäsie (BKG), and European Space Agency's Space Operations Centre (ESA/ESOC)—the Chinese Academy of Sciences (CAS), Wuhan University. Finally, National Research Canada (NRCan), GFZ, GMV, and CNES are the Natural Resources Canada, Deutsches GeoForschungs Zentrum, Aerospace and Defence, and Centre National d'Etudes Spatiales, besides the official corrections produced by the international GNSS services (IGS).

Three IGS official RT orbital and clock corrections, IGS1, IGS2, and IGS3, were recently renamed to SSRA01IGS1, SSRA02IGS1, and SSRA03IGS1, respectively. The software used to construct the **SSRA01IGS1** Single-epoch combination solution was created by ESA/ESOC. This product's solution epochs are totally autonomous, allowing IGS to reach the total accuracy available at the outset of product development. Each AC solution's clocks are aligned by subtracting a standard offset calculated by processing CNES from all satellite clocks at each epoch. IGS provides two

forms of SSRA01IGS1 solution to accommodate the satellite mass and antenna phase center calculations. It is worth mentioning that this solution provides corrections to the GPS only.

SSRA02IGS1 is a Kalman filter composite generated by BKG's BNC program. Unlike SSRA01IGS1, this solution required several minutes to converge to the suitable accuracy. One of the arriving AC solutions is parsed for orbit data. ACs estimates of satellite clocks are utilized as pseudo-observations in the Kalman Filter correction method. Currently, the SSRA02IGS1 provides corrections for GPS, GLONASS, and Galileo satellites.

SSRA03IGS1 This is the same product that was initially known as IGS03/IGC03, an experimental combination product that used BKG's BNC software to calculate a Kalman filter combination of GPS and GLONASS corrections. Currently, this stream provides corrections to BeiDou and Galileo besides GPS and GLONASS.

Contrary to free PPP services, for instance, IGS or primary ACs, there are commercial PPP service providers, for example, Leica Geosystem, VERIPOS, Trimble RTX, TerraStar, StarFire, and OmniSTAR (Hexagon, 2022; Leica Geosystems, 2022; OmniSTAR services, 2022; TerraStar Correction Services, 2022; Trimble Positioning Services, 2022; VERIPOS, 2022). The PPP service providers use a system of ground reference stations to gather correction information for each satellite's various signals. Geostationary satellites transmit the adjustments computed using this data to the receivers of paying customers. Alternatively, it can be delivered to GNSS users through internet communications.

3.4 Current tools for real-time precise point positioning

Many GNSS commercial, scientific, and educational GNSS software packages are currently available. They provide many coordinates solutions through RTK, NRTK, VRS, and other services. However, limited software is capable of dealing with PPP and RT-PPP.

Different research centers and some universities provide open-access PPP and RT-PPP tools, some of which encounter maintenance and updating problems. This section provides a literature review regarding the RT-PPP tools. The performance of those tools is varied in accuracy and converging time terms (Alcay & Atiz, 2021; Atiz et al., 2021).

3.4.1 BNC

An open-source program called the BKG Ntrip Client (BNC) was created for several real-time GNSS applications. BNC also manages HTTP communication and transmits incoming GNSS output to a serial or Internet Protocol (IP) port. The BNC is distinguished from other software as it is executable with different operating systems. Additionally, the possibility of using operating systems such as Debian and Raspbian permits outdoor applications (Bundesamt für Kartographie und Geodäsie, 2022).

The BNC software performs many tasks such as navigation and observation conversions with formats such as Radio Technical Commission Maritime Service /Receiver Independent Exchange Format (RTCM/RINEX), storing correction SSR streams, RINEX editing, including splitting and concatenating for traditional RTK, and providing corrections from a close reference base station to a serially connected receiver. For PPP measurements, it is possible to work with both RT and post-processing modes within the software. Additionally, it is possible to evaluate different coming streams. Regarding the correction stream, the BNC combines broadcasted SSR corrections from many different ACs(Bundesamt für Kartographie und Geodäsie, 2022; Federal Agency for Cartography and Geodesy, 2022).

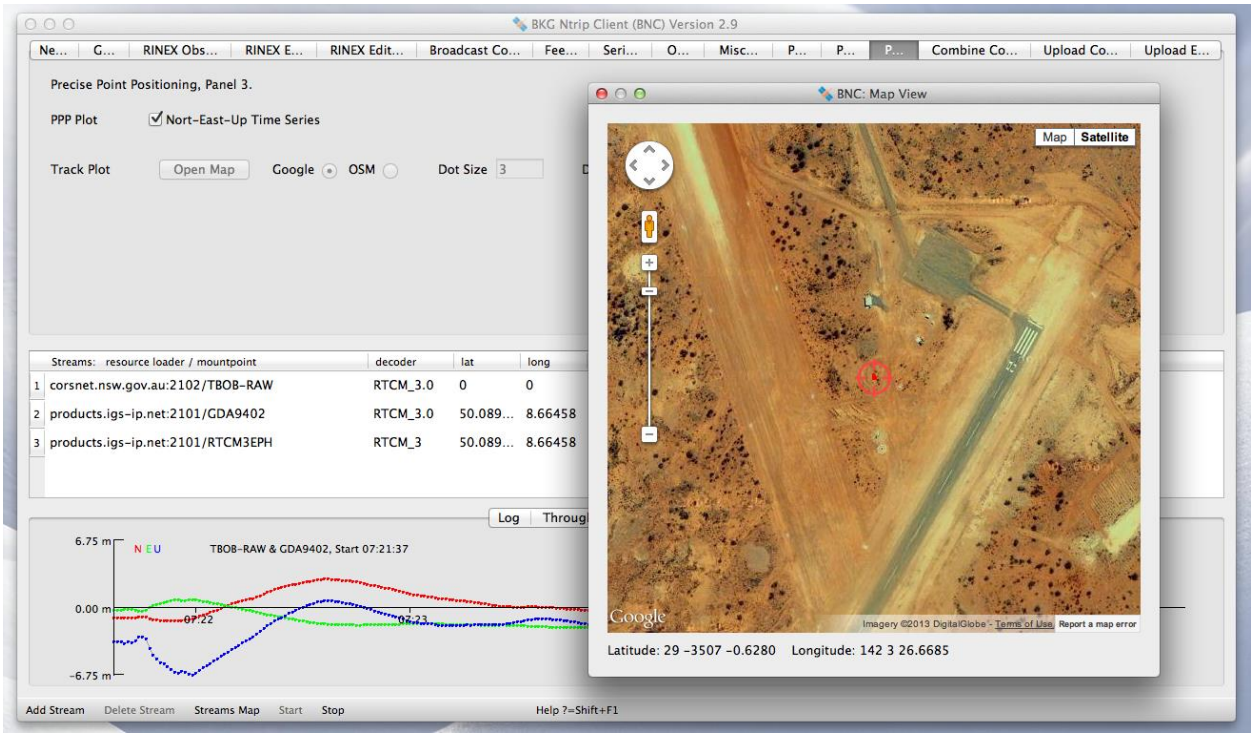

Figure 3.1 BNC interface.

(Source: (Bundesamt für Kartographie und Geodäsie, 2022)).

Many GNSS researchers have used the BNC software. It is involved in many applications, such as precise kinematic positioning, RT corrections evaluations, and monitoring applications (Alcay & Atiz, 2021; Charoenphon & Satirapod, 2022; Galera Monico et al., 2019; Qafisheh et al., 2022)

3.4.2 RTKLIB

The first RTKLIB release was created in 2006. It was initially formed by the Tokyo University of Marine Science and Technology mainly for educational purposes as open-source software. RTKLIB supports various GNSS features such as Multi-GNSS standard and precise positioning, RT-PPP, and post-process PPP. Additionally, it supports Hypertext Transfer Protocol /File Transfer Protocol (HTTP/FTP), local log files, serial, Internet Protocol/Transmission Control Protocol (IP/TCP), and NTRIP for external communication. Many GNSS investigators widely use the RTKLIB software. It is elaborate in many applications such as Driving simulations, smartphones, the safety of life, RTK, UAV, and RT corrections evaluations and monitoring applications

(Angrisano et al., 2020; Kaleev et al., 2021; Kaleev & Saburova, 2018; Lim et al., 2021; Takács et al., 2017).

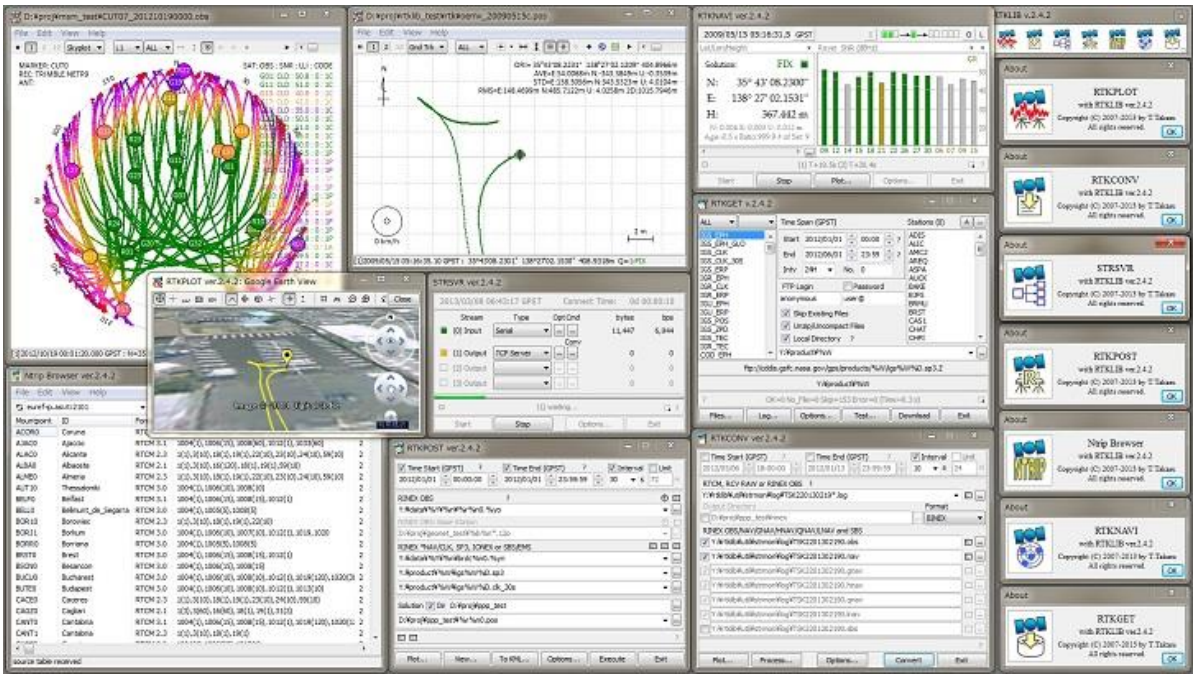

Figure 3.2 RTKLIB interface.

(Source: https://www.rtklib.com/rtklib.htm).

3.4.3 PPP-WIZARD

Unlike BNC and RTKLIB, the PPP-wizard is available to download on request. The CNES has created the software. The specific preference for using PPP-WIZARD over other software is the ability to perform the ambiguity resolution technique with zero differences. The benefits of this approach are that compared to the conventional PPP approaches, the precision is better than one order of magnitude. It is not specifically a local augmentation method, does not predict atmospheric variables, and requires a sparse station network. It is equivalent to that used for the GALILEO Commercial Service or that used in SBAS systems (Centre national d'études spatiales, 2022). The software involves many research activities, especially for solving ambiguities (Jokinen et al., 2013; Li et al., 2019).

3.4.4 gLAB

A software package called gLAB was created by the experts in astronomy and geomatics (gAGE) at the Universitat Politècnica de Catalunya (UPC). Additionally, the capability for various navigation constellations is incorporated, enabling the execution of some data analysis using Multi-GNSS data under the terms of an ESA agreement. It is a flexible, dynamic teaching tool for processing and analyzing GNSS data.

The tool enables both standalone GPS location and PPP by centimeter-level accurate modelling of GNSS positioning. This allows for the independent assessment of each error contributor, which has significant educational benefits. Various standard formats, including RINEX-3.00, SP3, ANTEX, and SINEX files, are supported by the software. Additionally, the capability for various navigation constellations is incorporated, enabling the execution of some data analysis using real Multi-GNSS data (Universitat Politecnica de Catalunya, 2021). The gLAB supports various research activities (Cahuasqui et al., 2022; Teresa Alonso et al., 2021; Universitat Politecnica de Catalunya, 2021).

3.4.5 GipsyX

As in the case of PPP-WIZARD, the GipsyX is available to download on request and uses the PPP processing technique. The earth tracking application groups at the JPL create and operate GipsyX. It replaces the old version of software GNSS-Inferred Positioning System and Orbit Analysis Simulation Software (GIPSY-OASIS); this software provides many solutions, such as Analysis of GNSS data, centimeter-level, accurate timing, and positioning using GNSS. This software is distinguished as it utilizes JPL's GPS orbit and clock components for single-receiver ambiguity resolution. It is involved in many applications and research activities. Unlike BNC, the GipsyX implements different composite models such as high-order earth gravity corrections, atmospheric drag, solid and ocean tide gravity fields, the third body effects from the Moon, Sun, and other planets, and solar radiation pressure (Bertiger et al., 2020; Jet Propulsion Laboratory, 2021).

3.4.6 GMV MAGIC-PPP

MAGIC-PPP is a global system that enables users of GNSS to identify their location or trajectory to within centimetres. It uses the latest version of GMV's PPP models, which are based on GNSS corrections, supports rapid convergence, and employs hybridization strategies with outside sensors for increased location consistency. The MAGIC-PPP provides many PPP services, which can be implemented by post-processing, web service, and PPP mail. The MAGIC-FAST feature is distinguishing as it significantly improves the converging time. Unlike BNC and RTKLIB, the MAGIC-PPP services are available to registered users (GMV Innovating Solutions S.L., 2022).

The MAGIC-PPP corrections streams and the solution services have been widely used in many scientific applications (Guo, 2015; Kirschenstein et al., 2018; Krasuski, 2017; Krasuski et al., 2018).

3.4.7 G-Nut/Geb

The main goal of the G-Nut software is to emphasize and encourage interdisciplinary exploitation of GNSS observations, which serve as the cornerstone of the G-Nut library and specialized user applications. According to its evaluations, the G-Nut project is currently in the testing phase. The fundamental data members and library functions have been put into place with the initial applications. Processing that can be done both offline and in RT has shown to have robust functionality. The software is a part of the project and has been operated by the Research Institute of Geodesy and Topography and Cartography and the Pecny Observatory in the Czech Republic (Geodetic Observatory Pecny, 2012; Research Institute of Geodesy, 2020). The G-Nut library is an open-source library that contributes to many research activities (Dousa & Vaclavovic, 2014; Vaclavovic et al., 2013). The software is distinguished as it provides several PPP approaches that can operate in real-time and post-processing modes.

3.4.8 Bernese tool

The Astronomical Institute at the University of Bern (AIUB) developed the scientific, high-precision, Multi-GNSS data processing package recognized as the Bernese GNSS Software. For its IGS and European (EUREF/EPN) actions, CODE uses it as an example. The software is continuously being developed and improved. The software package is operable in different operating systems (Bernese GNSS Software, 2022; Rolf Dach et al., 2015).

3.4.9 Other tools

Besides the pre-mentioned open-source software, packages, and libraries, some commercial software is involved in RT-PPP, such as RTNet and Trimble Business Center (TBC). Additionally, for post-process PPP measurement, there are available online position services like AUSPOS, OPUS, and CSRS-PPP (GPS Solutions, 2022; Jet Propulsion Laboratory, 2022; NGS, 2022; NRC, 2022; Trimble, 2022).

3.5 Current limitations of precise point positioning and real-time precise point positioning

3.5.1 Ambiguity resolutions

The described PPP model in section 3.2.2 includes $\widehat{\dot{B}_C}$ term, which describes the approximation of ambiguity bias. Due to the problem of ambiguity fixing in PPP, this approximation needs more time to converge to the right solution. The converging time depends on the quality of the PPP model, satellite geometry, and observational noises. The ambiguities in section 3.2.2 are treated as not integer numbers. This solution is called float ambiguity. Alternatively, it is possible to fix the ambiguity with some techniques. The number of wave cycles between the satellite and receiver could be treated as an integer value representing the integer number of the cycles in the transmission path; additionally, to the integer number, it is also possible to measure the cycle fractions. The high-quality GNSS receivers implemented with the phase carrier tracking units allow the receiver to count the cycle fractions.

$$B_{1,REC}^{Sat} = \lambda_1 N_{Rec,1}^{Sat} + b_{1,REC} + b_1^{Sat} \tag{3.14}$$

$N_{Rec,1}^{Sat}$: represents the integer number of cycles between the GNSS satellite and receiver corresponding to the signal L1; for instance, similarly, it is possible to write equations to other signals transmitted from the satellite, λ_1 represent the wavelength ($b_{1,REC}, b_1^{Sat}$) represent the cycle fraction in the receiver and satellite sides. The ambiguity-fixing procedures use the ambiguities in the integer structure to fix them correctly, speeding up convergence and resulting in excellent accuracy.

The fixing approach can be implemented in relative positioning through double differences in the measurements. The differences allow for eliminating the satellite and receiver cycle fractions. The zero differences are an absolute ambiguity fixing approach used in PPP-AR (PPP with ambiguity resolution).

Integer least-squares and integer bootstrapping are two popular methods for resolving integer ambiguities (Blewitt, 1989; Teunissen, 2001). The integer bootstrapping uses least-squares ambiguity cross-correlation adjustment, which is optimum in the sense of increasing the likelihood of proper ambiguity resolution and provides an exceptionally smooth execution of this approach (Teunissen, 2001). In any event, the case where the integer ambiguity resolution process fails must be taken into account since the incorrectly corrected ambiguities may result in significant distortions in the actual values. Because of this, ambiguity verification is a significant problem. Many tests might be applied to determine whether or not to adopt the integer solution (Brack, 2017; Wang et al., 2022; Yue et al., 2022).

Strategies for integer ambiguity correcting in PPP have been the topic of extensive research. They have greatly improved in recent years as the precision of satellite orbital and clock corrections enhanced to allow the use of PPP. These strategies include applying wide-lane and narrow-lane combinations. Additionally, some corrections streams currently contain satellite carrier phase biases (Geng et al., 2022).

The determination of the fractional cycle bias (FCB) and Integer Recovery Clock (IRC) enhances ambiguity-fixed. FCB and IRC are proposed by (Collins et al., 2010; Ge et al., 2008; Laurichesse et al., 2008). They highlighted that because a particular satellite pair's single-difference ambiguities originate from double-difference ambiguities that are close to integers, they must have an equal

fractional portion. Additionally, they demonstrated how FCBs could be predicted using single-difference observations from a network of reference stations and how the calculated FCBs could be utilized to completely eliminate the satellite FCBs in a PPP approach.

The evaluation of how Multi-GNSS affects GNSS PPP ambiguity can be found in Li et al. (2019), who have utilized the multi-frequency signals to allow a variety of combinations on different frequencies, which can improve the PPP performance in terms of ambiguity resolution. That study shows it can improve PPP accuracy and converging time of simulated GALILEO PPP data utilizing GPS + GALILEO + BeiDou constellations. This study supported the concept that employing the three systems together rather than individually would provide the best performance to resolve ambiguities (Nadarajah & Teunissen, 2013). Capilla et al. (2016) and Pan et al. (2017) showed that using Multi-GNSS PPP improves the PPP converging time.

3.5.2 Initialization period and noise of ionosphere-free combination

As part of an analysis of the current state of PPP converging time, different researchers applied various approaches to estimate PPP converging time. For instance, Martín et al., (2011), define it as the time required to reach centimeter accuracy; however, a level of decimetre was applied by (Bisnath & Gao, 2009a), and other researchers predefine the converging time (Zumberge et al., 1997). Kouba and Héroux, (2001), showed that two to three hours were required to reach centimeter accuracy. Reaching a sub-decimetre level of accuracy was achievable for kinematic PPP (Colombo et al., 2004) within 30 minutes or more. More or less, the same results were found (Héroux et al., 2004; Landau et al., 2009) with 90 minutes for converging time. Martín et al., (2011), deduced that there is no significant reduction in the converging time by using GLONASS and GPS with two two-hour converging periods to reach a centimeter level of accuracy. Martín et al., (2011), compared PPP results using GPS and GLONASS in combination with GPS-only observations. They concluded that there is no significant impact in reducing the convergence time. However, they recommended further investigation to examine the PPP performance, especially since the number of operational satellites will increase soon (Martín et al., (2011)). Xu et al., (2017), showed that combining BeiDou + GPS improved the converging time by 18.5% concerning only BeiDou-PPP. Additionally, the research showed significant improvement in the coordinate accuracy obtained by combining the pre-mentioned constellations (Xu et al., 2017).

Using Multi-GNSS PPP approaches can help to reduce convergence time. Afifi and El_Rabbany, (2016), investigated the effect of utilizing Multi-GNSS PPP on the initialization period. The study concluded by using combinations of BeiDou +GALILEO + GPS observation, enhancing the RT-PPP converging time by 25% (Afifi & El-Rabbany, 2016). Nadarajah et al., (2018), conclude that the converging time could be reduced to around half the period if the PPP was performed using GLONASS, GPS, and GALILEO instead of using GPS alone. Lou et al. (2016) found that the Multi-GNSS PPP enhanced the converging time by 60%. Similar results were confirmed using Multi-GNSS PPP AR (Aggrey & Bisnath, 2019b). A recent study shows that the improvement of converging time is possible using Multi navigation constellations; this research studies the effect of changing elevation angles with respect to Multi and alone navigation constellations (Zhao et al., 2020). Another Multi-GNSS PPP study showed that BeiDou with GPS + GLONASS significantly improved PPP performance in converging time and accuracy (Huang et al., 2016). Ogutcu et al., (2021), showed that BeiDou enhances the PPP converging period for GALILEO with 6%, GPS with 13%, and 10% for GLONASS. The study also examined the PPP initialization time concerning several cut-off angels (Ogutcu et al., 2021)

Hesselbarth and Wanninger, (2008), showed that a high-rate clock product could significantly reduce the converging time. Finally, the enhancement of the PPP converging time could be achieved by using precise ionospheric and tropospheric products (Li et al., 2016; Li et al., 2019; Shi & Gao, 2014; Zhao et al., 2020)

According to Su and Jin, (2018), the PPP method's average convergence time for the BeiDou, GPS, GLONASS, BDS+GPS, and Multi GNSS is 55.89 minutes, 25.88 minutes, 33.30 minutes, 20.50 minutes, and 15.71 minutes, respectively. Li and Pan, (2021), recently investigated PPP Multi-GNSS different product's performance and found in terms of RT-PPP converging time 8.7, 5.2, and 11.2 minutes for the components of the prementioned directions.

Zheng et al., (2022), confirmed that using GLONASS and GPS improves the converging time and the accuracy of estimation ZTD. Xia et al., (2022), proposed an RT model for ZTD that indicates a significant reduction in converging time, especially for up components.

3.5.3 Latency

The user uses the orbit and clock products at various latencies. The latency time can be defined as the delay produced in transmitting the products in the IGS or ACs. NTRIP is the protocol for integrating these solutions for IGS RTS Service and disseminating them online with RTCM SSR correction format. The amount of time needed for the computer system running the RT-PPP solution (Johnston et al., 2017), can also produce a delay component.

Hadas and Bosy, (2014), raised problems like latency or the switch from global to individual AC products that must be considered. The same authors demonstrated that combining official IGS products affected the latency values. Accordingly, the coordinate's availability and accuracy degraded (Martín et al., 2013; Qafisheh, 2020). Zhang et al. (2018a) showed that the latency is noticeable for RT products and is considered part of this research's availability. Pelc-Mieczkowska & Tomaszewski, (2020), evaluate the SSR corrections concerning the latency impact on the radial, along, and cross-track components. The researchers investigated the product's latency and found that for every three minutes, latency impacted orbital correction with 5 centimetres error for each component. However, the situation is worse for the latency in clock corrections; the same amount of error corresponds to one-minute latency. The research shows that all research stations' mean absolute coordinate residual error reaches 2.87m, 3.07m, and 5.75m for the north, east, and vertical. The low prices accuracy can be justified by the fact that Pelc-Mieczkowska & Tomaszewski, (2020), studied the latency impact for Single Point Position. On the contrary, Martín et al., (2013), found that the PPP positioning accuracy could be affected by 15 to 30 centimetres if the latency values were between 30 to 40 seconds.

Zhang et al., (2018), mentioned that the IGS combination products show 28 to 26 seconds of latency. On the other hand, the latency for individual AC products for instant CLK22 was 3 seconds. The research confirmed that the latency value affects both the availability and the accuracy of PPP measurements.

The same authors evaluated various RT products from IGS and other ACS. The study found the latency values for IGS01, IGS03, CLK22, CLK52, and CLK90 streams are 24-28, around 27, around 3, less than 10, and around 8 seconds, respectively. Similar results were found (Pelc-

Mieczkowska & Tomaszewski, 2020) with 8 seconds for CLK90 and IGS01 above 24 seconds. The latency values are not constant and vary concerning correction stream type and communication quality. The mean latency value of the IGS03 SSR is around 32 seconds (Qafisheh et al., 2020).

3.5.4 Availability and the quality of state space representation corrections

Another part of an analysis of the current state of PPP regards the quality and the availability of correction products. PPP service providers disseminate RTS, which provides access to precise real-time products used for RT applications. The quality and availability of those products can be found in Hadas and Bosy (2014). The analysis revealed that the GPS and GLONASS satellite systems have data availability rates above 92%. Additionally, it compared actual orbits and a clock to IGS final products. The investigation concluded that the 3D orbital precision of GPS and GLONASS is 48 mm and 84 mm, respectively, while the clock accuracy is 0.28 ns for GPS and 0.82 for GLONASS. However, research on products and standardization is still needed.

A more comprehensive and recent study related to the assessment of Muti-GNSS correction products was done by (Kazmierski et al., 2020). This study investigates CNES RT orbital and clock corrections. The most precise orbital products are available for GPS, according to studies. However, accurate atomic clock correction products recover systematic inaccuracies in GALILEO's orbits. Despite having high-quality orbits, the GLONASS satellites have inadequate clocks, which is the same as the Chinese BeiDou system. A similar evaluation for the same CNES product was investigated by (Kazmierski et al., 2018); the research comparison between CODE/ CNES products during one one-month, the 3D orbital RMS between the CODE and CNES for GPS, GLONASS, GALILEO, BeiDou MEO, and BeiDou IGSO was 5, 10, 18, 18, and 36 cm, correspondingly. BeiDou geostationary orbital errors are higher than one meter.

Guo et al., (2017), assessed and compared the quality of the precise products between different ACs. According to the findings, orbit evaluations for GALILEO, BeiDou MEOs, BeiDou IGSOs, and QZSS show similarities of roughly 0.1-0.25 m, 0.1-0.2 m, and 0.2-0.4 m, respectively. However, the BeiDou GEO orbits have the weakest alignments, with only a few meters of agreement. For clock evaluations, the results show that BeiDou IGSOs and MEOs have 0.15–0.8

ns, and QZSS from 0.4-0.8 ns, clock assessments of individual ACs have uniformity of 0.2–0.4 ns for GALILEO.

The findings demonstrate that the CNES and WHU analysis centers offer the most comprehensive and high-quality solutions. Qafisheh et al. (2022) investigated the assessments of Multi GNSSs' RT products, showing that, in general, they have better than 5 cm and 0.15 ns, respectively. GPS seems to have the highest orbit and clock accuracy. GALILEO, BeiDou-3, GLONASS, and BeiDou-2 are next in order (Li et al., 2022).

Additional recent research showed that the satellite orbit quality of CLK93 solutions is 4, 5, 12, and 16 cm used for GPS, GALILEO, GLONASS, and BDS, respectively, compared to the final accurate products of GFZ Multi-GNSS products. The RMS accuracy of GPS, GALILEO, GLONASS, and BeiDou, according to the CLK93 satellite clock, is 0.3, 0.4, 2.5, and 1.8 ns, respectively (Wang et al., 2020).

Regarding accuracy and availability, Zhang et al., (2018), have investigated nine RT products and found that the average availability is more than 99.3% for all RTS products except CLK70.

Comparison performance between ultra-rapid and RT correction products was investigated by Elsobeiey and Al-Harbi, (2016); the research showed a significant improvement in using RT correction products concerning ultra-rapid products.

Bahadur and Nohutcu, (2019), investigated the availability of orbital and clock correction products, and the orbital correction products availability is around 99.8%, 89%, 92%, and 87% for GPS, GLONASS, GALILEO, and BeiDou, respectively on the other hand, the availability of clock products is achieved roughly of 99.8%, 87%, 91% and 86% for GPS, GLONASS, GALILEO, and BeiDou respectively.

The elevation angle also influences the availability of PPP solutions, in other meaning. Wu et al. (2021) found that the best availability of PPP solution can exist if the elevation angle of satellites covers nearly 20 degrees, with 98% of PPP solution availability.

The solution continuity and availability are related to the availability of both clocks and orbital corrections. Qafisheh et al., (2022), investigated the availability of GPS and GLONASS clock correction through the years 2013,2014, 2015,2019, and 2021. They found that GPS clock products are more available rather than GLONASS.

3.5.5 The effect of tropospheric and ionospheric layers on the precise point positioning performance

The last part of the current state of PPP construction concerns atmospheric studies. The investigation's first component examines tropospheric research to comprehend its influence better. The Zenith Wet Delay (ZWD) and the Integrated Water Vapor (IWV) approximations are required. The Saastamoinen model instantly utilizes the station's altitude, latitude, and pressure data (Saastamoinen, 1972). With the aid of the temperature data, the ZWD was converted to IWV (Bevis et al., 1992). Hobiger et al., (2008), illustrated that improving the numerical weather model can enhance PPP accuracy. For example, Hadas et al., (2013), proved that utilizing the Saastamoinen model is insufficient for PPP applications, so they proposed using the regional tropospheric model.

Aggrey and Bisnath, (2019a), presented that GIMS and tropospheric zenith delay corrections significantly affect both convergence time and station accuracy. The research mentioned that the tropospheric delay highly influences the converging time in PPP. They investigated the impact of several tropospheric models and parameters; some showed that station accuracy could vary with values between 20% and 30% concerning weather conditions.

The positioning performance assessment study investigates tropospheric delay retrieval over a single day of observation. The observations are based on single-system PPP solutions using precise products from several IGS and MGEX ACs. The positioning results were evaluated using static and RT-PPP modes, while tropospheric delays were obtained using static PPP mode. This research evaluates positioning quality and tropospheric delay retrieval in a single day of observations using only one PPP solution and accurate products from several IGS and MGEX ACs. Whereas the tropospheric delays were acquired using the coordinate-fixed PPP method, the positioning

performance is analysed using the coordinate-static and coordinate-kinematic PPP modes (Zhou et al., 2019).

The online positioning services (Astudillo et al., 2018) showed good agreement in the estimation of ZTD between several PPP online processing providers.

The tropospheric corrections typically included the ZTD and the horizontal gradients calculated from relative positioning or PPP. The carrier phase residuals, however, can partially absorb the anticipated tropospheric delays. Consequently, reconstructing Slant Tropospheric Delay (STD) is necessary. Based on the repetitive investigations of Xiong et al. (2019), the proposed STD model could improve the 3D accuracy to 0.5 cm,1 cm, and 1.2 cm in the south, north, and up components (Xiong et al., 2019).

According to Su and Jin, (2018), Zenith Hydrostatic Delay (ZHD) is responsible for 90% of the overall delay Regarding the PPP solution. The study looked at how ZHD estimation could be improved by utilizing tropospheric models and actual meteorological data (Su & Jin, 2018). The findings indicate that by employing meteorological data for ZHD correction, various GNSS PPP solutions can attain positioning accuracy levels of several millimetres. Zheng et al. (2022) confirmed that using GLONASS and GPS improves the estimation accuracy of ZTD. The RT model for ZTD

has been established by (Xia et al., 2022). The established model showed better accuracy concerning the GNSS re-proceed solution with 1.44 centimetres. The wet delay, which results from rain, snow, or fog, could count for more than half of the delay, which the troposphere contributes to (Lehtola et al., 2022).

The accuracy of the hydrostatic and wet delays at an elevation angle of 4 degrees was significantly enhanced by adopting the second horizontal gradient order, compared to the traditional method, by almost 60% (Zhou et al., 2022).

Regarding the impact of the Ionosphere, the final section of the investigation into the state of PPP is concerned. The Ionospheric delay could be reduced using an Iono-free combination; however, doing so increases both observational noise and convergence time. The Iono-free combination is a restricted approach and could be utilized only for those receivers capable of tracking more than

one single frequency. Single-frequency users employ other elimination approaches, such as ionospheric models or worldwide ionospheric maps. The benefits of using the prementioned models on PPP single frequency measurements were investigated by (Cai et al., 2017; Gao et al., 2017; Ning et al., 2018). Creating regional Ionospheric models can shorten the PPP convergence period (Yao et al., 2013). The regional and global Ionospheric models can significantly reduce the convergence time and improve the coordinate accuracy. The constrained model showed that the accuracy with the first epoch could reach 40 and 20 centimetres, respectively, concerning the use of the global or regional Ionospheric model (Xiang et al., 2020). The same researchers confirmed a significant reduction to 7.5 minutes for the converging time. For these models, it is required to estimate the Total Electron Content (TEC), the overall quantity of electrons included on a radio signal's path between GNSS satellites and receivers. The forecasting of the TEC quantities could enhance the mapping of ionospheric models. Consequently, it could improve PPP measurements and GNSS observations in general (Maglambayan & Macalalad, 2022; Meyer et al., 2006; Muafiry et al., 2022; Rukundo, 2022).

Many researchers confirmed that the second-order Ionospheric models (Elsobeiey & El-Rabbany, 2011, 2012) as well as utilizing the Multi-GNSS PPP (Gao et al., 2017; Ning et al., 2018) could enhance PPP accuracy and converging time for GNSS users (Xiang et al., 2020).

Rapid Ionospheric oscillations, called scintillation, occur in different regions of our atmosphere. Consequently, it affects the TEC, which consequently affects the PPP measurements with respect to achieved accuracy, reliability, availability, and converging time. Zhang et al., (2014), minimize positioning errors as there are ionospheric perturbations. The findings demonstrate that the enhanced method may avoid needless refusal or re-initialization and can reduce the utilization of phase ambiguities without compromising the precision and dependability of the PPP solution. Numerous researchers looked into how ionosphere scintillations impacted GPS measurement (Dal'Cól et al., 2022; Doherty et al., 2003; Gwal et al., 2022; van Dierendonck & Hua, 2001; Zhang et al., 2014). This research also extended to cover the scintillations on other navigation satellites systems (Dal'Cól et al., 2022; de Oliveira Moraes et al., 2018; de Souza et al., 2022; C. Li et al., 2022; Luo et al., 2018; Vasylyev et al., 2022; Yang & Morton, 2020).

Liu et al., (2021), examined the effectiveness of the worldwide Vertical Total Electron Content (VTEC) provided by the entire Real-Time Global Ionospheric Map (RT-GIM). The study concluded that the RT-GIM model from UPC has similar accuracy to post-processed GIM. The IGS RT-GIMs show evident applications for RT services, such as transmission error adjustment parameters for radio signals, space weather monitoring, and global natural hazard detection.

Chapter 4 Early Warning System

4.1 Introduction

The global population is significantly increasing, which leads to substantial urban expansion, including high demand for building skyscrapers, dams, megastructures, cities, and offshores. In certain areas, those structures are exposed to environmental conditions such as wind load, landslides, ground subsidence, earthquakes, and tsunamis in certain areas. Therefore, such hazardous events could lead to massive destruction, which leads to structural failures, death tolls, injuries, and infrastructure loss.

Saving lives, avoiding economic losses, and preventing structural failures are possible by monitoring these hazardous phenomena through the ground or spatial movement. EWSs are essential to prevent economic and human losses. An EWS is defined as "an integrated system of hazard monitoring, forecasting and prediction, disaster risk assessment, communication and preparedness activities systems, and processes that enable individuals, communities, governments, businesses, and others to take timely action to reduce disaster risks in advance of hazardous events" (United Nations & UN-SPIDER Knowledge Portal, 2021).

According to the United Nations Office for Disaster Risk Reduction (UNDRR) (United Nations & UN-SPIDER Knowledge Portal, 2021), EWSs could be categorized according to the hazard type. Consequently, EWSs realized geological risks like landslides, earthquakes, volcanoes, and tsunamis, including extreme weather events, such as flash floods, droughts, hurricanes, extreme heat and cold weather waves, wildfires, health and biological hazards, and crop and livestock illnesses. Accordingly, the UNDRR and the World Metrological Organization founded in 2015 the International Network for Multi-Hazard Early Warning Systems (IN-MHEWS), (World Metrological Organization, 2018).

4.2 The changing shape of the earth: natural land deformation

A variety of natural events, such as earthquakes, landslides, volcanic and glacial movements, and tectonic plate movements, cause land deformations. Natural land deformations can potentially have far-reaching consequences on the environment and the earth's inhabitants. The consequences arising from natural land deformation encompass both human casualties and economic repercussions. Understanding Earth's long-term changes and anticipating potential threats, both of which can be aided by research into natural land deformation, is of paramount importance. Several techniques like surveying, remote sensing, navigation, and geodesy could be used to investigate natural ground deformation patterns. These techniques enable gathering and examining vital information that improves our knowledge of the Earth's dynamic processes and allows us to predict potential geological dangers. The subsequent section of this chapter provides a concise overview of the prominent natural land deformation occurrences of utmost significance.

4.2.1 Earthquakes activities

Our planet Earth's structures contain various layers; mechanical, physical, and chemical properties vary concerning each layer. The seismic wave is used to define layer boundaries. The earth's layers differ by density, temperature, and seismic wave speeds. A Low-Velocity Zone (LVZ) is formed when a seismic wave experiences more impedance when interacting with the rocky melting materials, which decreases its traveling speed. Understanding the asthenosphere is crucial for scientists as it acts as a soft substratum on which the rigid lithosphere floats. The lithospheric plates are subjected to heat conventions, which result in the movements of tectonic plates. The movement directions lead to constructing converging or diverging margins. The plate tectonic theory was introduced by Alfred Wegener (Coltice et al., 2019; Hallam, 1975). Alfred introduces the thermal convection current mechanism.

Figure 4.1 illustrates the movement directions of adjacent plates due to convection currents. The thermal convection mechanism led to the form of a subduction zone where adjacent plates converge. On the contrary, the Mid-oceanic ridge formed due to the divergent movements. Figure 4.1 A right and left strike-slip are presented in A and B, and C presents an oblique-slip case. However, S and E show a Dip-slip situation.

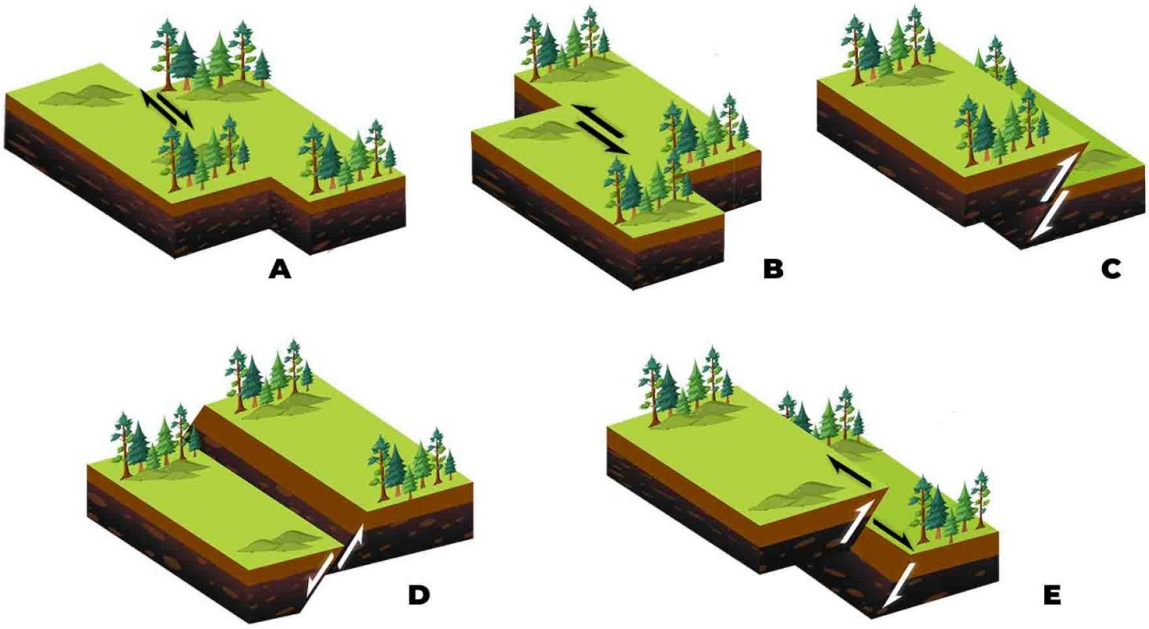

Figure 4.1 Faulting mechanism types.

(Prepared by the author).

The earthquake hypo-center is located at the weakest point along the tectonic plate boundary. Plate tectonics collisions are responsible for forming deformation activities such as earthquakes, volcanic eruptions, and tsunamis (Gunawardana, 2016; Sucuoğlu et al., 2014). This action released energy from the earthquake hypo-center, forming seismic waves.

Regarding traveling speed, magnitude, and direction, seismic waves are classified into four types: Primary wave (P-wave), Surface wave (S-wave), Love wave, and Rayleigh wave. The seismic wave speed variations are related to the density of rock materials (Er et al., 2010). In order to explain how the surface interacts with seismic waves, the terms Peak Ground Velocity (PGV), Peak Ground Acceleration (PGA), and Peak Ground Displacements (PGD) have been utilized. PGV displays the velocity of an earthquake's shaking at a specific location on the ground. The peak ground velocity is the maximum rate of shaking ever observed at a particular location during

an earthquake. However, PGA is the change in acceleration or velocity for a unit of time. The PGD also demonstrates the peak extent to which the earthquake altered the locations of surface points (EBI Consulting, 2022; Masi et al., 2011; Sucuoğlu et al., 2014). Table 4.1 shows different recorded parameters regarding the well-known El Centro 1940, Northridge 1994, and Tangshan 1976 earthquakes (Liu et al., 2016; Malhotra, 2003).

Table 4.1 Extremes earthquakes recorded.

Earthquake name	Magnitude (Mw)	PGA (m/s2)	PGV (m/s)	PGD (m)
El Centro	6.9	3.417	0.373	0.403
Northridge	6.7	0.568	0.515	0.0847
Tangshan	7.6	1.458	0.41	0.533

Figure 4.2 illustrates different types of seismic waves with respect to the direction of the wave and surface oscillations. A, B, C, and D represent earthquake P, Love, S, and Rayleigh waves, respectively.

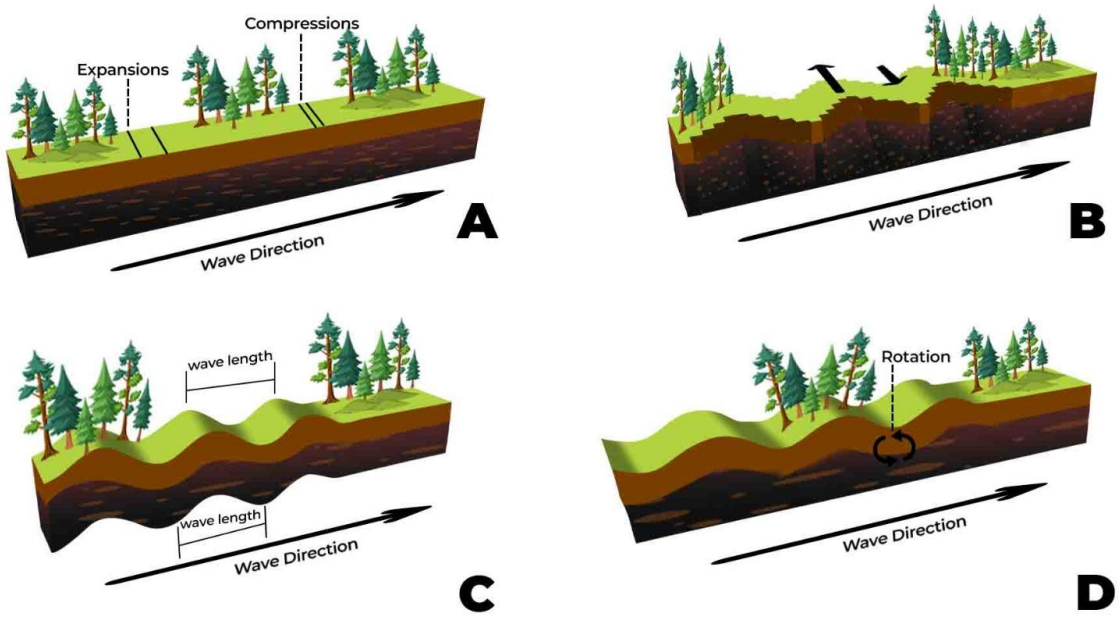

Figure 4.2 Seismic wave's primary types.

(Prepared by the author).

The GNSS measurements are crucial in determining the peak displacements during shaking caused by an earthquake. The superiority of using GNSS against traditional seismic sensors is evident as it can determine the actual effect of the earthquakes' magnitude on the earth's surfaces (Kaftan & Melnikov, 2017; Urtiaga et al., 2022; Yang et al., 2020). Consequently, if the surface point displacement is calculated, it is possible to determine the actual magnitude and direction of the seismic wave. Rayleigh and S waves experience vertical movements of the surface. Accordingly, these vertical movement motions are more likely to trigger tsunami events.

4.2.2 Tsunami activities

Another type of risk brought on by the earth's activities is a tsunami. Unlike other earth risks, tsunami waves can subsequently start after undersea landslides, volcanic eruptions, or submarine earthquakes, followed by extremely fast waves that can potentially cause destruction and land flooding (Geoscience Australia, 2020; Goff & Chagué-Goff, 2022). Tsunami waves vary in wave speed and amplitude. Wave amplitude could be varied between several centimetres to hundred meters. The Lituya Bay tsunami initiated the most considerable recorded height of around 250 meters (Mader & Gittings, 2002).

Wave speed varies concerning the depth of the wave beneath sea level. The speed magnitude varies between 500 and 25 miles per hour (National Oceanic and Atmospheric Administration, 2018).

4.2.3 Landslides activities

The landslide phrase refers to the phenomena of the landform that results from the downward drift of soil and rock materials under the influence of gravity. Various factors, including human actions such as material excavations, the influence of unstable construction filling materials, reservoir rapid filling/withdrawal, deforestation activities, and mining operations, could cause the landslide event. Natural factors also play an essential role in landslide formation, including rainfall, snowmelt, flash flooding, earthquakes, weathering, or exposure to multiple freezes/thaw cycles. The landslide classification varies concerning the failure mechanism, slope characteristics, mass types, and layers. The failure mechanism could be as topple, slide, fall, spread, or flow forms. However, regarding the mass type, the slope materials can have soil, rock, or composed materials.

Accordingly, the amounts and the speed of drifting materials vary with the landslide types (Zeni et al., 2015).

4.2.3.1 Falls

This type of landslide commences with rocky or soil mass drifting from cliffs or steep slopes. A detachment of drifting material from the original slope mass releases the landslide mass. Those materials travel at rapid to extreme speeds. The mass volume could vary from individual rocks or small amounts of soil to massive blocks with more than thousands of cubic meters (Highland & Bobrowsky, 2008).

4.2.3.2 Topple

The topple landslide results from rotational forward drifting above the gravity center. This rotation occurs due to the exerted weight of upslope materials. The Topple landslide's mass travel velocity ranges from relatively rapid to extremely slow. Occasionally, speeding along the traveling path occurs depending on the steeping slope (Highland & Bobrowsky, 2018, 2008).

4.2.3.3 Rotational slides

This type of slide mainly occurs in the homogeneous filling material. Contrary to Topple forward rotational drifting, the rotational slides occur about the axis parallel to the direction of the slope contours. The movement starts exceeding the ultimate sharing strain due to the homogeneity. Along the rupture surface, the drifting material flows as a relatively cohesive mass with minimal distortion. The speed varies from 0.06 meters per year to 1.5 m monthly (Crozier, 2010; Highland & Bobrowsky, 2008).

4.2.3.4 Translational landslide

In a translational landslide, there is no rotational movement or backward tilting as the mass flows outward, or down and outward, along a predominantly planar terrain. In contrast to rotational slides, this slide form can expand if the rupture surface is sufficiently sloped. The velocity can differ from a range of 1.5 meters (Highland & Bobrowsky, 2008).

4.2.3.5 Spreads

A cohesive soil or rock mass that has expanded along with mass subsidence above weaker underlying material. Spreads may be caused by the fine underlying materials liquefying or flowing. Block liquefaction and lateral spreading are a few different forms of landslide spreads. After various triggering events, like an earthquake, the travel velocity may be slow to moderate and occasionally quick. The landslide mass may gradually spread over time at a few millimetres to tens of meters per day (Highland & Bobrowsky, 2008; USGS, 2020a).

4.2.3.6 Flow

A flow is a continuously moving object in space with short-term, closely spaced surface shear. This type of landslide has a different form, such as debris flows, which are rapid material movements in which water, loose soil, and occasionally rock combine to form a slurry that travels downhill—volcanic debris flows, which is a word from Indonesia. Lahars are volcanic mudflows, as well. These volcanic slopes are where these flows first appear. Debris avalanches generally occur from an unstable slope collapsing and the shattered debris being swiftly moved away from the slope. They are enormous, high-speed, and frequently open-slope flows. Generally, this occurs from an unstable slope collapsing and the shattered debris being swiftly moved away from the slope. Earth-flow occurs on gentle to moderate slopes, typically in fine-grained soil, like clay or silt, but it can also be found in bedrock that is very weathered and clay-bearing. A slow earth-flow is popularly known as creep, which is the imperceptibly slow, persistent descent of slope-forming soil or rock. Internal shear stress, which is enough to cause deformation but not enough to cause failure, causes the creeping movement flows. Permafrost failures in permafrost conditions can happen on gentle slopes and involve the movement of fine granular materials, previously ice-rich soil (Geertsema & Highland, 2011; Highland & Bobrowsky, 2018, 2008). Figure 4.3 illustrates the pre-mentioned landslide types, the nature of landslide flow, flow materials, and landslide traveling speed. It is worth mentioning that the landslide traveling speeds vary from a slow speed of 1 centimeter per year to a modest speed of around 1 kilometre per hour to a rapid and highly rapid speed of more than 5 kilometres per hour. The variation in traveling speed is highly related to cliff angle slope, landslide material type, and water content.

Figure 4.3 Landslide mass movements classification

(Prepared by the author).

4.2.4 Volcanic activities

The converging plate tectonics margins result in subduction zone creations. Oceanic plates subduct below the continental plates; this action results in melting subducted rocky materials. On the contrary, at the diverging margins, the earth's crust is subjected to tension forces, resulting in thinning of the earth's crust. Consequently, melting rocky materials have lower density regarding the surrounding rocks. Subsequently, these materials rise to upper rock layers and are possibly stored in the magma chamber. Over several years, the magma collects in the chamber below the surface. The trapped melting rocky materials and the stuck gases are responsible for the trigger of eruption. Before the eruption, the magma rises, resulting in deformation, tilt changing, and surface uplifting.

Volcanic activity releases volcanic ash, molten rocks, and gases. Volcanic eruptions usually involve earthquake activities, land uplifting, and other surface deformation. The temperature of melting materials can vary between 700 to 1200 Celsius. These materials are subjected to colling when they interact with cold air above or with sea water if the eruption occurs at seafloors. The density, viscosity, and temperature of volcanic materials affect the volcanic shapes—the intensity of volcanic eruptions related to the pressure of trapped materials (Sheets & Grayson, 2013).

4.3 The behavior of structures under load: structural deformation

Deformations occur in artificial structures when loads exceed their safe design limits. These structural deformations could be classified into three categories. The first category contains natural loads that impact structures, including wind and snow loads, soil instability due to freezing-thaw cycles, variation in soil water content due to changing groundwater table levels, and the expansions and contractions of structural materials due to thermal loads. The second category includes artificial loads that affect structural behaviors, including structural weight, called dead loads, and building objects, weights, and people's furniture, called live loads. The third category contains the impact loads such as earthquakes, landslides, and tsunamis, which are sudden loads affecting structures. All the above-mentioned loads and forces could lead to structural deformations, for example, could cause structural crakes, vibrations, inclinations, and subsidence or uplifting (Day, 2012; Gaylord et al., 1997; Peck et al., 1991; Peng, 1992).

Several variables, including structure design, soil, construction materials, and the surrounding environment, influence the accepted range for structural subsidence. Any structure will experience some degree of subsidence over time depending on factors like weight, variations in soil moisture, and other external variables (Peng, 1992).

However, if the structure settles too much, it can become unsafe. As a result, the expert's recommendations specify the maximum permissible settling of the structure, considering its intended use and the type of foundation system used. The structural engineering guidelines state that half inches of the settlements are acceptable for residential buildings; however, more constraints regarding commercial buildings recommend that the subsidence not exceed 0.25 inches. There should also be no more than a 1/4 inch of settling per year. These rules are based on factors such as soil type, construction materials, and foundation design (Peng, 1992; Scheck & Bayer, 1999).

On the other hand, the Building Code Requirements for Structural (ACI 318-14) specify that the allowable subsidence of beams and slabs did not exceed 1 cm corresponding to the 2.40 meters length (Committee, 2008).

Investigations concerning the structural cracks. Concluded that numerous causes, including temperature fluctuations, shrinkage, subsciences, and dead/live loads, can cause structural cracks, from little surface cracks that are mainly aesthetic to larger cracks that could compromise the building's structural stability. Accordingly, the cracks vary in terms of their shape and direction.

The investigations showed that different specifications regarding the crack's dimensions and shape had been utilized, accommodating structural types and usage. For instance, high-constraint specifications and acceptable crack dimensions are required for water storage and treatment units. Table 4.2 shows the American Concrete Institute (ACI) acceptable crack width accommodating the structural surrounding environments.

Table 4.2 Reasonable cracks dimension ACI 318.

Exposure condition	Crack width	
	in	mm
Dry air or insulation members	0.016	0.41
Humidity conditions	0.012	0.30
Deicing chemicals	0.007	0.18
Seawater environments	0.006	0.15
Water storage structure	0.004	0.10

ACI demonstrates that the pre-mentioned figures represent a guideline for allowable concrete cracks. It is worth highlighting that even though a crack in a concrete structure is within acceptable bounds, it should still be taken seriously. Cracks can damage the building's structural stability and allow water and other substances to seep through the concrete, causing more damage (Committee, 2008).

In terms of the impact loads caused by earthquakes and wind loads investigations. The two primary types of loads that impact a structure are horizontal forces, which can cause displacement of the entire structure or a portion of it. Structural engineering guidelines accept the minimum displacement value that does not impact the building's stability (Day, 2012).

In terms of structural means, they have been employed to avoid structural failure and enhance structural stability. The structural subsidence could be minimized by utilizing several approaches, including soil replacement, soil grouting, mat foundations, settlement joints, or pile foundations. On the other hand, the impact loads resulting from wind and earthquakes could be prevented by utilizing the share walls or implementing the foundation's shock absorption mechanism.

It is not sufficient to initiate early warnings for structural evacuations and initiate structural safety regulations using the PPP technique or other GNSS positioning approaches only. Due to the fact that even if the structure is subjected to deformations or settlements exceeding the limits of the aforementioned guidelines, this does not necessarily mean that the structure is not stable or going to collapse. Consequently, initiating evacuation warnings requires several engineering steps. Review the structural design, then utilize structural evaluation tools such as a Schmidt hammer, steel scanner device, and concrete core test—subsequently, the foundation and soil evaluations. With the aid of surveying and GNSS measurements, the structural engineer can evaluate the

building's stability and decide whether or not to initiate evacuation warnings—several high-computation software such as E-taps, SeismoSignal, Xtract, and Sap2000 can be used to help with this decision (Chadwell & Imbsen, 2004; Computers and Structures, 2023; Seismosoft, 2019; Sekhar & Das, 2017). SeismoSignal software can instantly evaluate building behavior by simulating real-earthquake seismic waves (Seismosoft, 2019). Section 4.10 demonstrates several studies implementing the RT-PPP approach for structural monitoring.

4.4 The necessity of an early warning system to prevent risks and natural hazards

Numerous international agreements at different government levels have emphasized the value of early warnings. EWS are essential tools for preventing new disaster risks and reducing current disaster risks, according to the 2015 Sendai frameworks for disaster risk reduction from the United Nations (Zia & Wagner, 2015). This framework also emphasizes that by 2030, EWSs must have undergone significant evolution to increase disaster risk reduction. Zhou et al., (2014), mainly focused on EWSs as one of the five most important actions with the Hyogo framework for action. Populations in urban regions that are particularly exposed to earth crust deformations have dramatically increased during the past several years. EWSs can initiate timely mitigation measures before the advent of destruction to such regions. The EWS technologies can also improve community responses by decreasing damage and injuries and by strengthening operations for both the public and private divisions**.** Providing early warnings is crucial to prevent life and economic losses. The time before the destruction's arrival allows for performing protection arrangements.

These arrangements include city and structure evacuations, shelter openings, automatic initiation of protective measures for critical infrastructure like opening firehouse doors, breaking off rapid transport vehicles, traffic management to prevent accidents, and stopping lifts.

Stakeholders, emergency services, and civil defense teams depend on the response time prior to the arrival of destruction. EWS alerts are preferred since they give the public and crews more time to make essential safety preparations. This time varies according to the geo-hazard type and the implemented EWS.

National Oceanic and Atmospheric Administration (NOAA) and Our World in Data provide free access to natural disasters, including earthquakes, tsunamis, landslides, and volcanic activities.

The database also provides the consequences of those hazards in terms of death numbers, amount of destroyed or damaged house units, and the economic losses due to the disaster events. Additionally, various information is provided, such as the locations of events, number of injured and missing people, earthquake magnitudes, speed, and height in case of using the tsunamis database. Table 4.3 contains different website links where more information can be found regarding natural hazards databases (National Centers for Environmental Information (NCEI), 2022a, 2022b, 2022c; Our World in Data, 2022).

Table 4.3 Natural hazards databases.

Natural hazard type	Database website link
Tsunamis	**https://www.ngdc.noaa.gov/hazard/tsu.shtml**
Earthquakes	**https://www.ngdc.noaa.gov/hazard/earthqk.shtml**
Volcanic	**https://www.ngdc.noaa.gov/hazard/volcano.shtml**
Landslides	**https://ourworldindata.org/natural-disasters**

Based on Table 4.3 databases, the archive data have been used to create Figures 4.4 to 4.10. Those Figures show the natural hazard indicators regarding the number of deaths, destroyed and damaged houses, and economic losses regarding earthquakes, tsunamis, volcanoes, and landslides.

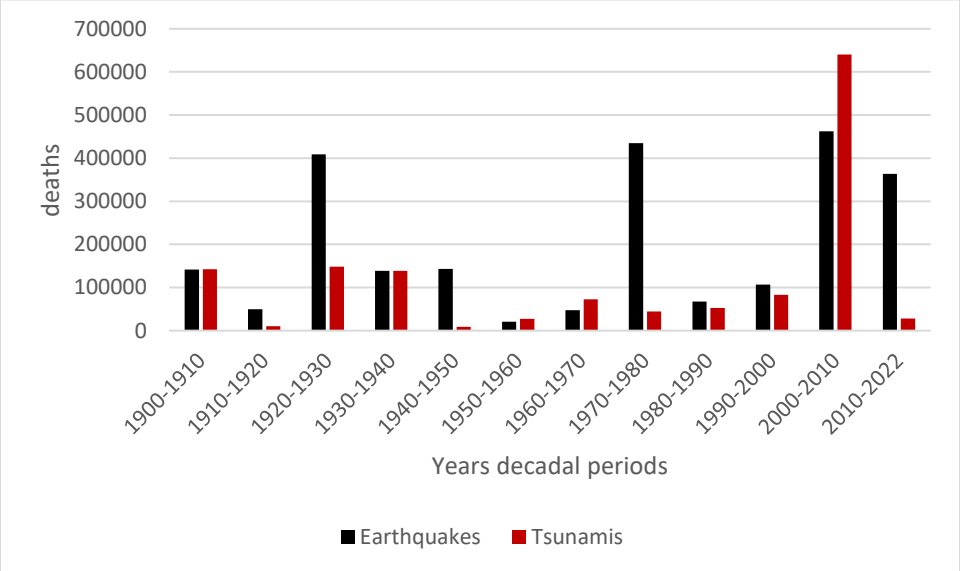

Figure 4.4 Deaths from earthquakes and tsunamis.

(Prepared by the author based on data from Table 4.3 Natural hazards databases).

Figure 4.5 shows the economic losses due to earthquakes and tsunamis from 1900 till now. Additionally, Figure 4.6 shows the corresponding number of houses damaged or destroyed due to earthquakes and tsunamis in the same period.

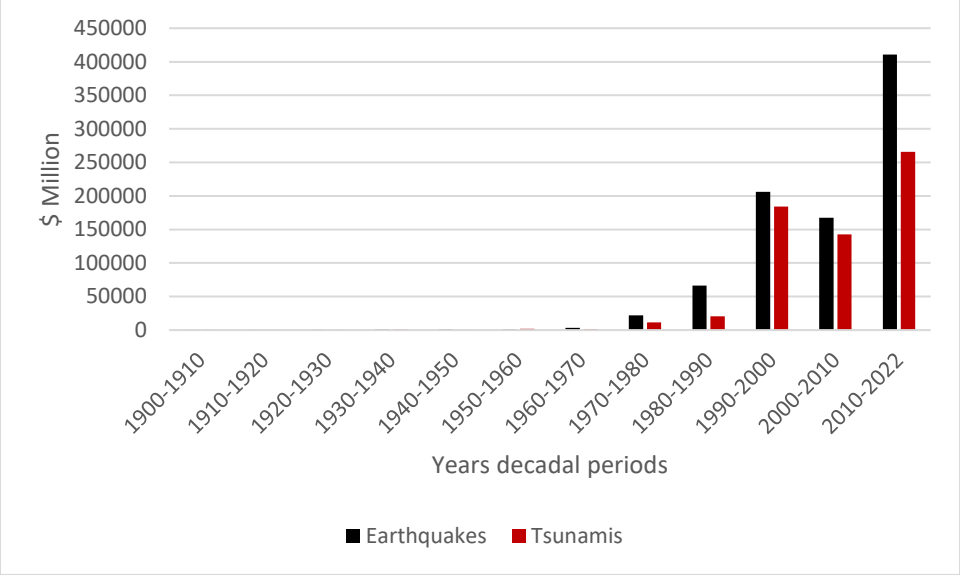

Figure 4.5 Economic losses of earthquakes and tsunamis.

(Prepared by the author based on data from Table 4.3 Natural hazards databases).

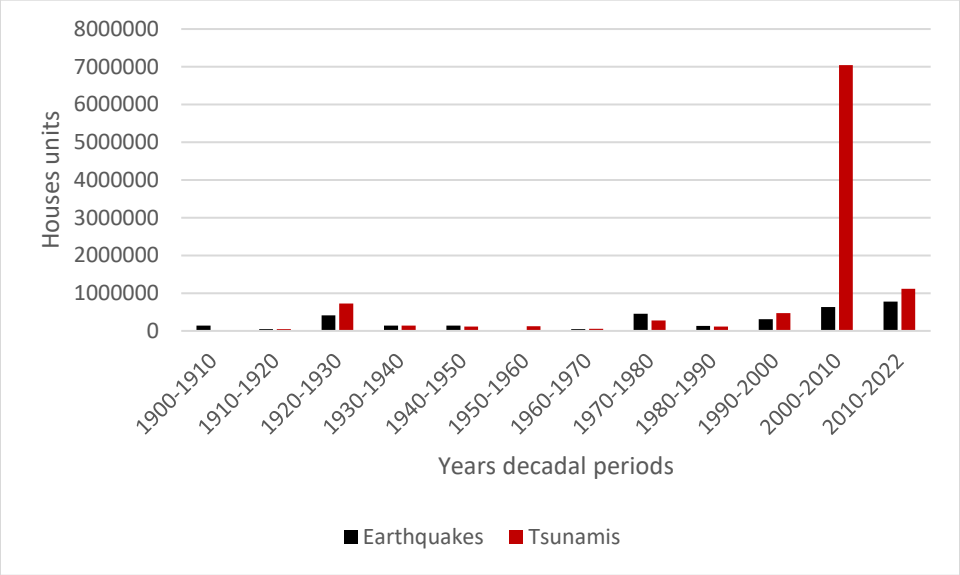

Figure 4.6 Number of damaged/destroyed houses by earthquakes and tsunamis.

(Prepared by the author based on data from Table 4.3 Natural hazards databases).

Figure 4.7 shows the number of deaths regarding landslides and volcanic activities from 1900 till now; furthermore, Figure 4.8 shows the number of people left homeless due to volcanic eruptions or landslides.

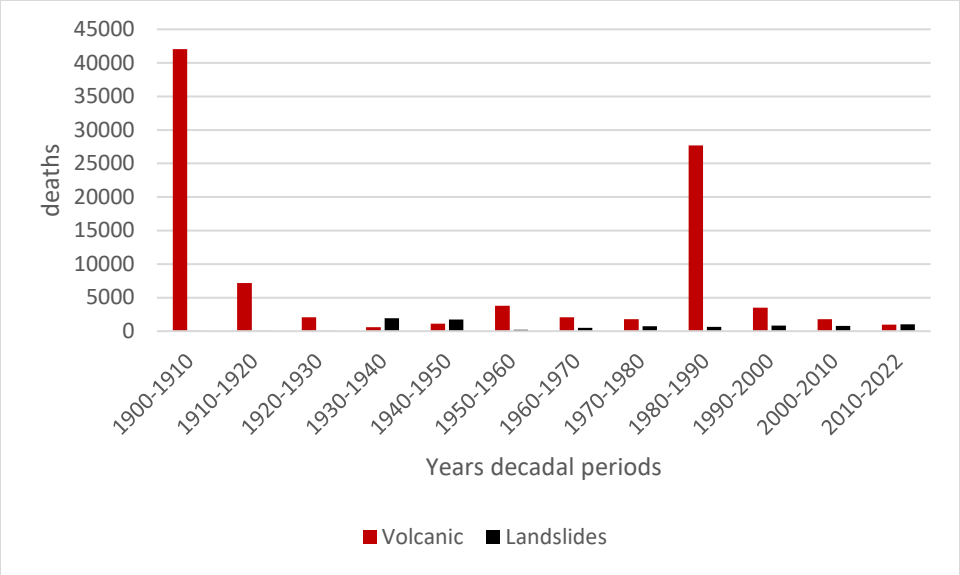

Figure 4.7 Volcanoes and landslides deaths.

(Prepared by the author based on data from Table 4.3 Natural hazards databases).

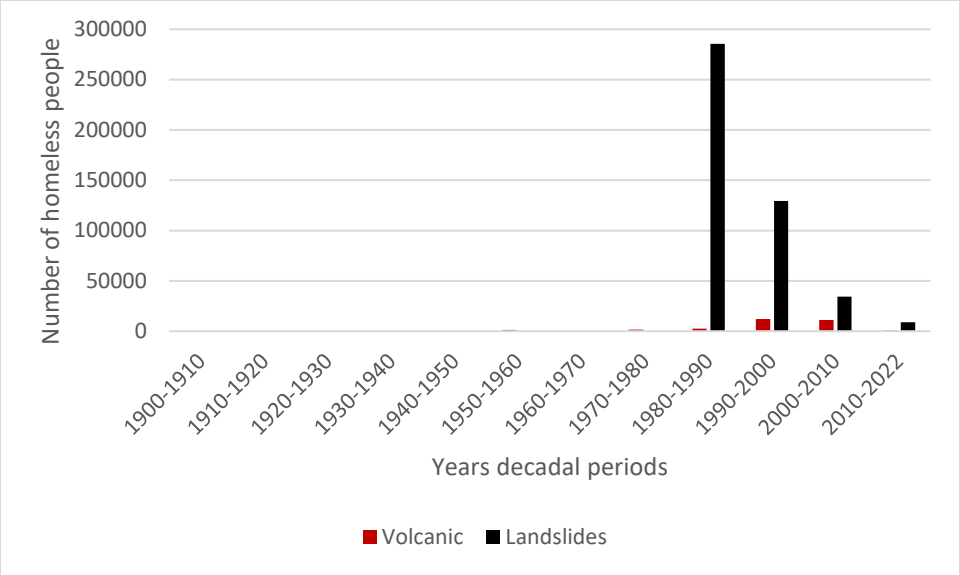

Figure 4.8 Number of homeless people due to volcanoes and landslides

(Prepared by the author based on data from Table 4.3 Natural hazards databases).

Figure 4.9 and Figure 4.10 shows the economic losses due to volcanic and landslide activities. Figure 4.9 shows the economic losses in terms of millions of US dollars. However, Figure 4.10 shows the economic losses as a percentage of the world's Gross Domestic Product (GDP).

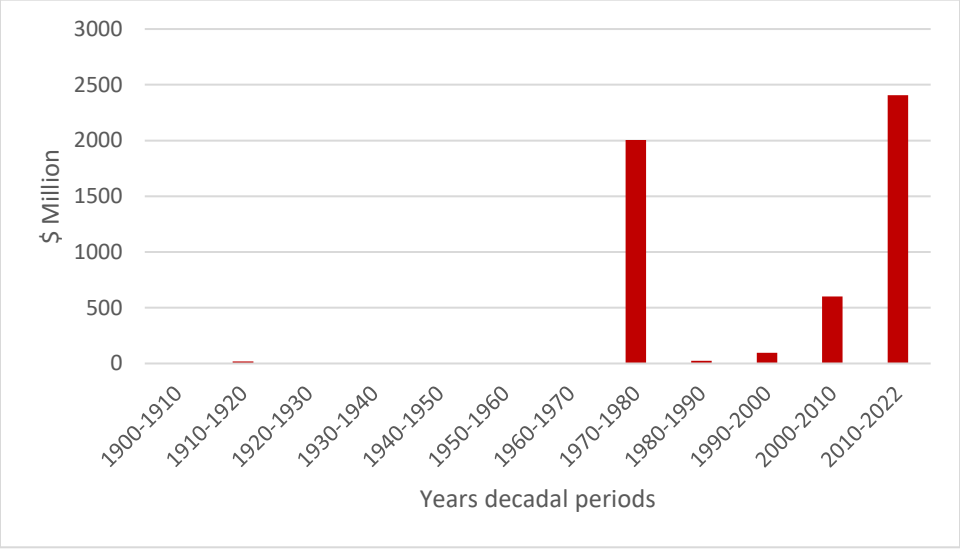

Figure 4.9 Economic losses due to volcanic.

(Prepared by the author based on data from Table 4.3 Natural hazards databases).

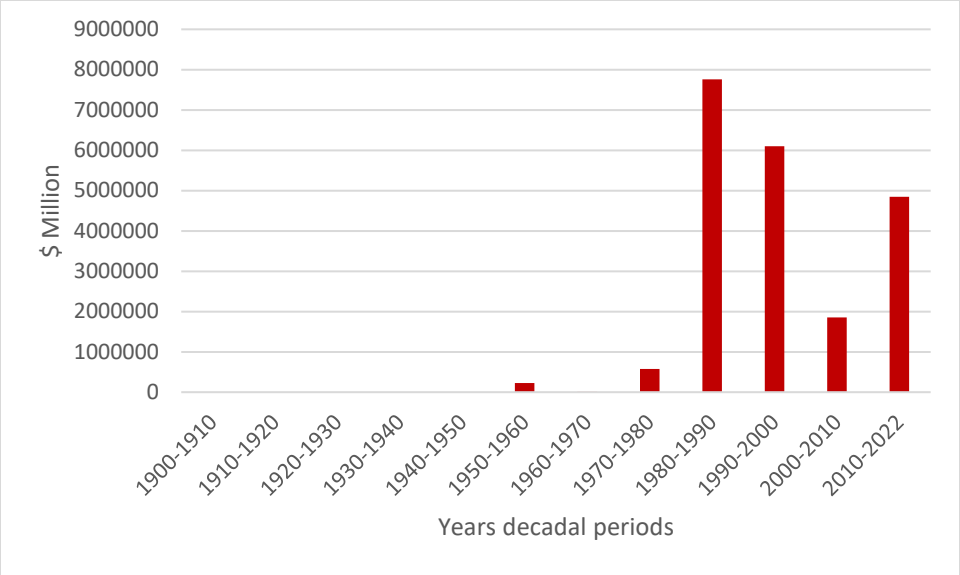

Figure 4.10 Economic losses due to landslides.

(Prepared by the author based on data from Table 4.3 Natural hazards databases).

The good archiving of the natural hazards events and their consequences demonstrate a striking increase in deaths, economic losses, and destroyed homes, particularly between 2000 and 2022, despite the advent of the newest and most advanced technologies. Additionally, the growing global population makes people more vulnerable to natural disasters. Global warming raises more issues related to natural hazard disasters, including glacier melting and sea level rises, which lead to more deformation activities, especially with land subsidence and uplifting. In addition to triggering more landslide events; thus, implementing well-designed EWSs can avoid all of these losses.

4.5 Earthquakes, tsunamis, landslides, and volcanic early warning systems

The *earthquake early warnings* depend on both earthquake magnitude and hypo-center location. It is a challenge for earthquake alert centers to initiate warnings if the hypo-center is near urban areas. On the contrary, the early warning could be initiated earlier if the hypo-center is remote enough from urban areas.

The speed at which seismic waves propagate from a rupturing fault during an earthquake is essential to implement an earthquake EWS efficiently(Sheen et al., 2014). P-waves and S-waves propagate through the earth's shallow layers when rupture occurs. P-waves move faster than S-

waves, yet S-waves are more harmful than P-waves because of their great amplitude, which causes crust shaking. When an earthquake event occurs due to the superiority of the P-wave speed, the seismic stations record the arrival of P-waves and transmit the recordings to the master control station, where data interpretation is used to estimate the arrival of S-waves. The amount of time that passes between the arrival of P-waves and S-waves is called the "lead time." Studies show that this time could vary from a few seconds to several tens of seconds before reaching the surface seismic waves (Alcik et al., 2009; Cochran et al., 2018; McGuire et al., 2021; Parolai et al., 2017).

Differently, the lead time initiated with *Tsunami warning systems* could vary from a few minutes to several minutes depending on the locations of both earthquakes and offshore cities (Alcántara-Ayala & Oliver-Smith, 2019; Amato, 2020; K. Chen et al., 2020; Kamogawa et al., 2016; Sobolev et al., 2007; Srinivasa Kumar & Manneela, 2021; Tsushima & Ohta, 2014).

The *landslide's early warnings* could be initiated several minutes to 24-48 hours or more before the landslide event (Alcántara-Ayala & Oliver-Smith, 2019; Capparelli & Tiranti, 2010; Pecoraro et al., 2019). This time variation could be illustrated as the landslides could be induced through different triggers such as rainfall, variation of the groundwater table, soil erosion, volcanic eruptions, earthquake activities, and artificial disturbance activities (USGS, 2020b).

The *early volcanic warnings* could initiate warnings within hours, days, or even months before the eruptions (Alcántara-Ayala & Oliver-Smith, 2019; Sparks, 2003). The variation in leading time is related to various volcanic types. Different phenomena could be observed before the eruption, like surface inflation, volcanic slope variations, and rising temperature—increased sulphur dioxide levels and increased seismic activities. The leading time could vary concerning the priory observed signs related mainly to the volcano types.

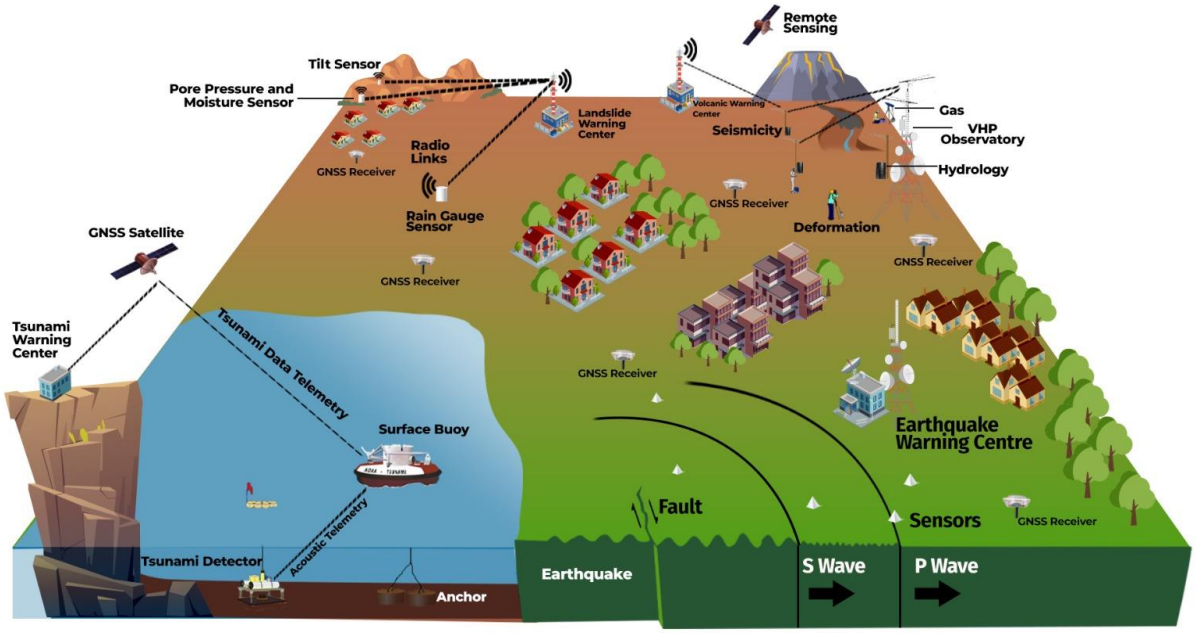

Figure 4.11 Multi-geo-hazard early warning system

(Prepared by the author).

Figure 4.11 represents establishing a comprehensive EWS, consisting of several monitoring elements such as seismic, rain gauge, tilt, gas, and surface Buoy sensors, incorporation with the master control station, and alerting communication units.

4.6 Early warning system methods

Different phenomena are associated with geo-disasters, like surface deformations, earthquakes, and volcanic eruption triggers. Consequently, many methods have been utilized to track pre-mentioned phenomena. These methods could be classified into the following categories (Ewert et al., 2005; Pecoraro et al., 2019; Sheen et al., 2014; Zang et al., 2022):

1. Geotechnical methods include methods such as inclinometer, borehole, embedded extensometers, differential monitoring stability, tiltmeter, optic fibre, crakes-meter, piezometer, perforated standpipe, tensiometer, and thermocouple psychrometer.
2. Remote sensing data also monitor deformations with cameras, ground and air-based lidar, ground-based and interferometric-based synthetic aperture radar, ground penetrating radar, satellite sensors, and UAVs.
3. Geodetic methods have also been used as an EWS means, including GNSS, total stations, and interferometric.
4. Hydrological tools have been utilized in monitoring, like water level meters, hydrometers, and spring sampling.
5. Geophysical methods: geophone, seismometer, and accelerometers.
6. Metrological means: Rain gauge, weather station, particulate matter measuring device, and barometer. Sulphur dioxide detectors.

These methods could be integrated with the advanced Internet of Things, machine and deep learning, reliable communication systems, and artificial intelligence. These integrations enhance the availability, reliability, and integrity of EWS (Bilal et al., 2022; Qafisheh et al., 2021; Suwarno et al., 2021; Xu et al., 2020). From a geodetic point of view, the integrations between geodetic techniques include SAR, lidar, and GNSS. Such integrations are essential in terms of having a comprehensive view of deformation events in terms of deformation magnitude, event duration, and deformation type. It could also be a solution to combine low-accurate RT measurements with high-accurate observations obtained from post-process procedures or quasi-real-time methods. For instance, an mm accuracy could be achieved through SAR methods (post-process mode). On the other hand, a decimetre or sub-decimetre level of accuracy is achievable by applying the RT-PPP

method. In addition, some geodetic techniques are suitable for long-term monitoring, and others are ideal for mentoring instantaneous deformation events.

Contrary to traditional EWSs, RT-PPP, Quasi RT-PPP, and DGNSS could initiate prior warnings concerning traditional EWSs. The ability to accurately position and assess the coordinate time series analysis and the RT nature of the data. Accordingly, some events that cause the earth's crust to deform may be observed before the event trigger occurs.

4.7 Examples of current DGNSS-based early warning systems

The ability to obtain highly accurate positioning via DGNSS technologies paves the way for it to be used as a major tool for surface deformation (Farzaneh et al., 2022; Gümüş & Selbesoğlu, 2019; Jäger et al., 2005; H. Tang & Xu, 2019; Wu et al., 2020; Yang et al., 2016). Accordingly, DGNSS techniques have been implemented to monitor deformations resulting from natural hazards like tsunamis, earthquakes, landslides, and volcanic activities (Cina et al., 2013; Cina & Piras, 2015; le Mével et al., 2015; Li et al., 2021; Lin et al., 2021; Miura et al., 2004; Pirotti et al., 2015; Xu et al., 2020; Zedek et al., 2021). Additionally, these technologies have been widely utilized for monitoring mega structures such as dams, bridges, and skyscrapers (Cefalo et al., 2017; Q. Chen et al., 2018; Roberts et al., 2019; Xi et al., 2021; Xiao et al., 2019). Consequently, the approaches of the DGNSS are utilized as a primary early warning systems technique for environmental disasters. Following are some EWS projects.

4.7.1 Pacific Tsunami Warning and Mitigation System (PTWS)

The PTWS is regarded as one of the fundamental pillars of the authorized tsunami early warning supplier’s system under the United Nations Educational, Scientific, and Cultural Organization (UNESCO) (NOAA, 2022).

In order to provide a more precise and timely evaluation of the intensity and form of earthquakes and tsunamis, At the beginning of 2010, the prototype of the GPS-aided Real-Time Earthquake and Tsunami Alert System (GREAT) project was set up. GPS data is utilized to strengthen NOAA's Pacific Tsunami Warning Center's (PTWC) tsunami and earthquake warnings and the United States Geological Survey (USGS) operational responses (Bar-Sever et al., 2009).

In order to provide early tsunami warnings, NOAA utilizes Deep Ocean Assessment and Reporting Tsunami (DART) stations. The station contains several sensors, such as water pressure, a thermometer, GNSS receivers, and a communication system. After the GREAT project, NASA initiated the GPS Aided and DART Ensured Real-Time (GADER) project (NASA, 2013). The DART onboard GNSS system operates differentially and uses NASA's Differential GPS (DGPS) network. The combination of DART RT sensing data and DART's accurate locations enhances the capability of initiating tsunami early warnings (Meinig et al., 2005; Titov et al., 2017).

4.7.2 ShakeAlert earthquake early warning system for the west coast of the United States

The ShakeAlert was founded as a result of cooperation between USGS and several US academic universities to implement EWS for the US West Coast. The ShakeAlert system's goals are to recognize and classify earthquakes shortly after they start, estimate the expected magnitude and the surface ground movements that will follow, and make notifications available for distribution to vulnerable individuals and infrastructure (Burkett et al., 2014; ShakeAlert, 2016). The University Navigation Signal Timing and Ranging NAVSTAR Consortium (UNAVCO) took part in developing and testing the ShakeAlert system for the country's west coast. It participated with 151 GNSS sites to be integrated with the system. Those GNSS stations provide RT-GNSS data combined with seismic data, leading to a better understanding of earthquakes and tsunami events (UNAVCO, 2020).

4.7.3 TRUAA early warning system

TRUAA system is similar to the shake alert system in the US; TRUAA is currently in the testing stage, covering Israel and Palestinian territories. The Dead Sea Fault and its accompanying branches, including the Carmel Fault, are this region's primary causes of earthquakes. It is worth mentioning that the country's shape reveals a limitation in providing adequate time for warnings. For instance, Jerusalem is just 30 km away from the Dead Sea; this gives the TRUAA a 3-second lead time. The system could be enhanced with more cooperation in the eastern Mediterranean countries. Currently, three GNSS sites aid the EWS with RT data, which is projected to increase soon (Allen et al., 2012; Nof & Kurzon, 2021).

4.7.4 GNSS-based Upper Atmospheric RT Disaster Information and Alert Network (GUARDIAN)

GUARDIAN is a near RT alert system that relies on JPL GNSS network data. Currently, JPL operates 78 stations in the Pacific region. Accordingly, GUARDIAN alert streams presently cover the premonition regions, but the system architecture could be extended to cover more regions or works globally. The energy releases natural hazards; moreover, the effect of the ground shaking also disturbs the atmosphere. GUARDIAN uses both ionospheric disturbances and total electron content to track and monitor the earth's activities.

The RT responses design is based on three symbiotic components: Creating the TEC time series is the first step. The second step is the collection of 1 Hz GNSS observations and processing them with Deep Learning (DL). The third step is determining if drifting ionospheric turbulences are caused by the TEC time series in RT. Finally, the inverse model ling's final objective is to use ensemble modelling to extract tsunami features from the TEC data (Martire et al., 2021). The ionosphere responds to natural disasters with delays between 8 and 40 minutes. The size of TEC perturbations is frequently inversely proportional to the actual occurrences (Pathy et al., 2019).

4.7.5 GNSS/LPS/LS-based online Control and Alarm System (GOCA)

The GOCA system has been created and maintained by the Institute of Applied Research (IAF) at Karlsruhe University. GOCA composes various geodetic sensors such as GNSS, Local Positioning systems (LPS), Local Sensors (LS), online control units, and alarm systems. GOCA involves the DGNSS in monitoring the movements of the earth's surface. GOCA is intended for online monitoring and warning in the case of safety-relevant buildings and geotechnical facilities such as dams, in addition to its use in natural disaster prevention (GOCA Project, 2017; Jäger et al., 2006).

4.7.6 Japan's early warning system

The Japan Metrological Agency provides a comprehensive EWS for natural hazards like extreme weather events, landslides, earthquakes, and volcanic activities (Japan Meteorological Agency, 2022c, 2022b, 2022a). DGNSS observations aid the EWS with RT data over Japan. The Japanese Authority of Geospatial Information aids the EWS with 1300 CORS. These stations are considered pillars for crustal deformation monitoring and updating the Japanese geodetic datum. It is worth mentioning that some of those stations contribute to MGEX and IGS networks (Geospatial Information Authority of Japan, 2021, 2022).

4.7.7 GeoNet

Toka T Ake Earthquake Commission (EQC), the Institute of Geological and Nuclear Sciences (GNS Science), and Land Information New Zealand (LINZ) have developed a collaboration to create the GeoNet project (GeoNet, 2022a; GNS Science, 2022; Toka Tū Ake EQC |, 2022). In order to create and maintain a cutting-edge geological risk warning system in New Zealand, the GeoNet project was started in 2001. GeoNet gives the general public information on hazards, such as earthquake reporting and volcanic activity alerts (GeoNet, 2022b). It can also retrieve whole data sets, including GPS Rinex files, earthquake hypocenters, and sensor waveform data. The research community has free access to this data. Unlike the prementioned EWS, GeoNet does not provide early warning for earthquakes, tsunamis, and landslides. However, it provides various alerting levels for volcanic activities across the country (Becker et al., 2020; GeoNet, 2022a).

4.7.8 Indonesia Tsunami Early Warning System (InaTEWS)

Since 2007, the Indonesian National Tsunami Warning Center has offered to act as a tsunami watch provider alongside India, Australia, Malaysia, Thailand, and Iran to offer alert services to the prementioned member states. InaTEWS was built under the direction of UNESCO's intergovernmental oceanographic commission. Numerous services are offered by InaTEWS, including SMS and voice notifications, information about earthquakes and tsunamis, and access to past events (Agency for Metrological Climatology and Geophysics, 2022).

Rather than using traditional seismic sensors alone, a new methodology for early tsunami warning was implemented by the German Indonesian Tsunami Early Warning System (GITEWS) project, which uses more sensor systems and assigned components than previous systems. The GITEWS project's GNSS-based elements project enhance sea level estimation and identifies co-seismic land mass deformations with lower latency. Besides the traditional seismic sensors, InaTEWS deployed GNSS sensors on sea surface buoys, land, and tidal gauges; GNSS sensors are also used as RT reference stations, either independently or in conjunction with seismic sensors (Falck et al., 2010).

4.7.9 Early-Warning and Rapid Impact Assessment with real-time GNSS in the Mediterranean (EWRICA)

The EWRICA is a proposed project funded by the Federal Ministry of Education and Research in Germany. This project aims to establish an EWS prototype with RT GNSS observations. The EWS prototype is subjected to cover Europe and the Mediterranean regions. Unlike the USA, Chile, and Japan, only a few European countries, such as Greece and Italy, implement GNSS networks for robust ground displacement measurements (Maorong, 2022).

4.7.10 Local landslides early warning systems

Unlike earthquakes and tsunamis, landslides could be induced by many trigger events. In order to initiate landslide warnings, various monitoring methods need to be implemented. The implementation of the DGNSS technique is crucial for warning initiation. Accordingly, comprehensive research by Pecoraro et al. (2019) showed that the DGNSS contributes to several landslide EWS.

4.7.11 Precise point positioning deformation studies

Recently, RT and post-processing PPP measurements have been involved in many monitoring activities. These activities include monitoring many crustal deformations. Post-processed PPP methods could achieve more acceptable accuracies, which enhance motion detections. However, the post-procced PPP (static PPP) is not an RT solution. Alternatively, RT-PPP is ideal for RT monitoring but has more limitations than static PPP.

Several studies investigated PPP measurements regarding earth surface deformations. Wang et al. (2013) applied the PPP method to a creeping landslide in Puerto Rico as a case study. The research used PPP in its static form, which is suitable for monitoring such types of landslides. The creeping landslide, also called slow flow landslide, is distinguished through the slow flow motions of a landslide over a long period. The landslide mass flows over a rock or solid materials lying in slope terrains. This type of slow motion usually results in deformation without surface rupturing. The study investigated two years of GPS measurements collected in the study area. After removing outliers and avoiding data collection during extreme weather events, the static PPP accuracy could achieve 2-3 mm in horizontal components. In contrast, the vertical component reaches 8 mm with one day of observation sessions.

Regarding static-PPP earthquake detection studies, Zang et al. (2022) utilized Multi-GNSS experiments with high-rate data. The study justified the uses of the final clock and ephemeris products as a result of low BeiDou ephemeris accuracy; the study confirmed that the uses of Multi-GNSS provide the highest accuracy. The research investigated the displacements of various stations 5 minutes prior to the earthquake events. The result showed that the best-calculated displacements were achieved utilizing multi-constellations with 0.22 cm, 0.25 cm, and 0.53 for east, north, and vertical components, respectively.

Similarly, Zhiping (2016) investigated four IGS stations during the 2011 massive Japan earthquake. The study implemented static PPP to investigate earthquake deformations. The research results demonstrated that some IGS stations experienced deformation displacements of (1.61 to 1.20) meters during the earthquake (Zhiping et el., 2016).

Numerous researchers examined RT-PPP measurements regarding earth crust deformations. In 2008, GFZ initiated the GPS-SurfacE Deformations within Seconds (G-SEIS) project. The project design is to develop a new set of multi-parameter stations that operate independently and alone for extended periods. The project's final deliverable is to construct a GNSS software that deals with RT-GNSS observation, allowing reporting deformations within seconds of events (Helmholtz-Zentrum Potsdam, 2008).

Various studies presented the applicability of RT-PPP in monitoring deformations. Martín et al. (2015) validated RT-PPP capabilities as a possible tool to monitor deformations. This research conducts three types of experiments regarding RT-PPP. The study investigated the RT-PPP performance regarding permanent stations, kinematic situations, and simulated displacements. Ten IGS globally distributed permanent stations have been chosen for the first experiments. In this experiment, 24 hours of continuous RT-PPP observations were stored. The results showed that 0.20-0.25 meters coordinate accuracy is achievable after a short initialization time; however, this accuracy could be improved after one hour. The kinematic situation showed less accurate results as the GNSS receiver encountered signal loss, multi-path difficulties, and increasing latency effect due to utilizing the mobile network and vehicle dynamic actions. The coordinates accuracy reaches 0.15 meters and 0.25 meters for horizontal and vertical components, respectively. Martín et al. (2015) concluded that these results could apply to some applications, such as fleet management and location-based services. The distinguishing feature of this study is that it validates the ability to observe 0.30 meters of simulated displacements through RT-PPP measurements (Martín et al., 2015). Chen et al. (2009) evaluated the EPOS-RT software for monitoring deformations. Similar to Martín et al. (2015) experiments, the research has been done with simulated motions on a horizontal linear table. The research implemented different types of deformation, including vertical vibrations and vertical and horizontal movements. The research finding was for RT and post-processing positioning solutions based on PPP revealed mm horizontal positioning precision. The study demonstrated that the RT-PPP precisions are feasible for various applications. Tao et al. (2021) TFM-CNN, an abbreviation of Time-Frequency Mask Convolution Neural Network, to mitigate multi-path errors investigated the magnitude of the multi-path concerning various environments; the research concluded multi-path removal's effectiveness in improving deformations detections (Tao et al., 2021).

Some investigations showed the suitability of RT-PPP application in structure monitoring. Kaloop et al. (2017) investigated different monitoring scenarios, such as RTK, RT-PPP, and DGNSS, as a tool for structural health monitoring. The researchers confirmed that the very accurate coordinates of the monitoring stations are now efficiently measured at minimal cost using the NRTK and PPP-GNSS technologies.

Tang et al. (2017) utilized both RT-PPP and double differences for Severn Suspension Bridge monitoring in the United Kingdom. The study concluded that double differences, RT-PPP time series, and frequency domain analysis produced comparable outcomes. RT-PPP results indicated 70 centimetres of the vertical, whereas the lateral variations could reach around 34 centimetres. The research referred to these variations as the bridge's mass traffic flow.

Regarding the RT-PPP and double differences coordinates assessments, the study showed that the RMS reached around 8 centimetres within five hours of observations (Tang et al., 2017). However, DGNSS or double differencing encountering inaccurate deformation results as the deformation affects both base or GNSS network receivers and rover in a more or less similar time. On the contrary, the global RT-PPP solution could overcome the prementioned problem by utilizing the global positioning technique.

Many investigated the performance of RT-PPP for landslides or high steep slope stability monitoring. Capilla et al. (2016) utilized simulated deformation observations, and a rod sliding bar was used to simulate deformation in both vertical and horizontal directions. The research experiments emphasized that the possibility of detecting landslide monitoring is achievable using GPS and GLONASS RT-PPP measurements; the study also showed a remarkable accuracy improvement when PPP is implemented using ambiguity resolution. The research confirmed that the PPP methodology has a promising future and can be utilized, together with other geophysical tools, in RT monitoring systems to identify movements in specific locations, assisting in developing EWS. PPP could significantly improve catastrophe mitigation or prevention, especially in places without a nearby network infrastructure.

Lian et al. (2020) used diverse RT GNSS techniques to determine high-steeps' stability. The monitoring system consisted of 8 implemented stations distributed in the landslide area. Those stations are operated with RT-GNSS data through RTK or RT-PPP. GNSS observations were used

to obtain relative displacements to assess the landslide stability. According to the study's findings, the study implements nonlinear Kalman filtering of double-differential and three-differential procedures with an improved ionospheric correction model. Horizontal precision was greater than 3 millimetres, while elevation accuracy was 5 millimetres.

Ruhl et al. (2017) confirmed that the accuracy of the RT-GNSS observations with seismometers was higher than that of the stand-alone seismometer. The study implemented 1,300 tests for the geodetic warning system with actual time-dependent simulated earthquakes; they concluded that traditional seismometers underestimate the magnitude of large simulated earthquakes. Thus, the study emphasizes that RT-GNSS measurements are crucial in earthquake early warning systems. Additionally, The RT-PPP method improves the detection of actual crust movements regarding the global solution.

When GNSS network solutions, virtual reference stations, or local base stations are absent or have insufficient coverage in a particular location, the RT-PPP may be the only monitoring option. This method can be used in remote places or areas with inadequate infrastructure. Moreover, Tang et al. (2017) research emphasizes the superiority of RT-PPP over double differences, especially if the monitoring sites are far away from the base receiver or GNSS network solutions.

Desertic, arctic, antarctic, or rough terrain areas are ideal for RT-PPP and PPP operating areas (Bezcioglu et al., 2019). Barker et al. (2002) revealed that a different strategy must be used to increase accuracy in an offshore environment than on land. Creating an RTK network or adding nearby reference stations is not always possible. On the other hand, the vast oceans provide a setting that is almost perfect for RT-PPP monitoring. Buildings or tree leaves do not obstruct navigation signals in any way. The antenna can typically see all satellites over the horizon, and GNSS receivers on board a ship rarely encounter cycle slips (Barker et al., 2002). Thus, this method is ideal for positioning in regions such as offshores, coastal, or island areas; additionally, it is suitable for maritime positioning. Alkan et al. (2017) also looked into the PPP readings in both modes in marine areas. The study found that numerous maritime applications could be carried out with the RT-PPP accuracy levels. PPP could be applied to maritime implementation in accurate hydrographic surveying, marine geodesy, and oceanography (Alkan et al., 2017).

As a result of melting glaciers in both the Arctic and Antarctic regions and the rising sea levels consequences brought on by global warming (Bezcioglu et al., 2019), there are more significant problems with land subsidence and uplifting, increasing landslides events as a result of frequent flash floods. Thus, more regions and populations will be impacted by more natural hazards. Consequently, more lives and economic losses are projected to increase, especially in vulnerable populations.

It also appears from these studies that the use of RT-PPP solutions is essential to the early detection of natural hazards. Additionally, the use of RT-PPP may be the best solution in many areas; however, the use of RT-PPP as a method of EWS is still in progress due to the lack of accuracy, long initialization time, RT correction product outages, and other limitations.

The evolution of RT-PPP as a strategy for implementing an EWS might be regarded as one of the novel aspects of this thesis. Therefore, machine learning prediction tools were used to improve the quality of RT corrections by solving latency (Qafisheh et al., 2022; Qafisheh, 2020). More results regarding solving latency problems can be found in Chapters 6 and 7. Additionally, machine-learning classification algorithms have been utilized to establish EWS (Qafisheh et al., 2021). In Chapters 6 and 7, further outcomes relating to EWS can be found. In the design of this system, three matrices were developed, which indicate three different levels of services. This process will generate an early warning protocol only if the probability of deformations is very high. Accordingly, the RT-PPP utilizing the Multi-GNSS observations enhances the RT corrections in addition to the expansion of the Multi-GNSS network. Besides, it boosts the ionospheric and the tropospheric models or products. Integrating these with the machine or deep learning algorithms will increase RT-PPP reliability.

Consequently, all will pave the road to utilizing these techniques in EWS. Through the literature conducted in this chapter, we can conclude that the natural hazard risks, which include earthquakes, landslides, volcanoes, and others, significantly affect human lives and lead to many losses at the human or economic levels. Implementing a well-designed EWS can break all of these losses.

Chapter 5 Machine Learning

5.1 Introduction

"ML" was first used in 1959 by the early computer scientist Arthur Samuel. In the same time frame, self-learning computers were also introduced (Lindsay, 1964; Samuel, 1959). However, using ML notions to solve various problems is not always optimal. As a rule of thumb, always finding solutions without using ML algorithms delivers simplicity and reduces execution time and ambiguity. Therefore, applying ML has several benefits and drawbacks. ML has become an essential component for various applications due to several advantages, including the capability of pattern recognition and self-learning. It is also supported by a large community and the suitability to deal with high-dimensional data.

On the contrary, several disadvantages appear, such as results interpretation difficulties and the vulnerability to introducing high error, especially with an over-fitting or bad selection of training and test data from the original dataset, wrong adjustment of internal hyperparameters of a specific ML algorithm, or choosing the wrong ML model. Moreover, ML needs an extensive database to train their models well. Some applications require massive computational resources with long periods of training. The ML models conclude several steps essential to properly implement data preparation, model parametrization, and results assessments. Figure 5.1 shows the main steps in the ML life cycle. However, the life cycle could be extended to cover the system deployment and the user's feedback to represent the actual scenario.

Numerous ML models have been created mainly by mathematicians and statisticians. Several ML models could be implemented either with supervised or unsupervised learning. The primary distinction between supervised and unsupervised learning is the nature of the data used earlier. Unsupervised learning uses datasets that have not been labelled, while supervised learning relies on such labels. When we discuss data being "labelled," we mean it has the correct answer already attached to it. According to data patterns, application types, and resource availability, the most appropriate ML model must be chosen to increase result accuracy, reduce complexity, and boost performance. Consequently, the chosen ML mode could solve clustering, classification, or regression problems.

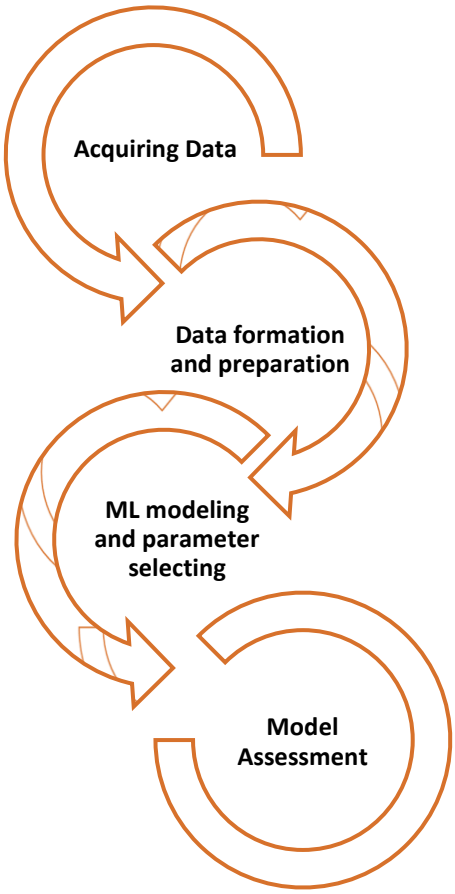

Figure 5.1 Machine learning phases

(Prepared by the author).

5.2 Supervised Learning

The two types of problems for which supervised learning is applicable are prediction and classification. Given a labelled dataset, the purpose is to understand modelling from inputs x to results y.

$$Z = \{(x_i, y_i)\}_{i=1}^{N}$$

Where: Z is the dataset for training, and N is the number of giving learning samples.

The input x is a dimensional vector containing several fragments of information called features or attributes. This vector might be just columns with information related to the results, a simple image, a sequence of sentences, an email, a graph, a molecular form, or time series. Similarly, the y vector is the label, which could be a nominal or categorical vector.

$$y_i \epsilon \{1, \ldots \ldots, h\}$$

Supervised learning is considered a regression problem if y_i represent a continuous variable; the ML aims to predict the y_i given a x_i. On the contrary, classification problems deal with categorization. The ML problem is to classify y_i event with a given x_i. Many popular ML models, including linear and logistic regressors and classifiers, Support Vector Machines (SVMs), Nearest Neighbours (NNs), Decision Trees (DTs), Random Forests (RFs), Neural Networks (NNs), and Extreme Gradient Boosting (XGB), all have their roots in the supervised learning paradigm (James et al., 2013; Murphy, 2012).

5.3 Unsupervised learning

Unsupervised learning is suitable for clustering and descriptive research; it is mainly utilized to gain knowledge from a given dataset. The ML goals to establish or recognize existing patterns within a given $Z = \{(x_i)\}_{i=1}^{N}$. Since the z vector does not contain the corrected answers. As a result, the ML could not be evaluated like supervised learning would have due to the absence of the truth vector. Supervised learning is the foundation of many well-known ML models, such as K mean and hierarchical clustering, Density-Based Spatial Clustering of Applications with Noise (DBSCAN), and Principal Component Analysis (PCA) (James et al., 2013; Murphy, 2012).

5.4 Reinforcement Learning

In contrast to supervised and unsupervised learning, this sort of learning uses trial and error to identify the most effective outcomes. The fields of game design, robotics education, and autonomous vehicles all rely heavily on this kind of learning (Sutton & Barto, 2018). The learning procedures are entirely autonomous, based on the rewards or actions from each learning phase.

Reinforcement learning uses techniques like Monte Carlo and deep neural networks (Duda et al., 2000; Sutton & Barto, 2018).

5.5 ML classification and regression models

This part briefly summarizes some of the ML algorithms utilized and investigated in this thesis. Most of these ML models could be used for classification or regression tasks. Chapter 6 illustrates the methodological research implementations of the ML models applied through. The ML algorithms outcomes comparison interpretation and discussions can be found in Chapters 7 and 8.

5.5.1 Linear model

Linear ML is considered one of the most popular supervised ML algorithms. The linear model is widely implemented in several applications that solve regression or classification tasks. In the case of regression, the linear ML attempts to predict results following a training phase on available data. When it comes to classifying new events regards, utilizing ML for classification problems; consequently, its goal is to build the decision boundary that will be used to place them in one of several preexisting categories (Borovcnik et al., 1991). Equation 5.1 represents the linear equations that can be used for classification or regression tasks.

$$y(x) = w^t x + \in \tag{5.1}$$

Where $w^t x$ signifies the scalar or the inner products of the weight and the input vectors. At the same time, $\in$ regards the classification tasks represent the classification error. Alternatively, the regression scenario $\in$ represents the residual mistake between the linear forecasts and the actual response values (Murphy, 2012; Svensen & Bishop, 2009).

5.5.2 Logistic model

Nelder and Wedderburn suggested this approach in 1972 as a way to apply linear regression to situations where it would not usually be appropriate (Nelder & Wedderburn, 1972). Equation 5.2 represents the relation between the probability outcome vector on the equation's right side, which always lies between zero and one. The linear input vector is on the left equation part (James et al., 2013).

$$\log\left(\frac{\mathcal{P}(x)}{1-\mathcal{P}(x)}\right) = \beta_0 + \beta_1 x \quad (5.2)$$

To sum up, depending on the probability, logistic classification is a classification method used to determine the probability of categorical value. In contrast, logistic regression is a regression method used for binary classification (Bishop & Nasrabadi, 2006; Swamynathan, 2019).

5.5.3 Polynomial model

Polynomial functions are used in the polynomial regression or classifier model as an ML model to fit a curve to a data set. In this paradigm, a polynomial function represents the connection between the input and target variables. Input-output relationships that do not follow a linear or logistic model could be modeled with the polynomial algorithm. The polynomial model can predict more complicated patterns in the data than linear regression, allowing for non-linear correlation between the independent. Equations 5.3, 5.4, and 5.5 represent the model's complexity, proportional to the polynomial degree (Bishop & Nasrabadi, 2006; Hastie et al., 2009a). Polynomials of increasing degrees are used to characterize different types of models; however, they are subjected to overfitting (Tan et al., 2016). A linear model has a degree of 1, a quadratic model has a degree of 2, a cubic model has a degree of 3, and the last equation represents the polynomial function with n degrees (Swamynathan, 2019).

$$Z = m_1 X + m_2 x^2 + c \quad (5.3)$$

$$Z = m_1 X + m_2 x^2 + m_3 x^3 + c \quad (5.4)$$

$$Z = m_1 X + m_2 x^2 + m_3 x^3 + \cdots + m_n x^n + c \quad (5.5)$$

5.5.4 Decision tree

A decision tree ML algorithm seeks to identify, at each node, the optimal data split that maximizes class separation or minimizes prediction error. Since decision trees are simple to read, they are popular for exploring data and demonstrating complicated relationships. They can also handle categorical and numerical data and resist outliers and null values. They, however, tend to overfit, particularly when the tree is permitted to expand excessively profoundly, and they can be sensitive

to minor changes in the data. Many methods are available for overcoming these limitations., including pruning, ensembling, and random forests (Tan et al., 2016).

The decision tree splitting relies upon measuring the impurity of the data, such as the Gini impurity or entropy, and choosing the split that reduces the impurity the most. The impurity term refers to heterogeneity in a set of examples or data points. In order to create homogeneous data clusters, the DT algorithm creates feature splitting through several tree nodes. Consequently, several approaches could be utilized to improve splitting efficiency or enhance homogeneity, such as the Gini impurity, which subtracts the squared probabilities of every dataset from 1, and the Gini impurity is determined. One result denotes the greatest impurity, where the data events are evenly distributed across all categories.

In contrast, if the Gini calculations show a zero value that denotes absolute purity, it illustrates that all data events fall into the same category. However, the Entropy mathematical perspective is based on adding the negative logarithm of the probabilities of each data category multiplied by their probabilities; similar to Gini, this approach leads to zero and one results. A decision tree's gain is the amount of impurity it eliminates when the data is partitioned according to some criterion.

Equations 5.6 and 5.7 represent the entropy and gain equation, respectively (Borovcnik et al., 1991; Buntine et al., 1992; Drummond & Holte, 2000; Duda et al., 2000; Peixeiro, 2019; Quinlan, 1986).

$$E(s) = -\sum_{i=1}^{k} p_{i\, log_k(pi)} \quad (5.6)$$

Where:

E: represent the entropy.

Pi: proportion of data of each class.

$$G(S,Q) = E(s) - \sum_{i=1}^{k} p_i\, E(S,Q_i) \quad (5.7)$$

Where:

$G(S,Q)$: denotes the information gained in the original data set due to Q feature splitting.

$E(s)$: entropy of the original data set.

Pi: proportion of data of each class.

$E(S, Q_i)$: entropy of the new split class of data.

5.5.5 Random Forest (RF)

Like the pre-mentioned ML algorithms, the random forest is a supervised learning model for regression and classification problems. The model's name indicates the methodological notions behind it. Mitigating over-fitting drawbacks regards the implementation of the decision tree model; the fundamental concept of random forest is to build multiple decision trees and then aggregate their results to obtain the final prediction with high precision that any individual decision tree that forms the forest. A randomly assigned sample of the training examples and a selected subset of the attributes are used to train each tree in the forest model. This method mitigates over-fitting, and the data and attributes used to create an individual tree in the model are varied (Borovcnik et al., 1991; James et al., 2013; Swamynathan, 2019; Tan et al., 2016). Rodríguez et al. (2006) represent the random forest methodology divided into the training and prediction phases.

- **Phase one (training):**

Considering

X: the training examples set's object.

Y: is the label of the training examples.

L: are the ensemble's total number of classifiers.

$\begin{cases} w_1 \\ . \\ . \\ w_2 \end{cases}$: the labels classes set.

Aimed at $i = 1 \ldots \ldots \ldots \ldots . L$

Prepare the matrix of rotation R_i^a where $R_i^a$is equal to

$$\begin{bmatrix} a_{i,1}^{1} a_{i,1}^{2} \dots \dots a_{i,1}^{M1} & 0 & \dots & 0 \\ 0 & a_{i,2}^{1} a_{i,2}^{2} \dots \dots a_{i,2}^{M2} & \dots & 0 \\ \vdots & \vdots & \ddots & \vdots \\ 0 & 0 & \dots & a_{i,k}^{1} a_{i,k}^{2} \dots \dots a_{i,k}^{Mk} \end{bmatrix}$$

Feature splitting to the K subset construction $F_{i,J} = for\ j = 1 \dots \dots \dots \dots . K$

For the j vector

Consider $X_{i,J}$ the dataset X for the feature in $F_{i,J}$

Remove from $X_{i,J}$ A random group of classes.

Select from $X_{i,J}$a bootstrap sample with 75 % as $\grave{X_{i,J}}$.

Applies the principal component analysis to the previous sample.

Arranging the $C_{i,J}\ for\ j = 1 \dots \dots \dots \dots . K$ in R_i^a Rotation matrix.

Build the G_i classifier by utilizing $(XR_i^a\ , \mathrm{Y})$ as a training example.

- **Phase two:**

For every entity x, the RF aims to assign x to the most confident class.

A random forest uses a collection of decision trees to produce a forecast based on the given dataset. After all the trees have made their predictions, the ultimate prediction is arrived at by a simple majority vote. Compared to other ML methods, Random Forest has many benefits. It has a high degree of accuracy and can process many input attributes without becoming overfitting. It also tolerates missing values and noisy data with ease. Compared to more straightforward models like linear regression, random forest training can be time-consuming, and the resulting output can be ambiguous (Rodríguez et al., 2006). More information regarding the algorithm's methodological background can be found (Rodríguez et al., 2006).

5.5.6 Extreme Gradient Boosting (XGB)

The extreme gradient boosting model is considered a broadly utilized machine learning algorithm. The model relies on an ensemble learning approach combining several weak models to create a robust model. The outputs of each weak classifier or regressor are consequently aggregated, resulting in improving the performance of the combined model. XGB relies on boosting the ensemble learning approach. This includes operating by sequentially learning base models so that each succeeding model concentrates on the instances with which the preceding models had difficulty. As the models are refined iteratively, the incorrectly classified cases are given extra weight at each phase. The model depends on the decision tree classifier. However, instead of performing the training concerning the actual figures or labelling, the model performs the training to minimize the residual with the gradient technique. Findings into feature importance are provided by XGBoost, which allows one to evaluate the relative importance of input variables for prediction. This capacity makes it easier to choose useful features and improves comprehension of the underlying data patterns. Additionally, XGBoost is capable of handling missing values in datasets by figuring out the best way to handle blank records while building the tree, eliminating the need for intensive data preprocessing (Chen et al., 2015; Chen & Guestrin, 2016; xgboost developers, 2022).

Additionally, the method has built-in cross-validation features that let users quickly assess and modify modelling hyperparameters. With a wide range of optimal solutions and assessment measures, it demonstrates versatility by enabling both classification and regression applications. As a result, users can customize XGBoost to meet their unique needs (XGBoost developers, 2022).

5.5.7 K Nearest Neighbours (KNN)

The KNN ML model belongs to the nearest neighbour's machine learning approach; this approach can be implemented in several ways, including, Nearest to the mean, K Nearest Neighbours, and the Naïve Bayes. These ML models could be utilized for several regression and classification tasks. Since this is the case, the NN ML model predicts or classes new entities to the most similar value in regression or the most similar category in classification tasks. As a result, KNN and the Nearest to the mean can improve classification and prediction accuracy. Regression decisions can be made

by considering the K entities most closely related to the prediction or classification boundaries. Alternatively, the nearest to the mean predicts or classifies entities according to the neighbouring mean clustering value. Various metrics, such as Euclidean and Manhattan distance, can be used to calculate how far away a new data point is from its closest neighbours (International Business Machines Corporation, 2022). The algorithm forecasts the value of a new data point in the context of regression by averaging the values of its k nearest neighbours (Duda et al., 2000; Hastie et al., 2009a).

NN group models are a simple and versatile ML algorithm utilized for non-linear and linear datasets. It is also efficient when the boundary of the decision is complicated and not easily separable employing a linear method. However, KNN can be computationally costly, especially when the data set is enormous. It requires computing the distance between the newest data point with respect to all the points in the training group (Borovcnik et al., 1991; James et al., 2013). Additionally, the choice of K can significantly impact the algorithms' performance, so it is vital to correctly choose a specified value for K. The K-nearest neighbour rule, developed by Fix and Hodges in 1951, is a non-parametric approach to classifying patterns. However, it is highly recommended to implement an odd K value for even categorizing tasks and to avoid choosing K values as multiple to the number of desired categories (Swamynathan, 2019).

5.5.8 Support Vector Machine (SVM)

Many researchers and practitioners turn to Support Vector Machine (SVM) as a robust and widespread ML technique for classification or regression analysis (Awad & Khanna, 2015). This technique falls under supervised learning, in which an ML algorithm uses training examples data to predict or categorize new data. An essential step in SVM's operation is constructing a classification boundary (hyperplane) that splits data into homogeneous groups. This method prefers boundary maximization by increasing the margin or the distance between the nearest data points in each class and the threshold. "Support Vector Machine" comes from "support vectors," which are the set of closest data points. The SVM approach is versatile enough to include linear and non-linear input by projecting it into a multidimensional space and then using a linear boundary to divide the data into classes (Cortes et al., 1995; Guyon et al., 2011). The kernel technique is used to affect this adjustment. Examples of kernels used in SVMs are linear,

polynomial, Radial Basis Function (RBF), and sigmoid (Mongillo, 2011; Schölkopf et al., 2002). SVM implementations have many parameters that must be set in addition to the premonition kernels (Guyon et al., 2011). SVM's capable of handling high-dimensional data and maintaining performance when there are multiple features in the dataset, and it is considered one of its main strengths (Schölkopf et al., 2002). Modifying the cost function used to improve the border can also deal with imbalanced datasets, in which the group is much more numerous than the others' optimization-based technique, making it computationally cost-efficient, even for massive datasets (Murphy, 2012).

Furthermore, SVM models are easily interpretable because they rely on the support vectors, not the entire dataset. Finally, SVMs are a powerful and flexible ML technique that can be applied to various problems in classification, regression, and anomaly detection. SVM is still a popular option for many applications in domains including biology, economics, and computer vision despite its drawbacks, such as its vulnerability to the selection of kernel function and the difficulties in readability for non-linear boundaries (Bishop & Nasrabadi, 2006; Hastie et al., 2009b).

The following formulas define the SVM soft margin:

$$minimize_{\ w,b,\xi} = \frac{1}{2} w^T w + C \sum_{i=1}^{m} \xi_i \tag{5.8}$$

Subjected to $y_i(w^T x_i + b) \geq 1 - \xi_i, \xi_i \geq 0, \quad for\ 1 \leq i \leq m$

Where w denotes the width of the margin, b denotes the bias, ξ indicates the slack variable that permits some unexpected events or mistakes to occur in the margin, and the trade-off margin width is shown by C value. The gamma (γ) hyperparameter can also be used for some SVM kernels. The gamma hyperparameter can control the model variance (SMOLA, 2004).

5.5.9 Autoregressive integrated moving average

A well-known time series forecasting method that integrates moving average, differencing, and autoregression components is the Autoregressive Integrated Moving Average (ARIMA) model. It is commonly used in forecasting data with temporal dependencies, such as environmental, financial, and economic variables. The ARIMA model, which belongs to the linear time series

models category, is well known for its ability to recognize complicated data patterns (Sneeuw et al., 2012; Van Le & Nishio, 2019; Ye et al., 2012).

Three parameters are involved in adjusting the model, which are p, d, and q

The "p" represents the order of autoregression in an ARIMA (p, d, q) model, which determines the number of lagged data for prediction. A more complicated model that makes predictions by considering more past data points has a higher "p" value. The autoregressive component is essential for modelling serial correlations because it helps to capture the memory and inertia displayed by the time series.

The time series data is differentiated as part of the integration process to make it stationary. Stationarity is a crucial presumption for many time series models, including ARIMA. A stationary time series means that the time series has a constant mean and variance value, and autocovariance over time makes the modelling scheme easier. The order of differencing used to achieve stationarity is represented by the parameter 'd', which eliminates trends or seasonality within the time series data. While the ‘q’ value showed how many lags of previous errors must be considered when determining the time series's prediction value (Box et al., 2011; Hyndman & Athanasopoulos, 2018).

The following is an ARIMA (p, d, q) model's generic equation:

$$y'_t = g + b_1 y'_{t-1} + b_2 y'_{t-2} + \cdots + b_p y'_{t-p} + r_1 \varepsilon_{t-1} + r_2 \varepsilon_{t-2} + \cdots + r_q \varepsilon_{t-q} + \varepsilon_t \quad (5.9)$$

where g is a constant, ε_t represents the noise, and y'_t Indicates that the series is differenced to ensure time-series stationarity. However, the parameters b_1 to b_q and r_1 to r_q having higher q values in b and r terms represent that the model needs to consider more historical data within differentiates processes and within the weighted moving average process, respectively—higher "q" results in a more complex model taking more prior errors for more accurate prediction. The moving average component aids in modelling and incorporating randomness and noise into the data.

The ARIMA model, which provides an adaptable framework to capture the numerous interactions in temporal data, is a valuable tool in time series analysis. Because it includes moving averages,

differencing, and autoregression components, it enables researchers and analysts to make precise predictions and learn essential things about the dynamics of complicated time series phenomena.

5.6 Python ML libraries

There is a wide variety of machine-learning Python libraries. Some libraries have open-source licenses, while others may require prepaid credits to implement. These libraries could be used across the various stages of ML, such as data preprocessing, ML system development, ML assessment and evaluation, and ML visualization and reporting. The examples provided in Section 5.6 are taken from commonly used libraries (Swamynathan, 2019).

Matplotlib is a package that allows users to create data visualizations with granular levels of information by utilizing a variety of low-level plotting algorithms (Matplotlib, 2023).

Seaborn is the name of a library that offers a variety of high-level visualization technologies in the context of creating data visualizations that are both useful and attractive (Seaborn, 2022; Waskom, 2021).

Plotly library is another visualization library that allows Python users to generate several graphs such as scatter and line plots, histograms, heatmaps, geo-maps, and others (Plotly, 2023).

NumPy is a library that supports massive, multiple-hierarchical arrays and matrices and various mathematical operations that can be utilized while working with various data structures (NumPy, 2023).

Pandas is a toolkit that allows users to manipulate and analyse enormous datasets easily, providing high-performance data structures and data analysis techniques that are also simple (Pandas, 2023).

Keras is a high-level Application Programming Interface (API) that appears at the top of TensorFlow and offers a user-friendly interface for constructing deep learning models (Keras, 2023).

PyTorch is a popular open package that Facebook initially designed. It offers a variety of methods and APIs that may be used for constructing and training deep learning architectures (Pytorch, 2023).

TensorFlow is a library made by researchers and is used for constructing deep learning models and their training. It offers various APIs for constructing and implementing models in various production scenarios (TensorFlow, 2023).

A library that offers a variety of supervised and unsupervised ML algorithms, in addition to features for model selection, evaluation, and the preprocessing of data, is called **scikit-learn**. This library is quiet, and the acronym for scikit-learn can be shortened to sklearn (Scikit-learn, 2023).

The **Python pickle** library is a built-in module that lets Python objects be serialized and deserialized. Serialization turns an object into a stream of bytes that can be saved in a file or sent over a network. On the other hand, deserialization is putting the object back together from the serialized byte stream (Python, 2023).

5.7 Metrics and models accuracy assessments

The ML cycle contains several steps or phases. However, it is crucial to answer the questions regards:

Is the applied model well-performing?

Or does the researcher add more complexity to the model, leading to model overfitting?

Or does the applied model extensively consume the resources?

The pre-mentioned questions could be investigated through different metrics; the advantages of existing the truth values in supervised learning can ease the model performance investigations. Consequently, the R-squared for the goodness of model fitting, root mean squared error, and the mean absolute error are several ways to utilize mathematical equations to assess the supervised ML regression tasks (Murphy, 2012). Regarding the supervised classification problems, several assessment metrics like accuracy, precision, recall, F1 score, confusion matrix, sensitivity, specificity, misclassification error, and Area Under the Receiver Operating Characteristic Curve (AUC-ROC) are only a few measures that can be used to evaluate a model's performance. Alternatively, unsupervised ML tasks aim for data grouping utilizing feature similarity. Accordingly, the model performance could be assessed through several metrics, such as silhouette,

homogeneity, and completeness scores. Similarly, some visualization methods include principal component analysis.

Overall, the task and the nature of the data used will determine the most appropriate evaluation strategy; the right approach must be taken to guarantee a consistent and reliable assessment of the ML model. Some supervised regression and classification matrices are illustrated below (Fawcett, 2006).

5.7.1 R^2 for the goodness of fit

R^2 represents statistical measurement with values ranging from zero to one; this measurement assesses the separation between the scatter points and the regression line. The higher R^2 values represent lower variances between the fitting regression line and the modeled data set. Inversely, small R^2 values indicate higher variances between the line of regression and the modeled data points. Equation 5.9 represents the mathematical equation utilized for obtaining R^2 values.

$$R^2 = 1 - \frac{\sum SSR}{\sum SST} \tag{5.9}$$

Where the $\sum SSR$ in the numerator indicates the total sum of square residuals and $\sum SST$ in the denominator refers to the summation of the squared deviations between the observed values and the average (mean) value (Swamynathan, 2019; Tan et al., 2016).

5.7.2 Root Mean Squared Error (RMSE)

The root-mean-squared error (RMSE) is a statistical metric that measures how near the prediction is to the actual value. The lower the RMSE, the higher the approximation of the model to the dataset. The average of the squared discrepancies between the observed and predicted observations is used to determine the RMSE. Equation 5.10 represents the mathematical equation utilized for obtaining RMSE values. Zero root-mean-squared error would indicate that the model fits the data perfectly, which is rarely the practice case.

$$RMSE = \sqrt{\frac{1}{n}\sum_{i=1}^{n}(y_i - \hat{y}_i)^2} \tag{5.10}$$

Where the n in indicates the total number of observations and $(y_i - \hat{y}_i)^2$is the squared of the differences between each entity and the mean value (Murphy, 2012; Swamynathan, 2019).

5.7.3 Mean Absolute Error (MAE)

The MAE statistic measures the discrepancy between the values observed and those predicted by a model. Similarly, RMSE is typically used to assess a regression model's accuracy, but instead of using the square of the differences, it uses the differences' absolute values. In conclusion, MAE measures the average size of the mistakes in a regression model. It is a helpful method of comparing the effectiveness of various models or assessing the general accuracy of a model's forecasts. In comparison to RMSE, MAE emphasizes the magnitude of severe prediction mistakes, whereas RMSE emphasizes the magnitude of prediction errors that are tiny but nonzero. The MAE calculation equation is shown in Equation 5.11.

$$MAE = \frac{1}{n}\sum_{i}^{n}|y_i - \hat{y}_i| \tag{5.11}$$

Where the n in indicates the total number of observations and the term $(y_i - \hat{y}_i)$ is the difference between each entity and the mean value (Swamynathan, 2019).

5.7.4 Prevalent employed performance indicators regarding the confusion matrix

A confusion table is constructed by analyzing a test data set's prediction and actual class labels. That is commonly utilized to measure the efficacy of a binary classification model. There are four elements in the matrix: True Positive (**TP**) indicates the number of examples where the matching between actual and model-predicted labels is established as positive, False Positive (**FP**) denotes the sample number that the model incorrectly predicts them as positive, but the actual label is negative, True Negative (**TN**) indicates the number of entities where the model predictions and actual label are both have a negative label, and lastly, the False Negative (**FN**) is the number of the samples having positive labels, and the model is incorrectly predicting them as negative (Fawcett, 2006). Table 5.1 illustrates the confusion matrix elements. The APL, ANL, PML, and NML abbreviations mean Actual Positive Label, Actual Negative Label, Positive Model label, and Negative Model label, respectively. Additionally, N indicates the total number of samples with

positive labels, while P is the total number of samples with negative labels (Murphy, 2012; Swamynathan, 2019).

Table 5.1 Confusion matrix elements. APL and ANL represent the actual positive and negative labels. PML and NML signify the ML model's positive and negative prediction labels. TP, TN, FP, and FN represent true positive, true negative, false positive, and false negative, respectively. P denotes the sum of positive events, while N signifies the total number of negative events.

Confusion matrix	**Actual labels**	
Model forecasts labels	**APL**	**ANL**
PML	**TP**	**FP**
NML	**FN**	**TN**
Total	**P**	**N**

Accordingly, several statistical measures are utilized to investigate the ML model's performance, similar to FP and TP rates, precision, accuracy, Recall a, and F-measure. Equations 5.12 to 5.17 show the mathematical formulas for the pre-mentioned performance indicators.

$$FP\ rate = FP\ /\ N \tag{5.12}$$

$$TP\ rate = TP\ /\ P \tag{5.13}$$

$$Precision = TP\ /\ (TP + FP) \tag{5.14}$$

$$Recall = TP\ /\ P \tag{5.15}$$

$$Accuracy = TP + TN\ /\ (P + N) \tag{5.16}$$

$$F - measure = 2 * Precision * Recall\ /\ (Precision + Recall) \tag{5.17}$$

Consequently, graphical indicators, such as receiver operating characteristics and area under the curve, can be constructed using the FP and TP rates. The FP rate represents the number of events the classifier misclassifies as positive events but belongs to the negative events class. In contracts, the TP represents the number of events that the classifier succeeds in classifying as positive events, and they belong to the positive class. The TP is also known as sensitivity. Additionally, the precision represents the ability of classifiers regarding positive predictions. The ability of

classifiers regarding the true positive and negative predictions, called accuracy, represents the classifier's overall accuracy. The F-measure is the combined metric that is considered more robust in terms of evaluating the model's ability regarding positive events.

A classifier's capabilities and limitations can be understood by examining these performance indicators, such as the FP rate, TP rate, precision, accuracy, and F-measure.

5.7.5 Receiver Operating Characteristics (ROC)

ROC is a graphical metric that investigates the ML model's performance. Changes to the model's classification thresholds, followed by the TP rate and FP rate calculations at each threshold, generate the ROC curve. The curve thus obtained illustrates how the relative values of TP rate and FP rate are varied as a function of threshold; accordingly, evaluation of classifiers trained with ML model. The ROC curve nearest to the top left corner of the graph indicates a high TP rate and a low FP rate throughout various threshold ranges. Equations 5.12 and 5.13 illustrate the TP and FP rates formulas (Fawcett, 2006; Murphy, 2012; Swamynathan, 2019).

5.7.6 Area Under Curve (AUC)

The AUC is a graphical metric relying on the ROC curve. This metric is based on calculating the area under the ROC curve. The area under the ROC curve plots the TP rate on the y-axis against the FP rate on the x-axis. Consequently, AUC is measured. As a result, there is a direct correlation between the AUC and classifier performance. The maximum AUC value is one, and as much the ROC has an area near one, this indicates a likely highly accurate classifier. AUC values close to 0.5 demonstrate that the classifier is no more effective than random classifiers.

Accordingly, whenever there is an imbalanced distribution of class entities, the AUC is a helpful metric for assessing the performance of binary classification techniques. Since it provides a single score that sums up the model's overall performance, it is also a common metric for identifying the suitable model from a set of investigated models (Fawcett, 2006; Murphy, 2012; Swamynathan, 2019).

Eventually, it is worth highlighting that the above metrics' values range between one and zero. The optimum values for measures like false positive rate, true positive rate, precision, and accuracy in

machine learning techniques depend on the specific problem that research is attempting to solve, and there is no general "optimal" value for these metrics. The recommended values vary according to the nature of the data and the accuracy balance that the researcher will make.

5.8 GNSS ML applications

Recently, there has been an expansion in the prevalence of solutions that combine ML and GNSS. As a result of these solutions, GNSS models are more precise, trustworthy, and stable than ever before, and the use of GNSS has expanded greatly without the typical GNSS restrictions. Many researchers have investigated combining GNSS and ML in several domains, such as seismic applications, geoid modelling, indoor and outdoor applications, multipath mitigation, GNSS error prediction and outlier detections, location-based services, and human mobility, and widely in the domain of signal spoofing and antijamming techniques, and water vapor. In recent years, researchers' attention has been focused on how to combine ML with GNSS. Here, we will cover some recent research that has integrated ML with GNSS.

Gitis et al. (2021) analyse the GPS time series data for Japan and California regions. The study aims to predict earthquakes using the time series coordinates movement investigations. Gitis et al. (2021) associated comparison for earthquake prediction. Several models have been investigated, such as random forecast, spatial density, spatial-temporal GPS, and seismic data. The research applied methodology includes training the models with time series and earth catalogue data and eventually creating the spatio-temporal alarm map for earthquakes that have a magnitude greater than 5.5 on the Richter scale. The research was conducted to answer the following questions:

a) Will earthquakes be reliably predicted using space geodesy data? Furthermore, b) Does adding spatial geodesy data to seismological data enhance earthquake forecasting? The research concludes that earthquakes can be reliably predicted using GPS data (Gitis et al., 2021).

GUARDIAN is a near RT system utilized in Pacific regions for initiating Tsunami alerts. Akyol et al. (2020) examined using ionospheric data and ML to predict earthquakes. The study techniques are based on the SVM to determine if a spatial or temporal ionospheric anomaly is associated with a potential earthquake trigger. The applied technique provides the model with an ability of around 80 percent for earthquake detection (Akyol et al., 2020).

Typical Geoid model calculation uses the least-squared, polynomial fitting, and finite element methods to fit a gravimetric geoid model to GPS\levelling points to improve precision and accuracy. Several studies implemented ML models to improve the Geoid model's accuracy. These researchers, for instance, applied artificial neural networks, Minimax Probability Machines (MPM), Gaussian Process Regressions (GPR), SVM, and multivariate adaptive regression splines. The studies confirmed the ability of ML models to improve the Geoid model results (Kaloop et al., 2022; Kavzoglu & Saka, 2005; Zaletnyik et al., 2008).

Inertial Navigation Systems (INS) have been widely used in GNSS-dependent applications. Accelerometers, gyroscopes, inertial measurement units, micro-controllers, and other components are all found within an INS system. Moving objects' position, velocity, and altitude can be better calculated when the INS and GNSS are combined. In recent years, numerous ML methods have played critical roles in enhancing positional precision in geographically ambiguous times, such as when GNSS is unavailable. Xu et al. (2010) investigated the least-squared SVM and Kalman filter as integrator methods for GPS and INS. The study found that SVM can avoid overfitting problems, as studied through the research study (Xu et al., 2010).

Similarly, Wang et al. (2018) proposed a novel extreme ML that relies on fading filter and comparing the results with commonly used neural learning networks, including several inputs, hidden and outputs layers. According to the research, GPS outages reduce the navigation system's accuracy, but the new approach outperforms traditional neural network learning algorithms regarding positioning accuracy and learning speed (Wang et al., 2018). Accordingly, some applications could take advantage of the pre-mentioned combinations. The research regarding UAV flight controls demonstrated that the adaptive Kalman filter with random forest and fuzzy logic could classify GNSS accuracy more accurately than the others. Comparing the onboard solution to the overall positioning result obtained in this study showed an accuracy improvement of almost 50% (Zhang & Hsu, 2018).

Some GNSS signal-domain applications have also enhanced from the recent rise of machine and deep learning. Several studies investigated the multiple approaches to mitigate multipath error. Modelling this error source is challenging since it is closely correlated to the environment and

fluctuates with satellite elevation angles. Because of this, several GNSS manufacturers shield their products from the reflected signals. Accordingly, Orabi et al. (2020) proposed a neural network model that relies on features such as signal time delay and power attenuation. The proposed model was inspected in a challenging multipath environment. The study confirmed that the proposed deep learning model is more accurate than traditional methods (Orabi et al., 2020). Previously, Quan et al. (2018) applied convolution neural networks to improve high GNSS precision applications. The study concluded that 80% of multipath measurements could be detected, leading to coordinates accuracy improvement with around 18 to 30 % (Quan et al., 2018).

Similarly, there is a proposed approach called "Time-Frequency and Convolution Neural Networks." The approach was trained in concrete roofs, grass, shrubs, water bodies, and near glassy buildings; the research showed that the applied approach could enhance the monitoring of GNSS applications (Tao et al., 2021). The SVM is similarly utilized as an ML classifier to detect multipath signals (Suzuki & Amano, 2021).

Multiple machine-learning approaches and efforts have been aimed at increasing GNSS precision under extreme conditions. One such method was applying a bagging tree-based algorithm to adjust the range measurements based on a prediction of the pseudorange error derived from the signal-to-noise ratio and the satellite elevation angles (Qin et al., 2021). Other methods include long-short time memory and recurrent neural network learning models in GNSS error prediction (Yang et al., 2019). Alternatively, an artificial neural network as a map-matching model could be utilized to avoid the GNSS drawbacks in urban canyons (Hashemi & Karimi, 2016).

Numerous sensors, such as gyroscopes, accelerometers, inertial measurement units, and GNSS sensors, are used in mobile devices nowadays. Recent advances in ML and the extraction of mobile sensor observations have piqued the interest of many academics and opened up a wide range of potential new uses for mobile device usage. Accordingly, numerous investigations have been carried out on utilizing ML approaches as learning methods to understand, classify, and predict daily human activities (Lee & Kwan, 2018; Tanaka et al., 2015; Zheng et al., 2008). Additionally, the GNSS and ML techniques have been examined in transportation domains; vehicles and human trajectory recognition, travel time forecasting, transportation classification, and traffic flow

predictions are examples where GNSS, smartphones, and ML could be exploited (Hofleitner et al., 2012; Qi et al., 2014; Wang et al., 2018).

GNSS signals face many challenges, including interference, jamming, and spoofing; still, besides encrypting, the GNSS signals fake signals affect the GNSS systems. These challenges could lead to severe problems for some applications such as automated vehicles, UAVs, the safety of life applications, and traffic fleet management. Consequently, ML has been utilized to predict or classify the hacked signals; Accordingly, the protection of the GNSS could be improved (Campos et al., 2020; Gallardo & Yuste, 2020; Manesh et al., 2019; Wang et al., 2021; Wang et al., 2020; Wei et al., 2022; Yang et al., 2022).

5.9 Harnessing the power of machine learning in establishing robust early warning systems

The disaster risks can be significantly reduced with the help of Early Warning Systems (EWS). They are crucial resources for early warning of impending danger in order to implement preventative measures in high-risk areas. EWS systems provide early warnings, allowing communities to organize efficient responses and reduce losses across the public and private sectors. When it comes to saving lives and limiting financial damage, early warnings take center stage. The time before the destruction begins is a crucial opportunity for taking precautions and stepping up preparations, as the research utilizes the RT-PPP measurements in establishing the EWS to detect the deformations and initiating early warnings through a series of experiments. The RT-PPP experiments enrich the research with a considerable database containing abroad features with entities that vary in accuracy, the direction of deformations, the number of satellites used, the utilized corrections streams, and other features. Machine learning provides several advantages in establishing the RT-PPP EWS, including improving EWS accuracy, providing different metrics to evaluate EWS performance, and providing the ability to handle a high feature-space database, automation, and feature importance analysis.

Machine learning has many benefits overall, notably automation of decision-making, productivity, pattern recognition, increased accuracy, handling complexity, adaptation, customization, continuous improvement, scalability, and flexibility. These advantages make machine learning an

effective tool for many different industries and applications, fostering innovation and enhancing decision-making.

Chapter 6 Research Methodology

6.1 Introduction

The primary objective of this chapter is to provide a comprehensive account of the main work packages and stages employed in this study. All research stages were carefully planned to address the research questions. These main stages encompassed an inquiry into research novelty and a literature review, followed by an examination of the potential beneficiaries of the research. The investigation covered the improvement of RT satellite corrections caused by the latency as one of the main reasons for not accurate and precise results in the RT-PPP, and developing and exploring the EWS as a tool for mitigating various natural hazards. As a result, several investigations have been conducted, including selecting IGS combined satellite corrections and assessing the impact of latency on RT-PPP coordinates (IGS, 2020a).

Subsequently, in the first section of this chapter, various ML approaches were explored to mitigate the latency values. The primary focus of this investigation was to evaluate the performance of these approaches by applying various parameters such as signal analysis, data splitting, and data cleaning. The model's performance was assessed using statistical tests to compare the actual clock corrections and IGS station coordinates with the model's predicted values and IGS station coordinates.

The following section of this chapter centers on the investigations conducted to establish an EWS. The initial step was designed to test the performance of RT-PPP under various elevation mask angles and different combinations of GNSS constellations and corrections. Next, a platform was developed to simulate deformations, and numerous experiments were conducted to replicate natural deformation events. These experiments encompassed variations in deformation magnitudes, directions, and elevation mask angles. Daily GNSS measurements were collected with simulated deformations, designing and developing a platform to gather vast amounts of data for training ML models; this was followed by determining experiment variables, including dependent, independent, extraneous, and control variables. Subsequently, different phases were implemented to clean, repair, and prepare the stored GNSS observations, including data labelling. The accuracy and integrity of the applied ML approaches were then assessed. This phase extended to investigate

different accuracy metrics (Fawcett, 2006), including several probabilities, such as the probability of true, false, and out-of-service detections. In order to make the research findings more easily reproducible, each of the stages that were discussed previously will now be broken down into their respective sections. An overview of the research methodology is illustrated in Figure 6.1.

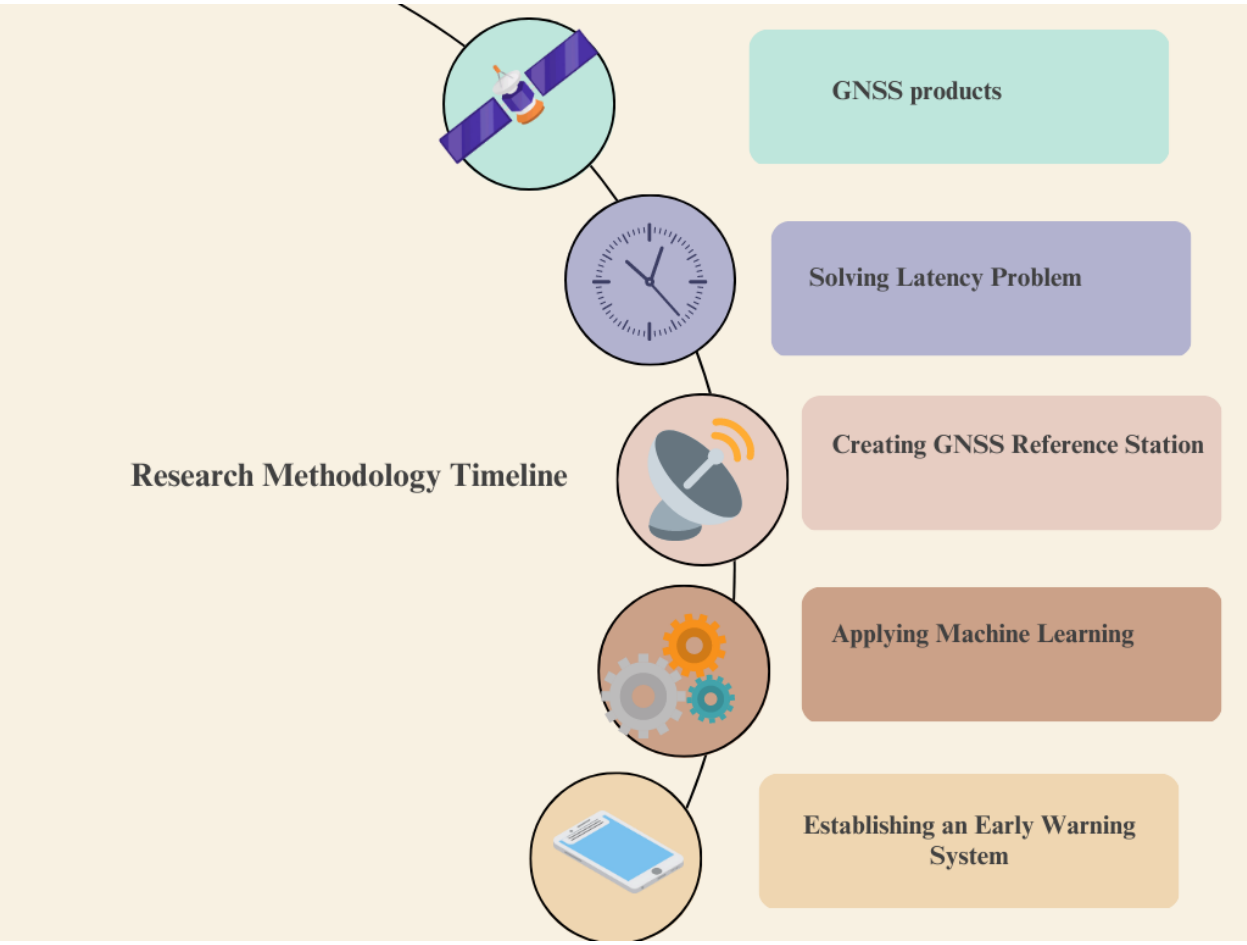

Figure 6.1 Research milestones

(Prepared by the author).

6.2 Research methodology concerning the reduction of latency impact of GNSS products in real-time precise point positioning technique

RT-PPP is widely adopted as a positioning technique due to several advantages (Bezcioglu et al., 2019; Odijk et al., 2015; Teunissen & Khodabandeh, 2015) that were presented in previous chapters. However, this method faces various challenges, including signal and correction interruptions, ambiguity resolutions, computational requirements, specialized software, and data latency. This chapter specifically focuses on the methodological perspective utilized in this research to overcome the latency problem (Martín et al., 2013; Qafisheh et al., 2022; Qafisheh, 2020). In RT-PPP, the SSR products must be expeditiously transmitted from ACs or IGS to GNSS users. Any delay in transferring data and products may result in extending the delivery time period, leading to the utilization of outdated corrections and, consequently, inaccurate positioning coordinates. The latency impact can significantly degrade the RT-PPP corrections, initialization time, and final RT coordinates.

Consequently, several studies confirmed the latency effect of coordinates accuracy and availability latency. Forty seconds of latency could lead to more than half a meter regarding the driven RT coordinates (Martín et al., 2013). Moreover, the latency also impacts the availability of RT-PPP solutions (Hadas & Bosy, 2014; Qafisheh et al., 2022). Furthermore, the research highlights significant concerns regarding the impact of latency, not only on RT-PPP measurements but also on the performance of RT-PPP EWS.

The BNC software can extract and store the correction stream latency value. Therefore, it was considered as an ML time-series training feature. Consequently, this led the research to train the ML models with high and low latency correction streams with the idea of predicting the actual correction stream value (no latency) using previous values (values received on the user side with latency).

Several ACs offer RT corrections, which consist of SSR products with necessary information such as satellite phase and code biases, satellite orbital and clock corrections, and ionospheric modelling (IGS, 2020b). However, latency affects all of the corrections, as mentioned above. In particular, due to the onboard satellite clock's inherent nature, it is necessary to transmit the clock corrections

with a high sampling rate to mitigate satellite clock instability, frequency fluctuations, and oscillations. Satellite phase and code biases, satellite orbital parameters, or ionospheric modelling are transmitted with a low sampling rate (several minutes), so the impact of latency is not as critical as satellite clock corrections are. Figure 6.2 summarizes the flow chart of the implemented research work packages and phases.

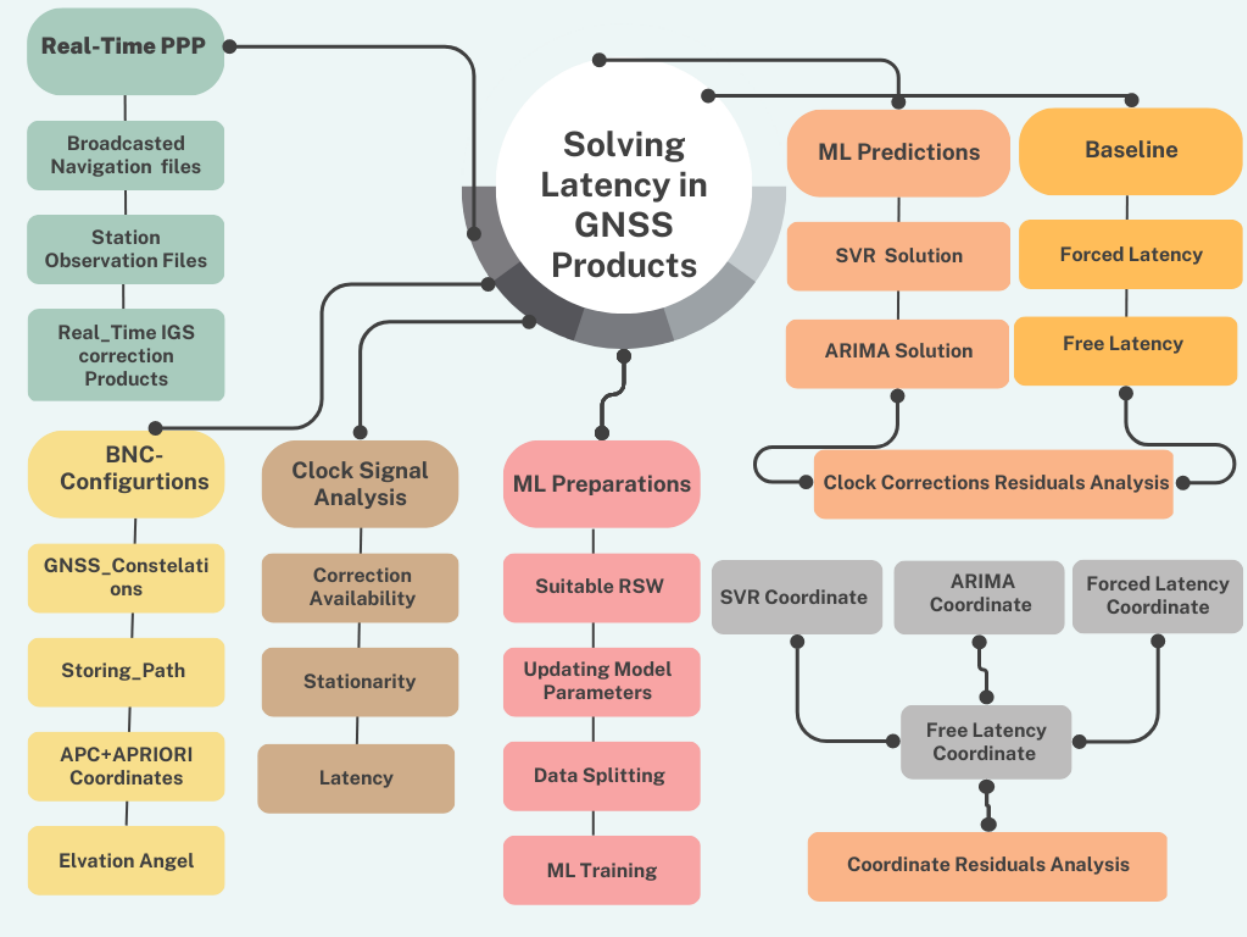

Figure 6.2 Solving latency flowchart

(Prepared by the author).

The following work packages and phases were implemented in this research regarding solving latency:

6.2.1 Work package 1 (RT-PPP data acquisition)

The first work package was designed to obtain RT-PPP observations. The BNC software and its C++ complementary library were utilized in this package. The following phases were implemented in RT mode.

- ❖ Phase 1:

This phase chooses the IGS/ACs correction as the official IGS/ACs correction product. In the case of the IGS, it delivers orbital corrections, code biases, and clock corrections at one-minute intervals and ten-second intervals, respectively. The four GNSS constellations (GPS, Galileo, BeiDou, and GLONASS) are now supported by IGS corrections.

- ❖ Phase 2:

The BNC software was implemented in RT-PPP mode in the next stage using IGS03 correction streams. At the same time, several IGS permanent stations were selected, namely, NYA1, HOFN, UNBJ, BRST, ANKR, REUN, NTUS, THU2, and KERG. Table 6.1 provides approximate locations, the station's name, and the station's country.

Table 6.1 Research IGS selected stations.

St.name	φ	λ	Link to the station's log file	Country
BREST	48.38	-4.497	https://www.igs.org/imaps/station.php?id=BRST00FRA	France
ABMF	16.262	-61.528	https://www.igs.org/imaps/station.php?id=ABMF00GLP	Guadeloupe
REUN	-21.208	55.572	https://www.igs.org/imaps/station.php?id=REUN00REU	France
ANKR	39.888	32.759	https://www.igs.org/imaps/station.php?id=ANKR00TUR	Turkey
UNBJ	45.95	-66.642	https://www.igs.org/imaps/station.php?id=UNBJ00CAN	Canada
HOFN	64.267	-15.198	https://www.igs.org/imaps/station.php?id=HOFN00ISL	Iceland
KERG	-49.351	70.256	https://www.igs.org/imaps/station.php?id=KERG00ATF	France
NTUS	1.346	103.68	https://www.igs.org/imaps/station.php?id=NTUS00SGP	Singapore
NYA1	78.93	11.865	https://www.igs.org/imaps/station.php?id=NYA100NOR	Norway
THU2	76.537	-68.82	https://www.igs.org/imaps/station.php?id=THU200GRL	Greenland

The stations listed in the previous table were selected to be globally distributed to examine the proposed study methodology. Figure 6.3 provides a map showing the selected IGS stations.

❖ Phase 3:

Several trials were conducted to acquire RT-PPP data for the research; the first pilot test began on 13th December 2019 and lasted three days. For three days, the BRST station acquired continuous RT-PPP observations; simultaneously, the correction stream values and the navigation files were stored for the research investigations.

The study then expanded to include more stations over an extended period to check the evolution of the IGS/ACs products. That explains why the research utilized archived RT-PPP for the prementioned IGS stations during 2013, 2014, 2015, 2019, and 2021. As a result, the suggested approach to solving the latency problem could be tested with multiple stations at various times. With this analysis, it is possible to thoroughly assess the performance of ML prediction models.

Consequently, one day was selected from the pre-mentioned years. Table 6.2 shows the station's names and the data availability during the research days. The THU200GRL was eliminated from investigations due to data unavailability in 2019 and to provide consistency through the research years. The selected IGS stations and IGS03 correction stream have been added to the stream canvas after selecting the required streams, including IGS stations, broadcast navigation, and target correction streams.

Table 6.2 Stations names and data availability.

Station	29/10/2013	13/01/2014	25/02/2015	14/12/2019	21/05/2021
BRST00FRA	√	√	√	√	√
ABMF00GLP	√	√	√	√	√
REUN00REU	√	√	√	√	√
ANKR00TUR	√	√	√	√	√
UNBJ00CAN	√	√	√	√	√
HOFN00ISL	√	√	√	√	√
KERG00ATF	√	√	√	√	√
NTUS00SGP	√	√	√	√	√
NYA100NOR	√	√	√	√	√
THU200GRL	√	√	√	X	√

Figure 6.3 The research selected IGS stations

(Prepared by the author).

6.2.2 Work package 2 (BNC configurations)

The second work package provided the utilized software with all required parameters. The following details describe the current work package's steps and configurations.

The current work package provided the BNC software with all the parameters to operate in the RT mode. The BNC setup folder usually contains several configuration setup examples. The

09_PPPNet.bnc configured example was re-configured with the prior station's coordinates. Additionally, to correct the RTCM observations, the APC offsets and variations were provided to the BNC through the IGS ANTEX file. IGS provides access to several files, including the IGS antex, found at https://files.igs.org/pub/station/general/.

Further arrangements were made regarding the GNSS constellations, which included the selection of codes and phase observation for GPS and GLONASS. During the implementation of the experiments, corrections for the GNSS constellations mentioned above were provided by the IGS03 product. Another aspect of the research focused on selecting an appropriate minimum elevation angle mask for satellites. Based on recommendations from the BNC and other researchers, an elevation angle of 10 degrees was selected to avoid noisy code and phase observations from GNSS satellites with 10 degrees or lower elevation angles (Weber & Mervart, 2007; Wu et al., 2021)

The later stage was designed to provide BNC with the required paths for the sake of storing broadcasted corrections, the RINEX station's observation files, broadcasted navigation files, the latency value, and the RT-PPP station's coordinates for further implementation (German Federal Agency for Cartography and Geodesy, 2022; Weber & Mervart, 2007).

6.2.3 Work package 3 (ML training and clock correction analysis)

The third work package includes several phases regarding the implementation of the ML models. The phases were distributed to cover investigations regarding choosing the appropriate machine learning algorithms and the suitable Rolling Sliding Window (RSW) length to train the ML prediction models—a selection of the suitable periodic time to update the prediction model parameters. Furthermore, several tasks focused on investigating the stationarity and the availability of the clock correction signals.

- Phase 1:

The process of choosing appropriate ML algorithms requires statistical analysis to perform a stationary evaluation of the temporal signal, which is usually called as time series forecasting. If the signal exhibits stability, i.e., the absence of trends, seasonality, or cyclical patterns, a significant proportion of ML algorithms, including decision trees, neural networks, and XGB, cannot be used

since those methods cannot predict future values in a time series forecasting (Hyndman & Athanasopoulos,2018). The predicted values are indistinguishable from the most recent observation in such scenarios, because the best probability for the next value is simply as the previous observation value. Accordingly, the Kwiatkowski–Phillips–Schmidt–Shin (KPSS) statistical test was applied for 8 minutes RSW for various GNSS satellite blocks (Kwiatkowski et al., 1992). Table 6.3 shows the percentages of the RSW with or without stationary behavior. It is worth mentioning that this test was investigated in the sample of the data collected from the 2019 prementioned pilot experiment.

Finally, the intended interpretability of the model, the amount of available data, the intricacy of the relationships within the data, and the dataset's features all help determine the best model to use. The SVM, linear regression and ARIMA models are suitable to be utilized over stationary time series data (Box et al., 2015; Hyndman & Athanasopoulos, 2018). So, they are used in this research. It is worth mentioning that the ARIMA considers enhanced linear regression as it considers both the error and data trend of the trained and tested data.

Table 6.3 Clock correction and stationarity behavior.

Satellite Block	Percentage of periods with stationarity behavior	Percentage of periods with non-stationarity behavior
IIF	76.99	23.01
IIR	88.28	11.72
IIRM	89.64	10.36
K	62.11	37.89
M	61.02	38.98

- Phase 2:

Further analysis in this phase was established concerning investigating the availability of satellite clock corrections. During this phase, the archived satellite clock corrections were investigated to check the availability of the clock corrections (IGS, 2020). The RT corrections experienced times of outages and interruptions. As a consequence, it produces an unavailability of RT-PPP solutions. During this phase, one day was selected for each year of the archived RT corrections to examine the outages of clock corrections.

- Phase 3:

The Python script was utilized during this phase in order to examine the latency value of the stored broadcasted IGS03 correction. The results showed that the average latency for the IGS03 SSR stream is 31.6 seconds, with maximum and minimum values of 32.2 and 31.3 seconds, respectively. This investigation was carried out on the data obtained during three days of continuous RT-PPP measurements starting from 13th December 2019.

6.2.4 Work package 4 (ML prediction/implementation)

The fourth work package was devoted to construction solutions from the prediction models, and a simulation latency solution was created.

- Phase 1:

The same pilot study data set is again examined during this phase to check the suitable RSW length for SVR and ARIMA. Several RSWs with lengths of 1,2,4,8, and 16 minutes were examined. On Wednesday, 13th December 2019, the one hour of clock corrections in this experiment was examined. The research establishes four solutions in the current phase; thus, the simulation of the following scenarios was constructed: the latency-free solution, which reflects the ideal situation where the clock correction is delivered to the users without latency. The forced latency solution was the clock correction delivered to the GNSS users with a stream latency of 30 seconds for the combined product and 15 seconds for the ACs products. It is worth mentioning that this solution simulates a typical RT-PPP situation; thus, the BNC software post-processing the RT-PPP files where the latency value has been added artificially. On the contrary, the ARIMA and SVR solutions are emulating scenarios if the GNSS users consider utilizing the ML prediction models to overcome the latency.

The standard deviation of the clock correction residuals derived by subtracting the forced latency and SVR and ARIMA forecasts with respect to the free latency have been calculated. The STDP denotes the standard deviation of the subtracted clock correction among the ML prediction models with respect to the free latency, and STDL signifies the standard deviation of the subtracted clock correction among the forced latency with respect to the free latency. Results show that an RSW of

8 minutes for the ARIMA model and 1 minute for the SVR model is a practical trade-off between prediction accuracy and processing time.

As a summary, the main results of this phase (extensively founded and explained in the next chapter) can be found in Tables 6.4 and 6.5, where the standard deviations of the prediction models with the forced latency solution with free latency solutions are compared.

Table 6.4 ARIMA prediction standard deviations in comparison with a free-latency solution.

Satellite PRN		**RSW duration in minutes**				
		1	**2**	**4**	**8**	**16**
G32/IIF	STDP	0.015	0.016	0.016	0.009	0.012
	STDL	0.016	0.016	0.016	0.016	0.015
		Required processing time in seconds				
		2m56s	4m35s	4m40s	5m26s	6m16s
G05/IIRM	STDP	0.040	0.036	0.033	0.024	0.024
	STDL	0.040	0.040	0.040	0.041	0.041
		Required processing time in seconds				
		3m20s	6m45s	7m02s	7m46s	10m59s
G23/IIR	STDP	0.016	0.015	0.013	0.010	0.007
	STDL	0.017	0.017	0.017	0.017	0.017
		Required processing time in seconds				
		3m34s	6m13s	6m52s	7m04s	8m39s
R09/K	STDP	0.026	0.026	0.019	0.016	0.015
	STDL	0.028	0.028	0.028	0.030	0.029
		Required processing time in seconds				
		2m45s	4m18s	3m54s	4m13s	5m13s
R15/M	STDP	0.014	0.016	0.012	0.022	0.019
	STDL	0.016	0.016	0.016	0.028	0.027
		Required processing time in seconds				
		2m41s	4m59s	5m02s	4m53s	4m58s

Table 6.5 SVR prediction standard deviations in comparison with a no-latency solution.

Satellite PRN		RSW duration in minutes				
		1	**2**	**4**	**8**	**16**
G32/IIF	STDP	0.011	0.016	0.022	0.029	0.034
	STDL	0.016	0.016	0.016	0.016	0.015
		Required processing time in seconds				
		20s	20s	21s	24s	26s
G05/IIRM	STDP	0.027	0.033	0.039	0.047	0.051
	STDL	0.040	0.040	0.040	0.041	0.041
		Required processing time in seconds				
		20s	20s	21s	24s	25s
G23/IIR	STDP	0.012	0.018	0.025	0.028	0.031
	STDL	0.017	0.017	0.017	0.017	0.017
		Required processing time in seconds				
		20s	20s	15s	23s	26s
R09/K	STDP	0.018	0.025	0.031	0.041	0.058
	STDL	0.028	0.028	0.028	0.030	0.029
		Required processing time in seconds				
		20s	20s	21s	23s	25s
R15/M	STDP	0.010	0.015	0.023	0.041	0.051
	STDL	0.016	0.016	0.016	0.028	0.027
		Required processing time in seconds				
		20s	23s	20s	23s	26s

- Phase 2:

This phase established prediction model parameterization updating. Based on stored data, the prediction model architecture should be upgraded by searching and modifying optimal hyperparameters. The goal is to find the optimal update frequency for the hyperparameters. Subsequently, the optimal values for those hyperparameters can be determined. Accordingly, this resulted in evaluating predictive performance with various combinations of C and gamma hyperparameters in the SVR model and (p, p, d) in the ARIMA model. Therefore, the research investigating usage-wide hyperparameter dimensionality in both models for more reliable forecasts (Piccolo, 1990).

In SVR, a high C value suggests the model does not allow faults to violate the margin, reducing the margin; the lower it is, the more faults' values are allowed. In order to regulate interpolation and extrapolation behaviour, the gamma parameter controls the Gaussian function's variance (Guyon et al. 1993). p regulates the number of lags needed for linear regression, d regulates the

level of differencing needed for signal stationarity, and q manages signal error propagation in the Model parameters (Clarkson et al., 2012; Drucker et al., 1997).

As a summary of this phase, it can be concluded that choosing the optimal automatic update frequency for hyperparameters is a task that should follow the prediction model implementation. From 13th to 16th December 2019, the updating intervals of 0.25, 0.50, 1, 2, 3, 4, and 6 hours were evaluated. The experiments led to the choice of a one-hour refresh rate for SVR. The set of hyperparameters to determine in the SVR method might be quite broad to ensure that the correct values are chosen parameters. An hourly rate maintains a proper balance between calculation time and accuracy. The list of ARIMA model hyperparameters is relatively short—it ranges from 0 to 3 for the p and d parameters and from 0 to 1 for the q parameter. Because of this, finding hyperparameters is a quick process, and fixing them takes eight minutes of calculation time (Schölkopf et al., 2002; Smola & Schölkopf, 2004). The research considers utilizing the default initialization parameters for both models' unit time reaches 8 minutes in the case of utilization of the ARIMA model. However, the utilization of the default initialization parameters was extended to one hour if the GNSS user relied on the SVR model. It is worth mentioning that the research utilized RSW to train and update the utilized parameters for ML prediction models; this could be justified firstly, the RSW is suitable for clock corrections as new and relevant data are incorporated to improve the prediction and parameter selection accuracy, and secondly, the RSW dropped the outdated clock corrections. In addition, this overcomes the disadvantages if the expanding, fixed-size, overlapping, and thumbing windows have been utilized.

6.2.5 Work package 5 (Prediction and solution creation)

The last work package improves the ML model's performance through several investigations regarding the mode of training, hyperparameter selection, and determining the updating rate of those parameters. The following steps in the current work package deal with predicting the clock corrections. By implementing SVR and ARIMA.

- Phase 1:

The preselected RSWs were utilized for training the ML prediction models. Accordingly, the ARIMA and SVR models predicted the clock correction within 30 seconds to overcome the latency. The selected IGS station and the research day are described in Tables 6.1 and 6.2.

- Phase 2:

Three correction files were created to hold the clock corrections: **ARIMA, SVR, and forced latency**. The first two files hold the new predictions regarding the clock corrections. However, the last file holds the shifted values simulating the latency impact.

- Phase 3:

The last phase paves the road to statistically assessing the ML model's performance. Accordingly, the residuals were calculated from the ARIMA, SVR, and forced latency for the RT corrections without the latency impacts. Consequently, the next chapter illustrates the results in terms of comparisons regarding the standard deviation and the range concerning the pre-mentioned solutions.

6.2.6 Work package 6 (RT-PPP coordinates assessment)

The final work package focused on investigating the impact of the pre-mentioned solutions on RT-PPP coordinates; thus, the BNC software was configured with stored navigation, observation, and four solutions stored files to operate in post-processed mode (Weber & Mervart, 2007).

- Phase 1:

The observation, navigation, and RT correction were acquired from the IGS archived data covering the research years and IGS stations in the current phase. The BNC is configured to implement the RT-PPP with post-proceed mode. Consequently, the BNC was provided with the path to store RT-PPP coordinates. Accordingly, four coordinate solutions were created through the current phase. Namely, SVR and Arima's prediction coordinate solutions and forced and free latency coordinate solutions.

- Phase 2:

The last phase in the current work package was designed to provide the coordinate residuals by subtracting the solution coordinates from the corresponding free-latency RT coordinates (ideal solution). Consequently, that yields to have residuals for several solutions. Chapter 7 illustrates the results in terms of comparisons regarding the standard deviation and the range concerning the pre-mentioned solutions.

6.2.7 Work package 7 (Data interpretation)

During the earlier research stage, the emphasis was on comprehending, interpreting, and presenting the results. Python visualization libraries, including Pandas, Plotly, Matplotlib, and Seaborn, were utilized. Tableau and Excel have also been employed (Matplotlip, 2012; Microsoft, 2023b; Pandas, 2023; Plotly, 2023; Seaborn, 2022; Tableau Software, 2023). The software mentioned above, and libraries were utilized to produce vital graphical representations, such as standard deviation and range analysis of latency and ML algorithm solutions. In addition, scatter plots were generated to compare the ML model prediction-driven coordinates with those derived from forced latency solutions.

6.3 Research methodology regards establishing RT-PPP early warning system

Employing GNSS information from a single receiver, RT-PPP can generate accurate location estimates in RT. The approach is a cost-effective and more versatile positioning option because it does not rely on a network or differential GNSS solutions.

Providing RT global positioning solutions is a significant benefit of RT-PPP. This means users can receive accurate and reliable positional information in RT, even in remote or isolated areas. This capability is beneficial for monitoring natural disasters such as landslides, volcanic eruptions, tsunamis, and earthquakes (Capilla et al., 2016; Ewert et al., 2005; McGuire et al., 2021; Tsushima & Ohta, 2014; Zedek et al., 2021).

The fact that RT-PPP uses a global infrastructure of permanent GNSS stations is an additional benefit. These stations are spread globally and offer continuous data essential to the accuracy and dependability of RT-PPP SSR products. Furthermore, RT-PPP can be used in areas far from the

coverage of GNSS network corrections, such as polar, desert, and rough terrain areas (Barker et al., 2002; Bezcioglu et al., 2019).

Overall, the RT-PPP is a powerful and versatile tool for precise positioning in RT. Its numerous advantages, including global positioning, cost-effectiveness, and reliability, make it a preferred method for many applications. The following packages and phases were designed to establish an RT-PPP early warning system (Bezcioglu et al., 2019; Odijk et al., 2015; Teunissen & Khodabandeh, 2015). The pre-experimental research design has been carried on through work packages 1 to 4; however, the rest of the work packages are devoted to the true experimental research design. Figure 6.4 summarizes the flow chart of the main research work packages.

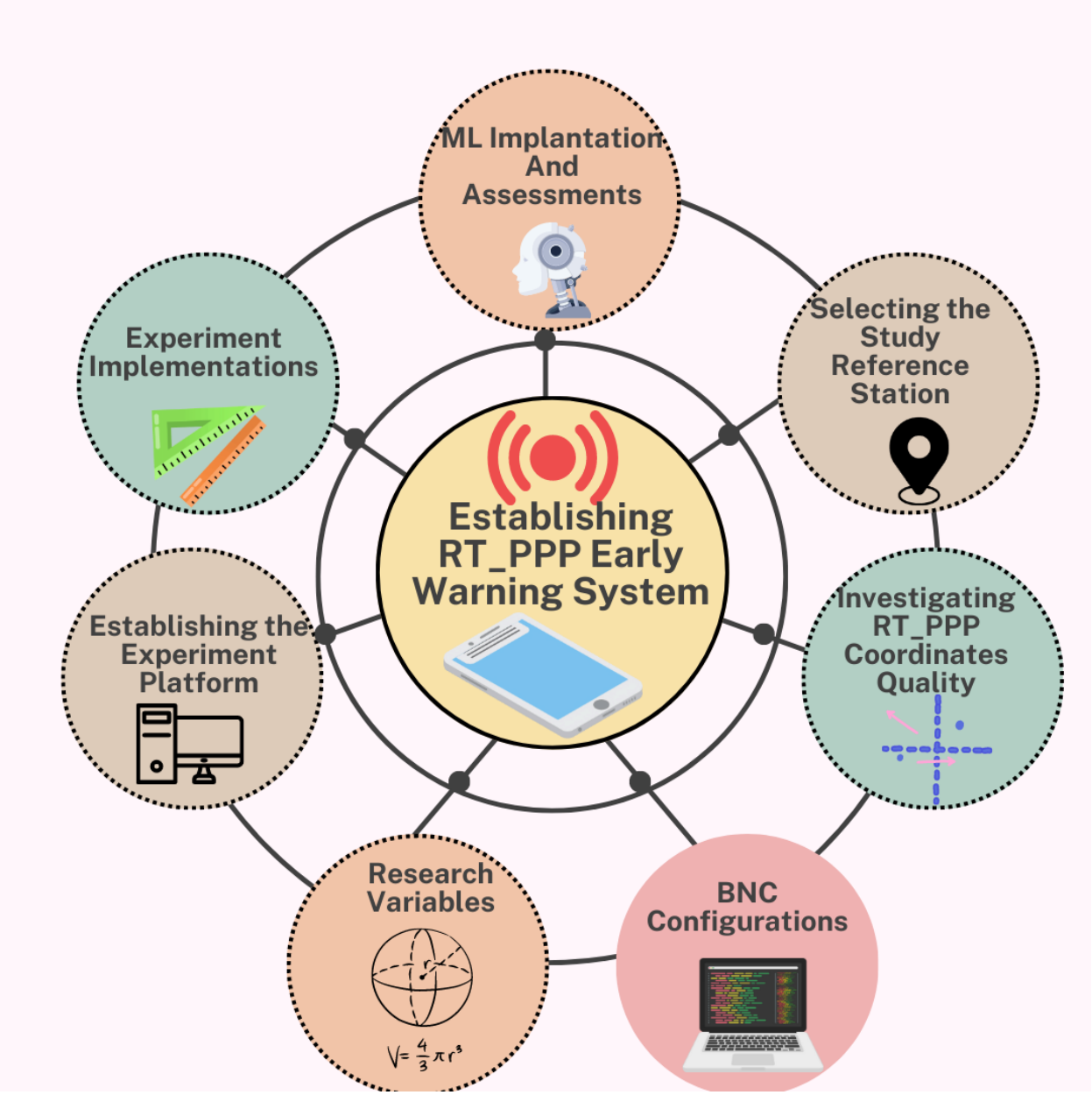

Figure 6.4 Establishing RT-PPP early warning system flowchart

(Prepared by the author).

6.3.1 Work package 1 (Selecting the study reference station)

During the investigation of the present work package, several phases were developed to establish the study reference station. In order to ensure practical training of the ML model, it is recommended to provide numerous training examples that vary in station locations, diverse data quality, and utilize different manufacturing GNSS receivers. Selecting multiple stations that differ in satellite availability, sky, and environmental conditions is also crucial (Quan et al., 2018; Tao et al., 2021; Wu et al., 2021). Consequently, these stations must be distributed globally to fulfil all the pre-mentioned requirements. However, due to the substantial number of experiments conducted in this research, the following phases were designed to address the challenges associated with station diversity.

- Phase 1:

The selection of the study reference station on the rooftop of the researcher's university building was based on the aim of circumventing the challenges associated with long experiment periods, the complexities involved in implementing global experiments, the substantial number of experiments required, Covid restrictions, and the size constraints of the machine platform. These challenges would have been dominant if multiple stations had been chosen for the study. Moreover, the IGS permanent stations are unsuitable for use due to the nature of station construction and the impossibility of performing experiments on these stations.

- Phase 2:

The second phase is devoted to acquiring the reference station coordinates; thus, two static observation sessions were carried out over 24 hours on 28th February 2021 and 18th March 2021, respectively. Consequently, the RINEX observation file was post-processed utilizing Online Positioning Services (US Department of Commerce, NOAA, 2020). Subsequently, Table 6.6 shows the station post-processed coordinate in ITRF 2014 format. Figures 6.5 and 6.6 show the research reference station location, a BNC software plotting tool provided, and the center station location of the produced streams used in the experiment.

Table 6.6 Reference station ITRF cartesian and polar coordinates obtained during the 18th March 2021 session.

Coordinate Value	Value	σ (m)
X	4455833.612 m	0.007
Y	3127063.828 m	0.006
Z	3314433.169 m	0.005
Latitude	31° 30' 25.17194" N	0.003
Longitude	35° 03' 38.99417" E	0.004
Ellipsoidal height	928.314	0.009

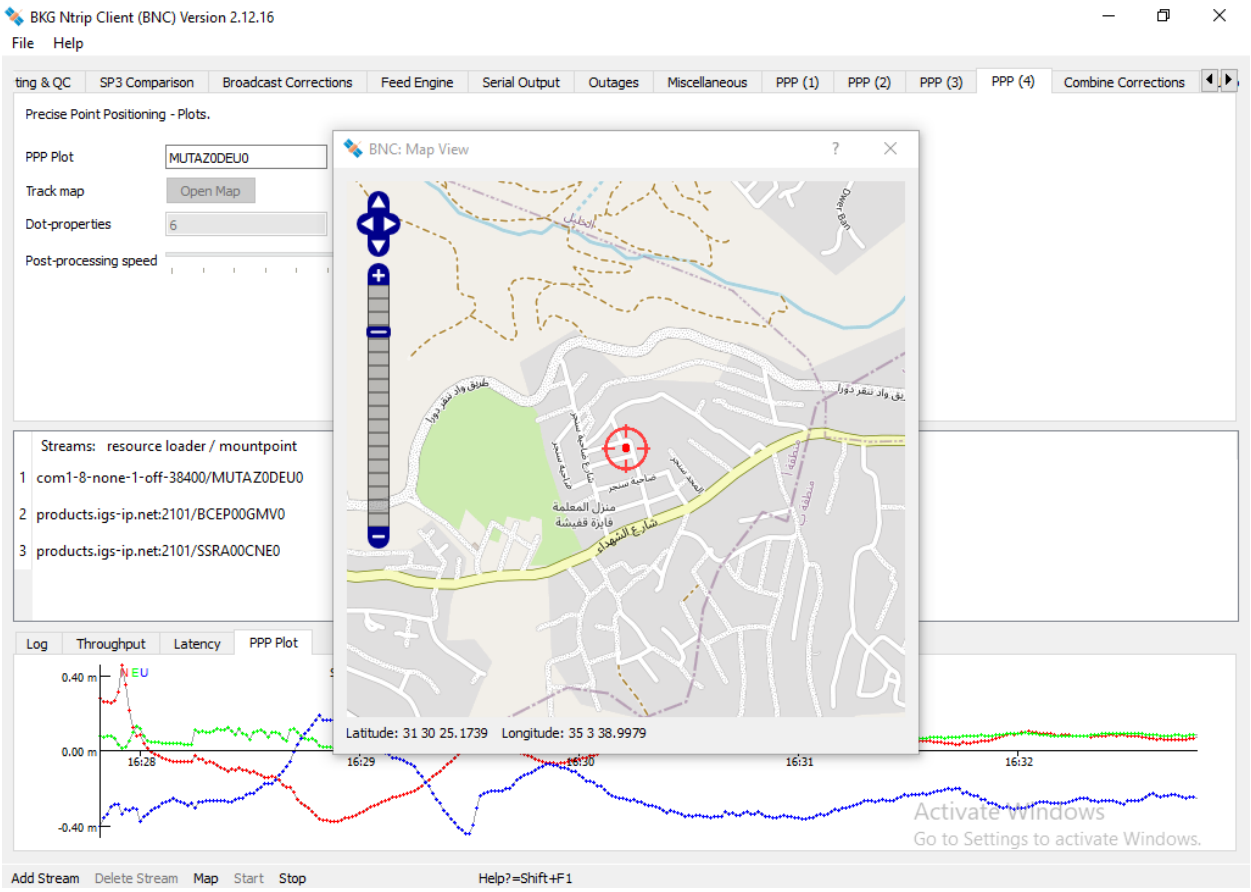

Figure 6.5 The research reference station

(Prepared by the author).

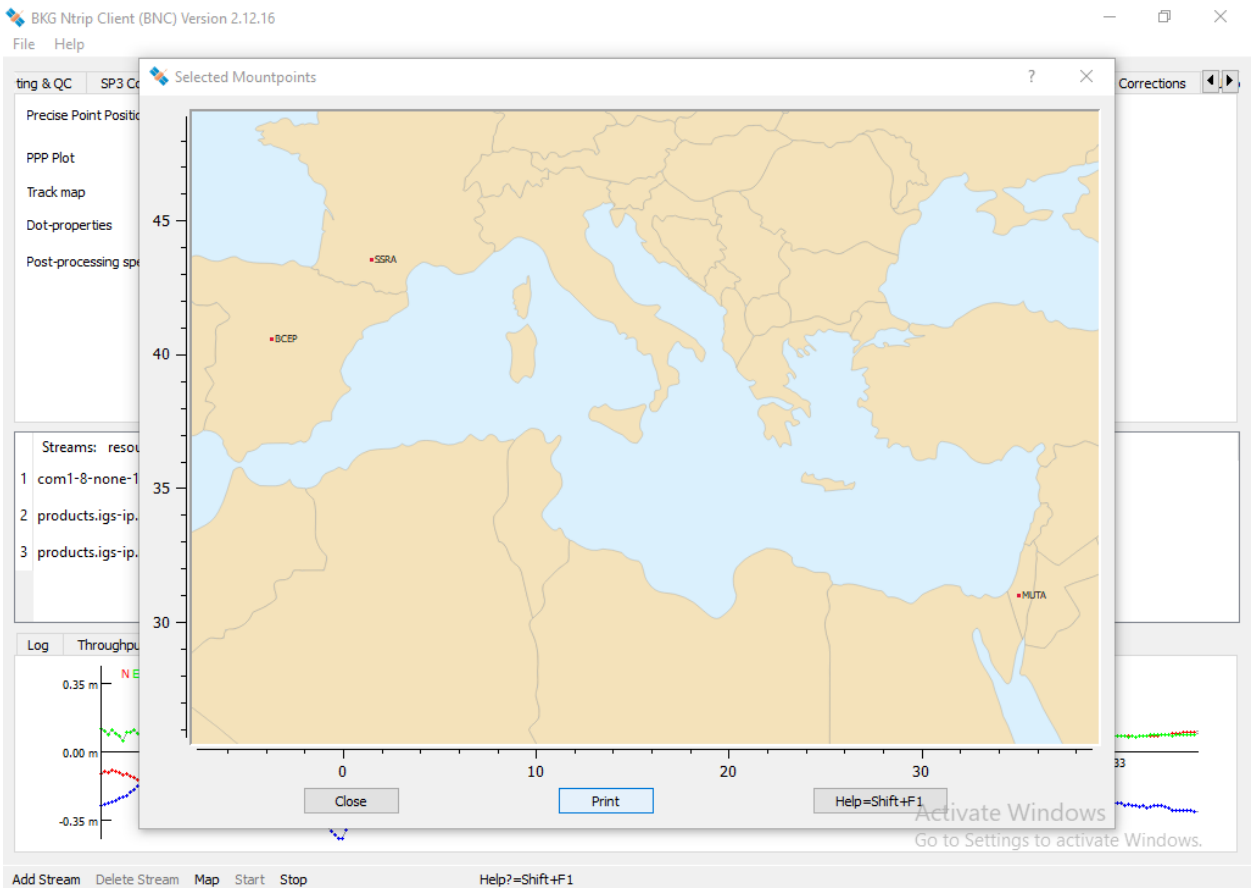

Figure 6.6 The research map of the reference station with utilized stream locations

(Prepared by the author).

❖ Phase 3:

The third phase is dedicated to ensuring the acquisition of diverse quality RT-PPP raw data. The number and the geometry of tracked satellites influence the RT-PPP measurement quality. RT-PPP is sensitive to the number of tracking satellites and the satellite's geometry above the sky of the GNSS users. Consequently, this research examines using different elevation angles to emulate different environmental situations scenarios. This research used various elevation angles: 0, 10, 20, 30, 40, 50, and 60 degrees (Wu et al., 2021).

The BNC software uses quality control codes, ensuring that the GNSS users will not configure it with extreme parameters. Those configurations could lead to considerable errors in coordinates accuracy and solution availability. These quality control establishing thresholds allow the BNC

users to use elevation angles between zero and twenty degrees. The maximum waiting time for clock corrections is twenty seconds; some constraints are related to the minimum number of satellites required to perform the PPP. Consequently, the research configured the open-source codes of the BNC software. Afterward, the BNC was recompiled with newly configured codes to investigate the premonition elevation angle values. Figures 6.7 and 6.8 show the BNC widget with a new configuration that allows the research to use different elevation angles (Bundesamt für Kartographie und Geodäsie, 2022).

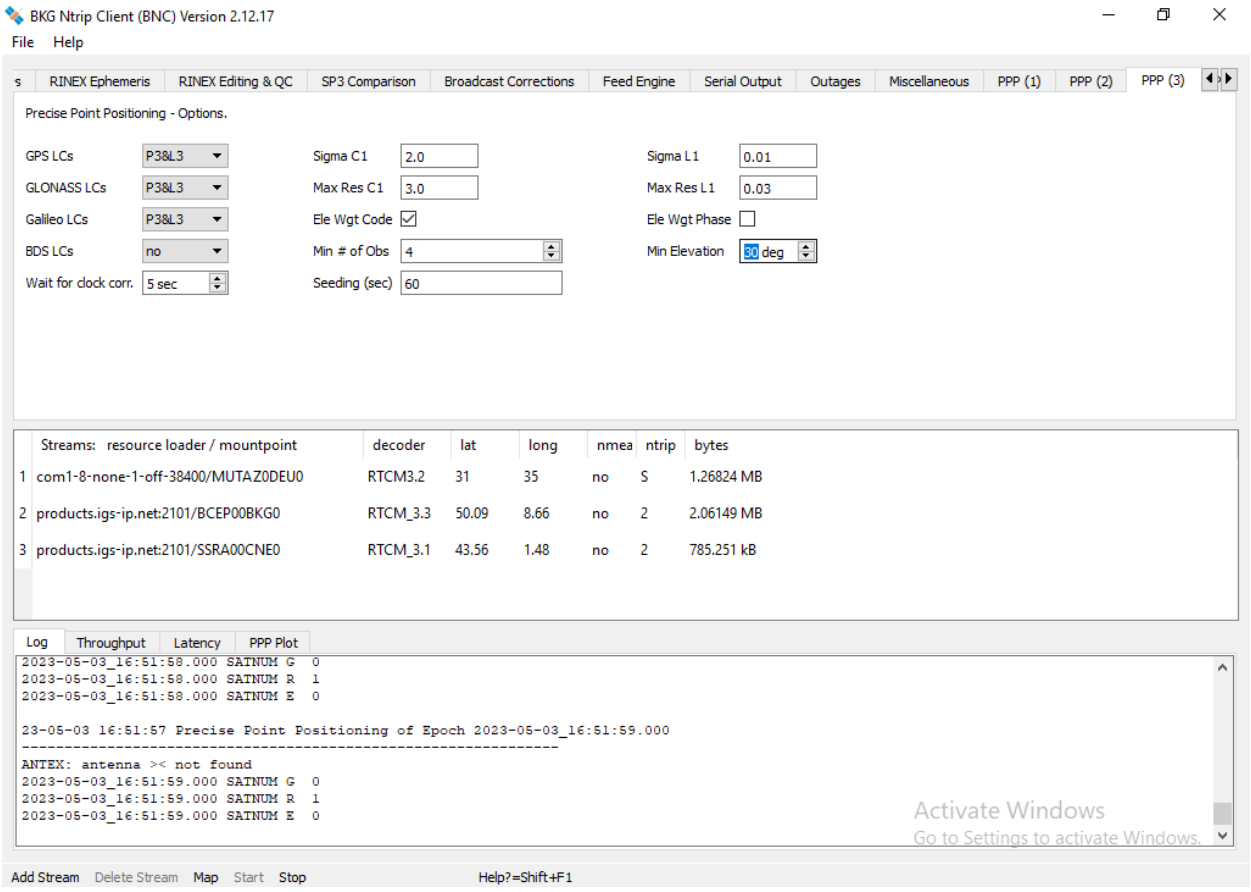

Figure 6.7 Recompile BNC software with widget utilizes a 30-degree mask angle.

(Prepared by the author).

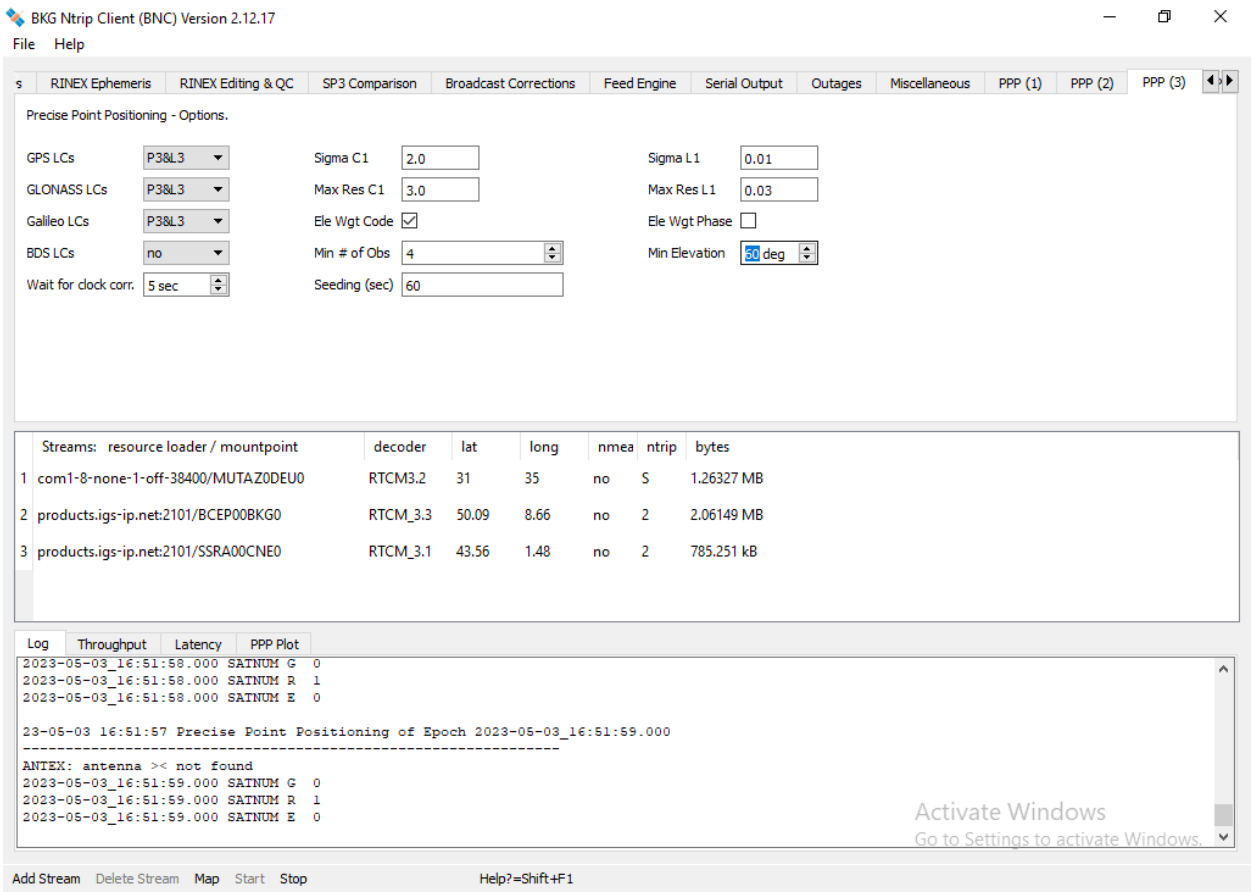

Figure 6.8 Recompile BNC software with widget utilizes a 60-degree mask angle.

(Prepared by the author).

❖ Phase 4:

In the final stage, the information about the RT-PPP measurements was stored. This stored information facilitates the research aimed at investigating the correlation between different variables. The correlation information is expressed as a coefficient ranging from -1 to 1, with a value of 1 indicating the highest positive correlation, -1 representing the highest negative correlation, and 0 indicating the absence of correlation (Pearson, 1920). The correlation analyses were conducted among variables, including tropospheric error, satellite number, latency, phase residuals, elevation angles, obtained coordinates, coordinate accuracy, and root mean squared errors.

6.3.2 Work package 2 (RT-PPP coordinates quality investigations)

This WP2 included essential investigations required to perform the real-time PPP experiments reasonably; this led us to examine the BNC open-source software, The GNSS receiver, and the station environment in static form.

- Phase 1:

The RT-PPP investigations led this study to explore the use of the BNC software with different navigation satellite system combinations. These combinations include working with (GPS, GPS+ GLONASS, GPS+GLONASS+Galileo) the best accuracy was achieved using the GPS +GLONASS combination. Even though the experiment was carried on in different navigation satellite systems, these results match the research findings done by (Kiliszekn & Kroszczyński 2020).

- Phase 2:

Various elevation angle values were used in this research, and the values of these angles were (0, 10, 20, 30, 40, 50, and 60) degrees to assess the RT-PPP regarding the accuracy and solution availability.

- Phase 3:

The latencies of the correction streams also influence the quality of real-time PPP measurements. Thus, the correction streams have been used with different latencies (SSRA00CNE short latency stream and IGS03 high latency stream).

6.3.3 Work package 3 (BNC configurations)

The third work package provided the utilized software with all required parameters. The following phase details describe the steps and configurations of the current work package.

- Phase 1:

The current phase was devoted to providing the BNC software with all the parameters to operate in the RT mode. First, the BNC setup folder contains several configuration setup examples. The

10_PPPQuickStart.bnc configured example was re-configured to obtain serial streams. The required configuration regards the mount point's name, RINEX format, approximate latitude and longitude, port name, baud rate, data bit, and flow control provided (German Federal Agency for Cartography and Geodesy, 2022). Next, the priory coordinate file was adjusted to hold the coordinate value obtained from the previous work package. Additionally, to correct the RTCM observations, the receiver APC offsets and variations were provided to the BNC. In addition, the receiver height above the station marker was also provided in the same file (German Federal Agency for Cartography and Geodesy, 2022).

- Phase 2:

SSRA00CNE and IGS03 correction streams were added to the stream canvas to train the ML models with different training samples with various latency values. In this phase, further arrangements were made regarding the GNSS constellations. The elevation angle mask with an elevation angle of 10 degrees was selected to avoid noisy code and phase observations from GNSS satellites with 10 degrees or lower elevation angles. In addition, several elevation angles were utilized, including 10, 20, 30, and 35 degrees, for the sake of learning models with several scenarios that simulate sky conditions. Accordingly, that was followed with a selection of the mandatory paths to store the broadcasted corrections, the RINEX station's observation files, broadcasted navigation files, the latency value, and the RT-PPP station's coordinates for supplementary implementation.

6.3.4 Work package 4 (Research variables investigation)

The current research work package has investigated different variables to ensure accurate modelling for the EWS. This investigation is essential to design properly the research experiments to fulfil the research hypothesis; the research investigations lead to include the phases:

- Phase 1:

Phase one was to prepare the ML models with essential variables to classify deformation events. First, the BNC software was configured with different configurations, saving the required information for establishing classification variables. Those configurations led the research to

access various details regarding the orbital and clock correction files, log files, PPP files, and National Marine Electronics Association (NMEA) files.

Accordingly, this allows having information related to orbital and clock corrections for each satellite, latency information, 3D coordinates, 3D displacements of the receiver over station marker location, tropospheric error, Horizontal Dilution of Precision (HDOP), and satellite number.

Secondly, this part of the research is required to provide the ML models with additional calculated variables. Consequently, the following components were calculated from measurements. Position and horizontal root mean squared error was calculated from the derived observations. Moreover, the average value of residuals for the code and phase observation was calculated concerning the ionosphere-free linear combination of code/phase. Moreover, the east-north-up displacements for the current observation have been compared with the last ten a priori east-north-up displacements.

The last part deals with quality control indicators.

Different indicators can be obtained from the BNC files. In this research, we add four indicators related to the speed and course of the receiver's ground over the marker location. Additionally, the NMEA protocol provides the GNSS users with receiver and position quality indicators and warnings. More information regarding those warnings and the used NMEA sentences can be found (NovAtel a, 2022; NovAtel b, 2022).

- Phase 2:

The second phase was regarding the variables classification to enhance the understanding of the research experiment's variables. Moreover, it provides other researchers with reproducibility to construct a comparison and further studies.

- **Independent Variables (IV):** Those variables are independent, and the researchers assume that they influence the availability and quality of the real-time PPP measurements; consequently, they affect the EWS ML algorithm's accuracy and performance. Table 6.7 includes the research independent variables.
- **Extraneous Variables (EV)** are external variables that influence the IV. Some EVs could be controlled; consequently, controlling these variables could improve the research

reproducibility and reliability. The research divided these variables into two groups: confounding and control variables.

- **Confounding Variables (COV):** represents the uncontrolled extraneous variables such as wind speed, temperature, pressures, and humidity. Table 6.9 includes the research confounding variables.
- **Control Variables (CV):** represents all variables the researcher can control through research activities, such as satellite elevation mask angles, the receiver displacement values, displacement movement directions as controlled by the research engine, correction streams, labelling values, and measurement time. Table 6.8 includes the research control variables.

❖ **Dependent Variables (DV):** Those variables are driven by RT-PPP measurements and are influenced by IVs, EVs, and CVs. Some research DVs include the displacement components regarding topocentric frame, driven station cartesian coordinates, coordinates residuals, horizontal and position RMSE, course, and speed over the ground. Table 6.10 includes the research-dependent variables.

Table 6.7 Research experiments independent variables.

Variable name	Type	Variable description
Sat-number	IV	Satellites number above the GNSS user sky.
Tropo	IV	Tropospheric corrections were driven from the Saastamoinen model.
Tropo-error	IV	Tropospheric error from the Saastamoinen model.
Index	IV	The index indicates the timestamp of real-time measurements.
HDOP	IV	Horizontal dilution of precision.

Table 6.8 Research experiments control variables.

Variable name	Type	Variable description
Elevation angle	CV	The satellites having elevation angles less than (10,20,30 and 35 degrees) will be discarded from tracking during several experiments.
Displacements values	CV	Represents the movements exerted with the Computer Numerical Control CNC machine or manually through the roller device. The displacement values are listed in the experiment details table.
Type of movements	CV	Represent the direction of movements, including vertical, horizontal, and 3D.
Correction streams	CV	Two correction streams were used (IGS03 and SSRA00CNE).
GNSS constellations	CV	Denotes the utilized GNSS constellations during RT-PPP experiments.
Receiver antenna height	CV	Represent the height of the GNSS receiver above the station marker location.

Table 6.9 Research experiments confounding variables.

Variable name	Type	Variable description
Wind Speed	COV	The velocity of the wind over the research station.
Temperate	COV	The temperature during the experiment.
Pressure	COV	Air pressure over the reference station.
Humidity	COV	The air moisture content during experiments.
Weather condition	COV	Such as rain, dry, haze, or fog.
Satellites-Along-track **Satellites-clock-corr** **Satellites-Out-of-plane** **Satellites-Radial** **Satellites-Velocity of A long-track** **Satellites-Velocity of Out-of-plane** **Satellites-Velocity of Radial**	COV	Orbital and clock corrections. It is worth noting that those variables were stored for each tracked satellite in the research database.
Position-fix **Receiver-warning**	COV	Quality indicators.
Corrections stream latency	COV	Represent the amount of latency during the research experiments, including low latency correction streams such as SSRA00CNE with around 15 seconds and high latency correction streams IGS combined correction with a latency value of around 35 seconds.
Multipath error	COV	Indicates the amount of error as it is affected by reflected GNSS signals.

Table 6.10 Research experiments dependent variables.

Variable name	Type	Variable description
dE-true	DV	East, North, and Up components of displacement computed on the local plane coordinate system
dN-true	DV	
dZ-true	DV	
X	DV	Geocentric cartesian coordinates GRS80.
Y	DV	
Z	DV	
dx	DV	Coordinates residuals.
dy	DV	
dz	DV	
E-diff-i	DV	East displacement values concerning a priori last ten observations (value of i from (1 to 10)).
N-diff-i	DV	North displacement values for a priori last ten observations (value of i from (1 to 10)).
Up-diff-i	DV	Up displacement values to a priori last ten observations (value of i from (1 to 10)).
Position-RMSE	DV	3D Root Mean Squared Error.
Horizontal-RMSE	DV	2D Horizontal Root mean squared error.
Course-og	DV	Course overground.
Speed-og	DV	speed overground.
Target	DV	The target variable includes centered, misplaced, and out-of-service labels; the labelling function followed the type of movements and the coordinate residuals.

6.3.5 Work package 5 (Description of proposed engines)

The necessity for considerable amounts of data during ML training, testing, and validation stages is a significant challenge. These fundamental problems extended to the necessity of data cleaning and preparation in formats usable by ML. Consequently, the current work package investigated several phases designed to create a suitable proposed engine to collect the several types of deformation and non-deformation events.

- Phase 1:

After revisions of different ways to generate relevant data to model and test the EWS, the CNC laser machine was selected as a suitable machine to perform experiments, table 6.11 includes details of the selected machine.

Table 6.11 Machine frame manufacturing descriptions.

Brand	**Eleks Maker.**
Model	EleksLaser-A3 pro.
Working Voltage **Working Current**	Working Voltage: DC 12V. Working Current: DC 2.5A.
Weight	4.60kg.
Machine material	Stainless Steel and Acrylic.
Working area	One squared meter.

Figure 6.9 shows the different machine components; Table 6.12 describes the machine parts (Xu & Newman, 2006).

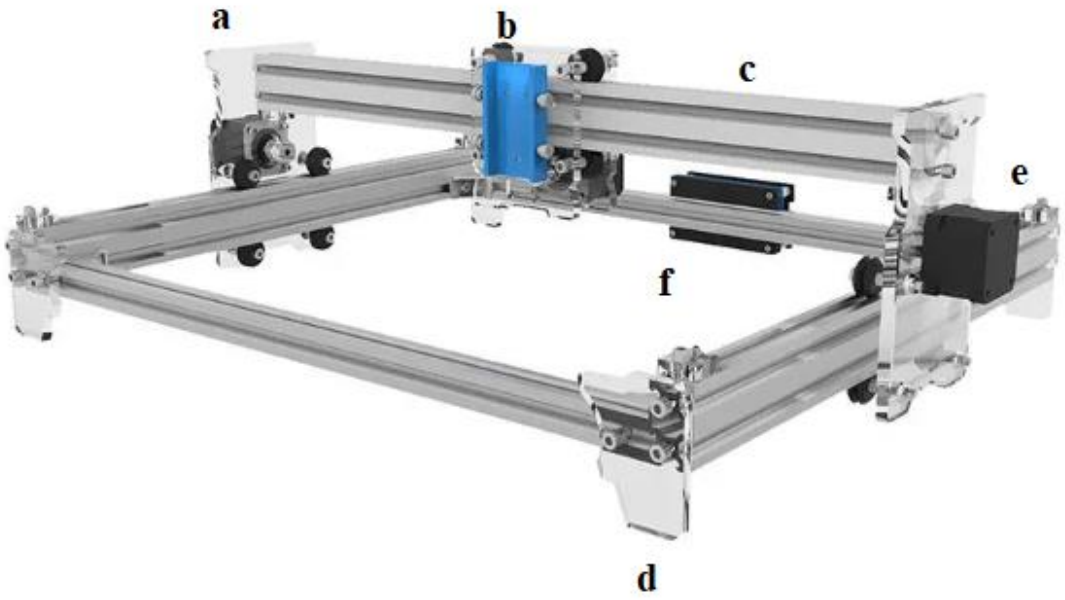

Figure 6.9 CNC Machine

(Prepared by the author).

Table 6.12 Machine frame part descriptions.

Part name	Part description
A	First horizontal stepper motor.
B	Longitudinal stepper motor.
C	Machine arm.
D	Machine holder.
E	Second horizontal stepper motor.
F	The Machine microcontroller.

- Phase 2: In this stage, we are working to overcome the restrictions research machines impose. The apparatus and its supplementary parts for the experiment, including the GNSS receiver, computer, monitor, cable holder, and vertical and horizontal adjustment accessories, were kept and carried on a portable table. Figure 6.10 and Table 6.13 show the machine with supplementary devices and tools utilized in horizontal experiments.

Figure 6.10 Research engine (horizontal deformations)

(Prepared by the author).

Table 6.13 Machine frame part descriptions.

Device	Device explanation
A	GNSS receiver (19 cm x 10.4 cm, 1.52 kg)
B	Monitor
C	Cables hanger
D	Spirit level
E	Rod leveling bubble
F	Plumb bob
G	personal computer
H	Horizontal bar (1 meter)
I	Longitudinal bar (1 meter)
J	CNC microcontroller
K	Detachable tribrach
L	CNC stepper motor
M	Station marker

- Phase 3:

The last step of the current work package focused on fixing the vertical displacement problem. Thanks to its two stepper motors, the machine could move horizontally, but it was vertically in place. The GNSS receiver was carried on a pole; a roller was attached to the pole to extract motion in the vertical plane. Figure 6.11 and Table 6.14 show the research engine with supplementary devices and tools utilized in vertical and 3D experiments.

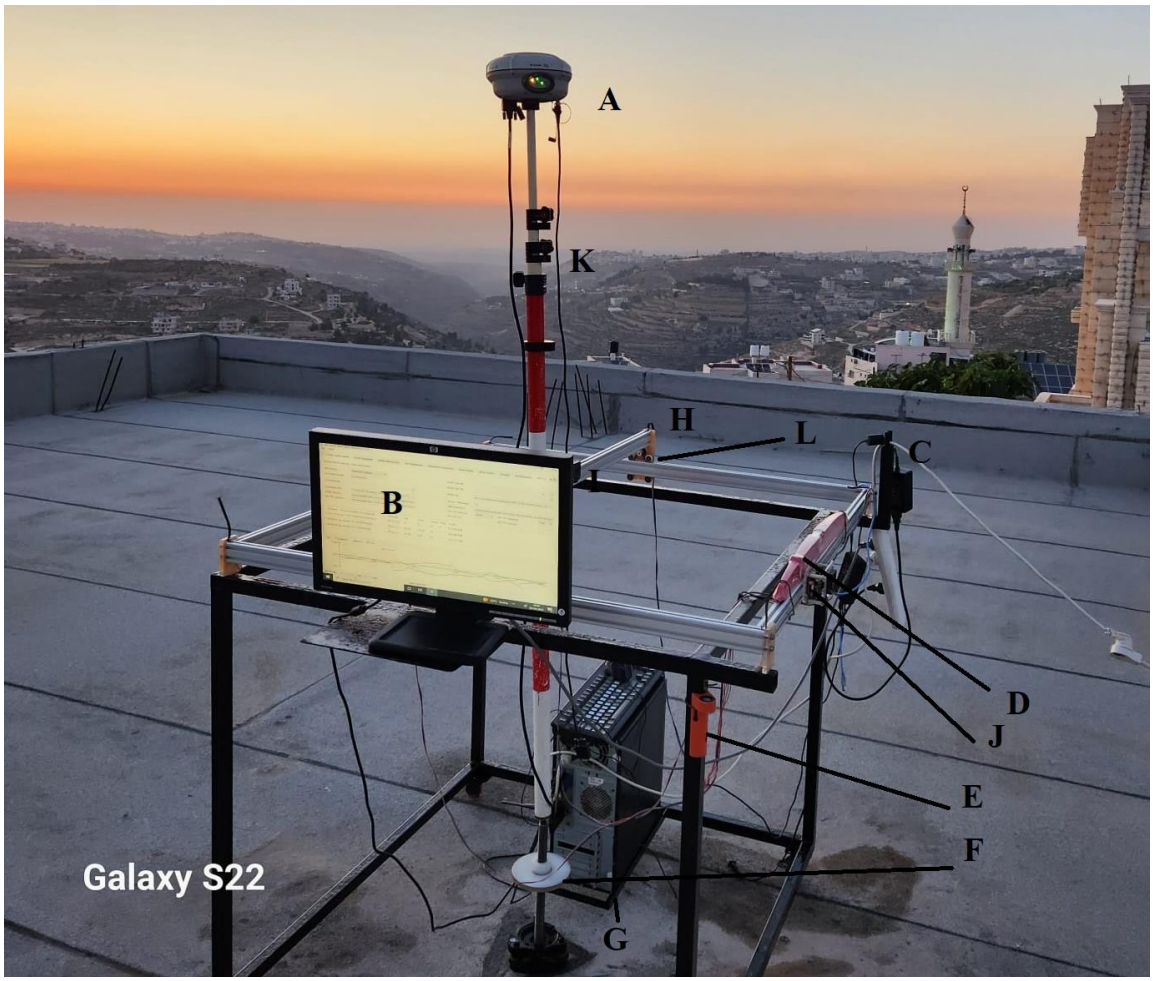

Figure 6.11 Research engine (vertical and 3D deformations)

(Prepared by the author).

Table 6.14 Research engine frame part descriptions.

Device	Device explanation
A	GNSS receiver
B	Monitor
C	Cables hanger
D	Spirit level
E	Rod leveling bubble
F	Vertical roller (0.5 meters)
G	PC
H	The horizontal bar (1 meter)
I	longitudinal bar (1 meter)
J	CNC microcontroller
K	Rod 1-4 meter
L	CNC stepper motor
M	Station marker

6.3.6 Work package 6 (Ranges of deformation and subsidence, time span)

The last packages were related to the experiment's preparation. The research examines the ML models with different deformations on the sixth work package. This investigation includes the following phases:

- Phase 1:

This phase focused on the studies of various amounts of displacements ranging from (1 to 20cm). The choosing displacement range could be justified as a trade-off between RT-PPP accuracy and various displacement values, as represented previously in Chapter 4. Accordingly, the research examines three types of motions, horizontal, vertical, and 3D, to mimic different deformation situations, including land subsidence, land uplifting, and horizontal or 3D deformations.

Firstly, the deformation events with values equal to d cm were exerted using the CNC machine with the aid of the manual roller device to exert the vertical movements. That led the research to prepare different x, y, and z values in the machine coordinate system to exert different displacements (d) to simulate the deformation events that could occur in any direction. The following equation shows the x, y, and z constraints used in d establishing, where x and y correspond to planar coordinates in the horizontal plane and z to the vertical component.

$$x^2 + y^2 + z^2 = d^2 \quad (6.1)$$

The last step led us to pick a range of x and y, which examined the ML models model with different d values. The following table shows the values of x, y, z, and d.

Table 6.15 Deformation displacement components values. d is obtained precisely as a combination of x, y, and z components.

X range (cm)	Y range (cm)	Z range (cm)	d (cm)
From -20 to 20	-20-20	-20-20	20
From -15 to 15	-15-15	-15-15	15
From -10 to 10	-10-10	-10-10	10
From -5 to 5	-5-5	-5-5	5
From -3.75 to 3.75	-3.75-3.75	-3.75-3.75	3.75
From -2.5 to 2.5	-2.5-2.5	-2.5-2.5	2.5

❖ Phase 2:

After setting up the machine with the displacement values shown in Table 6.15, forty-eight experiments were conducted with the following considerations.

- Horizontal experiments with different d values are shown in the table above. Consequently, to ensure randomization movements of the CNC machine, a dataset sample with 48 random x and y values was chosen each time. The research used the 48 different random x and y values with the desired amount of displacement. The 48 points allow us to do experiments with 24-hour lengths with 15 minutes for each round trip between the station marker and the displaced point's location. The 24 hours have been chosen to investigate PPP solutions daily and nightly with different ionospheric effects.
- The manual roller device has been used for vertical experiments to exert movements in up and down directions. The movement values ranged from 1cm to 20 cm; the experiment periods varied between 12 and 24 hours. The GNSS receiver remained and left the station marker location within 1-2 hours.
- For 3D experiments, CNC and manual roller devices have been used to exert the desired movements. The movement values ranged from 1cm to 20 cm; the experiment periods

varied between 12 and 24 hours. The GNSS receiver remained and left the station marker location within 1-2 hours.

It is worth mentioning that machine coordinates components, traveling speed, and waiting time were all uploaded to the machine microcontroller utilizing the g-code (Gleadall, 2021; Latif et al., 2021; Xu & Newman, 2006).

- ❖ Phase 3:

During this phase, the research prepared the labelling function. This function labels the GNSS measurement event according to the GNSS receiver status. Consequently, this variable label holds three different classes:

1. Centered: means that the receiver occupied the station marker location.
2. Misplaced: means that the receiver occupied points with displacement distance (ds) away from the station marker.
3. Out of service means that the receiver occupied points located with ds away from the station marker or occupied the station marker location, but biases lead to tremendous errors. The ds have been chosen to be 30 cm. The justification for choosing the ds to be 30 cm could be illustrated as the RT-PPP measurements indicate the displacements with a 30 cm value greater than exerted movements (20 cm).

The RT-PPP introduces blunders or outliers measurements. This research shows that multipath error, elevation angles, latency, satellite geometry, and the number of satellites led to having values of displacements with more than 0.5 meters in all directions. That led us to add the third level of class, which is out of service. So, all measurements having displacement errors equal to or more than 0.30 meters were labelled as out of service. The researcher considers this labelling due to insufficient certainty to rely on those measurements to initiate warning alerts. Additionally, NMEA sentences contain GNSS quality indicators, such as the health of the used satellite, the GNSS receiver measurements mode, the receiver, and the GNSS constellation status. Any measurements with invalid GNSS quality indicators were added to this class.

The following equation shows the labelling function used during this research:

$$f(x) = \begin{cases} 0, & \sqrt{x^2 + y^2 + z^2} \in 0 + \boldsymbol{\varepsilon} \\ 1, & \sqrt{x^2 + y^2 + z^2} \in d^2 + \boldsymbol{\varepsilon} \\ 2, & \sqrt{x^2 + y^2 + z^2} \in d^2 + \boldsymbol{\varepsilon} + bias \end{cases} \quad (6.2)$$

Where:

x, y, z denoted the displacement in cm.

d^2 the total travel distance in cm.

$\boldsymbol{\varepsilon}$: Measurements error.

0: denotes that the receiver occupied station marker locations

1: represents that the receiver is Misplaced with d distance from the station marker location.

2: denotes that the receiver experienced tremendous bias errors.

6.3.7 Work package 7(Experiments implementations)

This section provides a brief overview of the experiments; in total, there were 48 experiments conducted to investigate various aspects of RT-PPP measurements. The experiments were designed to examine different types of deformation, including 24 vertical, eight horizontal, and 16 three-dimensional deformations. The experiments yielded a total of 4,299,510 events, which were distributed across 2,205,918 centered events, 645,822 out-of-service events, and 1,447,770 misplaced events. The event distribution percentages of the centered, out-of-service, and misplaced events are 51.3%, 15%, and 33.7 %, respectively. For the sake of ML, training is recommended to utilize an equal percentage of each class because the RT-PPP measurements do not converge when the system is not robust enough. Accordingly, it can be seen from the experiment results that the number of the collected RT-PPP observations is reversibly proportional to the elevation angle. Tables 6.16, 6.17, and 6.18 show that the number of collected RT-PPP observations for 24-hour experiments is reversibly proportional to the selected elevation angle (10, 20, and 35 degrees). Similarly, this correlation is also valid for the utilized stream regarding latency. Moreover, the experiment's randomization affects the event distributions.

The latency values of the correction streams used in the RT-PPP measurements were also investigated, with experiments conducted using both the SSRA00CNE and SSRA00IGS streams, with latency values of approximately 15 and 35 seconds, respectively. In addition, the experiments were designed to train machine learning algorithms in different station situations. This involved conducting 31 experiments at an evaluation angle of 10 degrees, nine experiments at an angle of 20 degrees, four at 30 degrees, and four at 35 degrees.

Furthermore, the BNC software was configured to neglect satellites with an elevation below a specified mask elevation angle. During data collection, various degrees of displacement were applied through the CNC machine. The experiment periods were also extended from 12 to 24 hours to ensure adequate data were collected during different ionospheric conditions (Andrei et al., 2009; Feltens & Schaer, 1998; Wang & Rothacher, 2013). Tables 6.16, 6.17, and 6.18 show the research experiment, including details of manipulated variables.

Table 6.16 Details description of the research experiments regarding horizontal movements.

Displacement value (cm)	Period (h)	Movements periods (h)	Date of Start	End Date	# Of events	Elevation Angle	Correction Stream	Latency
10	24	0.25	2021-11-10 18:18:55	2021-11-11 18:29:19	101965	10	SSRA00CNE	Low
15	24	0.25	2021-11-09 18:01:55	2021-11-10 18:15:59	102430	10	SSRA00CNE	Low
1	24	0.25	2021-12-11 09:28:35	2021-12-12 05:39:15	86328	10	SSRA00CNE	Low
2.5	24	0.25	2021-12-03 12:21:58	2021-12-04 14:09:54	110746	10	SSRA00CNE	Low
20	24	0.25	2021-11-07 16:01:10	2021-11-08 15:46:59	99131	10	SSRA00CNE	Low
2.5	12	0.25	2021-12-13 06:21:39	2021-12-14 07:37:04	32657	10	SSRA00CNE	Low
3.75	24	0.25	2021-11-25 16:05:40	2021-11-26 19:53:14	118804	10	SSRA00CNE	Low
5	24	0.25	2021-11-22 13:08:04	2021-11-23 13:09:09	101284	10	SSRA00CNE	Low

Table 6.17 Details description of the research experiments regarding vertical movements.

Displacement value (cm)	Period (h)	Movements periods (h)	Date of Start	End Date	# Of events	Elevation Angle	Correction Stream	Latency
10	12	1	2022-01-08 06:06:46	2022-01-08 18:01:49	51210	10	SSRA00CNE	Low
10	24	random	2022-04-10 18:02:06	2022-04-11 19:43:04	101041	10	SSRA00CNE	Low
15	12	1	2022-01-11 08:53:23	2022-01-11 21:12:24	52770	10	SSRA00CNE	Low
2.5	12	1	2022-01-09 08:43:44	2022-01-09 21:04:34	52920	10	SSRA00CNE	Low
20	12	random	2022-01-12 07:08:31	2022-01-13 20:09:24	158463	10	SSRA00CNE	Low
20	24	random	2022-04-14 21:40:34	2022-04-15 22:19:54	105880	10	SSRA00CNE	Low
2	24	random	2022-04-16 07:26:37	2022-04-16 20:31:00	99280	10	SSRA00CNE	Low
3.75	24	random	2022-04-08 08:36:06	2022-04-09 08:48:59	98218	10	SSRA00CNE	Low
5	12	1	2021-12-18 07:20:30	2021-12-18 20:00:04	52899	10	SSRA00CNE	Low
10	24	random	2022-04-22 09:18:54	2022-04-23 13:57:49	103134	10	SSRA00IGS	High
15	24	random	2022-04-23 14:00:26	2022-04-24 13:29:09	84523	10	SSRA00IGS	High
20	24	random	2022-04-24 13:30:59	2022-04-25 13:31:59	85129	10	SSRA00IGS	High
2	24	random	2022-04-17 23:24:56	2022-04-19 00:46:24	91290	10	SSRA00IGS	High
3.75	24	random	2022-04-19 21:25:09	2022-04-20 21:29:34	86666	10	SSRA00IGS	High
5	24	random	2022-04-20	2022-04-21	83615	10	SSRA00IGS	High

			21:32:32	20:46:04				
10	24	random	2022-05-28 19:56:45	2022-05-29 19:16:49	99320	20	SSRA00CNE	Low
15	24	random	2022-05-29 19:21:05	2022-05-30 18:42:15	100000	20	SSRA00CNE	Low
2.5	24	random	2022-05-26 16:41:42	2022-05-27 09:52:04	73653	20	SSRA00CNE	Low
20	24	random	2022-05-30 18:48:06	2022-05-31 20:22:19	109230	20	SSRA00CNE	Low
5	24	random	2022-05-27 20:05:40	2022-05-28 19:54:29	71712	20	SSRA00CNE	Low
10	24	random	2022-06-02 17:16:05	2022-06-03 11:43:49	78460	35	SSRA00CNE	Low
5	24	random	2022-06-01 19:21:32	2022-06-02 17:13:44	64930	35	SSRA00CNE	Low
15	24	random	2022-06-02 17:15:59	2022-06-03 11:43:49	78458	35	SSRA00CNE	Low
20	24	random	2022-06-03 11:48:10	2022-06-05 20:27:24	129253	35	SSRA00CNE	Low

Table 6.18 Details description of the research experiments regarding 3D movements.

Displacement value (cm)	Period (h)	Movements periods (h)	Date of Start	End Date	# Of events	Elevation Angle	Correction Stream	Latency
10	24	random	2022-05-03 15:49:38	2022-05-04 14:01:09	95158	10	SSRA00CNE	Low
15	24	random	2022-05-04 14:02:43	2022-05-05 04:00:44	60022	10	SSRA00CNE	Low
20	24	random	2022-05-05 08:57:02	2022-05-06 03:03:44	72138	10	SSRA00CNE	Low
5	24	random	2022-05-01 14:32:32	2022-05-02 18:31:39	119906	10	SSRA00CNE	Low
10	24	random	2022-04-26 14:10:14	2022-04-27 14:36:29	83652	10	SSRA00IGS	High
15	24	random	2022-04-29 14:04:09	2022-04-30 15:13:39	90570	10	SSRA00IGS	High
20	24	random	2022-04-30 15:16:37	2022-05-01 11:21:59	70359	10	SSRA00IGS	High
5	24	random	2022-04-25 13:34:30	2022-04-26 14:07:49	88239	10	SSRA00IGS	High
10	24	random	2022-05-07 13:10:23	2022-05-08 13:49:49	105560	20	SSRA00CNE	Low
15	24	random	2022-05-08 13:55:40	2022-05-09 14:52:14	105946	20	SSRA00CNE	Low
20	24	random	2022-05-09 14:55:03	2022-05-10 18:00:19	115826	20	SSRA00CNE	Low
5	24	random	2022-05-06 05:52:46	2022-05-07 13:07:54	133804	20	SSRA00CNE	Low
10	24	random	2022-05-12 08:03:55	2022-05-12 22:33:06	46614	30	SSRA00CNE	Low
15	24	random	2022-05-14 20:03:52	2022-05-15 15:28:54	55219	30	SSRA00CNE	Low
20	24	random	2022-05-25 18:54:55	2022-05-26 09:17:50	60414	30	SSRA00CNE	Low
5	24	random	2022-05-10 18:06:48	2022-05-11 15:51:03	85678	30	SSRA00CNE	Low

6.3.8 Work package 8 (Machine learning implantation and assessments)

In this research, different ML models were investigated as tools for establishing an early warning system, including decision trees, random forest, logistic regression, K nearest neighbours, XGB, and support vector regression. In future studies, the researchers intended to apply deep learning methods such as Convolutional Neural Networks (CNNs), Recurrent Neural Networks (RNNs), Long Short-Term Memory (LSTM), and Gated Recurrent Units (GRUs). Accordingly, the research demonstrates a robust comparison between the selected ML models. Different performance matrices such as accuracy, precision, recall, and f1-score could be used for model performance investigation (Fawcett, 2006). The flowing phases were implemented in the current work package:

- Phase 1:

Phase one of the research involved data cleaning and preparation to investigate missing values in the entire database. Our investigations revealed that the missing values were due to different sampling intervals and the unavailability of SSR products in the received streams. For instance, the orbital corrections were sampled at 1 minute, while the clock corrections were sampled at 10 seconds, extending to 30 seconds to sample the latency value. It is worth noting that the nature of the variables determines the sampling rate; for instance, it is adequate to sample the latency within 30 seconds since the variation of the internet speed would not undergo significant changes. Similarly, the study showed that the clock correction required a higher sampling rate than the orbital correction because the clocks equipped onboard satellites have a high variation rate due to clock frequency instability.

Moreover, the BNC software could not calculate coordinates during some periods due to geometry or the number of satellites. Additionally, corruption or communication interruptions in the correction products could affect the availability of coordinates. Therefore, in this step, the researchers had the option of eliminating rows where null values existed or using the nearest filling methods. In this regard, the nearest filling method was adequate to avoid losing data collection based on the nature of the variables. However, missing entities were dropped from the database where coordinate values were missing. During this phase, the research extracted variables such as

observation time and measuring coordinates to generate a generic model that can be applied to any monitoring station.

- ❖ Phase 2:

At this research stage, we reach the point that allows us to start training, validating, and testing the ML models. The 48 experiments will enable the ML model's investigation with adequate measurement events. Moreover, the CNC and manual motions were designed to lead the receiver to collect measurements over station marker locations with different periods and Misplaced points. That allows the research to train the ML models with unbiased amount measurements in quantity. The first step in phase 2 was dedicated to data scaling. This study utilized the standard scaler, a machine learning feature normalization, and a preprocessing technique to create consistent values for dataset variables. It is included in Python's scikit-learn toolkit and is used prior to training a model for machine learning.

This procedure is used to normalize continuous numerical features to a common scale. The standard scaler analyses each feature separately and then aggregates the data for that feature to determine its mean and standard deviation. This step is essential for some ML models where the magnitude of variable values affects classification accuracy. Applying a standard scaler ensures that features have uniform scales, which benefits various machine learning algorithms sensitive to feature scales (such as linear regression, logistic regression, and support vector machines).

The second step was dataset splitting. Those investigations were essential to ensure that the ML models used data samples from the whole data population in the three phases of training, testing, and validation. In this step, the research led us to divide the research database into three sub-datasets: The 48 experiments were adequate to conduct the research using 40% of data for ML model training, 30% for testing ML models, and the rest of the data for models' validation. The default values used for training and testing usually equal 70% and 30% as a role of thump. However, in this study, we used the premonition data splitting percentage to ensure the model was trained, validated, and tested in three different data sets. Additionally, all the measurements were shuffled randomly before creating the three datasets to ensure the removal of time and distance dependency (Hastie et al., 2009; Swamynathan, 2019; Tan et al., 2016).

❖ Phase 3:

This phase introduced the background for the confusion matrix and the EWS probabilities. The confusion matrix is a prevalent measure used while solving classification problems. It can be applied to binary classification as well as to multiclass classification problems. An example of a confusion matrix for three classification classes is shown in the table below.

The confusion matrix consists of six essential characteristics (numbers) used to define the measurement metrics of the classifier. These six numbers are:

- **TP (True Positive):** TP represents the number of misplaced events from the marker location, and ML models correctly classify them.
- **TN (True Negative):** TN represents the number of events centered (no motion) above the marker location, and ML models correctly classify them.
- **TNE (True Neutral):** TNE represents the number of events that are correctly out of service and correctly classified with ML models. Those events are named neutral because the research is not sure enough if those events are centered (no motion) or misplaced from the station marker location.
- **FP (False Positive):** ML models classify as misplaced or out-of-service observations that are really centered. FP is also known as a *Type I error*, causing a false alarm of the EWS.
- **FN (False Negative):** ML models classify as centered or out-of-service observations that are really misplaced. FP is also known as a *Type II error*. It is causing no alarm when the EWS should generate it.
- **FNE (False Neutral):** ML models classify as centered or misplaced observations that are really out of service. FP is also known as a *Type III error*, causing, in the case of misplaced bad classified observations, a false alarm of the EWS.

Table 6.19 Confusion matrix elements.

Actual Label \ Predictions			
	#Of Events with Truly Non-Motion Detection **TN**	#Of Events with False Non-Motion Detection **FN**	#Of Events with False Non-Motion Detection **FN**
	#Of Events with False Motion Detection **FP**	#Of Events with Truly Motion Detection **TP**	#Of Events with False Motion Detection **FP**
	#Of Events with False Out of Service Detection **FNE**	#Of Events with False Out of Service Detection **FNE**	#Of Events with Truly Out of Service Detection **TNE**

This research used the accuracy value as a performance indicator. Moreover, in this study, seven different probabilities have been investigated utilizing the following equations:

$$\text{The Probability of Truly Non} - \text{Motion Detection} = \frac{\text{TN}}{\text{TN} + \sum \text{FN}}\% \quad (6.3)$$

$$\text{The Probability of False Non} - \text{Motion Detection} = \frac{\sum \text{FN}}{\text{TN} + \sum \text{FN}}\% \quad (6.4)$$

$$\text{The Probability of True Motion Detection} = \frac{\text{TP}}{\text{TP} + \sum \text{FP}}\% \quad (6.5)$$

$$\text{The probability of Flase Motion detections} = \frac{\sum \text{FP}}{\text{TP} + \sum \text{FP}}\% \quad (6.6)$$

$$\text{The probability of Truly Out of Service Detection} = \frac{\text{TNE}}{\text{TNE} + \sum \text{FNE}}\% \quad (6.7)$$

$$\text{The probability of False Out of Service Detection} = \frac{\sum \text{FNE}}{\text{TNE} + \sum \text{FNE}}\% \tag{6.8}$$

$$\begin{aligned}\text{The probability of False } Classifications\ \% \\ = \text{The Probability of False NonMotion Detection} \\ + \text{ The probability of Flase Motion detection} \\ + \text{The probability of False Out of Service Detection}\end{aligned} \tag{6.9}$$

$$\text{ML model's accuracy} = \frac{\text{TN} + \text{TP} + \text{TNE}}{\sum \text{Events}}\% \tag{6.10}$$

The probabilities equations above are explained in the following probabilities matrix.

Table 6.20 EWS probability matrix elements.

		Predictions		
Actual Label		Probability Of Truly Non-Motion Detection	Probability Of False Non-Motion Detection	Probability Of False Non-Motion Detection
		Probability Of False Motion Detection	Probability Of True Motion Detection	Probability Of False Motion Detection
		Probability Of False Out of Service Detection	Probability Of False Out of Service Detection	Probability Of Truly Out of Service Detection

- Phase 4:

The ultimate stage pertained to constructing a performance comparison among different ML models utilizing the abovementioned metrics. The performance analysis was constructed separately for each type of experiment. Accordingly, the research concludes with an assessment of EWS performance with respect to horizontal, vertical, and 3D deformations. Consequently, this is followed by examining the feature importance investigation; this is essential to reduce the feature space dimensions, enhancing the ML model's performance and accuracy. Eventually, EWS ML models were exported in Python Pickle (PLK) format to ease the implementations (Python, 2023). The exported EWS ML models include a vertical model that emulates the uplifting and land subsidence, a horizontal model that simulates the horizontal deformations, and 3D models to mirror the generic model. It is worth mentioning that the deformation monitoring users could select suitable models according to their monitoring needs.

6.3.9 Work package 9 (Data interpretation)

In the previous research phase, the focus was on understanding, interpreting, and presenting the outcomes. Python visualization libraries, Pandas, Plotly, Matplotlib, and Seaborn, were employed for this purpose. Additionally, Tableau and Excel were used in the current phase (Matplotlip, 2012; Microsoft, 2023b; Pandas, 2023; Plotly, 2023; Seaborn, 2022; Tableau Software, 2023). The software mentioned above and libraries were used to generate critical figures, such as features correlation matrices, feature importance, and event distribution analysis for displacement movement types, and utilized correction streams and elevation angles. Furthermore, numerous charts and figures were produced to examine the correlation between elevation angles and displacement values. Subsequently, the performance of ML models With respect to the achieved accuracy and true/false alarm warning probability was analysed through various charts. Notably, several comparison tables were generated to compare and contrast the performances of different ML models.

6.3.10 Work package 10 (Azure platform)

The final study deliverable was expanded to deploy an external portal to validate the research findings. Consequently, the Microsoft Azure cloud computing platform provides solutions and capabilities for developing, distributing, and managing cloud-based software. Subsequently, the research database was stored in the platform cloud. Azure automatically generated the automatic ML baseline to investigate the performance of numerous ML models (Microsoft, 2023a). It is worth highlighting that the Azure-generating ML models can be exported; accordingly, the Python pickle library can be used to read the model (Python, 2023).

Consequently, it can be utilized by incorporating the BNC software as a core of establishing EWS. Accordingly, the RT-PPP observations can be used as inputs for the trained Azure-generating ML model for initiating deformations early warnings.

Chapter 7 Results and Discussions

7.1 Introduction

Improving RT corrections enhances the RT-EWS execution. Previous discussions have highlighted several challenges with RT corrections, such as latencies, availability, and outliers. Since RT corrections rely on data transmission over the internet, they are susceptible to spoofing and cyber-attacks. Additionally, explained error sources and the continuity of correction streams can influence the quality of PPP measurements. Consequently, as mentioned earlier, these issues can significantly impact the performance of RT-PPP and the EWS, which rely on RT-PPP measurements. The first part of this chapter presents research findings focused on the latency problem in RT corrections. The chapter contains the results obtained regarding the investigations on the availability of clock correction, the maximum clock correction consecutive difference value as it indicates leaps in clock correction values. The chapter also shows the SVR and ARIMA evaluation performance in terms of statistical analysis. The finding extended to cover all research years' mean, range, and standard deviation comparisons. This is followed by the simulated results, which regard the obtained prediction values and their influences on the RT-PPP coordinates performance. As the research extended to cover several years, the IGS RT corrections improved, allowing the researchers to investigate the performance of the applied ML concerning Galileo and BeiDou besides the primary GPS and GLONASS systems. Accordingly, this chapter includes a comparison analysis regards the comprehensive analysis carried out on 2021 RT correction data.

The chapter introduces substantial results, provided by the integration of the experimental device with the reference station for simulating displacements; this follows with the analysis of feature correlation analysis and concludes with the feature correlation matrix. Tropospheric error, tracked satellite number, delay, phase residuals, elevation angles, acquired coordinates, coordinate precision, and root mean squared errors were all subjected to correlation studies. Following the initial phase, the research experiments were systematically manipulated by employing multiple elevation angles and diverse correction streams, subjecting them to various artificial deformations that varied in magnitude and direction. Consequently, the resulting measurements of RT-PPP exhibited variations in terms of their quality and accuracy. Training and testing the RT-PPP EWS

machine-learning models with diverse RT-PPP measurements were possible, subsequently enhancing the EWS performance.

Chapter seven also contains results regarding the event distribution with respect to the latency of the used stream, elevation angle, and type of exerted deformations, followed by assessment results of RT-PPP EWS ML models; this evaluation contains several probabilities analyses, such as the RT-PPP EWS probabilities of initiating true warning regards motion/non-motion/out of service detection in addition to the RT-EWS probabilities of initiating false warning regards motion/non-motion/out of service detections.

7.2 Latency results

As described earlier in the previous chapters, the investigation results regarding the stationarity of the clock correction time-series data is an essential primary step for choosing suitable ML prediction models. Consequently, the SVR and ARIMA have been utilized in this study. Chapter six introduced the study findings regarding the RSW investigations, which led the research to utilize RSW with a period of 8 and one minute to train ARIMA and SVR, respectively. Additionally, the RSW with a period of 8 minutes and one hour was used to update the model hyperparameters to the ARIMA and SVR, respectively. The third work package in chapter six investigated the unavailability of RT-PPP correction as the stream results were subjected to encounter periods of outages and interruptions. Table 7.1 shows the research findings regarding the availability of clock corrections during the research years, considering that the investigation was carried out within one day. During this period, the clock corrections encountered periods of outages. It can be seen from the table data that some satellite blocks encounter a period of interruptions. For instance, the GLONASS-K block showed 10-26 % of clock corrections unavailability, corresponding to 2-6 hours of interruption periods. Moreover, it encounters a reduction in the availability of corrections; around 24% of the reduction was found between 2013 and 2021. These interruptions degrade the RT-PPP solution in terms of quality and availability.

Table 7.1 The availability of clock correction behavior.

Date	Satellite Block	Clocks corrections availability (%)
29/10/2013	GPS-IIF	98.13
	GPS-IIR	99.97
	GPS-IIRM	99.97
	GLONASS-K	100
	GLONASS-M	96.88
13/01/2014	GPS-IIF	96.07
	GPS-IIR	99.90
	GPS-IIRM	99.96
	GLONASS-K	100.00
	GLONASS-M	98.00
25/02/2015	GPS-IIF	99.07
	GPS-IIR	99.96
	GPS-IIRM	99.93
	GLONASS-K	98.77
	GLONASS-M	99.62
14/12/2019	GPS-IIF	98.34
	GPS-IIR	99.97
	GPS-IIRM	100.00
	GLONASS-K	89.88
	GLONASS-M	99.16
21/05/2021	GPS-IIF	99.46
	GPS-IIR	91.48
	GPS-IIRM	99.89
	GLONASS-K	76.11
	GLONASS-M	96.05

The RT-PPP pilot experiment was also analysed for data on the most remarkable clock correction leaps anticipating the implementation of machine learning prediction; this could be justified by the ML prediction models encountering performance challenges due to unexpected leaps. Consequently, as part of this analysis of the clock correction, the research subtracted each consecutive clock correction value, and the Python codes were utilized to return the maximum for each GNSS satellite. We then categorized the mean value of the maximums for each satellite cluster with respect to the clock correction leaps. The average of the highest difference between two consecutive clock correction values is displayed in Table 7.2. It demonstrated that the difference, or jump, in clock correction values for GPS block IIF satellites might approach nearly

twelve meters. Subsequently, those jumps in clock corrections affect the coordinate's availability, accuracy, and prediction performance.

The result concludes that, for instance, the GPS-IIF showed an improvement of around 84% reduction with respect to 2013; in 2021, clock correction data shows that a similar improvement performance was achieved regarding the GPS-IIR blocks with an improvement of 92.5%. Additionally, the GPS-IIRM block showed an improvement in minimizing the clock correction jumps by around 89% between 2013 and 2021. However, the GLONASS satellite constellation shows minimal improvements regarding the clock correction leaps compared to the GPS. For instance, GLONASS block K shows an 18% improvement regarding clock correction leaps.

On the contrary, the GLONASS-M block showed a degradation of around 53% between 2013 and 2021. It is worth mentioning that the GLONASS-K is the newest block for the GLONASS constellation, and it contains two versions, K1 and K2 blocks. It is worth emphasizing that the onboard satellite clock's stability influences the clock correction leaps accordingly; the GPS constellation demonstrated better enhancement through the research years.

The stability of satellite clocks influences the positioning performances as well as its effects on the ML prediction model's results. The chapter results regarding the clock corrections mean, range, and standard deviation assessments showed a lower enhancement regarding the clock corrections range analysis over the standard deviation evaluations. It is worth noting that those leaps' percentages are slightly small compared to the entire clock corrections population.

Table 7.2 The average of cock corrections maximum consecutive average.

Year	Satellite Block	Average of Maximum consecutive differences (meters)
2013	GPS-IIF	11.68
	GPS-IIR	2.16
	GPS-IIRM	2.15
	GLONASS-K	0.50
	GLONASS-M	1.27
2014	GPS-IIF	0.75
	GPS-IIR	0.26
	GPS-IIRM	0.48
	GLONASS-K	1.25
	GLONASS-M	1.04
2015	GPS-IIF	0.27
	GPS-IIR	0.37
	GPS-IIRM	0.29
	GLONASS-K	0.49
	GLONASS-M	1.41
2019	GPS-IIF	0.11
	GPS-IIR	0.31
	GPS-IIRM	0.19
	GLONASS-K	0.43
	GLONASS-M	0.63
2021	GPS-IIF	0.16
	GPS-IIR	0.16
	GPS-IIRM	0.22
	GLONASS-K	0.41
	GLONASS-M	1.95

7.2.1 ML prediction models' assessment regards the latency issues.

Chapter Six, work Package Five utilized the SVR and ARIMA prediction model to overcome the latency effect of RT-PPP products. The statistical assessment was carried out in this research by performing range, standard deviation, and mean comparisons regards the model's prediction clock corrections. Thus, to create a reliable comparison, the standard deviation of the clock correction residuals was derived by subtracting the SVR and ARIMA forecasts with respect to the free

latency. On the other hand, the standard deviation of the clock correction residuals was derived by subtracting the forced latency with respect to the free latency; that allowed the researchers to compare the performance of prediction models with respect to an ideal situation where the latency value does not impact the GNSS users from one side. On the other side, the research compared the RT situation where the latency impacts the GNSS users with respect to the ideal situations. The range and mean assessment were carried on similarly for SVR, ARIMA, and forced latency solutions. It is worth noting that the analysis of the mean of the residuals had been eliminated due to the similarity of the obtained results, which found the zero mean value of the clock correction subtracting from the forced latency, SVR, and ARIMA forecasts with respect to the free latency; this finding could be justified as a result of similarities among the four clock correction signals, for instance the free latency and forced latency signals are nearly similar due to the slight shifting of the correction values ahead with the latency value which the research utilized in order to simulate the latency effect (30 seconds in the case if the IGS combined products). However, the SVR and ARIMA constructed signals are more similar to the free latency signal due to the likeness between the predicted and free latency clock correction values. Figure 7.1 delineates the graphical representation of research-oriented clock correction signals. The initial signal within the plot describes the free-latency time-series signal, thereby encapsulating clock correction values devoid of latency-induced influences. In contrast, the subsequent signals, ARIMA and SVR, correspond to predicted clock correction values inferred by the machine learning models. The forced-latency example is established, wherein a 30-second shifted head artificially displaced clock correction values to simulate latency impacts. A pronounced likeness across all the research signals is discernible from the graphical exposition. It is essential to recognize that the illustrated figure embodies the clock correction value acquired at the beginning of May 22, 2021, about the GPS G01 satellite. A visible similarity prevails among the research time-series signals. The figure illustrates that the ARIMA and SVR solutions establish higher similarities to the free-latency solutions more closely than the forced-latency solution. Accordingly, the pre-mentioned related issues justify that the research assessment of residual mean analysis was omitted due to the convergence of outcomes, which revealed a nearly zero mean value for the clock correction solution subsequent to the residual values derived by deduction of the SVR, ARIMA forecasts and forced-latency with respect to the free latency.

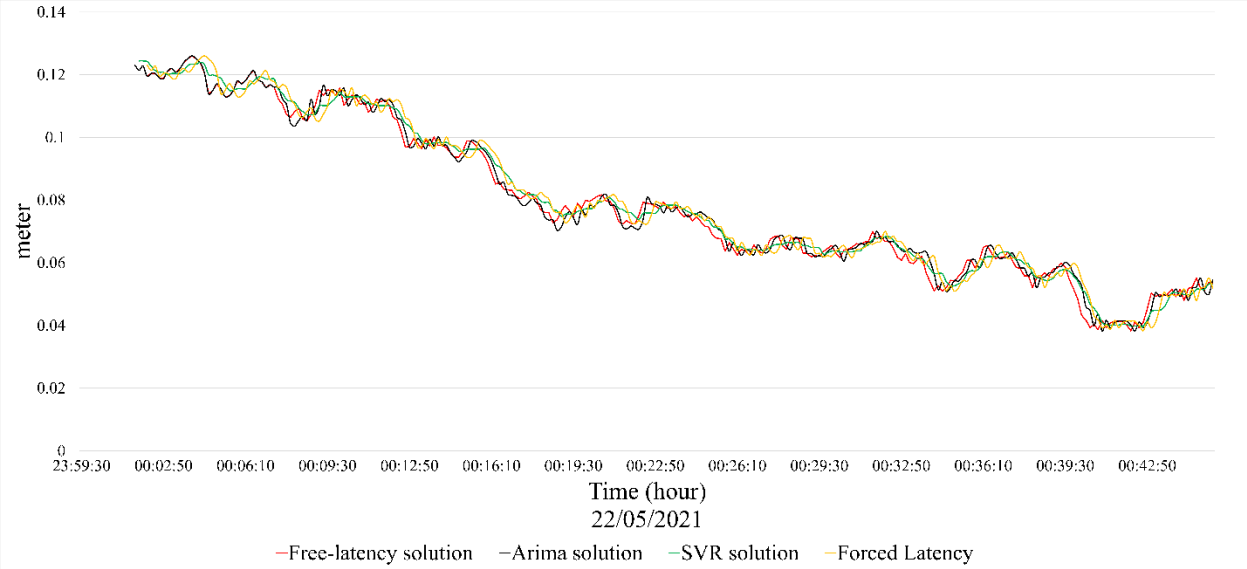

Figure 7.1 Temporal evolution of IGS03 clock correction solutions: Analyzing time series signals

(Prepared by the author).

After the initial data from the pilot study had been analysed, researchers could look into how well the applied ML worked with Galileo and BeiDou in addition to the primary GPS and GLONASS systems because the study lasted for multiple years, and since IGS RT corrections improved. In light of the exhaustive research performed on the RT correction data for 2021, this chapter provides a comparison results analysis. It is worth mentioning that the rest of the results regarding all the research years can be found in the appendices section. Figures 7.2 to 7.5 show the standard deviation comparison with respect to the three solutions for BeiDou, GLONASS, Galileo, and GPS constellation*s*.

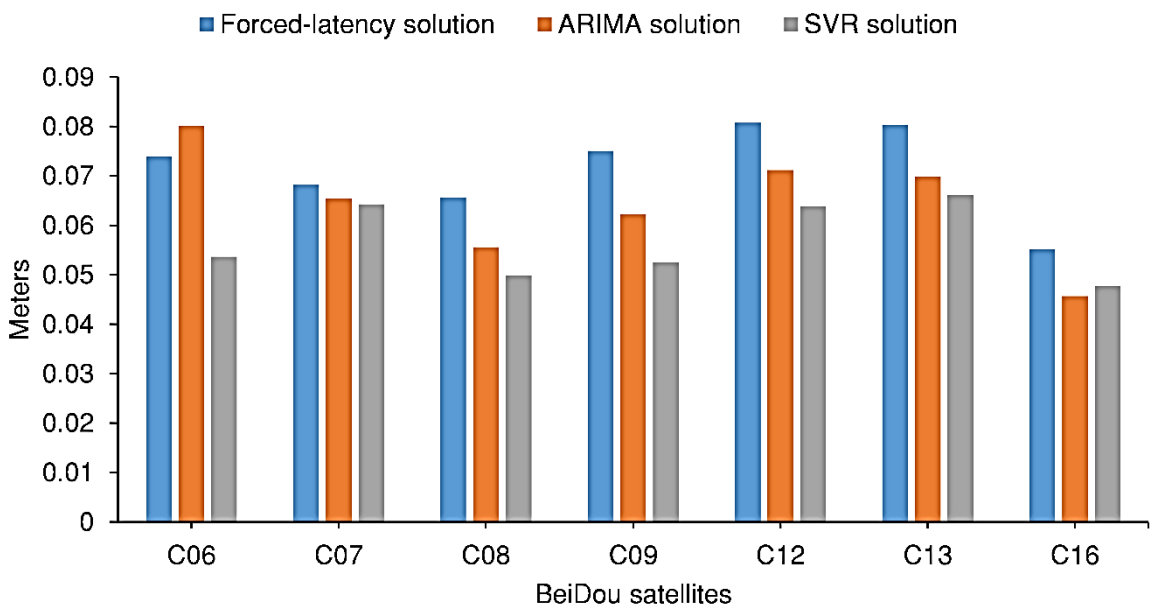

Figure 7.2 IGS03 standard deviations in meters for BeiDou satellites according to 2021 data

(Prepared by the author).

The study outcomes about the standard deviation improvements with respect to the BeiDou satellite system revealed that satellite C09 exhibited the most favourable outcomes regarding the performance of the SVR and ARIMA ML prediction models. Notably, the SVR model demonstrated a performance enhancement of 30 percent, while the ARIMA model showcased a 17 percent improvement compared to the forced latency. Moreover, an analysis of satellite C07 indicated a minimal 5 percent increase in SVR performance due to the latency impact. Conversely, findings from satellite C06 demonstrated that the employment of the ARIMA solution marginally elevated the latency effect by 8 percent.

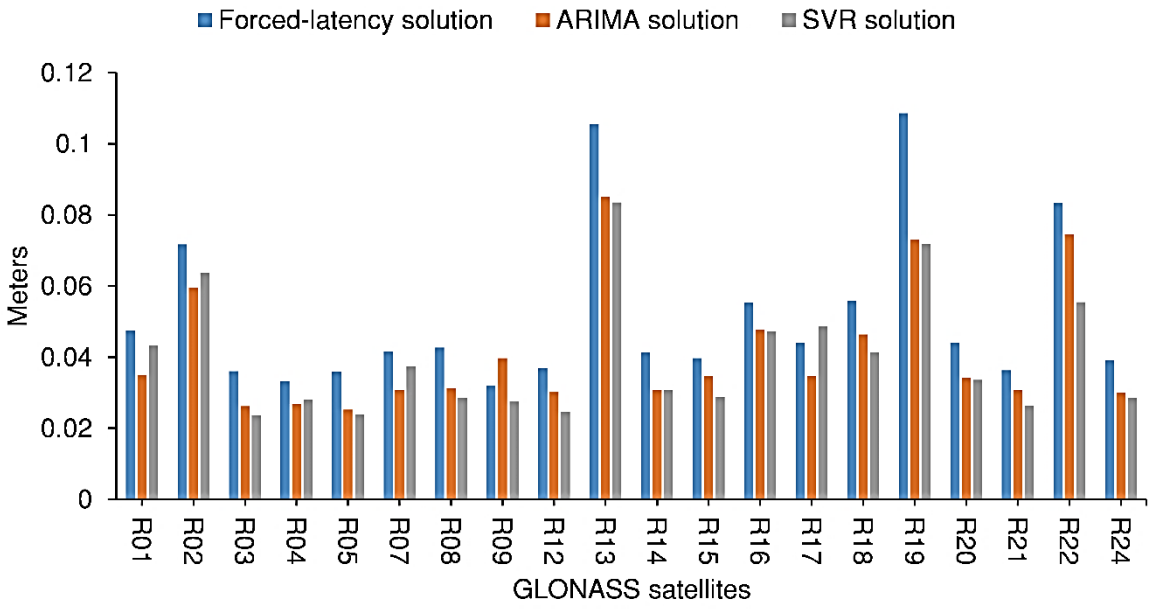

Figure 7.3 IGS03 standard deviations in meters for GLONASS satellites according to 2021 data

(Prepared by the author).

The study results about the standard deviation enhancements with respect to the GLONASS satellite system exposed that satellite R19 exhibited the most advantageous outcomes regarding the performance of the ARIMA. With respect to the SVR ML prediction model, the most valuable outcome is dedicated to the R22. Remarkably, the SVR model established a performance enhancement of 34 percent, while the ARIMA model showcased a 33 percent improvement compared to the forced latency. Conversely, an analysis of satellite R17 indicated a slightly increased latency impact of 10 percent regarding the SVR performance. Moreover, findings from satellite R09 demonstrated that the employment of the ARIMA solution elevated the latency effect by 24 percent. It is worth mentioning that R17 and R09 GLONASS satellites are the only satellites showing degradation of the applied ML prediction models.

The research findings addressing the influence of the prediction ML models on the Galileo satellite system are depicted in Figure 7.4. According to the study's findings on standard deviation enhancements for the Galileo satellite system, satellite E01 displayed the best results regarding ARIMA performance, and satellite E08 displayed the best results regarding SVR ML prediction models. Remarkably, the ARIMA model showed a 36 percent improvement for the E15 satellite

compared to the forced latency, while the SVR model showed a performance improvement of 37 percent for the E08 satellite. Additionally, due to the latency impact, an investigation of satellite E24 showed a minor 5 percent improvement in SVR performance.

On the other hand, a study of satellite E24 revealed a 10 percent increase in latency impact on the ARIMA performance. It is important to note that the E24 Galileo satellite is the only one that exhibits a decline in the ARIMA prediction model's performance.

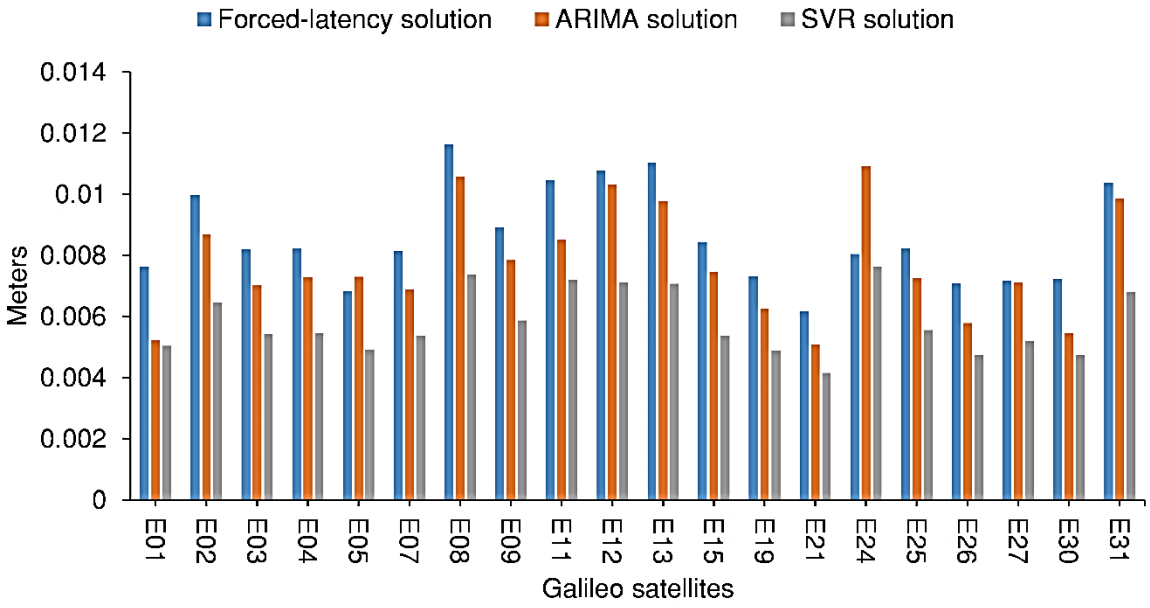

Figure 7.4 IGS03 standard deviations in meters for Galileo satellites according to 2021 data

(Prepared by the author).

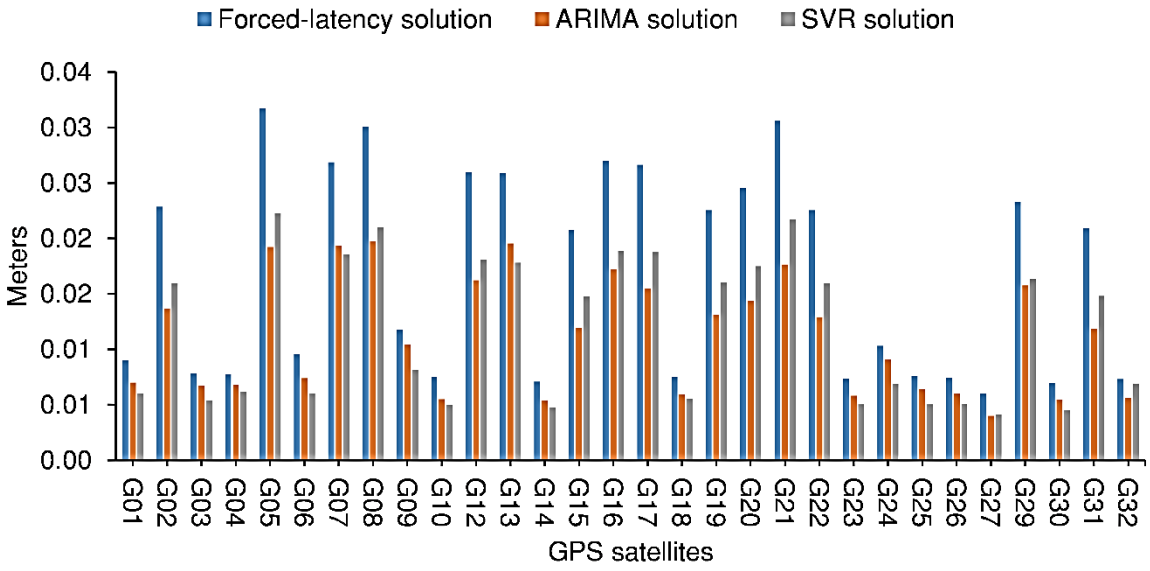

Figure 7.5 IGS03 standard deviations in meters for GPS satellites according to 2021 data

(Prepared by the author).

The research outcomes about the impact of prediction ML models on the GPS satellite system are graphically depicted in Figure 7.5. The investigation revealed noteworthy findings regarding the influence of the SVR and ARIMA ML prediction models on the clock corrections standard deviation enhancements. Notably, satellite G06 exhibited the most favourable results in terms of SVR performance, whereas satellite G31 showcased superior outcomes for the ARIMA ML prediction models compared to the forced latency; the ARIMA model exhibited a substantial 43 percent improvement for the G21 satellite, whereas the SVR model demonstrated a performance enhancement of 37 percent for the G08 satellite. Furthermore, an examination of the latency impact on satellite G32 indicated a minor 5 percent improvement in SVR performance, whereas implementing the ARIMA model results in an 11 percent enhancement for the G09 satellites. It is crucial to emphasize that the SVR and ARIMA ML models can improve the standard deviation performance of all GPS satellites, thus mitigating the latency effect effectively. Table 7.3 shows the statistical assessments for the research solutions over several research years.

Following the previous standard deviation assessment, the research analyses were extended to evaluate the range performance. It is important to note that the range is a sensitive statistical

indicator. As clock corrections encounter a period of interruptions, fluctuations, and the most critical effect of the clock jump period, all of the issues could affect the ML model's performance accordingly; if the prediction models are due to the previous issues raising or reducing the clock corrections expectations, that lead to degraded range enhancement. Table 7.4 shows the range of statistical assessments for the research solutions over several years.

Figures 7.6 to 7.9 show a range comparison with respect to the three solutions for BeiDou, GLONASS, Galileo, and GPS constellations.

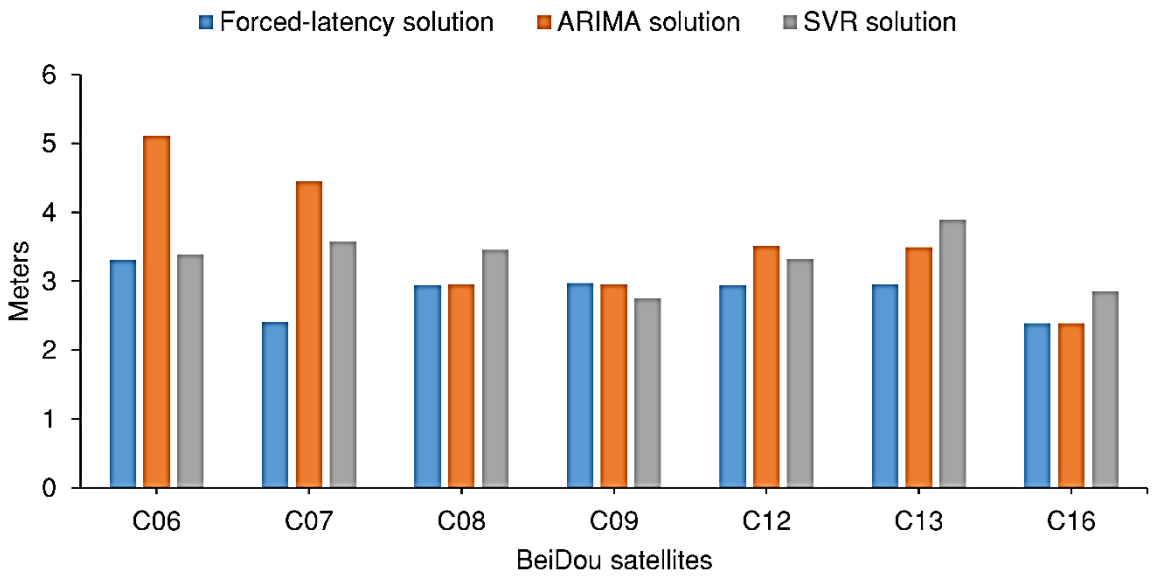

Figure 7.6 IGS03 range differences in meters for BeiDou satellites according to 2021 data

(Prepared by the author).

The study outcomes about the range improvements with respect to the BeiDou satellite system revealed that satellite C09 exhibited the most favourable outcomes regarding the performance of the SVR and ARIMA ML prediction models. Notably, the SVR model demonstrated a performance enhancement of 7 percent, while the ARIMA model showcased a 1 percent improvement compared to the forced latency. Conversely, findings from satellite C07 demonstrated that the employment of the ARIMA and SVR solution elevated the latency effect by 85 percent and 49 percent, respectively.

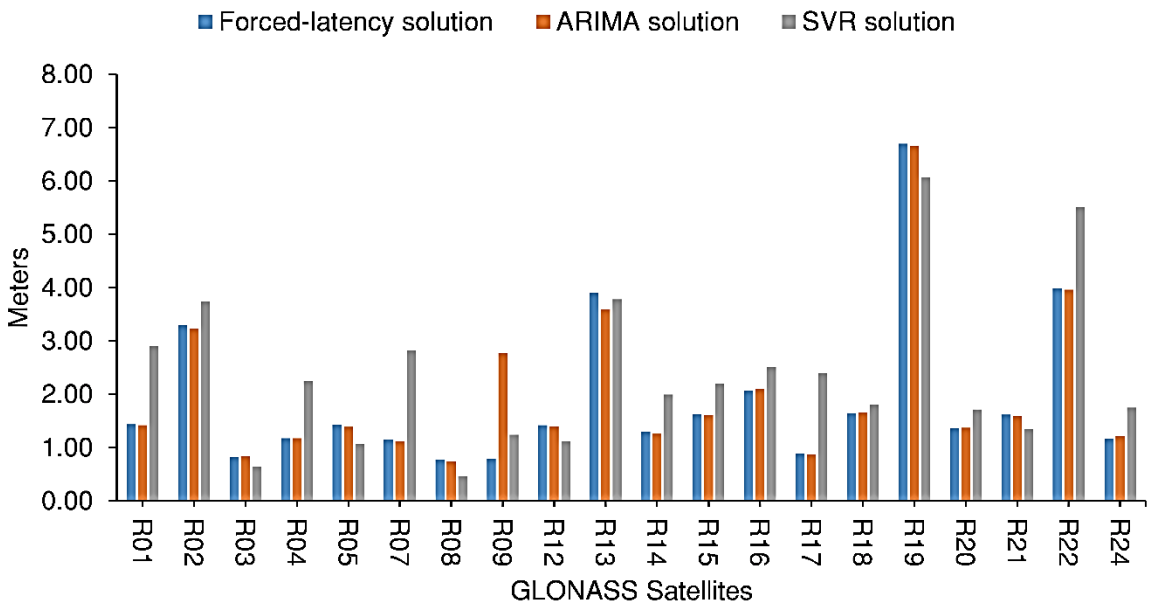

Figure 7.7 IGS03 range differences in meters for GLONASS satellites according to 2021 data

(Prepared by the author).

The study results about the range enhancements with respect to the GLONASS satellite system exposed that satellite R08 exhibited the most advantageous outcomes regarding the performance of the SVR prediction model. Noting, the model established a performance enhancement of 40 percent, while the ARIMA model showcased around 8 percent improvement compared to the forced latency to the R13 GLONASS satellite. Conversely, an analysis of satellite R09 indicated a slightly increased latency impact of 25 percent regarding the ARIMA performance. Moreover, findings from satellite R17 demonstrated that the employment of the SVR solution elevated the latency effect by 17 percent.

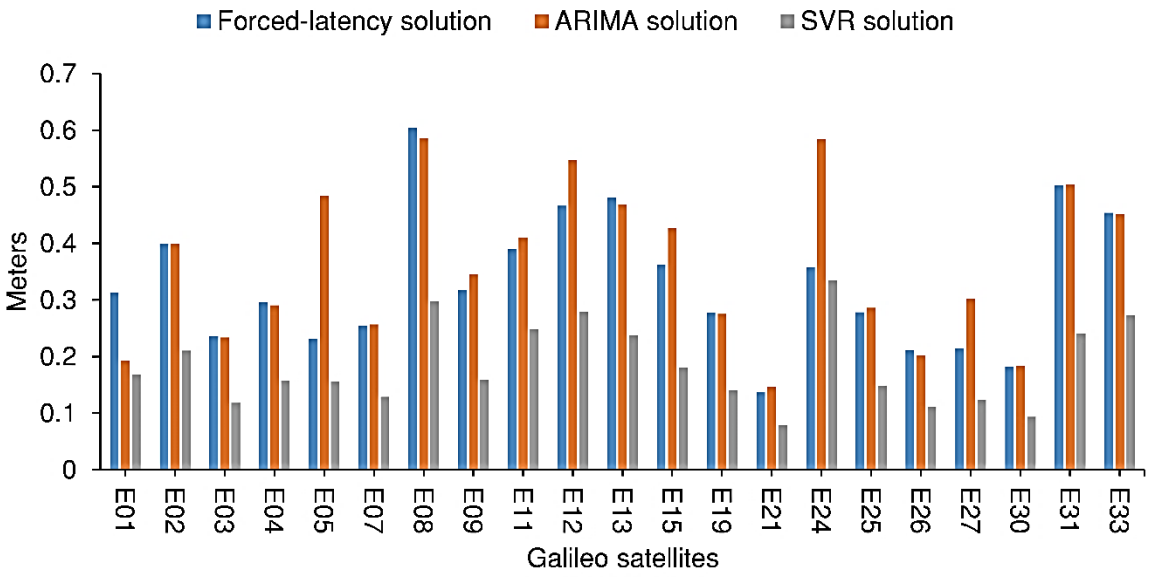

Figure 7.8 IGS03 range differences in meters for Galileo satellites according to 2021 data

(Prepared by the author).

The research findings addressing the influence of the prediction ML models on the Galileo satellite system are depicted in Figure 7.8. The study's findings on range enhancements for the Galileo satellite system show that satellite E01 displayed the best results regarding ARIMA performance, and satellite E31 displayed the best results regarding SVR ML prediction models. Remarkably, the ARIMA model showed a 38 percent improvement for the E01 satellite compared to the forced latency, while the SVR model showed a performance improvement of 52 percent for the E31 satellite. Additionally, regarding the latency impact, an investigation of satellite E24 showed a 6 percent with minor improvement in SVR performance to all Galileo satellites. Additionally, the E05 Galileo satellite shows a degradation of the enhancement regarding the range evaluation by 11 percent. It is important to note that the Galileo satellite system exhibits a remarkable enhancement in range analysis compared to the GLONASS and BeiDou constellations.

The research outcomes about the impact of prediction ML models on the GPS satellite system are graphically depicted in Figure 7.9. The analysis revealed noteworthy findings regarding the influence of the SVR and ARIMA ML prediction models on the clock correction range improvements. Notably, satellite G06 exhibited the most favourable results in terms of SVR performance, whereas satellite G07 showcased superior outcomes for the ARIMA ML prediction models compared to the forced latency; the ARIMA model exhibited a substantial 21 percent improvement for the G08 satellite, whereas the SVR model demonstrated a performance enhancement of 61 percent for the G06 satellite. Furthermore, examining the latency impact on satellite G03 indicated a minor 26 percent improvement in SVR performance. Conversantly implementing the ARIMA model results in a 13 percent range degradation for the G29 satellites. It is crucial to emphasize that the SVR and ARIMA ML models notably improve the standard deviation and range performance for most GPS and Galileo satellites, thus mitigating the latency effect effectively. These results could be justified in implementing high-stability satellites in both systems.

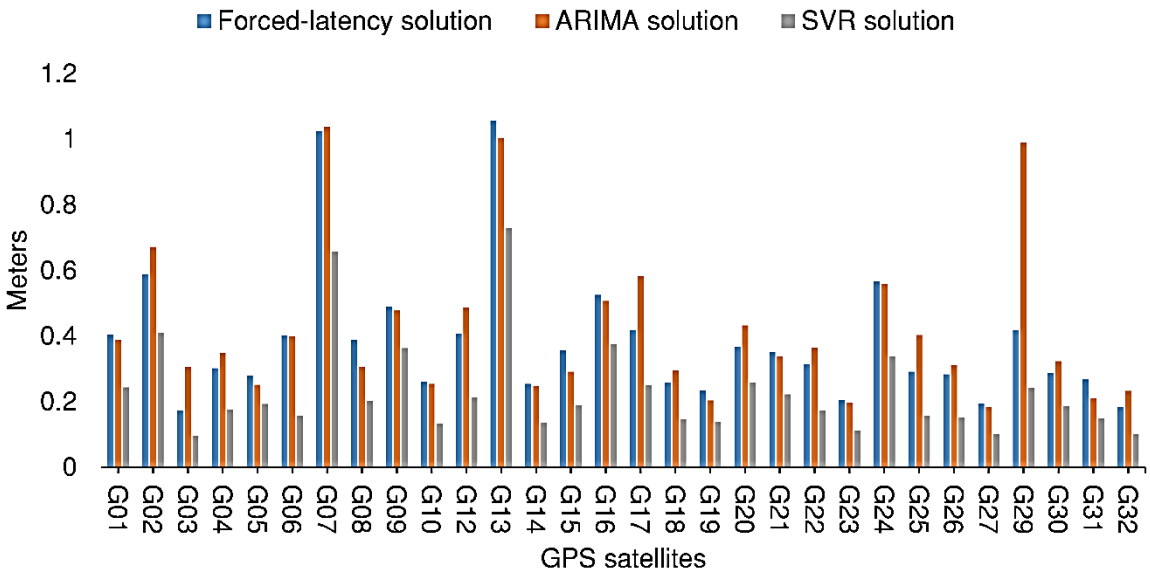

Figure 7.9 IGS03 range differences in meters for GPS satellites according to 2021 data

(Prepared by the author).

Eventually, the previous research finding in this section summarizes the performance of the utilized prediction ML models through the research years. Tables 7.3 and 7.4 show the ultimate research finding in terms of standard deviations and the average of the range, which have been calculated from the residuals obtained by subtracting the clock correction values among the research solution with respect to the free-latency solution. Remarkably, the ARIMA model showed outstanding performance for the GPS-IIRM block, reaching around 33 percent in 2014 and 2019, and notably, the GPS-IIF block showed a reduction of standard deviation, reaching 50 percent in 2015. The GPS-IIR and GPS-IIRM satellite blocks show Similar results with respect to the 2021 research year. However, the ARIMA showed minimum model improvement concerning the GLONASS-K satellite block. Note that the ARIMA model shows an ability to reduce the standard deviation for the majority of GNSS satellite blocks.

On the other hand, the SVR model shows a slightly similar performance. For instance, the standard deviation improved for the GLONASS-K satellite block by 25 percent and 14 percent in 2013 and 2015, and it reached the same satellite block with around 31 percent enhancement concerning standard deviation enhancement in 2021.

It is worth noting that the figures in the table were categorized for each satellite block. Thus, irregular behaviour from the individual satellite could disturb the average, driven values.

Table 7.3 Clock corrections standard deviations of all researched years.

Solution	Satellite Block	2013	2014	2015	2019	2021
Forced-latency solution	GPS-IIF	0.39	0.04	0.02	0.03	0.01
	GPS-IIR	0.11	0.03	0.03	0.02	0.02
	GPS-IIRM	0.12	0.03	0.03	0.03	0.02
	GLONASS-K	0.04	0.07	--	0.14	0.04
	GLONASS-M	0.06	0.06	0.06	0.05	0.05
ARIMA model	GPS-IIF	0.34	0.03	0.01	0.02	0.01
	GPS-IIR	0.09	0.02	0.02	0.02	0.01
	GPS-IIRM	0.10	0.02	0.02	0.02	0.01
	GLONASS-K	0.04	0.07	--	0.13	0.03
	GLONASS-M	0.05	0.05	0.05	0.04	0.04
SVR model	GPS-IIF	0.32	0.03	0.01	0.02	0.01
	GPS-IIR	0.09	0.02	0.02	0.02	0.01
	GPS-IIRM	0.11	0.02	0.02	0.02	0.01
	GLONASS-K	0.03	0.06	--	0.09	0.03
	GLONASS-M	0.05	0.05	0.04	0.04	0.04

The research findings about range assessment are demonstrated in Table 7.4, which shows the capacity of the ARIMA model to enhance the range results; specifically, in 2013, the ARIMA model was observed to improve the range accuracy by approximately five meters for the GPS-IIF block. In addition, the ARIMA model shows range reduction improvements to the latency solution by around 27 percent and 15 percent in the research years 2013 and 2019, respectively. Notable improvements were observed with the SVR model for different GPS satellite blocks across the study years. The SVR model exhibited an outstanding enhancement of approximately 19 percent for the GPS-IIF block, 46 percent for the GPS-IIR block, and around 57 percent for the GPS-IIRM block in the years 2015, 2019, and 2021, respectively. However, it is worth noting that in 2013, the SVR model was found to increase the latency impact by approximately 4.80 meters for the GPS-IIF block. The SVR model's poorest performance was identified in 2014 and 2015, particularly for the GLONASS K and M satellites block, where degradation in range evaluation of 31 percent and 23 percent was observed, respectively. On the contrary, the SVR model with respect to the GPS-IIRM block showed the capacity to enhance the range performance with around 23, 25, and 57 percent, with respect to the research years 2014, 2019, and 2021.

Table 7.4 Average of clock correction ranges of all researched years.

Solution	Satellite Block	2013	2014	2015	2019	2021
Forced-latency solution	GPS-IIF	18.79	1.54	0.51	1.06	0.38
	GPS-IIR	4.41	0.84	0.77	0.68	0.40
	GPS-IIRM	4.55	0.87	0.82	1.25	0.37
	GLONASS-K	1.11	2.57	--	9.72	0.78
	GLONASS-M	2.49	2.54	2.14	2.52	1.99
ARIMA model	GPS-IIF	13.80	1.59	0.53	0.90	0.40
	GPS-IIR	4.03	0.84	0.74	0.71	0.41
	GPS-IIRM	4.13	0.88	0.88	1.21	0.47
	GLONASS-K	1.11	2.57	--	9.03	0.74
	GLONASS-M	2.70	2.25	2.05	2.49	2.06
SVR model	GPS-IIF	18.59	1.81	0.43	0.92	0.23
	GPS-IIR	4.07	0.76	0.69	0.38	0.26
	GPS-IIRM	4.36	0.68	0.98	0.91	0.20
	GLONASS-K	0.82	3.95	--	10.17	0.46
	GLONASS-M	3.03	3.04	2.74	3.07	2.46

7.2.2 Coordinates assessment regarding the latency issues.

The stored navigation, correction, and observation files were reused in post-processing mode to evaluate the impact of the clock correction prediction on the performance of RT-PPP coordinates. Consequently, the IGS03 files were recreated to hold clock correction prediction values. Subsequently, this idea allows the research to assess the SVR and ARIMA ML prediction models on the RT-PPP performance. Accordingly, the BNC software was reconfigured to perform RT-PPP with respect to SVR, ARIMA, and free and forced latency. Therefore, the impact of the ML prediction models could be assessed. It is worth mentioning that several versions of the BNC software were utilized in order to accommodate the evolution of GNSS files. This section also contains the result finding regarding coordinates availability for the ML prediction solutions.

It should be noted that the availability of the RT-PPP has remarkably improved during the research study years. Figures 7.10-7.13 show ABMF coordinate scatter plots as representative examples for all research IGS stations, summarizing the study's findings and introducing the most recent data (2021), noting that ten IGS permanent stations have contributed to this evaluation and that the

study period has been expanded to include 2013, 2014, 2015, 2019, and 2021 years. Figure 7.10 shows that the ARIMA and SVR coordinates solutions have more tendency to be distributed around the figure origin, indicating the ability of both ML models to mitigate the latency impact. It is worth noting that the figures represent the coordinates residuals in the local horizontal coordinate system.

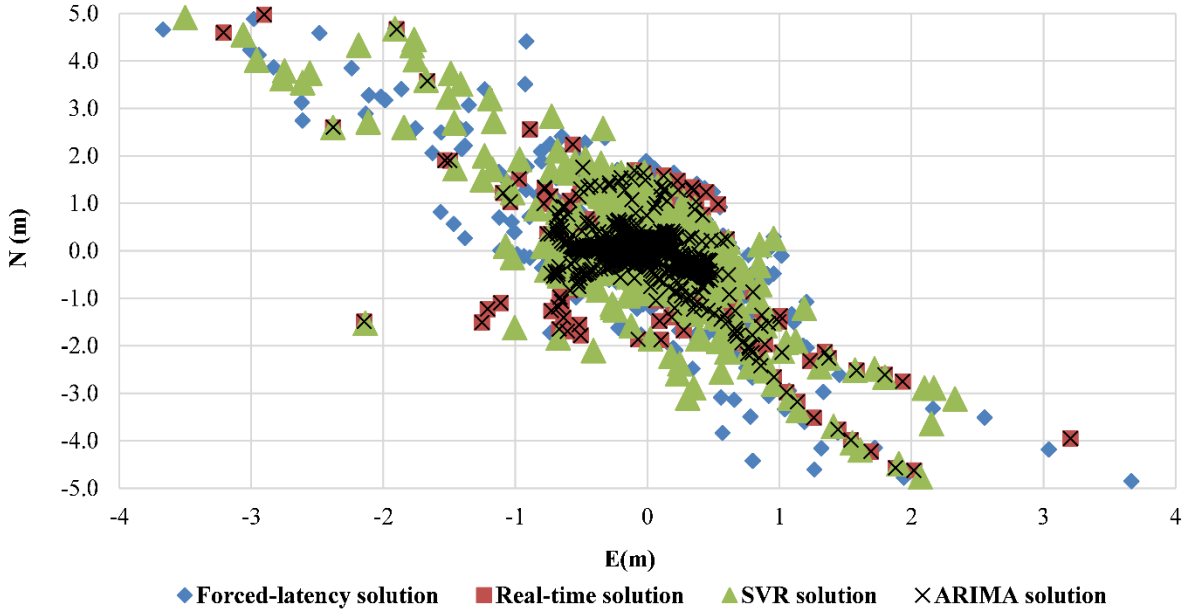

Figure 7.10 ABMF station coordinates solutions residuals according to 2021 data.

(Prepared by the author).

Figures 7.11 and 7.12 show that the ARIMA model improves the performance of the forced latency solution. Noting that the SVR solution also performs better than the forced latency solutions. However, similar performance regarding the Up component can be visualized in Figure 7.13, remarking that the Up-coordinate component witnesses notable oscillations concerning all research solutions. Figures 7.11 to 7.12 indicate the east, north, and up components within the local horizontal coordinate system.

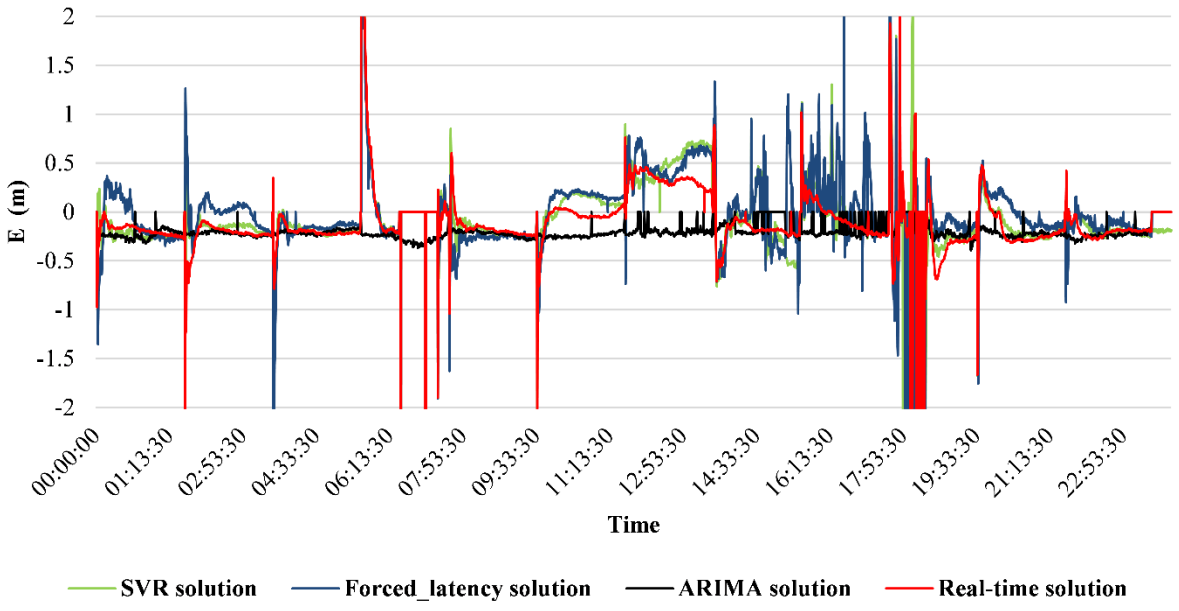

Figure 7.11 ABMF station east component residuals according to 2021 data

(Prepared by the author).

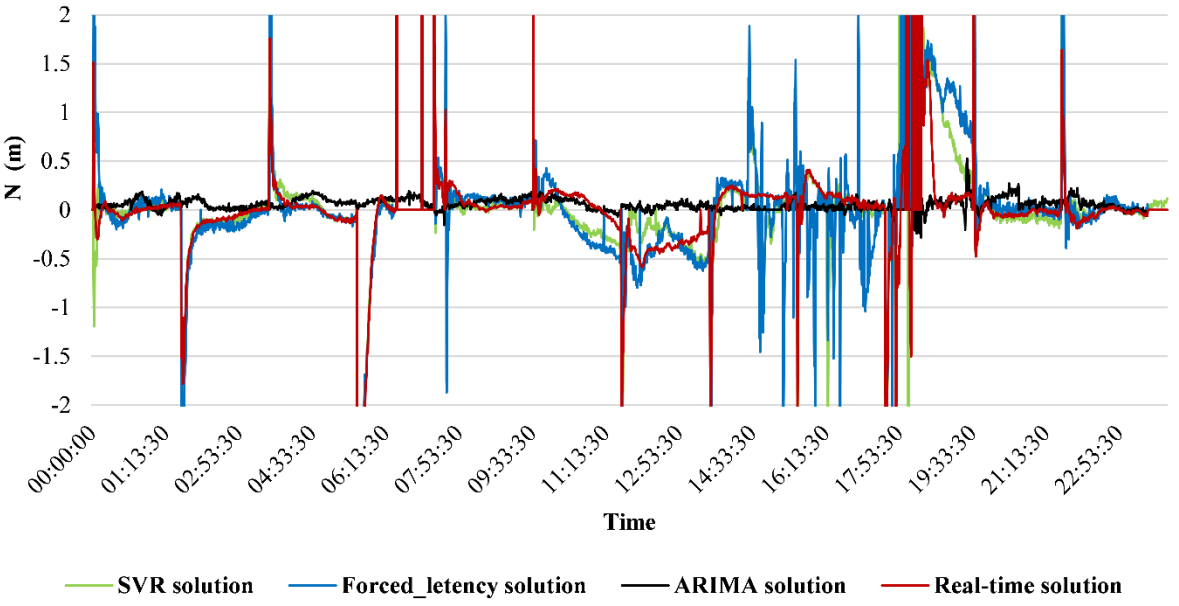

Figure 7.12 ABMF station north component residuals according to 2021 data

(Prepared by the author).

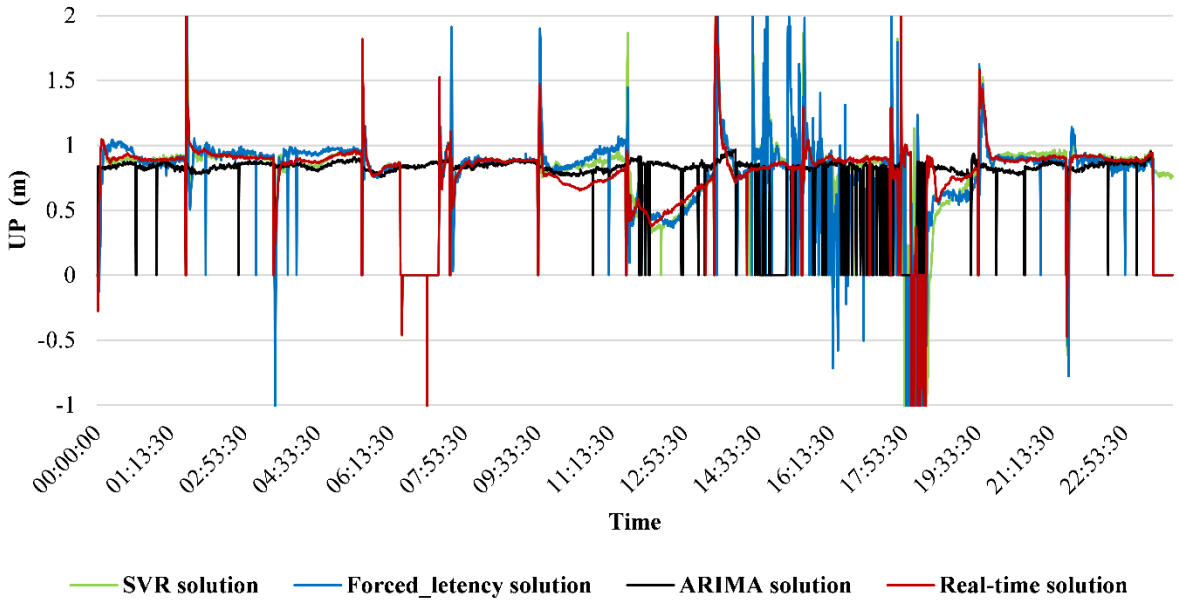

Figure 7.13 ABMF station Up component residuals according to 2021 data

(Prepared by the author).

In order to demonstrate the section results, all the researched stations through the investigation years were subjected to statistical assessment regarding the standard deviations, mean, and range analysis to the obtained coordinates from several solutions. Table 7.5 demonstrates the research three-dimensional coordinates findings concerning overcoming the latency, and the units of the figures table are in meters. All the statistical indicators have been calculated with respect to the coordinate residuals obtained by subtracting the coordinates solutions with respect to the free latency coordinates. Means, standard deviations, and ranges' averages have been calculated with respect to all coordinates' residuals. The research assessments show means, standard deviations, and ranges of average performance improvements when using the SVR and ARIMA solutions over the forced-latency solutions. The ARIMA and SVR model remarkably improve the mean coordinates value by 17 and 13 percent, respectively. In addition, the coordinate standard deviation improves by 13 and around 31 percent for the ARIMA and SVR solutions, respectively. However, the range performance shows the ability of the SVR solution to enhance the range coordinates by 11 percent.

Conversely, the ARIMA model slightly increases the range average by 3 percent with respect to the forced-latency solution. It can be concluded that the SVR and ARIMA models can mitigate the latency impact on the RT-PPP coordinates. However, the SVR model shows superior performance with respect to the coordinate standard deviation improvement. Accordingly, a notable performance for the SVR and ARIMA models, regarding the coordinates mean assessment, was found in 2014 and 2015, with the ability to enhance the mean coordinate value by around 50 percent. In addition, the same research years showed the enhancement of the standard deviation performance by 40 percent with respect to the ARIMA model and 20 percent to the SVR model. Regarding the coordinates range assessment, the ARIMA model shows enhancement of the range values with 15, 39.5, and around 1 percent with respect to the research years 2013,2015,2019, respectively.

On the other hand, the SVR model notably improves the coordinate range values by 13,13.5 and 23 percent concerning the research years 2013, 2015, and 2021, respectively.

Table 7.5 shows 3D coordinates results from the research assessments regarding all the study research years, and all studied IGS stations. Where the table units are in meters; however, the 3D coordinates results were aggregated in order to show the performance of all the research stations.

Table 7.5 3D coordinates results from evaluation regarding all the study research years (the table units are in meters).

Statistical indicators	Solution	Average of all years	2013	2014	2015	2019	2021
Mean	Forced-latency solution	0.23	0.04	0.07	0.51	0.40	0.14
	ARIMA model	0.19	0.04	0.04	0.22	0.42	0.21
	SVR model	0.20	0.06	0.04	0.40	0.41	0.10
Standard deviation	Forced-latency solution	0.84	0.60	0.47	1.26	0.76	1.11
	ARIMA model	0.73	0.66	0.44	0.75	0.70	1.12
	SVR model	0.58	0.58	0.38	1.43	0.69	0.75
Range	Forced-latency solution	11.52	13.74	7.74	7.79	11.01	17.33
	ARIMA model	11.90	11.68	8.92	4.71	10.94	23.27
	SVR model	10.25	11.95	8.20	6.75	11.34	13.20

The research latency assessments were extended to evaluate the ML prediction models regarding the coordinates' availabilities. Ten IGS permanent stations have been involved in the current assessment, and the research has been prolonged to cover the years 2013, 2014, 2015, 2019, and 2021. Table 7.6 shows the availability assessments of all IGS research stations during the investigation years, where more evaluation of the stations can be found in the appendices sections. The table shows the availability of ML prediction models with respect to the forced latency solution. Noting that, for example, the ARIMA and SVR model's ability to enhance the station's coordinate availability by around 5 percent with respect to 2013 and 2015. It is of notable import to recognize that Table 7.6 figure expresses the coordinates availability within 24 hours of RT-PPP observations value acquired through several research years. For example, All IGS stations in 2015 showed that the forced-latency solution led to the unavailability of RT-PPP solutions for more than 12 hours. However, the ARIMA and the SVR solutions improve the RT-PPP coordinates performance, resulting in reducing the unavailability of RT-PPP solutions to around 10.5 hours, which corresponds to improved availability with nearly 8 hours in the case of utilizing the ARIMA prediction model and with about 5 hours in the case of using the SVR model. Table 7.6 shows the solution's performance with respect to the researched years. The percentage of coordinates availability had been calculated as an average for all research stations.

Table 7.6 Availability of the RT-PPP coordinates solutions of selected research stations.

	Percentage of coordinates availability (%)		
All research Stations	**Forced-latency**	**ARIMA**	**SVR**
2013	81.67	86.06	84.73
2014	90.11	91.88	92.33
2015	46.75	50	54.62
2019	92.77	93.55	93.66
2021	83.66	84.66	84.77

7.3 RT-PPP EWS results

Using only one GNSS receiver, RT-PPP can produce reliable real-time location estimation. It does not require a network or differential GNSS solutions; thus, the method reduces costs and provides more flexibility in location. One of RT-PPP's main advantages is that it can provide real-time global positioning solutions; this shows that GNSS users in remote areas can still obtain precise location data in RT. RT-PPP EWS foundational results regard the initial work packages introduced in Chapter Six, third section. The first work package established the research reference station; the main stages utilized in station creation were demonstrated in detail in the previous chapter. Two sessions were conducted over 24 hours on the twenty-eighth of February 2021 and the eighteenth of March 2021 to obtain the reference station coordinates. Accordingly, the stored observation files were processed to utilize the online position services and followed by several experiments that utilized various elevation angles in RT-PPP mode to check the PPP's availability and performance. Those two sessions day were observed utilizing ten-degree mask elevation angles.

Later, from the tenth of September through the 20th, 2021, Seven RT-PPP sessions were conducted over 24 hours to evaluate the RT-PPP performance utilizing 0,10,20,30,40,50 and 60 degrees of satellite elevation mask angle. Subsequently, the stored RT-PPP observation files were subjected to investigate the variable correlations. The RT-PPP measurements were stored with respect to different elevation angle values. Table 7.7 presents the research outcomes regarding the seven RT-PPP sessions, which were carried out by manipulating various elevation mask angles. The table showcases the range assessments of the error components in the east, north, and up directions, which had been calculated with respect to establishing research station coordinates. Additionally, the final columns of the table illustrate the availability of the RT-PPP solution across various satellite elevation mask angles. Notably, the most precise results were obtained when employing a 10-degree elevation angle, aligning with the research findings and recommendations by Weber and Mervart (2007) and Wu et al. (2021). Conversely, adopting a 50-degree elevation mask angle resulted in substantial errors across all coordinate components. Moreover, the findings indicate that a 60-degree elevation mask angle led to insufficient convergence of the RT-PPP solution.

Table 7.7 RT-PPP coordinates component error ranges.

Elevation angle	East range (m)	North range (m)	Up range (m)	Solution availability (%)
0	7.47	7.27	18.96	91.67
10	0.11	0.14	0.38	99.96
20	11.46	14.28	50.74	99.94
30	6.23	20.24	120.36	96.63
40	5.50	26.34	218.65	52.71
50	16.39	70.84	263.05	7.44
60	-	-	-	0.00

The seven RT-PPP sessions investigations extended in work package one aim to explore the correlation association between the research variable. Coefficients ranging from -1 to 1 are used to denote the level of correlation; values of 1 indicate the strongest positive correlation, -1 the strongest negative correlation, and 0 no correlation at all (Pearson, 1920). The correlation analyses were conducted among the following research variables: tropospheric error, satellite number, latency, phase residuals, elevation angles, obtained coordinates, coordinate accuracy, and root mean squared errors. Figure 7.14 shows the correlation matrix among all the research variables.

A correlation matrix was constructed to analyse the relationship between various factors using the recorded RT-PPP measurements obtained from the tenth of September through the 20th. A continuous data collection period of seven days was employed for this purpose. The correlation matrix revealed a strong positive correlation between the RT-PPP coordinates and the errors associated with coordinate determination. Conversely, a negative correlation was observed between the RT-PPP vertical error and tropospheric delay, as is spected. Furthermore, significant negative correlations were observed between the satellite's elevation mask angle and latency, the number of tracked satellites, and the root mean squared error of the phase measurements.

It is essential to highlight that the horizontal and positional root mean squared error exhibited a positive correlation with the station coordinates and the error components of the coordinates. It is worth noting that the number of observations influenced the correlation results. For instance, as the satellite elevation angle increased, the availability of the RT-PPP solution decreased, resulting in weakened correlation levels. Those experiments enrich the research regarding the best-utilized elevation angle, the RT-PPP availability performance, and the relevant research variables for

establishing the early warning system. The impact of satellite geometry, the number of tracked satellites, and satellite elevation mask angle on the driven coordinate accuracy and availability are well-known. However, the study's primary concern is investigating the most relevant research variables. Enriching the proposed RT-PPP ML models with sufficient RT-PPP measurements varying for an instant in the number of GNSS used satellites, constellation geometries, and coordinate accuracy. Consequently, the research's primary notation is to perform the experiments in several site locations; these locations have various sky conditions, including performing the research experiments near high buildings, urban canyons, or over, for example, a mountain area where the station has a complete open sky environment to achieve diversity RT-PPP observations. The BNC open-source software allows the researchers to modify and recompile the original software code, allowing the research to simulate several station environment conditions.

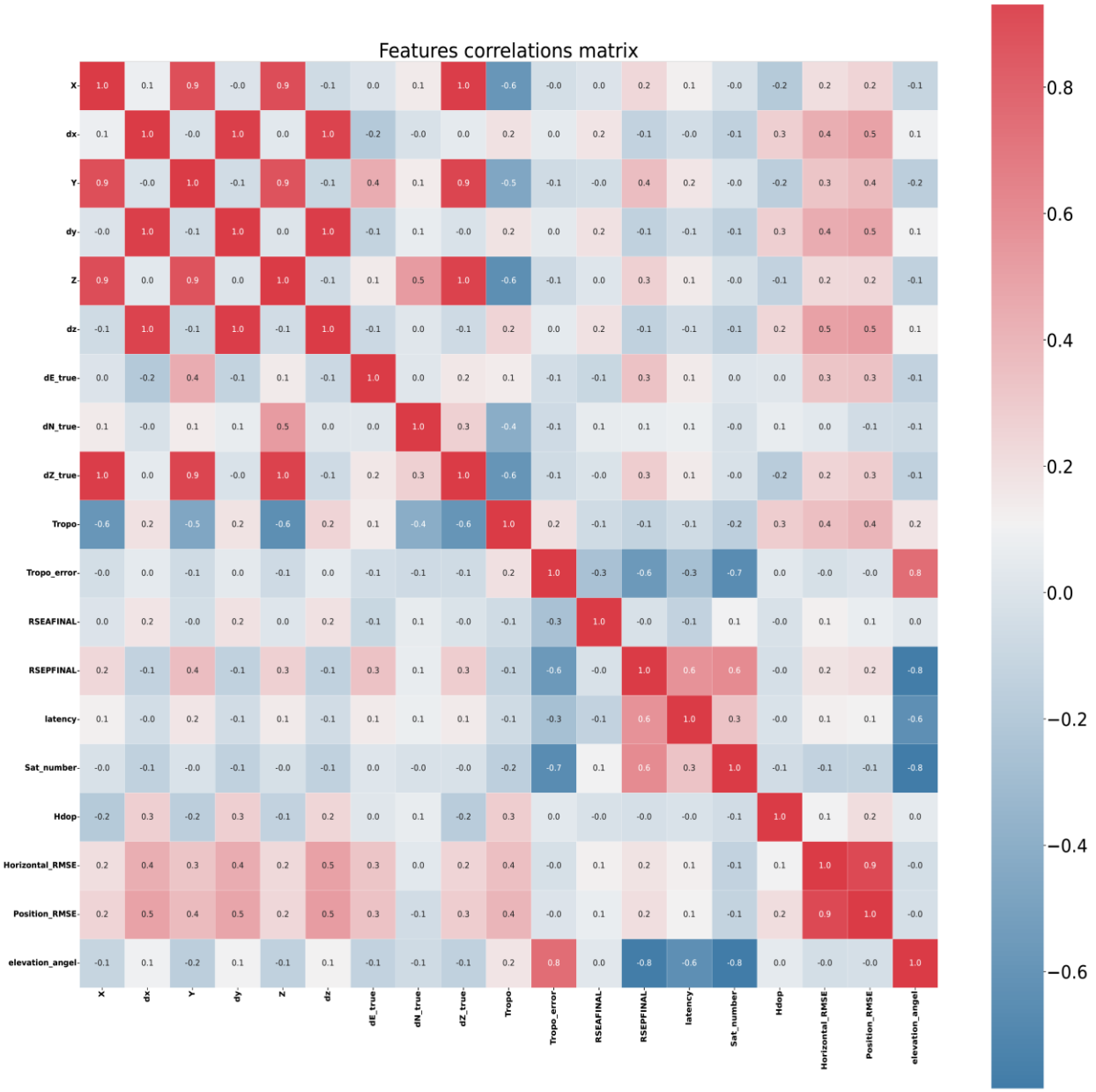

Figure 7.14 Variable correlation matrix

(Prepared by the author).

The results regard establishing the RT-PPP EWS extended to cover the research finding obtained from the fourth work package, which was constructed to demonstrate the research variable, including orbital and clock corrections for each satellite, latency information, 3D coordinates, 3D displacements of the receiver over station marker location, tropospheric error, Horizontal Dilution

of Precision (HDOP), and the solution utilized satellite number. Subsequently, that allows the research to classify the experiment events obtained from the seventh work package regarding deformation directions, streaming latency, and elevation angles concerning centered misplaced classes.

Figure 7.15 illustrates the distribution of the events concerning the type of experiments. The figure's vertical axis shows the centered and misplaced categories, and the pie chart in front represents the distribution of events observed during V, H, and 3D deformation experiments. The figure shows good research event distributions; for example, the misplaced research events were distributed as 27.15, 39.67, and 33.18 percent with respect to the horizontal, vertical, and three-dimensional deformation simulation experiments. At the same time, the research center events were distributed as 17.31, 31.52, and 57.17 percent with respect to the horizontal, vertical, and three-dimensional deformation simulation experiments; the percentage differences among the categories could be justified as a result of exiting the RT-PPP outliers measurements in addition to carry out slightly more experiments regards vertical deformation simulation experiments to compensate GNSS low vertical accuracy. The out-of-service category was eliminated from the figure as it contains the outlier event, which holds a lower percentage concerning the primary research categories. In addition, the random distribution of the RT-PPP outliers among the event categories. It is worth mentioning that the research event term denotes individual RT-PPP observation.

It is worth noting that the research cannot control the distribution of the event as it contains the outliers RT-PPP measurements, which are affected by poor satellite geometry (elevation mask angle), extreme latency, and high HDOP values, consequently leading to unequal classification percentages.

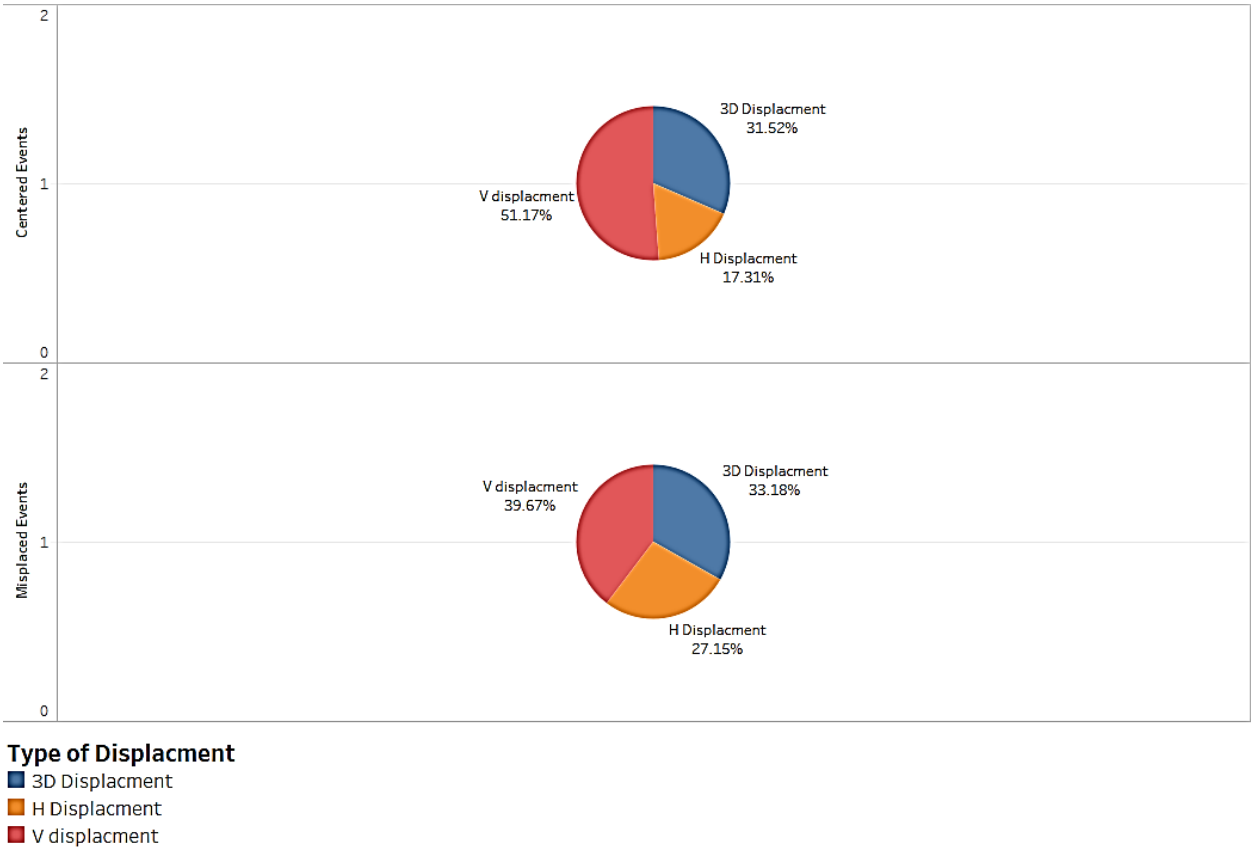

Figure 7.15 Events distribution regarding the deformation movement directions

(Prepared by the author).

Figure 7.16 describes the distribution of research events concerning the utilized stream. The figure's pie chart represents the distribution of events concerning the SSRA00CNE low latency stream and SSRA00IGS high latency streams. The percentage of the three-dimensional events observed utilizing SSRA00CNE and SSRA00IGS streams is 24.83 and 7.82 percent, respectively. The SSRA00CNE were utilized in vertical and horizontal experiments with 37.08 and 17.71 percent, respectively. The SSRA00IGS stream holds 12.56 percent of the all-event population. It is worth mentioning that the research utilized SSRA00CNE more frequently rather than SSRA00IGS to reduce the latency impact and improve the RT-PPP EWS performance.

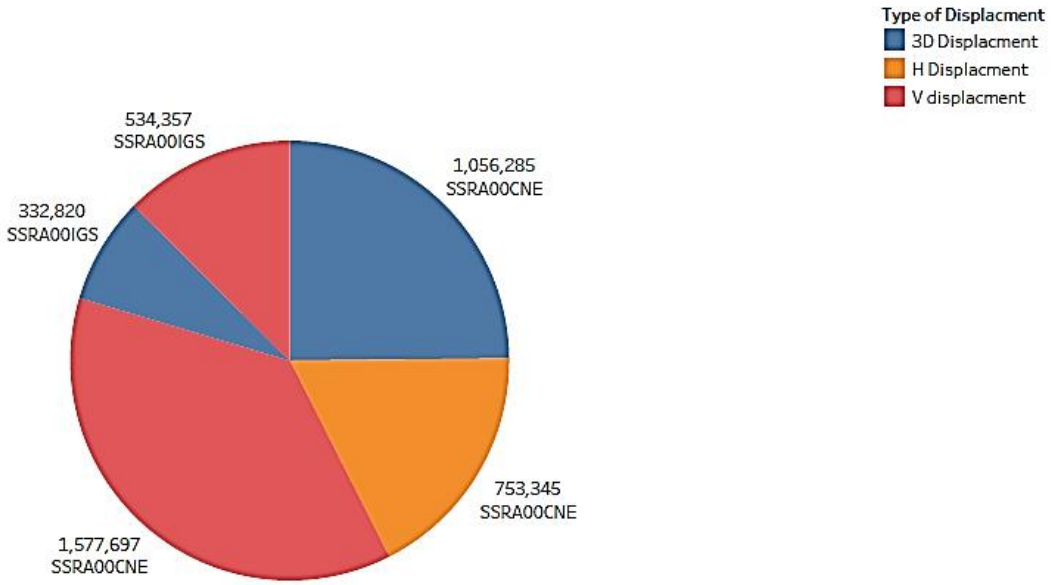

Figure 7.16 Events distribution regarding the utilized stream

(Prepared by the author).

7.3.1 Selection of noise-free measurements with satellite elevation angle

From the eleventh of October 2021 until the fifth of October 2022, 48 experiments were carried out. The research engine was utilized for simulation deformations in various directions; the RT-PPP was stored continuously for 24 hours during these sessions. Six sessions were conducted for 12 hours period. It is worth mentioning that the stored RT-PPP varied in stream latency and utilized elevation mask angles, magnitude, and direction of simulated deformations. The present experiments were designed to investigate the optimal satellite elevation angle to obtain noise-free measurements (in terms of manipulating the angle amount). Additionally, these experiments have significantly expanded the research data repository with a diverse range of PPP observations, enabling more effective training and evaluation of the researched machine learning model used for establishing the EWS.

Figure 7.17 describes the research events distributions concerning the detection of noise-free measurements, affected by multipath local effects selecting the best elevation angle. The figure's pie chart represents the distribution of research events concerning 10,20,30, and 35 degrees of mask elevation angle. Obviously, eliminating higher elevation mask angles may be advisable due to the unavailability of an RT-PPP solution when employing extreme elevation angles. A series of seven RT-PPP sessions conducted from the tenth of September to the 20th, 2021, revealed that utilizing a 50-degree angle resulted in a 7.44% success rate for the RT-PPP solution. Table 7.8 shows the availability of the RT-PPP solution with respect to utilizing various satellite elevation mask angles. Consequently, it is reasonable to advocate for the exclusion of elevated mask angles in order to circumvent these limitations and enhance the reliability and efficacy of the RT-PPP methodology. The figure shows that 64.41 percent of events were observed with a 10-degree elevation mask angle, and 21.51 percent were observed utilizing a 20-degree elevation mask angle. 5.83 and 8.25 percent were measured utilizing a 30 and 35-degree elevation mask angle. It is shown from the figure that the percentage of the research events with 10 degrees elevation mask angle is dominant among the utilized mask angles. The result obtained from the previous investigation showed the expected negative correlation between the elevation mask angle and the availability of the RT-PPP solution.

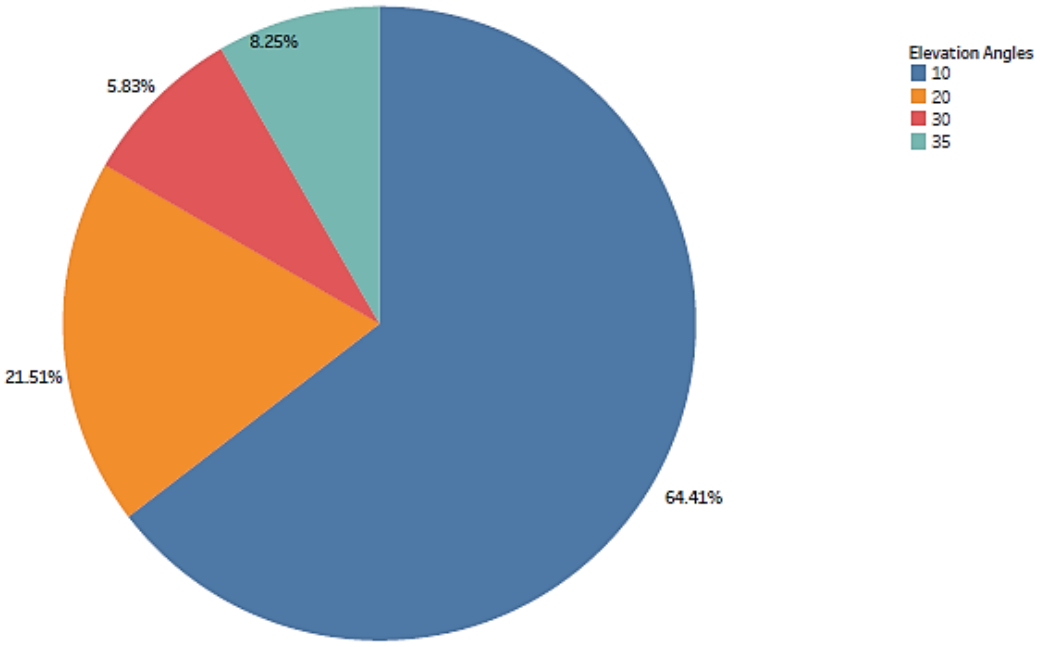

Figure 7.17 Events distribution regarding the utilized elevation angles

(Prepared by the author).

The following illustrations show the impact of utilizing 10- and 20-degree satellite elevation mask angles, the effect of changing the elevation angles on the performance of RT-PPP technique, and the impact on the number of out-of-service events. Two sessions have been selected out of 48 experiments for the sake of summarizing. The first session represents a 20 cm horizontal deformation simulation experiment held on the seventh of October 2021. At the same time, the second session represents a 20 cm three-dimensional simulation, noting that to reach the 20 cm amount of 3D simulated deformation level of displacement, it is worth mentioning that the utilized sampling frequency was one second during the experiments. The research randomly distributed the pre-mentioned displacement magnitude among the east, north, and up components. The experiment was held on the ninth of May, 2022. It is worth noting that the experiments encountered discontinuity periods due to weather conditions, electricity, and internet interruptions, forcing the research to repeat some experiments to conserve the experiment's consistency. Figures 7.18 to 7.26 show the research findings regards the impact of satellite elevation mask angle on the RT-PPP performance. Figure 7.18 shows the scatter plot for the 20 cm experiment utilizing a 10-degree

angle. The plot shows a well-distributed pattern among the centered, misplaced, and out-of-service events. Figure 7.18 utilizes the local horizontal coordinate system to show the east and north displacement components of RT-PPP observations. Figure 7.19 shows the trend of the HDOP values during the experiments, noting that the HDOP average value during 24 hours was around 1.3.

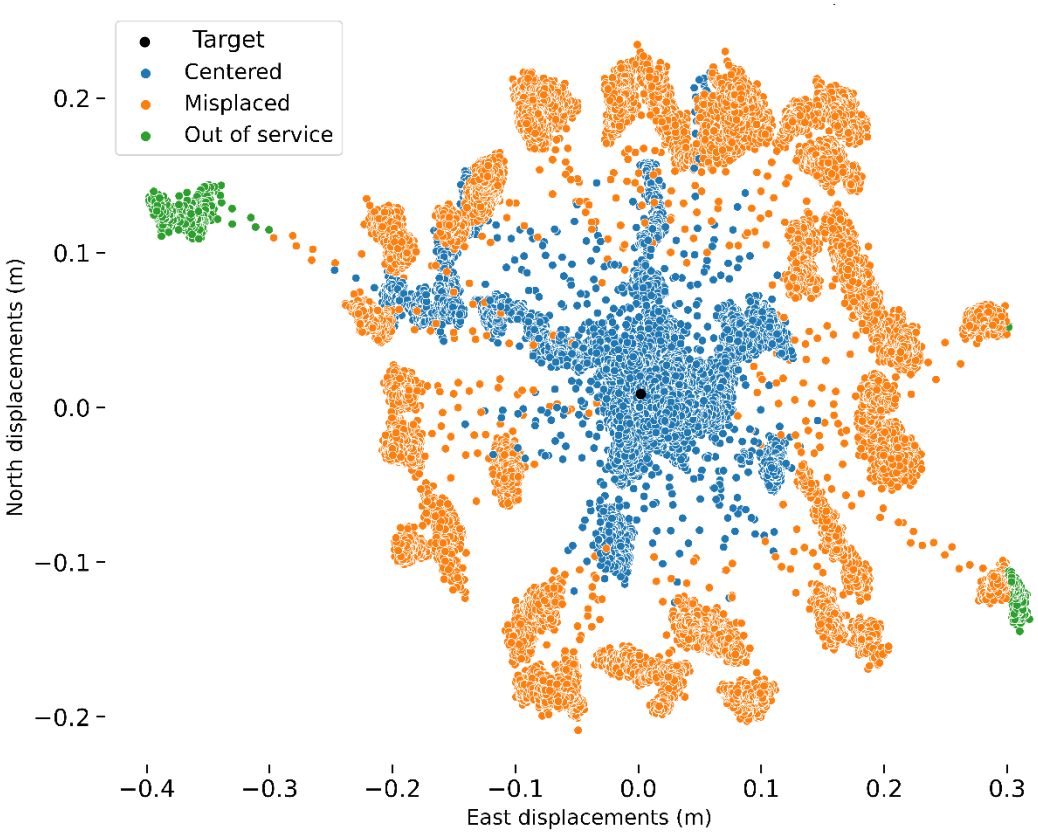

Figure 7.18 Displacements scatter plot with 10 degrees elevation angle

(Prepared by the author).

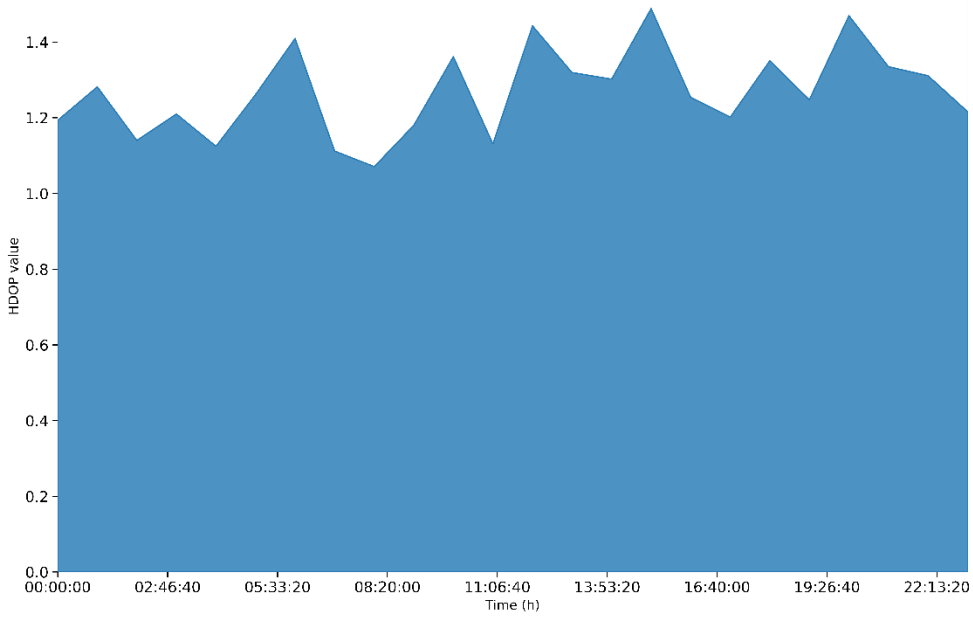

Figure 7.19 Horizontal dilution of precision with 10 degrees elevation angles

(Prepared by the author).

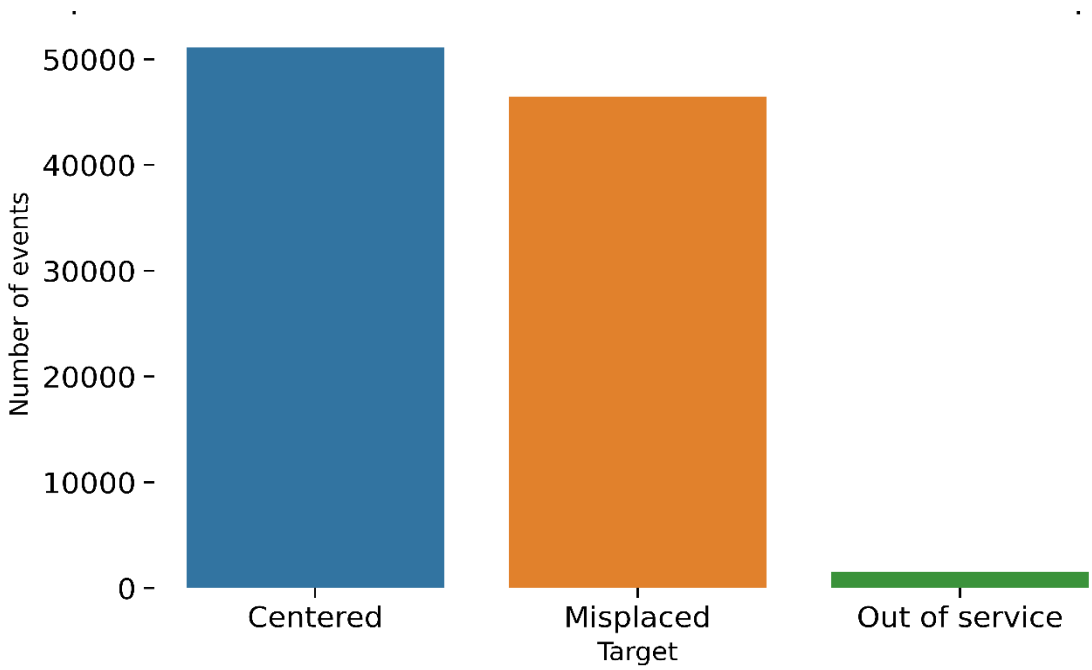

Figure 7.20 Experiment event distribution with 10 degrees elevation angles

(Prepared by the author).

Figure 7.20 shows the count plot of event distribution during the experiment; it is worth noting that both centered and misplaced categories nearly have the same number of RT-PPP observations. However, the out-of-service category contains slightly small percentages of RT-PPP observation crossing the outliers threshold (30 cm). Figures 7.21 to 7.23 illustrate the histograms of the east, north, and up displacement components of the RT-PPP observations. The experiment is only in the horizontal component; however, the RT-PPP up position is compared to the fixed vertical reference coordinate. It can be seen from the histogram distribution that the representation of outliers near the 30 cm and -40 cm level of displacements according to the error magnitude exceeds the exerted deformation (20 cm). The normal distribution of vertical events can be seen in Figure 7.23, where the data tend to concentrate around zero; this could be illustrated as the experiments do not exert any simulation in the vertical direction.

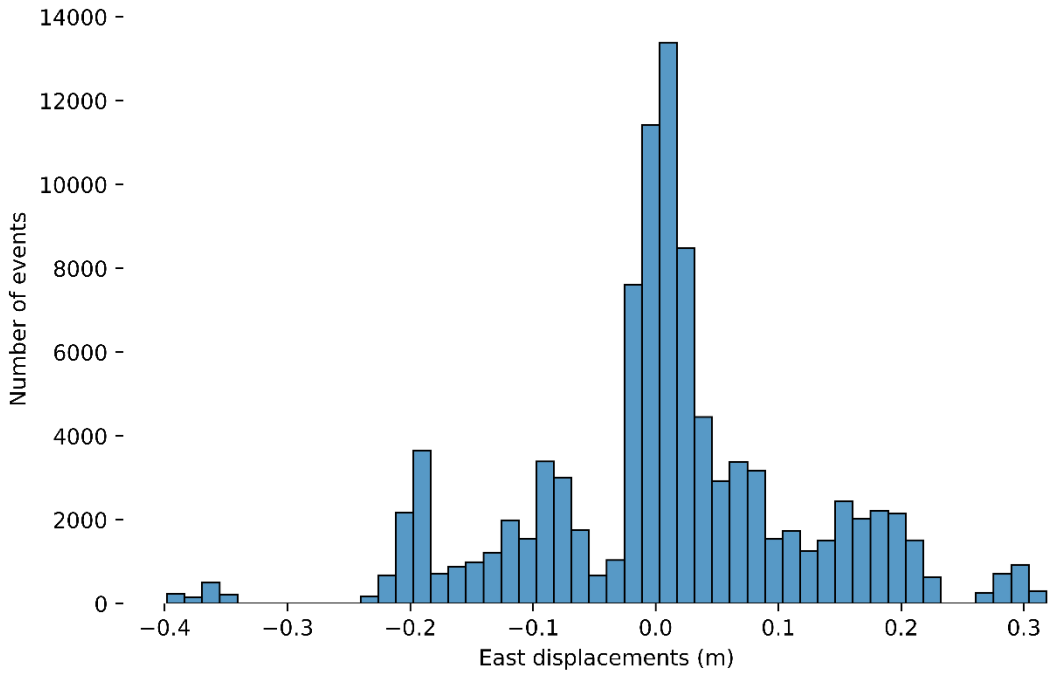

Figure 7.21 RT-PPP east displacements histogram with 10 degrees elevation angles

(Prepared by the author).

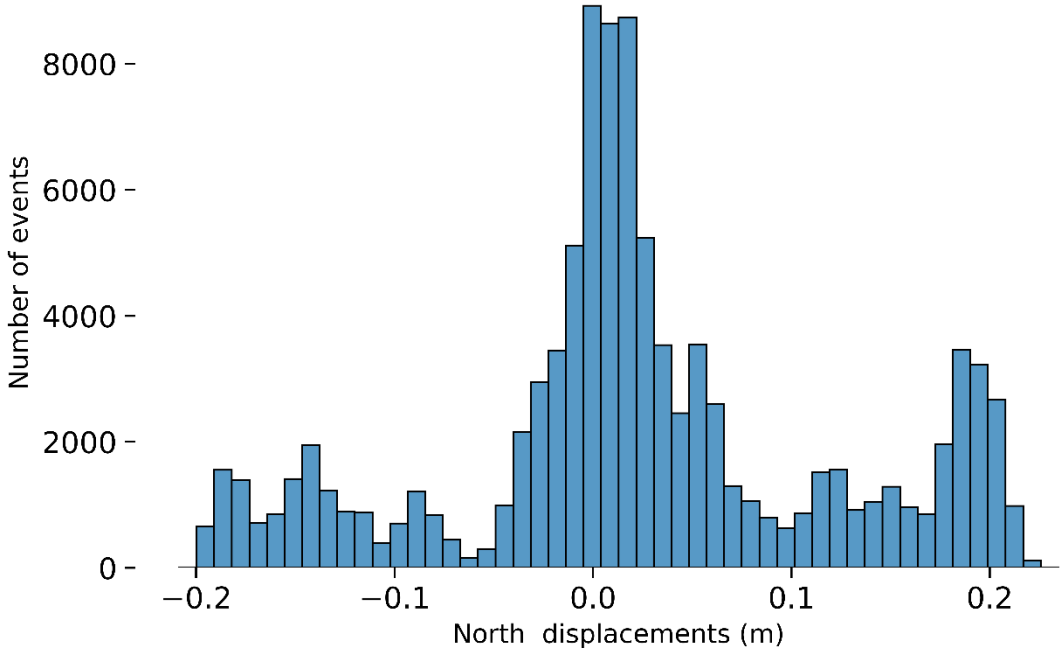

Figure 7.22 RT-PPP north displacements histogram with 10 degrees elevation angles

(Prepared by the author).

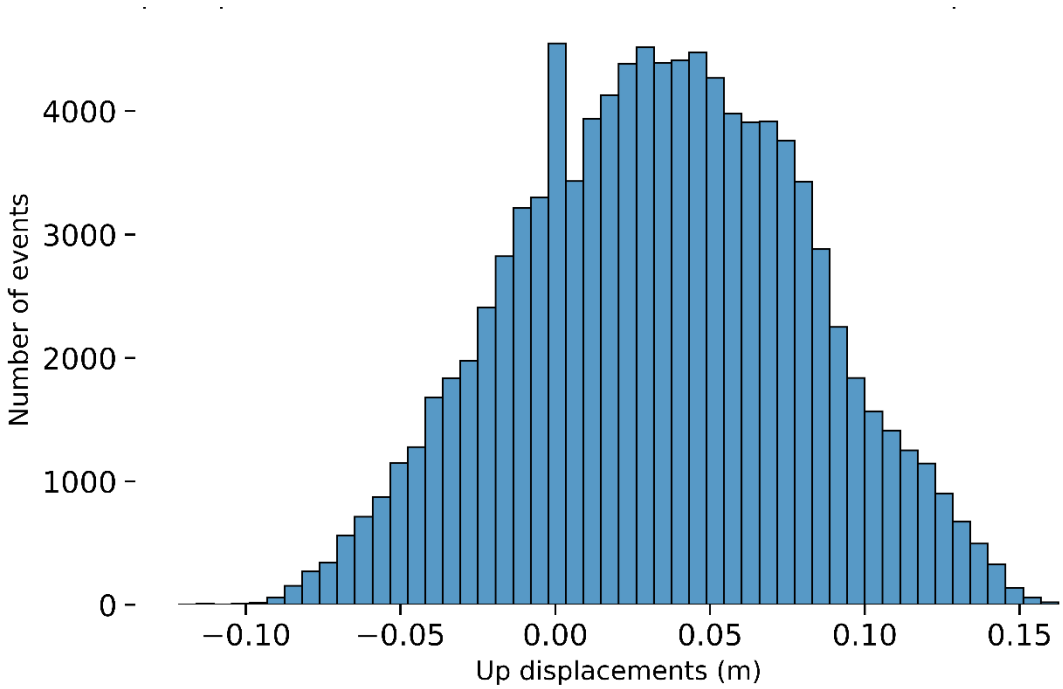

Figure 7.23 RT-PPP up-displacements histogram with 10 degrees elevation angles

(Prepared by the author).

Figures 7.24 to 7.29 show the research findings regarding the second session, which simulates a 20 cm three-dimensional level of deformations experiment held on the ninth of May, 2022. The experiment was carried out utilizing a 20-degree elevation mask angle. Figure 7.24 shows the scatter plot for the 20 cm experiment utilizing a 20-degree angle. The plot shows an unrecognized distributed pattern among the centered, misplaced, and out-of-service events. Noting, the vertical and horizontal figure axis enlarged to around 20 meters in both directions compared to Figure 7.18, where the vertical and horizontal axes range around 40 centimetres. Figure 7.24 utilizes the local tangent plane coordinate system to show the east and north displacement components. Figure 7.25 shows the trend of the HDOP values during the experiments, noting that the HDOP average value during 24 hours was around 2.3; this value has been doubled compared to the 10-degree elevation mask angle experiment. This experiment can be used to simulate less valid satellites for the computation of the solution or a bad PDOP satellite configuration.

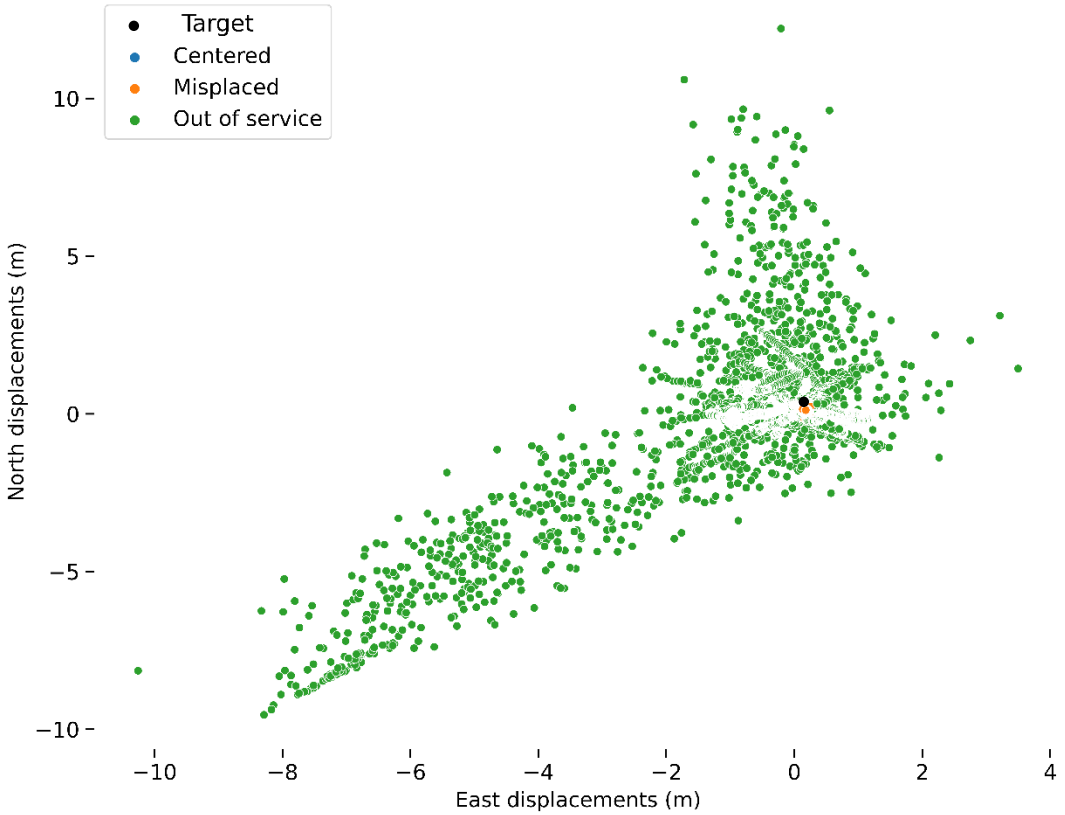

Figure 7.24 Scatter plot with 20 degrees elevation angle

(Prepared by the author).

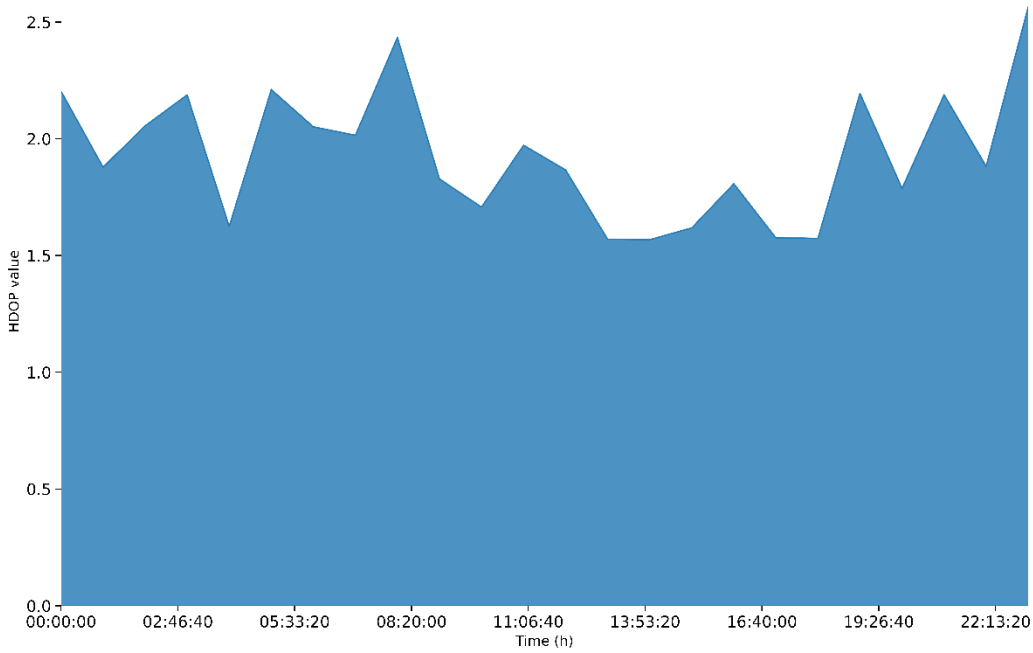

Figure 7.25 Horizontal dilution of precision with 20 degrees elevation angles

(Prepared by the author).

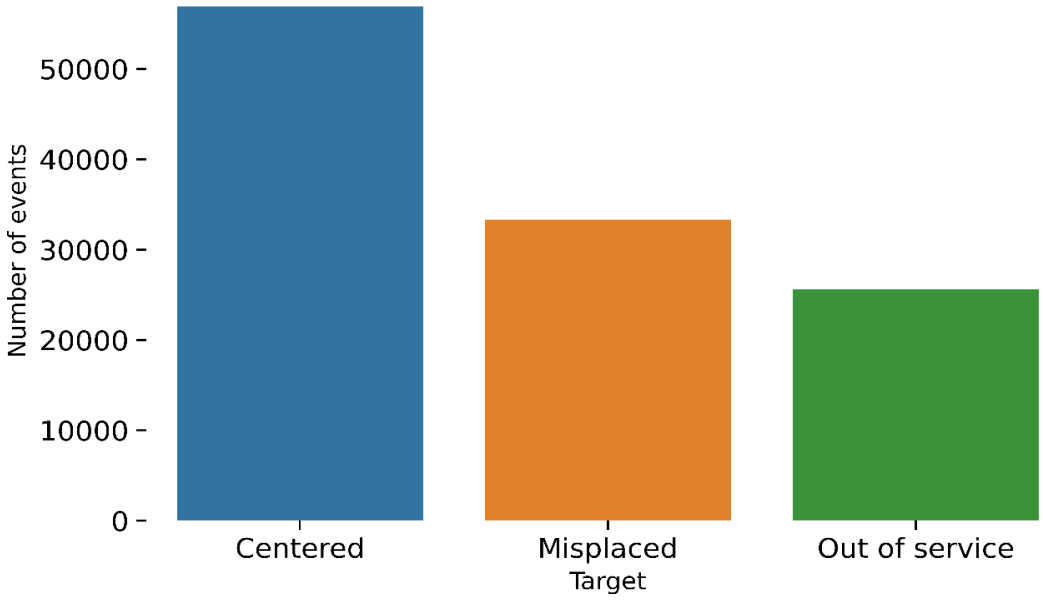

Figure 7.26 Experiment event distribution with 20 degrees elevation angles

(Prepared by the author).

Figure 7.26 shows the count plot of events distribution during the experiment; it is worth noting that both centered, out-of-service, and misplaced categories have various amounts of RT-PPP observations; this could be justified as the RT-PPP outliers measurements are normally distributed, and even they impact the distribution of RT-PPP measurements in the primary centered and misplaced categories. However, the out-of-service category contains significant percentages of RT-PPP compared to 10-degree experiments. Figures 7.27 to 7.29 illustrate the histograms of the east, north, and up RT-PPP displacement components. It can be seen from the figures that the exiting of significant outliers in three companies, the histogram axis enlarged in three plots with around 20 meters, indicating the existence of RT-PPP outliers events as a result of using higher elevation mask angel compared with Figures 7.21 to 7.23.

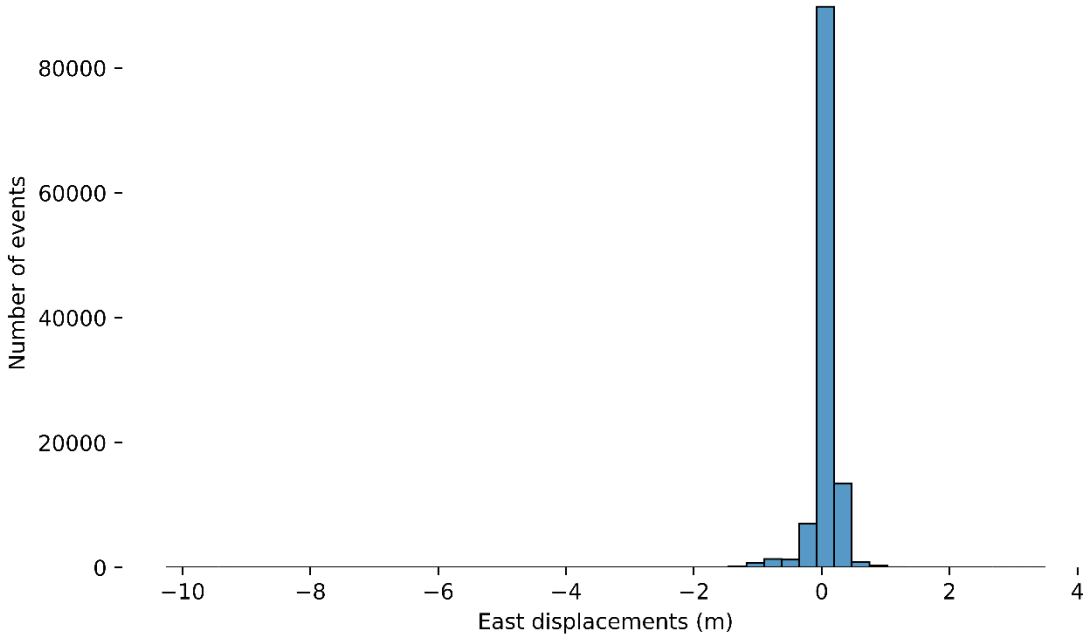

Figure 7.27 RT-PPP east displacements histogram with 20 degrees elevation angles

(Prepared by the author).

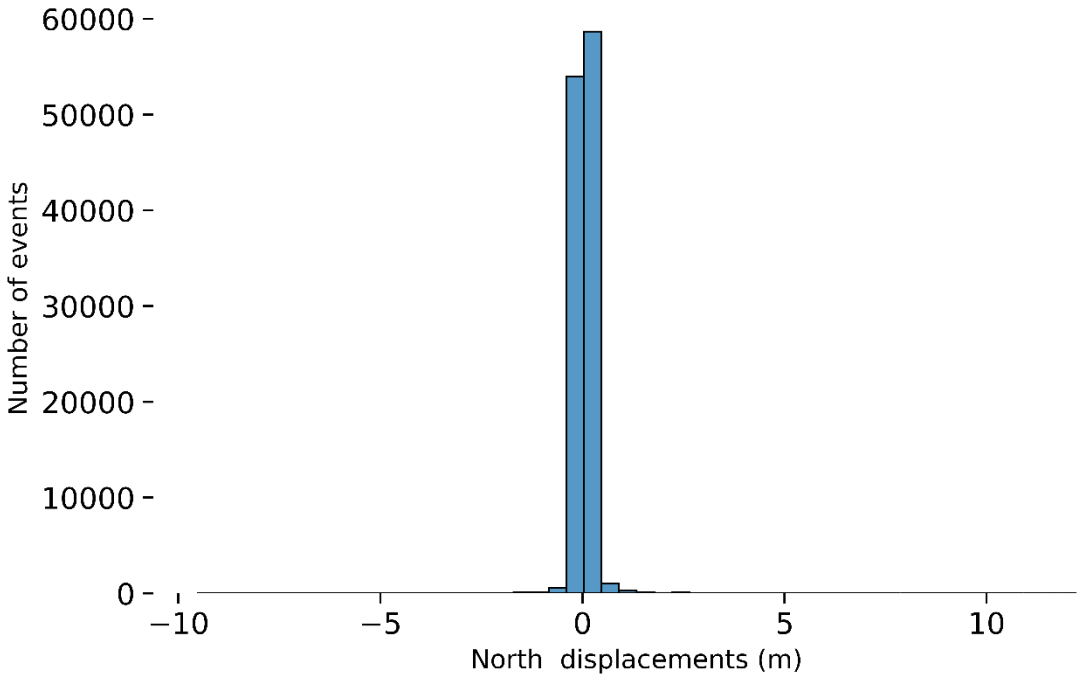

Figure 7.28 RT-PPP north displacements histogram with 20 degrees elevation angles

(Prepared by the author).

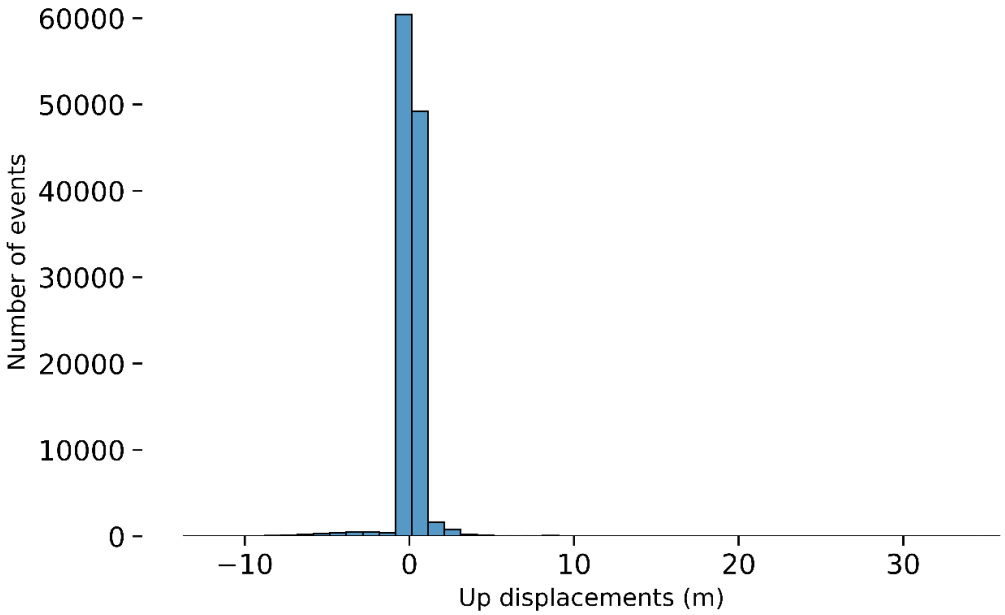

Figure 7.29 RT-PPP up-displacements histogram with 20 degrees elevation angles.

(Prepared by the author).

All the pre-mentioned illustrations highlighted the importance of utilizing proper satellite elevation angles. In other words, performing the RT-PPP measurement within a suitable station environment regarding the sky conditions is essential. Table 7.8 briefly summarizes the results regarding the 20 and 10-degree experiments. The results obtained from the 20 experiment proves the degradation of RT-PPP observation.

Table 7.8 RT-PPP coordinates component error ranges regarding 10 and 20 satellite elevation angles.

Elevation angle	East range (m)	North range (m)	Up range (m)
10	0.71	0.44	0.28
20	13.75	21.75	49.64

7.3.2 RT-PPP early warning system assessment results

The total number of research experiments reached 57, as mentioned in the previous section; two were carried out in static mode to obtain the study reference station coordinates, followed by seven sessions to investigate the impact of utilizing several elevation mask angles on RT-PPP besides exploring the RT-PPP variables correlations.

Upcoming Forty-eight experiments were conducted between the eleventh of October 2021 and the fifth of October 2022. The research engine was established to simulate deformations in different directions, with the RT-PPP being persistently recorded for a full day. In 12 hours, only six sessions were held. Note that the research manipulates the simulated deformations with different amount of magnitudes and directions. The elevation mask angles were manipulated with the following values (10,20,30,35 degrees), and the RT stream latency was changed in order to obtain various latency values. Those configurations were saved with RT-PPP within a 1-second sampling interval.

Forty-eight experiments were performed to probe different elements of RT-PPP measurements. Twenty-four vertical deformations, eight horizontal deformations, and sixteen three-dimensional deformations were all planned to be tested in the trials. Antecedent the training phase and testing of the RT-PPP EWS ML models, it is required to label RT-PPP observations to match the GNSS receiver locations. Three categories were established to match the GNSS receiver over the

reference station marker: centered, misplaced, and out-of-service. Out of a total of 4,299,510 occurrences, 2,205,918 were considered "centered," 645,822 were considered "out of service," and 1,447,770 were considered "misplaced" as a result of the tests.

These experiments add to our understanding of the optimal elevation angle for early warning systems, the RT-PPP availability, and the essential study variables. It is well understood that factors such as satellite geometry, the number of tracked satellites, and the satellite elevation mask angle all affect the precision and availability of the driven coordinates. However, the fundamental goal of the study is to explore the most critical research variables. Adding more RT-PPP data to the suggested ML models, with data varying for instant in the number of GNSS satellites employed, the constellation geometry, and the precision of the coordinates, thus improving the ability of the proposed RT-PPP EWS detections.

Various ML models were explored to establish an early warning system. These models included Decision Tree (DT), Random Forest (RF), XGBoost (XGB), Logistic Regression (LR), K Nearest (KN), and Support Vector Classifier (SVC). The research could be carried out with the 48 experiments provided since 40% of the data could be used for training ML models, 30% for testing ML models, and the remaining data could be used for validating the models. In most cases, 70% and 30% are utilized as the thump levels for training and testing, respectively. The research justifies utilizing 40% of data for training due to the complexity of the research machine learning models and the enormous size of the research database. However, the research was aware of this essential issue. Thus, several tests were conducted to compare the model's accuracy regarding training the ML model with 40 to 70 percent of the experiment data. The results show that the obtained accuracy is more or less within the same accuracy level despite the utilization of different percentages of experiment data. The RT-PPP EWS machine learning models are subjected to two levels of assessment; the first level of assessment is carried out through Chapter 6's work package eight, where the utilized ML classification models try to classify the RT-PPP test events to their belonging classes.

Consequently, the ML models could classify the event into three different categories: **Centered** class, where the measurements of the receiver were classified to be of the station marker. The second category, **Misplaced,** signifies that the receiver measurements are classified to occupied

points displaced from the station marker, (simulated deformation distance). The ultimate class is **Out of service,** which includes all RT-PPP measurements having displacement values more than 30 cm, which is greater than movements caused by the research engine (20 cm) plus the nominal RT-PPP level of accuracy which is nearly (10 cm) which are also proved by table 7.7 assessment table. In other words, the out-of-service classification category is supposed to contain all the measurements influenced by errors, biases, and measurement noises resulting from observations exceeding the 10- centimetres level of accuracy. It is worth noting that the research cannot rely on these observations to initiate the deformation early warnings due to the impact of the error sources.

Accordingly, the established confusion matrix contains several variables used to understand correctly Machine Learning classifications of the observations in comparison with the label of the same observations; those variables represent the assessment of the ML classification models performance in terms of TP (True Positive): TP is the number of events that are misplaced from the marker location and are correctly categorized by ML models, TN (True Negative): TN is the number of events that are centered (do not move) above the marker location, and ML models correctly classify them, TNE, which stands for "True Neutral," is the number of events that are out of service and correctly categorized by ML models. These events are called "neutral" because the researchers do not know for sure if they are centered (no movement) or displaced away from where the station marker is; on the contrary, the false classifications were also categorized into three different classes (False Positive): FP represents the number of misplaced events. ML models misclassify them; those events could be either out of service or centered over the station marker location.

FN (False Negative): The number of centered events is shown by FN. ML models misclassify them as out-of-service or centered events, but they are really displaced events. FNE, or False Neutral, is the number of out-of-service events the ML models misclassify as mislabelled or centered events. The same work package was extended to calculate the probabilities of initiation early warnings; this allows the research to establish the second level of assessing the RT-PPP performance. Six types of probabilities were calculated, namely, the probability of initiating true (motions/non-motions) detections, which indicates the ability of the RT-PPP EWS to detect whether the deformations occurred or not. Similarly, the probability of true (out-of-service) detections signifies

the ability of the RT-PPP EWS to inform the user that the obtained RT-PPP measurements are not robust enough to initiate proper (motions/ non-motions) detections.

On the other side, three false probabilities were constructed, which indicates that the RT-PPP EWS misled the users in the cases where the system-initiated motions/ non-motions/ out-of-service detections, and that does not match the reality at the station ground level—the research named those probabilities as false non-motion (FN), false motion (FP), and false out-of-service (FNE) detections. Subsequently, the investigation of RT-PPP EWS performance was investigated with respect to the following terms:

A. Accuracy indicates the ability of ML models to correctly classify the research events to their belonging category (centered, misplaced, and out-of-services). Accordingly, this metric had been calculated with respect to the test data.
B. Probability Of Truly Non-Motion Detection (POTNMD) signifies the EWS's ability to detect no deformation events.
C. Probability Of False Non-Motion Detection (POFNMD) indicates the EWS's tendency to non-initiate warnings coinciding with deformation occurrences. The reality shows that deformations or out-of-service occur at the station ground level; however, the EWS provides users with non-motion prediction -detection-. It is worth considering that the POFMD is a crucial aspect that must be minimized to avoid high economic and life losses.
D. Probability Of True Motion Detection (POTMD) signifies the EWS's ability to detect deformation events and emit a warning.
E. Probability Of False Motion Detection (POFMD) indicates the EWS's tendency to initiate false warnings. The reality shows that no deformations or out-of-service occur at the station ground level; however, the EWS provides users with motion prediction.
F. The Probability Of True Out-Of-Service Detection (POTOSD) signifies the EWS's ability to inform users that the RT-PPP measurements are not robust enough to rely upon.
G. The Probability Of False Out-Of-Service-Detection (POFOSD) indicates the EWS predicts Out-Of-Service observations, that is RT-PPP measurements are not robust enough to rely upon. However, the reality is that no deformation, or deformation, occurs at the station

ground level (this last is essential because no alarm is emitted when required in the deformation occurrences cases).

H. Probability Of Initiating False Classifications (POIFC) shows the overall tendency of EWS to initiate false classifications. The research aggregates all the previous false probabilities for the sake of a better comparison of the machine learning performance. Equation 7.1 shows the mathematical equation utilized for establishing POIFC.

$$\mathrm{POIFC} = \mathrm{POFNMD} + \mathrm{POFMD} + \mathrm{POFOSD} \tag{7.1}$$

For illustration, we analysed the per-mention probabilities associated with multiple machine learning (ML) models, specifically decision trees, random forest, XGB, logistic regression, K nearest neighbours, and support vector regression. Merely relying on model accuracy as the sole metric is deemed inadequate for selecting the most appropriate ML model to deploy in the proposed RT-PPP EWS. The research emphasizes the significance of the POTMD as a critical factor, as it signifies the model's capacity to detect crustal motions and initiate the necessary warnings, providing essential information to users and stakeholders for undertaking disaster precautions. Simultaneously, the POFNMD is regarded as a vital probability, representing the EWS's failure to activate the required warnings in timely instances when the motion really occurs. In summary, the selected ML model must have the highest accuracy and probability of true motion detection and have to reduce to nearly 0% for the false motion and out-of-services classifications due to the fact that the small probability of initiation of false warning or initiation of warnings could claim significant losses of lives and economics.

However, the research extended the probability investigation to POIFC as the sum of all false probabilities.

It is important to note that the probabilities associated with non-motion events and out-of-service detections are considered less significant to the EWS users than the POTMD and the POFNMD. In the event of generating false warnings for non-motion events, the EWS provides misleading information to users regarding geo-disaster occurrences that do not actually exist. Additionally, in the case of system out-of-service detections, it is well-established that the RT-PPP EWS lacks the necessary robustness to be relied upon.

Afterward, Chapter 6's Work Package 10 utilizes several visualization tools to ease the interpretations of the results. Before introducing the work package results, it is worth mentioning that they were broken down into four levels.

1. The evaluations of the RT-PPP EWS in terms of vertical displacements. Twenty-four experiments have been involved in this assessment. Those experiments were carried out from the tenth of October 2022 to the third of June 2022.
2. The evaluations of the RT-PPP EWS in terms of horizontal displacements. Note that eight experiments have been involved in this evaluation. Those experiments were carried out from the eighth of January 2021 to the twenty-second of November 2021.
3. The evaluations of the RT-PPP EWS in terms of three-dimensional displacements. Sixteen experiments have been involved in this assessment. Those experiments were carried out from the third of May 2022 to the eleventh of May 2022.
4. The evaluation of the RT-PPP EWS as a generic system noted that all the experimental data were utilized in this stage.

7.3.3 Simulated land subsidence and land-uplifting results

The twenty-four vertical deformation experiments that were carried out during Chapter 6's work package seven, showed that out of 48, were performed to probe different elements of RT-PPP measurements. The results are illustrated in Figures 7.30, 7.31, and 7.32. It is worth noting that the researcher tries to implement several assessment indicators in the created figures to summarize and compare the performance of the utilized ML models. The BNC was configured through the research experiments series, employing various elevation mask angles. This allowed us to emulate both unfavourable and favourable (HDOP) configurations. Concurrently, we manipulated similar RT streams to generate distinct scenarios, thereby facilitating the examination of high and low latency effects. At the same time, different amounts of vertical deformation values were exerted to enrich the research database with diverse RT-PPP observations. The figure's horizontal axis includes the utilized ML models, and the overall model’s accuracy is presented in the vertical axis. Table 7.9 abbreviations were utilized, and they either represent the figures with hue or sizes to discriminate the ML performance well. It is worth highlighting that the forthcoming results correspond to the research test events.

Figure 7.29 colours show POTNMD details; however, the symbol sizes show details that respect the POFNMD. The figure shows that the XGB and RF have superior performance with 99.92% and 93.76% POTNMD, respectively, to detect non-motion vertical deformations, and they also offer less probability of initiating false non-motion detections. On the contrary, the logistic regression shows the worst performance with respect to the achieved accuracy, POFNMD, and POTNMD. It is worth mentioning that this figure represents the performance of vertical deformations.

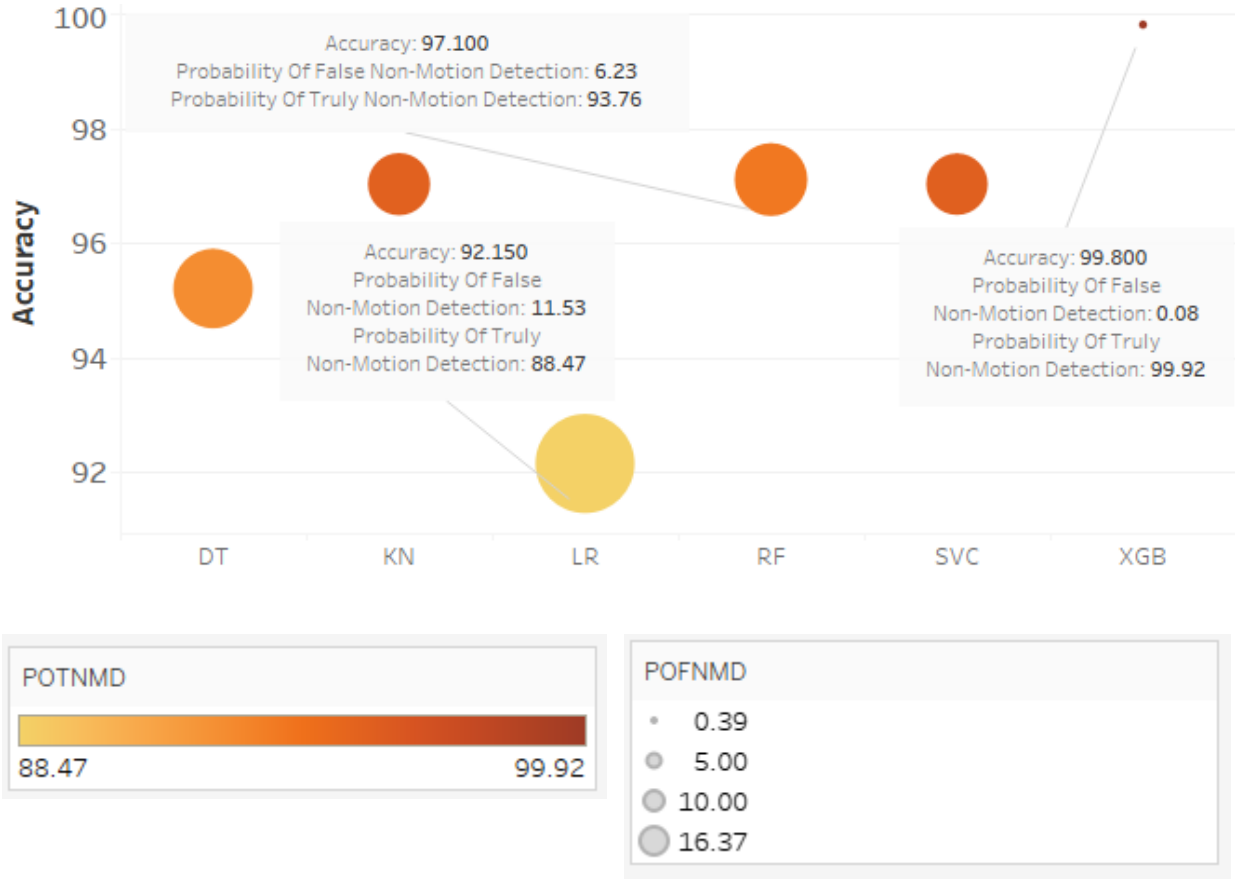

Figure 7.30 Vertical non-motion detections RT-PPP EWS performance

(Prepared by the author).

Figure 7.31 colours show POTMD details; however, the symbol sizes show details that respect the POFMD. The figure shows that the RF and XGB classifiers have superior performance, with 99.89% and 97.81% of POTMD, respectively, to detect vertical deformations, and they also offer less probability of initiating false motion detections. On the contrary, the logistic regression shows

the worst performance with respect to the achieved accuracy, POFMD, and POTMD. It is worth mentioning that this figure represents the performance of vertical deformations.

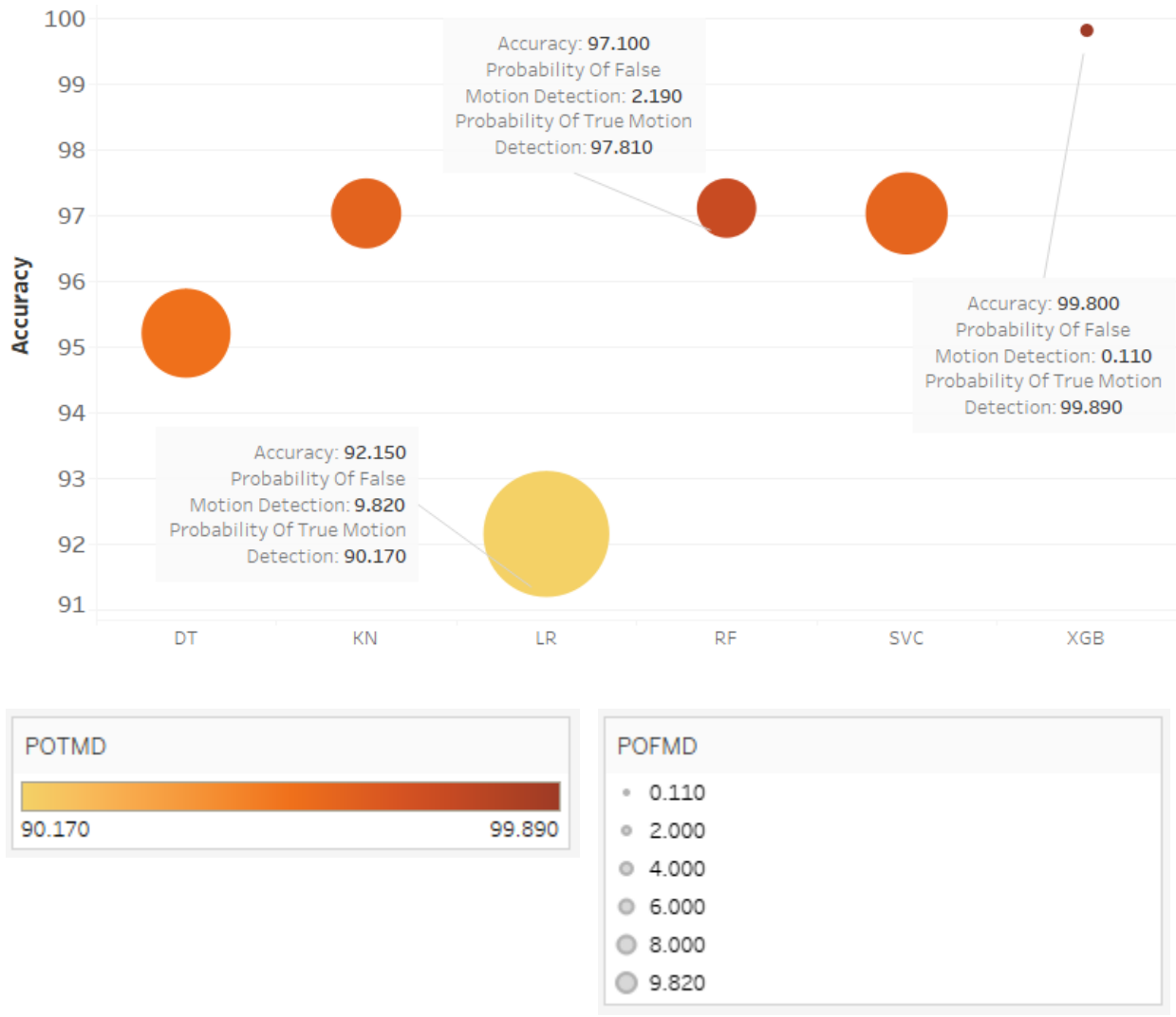

Figure 7.31 Vertical motion detections RT-PPP EWS performance

(Prepared by the author).

Figure 7.32 colours show POTOSD details; however, the symbol sizes show details that respect the POFOSD. The figure shows again that the RF and XGB have superior performance with a value of 99.84 % and 99.98% of the POTOSD, respectively. They also offer less probability of initiating false out-of-service detections. On the contrary, the logistic regression shows the worst performance with respect to the achieved accuracy, POTOSD, and POFOSD. It is worth

mentioning that this figure represents the performance of vertical deformations. Noting that the accuracy of all models represents good performance regarding the detection of out-of-service scenarios, it could be justified that the out-of-service category contains all outliers RT-PPP measurements. Thus, it is easy for the implementing models to detect them.

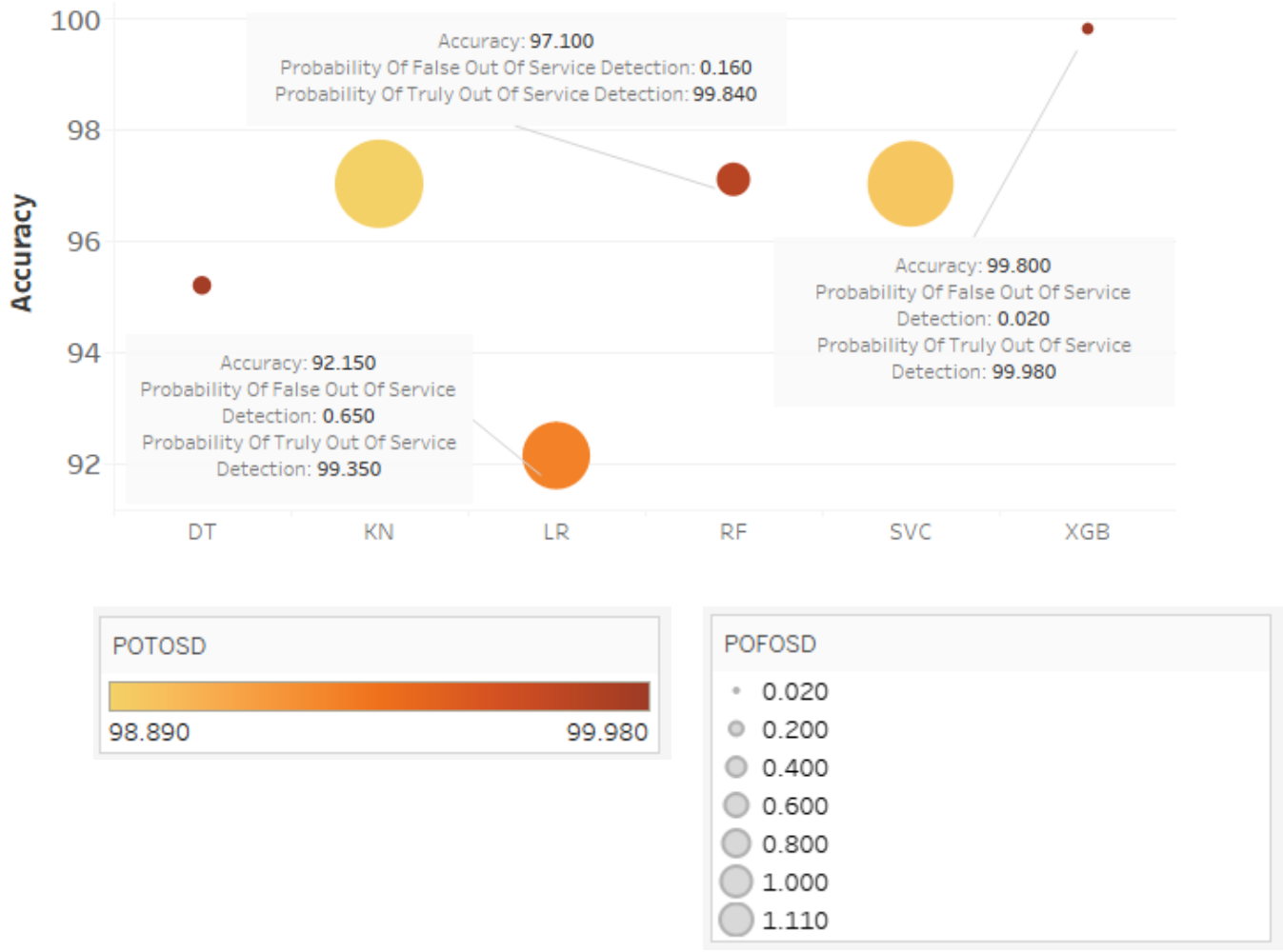

Figure 7.32 Vertical out-of-service detections RT-PPP EWS performance

(Prepared by the author).

7.3.4 Simulated horizontal deformation results

Eight horizontal deformation experiments were carried out during Chapter 6's work package, and 7 out of 48 were performed. The BNC was configured through the research experiments series, employing various elevation mask angles. This allowed us to emulate both unfavourable and favourable (HDOP) configurations. Concurrently, we manipulated similar RT streams to generate distinct scenarios, thereby facilitating examining high and low latency effects. At the same time, different amounts of horizontal deformation values were exerted to enrich the research database with diverse RT-PPP observations utilizing the research engine. The results are illustrated in Figures 7.33 to 7.35. It is worth noting that the researcher tries to implement several assessment indicators in the created figures to summarize and compare the performance of the utilized ML models. The figure's horizontal axis includes the utilized ML models, and the overall model's accuracy is presented in the vertical axis. Table 7.9 abbreviations were utilized, and they either represent the figures with hue and sizes to discriminate the ML performance well. The figures below were created to compare the MLAs' performance.

Similar to the previous section, the figures indicate that investigations have been carried out concerning 2D experiments. Figure 7.33 colours show POTNMD details; however, the symbol sizes show details that respect the POFNMD. The figure shows that the RF and XGB classifier performs better with 98.07% and 99.61% of POTNMD regarding horizontal deformations compared to the rest of the researched ML models. They also offer less probability of initiating false non-motion detections. On the contrary, the logistic regression shows the worst performance regarding accuracy, POFNMD, and POTNMD. It is worth highlighting that the forthcoming results correspond to the research test events.

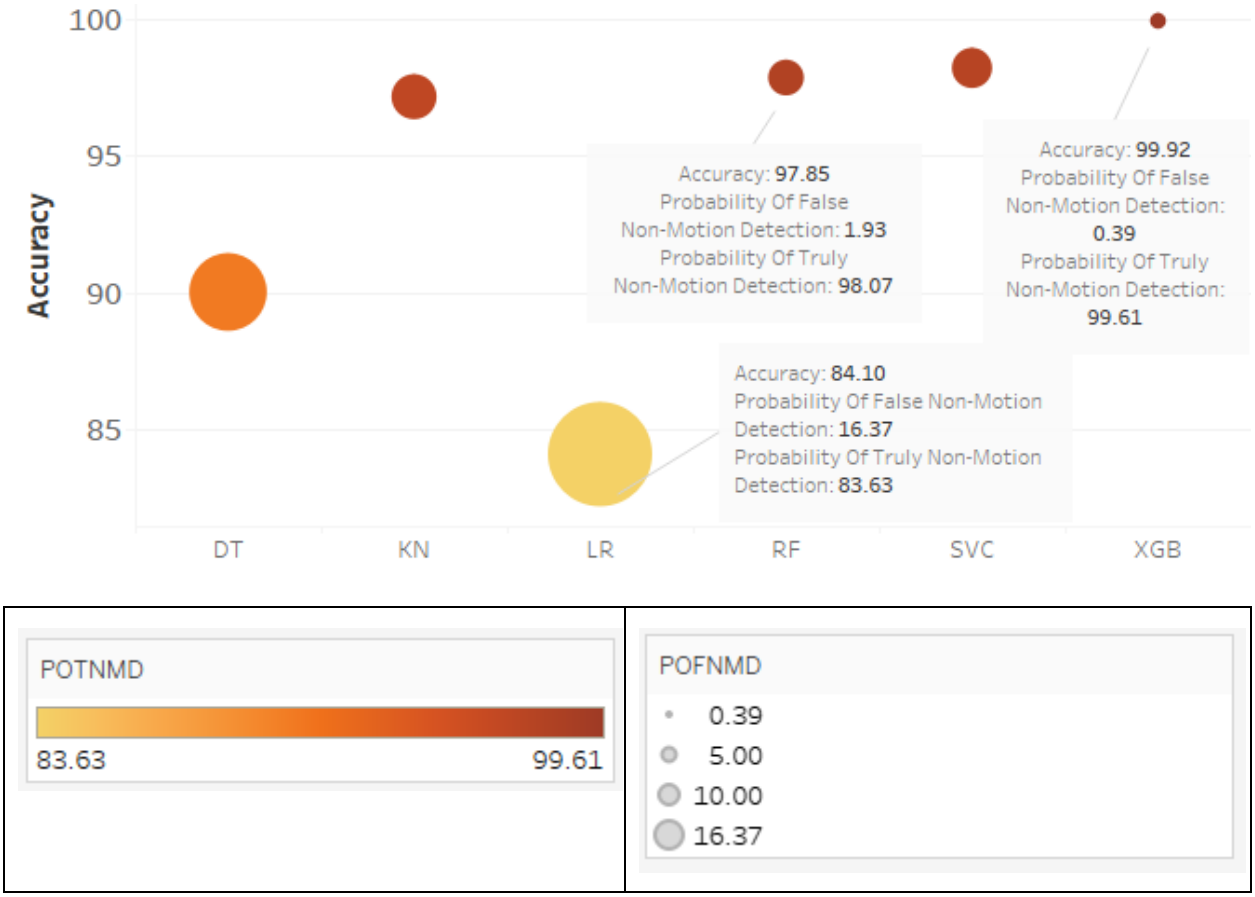

Figure 7.33 Horizontal non-motion detections RT-PPP EWS performance

(Prepared by the author).

Figure 7.34 colours show POTMD details; however, the symbol sizes show details that respect the POFMD. The figure shows that the RF and XGB classifiers perform better with 97.97% and 99.50 POTMD, respectively. Furthermore, they show the minimum probability of initiating false motion detections. Similar findings regarding SVC could be established. On the contrary, the logistic regression shows the worst performance regarding accuracy, POFMD, and POTMD. It is worth mentioning that this figure represents the performance of horizontal deformations.

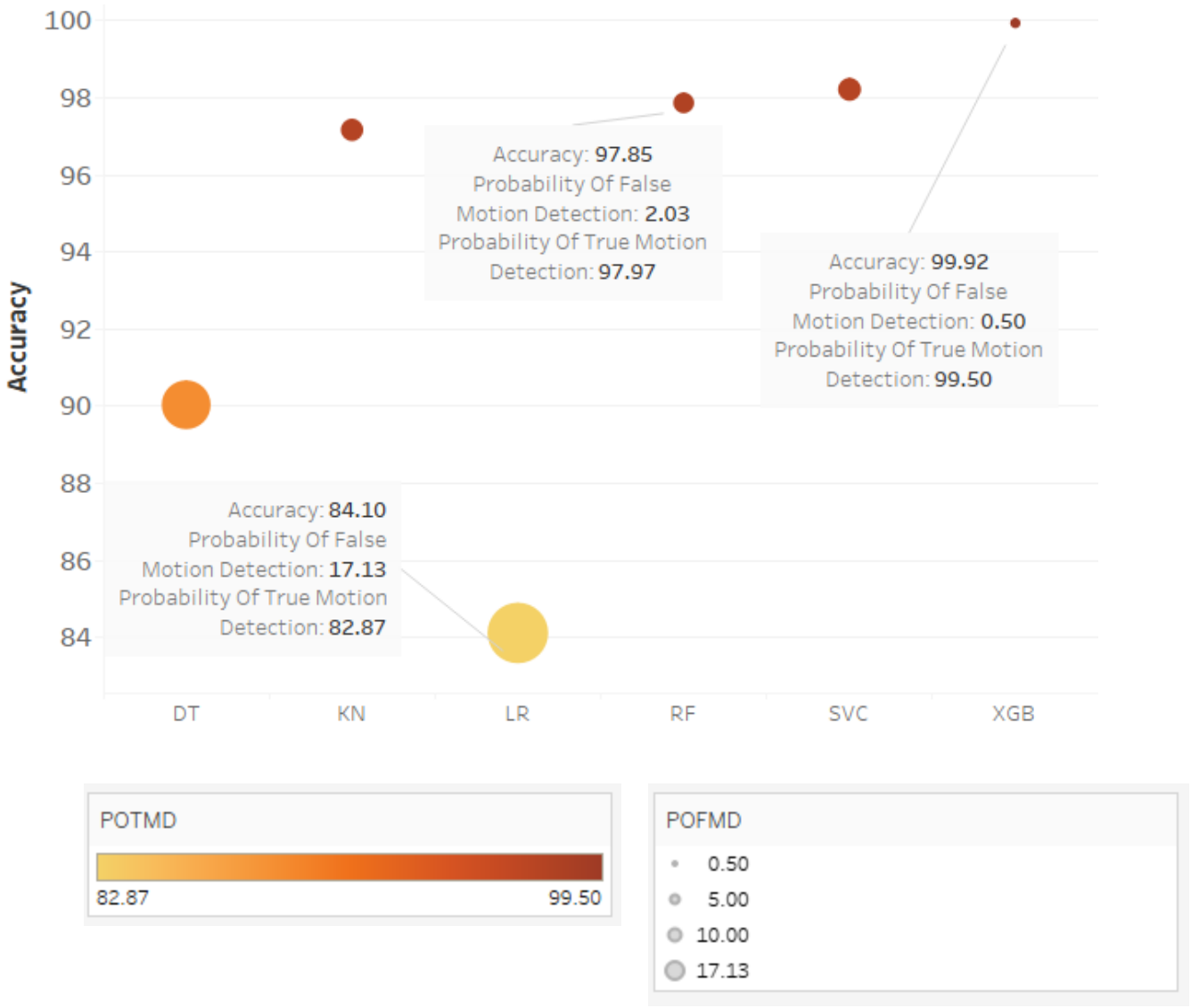

Figure 7.34 Horizontal motion detections RT-PPP EWS performance

(Prepared by the author).

Figure 7.35 colours show POTOSD details; however, the symbol sizes show details that respect the POFOSD. The figure shows that the RF and XGB classifiers have superior performance with 97.44% and 99.86 % POTOSD, and they also offer a minimum probability of initiating false out-of-service detections. On the contrary, the logistic regression shows the worst performance regarding accuracy, POTOSD, and POFOSD. It is worth mentioning that this figure represents the

performance of horizontal deformations. The fact that the out-of-service category encompasses all RT-PPP outliers supports the claim that all models have high accuracy with respect to out-of-service scenario detection; this makes their detection by the implemented models simple.

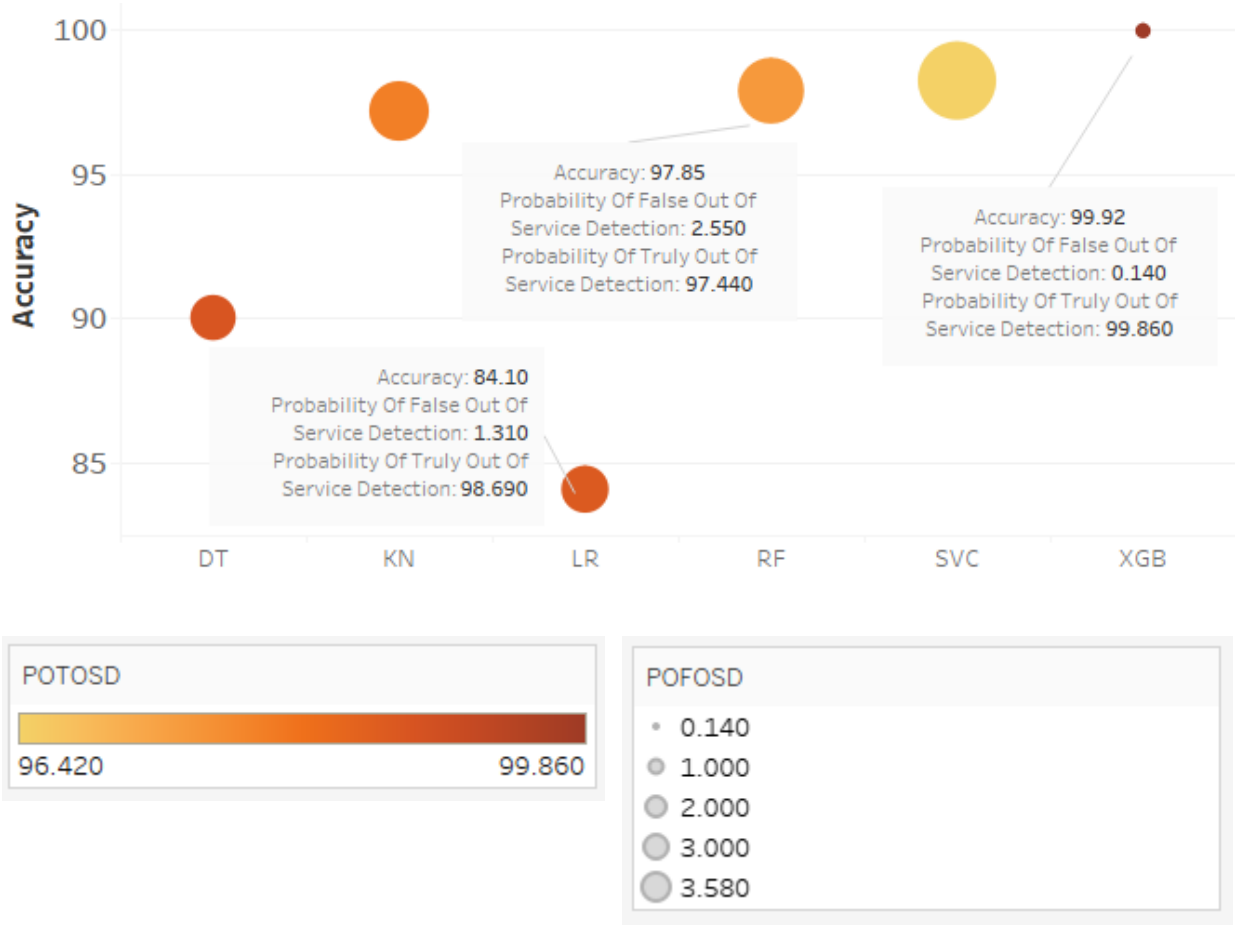

Figure 7.35 Horizontal out-of-service detections RT-PPP EWS performance

(prepared by the author).

7.3.5 Simulated 3D deformation monitoring results

Similar to the previous results regarding horizontal and vertical deformations, this section concludes the research findings regarding sixteen three-dimensional deformation experiments carried out during Chapter 6's work package 7 out of 48. It is worth highlighting that the forthcoming results correspond to the research test events. Figure 7.36 colours show POTNMD details; however, the symbol sizes show details that respect the POFNMD. The figure shows that the RF and XGB classifiers have superior performance with 99% and 99.96% of POTNMD, and they also offer a minimum probability of initiating false non-motion detections. On the contrary, the LR classifier shows the worst performance with respect to the achieved accuracy, POFNMD, and POTNMD. It is worth mentioning that this figure represents the performance of 3D deformations.

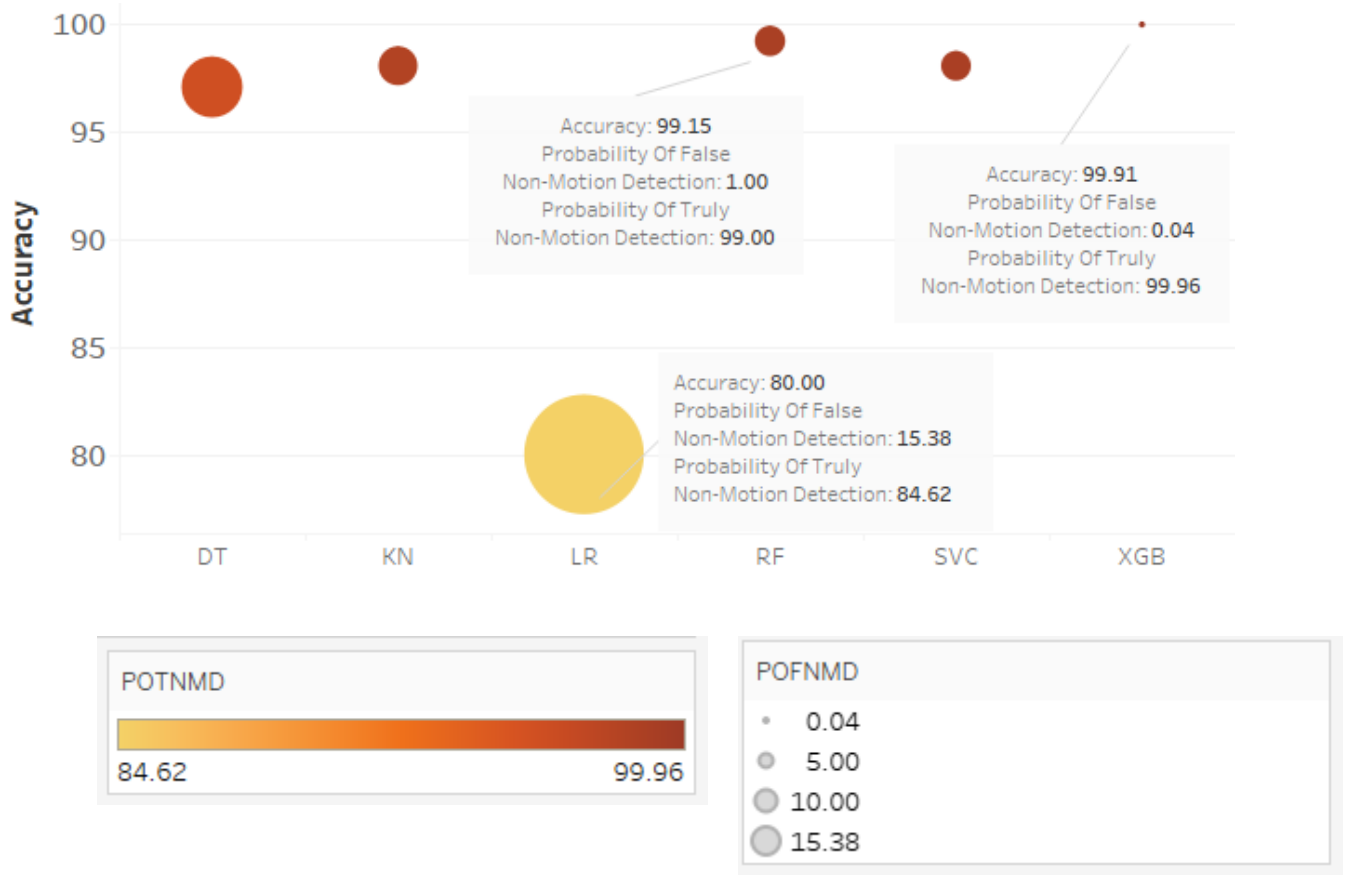

Figure 7.36 3D non-motion detections RT-PPP EWS performance

(Prepared by the author).

Figure 7.37 colours show POTMD details; however, the symbol sizes show details that respect the POFMD. The figure shows that the RF and XGB classifiers perform best with 99.92% and 99.99% of POTMD, respectively, and they show less probability of initiating false motion detections. On the contrary, the LR shows the worst performance regarding accuracy, POFMD, and POTMD. It is worth mentioning that this figure represents the performance of 3D deformations.

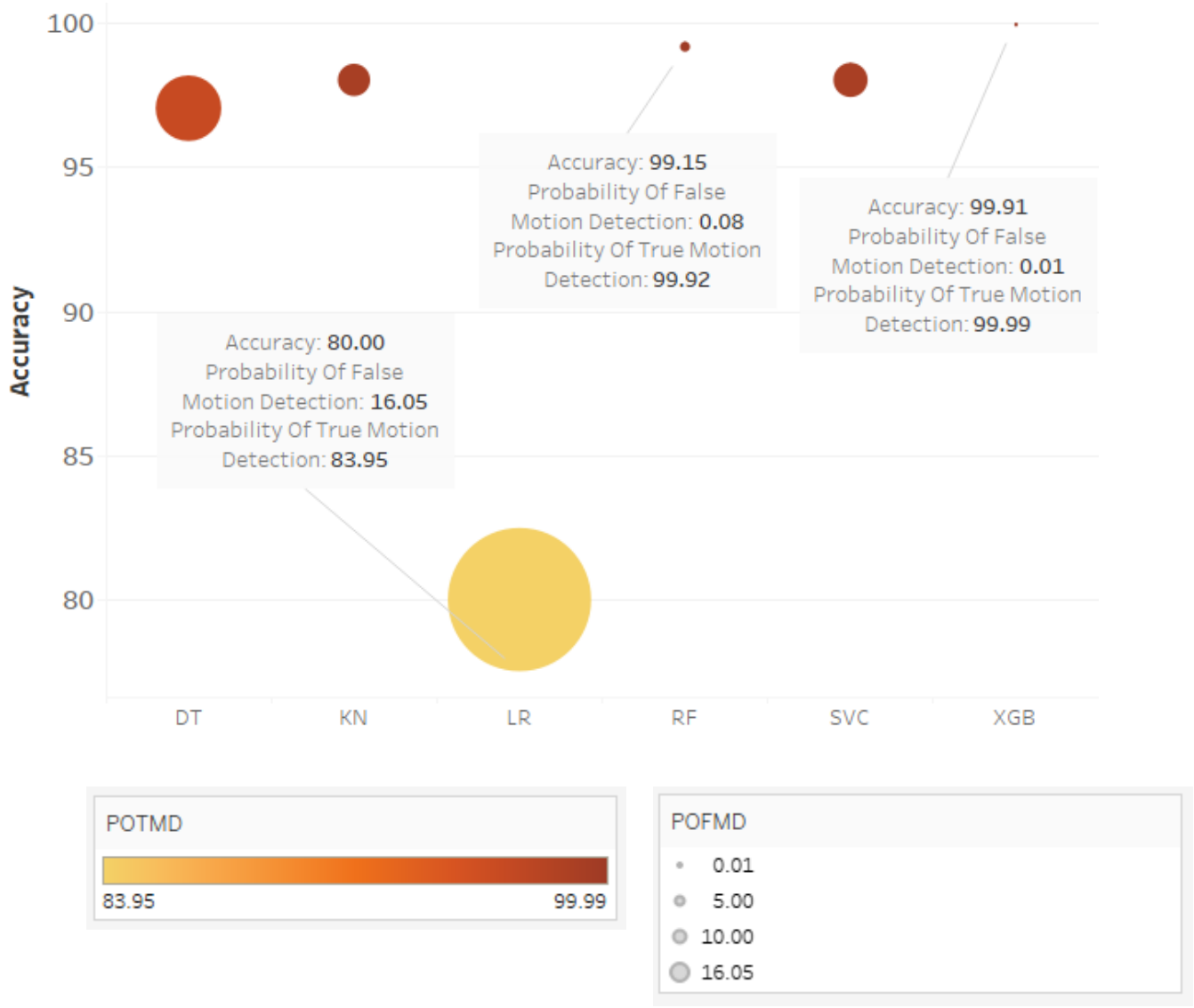

Figure 7.37 3D motion detections RT-PPP EWS performance

(Prepared by the author).

Figure 7.38 colours show POTOSD details; however, the symbol sizes show details that respect the POFOSD. The figure shows that the RF and XGB classifiers have superior performance with 99.08% and 99.99% of POTOSD, respectively, and they also offer a lower probability of initiating false out-of-service detections. On the contrary, the LR and the decision tree show the worst performance in accuracy, POTOSD, and POFOSD. It is worth mentioning that this figure represents the performance of 3D deformations. The notion that all models have good accuracy with respect to out-of-service scenario detection is bolstered by the fact that the out-of-service category includes all RT-PPP outliers. Because of this, it is easy for the implemented models to identify them.

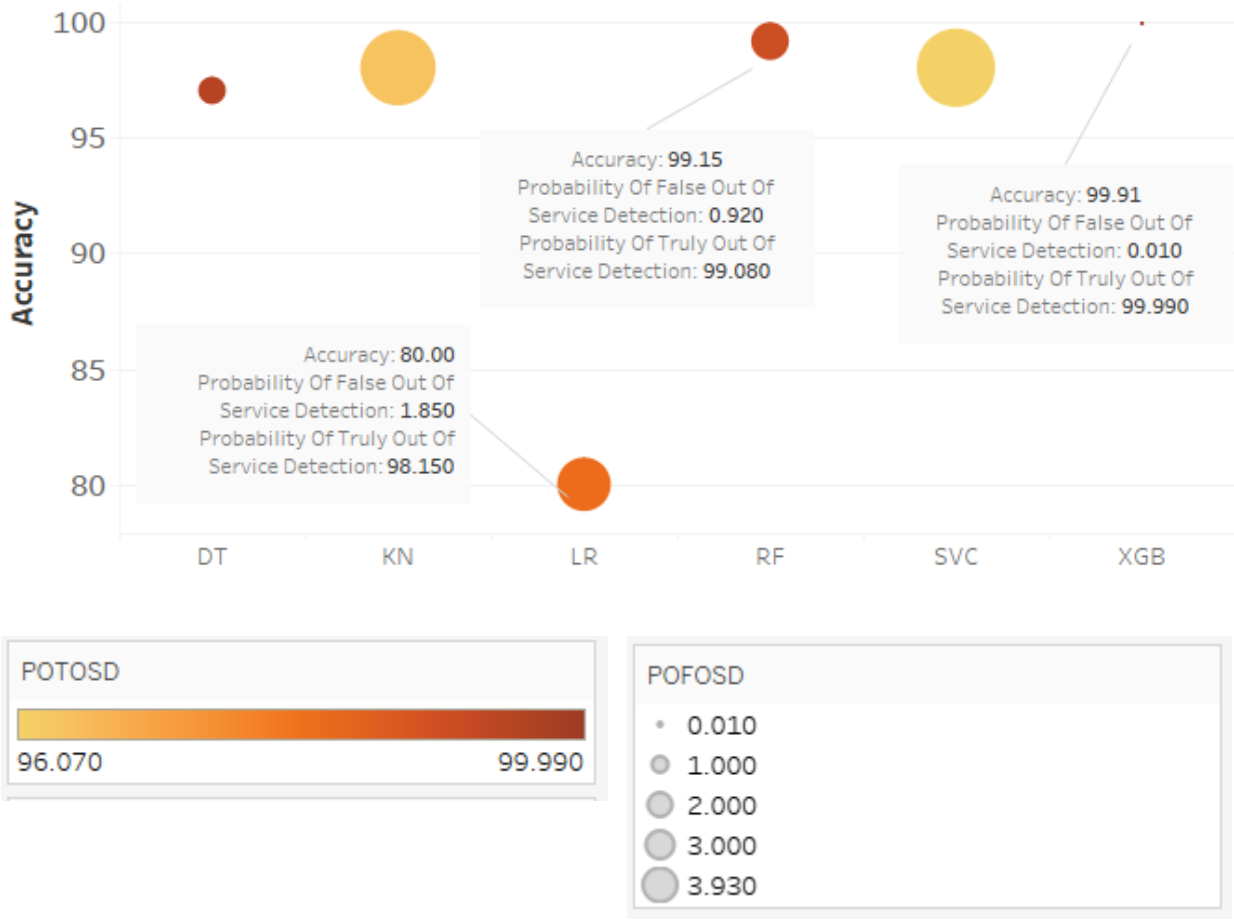

Figure 7.38 3D out-of-service detections RT-PPP EWS performance

(Prepared by the author).

7.3.6 Summarizing the results

To summarize the previous research finding results regarding vertical, horizontal, and three-dimensional deformations, Tables 7.9, 7.10, and 7.11 contain the final probability in terms of percentages regarding the RT-PPP EWS probabilities, noting that the POIFC was calculated as an aggregated figure with respect to all false warnings. The research established three different RT-PPP EWS adapting the situation if the users need to utilize an individual system suitable for land subsidence and uplifting, horizontal deformations, or three-dimensional deformations. It is worth highlighting that the section results correspond to the research test events.

The research emphasizes the significance of the POTMD and POFNMD as essential factors to be considered. The RF and XGB models show the best performance regarding the higher POTMD and minimal value of POFNMD. In addition, the overall accuracy of both models is superior to that of other investigation models. Simulated land subsidence and land-uplifting results show that the RF and XGB models demonstrate the probability of 97.81% and 99.89 percent of detecting vertical deformations out of all the deformation events, respectively. Regarding non-motion detections, The RF, KNN, and XGB models show the best performance regarding the higher Probability Of True None Motion Detections POTNMD and minimal value of Probability Of False None Motion Detections POFNMD. In addition, the models above showed accuracy performance with 97.10, 97.02, and 99.80 percent out of all the none-deformation events, respectively. Moreover, regarding the research concern regarding the initiation of false alarms, our investigations showed that the XGB model has the lowest value with respect to vertical POIFC, which reached 0.21 percent.

Simulated horizontal deformation results show that the RF, KNN, and XGB perform better than other investigation models; they can detect planer deformations, with 97.97, 97.65, and 99.50 percent of all the deformation events, respectively. The RF, KNN, and XGB models show the best performance regarding the higher horizontal POTNMD with 98.07, 96.93, and 99.61 percent out of all the none-deformation events, respectively, and minimal value of horizontal POFNMD. SVC showed similar performance regarding horizontal non-motion detections. Furthermore, our studies

revealed that the XGB model has the lowest value with regard to horizontal POIFC, which reached 1.03 percent out of all the out-of-services events, addressing the research worry regarding the commencement of false alarms.

Simulated 3D-deformation results show that RF, SVC, and XGB models fare well in terms of higher POTMD values, and POFNMD values are low. Furthermore, the total accuracy of the mentioned models is higher than that of investigation ML models. Regarding the 3D deformations compared to other inquiry models, the results demonstrate that the RF, SVC, and XGB have a higher detection probability for 3D deformations (99.92, 99.08., and 99.99%) concerning all the deformation events. For the maximum probabilities of non-motion detections and minimum probabilities value with respect to false non-motion detection events, the RF, SVC, and XGB models perform at 1, 0.96, and 0.04 percent of POFNMD with respect to all false non-motion detection events, respectively. Like vertical and horizontal results, the XGB model showed less likelihood of initiating a false warning with just 0.06 percent.

Contrary to the pre-mentioned ML models, The LR showed the worst performance regarding simulated vertical, horizontal, and 3D deformation, with accuracy reaching around 92, 84, and 80 percent, respectively. The model also showed a higher ability to initiate false warnings with respect to horizontal simulation results. The models showed a 34 percent probability of initiating false warnings. The LR classification ML model relies on classification data by creating a similar linear classification boundary, accordingly, due to the complex data distributions and higher dimensional space. Consequently, the lowest LR classification accuracy could be justified that the boundary established from the model above encounters challenges in separating the research events.

Table 7.9 RT-PPP EWS performance regards the vertical deformations.

Classifiers	Accuracy	POTNMD	POFNMD	POTMD	POFMD	POTOSD	POFOSD	POIFC
DT	95.20	92.59	7.41	95.09	4.91	99.95	0.05	12.37
RF	97.10	93.76	6.23	97.81	2.19	99.84	0.16	8.58
KNN	97.02	95.44	4.55	95.95	3.04	98.89	1.11	8.70
LR	92.15	88.47	11.53	90.17	9.82	99.35	0.65	22.00
SVC	97.02	95.55	4.45	95.82	4.18	98.95	1.05	9.68
XGB	99.80	99.92	0.08	99.89	0.11	99.98	0.02	0.21

Table 7.10 RT-PPP EWS performance regarding the horizontal deformations.

Classifiers	Accuracy	POTNMD	POFNMD	POTMD	POFMD	POTOSD	POFOSD	POIFC
DT	90.02	90.92	9.08	88.86	11.14	98.79	1.21	21.43
RF	97.85	98.07	1.93	97.97	2.03	97.44	2.55	6.51
KNN	97.15	96.93	3.07	97.65	2.35	97.91	2.09	7.51
LR	84.10	83.63	16.37	82.87	17.13	98.69	1.31	34.81
SVC	98.20	97.56	2.44	97.52	2.48	96.42	3.58	4.92
XGB	99.92	99.61	0.39	99.50	0.50	99.86	0.14	1.03

Table 7.11 RT-PPP EWS performance regards three-dimensional deformations.

Classifiers	Accuracy	POTNMD	POFNMD	POTMD	POFMD	POTOSD	POFOSD	POIFC
DT	97.02	96.00	4.00	96.63	3.37	99.51	0.49	7.86
RF	99.15	99.00	1.00	99.92	0.08	99.08	0.92	2.00
KNN	98.00	98.36	1.64	99.18	0.82	96.37	3.63	6.09
LR	80.00	84.62	15.38	83.95	16.05	98.15	1.85	33.28
SVC	98.00	99.04	0.96	99.08	0.92	96.07	3.93	5.81
XGB	99.91	99.96	0.04	99.99	0.01	99.99	0.01	0.06

Tables 7.9, 7.10, and 7.11 comprehensively illustrate the performance evaluation of the Real-Time Precise Point Positioning Early Warning System RT-PPP EWS with respect to vertical deformations, horizontal deformations, and three-dimensional deformations, respectively. The study underscores the significance of instituting an Early EWS that is tailored to address specific geological hazards, effectively adapting to varying types of deformations. Moreover, the research substantiates the rationale behind establishing an EWS calibrated for singular deformation modes, as this strategic approach contributes to the enhancement of EWS effectiveness and performance.

7.4 Generic model Azure analysis

The research study utilized the Azure platform as an additional investigation tool in order to address the critical nature of establishing the RT-PPP EWS and its impact on end-users. This was accomplished by using the platform as an additional investigation means. The purpose of the study was to check and validate the research conclusions, and Azure was used to accomplish this. This strategy ensured the delivery of a reliable and trustable model that end-users could rely on its performance. The current analysis uses all the research events collected through horizontal, vertical, and 3D experiments. Accordingly, the generated model could applied as a generic model for generalized displacements.

Microsoft Azure is a cloud computing platform that provides various services through Microsoft-managed data centers to assist individuals and businesses in developing, deploying, and managing applications and services. It offers a safe and dependable hosting environment and a wide range of tools that simplify application development, testing, and scaling. With the Azure platform, users can use the cloud to deploy AI and ML solutions, store data, run virtual machines, and develop web and mobile apps.

In addition to hosting virtual machines, Azure offers storage options, database management, networking features, and analytics applications. It is possible to build sophisticated, scalable applications by combining and integrating these services. Cognitive services, other Azure machine learning, and AI services let programmers incorporate AI capabilities into their software. The Azure automated machine learning utilizes several data scaling methods, including Standard Scaler Wrapper, which is a preprocessing method in ML that practices removing the mean and scaling to unit variance to make features more homogeneous. It ensures that the scales of the features are the same; this is important for algorithms that depend on the sizes of the features, like gradient descent-based methods. In addition, the preprocessing method called Max Abs Scaler scales features by dividing them by the maximum absolute value. This strategy preserves the sign and magnitude of the initial values as the data distribution is not subjected to any change. It is especially beneficial for sparse data when the mean and variance may not be accurate indications of the features of the data. However, the Sparce Normalizer is developed for sparse data, which is frequently found in text data or large datasets. It maintains the data's sparsity by scaling each

feature separately until its norm (magnitude) equals one. For methods that rely on the trigonometric similarity between data points, this may be helpful. Eventually, Singular Value Decomposition with Truncation (SVD), a dimensionality reduction approach called wrapper, is used to reduce the number of attributes in a dataset. The dimensions are efficiently decreased by splitting the dataset into three matrices and changing the lowest single values. It is frequently used to reduce noise and boost effectiveness in large datasets.

On the other hand, Azure automated machine learning utilizing several data ML models. An ensemble learning technique called Extreme Random Trees, often called Extra Trees, creates numerous decision trees by randomly choosing attributes and thresholds for each split. Adding more randomization than conventional decision trees seeks to reduce variance and overfitting. The average forecast from all the trees is the foundation for the final prediction.

Moreover, an efficient and quick gradient boosting framework is called Light GBM Light Gradient Boosting Machine (GBM). It employs a gradient-based method to identify the ideal splits and a histogram-based strategy for discarding features. Large datasets and categorical features can be handled with great ease by Light GBM, in addition to the pre-illustrated ML models, which are Logistic Regression, Random Forest, and XGBoost Classifier. The utilization of automated machine-learning methodologies facilitates the systematic exploration of the performance of machine-learning models through multiple iterative processes (Hastie et al., 2009a, 2009b; Murphy, 2012; Scikit-learn, 2023; Sutton & Barto, 2018). These iterations encompass a wide array of scaling techniques, allowing users to attain highly precise machine-learning models.

The research utilized one of the Azure services called automated ML. The service handles complicated decision-making by automatically selecting and configuring algorithms and model settings. In order to determine the optimal method and configuration for the data and prediction task, it employs state-of-the-art approaches to search for and assess candidates automatically.

Table 7.12 concludes the Azure research findings which correspond to the research test events. It is worth mentioning that the research does not control the Azure automated ML process and settings. Thus, the platform has investigated several ML models utilizing various data scaling methods. The process also included several iterations where the platform manipulated the model's parameters automatically. Azure utilizes several parameters such as learning rate, maximum

utilized features, minimum number of sample leaves, maximum tree depth, and utilized solver, and it applies Gini or entropy approaches.

The worst model performance with an accuracy of 50 percent was obtained utilizing the Random Forest with the Sparse normalizer scaling method. However, the same model showed the highest accuracy performance, with 99.9997 utilizing a standard scaler wrapper. The Azure research finding more or less matches the research investigations. For example, our study showed that the logistic regression had the worst performance, with accuracy achieved at 83 percent, which matches the Azure results with accuracy varying between 69 and 73 percent. The slight differences between the research and the Azure result are in reasonable range due to the implementation of various hypermeters and different data splitting percentages. The platform utilizes 70% for training and validation and 30% for ML testing.

On the contrary, the XGB and Random Forest show an accuracy of around 99 and 93 percent, respectively. The same models show accuracy reaching around 99.95 utilizing Azure automated ML. It is worth noting that automated ML does not include implementing the decision tree, K nearest, and support vector classifiers. The research justified the pre-mentioned model exclusions. Due to the high computational cost of utilizing the support vector machine and K nearest models, the decision tree exclusion could result from the model overfitting issues. The iteration column in Table 7.12 indicates how many platform iterations are required to return the best model accuracy for the chosen scaling method and the manipulated parameters.

Table 7.12 RT-PPP EWS Generic Azure assessments performance.

Scaling method	Model name	Accuracy	Iteration
Standard Scaler Wrapper	Extreme Random Trees	61.792	1
Max Abs Scaler	Extreme Random Trees	66.075	2
Max Abs Scaler	Extreme Random Trees	70.256	3
Max Abs Scaler	Extreme Random Trees	76.476	4
Standard Scaler Wrapper	Extreme Random Trees	85.573	5
Sparse Normalizer	Light Gradient Boosting Machine	85.978	1
Standard Scaler Wrapper	Light Gradient Boosting Machine	89.166	2
Max Abs Scaler	Light Gradient Boosting Machine	94.477	3
Max Abs Scaler	Light Gradient Boosting Machine	95.302	4
Standard Scaler Wrapper	Light Gradient Boosting Machine	95.443	5
Standard Scaler Wrapper	Light Gradient Boosting Machine	96.994	6

Standard Scaler Wrapper	Light Gradient Boosting Machine	97.501	7
Max Abs Scaler	Light Gradient Boosting Machine	98.33	8
Max Abs Scaler	Light Gradient Boosting Machine	98.875	9
Max Abs Scaler	Logistic Regression	69.53	1
Max Abs Scaler	Logistic Regression	71.622	2
Standard Scaler Wrapper	Logistic Regression	73.449	3
Sparse Normalizer	Random Forest	50	1
Sparse Normalizer	Random Forest	55.526	2
Truncated SVD Wrapper	Random Forest	71.432	3
Sparse Normalizer	Random Forest	73.007	4
Max Abs Scaler	Random Forest	80.378	5
Max Abs Scaler	Random Forest	90.508	6
Standard Scaler Wrapper	Random Forest	99.9997	7
Standard Scaler Wrapper	XGBoost Classifier	83.401	1
Standard Scaler Wrapper	XGBoost Classifier	86.071	2
Sparse Normalizer	XGBoost Classifier	93.583	3
Standard Scaler Wrapper	XGBoost Classifier	94.167	4
Standard Scaler Wrapper	XGBoost Classifier	94.45	5
Standard Scaler Wrapper	XGBoost Classifier	94.673	6
Standard Scaler Wrapper	XGBoost Classifier	96.598	7
Standard Scaler Wrapper	XGBoost Classifier	97.017	8
Standard Scaler Wrapper	XGBoost Classifier	97.366	9
Sparse Normalizer	XGBoost Classifier	98.329	10
Standard Scaler Wrapper	XGBoost Classifier	98.435	11
Standard Scaler Wrapper	XGBoost Classifier	99.175	12
Standard Scaler Wrapper	XGBoost Classifier	99.534	13
Max Abs Scaler	XGBoost Classifier	99.741	14
Standard Scaler Wrapper	XGBoost Classifier	99.769	15
Standard Scaler Wrapper	XGBoost Classifier	99.797	16

7.5 Feature importance and feature selection

The researchers probed the significance of the EWS feature, a central notion in machine learning; this allowed the study to examine every EWS feature used in RT-PPP and reevaluate which ones were most important.

The term "feature importance" is being used to describe the significance of individual features within a dataset in terms of their ability to aid the ML model forecasting or classification tasks. It aids in pinpointing the inputs that have the most impact on the model's performance. It is worth mentioning that several methods, such as correlation, feature importance metrics, premutation importance, and L1 Regularization, could be utilized to detect the most relevant feature. In this section, the research has investigated the relevancy of the data prepared to establish the RT-PPP EWS. Thus, the RF importance metrics method was utilized through the Azure platform. This method relies on the frequency with which a feature is utilized to partition the data, which is one metric on which algorithms like decision trees and random forests base their feature relevance scores. Accordingly, all experiment data were uploaded to the Azure Microsoft platform to investigate the feature's importance. Figure 7.39 shows the pie chart of the obtained results of the Azure platform. The findings clearly validate that among the variable attributes, the horizontal and positional Root Mean Square Error (RMSE) stand out as pivotal factors in the context of RT-PPP EWS. The established EWS is designed to categorize observations derived from the RT-PPP approach based on their disparity in relation to observations acquired at the established station marker location. Logically, the machine learning model would exploit the inherent advantages offered by the horizontal and positional RMSE values to discriminate between deformation and non-deformation events effectively. Furthermore, it is worth noting that the RMSE values exhibit substantial variations across the three distinct investigated categories, namely, misplaced, centered, and out-of-service categories.

Additionally, features like displacement components, latency, and the obtained tropospheric errors are crucial for the established EWS. It is significant to highlight that the deformation aspects, encompassing the horizontal and positional Root Mean Square Error (RMSE) and the east, north, and vertical displacement components, collectively constitute 80% of the importance concerning the entire features within EWS; this is succeeded by proportions of 6% and 4% correspondingly,

attributed to the tropospheric error and latency features. The other category includes the rest of the research features, such as the number of tracked satellites, Horizontal dilution of precision, RT-PPP coordinates residuals, elevation mask angle, and residuals of the carrier pseudoranges with respect to the Iono-free combination.

It is essential to highlight that it is imperative to recognize that the feature importance outcomes were notably affected by the number of RT-PPP observations. This effect stemmed from the inherent constraints associated with acquiring RT-PPP measurements—consequently, excessive HDOP value or an insubstantial number of used GNSS satellites impact the availability of RT-PPP observations. Hence, it becomes evident that the restricted accessibility and diminished quality of observations markedly influenced the relative significance ascribed to various features in the RT-PPP analysis.

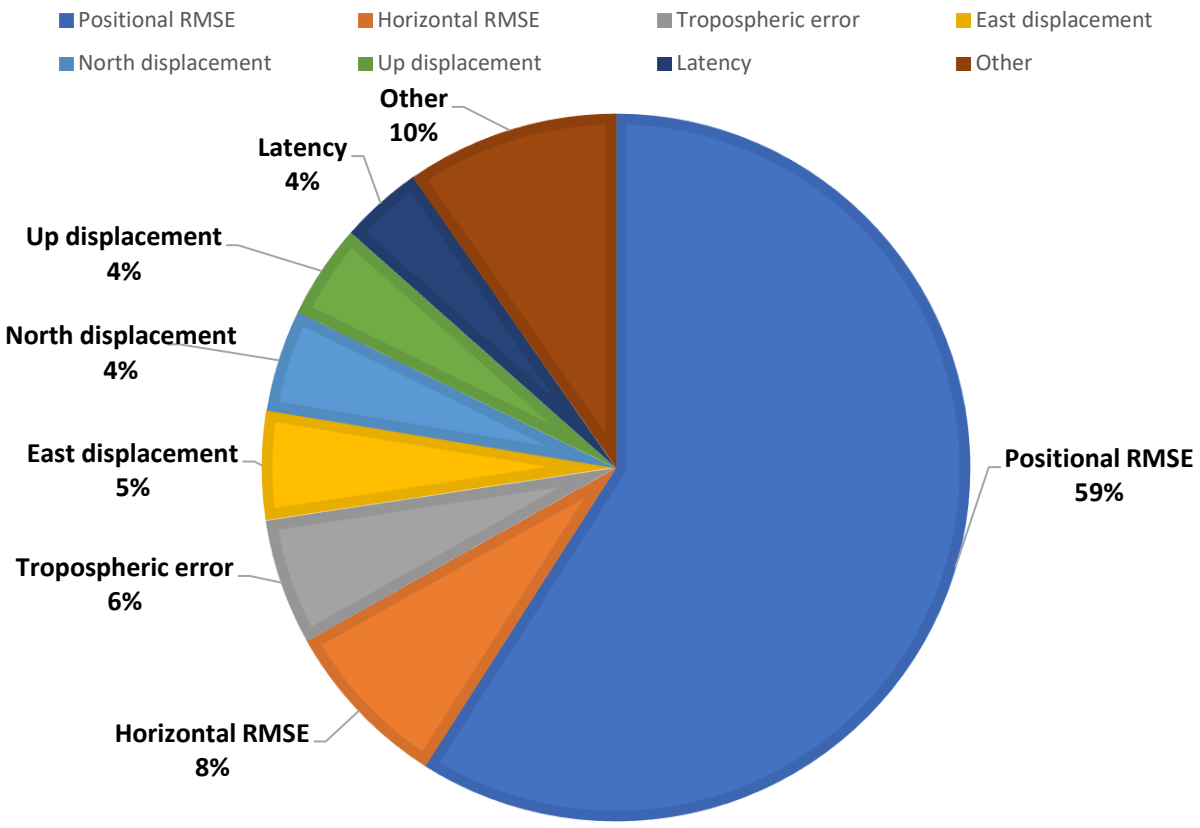

Figure 7.39 Research feature importance

(Prepared by the author).

Before the commencement of the research endeavour, the establishment of a comprehensive EWS and the related study's conclusions related to the inclusive RT-PPP EWS were presented. It is worth highlighting that the research dataset encompasses a total of 404 distinctive attributes involving approximately 1.7 million data instances. In this context, it is sensible to give attention to matters concerning computational complexity, the risk of overfitting, and the overall efficacy of the EWS.

7.6 Generic model

Selecting features as a subset based on the initial feature sets is fundamental in order to reduce computational complexity, prevent overfitting, and enhance model performance. Subsequently, to reduce the dimensional feature space and improve the execution and performance of the RT-PPP EWS, the notation of feature selection followed the above-mentioned results. Therefore, the RT-PPP EWS Generic model was trained and assessed utilizing east and north up-displacements and their residuals, position and horizontal RMSEs, speed and course overground, stream latency, satellite number, and the value of elevation mask angle.

Notably, the conducted research deliberately excluded the reference station coordinates as trained features to facilitate the generalization of the RT-PPP EWS for its applicability in diverse geographical locations (this means that the EWS required the deformations information as input, which was calculated concerning the station prior coordinates configured by BNC software for example). This approach enables the RT-PPP EWS to be more widely applicable and adaptable in various regions, enhancing its practical utility and accessibility across different geographic contexts.

The last results of this research were done by combining all the experiment data collected in the experiments tables in EWS work package seven, entitled experiments implementation; this combination allows training, validation, and testing of the RT-PPP EWS MLASs with data collected from all experiments; this enhanced the model's training and testing. Accordingly, the exported MLASs could be more reliable with respect to the achieved accuracy and detection probabilities as they trained with different correction streams, different magnitudes of elevation angles, various deformation magnitudes, different deformation directions, and different training

periods additionally, which allows training, testing, and validation of the models with adequate events.

Figure 7.40 colours show POTNMD details; however, the symbol sizes show details that respect the POFNMD. The figure shows that the SVC and XGB perform as the most accurate classifiers with 96.80% and 98.65% POTNMD, offering less probability of initiating false non-motion detections. On the contrary, the logistic regression shows the worst performance with respect to the achieved accuracy, POFNMD, and POTNMD. It is worth mentioning that this figure represents the performance of generic deformations.

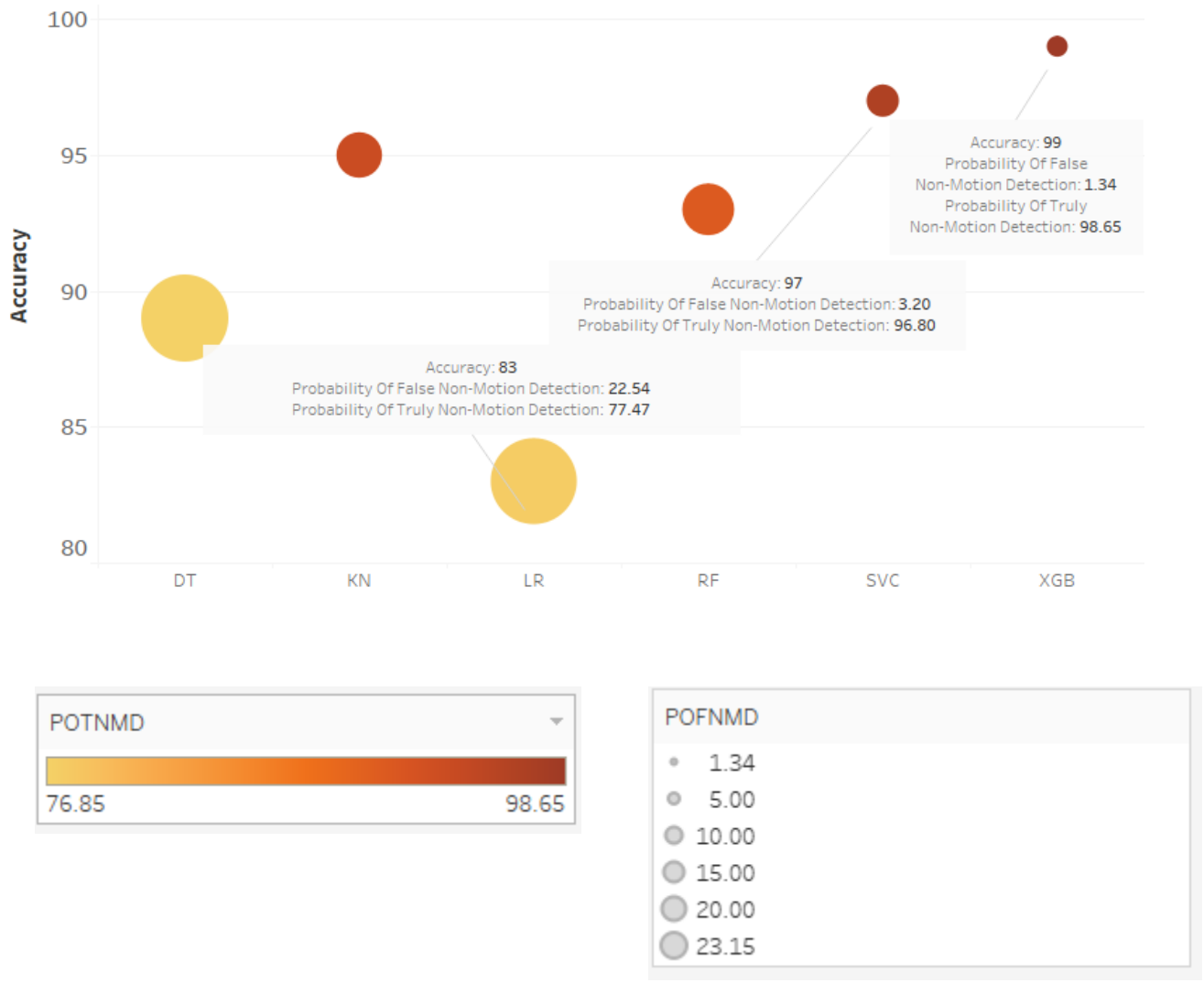

Figure 7.40 Non-motion detection RT-PPP EWS Generic MLAs performance

(Prepared by the author).

Figure 7.41 colours show POTMD details; however, the symbol sizes show details that respect the POFMD. The figure shows that the SVC and XGB perform superiorly with 97.29% and 98.85% of POTMD, and they are less likely to initiate false motion detections. On the contrary, the logistic regression shows the worst performance regarding accuracy, POFMD, and POTMD. It is worth mentioning that this figure represents the performance of generic deformations.

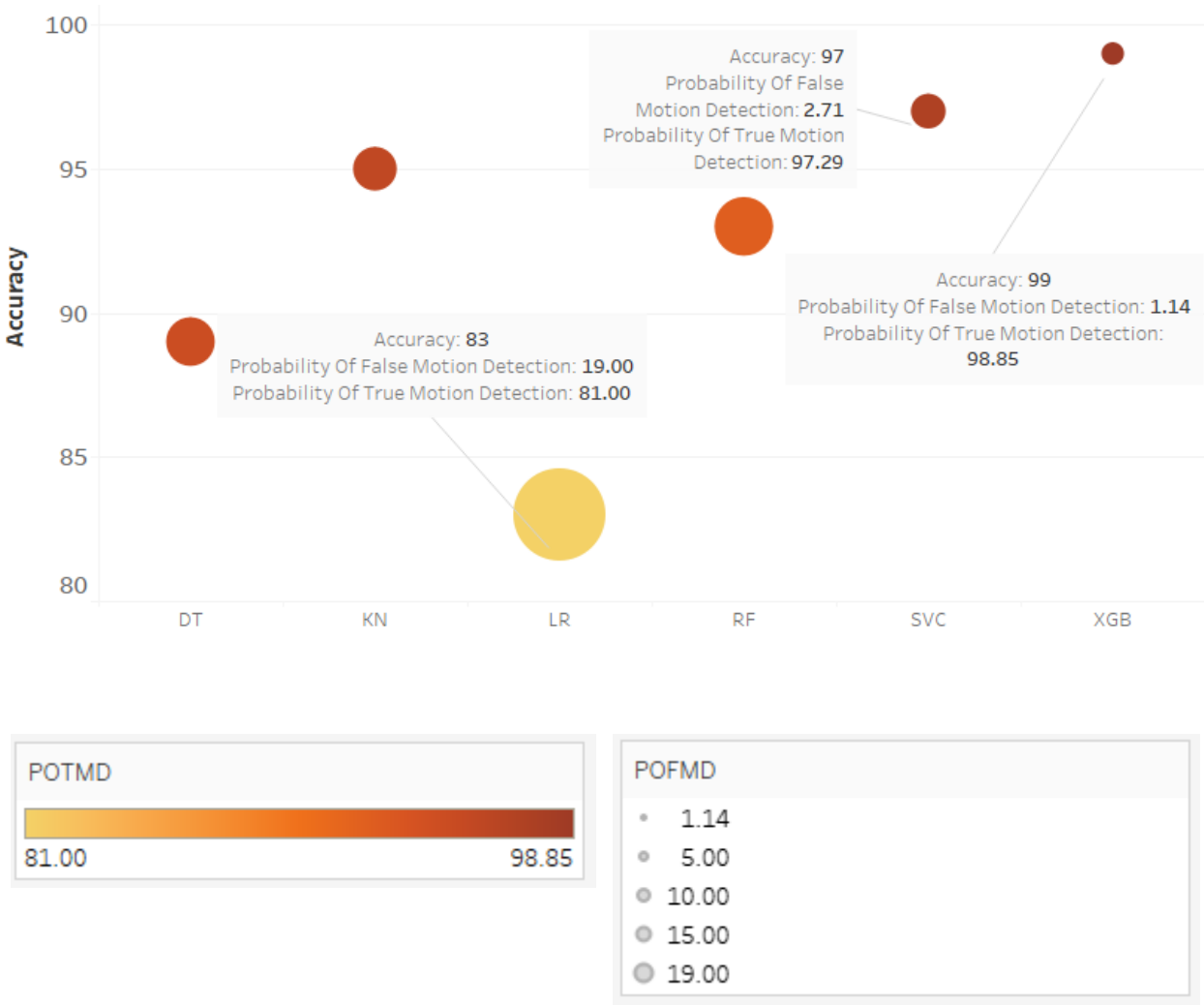

Figure 7.41 Motion detection RT-PPP EWS Generic ML models performance

(Prepared by the author).

Figure 7.42 colours show POTOSD details; however, the symbol sizes show details that respect the POFOSD. Again, the SVC and XGB are the most accurate classifiers, with an accuracy of 97% and 99.21% of POTOSD, respectively. Furthermore, they also offer less probability of initiating false out-of-service detections. On the contrary, the logistic regression and the decision tree show the worst performance in accuracy, POTOSD, and POFOSD. It is worth mentioning that this figure represents the performance of generic deformations.

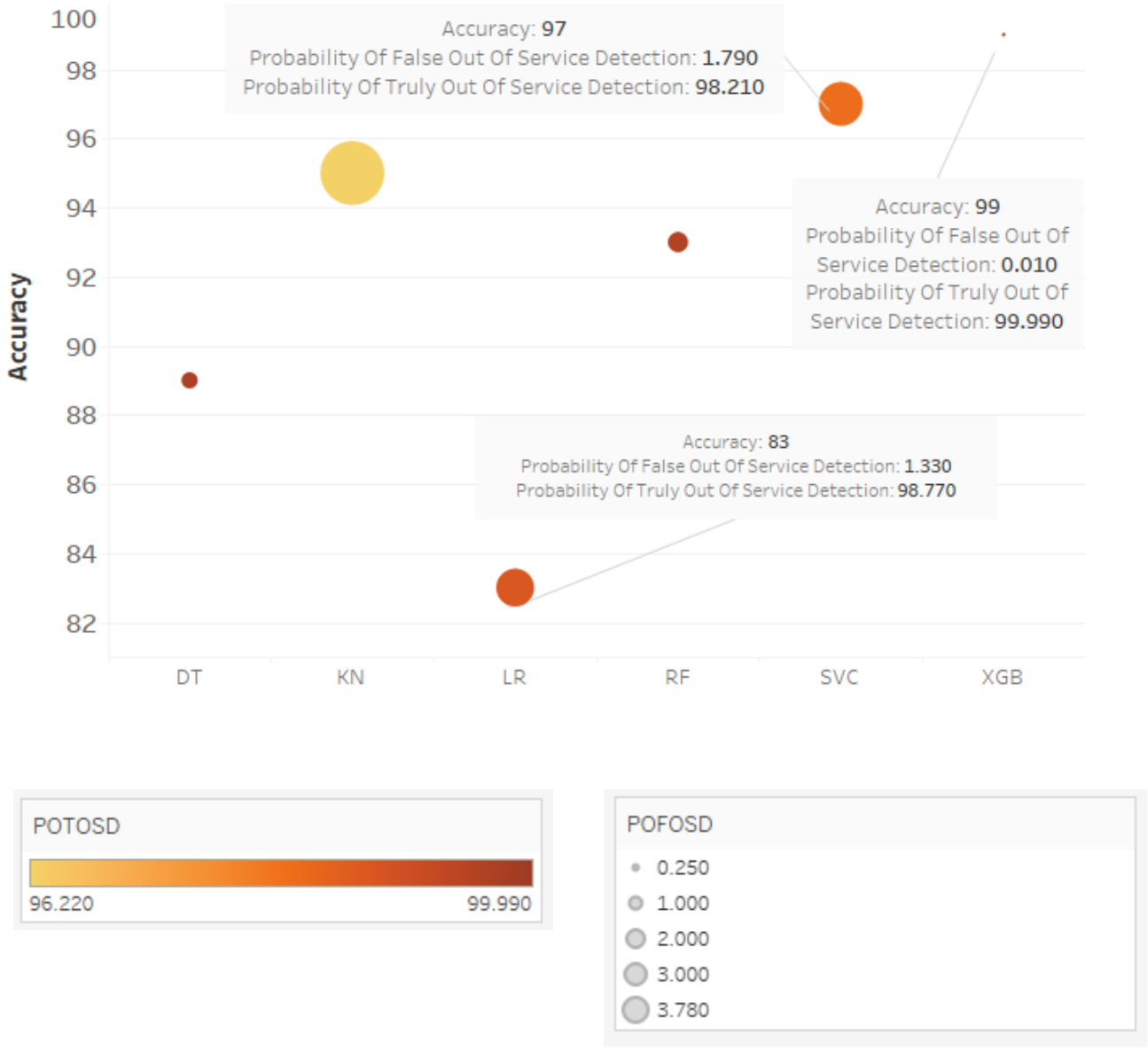

Figure 7.42 Out-Of-Service detections RT-PPP EWS Generic ML models performance

(Prepared by the author).

The forty-eight experiments were conducted between the eleventh of October 2021 and the fifth of October 2022. The research engine was established to simulate deformations in different directions, with the RT-PPP being persistently recorded for a full day. In 12 hours, only six sessions were held. Note that the simulated deformations' elevation mask angles, magnitude, and direction were used in the saved RT-PPP and that the stream latency changed. Accordingly, the research established the generic RT-PPP EWS, which has taken advantage of diverse RT-PPP collected through all research experiments. Noting that this step came after the research carried out regarding the importance of features, which concluded the research to utilize the most relevant features to proposed RT-PPP EWS, enhancing the system performance, reducing the computational cost, and avoiding data overfitting. Notably, the reference station coordinates were omitted on purpose from the conducted research in order to broaden the applicability of the RT-PPP EWS to a variety of places. The study aimed to create a method easily implemented in other locations without requiring precise and localized reference data. Hence, the authors omitted the coordinates of the reference stations. This method makes the RT-PPP EWS more portable and flexible, increasing its usability and availability in various geographical settings.

The research on the RT-PPP generic EWS showed that the XGB and SVC models show the best performance regarding the higher POTMD and minimal value of POFNMD. In addition, the overall accuracy of both models is superior to that of other investigation models. Furthermore, remarkably, they tend to have the minimum ability to initiate false alarms.

To summarize the previous research, Table 7.13 is presented, which contains all experiment events, including vertical, horizontal, and three-dimensional deformations. The table contains the final probability in terms of percentages regarding the RT-PPP EWS probabilities, noting that the POIFC was calculated as an aggregated figure with respect to all false warnings. The XGB and RF classifiers showed superior model accuracy compared to the other utilized models, with 97 and 99 percent overall accuracy. At the same time, the XGB showed the ability to initiate minimal false alarms with 2.48 percent, and it was 7.7 percent with respect to the SVC. Similar performances for both models were found regarding the ability of motion detection.

Table 7.13 RT-PPP EWS Generic ML models performance.

Classifiers	Accuracy	POTNMD	POFNMD	POTMD	POFMD	POTOSD	POFOSD	POIFC
DT	89	76.85	23.15	94.7	5.3	99.75	0.25	28.70
RF	93	91.2	8.2	92.3	7.7	99.62	0.38	16.28
KN	95	93.67	6.33	95.73	4.27	96.22	3.78	14.38
LR	83	77.47	22.54	81	19	98.77	1.33	42.87
SVC	97	96.8	3.2	97.29	2.71	98.21	1.79	7.7
XGB	99	98.65	1.34	98.85	1.14	99.99	0.01	2.481

7.7 Summary

The present chapter culminates with a concise synthesis of the study's findings. Primarily, the performance of the RT-PPP EWS is closely associated with implementing machine learning (ML) models. The preceding discussions indicate that the characteristics of RT-PPP measurements significantly influence the performance, which can be attributed to the fact that linear regression (LR) consistently exhibited suboptimal performance in most cases. The LR method represents an enhanced version of linear regression. Consequently, given the diverse distribution of research events, this model faces challenges in establishing robust classification boundaries among the research categories. Conversely, Decision Tree (DT) classifiers encounter issues related to over-fitting. As demonstrated by the study, the research database comprises 404 features and approximately 1.7 million entities, making it arduous for the DT model to handle such a substantial database effectively.

In contrast, the Random Forest (RF) classification model exhibits superior performance. This model employs an ensemble approach by combining multiple decision trees, and the final predictions are derived from aggregating the outputs of these trees. Consequently, it is capable of generating more precise and robust predictions. Additionally, the RF model is better for handling non-linear data. The Support Vector Classifier (SVC) demonstrates comparable performance by employing a radial kernel, enhancing the model's capacity to establish non-linear classification boundaries. As a result, it is suitable for detecting deformations that may occur in various directions and magnitudes. However, the XGBoost (XGB) performs well when it assesst to the test data. On the contrary, the performance of this model has deteriorated when evaluated on the entire research database.

The K-Nearest Neighbours (KNN) model performs well in certain instances. However, it is essential to acknowledge that the implementation costs associated with this model can be significant, particularly when determining the optimal value of K to be employed. Notably, the research findings align considerably with the results obtained from Azure, which indicate that RF and XGB are the most accurate models for deployment in the RT-PPP EWS.

Chapter 8 Conclusion, Discussions, and Future Works.

8.1 Conclusions and discussions

This chapter provides the essential summary and interpretations of the critical study findings. The research approaches the final chapter after completing multiple phases of investigations in which various improvements are presented throughout the thesis chapters.

According to the performed research experiments, the IGS03 clock corrections stream showed a mean latency of 31 seconds. Consequently, both SVR and ARIMA forecasting methods have been investigated and used to predict clock corrections to mitigate the latency impact by implementing the explained algorithms. Because of their known rate of change relative to clock corrections, latency effects on orbital corrections can be easily corrected because of the well-known orbital parameters. Hence, the research ignored it throughout the study investigations. It is worth noting that the latency analysis was carried out with respect to GPS and GLONASS navigation systems however, the research methodology could be extended to Galileo and BeiDou.

In the context of establishing RT-PPP EWS with the assistance of the RT-PPP technique and the machine learning models utilized in system creation, the system may generate very accurate real-time estimates and trigger early warnings to detect deformations and displacements.

It is worth mentioning that the research findings are valid with respect to the displacements having a magnitude equal to or less than 20 cm, which match the training displacement exerted with the research engine. However, for displacement values having a magnitude more than 20cm, it is suggested to re-training the developed ML models to adapt displacement values exceeding 20 cm; nevertheless, given the accuracy of the methodology developed for movements smaller than 20 cm, the probability of success for more significant movements should be equally high. It is worth highlighting that the research recommends using SVC or the XGBoost models as they provide the highest accuracy.

In conclusion, RT-PPP EWS is a globally deployable technology for monitoring and responding to geo-natural hazards. By adopting RT-PPP, the RT-PPP EWS could be utilized at a global scale, providing supportive RT warnings for local communities, stakeholders, and civil defence. To that

end, having access to such warnings far before a destructive event is crucial, as it paves the way for stakeholders to develop real-time protection and assessment applications and, if possible, evacuation procedures.

For the sake of establishing an RT-PPP early warning system, the reference station establishment installation and configuration were carried out. Accordingly, several days of static sessions were used to ensure the quality of the reference station coordinates. Additionally, seven days of RT-PPP coordinates were collected utilizing different elevation masks varied from 0 to 60 degrees in order to find noise-free measurements and to simulate bad GDOP scenarios. The researchers found an elevation angle with a ten-degree value was the most suitable, leading to error ranges of 11cm, 14 cm, and 38 cm in the east, north, and up directions, respectively. Regarding the availability of the RT-PPP solution, 99.96% was available utilizing a ten-degree elevation angle.

Beforehand, the research's findings regarding the RT-PPP EWS show that it is worth paying attention to the research results regarding the research variable relation. The research carried out two levels of investigations, including RT-PPP features correlations and RT-PPP EWS feature importance. The study justified the investigation levels regarding the variable's relations to ensure the consistency of the results.

Chapter 7 correlation matrix was created utilizing the stored RT-PPP measurements implemented after the station static sessions. Seven days of continuous RT-PPP measurements were invoked in this analysis. Accordingly, the correlation matrix shows a high positive correlation between RT-PPP coordinates and the coordinates-driven errors. A negative relation was constructed between the RT-PPP vertical error and tropospheric delay. Additionally, high negative correlations were established intermediate between the satellite's elevation mask angle and latency, the number of tracked satellites, and the root mean squared error of the phase measurements. It is worth noting that the horizontal and positional root mean squared error positively relates to station coordinates and the error coordinate error components. At this point, it is essential to note that the number of observations affected the correlation results.

Regarding the investigations of the importance of the RT-PPP EWS features, the Azure Microsoft platform was utilized to inspect the most relevant feature of the RT-PPP EWS. The platform results agreed with the research investigations. Figure 7.39 shows that the positional and horizontal

RMSEs are dominant regarding their relevancy to the RT-PPP EWS, as the EWS is planned to categorize observations derived from the RT-PPP procedure based on their difference concerning observations acquired at the established station marker location. It is fundamentally reasonable that the machine learning model would exploit the essential benefits offered by the horizontal and positional RMSE values.

However, the research shows that the most relevant features are the positional and horizontal RMSE, displacement components, tropospheric error, and latency values. It is worth noting that the relevancy of the other features was attenuating due to the nature of RT-PPP observations. The number of observations with high HDOP values is much less than those with small HDOP (in terms of manipulating the satellite elevation angle). This conclusion is also valid with respect to latency and the number of tracked satellites. It is also worth noting that the diversity of latency value was inadequate to raise the latency relevancy due to the utilization of two correction streams with latency values near 15 to 30 seconds. Similarly, the variety of mask elevation angles utilized led to the same results.

The research experiments have been carried out regarding three types of deformations (horizontal, vertical, and three-dimensional). Accordingly, the research designed and developed an engine that is able to exert simulated deformations in the desired directions and chosen magnitude. These deformations were exerted utilizing two stepper motors and a vertical roller. The deformations were controlled by implementing a g-code to the engine microcontroller, which allowed the research to store RT-PPP measurements during deformation/no deformation periods.

The RT-PPP EWS performance was initially assessed by the creation of the confusion matrix, which indicates the ability of the ML models to correctly classify the RT-PPP events with respect to motion/non-motion/out-of-service. Then, the research extends the RT-PPP EWS assessment with respect to various types of probabilities. Consequently, several types of probabilities have been calculated, including the probability of initiating true and false non-motion detections, the probability of initiating true and false motion detections, and similar probabilities with respect to the out-of-services. In addition, the RT-PPP EWS performance was evaluated with overall accuracy. However, which of the probabilities above is crucial to the RT-PPP EWS? or is the

overall accuracy sufficient to determine which of the utilized ML models is the most appropriate for RT-PPP EWS establishment?

Accordingly, the answers to these realistic questions can be illustrated with respect to the importance of the RT-PPP events. The RT-PPP measurements observed during the deformation periods are much more relevant to the EWS and stakeholders. Subsequently, the probability of initiating true motion detections is the most relevant indicator of the ML model's superiority. Nevertheless, the overall ML model's accuracy could be a general indicator of the RT-PPP EWS performance.

It is also worth highlighting that in establishing the generic EWS, the station coordinates have been eliminated to utilize the model without the limitations of the research reference station coordinates. Finally, the research recommends the use of high-rate GNSS receivers to have the advantages of reducing RT-PPP converging time and enriching the RT-PPP measurements in terms of the observation amount and, at the same time, using advanced techniques to solve the ambiguities. High-rated ultra-rapid products are also valuable for contrasting events detected in EWS as a control mechanism after events.

8.2 Research main findings

In this investigation, real-time data was examined, and clock corrections were predicted using RSW. Both models can then be utilized to deal with latency. In contrast to the real-time, which involves the latency impact, SVR and ARIMA models for the GPS satellite's clock corrections show a 28% decrease in standard deviation. Additionally, regarding GLONASS satellites, the ARIMA and SVR models decreased in standard deviation by 13% and 23%, respectively. A brief summary regarding the standard deviation improvements: The SVR model significantly enhanced various GPS satellite blocks over the study period. Notably, it displayed remarkable improvements of approximately 19 percent for GPS-IIF, 46 percent for GPS-IIR, and about 57 percent for GPS-IIRM between 2015, 2019, and 2021. However, in 2013, the SVR model increased latency by roughly 4.80 meters for GPS-IIF. Its weakest performance was in 2014 and 2015, especially for GLONASS K and M satellites, where range evaluation degraded by 31 percent and 23 percent,

respectively. Conversely, the SVR model notably improved range performance by around 23, 25, and 57 percent for the GPS-IIRM block in 2014, 2019, and 2021, respectively.

However, there has been a little increase in the SVR and ARIMA range discrepancies for GLONASS satellites, by about 2% and 16%, respectively. However, the SVR model predicts a 7 percent increase in range discrepancies for GPS.

In the context of research outcomes concerning 3D positioning, in contrast to real-time situations that include latency effects, the findings indicate a noteworthy enhancement in 3D positioning accuracy. Over the research period, the selected permanent GNSS stations revealed an average reduction in standard deviations of 13% for the ARIMA algorithm and 31% for the SVR algorithm. The mean value shows similar performance, with 17% for ARIMA and 13% for SVR. On the other hand, the range analysis showed improvement with 3% for ARIMA and 11 % for the SVR model.

The latency impact is mitigated with both models. The calculation results reveal that the SVR model is eight to nine times faster at processing data than ARIMA, suggesting that it may be a good alternative for overcoming the latency because of its ease of use and computational speed. If the GNSS receiver tracks signals from both the GPS and GLONASS constellations, it will need clock correction forecasts for about 55 satellites. The proposed prediction models can also predict clock corrections during data loss or discontinuity. Eventually, the research recommends utilizing the SVR model to overcome the latency due to the simplicity of implementation and execution speed; also, it showed more improvement relative to the ARIMA model. It is worth noting that the old format IGS03 streams did not include clock corrections with respect to Galileo and BeiDou; thus, the latency analysis was conducted concerning the GPS and GLONASS navigation systems, but the research approach might be extended to Galileo and BeiDou.

Regarding the RT-PPP EWS performance with respect to vertical deformations, Table 7.9 shows the superiority of the XGB model, with a probability of 99.89% to detect vertical deformation events and 99.80% overall accuracy. On the contrary, the worst performances were shown with decision tree and logistic regression, with the accuracy reaching 95% and 92%, respectively.

Regarding the RT-PPP EWS performance with respect to horizontal deformations, Table 7.10 shows a similar ascendancy of XGB with a probability of 99.50% to detect horizontal deformation events with respect to all deformation populations and 98% overall accuracy. On the contrary, the least optimal performances were shown with decision tree and logistic regression, with the accuracy reaching 90% and 84%, respectively. Regarding the RT-PPP EWS performance with respect to the three-dimensional, Table 7.11 shows a similar ascendancy of XGB with a probability of 99.99% to detect three-dimensional deformation events, with 99.91% overall accuracy. On the contrary, the least optimal performance was shown with the decision tree, with the accuracy reaching 97%. Eventually, the research evaluates the RT-PPP EWS concerning all kinds of deformations (Generic model). The research utilized all the research events and re-generated the establishment of the generic RT-PPP EWS, which can be a valuable tool for monitoring all deformations types. Accordingly, the evaluation of a generic RT-PPP EWS performance has been carried out. Table 7.13 shows the superiority of the support vector machine and XGB, with a probability of 97.29% and 98.85 to detect generic deformation events.

On the contrary, the least optimal performances were shown with decision tree and logistic regression, with the accuracy reaching 89% and 83%, respectively. It is also worth noting that the logistic regression indicated the highest false warning, reaching around 43%. It is essential to emphasize that the XGB model showed superior performance among other ML approaches; the model uses a gradient boosting approach, allowing it to combine the prediction from several decision trees. In addition, the XGB showed more capabilities for handling missing data and more speed execution.

The research verified the earlier evaluation of the RT-PPP Early Warning Systems (EWSs) on the test data; the research re-evaluated the XGBoost machine learning model performance during this stage. The research database was ranked hierarchically into four categories based on displacement levels: Equal to or less than 5 centimeters, 5-10 centimeters, 10-15 centimeters, and 15-20 centimeters. Accordingly, this allowed the research to more precisely assess the pre-mention machine learning model across different displacement magnitudes. Consequently, the following table presents the resulting model performance with respect to the achieved accuracy.

Table 8.1 RT-PPP EWS XGBoost performance with respect to several levels of displacements.

	level of displacements			
Classifier performance	1-5 cm	5-10 cm	10-15 cm	15-20 cm
XGB	86%	88%	89%	89%

While the XGBoost model performs well when trained on the total displacement dataset, its accuracy weakens when applied to data containing only minor displacements. This decrease is attributed to the inherent characteristics of RT-PPP measurements, which tend to exhibit more significant uncertainty at more minor displacement levels. This finding highlights the importance of considering the nature of the data when selecting and tuning machine learning models for Early Warning Systems (EWSs). Despite this challenge, the overall outcome demonstrates the potential of ML models to enhance EWSs' performance significantly.

8.3 Research novelty and main contributions

In the context of the research contributions and advancing knowledge, this study highlights the significance of latency's influence on RT-PPP performance, particularly concerning precision and accuracy. Our investigation explores the application of machine-learning models for predicting clock corrections in the context of IGS combination products. It is imperative to note that several Analysis Centers (ACs) offer distinct correction streams, but IGS products are regarded as the official standard, underlining their inherent reliability. The proposed machine-learning models exhibit substantial enhancements in the precision and availability of RT-PPP coordinates.

This study provides a detailed investigation into establishing the early warning system utilizing the RT-PPP technique; this technique has gained importance since the 1990s for GNSS positioning due to the cost-effectiveness of the RT-PPP technique is highlighted, as it eliminates the need for reference station data, distinguishing it from the traditional relative positioning approach. To achieve the highest accuracy level, RT-PPP requires employing pseudo-range and carrier phase observations on multiple frequencies, along with precise orbit and satellite clock correction products, accurate error modeling, and advanced analysis software. It is essential to note that RTT-PPP is highly sensitive to several error sources impacting early warning performance. Accordingly, the research offers the ability to utilize the ML models incorporated with the RT-PPP approach. One of the leading research contributions is to provide EWS users with several probability metrics.

Notably, these metrics are crucial for users in providing reliable information regarding deformation events or RT-PPP observations status.

Regarding the research applicability, the research utilizes several free, open-source software and machine-learning libraries. One of the essential aspects is that the developed research models can be integrated with web platforms or mobile devices for early warning dissemination. The RT-PPP EWS offers an affordable solution, particularly in economically challenged regions like developing countries. The cost of establishing traditional EWS systems could be excessively high in these areas, making the RT-PPP EWS a more viable option.

In the context of its societal impact, this thesis offers valuable insights that can benefit local communities, stakeholders, and the public sector. The development of an RT-PPP EWS carries the potential to significantly enhance emergency preparedness for a wide range of geo-natural hazards.

The findings derived from this research hold the promise of equipping emergency planners and managers with enhanced capabilities and a deeper understanding. The findings also contribute to better planning and executing emergency response strategies based on reliable real-time scenarios and well-informed assessments of expected damage. In this way, the knowledge generated by this thesis has the power to make a meaningful impact in the field of emergency management and response.

From an economic perspective, the insights gleaned from this thesis offer opportunities for businesses, the general public, and the private sector. They can leverage this knowledge to develop and implement strategies ensuring business continuity within an EWS. Moreover, there is potential for utilizing RT-PPP EWS in various engineering applications.

One of the strengths of RT-PPP EWS is its ability to provide advanced warnings about expected deformations at specific locations. This advanced notice empowers the formulation of preemptive plans, including decision models for effective responses to these warnings. The main objective is to reduce the impact of economic and life losses due to geo-natural hazards.

8.4 Future works

As with any investigation, some of the following issues could be considered as future works. Similar investigations could be established with simulations of the semi-real seismic waves, which results in real-surface deformations that could be implemented with a device such as a shaking table; this table was attached with actuators that could be utilized to exert natural seismic waves in terms of magnitude and direction. Regarding landslide, the simulation could be done with some lab for the instant coastal lab at Queen's University. Unfortunately, these capabilities are considered indoor applications. However, utilizing such a tool outdoors will aid the endeavours of testing the RT-PPP EWS with semi-natural trigger events (Prasad et al., 2004; Scaioni et al., 2013). Similar investigations could be established utilizing near-RT products to improve PPP measurement quality, which could be a solution for some geo-hazards disasters or slow-motion landslide detections. Additionally, it is worth mentioning that the possibility of establishing web and mobile applications relies on the research RT-PPP EWS. As the research considers the importance of features, it is possible to implement the RT-PPP EWS with the most relevant features, reducing system complexity and improving performance in terms of time response.

The researchers intend to extend the research investigations to cover deep learning methods such as Convolutional Neural Networks (CNNs), Recurrent Neural Networks (RNNs), Long Short-Term Memory (LSTM), and Gated Recurrent Units (GRUs).

8.5 Challenges

Several challenges during the research impeded the study, including internet and electricity interruptions. That led to re-implementing some experiments to ensure 24 or 12 hours of consistency among all the study experiments. In addition, some challenges impact the research development, including designing and developing the research engine used to simulate the deformations, implementing ML algorithms, and setting up the software and hardware to apply RT-PPP SSR products while performing the experiments. Also, another limitation overcome was ensuring the continuity of measurements and products during the research years.

Thesis Appendices

Appendix.A Ph.D. activities

Peer-reviewed journal and conference publications

1. Qafisheh, M. and Martín, A., (2020). Support Vector Regression Machine Learning Tool to Predict GNSS Clock Corrections in Real-Time PPP Technique. 10th International Conference on Localization and GNSS. Editorial Tampere University. http://localhost:8080/xmlui/handle/123456789/8516
2. Qafisheh, M., Martin, A. and Capilla, R., (2021), October. Proposed methodology for establishing an early GNSS warning system for real-time deformation monitoring. In Proceedings 3rd Congress in Geomatics Engineering (pp. 54-60). Editorial Universitat Politècnica de València. https://doi.org/10.4995/CiGeo2021.2021.12691
3. Qafisheh, M., Martín, A., Capilla, R. and Anquela, A.B., (2022). SVR and ARIMA models as machine learning solutions for solving the latency problem in real-time clock corrections. GPS Solutions, 26(3), p.85. https://doi.org/10.1007/s10291-022-01270-y

Oral presentations

1. Qafisheh, M. (2018), Water harvesting estimation using GIS in Bani Na'im area, GeoMundus Conference. University of Lisbon. https://geomundus.org/2018/docs/papers/Mutaz.pdf
2. Qafisheh, M., (2022), Establishing an early GNSS warning system using the random forest classifier, (D4G) first workshop on data science for GNSS remote sensing, Potsdam, Germany.https://www.d4g2022.de/assets/wajeh_qafisheh_mutaz_establishing_an_early_gnss.pdf.
3. Qafisheh, M. (2022), GNSS applications in deformation monitoring, scientific lecture. Palestine Polytechnic University.

Conference attendance and other activities

1. 15th gvSIG international conference (2019), 15th gvSIG international conference.
2. Second GATHER summer school, (2023), Delft, Netherlands, Integration of geodetic and imaging techniques for monitoring and modelling the Earth's surface deformations and seismic risk.

Appendix.B

Exploring Research Latency Results: A Compilation of Statistical Summaries

Table B.1 Statistical Summary of Forced-latency and ARIMA Solutions Based on 2021 Researched year (GPS Constellation).

Satellite number	Forced-latency solution			ARIMA solution		
	Range	Mean	Standard deviation	Range	Mean	Standard deviation
G01	0.2425923	0.0001085	0.006025058	0.1933353	8.61035E-05	0.005220321
G02	0.4100198	0.0001009	0.015970713	0.3994735	-0.000201412	0.008694859
G03	0.09445	-2.022E-05	0.00540538	0.2339769	0.000121918	0.00701327
G04	0.17607963	2.019E-05	0.006183142	0.2905434	3.61475E-05	0.007281985
G05	0.19275459	5.749E-05	0.022245371	0.4838452	1.2976E-05	0.007301457
G06	0.15739267	-2.57E-05	0.006024339	0.2569607	7.74965E-05	0.006884063
G07	0.65684864	-7.133E-05	0.018552802	0.5858155	-0.00016912	0.010580175
G08	0.20251691	-0.0006252	0.020996161	0.3458242	0.000110921	0.007840875
G09	0.3622961	3.175E-05	0.00813996	0.4105502	0.00052743	0.008516305
G10	0.13284787	-1.535E-05	0.004971752	0.5475101	-0.00011141	0.010324648
G12	0.21280906	3.859E-05	0.018061513	0.4680894	-0.000151317	0.009766211
G13	0.72899581	0.0001882	0.017803951	0.4269649	-9.29131E-05	0.007468114
G14	0.13625	-3.541E-06	0.004742415	0.2756723	-0.000121419	0.006264828
G15	0.188194	-2.752E-05	0.014743998	0.1471	-3.62254E-05	0.005080799
G16	0.3744491	-6.828E-05	0.018838709	0.5848918	8.53975E-05	0.010915265
G17	0.25022318	-3.174E-05	0.018762047	0.2862666	1.86833E-05	0.007254048
G18	0.1462	8.388E-06	0.005562395	0.2021954	-0.000104105	0.005785721
G19	0.13775	9.543E-06	0.015981269	0.3023924	-0.000161902	0.007122303
G20	0.2582425	3.355E-05	0.017494553	0.1832663	-0.000293467	0.005463953
G21	0.22114739	-6.67E-05	0.021738338	0.5040556	-0.00019042	0.009861672
G22	0.1719	-9.548E-05	0.015932264	0.4521063	0.000126736	0.008093199
G23	0.11095	4.245E-05	0.005035763	0.1970714	-0.000116728	0.005824991
G24	0.33847462	7.973E-05	0.006848151	0.5590929	-8.13942E-05	0.009069015

G25	0.15724768	-2.004E-05	0.005035397	0.4023711	8.31682E-05	0.006380366
G26	0.1500461	3.186E-05	0.005053892	0.3096443	-0.000112667	0.006029149
G27	0.101	1.815E-05	0.004104178	0.1826063	1.86827E-06	0.003983396
G29	0.24109753	-0.0001972	0.016329154	0.9906768	0.000163269	0.015765915
G30	0.18514675	5.218E-05	0.004488925	0.323118	0.000150001	0.005471266
G31	0.1481	0.000102	0.01482195	0.2098758	-5.57402E-05	0.01185754
G32	0.10055	9.002E-05	0.004994087	0.2318894	0.000196865	0.005589092

Table B.2 Statistical Summary of Forced-latency and ARIMA Solutions Based on 2021 Researched year (GLONASS Constellation).

Satellite number	**Forced-latency solution**			**ARIMA solution**		
	Range	Mean	Standard deviation	Range	Mean	Standard deviation
R01	1.4392	0.0002838	0.047574884	1.4175	-0.004842391	0.035080188
R02	3.2973	-0.0009229	0.071685933	3.2288755	-0.00269785	0.059512514
R03	0.8228	0.0003674	0.036036223	0.8343558	-0.002466368	0.026219265
R04	1.1752	-0.0001283	0.033143438	1.1728561	-0.001349691	0.026802764
R05	1.4248	-1.125E-05	0.035847068	1.3881723	0.000756801	0.025219866
R07	1.1576	0.0003233	0.041658492	1.1109375	0.00023347	0.03079878
R08	0.7756	-0.0003261	0.042652049	0.7355641	0.000797114	0.031308183
R09	0.786	0.0003299	0.031885044	2.7678	0.001041749	0.039696828
R12	1.4206	0.0003253	0.036951329	1.394448	0.000357314	0.03021514
R13	3.898	-0.000703	0.105613817	3.595	0.004146622	0.085031677
R14	1.2947	-2.402E-05	0.041359313	1.2575154	-0.003406227	0.030776507
R15	1.6237	6.543E-05	0.039728959	1.6091939	0.001001395	0.034638461
R16	2.0589	0.0001197	0.055291663	2.1001518	0.002976131	0.047843114
R17	0.8899	-0.0003097	0.04392278	0.8689604	-0.00487816	0.034685305
R18	1.6455	-0.0006105	0.055901801	1.6586715	-0.005105813	0.046390402
R19	6.6985	0.0010137	0.108546939	6.6629873	0.004358728	0.073193483
R20	1.3645	-0.0001963	0.044137188	1.3706107	0.003675574	0.0341831
R21	1.615	-2.588E-05	0.036284456	1.5879	0.001359578	0.030843932
R22	3.9854	0.0004891	0.083309277	3.9603	0.005712884	0.074576359
R24	1.1687	-0.0005145	0.039127911	1.2102882	0.000999694	0.029974769

Table B.3 Statistical Summary of Forced-latency and ARIMA Solutions Based on 2021 Researched year (Galileo Constellation).

Satellite number	Forced-latency solution			ARIMA solution		
	Range	Mean	Standard deviation	Range	Mean	Standard deviation
E01	0.3133	2.188E-06	0.007632889	0.1933353	8.61035E-05	0.005220321
E02	0.399	-5.438E-05	0.009973179	0.3994735	-0.000201412	0.008694859
E03	0.2358	-4.61E-05	0.008192608	0.2339769	0.000121918	0.00701327
E04	0.2957	5.657E-05	0.008216199	0.2905434	3.61475E-05	0.007281985
E05	0.2308	2.847E-05	0.006822393	0.4838452	1.2976E-05	0.007301457
E07	0.2544	-3.342E-05	0.008137304	0.2569607	7.74965E-05	0.006884063
E08	0.6042	8.606E-06	0.011625118	0.5858155	-0.00016912	0.010580175
E09	0.3173	-1.97E-05	0.008916212	0.3458242	0.000110921	0.007840875
E11	0.3904	0.0001007	0.010448456	0.4105502	0.00052743	0.008516305
E12	0.4667	-8.479E-05	0.010780535	0.5475101	-0.00011141	0.010324648
E13	0.4812	-6.975E-05	0.011035642	0.4680894	-0.000151317	0.009766211
E15	0.3628	-3.403E-06	0.008440842	0.4269649	-9.29131E-05	0.007468114
E19	0.2778	-1.222E-06	0.007306295	0.2756723	-0.000121419	0.006264828
E21	0.1368	4.36E-05	0.00616824	0.1471	-3.62254E-05	0.005080799
E24	0.3582	-0.000123	0.008041623	0.5848918	8.53975E-05	0.010915265
E25	0.2783	-0.0001372	0.008220023	0.2862666	1.86833E-05	0.007254048
E26	0.2112	8.935E-05	0.007090481	0.2021954	-0.000104105	0.005785721
E27	0.214	6.997E-05	0.007177271	0.3023924	-0.000161902	0.007122303
E30	0.1821	-0.0001093	0.007239238	0.1832663	-0.000293467	0.005463953
E31	0.5031	-8.965E-05	0.010371891	0.5040556	-0.00019042	0.009861672
E33	0.4541	0.0001654	0.009449467	0.4521063	0.000126736	0.008093199

Table B.4 Statistical Summary of Forced-latency and ARIMA Solutions Based on 2021 Researched year (BeiDou Constellation).

Satellite number	Forced-latency solution			ARIMA solution		
	Range	Mean	Standard deviation	Range	Mean	Standard deviation
C06	3.3134	9.186E-05	0.073928112	5.1122344	-0.001141059	0.080141373
C07	2.4017	0.000178	0.068217969	4.4549619	-0.000542798	0.065415696
C08	2.9437	0.0003028	0.065687497	2.9491	0.000248765	0.055580478
C09	2.9738	9.121E-05	0.075067673	2.9498635	0.00045637	0.062155475
C12	2.9449	-0.000387	0.080760591	3.5149685	-0.000194871	0.071148331
C13	2.9544	-0.0001571	0.080355769	3.4953962	-0.001478882	0.069792621
C16	2.389	-0.0002788	0.055188191	2.3877918	-0.000436515	0.045661109

Table B.5 Statistical Summary of Forced-Latency and SVR Solutions Based on 2021 Researched year (GPS Constellation).

Satellite number	Forced-latency solution			SVR solution		
	Range	Mean	Standard deviation	Range	Mean	Standard deviation
G01	0.2425923	0.0001085	0.006025058	0.2425923	0.000108474	0.006025058
G02	0.4100198	0.0001009	0.015970713	0.4100198	0.000100939	0.015970713
G03	0.09445	-2.022E-05	0.00540538	0.09445	-2.02228E-05	0.00540538
G04	0.17607963	2.019E-05	0.006183142	0.1760796	2.01895E-05	0.006183142
G05	0.19275459	5.749E-05	0.022245371	0.1927546	5.74945E-05	0.022245371
G06	0.15739267	-2.57E-05	0.006024339	0.1573927	-2.56987E-05	0.006024339
G07	0.65684864	-7.133E-05	0.018552802	0.6568486	-7.13307E-05	0.018552802
G08	0.20251691	-0.0006252	0.020996161	0.2025169	-0.000625247	0.020996161
G09	0.3622961	3.175E-05	0.00813996	0.3622961	3.1746E-05	0.00813996
G10	0.13284787	-1.535E-05	0.004971752	0.1328479	-1.53455E-05	0.004971752
G12	0.21280906	3.859E-05	0.018061513	0.2128091	3.85881E-05	0.018061513
G13	0.72899581	0.0001882	0.017803951	0.7289958	0.000188201	0.017803951
G14	0.13625	-3.541E-06	0.004742415	0.13625	-3.54147E-06	0.004742415
G15	0.188194	-2.752E-05	0.014743998	0.188194	-2.75157E-05	0.014743998
G16	0.3744491	-6.828E-05	0.018838709	0.3744491	-6.82827E-05	0.018838709
G17	0.25022318	-3.174E-05	0.018762047	0.2502232	-3.17416E-05	0.018762047
G18	0.1462	8.388E-06	0.005562395	0.1462	8.3877E-06	0.005562395
G19	0.13775	9.543E-06	0.015981269	0.13775	9.54287E-06	0.015981269
G20	0.2582425	3.355E-05	0.017494553	0.2582425	3.35547E-05	0.017494553
G21	0.22114739	-6.67E-05	0.021738338	0.2211474	-6.67013E-05	0.021738338
G22	0.1719	-9.548E-05	0.015932264	0.1719	-9.54809E-05	0.015932264
G23	0.11095	4.245E-05	0.005035763	0.11095	4.24511E-05	0.005035763
G24	0.33847462	7.973E-05	0.006848151	0.3384746	7.97265E-05	0.006848151
G25	0.15724768	-2.004E-05	0.005035397	0.1572477	-2.00431E-05	0.005035397
G26	0.1500461	3.186E-05	0.005053892	0.1500461	3.18617E-05	0.005053892
G27	0.101	1.815E-05	0.004104178	0.101	1.81497E-05	0.004104178
G29	0.24109753	-0.0001972	0.016329154	0.2410975	-0.000197232	0.016329154
G30	0.18514675	5.218E-05	0.004488925	0.1851467	5.21762E-05	0.004488925
G31	0.1481	0.000102	0.01482195	0.1481	0.000102036	0.01482195
G32	0.10055	9.002E-05	0.004994087	0.10055	9.00232E-05	0.004994087

Table B.6 Statistical Summary of Forced-Latency and SVR Solutions Based on 2021 Researched year (GLONASS Constellation).

Satellite number	Forced-latency solution			SVR solution		
	Range	Mean	Standard deviation	Range	Mean	Standard deviation
R01	1.4392	0.0002838	0.047574884	2.9074784	-0.001881633	0.043266353
R02	3.2973	-0.0009229	0.071685933	3.7364723	-0.000633557	0.063742643
R03	0.8228	0.0003674	0.036036223	0.6392295	-0.000512703	0.023600946
R04	1.1752	-0.0001283	0.033143438	2.2490016	-0.000151485	0.028055707
R05	1.4248	-1.125E-05	0.035847068	1.0696649	-1.67975E-05	0.023853336
R07	1.1576	0.0003233	0.041658492	2.8156381	-0.000263303	0.037424024
R08	0.7756	-0.0003261	0.042652049	0.4578783	0.000246109	0.028542634
R09	0.786	0.0003299	0.031885044	1.2361645	-0.000205609	0.027465517
R12	1.4206	0.0003253	0.036951329	1.1187802	-1.92381E-05	0.024609642
R13	3.898	-0.000703	0.105613817	3.7786614	0.00326581	0.083542946
R14	1.2947	-2.402E-05	0.041359313	1.9954199	-0.00041795	0.030829997
R15	1.6237	6.543E-05	0.039728959	2.1968304	0.001083651	0.028893278
R16	2.0589	0.0001197	0.055291663	2.5023811	-0.000405545	0.047261796
R17	0.8899	-0.0003097	0.04392278	2.3935327	-0.000780305	0.048591034
R18	1.6455	-0.0006105	0.055901801	1.8024029	-0.000658884	0.041210568
R19	6.6985	0.0010137	0.108546939	6.069628	0.002999953	0.071895664
R20	1.3645	-0.0001963	0.044137188	1.7125967	0.000233569	0.033612587
R21	1.615	-2.588E-05	0.036284456	1.3485566	4.95617E-05	0.026414347
R22	3.9854	0.0004891	0.083309277	5.5091662	0.001166272	0.055454863
R24	1.1687	-0.0005145	0.039127911	1.7510082	0.000359553	0.028574822

Table B.7 Statistical Summary of Forced-latency and SVR Solutions Based on 2021 Researched year (Galileo Constellation).

Satellite number	Forced-latency solution			SVR solution		
	Range	Mean	Standard deviation	Range	Mean	Standard deviation
E01	0.3133	2.188E-06	0.007632889	0.1677384	-2.2761E-05	0.005041362
E02	0.399	-5.438E-05	0.009973179	0.2108216	5.35989E-05	0.006452128
E03	0.2358	-4.61E-05	0.008192608	0.11845	3.82295E-05	0.005421445
E04	0.2957	5.657E-05	0.008216199	0.1573776	-3.39613E-05	0.005460063
E05	0.2308	2.847E-05	0.006822393	0.1561	5.80756E-05	0.004902011
E07	0.2544	-3.342E-05	0.008137304	0.1291	8.3188E-06	0.005377497
E08	0.6042	8.606E-06	0.011625118	0.2978977	3.49324E-05	0.007372286
E09	0.3173	-1.97E-05	0.008916212	0.1593499	1.24361E-05	0.005873336
E11	0.3904	0.0001007	0.010448456	0.2482925	-8.41862E-05	0.007201245
E12	0.4667	-8.479E-05	0.010780535	0.2790663	7.14513E-05	0.007102758
E13	0.4812	-6.975E-05	0.011035642	0.2375392	-8.82961E-06	0.007066179
E15	0.3628	-3.403E-06	0.008440842	0.1810533	1.15766E-05	0.005374827
E19	0.2778	-1.222E-06	0.007306295	0.1405	3.96453E-05	0.004875579
E21	0.1368	4.36E-05	0.00616824	0.07865	-4.21631E-05	0.004157578
E24	0.3582	-0.000123	0.008041623	0.3347953	3.63686E-06	0.007637891
E25	0.2783	-0.0001372	0.008220023	0.1489	8.43321E-05	0.005559676
E26	0.2112	8.935E-05	0.007090481	0.1107	-7.88363E-05	0.004740231
E27	0.214	6.997E-05	0.007177271	0.12375	-3.54981E-05	0.005184267
E30	0.1821	-0.0001093	0.007239238	0.09325	7.67774E-05	0.00474897
E31	0.5031	-8.965E-05	0.010371891	0.2405158	6.14339E-05	0.006813748
E33	0.4541	0.0001654	0.009449467	0.2725491	-0.000136056	0.006188497

Table B.8 Statistical Summary of Forced-Latency and SVR Solutions Based on 2021 Researched year (BeiDou Constellation).

Satellite number	Forced-latency solution			SVR solution		
	Range	Mean	Standard deviation	Range	Mean	Standard deviation
C06	3.3134	9.186E-05	0.073928112	3.3910286	-0.000143862	0.053622448
C07	2.4017	0.000178	0.068217969	3.5790423	0.000358543	0.064240714
C08	2.9437	0.0003028	0.065687497	3.4567693	-8.76279E-05	0.049835087
C09	2.9738	9.121E-05	0.075067673	2.7485396	-3.10583E-05	0.052523819
C12	2.9449	-0.000387	0.080760591	3.3196028	0.000897774	0.063779326
C13	2.9544	-0.0001571	0.080355769	3.8976156	-0.000530694	0.0660463
C16	2.389	-0.0002788	0.055188191	2.8526919	0.000652523	0.047680245

Table B.9 Statistical Summary of Forced-latency and ARIMA Solutions Based on 2019 Researched year (GPS Constellation).

Satellite number	Forced-latency solution			ARIMA solution		
	Range	Mean	Standard deviation	Range	Mean	Standard deviation
G01	0.439	-3.613E-05	0.011379166	0.4339853	-4.41702E-05	0.008128426
G02	0.6868	4.765E-05	0.025602174	0.6953653	-3.01627E-05	0.019208612
G03	0.4646	-6.798E-06	0.009647712	0.6188958	-3.72539E-05	0.008531705
G05	0.4297	0.0001105	0.036282182	0.4413021	-0.000366665	0.025746457
G06	2.6457	-0.0001671	0.038067975	2.4126195	-0.000553593	0.034647734
G07	0.466	0.0001324	0.026535446	0.4129953	-1.10131E-05	0.018498725
G08	3.2704	0.0001911	0.054260502	3.0090318	-0.000689485	0.046273303
G09	0.3946	5.072E-05	0.009933569	0.3871044	0.000141138	0.007593508
G10	0.2529	0.0001554	0.007726498	0.4581284	0.00015495	0.006723995
G11	0.41	0.0001501	0.026122454	0.3854307	-1.65461E-05	0.018124347
G12	0.499	6.621E-05	0.029919431	0.4859991	-0.000123251	0.021316726
G13	0.792	3.678E-05	0.023977226	0.9420543	6.44603E-05	0.017916058
G14	0.3403	0.0001124	0.02444168	0.3998357	-2.75838E-05	0.017052249
G15	0.9867	-8.8E-05	0.027099498	0.9944	-0.000117125	0.019116297
G16	0.5838	0.0002217	0.02844636	0.4629398	0.000581176	0.019791897
G17	1.8075	-0.000377	0.041137835	1.9738359	-0.000525577	0.033684771
G19	0.6637	0.0001123	0.026641516	0.6115783	-0.000175151	0.019020625
G20	0.5264	-6.058E-05	0.028871535	0.5259922	-0.000394131	0.020249099
G21	2.0832	-0.0001487	0.041166446	1.5970488	-0.000131469	0.030887137
G22	0.558	0.0001397	0.027393055	0.454868	0.000153579	0.019316472
G23	0.3479	0.0001953	0.023208843	0.3205696	9.45669E-05	0.015974863
G24	2.9563	2.747E-05	0.061249378	2.5095958	-0.001213923	0.045516449
G25	0.4358	-6.613E-06	0.010194386	0.1564608	3.58953E-05	0.005450238
G26	0.2492	0.0001346	0.008776027	0.232524	0.000205348	0.006065158
G27	0.2867	-3.086E-05	0.009109123	0.2707084	7.80461E-05	0.006868964
G28	2.1737	-7.109E-05	0.041901382	1.6810645	-0.00034719	0.027516877
G29	1.2161	-0.0003836	0.032993237	1.0296181	-9.85506E-05	0.022637389
G30	1.0351	-0.0001859	0.017255397	1.0922814	-0.000311344	0.017043753
G31	0.3414	-0.0001684	0.025143984	0.4167161	-0.000242301	0.017357018
G32	1.7505	-2.9E-05	0.020453667	1.1495947	-9.90823E-05	0.01767286

Table B.10 Statistical Summary of Forced-latency and ARIMA Solutions Based on 2019 Researched year (GLONASS Constellation).

Satellite number	Forced-latency solution			ARIMA solution		
	Range	Mean	Standard deviation	Range	Mean	Standard deviation
R01	1.2667	-0.0005381	0.044852227	3.1984203	-0.004149562	0.045009518
R02	2.3813	0.0005844	0.055542537	3.6873187	-0.001648612	0.053784796
R03	1.5971	6.946E-05	0.037646967	1.4047545	-0.002178903	0.030561641
R05	4.0259	3.052E-05	0.06280272	4.2670917	0.000144468	0.061074027
R07	0.89	0.0003981	0.037082986	1.3249966	0.002276881	0.030244021
R08	9.7221	-0.0014347	0.142262745	9.0260758	0.000296778	0.129630568
R09	0.8984	0.0005545	0.03063252	1.0475332	0.000267929	0.023797831
R11	17.3634	0.0004016	0.140465907	9.2257275	0.003806498	0.100330646
R12	1.1264	-0.000355	0.026631272	2.0801127	0.000524211	0.025061159
R13	1.9816	0.0009964	0.058822388	1.9040982	0.001508324	0.046231817
R14	4.3266	1.7E-05	0.055995512	4.3348	-0.002431407	0.053483545
R15	0.7268	0.0002005	0.025144312	0.8516591	-3.71552E-05	0.020583409
R16	1.54	-0.0015181	0.04266338	1.5176261	-0.000362108	0.037823468
R17	2.0802	-0.0001873	0.056832367	1.8941	-0.004174457	0.051473707
R18	1.4975	0.0004078	0.040167887	3.5882264	-0.00162776	0.047140766
R19	0.8576	0.0003168	0.033601727	1.1633837	0.001405383	0.024407277
R20	0.8354	-5.977E-05	0.039811917	0.9215725	0.002310314	0.032003372
R21	1.3452	-0.0004507	0.030431118	1.2508864	-0.000466248	0.025072136
R22	1.859	0.0003872	0.046212477	1.5991456	0.002692214	0.035672043
R23	1.2843	0.0001936	0.049984009	2.0200884	-0.003315627	0.045597329

Table B.11 Statistical Summary of Forced-latency and SVR Solutions Based on 2019 Researched year (GPS Constellation).

Satellite number	Forced-latency solution			SVR solution		
	Range	Mean	Standard deviation	Range	Mean	Standard deviation
G01	0.439	-3.613E-05	0.011379166	0.2401662	5.75456E-06	0.007155902
G02	0.6868	4.765E-05	0.025602174	0.4490141	5.6799E-06	0.016725165
G03	0.4646	-6.798E-06	0.009647712	0.2595149	-1.62033E-05	0.006640761
G05	0.4297	0.0001105	0.036282182	0.2551995	-7.87978E-05	0.023564363
G06	2.6457	-0.0001671	0.038067975	1.8422589	4.22479E-05	0.023598273
G07	0.466	0.0001324	0.026535446	0.2546985	-0.000219135	0.017494474
G08	3.2704	0.0001911	0.054260502	3.4005719	-0.000425012	0.036399809
G09	0.3946	5.072E-05	0.009933569	0.2421975	-4.37754E-05	0.006586248
G10	0.2529	0.0001554	0.007726498	0.13185	-0.000108034	0.005108184
G11	0.41	0.0001501	0.026122454	0.230093	-7.99941E-05	0.01747204
G12	0.499	6.621E-05	0.029919431	0.3333164	-1.37256E-05	0.019088182
G13	0.792	3.678E-05	0.023977226	0.476684	-7.33536E-05	0.015698894
G14	0.3403	0.0001124	0.02444168	0.1883986	-0.000135338	0.015960487
G15	0.9867	-8.8E-05	0.027099498	0.7703019	0.000197906	0.018346197
G16	0.5838	0.0002217	0.02844636	0.3066183	-0.000288169	0.018521159
G17	1.8075	-0.000377	0.041137835	1.6431365	0.000378356	0.029781711
G19	0.6637	0.0001123	0.026641516	0.4042983	-0.000147606	0.0173603
G20	0.5264	-6.058E-05	0.028871535	0.2941554	0.000227905	0.018832566
G21	2.0832	-0.0001487	0.041166446	1.2152302	0.000237225	0.026762567
G22	0.558	0.0001397	0.027393055	0.3275938	8.94911E-05	0.017751455
G23	0.3479	0.0001953	0.023208843	0.1761486	-0.000111299	0.015171014
G24	2.9563	2.747E-05	0.061249378	2.6238387	-0.000900496	0.037209757
G25	0.4358	-6.613E-06	0.010194386	0.2642173	-1.18048E-05	0.006815088
G26	0.2492	0.0001346	0.008776027	0.14075	-0.000147555	0.005956392
G27	0.2867	-3.086E-05	0.009109123	0.16835	2.44933E-06	0.006034831
G28	2.1737	-7.109E-05	0.041901382	1.2993118	0.000117287	0.029149388
G29	1.2161	-0.0003836	0.032993237	0.6557619	0.000208123	0.021404457
G30	1.0351	-0.0001859	0.017255397	1.7990917	-0.000452917	0.023479395
G31	0.3414	-0.0001684	0.025143984	0.2013592	0.000260472	0.016435871
G32	1.7505	-2.9E-05	0.020453667	0.9804059	-4.35585E-05	0.012437483

Table B.12 Statistical Summary of Forced-Latency and SVR Solutions Based on 2019 Researched year (GLONASS Constellation).

Satellite number	Forced-latency solution			SVR solution		
	Range	Mean	Standard deviation	Range	Mean	Standard deviation
R01	1.2667	-0.0005381	0.044852227	1.6459399	-1.47015E-05	0.036475206
R02	2.3813	0.0005844	0.055542537	1.6432151	-0.000215276	0.034669574
R03	1.5971	6.946E-05	0.037646967	2.674892	-0.000440744	0.036589049
R05	4.0259	3.052E-05	0.06280272	4.2750901	-0.000575576	0.040383806
R07	0.89	0.0003981	0.037082986	2.7426026	0.000476589	0.034814261
R08	9.7221	-0.0014347	0.142262745	10.168702	-0.000330068	0.089811404
R09	0.8984	0.0005545	0.03063252	0.6059657	-0.000523577	0.020421729
R11	17.3634	0.0004016	0.140465907	17.3529	0.000170097	0.138700751
R12	1.1264	-0.000355	0.026631272	0.7270242	0.000291128	0.01706238
R13	1.9816	0.0009964	0.058822388	2.35595	0.000318291	0.047560052
R14	4.3266	1.7E-05	0.055995512	4.2407982	-0.000493659	0.048550441
R15	0.7268	0.0002005	0.025144312	0.4907162	-0.000115515	0.016011171
R16	1.54	-0.0015181	0.04266338	1.7376004	0.000648761	0.034577753
R17	2.0802	-0.0001873	0.056832367	3.016321	-0.000465259	0.044202434
R18	1.4975	0.0004078	0.040167887	2.9616841	-0.000850659	0.038286375
R19	0.8576	0.0003168	0.033601727	1.3018625	-5.11668E-06	0.02431003
R20	0.8354	-5.977E-05	0.039811917	1.7986419	0.001424976	0.035755842
R21	1.3452	-0.0004507	0.030431118	2.6475604	-0.000199289	0.029528062
R22	1.859	0.0003872	0.046212477	2.0813513	-0.000566557	0.038279138
R23	1.2843	0.0001936	0.049984009	3.9600635	-0.000940583	0.060625801

Table B.13 Statistical Summary of Forced-latency and ARIMA Solutions Based on 2015 Researched year (GPS Constellation).

Satellite number	Forced-latency solution			ARIMA solution		
	Range	Mean	Standard deviation	Range	Mean	Standard deviation
G01	0.333	-5.273E-05	0.00909752	0.3242235	-0.000248144	0.007820062
G02	0.741	0.0002909	0.023296129	0.6939566	-0.000157102	0.014151568
G03	0.655	2.743E-05	0.0132895	0.828527	0.000289129	0.012921966
G04	0.981	6.408E-05	0.022790773	1.1181983	0.000518605	0.020421421
G05	0.317	-0.000114	0.028967581	0.2658293	0.000366258	0.018017528
G06	0.263	0.0002172	0.008778312	0.2722939	-0.000261065	0.006624563
G07	0.744	0.0004564	0.025195851	0.7117699	-2.00183E-06	0.015086769
G09	0.374	-3.047E-05	0.009704824	0.3795465	-0.000142499	0.007344769
G10	2.112	0.0004271	0.044316855	2.1084485	0.001877721	0.037006101
G11	0.898	-4.067E-05	0.02805203	0.8504914	0.000388717	0.017383585
G12	0.382	3.653E-05	0.028015979	0.4723849	-0.000294015	0.016836618
G13	0.941	-0.000111	0.030520925	0.8380023	0.000715787	0.020259934
G14	0.307	-3.299E-05	0.021447792	0.2868796	0.0001323	0.012654547
G15	0.328	-1.301E-06	0.021752809	0.3170153	-0.000304117	0.013030659
G16	0.466	5.521E-05	0.027292193	0.4744565	-2.58369E-05	0.016488228
G17	1.899	-0.0004291	0.04170652	1.9443379	-0.000103104	0.030319983
G18	0.293	6.857E-05	0.025589103	0.2856948	-0.000258349	0.015666896
G19	1.755	-0.0001725	0.055873003	1.776	0.000251468	0.046303807
G20	0.254	3.065E-05	0.023321096	0.207086	1.89975E-07	0.012958596
G21	0.353	7.342E-05	0.030232463	0.3017321	0.000327391	0.0177551
G22	0.748	-0.000128	0.025238698	0.7120039	-3.18399E-06	0.018090246
G23	0.557	-0.000157	0.022495126	0.6303225	0.000246582	0.016092017
G24	1.136	-0.0005361	0.03609758	1.0587767	-0.000465688	0.027043333
G25	0.336	-6.786E-05	0.010054452	0.3280871	0.000242557	0.007287116
G27	0.456	-8.986E-05	0.011311564	0.4597131	0.000363394	0.008312748
G28	1.27	0.0002574	0.034583084	1.2407854	-0.000460882	0.025277609
G29	0.269	0.0001061	0.022763163	0.4451302	-0.000193528	0.013630155
G30	0.278	2.979E-05	0.007920279	0.3726284	-0.000109973	0.006974728
G31	1.612	-0.0001265	0.03495725	1.6139954	-6.24661E-05	0.030165203
G32	0.382	-7.058E-05	0.011021359	0.3853837	-0.000299757	0.007730302

Table B.14 Statistical Summary of Forced-latency and ARIMA Solutions Based on 2015 Researched year (GLONASS Constellation).

Satellite number	Forced-latency solution			ARIMA solution		
	Range	Mean	Standard deviation	Range	Mean	Standard deviation
R01	0.546	3.038E-05	0.036121797	0.6246872	0.001927429	0.026325306
R02	2.316	-0.0008566	0.057919785	2.2845486	0.00453958	0.04922714
R03	1.408	-0.000362	0.048423642	1.381	0.003786403	0.037946382
R04	1.427	-0.0003837	0.055222001	1.3969241	0.005302176	0.042291043
R05	1.172	-5.923E-05	0.049744366	1.1879874	0.005245397	0.039238565
R06	0.849	-0.0001494	0.05369412	0.9650364	0.003747721	0.038902436
R07	0.95	-0.0006319	0.047715148	0.9102557	-0.003027989	0.033886877
R09	0.866	-0.0001759	0.038310681	0.8528298	0.003419693	0.027920203
R10	1.966	-0.0005616	0.056358779	2.0550822	0.003678198	0.045431847
R11	2.174	1.404E-05	0.050832264	2.1834255	0.001571883	0.041746199
R12	3.298	-0.001085	0.072087213	3.3540996	0.004663016	0.065447329
R13	2.935	-7.011E-05	0.072189921	2.8451702	-0.005133886	0.059270295
R14	1.359	-0.0008041	0.05047457	1.454824	0.003638915	0.038881329
R15	8.974	0.0032773	0.182034754	8.8736438	-0.001282992	0.162290778
R16	3.646	-0.0002614	0.060611247	2.1625603	0.002908539	0.04139812
R17	0.889	-0.0003324	0.04184499	0.8640992	0.002676213	0.031796108
R18	1.624	0.0003114	0.04024695	1.6203617	0.002753374	0.029822151
R19	2.267	3.629E-05	0.07224285	2.2440426	-0.008996875	0.057888453
R20	1.777	-0.0006339	0.05324257	1.8073263	-0.005339005	0.041808179
R21	1.006	-0.0002496	0.02980887	0.9765663	-0.00185674	0.019671132
R22	1.352	0.0003452	0.043962833	1.3590036	0.00285239	0.030168146
R23	3.085	0.0011883	0.063498515	3.0357151	-0.002284023	0.057313009
R24	2.797	0.0004878	0.062712622	2.7728655	-0.004225475	0.053038346

Table B.15 Statistical Summary of Forced-Latency and SVR Solutions Based on 2015 Researched year (GPS Constellation).

Satellite number	Forced-latency solution			SVR solution		
	Range	Mean	Standard deviation	Range	Mean	Standard deviation
G01	0.333	-5.273E-05	0.00909752	0.1924487	3.15784E-05	0.006142972
G02	0.741	0.0002909	0.023296129	0.5504991	-0.000226304	0.016644285
G03	0.655	2.743E-05	0.0132895	0.4237199	-3.49833E-05	0.008937737
G04	0.981	6.408E-05	0.022790773	2.3202496	-0.000731374	0.028321218
G05	0.317	-0.000114	0.028967581	0.1819994	4.01844E-05	0.020120922
G06	0.263	0.0002172	0.008778312	0.139491	-0.000184845	0.005976858
G07	0.744	0.0004564	0.025195851	0.5032971	-0.00038952	0.017427882
G09	0.374	-3.047E-05	0.009704824	0.1890757	5.91567E-05	0.006452327
G10	2.112	0.0004271	0.044316855	2.5987751	-0.000751572	0.030282738
G11	0.898	-4.067E-05	0.02805203	0.6310846	3.13898E-05	0.019922459
G12	0.382	3.653E-05	0.028015979	0.2269955	-0.000167331	0.019665018
G13	0.941	-0.000111	0.030520925	0.7594857	0.000174615	0.0215967
G14	0.307	-3.299E-05	0.021447792	0.1714283	-4.86474E-06	0.015047718
G15	0.328	-1.301E-06	0.021752809	0.1665	-5.17669E-05	0.015123994
G16	0.466	5.521E-05	0.027292193	0.2337279	-5.53705E-05	0.018719229
G17	1.899	-0.0004291	0.04170652	2.5795501	-0.000192909	0.038283339
G18	0.293	6.857E-05	0.025589103	0.1744984	-2.15692E-05	0.017984342
G19	1.755	-0.0001725	0.055873003	1.2457424	0.000234564	0.036743127
G20	0.254	3.065E-05	0.023321096	0.171	-2.42994E-05	0.016547734
G21	0.353	7.342E-05	0.030232463	0.1979976	-0.000174968	0.021221389
G22	0.748	-0.000128	0.025238698	1.2036612	0.000131297	0.019731682
G23	0.557	-0.000157	0.022495126	0.3672417	9.28789E-05	0.015688997
G24	1.136	-0.0005361	0.03609758	1.8663749	0.000943184	0.028149336
G25	0.336	-6.786E-05	0.010054452	0.1750008	8.16996E-05	0.006742096
G27	0.456	-8.986E-05	0.011311564	0.3234925	8.12575E-05	0.007788274
G28	1.27	0.0002574	0.034583084	0.8824857	-0.000221293	0.023956579
G29	0.269	0.0001061	0.022763163	0.166	-0.000199324	0.016015702
G30	0.278	2.979E-05	0.007920279	0.1415	-2.46425E-05	0.005475921
G31	1.612	-0.0001265	0.03495725	1.252299	-0.000250302	0.019426116
G32	0.382	-7.058E-05	0.011021359	0.2173868	6.46379E-05	0.007538734

Table B.16 Statistical Summary of Forced-Latency and SVR Solutions Based on 2015 Researched year (GLONASS Constellation).

Satellite number	Forced-latency solution			SVR solution		
	Range	Mean	Standard deviation	Range	Mean	Standard deviation
R01	0.546	3.169E-05	0.036123734	0.4952539	-0.001069845	0.024150453
R02	2.316	-0.0008581	0.05792304	3.115046	-0.000880811	0.039595199
R03	1.408	-0.000364	0.048426137	2.0864656	-0.000634598	0.038218841
R04	1.427	-0.0003865	0.055224681	2.8572086	-0.002017706	0.048486876
R05	1.172	-5.983E-05	0.049747276	2.8029139	-0.000975671	0.041211959
R06	0.849	-0.0001522	0.053696704	2.9692865	-0.001579809	0.053303796
R07	0.95	-0.0006328	0.047717897	2.1091777	0.000961383	0.035702542
R09	0.866	-0.0001763	0.03831296	0.5830814	-0.000336035	0.023808827
R10	1.966	-0.0005597	0.05636183	1.9591167	-0.001202508	0.036349565
R11	2.174	1.515E-05	0.050835271	1.7815994	-0.000685163	0.032111443
R12	3.298	-0.0010816	0.072090841	4.6359901	-0.000591722	0.046308089
R13	2.935	-6.68E-05	0.072193556	4.5838613	0.001948393	0.063549439
R14	1.359	-0.0008041	0.05047457	1.239425	3.36642E-05	0.034845299
R15	8.974	0.0032802	0.182045324	9.7999901	0.000789923	0.111780621
R16	3.646	-0.0002624	0.060614789	3.2288989	-0.000801528	0.039868304
R17	0.889	-0.000336	0.041846164	0.9986178	-0.0001299	0.028220689
R18	1.624	0.0003096	0.040249012	1.7041425	0.000160082	0.030413254
R19	2.267	3.961E-05	0.072246477	3.0979333	0.002123586	0.063916358
R20	1.777	-0.0006322	0.053245488	2.4684046	0.001203287	0.045748319
R21	1.006	-0.0002475	0.029810007	0.7721141	0.000195372	0.019789071
R22	1.352	0.0003419	0.043964403	1.1656203	-0.001079144	0.030127973
R23	3.085	0.0011912	0.063501724	4.3376799	0.000743657	0.041739872
R24	2.797	0.0004852	0.062715893	4.3994406	0.001362264	0.051252077

Table B.17 Statistical Summary of Forced-latency and ARIMA Solutions Based on 2014 Researched year (GPS Constellation).

Satellite number	Forced-latency solution			ARIMA solution		
	Range	Mean	Standard deviation	Range	Mean	Standard deviation
G01	1.401	0.0001835	0.055253245	1.7871542	-0.001296629	0.044621957
G02	0.393	9.189E-05	0.022393114	0.3989942	-0.000393805	0.014804224
G03	2.34	0.0002333	0.049821519	2.4822041	0.001129928	0.044415966
G04	0.665	0.0010956	0.021859628	0.687702	-0.000833242	0.017477782
G05	0.468	0.0002803	0.025069339	0.4623345	-5.78134E-05	0.016582966
G06	1.213	-0.0002899	0.026832343	1.2229745	0.000567175	0.019623317
G07	1.087	0.0003083	0.029197269	1.1568829	0.00031301	0.019428258
G08	4.594	0.0005506	0.071479703	4.6472443	-0.00095443	0.064395387
G09	3.144	-0.0017038	0.063806462	3.1626687	0.001576698	0.059152372
G10	0.503	-0.0015071	0.027405396	0.5166661	-0.000445392	0.018631386
G11	0.573	4.229E-05	0.024161554	0.597151	-0.00011349	0.015308076
G12	0.568	-8.98E-05	0.029799297	0.7035366	0.000207466	0.020828129
G13	0.463	-2.99E-05	0.034820628	0.4524916	0.000271384	0.024149105
G14	0.41	0.0001368	0.021958181	0.3956864	-5.32015E-05	0.014574374
G15	1.071	0.0002443	0.027394448	1.0583683	-0.000486138	0.019232217
G16	0.41	0.0001019	0.026958175	0.4290365	-0.00027835	0.017635582
G17	1.129	-0.0003564	0.034032555	1.099983	0.000509427	0.021570862
G18	0.346	1.784E-05	0.024690442	0.3826751	-9.94428E-05	0.016197407
G19	0.858	4.971E-05	0.02570127	0.7885742	-0.000291438	0.019685517
G20	0.31	-6.779E-05	0.023630047	0.3649347	0.000111614	0.015905719
G21	0.852	0.0001772	0.032818552	0.8544505	0.000443198	0.020416777
G22	0.324	-0.0001686	0.023599872	0.3140708	0.000213614	0.015527081
G23	0.323	3.013E-05	0.02178726	0.3375998	3.55564E-06	0.014867581
G24	1.248	0.0001137	0.036168179	1.1962703	0.000321761	0.027908781
G25	0.281	3.036E-05	0.011582443	0.2579192	0.000284218	0.009385093
G26	1.268	1.205E-05	0.023898477	1.2562432	-0.0002716	0.022119495
G27	4.372	0.0004042	0.061833612	4.3699304	0.000226882	0.044554784
G28	1.159	0.0005151	0.030138706	1.1932563	-8.94451E-05	0.022209893
G29	0.701	5.597E-05	0.028213086	0.6210117	0.000372959	0.019857597
G31	0.774	-7.404E-05	0.024939081	0.7435909	0.000140598	0.017810907
G32	0.747	-2.619E-05	0.016936275	0.7296885	0.000256055	0.013642087

Table B.18 Statistical Summary of Forced-latency and ARIMA Solutions Based on 2014 Researched year (GLONASS Constellation).

Satellite number	Forced-latency solution			ARIMA solution		
	Range	Mean	Standard deviation	Range	Mean	Standard deviation
R01	3.196	0.0007508	0.061083832	3.1808462	0.001584308	0.055829477
R02	0.878	0.0003754	0.043184594	0.884	0.003970491	0.033341775
R03	2.156	-8.14E-05	0.051500718	2.1418422	0.004543401	0.043808055
R04	1.086	-0.0003687	0.044296103	1.073	0.003050354	0.033297018
R05	2.22	-0.0008689	0.058844468	2.2063464	0.003471885	0.048621564
R06	2.304	0.0005897	0.066959618	2.277	0.002719121	0.055065941
R07	1.214	-0.0001212	0.048149976	1.188193	-0.003720146	0.037251863
R08	2.568	0.0005288	0.065546946	2.5738234	-0.003624479	0.066988353
R09	2.059	0.0002589	0.054998899	2.1846512	0.003255312	0.046283751
R10	2.115	-0.0013685	0.062275689	2.0573316	0.004006219	0.048504893
R11	3.665	0.0007402	0.068670347	3.5750126	0.002797231	0.049504816
R12	4.77	-0.0002072	0.080951725	5.2768954	0.004185526	0.074101277
R13	2.569	-0.0006623	0.061958837	2.5346446	-0.003595786	0.047965067
R14	1.591	0.0005733	0.048279358	1.56	0.002982737	0.037516862
R15	4.393	0.0011377	0.07940703	4.3236426	0.000954633	0.059364687
R16	2.812	-0.000617	0.062789581	2.81	0.004249444	0.055900387
R17	1.374	-0.0004767	0.051840694	1.3537087	0.004843452	0.042994493
R18	0.949	-0.0001396	0.046070593	0.8700777	-0.004360127	0.035076438
R19	1.385	0.0002779	0.036238509	1.3887056	-0.002020891	0.027384802
R20	2.217	-0.0003828	0.058276978	2.2029216	-0.004806924	0.040595848
R21	1.95	0.0001417	0.059359688	1.8849855	-0.003774	0.041810033
R22	3.094	-0.0007641	0.073533472	3.069454	0.004438201	0.062559975
R23	4.152	-0.0004156	0.083092957	4.1678945	-0.005850685	0.068386046
R24	2.626	0.0004903	0.064192913	2.6194197	-0.005768553	0.057042095

Table B.19 Statistical Summary of Forced-latency and SVR Solutions Based on 2014 Researched year (GPS Constellation).

Satellite number	Forced-latency solution			SVR solution		
	Range	Mean	Standard deviation	Range	Mean	Standard deviation
G01	1.401	0.0001835	0.055253245	2.0045171	0.000492485	0.046226332
G02	0.393	9.189E-05	0.022393114	0.2104222	0.000171523	0.015808521
G03	2.34	0.0002333	0.049821519	3.8904406	-0.000380691	0.042657973
G04	0.665	0.0010956	0.021859628	0.4914991	-0.000757814	0.015319372
G05	0.468	0.0002803	0.025069339	0.2753622	4.90234E-05	0.017763919
G06	1.213	-0.0002899	0.026832343	1.058493	0.000449811	0.0209067
G07	1.087	0.0003083	0.029197269	0.9264988	-1.14618E-05	0.021368584
G08	4.594	0.0005506	0.071479703	4.6664901	0.000876046	0.049720387
G09	3.144	-0.0017038	0.063806462	4.8743178	0.001018419	0.050983225
G10	0.503	-0.0015071	0.027405396	0.2655876	0.001479786	0.020497306
G11	0.573	4.229E-05	0.024161554	0.3386825	0.000240234	0.017028238
G12	0.568	-8.98E-05	0.029799297	0.2505425	0.000216186	0.020173389
G13	0.463	-2.99E-05	0.034820628	0.2679905	0.000201884	0.023392056
G14	0.41	0.0001368	0.021958181	0.2096137	9.06444E-05	0.015513525
G15	1.071	0.0002443	0.027394448	1.1924903	1.43543E-05	0.021710908
G16	0.41	0.0001019	0.026958175	0.2273141	9.52035E-05	0.018744393
G17	1.129	-0.0003564	0.034032555	0.7988042	0.000381241	0.023644392
G18	0.346	1.784E-05	0.024690442	0.178	0.00021972	0.017436819
G19	0.858	4.971E-05	0.02570127	0.6994925	9.40874E-05	0.018644438
G20	0.31	-6.779E-05	0.023630047	0.191	0.000245889	0.016702429
G21	0.852	0.0001772	0.032818552	1.5349727	6.57814E-05	0.02562605
G22	0.324	-0.0001686	0.023599872	0.1765	0.000314845	0.016805378
G23	0.323	3.013E-05	0.02178726	0.175	0.000209298	0.015330714
G24	1.248	0.0001137	0.036168179	1.0519948	0.000117586	0.026504788
G25	0.281	3.036E-05	0.011582443	0.1425	0.000236915	0.008133785
G26	1.268	1.205E-05	0.023898477	0.9041154	0.000239897	0.016489446
G27	4.372	0.0004042	0.061833612	4.369	-4.75265E-05	0.060097617
G28	1.159	0.0005151	0.030138706	0.8059043	-0.000224418	0.021123971
G29	0.701	5.597E-05	0.028213086	0.4245433	0.000176899	0.019648283
G31	0.774	-7.404E-05	0.024939081	0.5111543	0.000220962	0.017289343
G32	0.747	-2.619E-05	0.016936275	1.0227315	0.00023658	0.013760304

Table B.20 Statistical Summary of Forced-latency and SVR Solutions Based on 2014 Researched year (GLONASS Constellation).

Satellite number	Forced-latency solution			SVR solution		
	Range	Mean	Standard deviation	Range	Mean	Standard deviation
R01	3.196	0.0007508	0.061083832	4.3764882	-0.000817006	0.041672729
R02	0.878	0.0003754	0.043184594	2.5333078	-0.001618455	0.041832649
R03	2.156	-8.14E-05	0.051500718	2.1870055	-0.001320328	0.038612251
R04	1.086	-0.0003687	0.044296103	1.5547421	-0.001632041	0.037807062
R05	2.22	-0.0008689	0.058844468	1.7537802	-0.000363356	0.039847677
R06	2.304	0.0005897	0.066959618	3.4466792	-0.00148489	0.05708544
R07	1.214	-0.0001212	0.048149976	3.0473675	0.000843724	0.045744407
R08	2.568	0.0005288	0.065546946	3.946845	-0.000157942	0.060394081
R09	2.059	0.0002589	0.054998899	2.7261864	-0.002476592	0.051408929
R10	2.115	-0.0013685	0.062275689	2.5240879	-0.00088034	0.04834449
R11	3.665	0.0007402	0.068670347	3.2135363	-0.00102302	0.046457556
R12	4.77	-0.0002072	0.080951725	4.598991	-0.002015078	0.05663822
R13	2.569	-0.0006623	0.061958837	2.2336686	0.001830206	0.050946188
R14	1.591	0.0005733	0.048279358	2.9694963	-0.001310935	0.041482063
R15	4.393	0.0011377	0.07940703	4.327	-0.001379543	0.061894976
R16	2.812	-0.000617	0.062789581	4.3153534	-0.000781464	0.049277404
R17	1.374	-0.0004767	0.051840694	2.8417083	-0.000953287	0.040215181
R18	0.949	-0.0001396	0.046070593	2.6467751	0.000948304	0.043490281
R19	1.385	0.0002779	0.036238509	1.0654953	-0.000428741	0.02479094
R20	2.217	-0.0003828	0.058276978	2.8012833	0.000461361	0.05111428
R21	1.95	0.0001417	0.059359688	3.0195112	0.000551666	0.049125637
R22	3.094	-0.0007641	0.073533472	4.3056553	-0.000815026	0.059656891
R23	4.152	-0.0004156	0.083092957	4.4133408	0.001313659	0.076973645
R24	2.626	0.0004903	0.064192913	4.4096259	0.001313713	0.046104237

Table B.21 Statistical Summary of Forced-latency and ARIMA Solutions Based on 2013 Researched year (GLONASS Constellation).

Satellite number	Forced-latency solution			ARIMA solution		
	Range	Mean	Standard deviation	Range	Mean	Standard deviation
G01	4.524	2.214E-05	0.113219584	4.3152419	0.000412172	0.095546135
G02	4.528	-0.0001558	0.114644535	4.3049571	0.000164164	0.093243598
G03	4.494	0.0002644	0.116290877	4.2784164	-0.001286178	0.096421332
G04	4.56	-0.0003351	0.113958866	4.3278427	0.000445873	0.093641375
G05	4.503	-4.591E-05	0.116437751	4.2949872	0.000561348	0.097492565
G06	4.535	0.0009638	0.117282697	4.2983432	0.000362941	0.099880576
G07	4.522	5.031E-05	0.114858805	4.3006451	-0.000350223	0.094224093
G08	4.514	-0.0006172	0.115924161	3.8297485	0.000582576	0.093485941
G10	2.093	-0.0001111	0.040716172	2.0711608	-4.35132E-05	0.033694879
G11	4.555	6.956E-06	0.114827228	4.3499336	0.000494658	0.097802162
G12	4.592	-5.947E-05	0.117314368	4.2605202	-0.000602674	0.096164001
G13	4.519	-0.000176	0.116401185	4.2965723	0.000772992	0.095139006
G14	4.515	0.0001523	0.114742385	4.3019331	-0.000222713	0.093621963
G15	4.541	5.344E-05	0.114429518	4.3422824	0.000269116	0.095652011
G16	4.539	3.408E-05	0.115586249	4.3196209	-3.79106E-05	0.094362935
G17	4.532	0.0006339	0.115981819	3.4951773	0.000318554	0.091982881
G18	4.498	7.014E-05	0.11538383	4.2783514	0.000226329	0.092510829
G19	4.552	-8.115E-05	0.114826143	4.3060811	0.000476339	0.09741409
G20	4.532	0.00011	0.115456029	4.3089099	-7.5053E-05	0.092566479
G21	4.543	4.301E-05	0.116493919	3.5417132	5.6296E-05	0.090766801
G22	5.637	-0.0006785	0.13177722	4.2958216	0.000943751	0.094681005
G23	4.526	-9.552E-05	0.108120629	4.3755029	-0.000892741	0.091836013
G24	4.481	0.0004136	0.118878095	4.2971179	-0.000241948	0.097085816
G25	4.526	2.156E-05	0.113031117	4.3150795	-0.000390466	0.095131958
G26	147.307	0.0054262	2.82353352	130.9763	0.054327064	2.537043094
G27	4.52	7.234E-05	0.112938124	4.3110947	-0.000221453	0.095603441
G28	4.521	-0.0007756	0.114873917	4.2834156	3.70082E-05	0.096127893
G29	4.558	-0.0001834	0.115099847	4.2920824	7.3228E-05	0.095782971
G31	4.522	0.0001483	0.115037925	3.9272715	0.000611629	0.095028241
G32	4.521	-0.0002423	0.115831952	4.3003695	-0.000239713	0.100856781

Table B.22 Statistical Summary of Forced-latency and ARIMA Solutions Based on 2013 Researched year (GLONASS Constellation).

Satellite number	Forced-latency solution			ARIMA solution		
	Range	Mean	Standard deviation	Range	Mean	Standard deviation
R01	0.853	0.0003003	0.035914985	0.8531703	-0.002052058	0.028820784
R02	2.541	0.000814	0.0568916	2.4546138	-0.004255551	0.043121619
R03	1.657	0.0016703	0.049545305	1.6517581	-0.003139875	0.041400314
R04	1.78	5.539E-05	0.047432845	1.7253637	-0.002663364	0.039017396
R05	2.957	0.0017238	0.062555041	3.9096639	-0.000308441	0.061157744
R06	1.166	-0.0008132	0.056694957	1.4676263	-0.004229056	0.043612214
R07	4.214	0.0015586	0.089041173	4.2017113	0.005855935	0.078999295
R08	1.113	-0.0019857	0.042954156	1.1123399	0.001740154	0.035356772
R09	2.262	-0.0004124	0.060189454	2.4285843	-0.003144464	0.050467383
R10	2.779	-0.0020669	0.080693869	3.0012063	-0.005592663	0.065775092
R11	2.184	0.000432	0.051560356	2.1487829	-0.002099275	0.041310303
R12	2.696	-0.0012306	0.063993089	2.7533644	-0.004287944	0.046505488
R13	3.388	0.0009419	0.075902034	3.3497447	0.005327002	0.063409552
R14	2.916	0.000343	0.059521438	3.0064648	-0.005003884	0.058282652
R15	1.224	-0.0014188	0.053755267	1.1929346	-0.001165544	0.036636352
R16	4.268	0.0001423	0.070703202	4.1942219	-0.00274366	0.062728897
R17	1.535	-8.505E-05	0.053182272	1.5524009	-0.004959647	0.043219755
R18	2.972	-8.273E-05	0.06271845	3.5735753	0.002443143	0.064178235
R19	2.104	-0.0007655	0.045680332	2.1419604	0.001548186	0.037648472
R20	1.99	0.0003441	0.058459586	1.9873337	0.005920608	0.043840373
R21	4.826	-0.0012689	0.084729554	7.0830178	0.002348156	0.088289045
R22	1.798	0.0001876	0.047856472	1.7875452	-0.003606159	0.038810686
R23	1.513	-0.0007988	0.052560156	1.4760539	0.003903133	0.043132534
R24	1.392	0.0005482	0.051545399	1.5116174	0.004161983	0.040519649

Table B.23 Statistical Summary of Forced-latency and SVR Solutions Based on 2013 Researched year (GPS Constellation).

Satellite number	Forced-latency solution			SVR solution		
	Range	Mean	Standard deviation	Range	Mean	Standard deviation
G01	4.524	2.214E-05	0.113219584	4.1492422	-0.00037365	0.073135719
G02	4.528	-0.0001558	0.114644535	4.1432917	-0.000227278	0.075021847
G03	4.494	0.0002644	0.116290877	4.477	-0.001811847	0.129866273
G04	4.56	-0.0003351	0.113958866	4.4064989	-0.000756201	0.117789528
G05	4.503	-4.591E-05	0.116437751	4.1551009	-0.000572552	0.079307802
G06	4.535	0.0009638	0.117282697	4.3910009	-0.00179688	0.119698239
G07	4.522	5.031E-05	0.114858805	4.51	-0.001469496	0.11948479
G08	4.514	-0.0006172	0.115924161	4.1284808	-0.000107796	0.117825561
G10	2.093	-0.0001111	0.040716172	1.5289391	0.000208011	0.031116623
G11	4.555	6.956E-06	0.114827228	4.1359178	-0.000388268	0.074752672
G12	4.592	-5.947E-05	0.117314368	4.521	-8.92704E-05	0.120944704
G13	4.519	-0.000176	0.116401185	4.1764826	-0.000312175	0.078740916
G14	4.515	0.0001523	0.114742385	4.1321521	0.000157946	0.111521226
G15	4.541	5.344E-05	0.114429518	4.2393036	-0.000345716	0.111768622
G16	4.539	3.408E-05	0.115586249	4.18278	-0.00166823	0.112397664
G17	4.532	0.0006339	0.115981819	4.2801739	0.000916512	0.115059514
G18	4.498	7.014E-05	0.11538383	4.1559909	-0.000398024	0.074858751
G19	4.552	-8.115E-05	0.114826143	4.1752764	-0.000247086	0.074469071
G20	4.532	0.00011	0.115456029	4.129442	-0.000410075	0.075454325
G21	4.543	4.301E-05	0.116493919	4.516	-9.70959E-05	0.120648225
G22	5.637	-0.0006785	0.13177722	5.482002	-0.001821468	0.126179439
G23	4.526	-9.552E-05	0.108120629	4.1300565	-0.000223627	0.070807168
G24	4.481	0.0004136	0.118878095	4.512	-0.001794379	0.098906926
G25	4.526	2.156E-05	0.113031117	4.1743894	-0.00109998	0.111991553
G26	147.307	0.0054262	2.82353352	147.323	0.022490716	2.273495062
G27	4.52	7.234E-05	0.112938124	4.148937	-0.000444153	0.072977622
G28	4.521	-0.0007756	0.114873917	4.1712072	-4.18214E-05	0.077524381
G29	4.558	-0.0001834	0.115099847	4.1710375	-0.000177941	0.075243937
G31	4.522	0.0001483	0.115037925	4.502	4.6776E-05	0.121848107
G32	4.521	-0.0002423	0.115831952	4.3840011	-6.52526E-05	0.091893891

Table B.24 Statistical Summary of Forced-latency and SVR Solutions Based on 2013 Researched year (GLONASS Constellation).

Satellite number	Forced-latency solution			SVR solution		
	Range	Mean	Standard deviation	Range	Mean	Standard deviation
R01	0.853	0.0003003	0.035914985	1.5266318	-0.000655961	0.027008271
R02	2.541	0.000814	0.0568916	2.9135088	-0.002252255	0.053075546
R03	1.657	0.0016703	0.049545305	3.5725932	-0.002822408	0.048588235
R04	1.78	5.539E-05	0.047432845	1.812981	-0.000337851	0.034127235
R05	2.957	0.0017238	0.062555041	4.2265878	-0.001824568	0.050450013
R06	1.166	-0.0008132	0.056694957	1.221267	0.000308368	0.039905054
R07	4.214	0.0015586	0.089041173	5.5990409	0.001105644	0.061771656
R08	1.113	-0.0019857	0.042954156	0.8194638	0.002617234	0.028589356
R09	2.262	-0.0004124	0.060189454	2.3580313	-0.000138748	0.044426805
R10	2.779	-0.0020669	0.080693869	4.4440489	0.000337731	0.059846879
R11	2.184	0.000432	0.051560356	1.9432519	-0.000643363	0.036338333
R12	2.696	-0.0012306	0.063993089	3.6204901	-0.000538829	0.045437829
R13	3.388	0.0009419	0.075902034	4.2899901	0.001021206	0.051665549
R14	2.916	0.000343	0.059521438	2.8195463	-0.001512039	0.038555423
R15	1.224	-0.0014188	0.053755267	2.5734562	6.57325E-05	0.043025618
R16	4.268	0.0001423	0.070703202	4.248	3.89551E-06	0.052684294
R17	1.535	-8.505E-05	0.053182272	1.1820543	-0.000111345	0.035739941
R18	2.972	-8.273E-05	0.06271845	3.204991	0.000384649	0.051976204
R19	2.104	-0.0007655	0.045680332	2.2496893	0.001339152	0.034033721
R20	1.99	0.0003441	0.058459586	2.2869683	0.000310951	0.048529031
R21	4.826	-0.0012689	0.084729554	4.8086722	0.001228683	0.068592611
R22	1.798	0.0001876	0.047856472	3.0365085	-0.000540927	0.0406655
R23	1.513	-0.0007988	0.052560156	2.5263573	0.001418247	0.040713506
R24	1.392	0.0005482	0.051545399	1.2453906	0.000107334	0.036864281

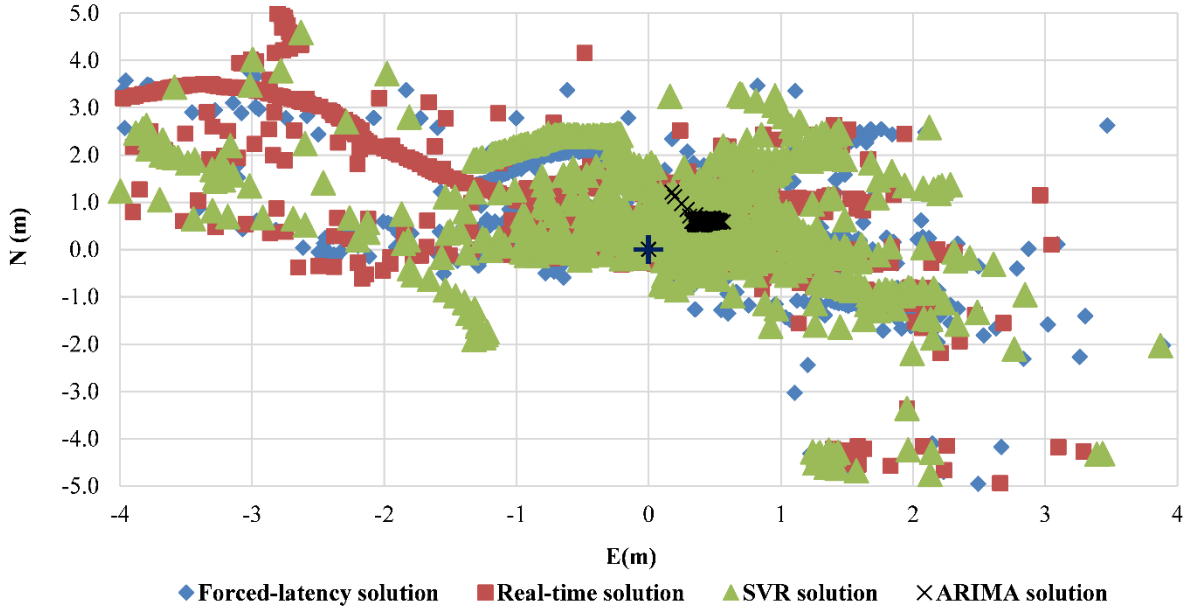

Figure B.1 BREST station coordinates solutions residuals according to 2021 data.

(Prepared by the author).

Figure B.2 ABMF station coordinates solutions residuals according to 2021 data.

(Prepared by the author).

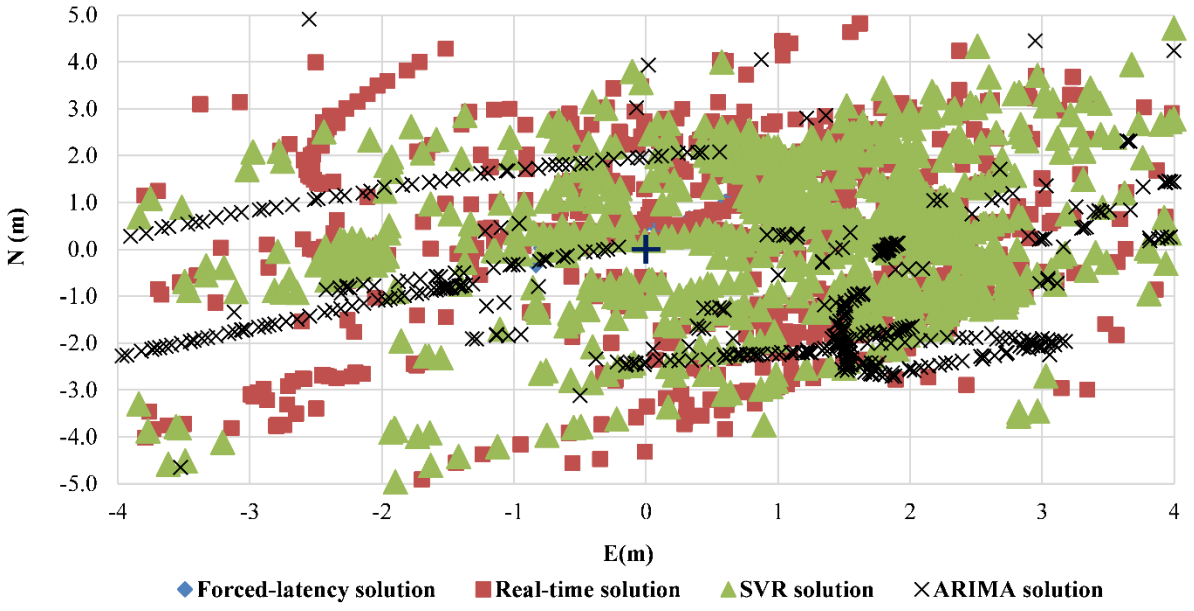

Figure B.3 ANKR station coordinates solutions residuals according to 2021 data.

(Prepared by the author).

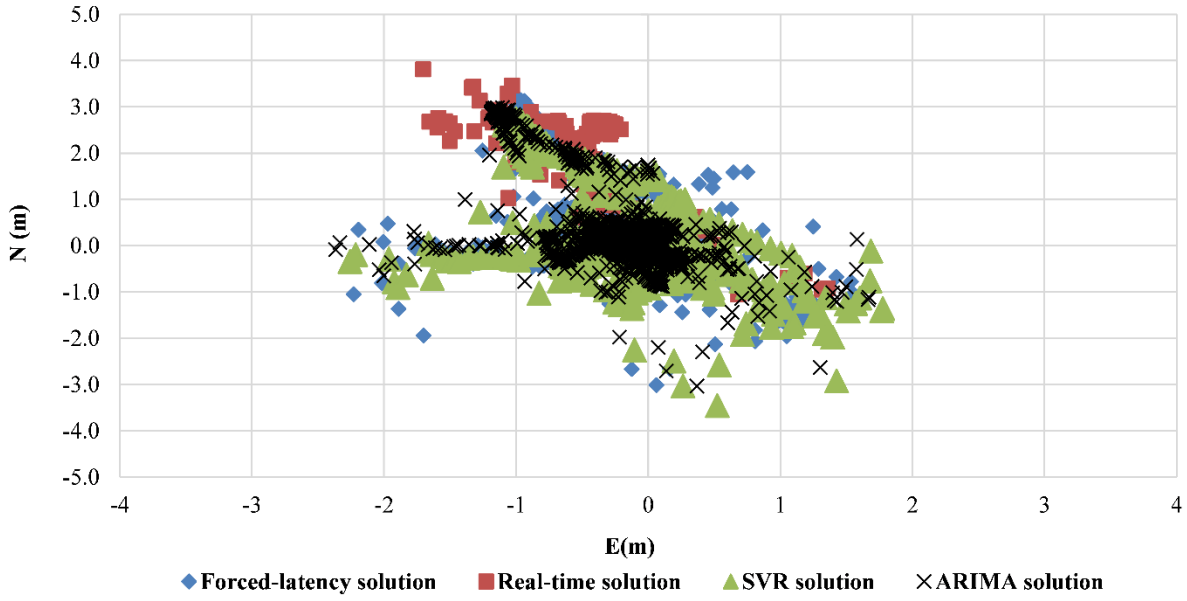

Figure B.4 UNBJ station coordinates solutions residuals according to 2021 data.

(Prepared by the author).

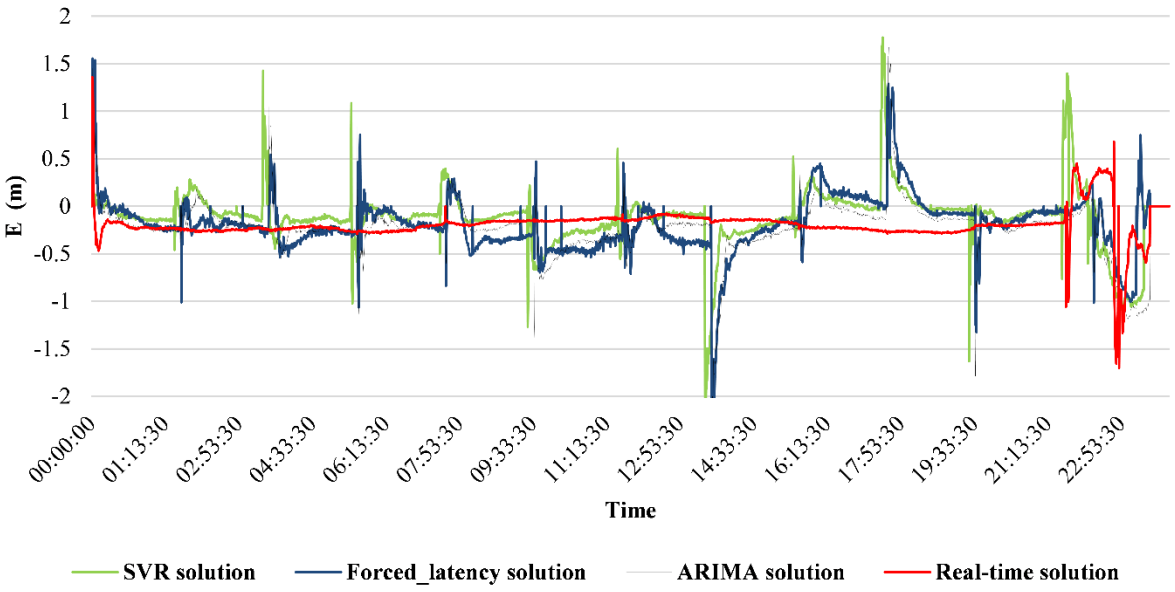

Figure B.5 UNBJ station east component residuals according to 2021 data

(Prepared by the author).

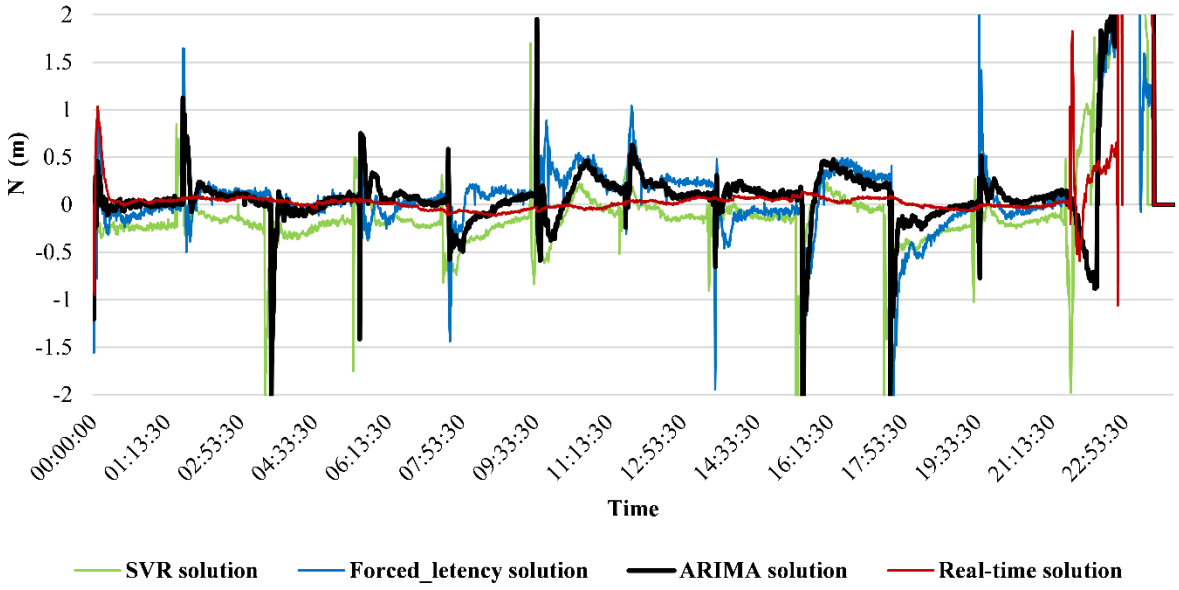

Figure B.6 UNBJ station north component residuals according to 2021 data

(Prepared by the author).

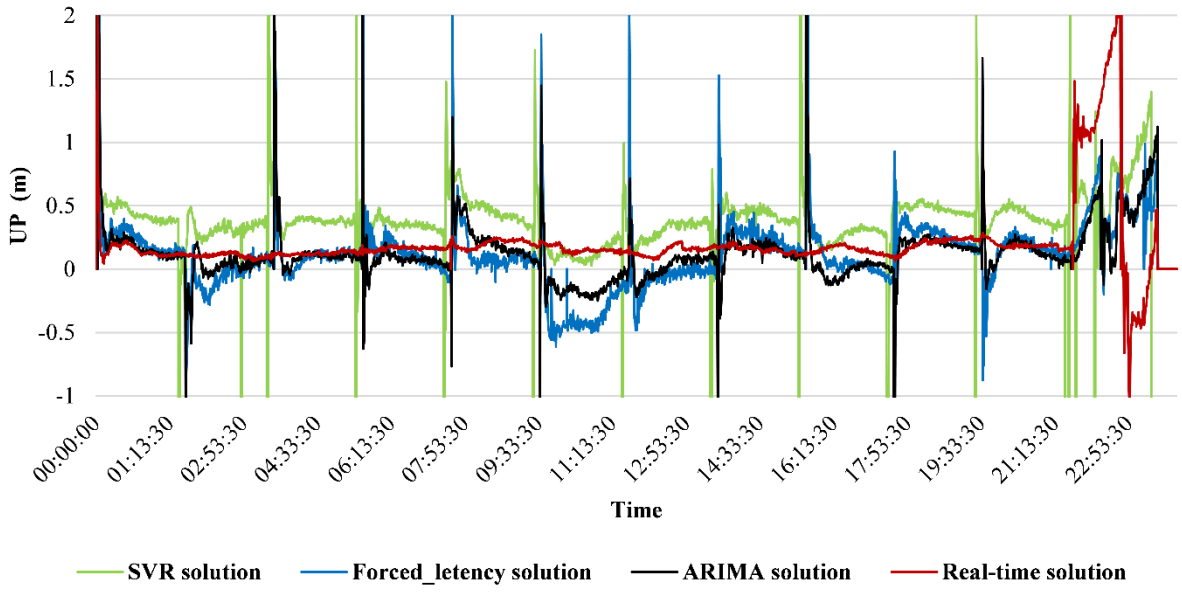

Figure B.7 UNBJ station Up component residuals according to 2021 data

(Prepared by the author).

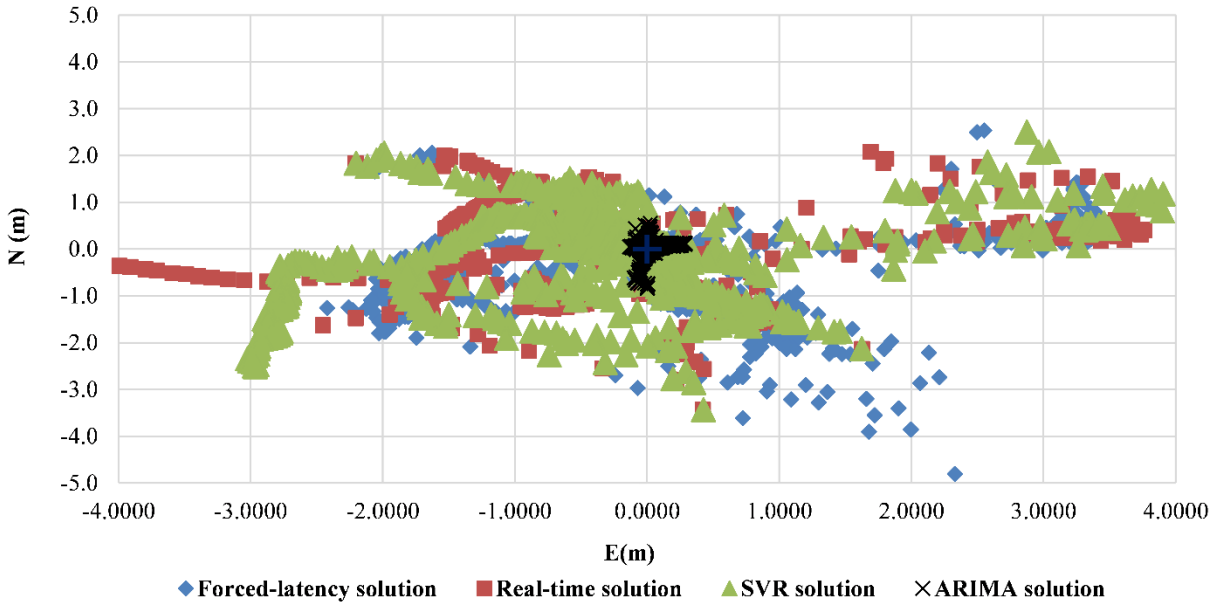

Figure B.8 HOFN station coordinates solutions residuals according to 2021 data.

(Prepared by the author).

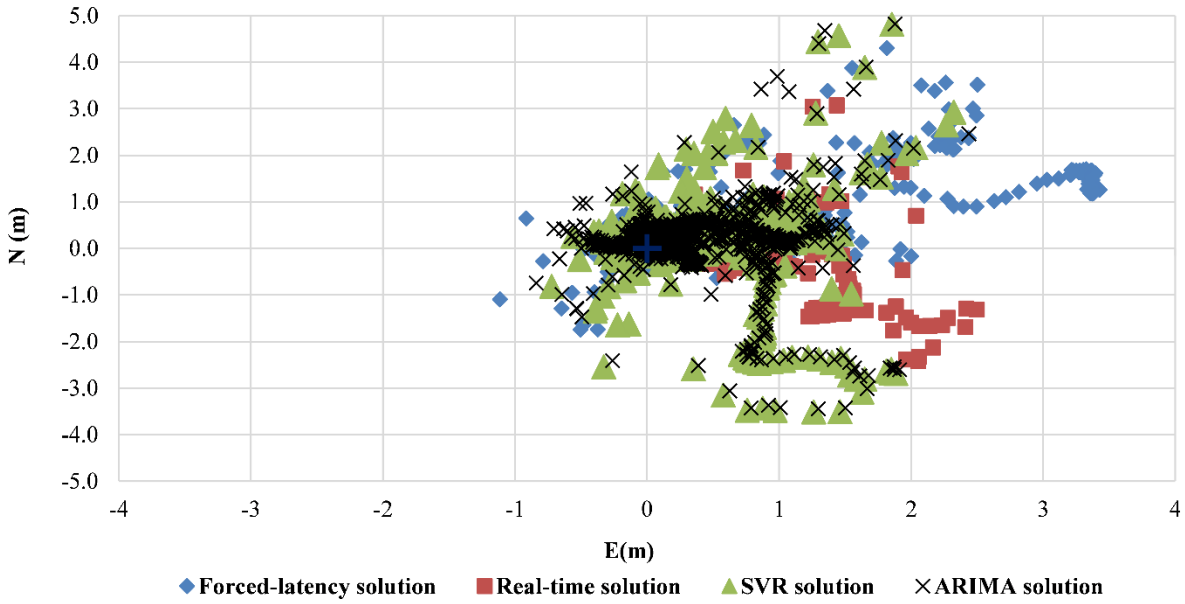

Figure B.9 KERG station coordinates solutions residuals according to 2021 data.

(Prepared by the author).

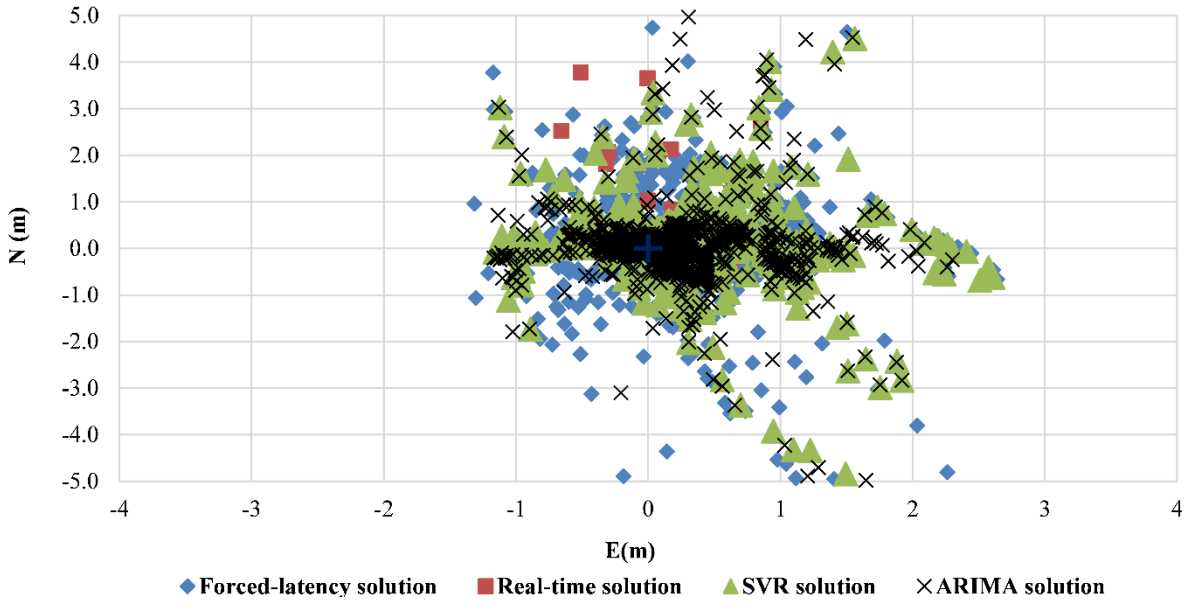

Figure B.10 NTUS station coordinates solutions residuals according to 2021 data.

(Prepared by the author).

Appendix.C

Analyzing RT-PPP EWS Research Experiment Comprehensive Statistical Summaries

Table C.1 Summary of 2-centimeters Vertical Displacement Experiment at 10 Degrees Elevation Angle with High Latency Stream.

Start date			**End date**			**Duration (hours)**	**# of events**
2022-04-17 23:24:56			2022-04-19 00:46:24			24	91290
	Coordinates components (m)			**Displacement components (m)**			**Latency**
	X	Y	Z	East	North	UP	Seconds
Mean	4455834	3127064	3314433	-0.16114	0.034825	-0.14608	32.06
Standard deviation	0.393469	0.654338	0.879729	0.41735	0.58147	0.919028	1.75
Minimum	4455823	3127055	3314425	-5.5291	-4.6009	-10.8696	30.22
Maximum	4455839	3127067	3314434	2.8829	3.5126	5.4947	41.67

Table C.2 Summary of 3.75-centimeters Vertical Displacement Experiment at 10 Degrees Elevation Angle with High Latency Stream.

Start date			**End date**			**Duration (hours)**	**# of events**
2022-04-19 21:25:09			2022-04-20 21:29:34			24	86666
	Coordinates components (m)			**Displacement components (m)**			**Latency**
	X	Y	Z	East	North	UP	Seconds
Mean	4455834	3127064	3314433	0.023592	-0.03255	0.054975	33.54
Standard deviation	0.148353	0.238717	0.318546	0.127974	0.300612	0.271516	1.57
Minimum	4455830	3127060	3314426	-1.604	-5.385	-7.1358	31.73
Maximum	4455836	3127066	3314440	1.3924	4.4135	6.759	42.89

Table C.3 Summary of 5-centimeters Vertical Displacement Experiment at 10 Degrees Elevation Angle with High Latency Stream.

Start date			End date			Duration (hours)	# of events
2022-04-20 21:32:32			2022-04-21 20:46:04			24	83616
	Coordinates components (m)			Displacement components (m)			Latency
	X	Y	Z	East	North	UP	Seconds
Mean	4455833	3127064	3314433	0.002814	-0.3725	-0.64498	26.07
Standard deviation	2.244827	1.485629	1.638109	0.604309	1.887514	2.449866	3.079
Minimum	4455824	3127059	3314426	-1.6821	-5.4618	-9.5415	22.75
Maximum	4455843	3127072	3314445	2.5602	3.8945	16.7481	36.62

Table C.4 Summary of 10-centimeters Vertical Displacement Experiment at 10 Degrees Elevation Angle with High Latency Stream.

Start date			End date			Duration (hours)	# of events
2022-04-20 21:32:32			2022-04-21 20:46:04			24	103134
	Coordinates components (m)			Displacement components (m)			Latency
	X	Y	Z	East	North	UP	Seconds
Mean	4455834	3127064	3314433	0.043	0.009764	0.114018	34.69
Standard deviation	0.066557	0.053325	0.048074	0.04623	0.028939	0.081301	0.33
Minimum	4455833	3127064	3314433	-0.073	-0.1553	-0.1729	30.47
Maximum	4455834	3127064	3314433	0.1917	0.123	0.3687	38.9

Table C.5 Summary of 15-centimeters Vertical Displacement Experiment at 10 Degrees Elevation Angle with High Latency Stream.

Start date			End date			Duration (hours)	# of events
2022-04-23 14:00:26			2022-04-24 13:29:09			24	84523
	Coordinates components (m)			Displacement components (m)			Latency
	X	Y	Z	East	North	UP	Seconds
Mean	4455834	3127064	3314433	0.021852	0.001917	0.053161	16.37
Standard deviation	0.098908	0.051432	0.064702	0.049906	0.028509	0.115373	0.34
Minimum	4455833	3127064	3314433	-0.0802	-0.1053	-0.2987	30.40
Maximum	4455834	3127064	3314433	0.1628	0.128	0.3431	42.82

Table C.6 Summary of 20-centimeters Vertical Displacement Experiment at 10 Degrees Elevation Angle with High Latency Stream.

Start date			End date			Duration (hours)	# of events
2022-04-24 13:30:59			2022-04-25 13:31:59			24	85129
	Coordinates components (m)			Displacement components (m)			Latency
	X	Y	Z	East	North	UP	Seconds
Mean	4455834	3127064	3314433	-0.05941	-0.40578	0.03534	31.81956
Standard deviation	1.574038	1.111771	2.27902	0.341906	1.653282	2.461163	0.258519
Minimum	4455829	3127059	3314418	-2.4168	-10.1569	-12.079	31.19
Maximum	4455845	3127072	3314436	5.5596	0.1887	13.5634	32.51

Table C.7 Summary of 2.5-centimeters Vertical Displacement Experiment at 10 Degrees Elevation Angle with Low Latency Stream.

Start date			End date			Duration (hours)	# of events
2022-01-09 08:43:44			2022-01-09 21:04:34			12	52920
	Coordinates components (m)			Displacement components (m)			Latency
	X	Y	Z	East	North	UP	Seconds
Mean	4455834	3127064	3314433	0.00191	0.0159	0.084142	13.86554
Standard deviation	0.043718	0.030175	0.040868	0.025083	0.022659	0.057874	0.382081
Minimum	4455834	3127064	3314433	-0.0671	-0.0565	-0.0668	13.06
Maximum	4455834	3127064	3314434	0.1591	0.3972	0.4714	19.3

Table C.8 Summary of 2-centimeters Vertical Displacement Experiment at 10 Degrees Elevation Angle with Low Latency Stream.

Start date			End date			Duration (hours)	# of events
2022-04-16 07:26:37			2022-04-16 20:31:00			24	99280
	Coordinates components (m)			Displacement components (m)			Latency
	X	Y	Z	East	North	UP	Seconds
Mean	4455833	3127064	3314433	0.016859	0.117826	-0.23043	15.76
Standard deviation	1.671532	0.706984	0.485649	0.417101	0.570332	1.740818	0.43
Minimum	4455816	3127058	3314430	-0.6474	-0.1391	-15.3946	14.8
Maximum	4455834	3127064	3314433	5.0239	8.9736	0.331	24.54

Table C.9 Summary of 3.75-centimeters Vertical Displacement Experiment at 10 Degrees Elevation Angle with Low Latency Stream.

Start date			End date			Duration (hours)	# of events
2022-04-16 07:26:37			2022-04-16 20:31:00			24	98219
	Coordinates components (m)			Displacement components (m)			Latency
	X	Y	Z	East	North	UP	Seconds
Mean	4455833	3127064	3314433	0.072063	-0.02337	-0.16253	14.13
Standard deviation	1.508415	0.896478	0.820706	0.367798	1.00537	1.614467	0.47
Minimum	4455817	3127054	3314426	-0.3394	-6.8425	-20.3132	13.09
Maximum	4455836	3127066	3314436	4.3178	6.4798	3.8183	26.33

Table C.10 Summary of 5-centimeters Vertical Displacement Experiment at 10 Degrees Elevation Angle with Low Latency Stream.

Start date			**End date**			**Duration (hours)**	**# of events**
2021-12-18 07:20:30			2021-12-18 20:00:04			12	52900
	Coordinates components (m)			**Displacement components (m)**			**Latency**
	X	Y	Z	East	North	UP	Seconds
Mean	4455834	3127064	3314433	-0.01014	0.013717	0.037007	20.31731
Standard deviation	0.03781	0.044361	0.028874	0.027794	0.02344	0.053938	5.061788
Minimum	4455834	3127064	3314433	-0.0732	-0.0515	-0.1131	13.03
Maximum	4455834	3127064	3314433	0.0859	0.0819	0.1804	32.39

Table C.11 Summary of 10-centimeters Vertical Displacement Experiment at 10 Degrees Elevation Angle with Low Latency Stream.

Start date			**End date**			**Duration (hours)**	**# of events**
2022-01-08 06:06:46			2022-01-08 18:01:49			12	51210
	Coordinates components (m)			**Displacement components (m)**			**Latency**
	X	Y	Z	East	North	UP	Seconds
Mean	4455834	3127064	3314433	-0.01213	0.028169	0.068581	13.76434
Standard deviation	0.061782	0.047156	0.044476	0.017054	0.026995	0.083662	0.373289
Minimum	4455834	3127064	3314433	-0.0694	-0.0318	-0.1226	13.01
Maximum	4455834	3127064	3314433	0.0387	0.0956	0.2692	23.18

Table C.12 Summary of 10-centimeters Vertical Displacement Experiment at 10 Degrees Elevation Angle with Low Latency Stream.

Start date			End date			Duration (hours)	# of events
2022-04-10 18:02:06			2022-04-11 19:43:04			24	101041
	Coordinates components (m)			Displacement components (m)			Latency
	X	Y	Z	East	North	UP	Seconds
Mean	4455834	3127064	3314433	-0.08568	0.09293	0.010834	16.49989
Standard deviation	0.168984	0.495776	0.468236	0.405231	0.338247	0.46365	0.530498
Minimum	4455833	3127060	3314431	-3.3461	-1.3797	-2.1234	15.48
Maximum	4455839	3127070	3314445	2.5575	6.2629	12.889	29.85

Table C.13 Summary of 15-centimeters Vertical Displacement Experiment at 10 Degrees Elevation Angle with Low Latency Stream.

Start date			End date			Duration (hours)	# of events
2022-01-11 08:53:23			2022-01-11 21:12:24			12	52770
	Coordinates components (m)			Displacement components (m)			Latency
	X	Y	Seconds	East	North	UP	Seconds
Mean	4455834	3127064	3314433	0.00093	0.012714	0.751067	13.79182
Standard deviation	0.072877	0.059827	0.054549	0.032805	0.01494	1.372916	0.471851
Minimum	4455834	3127064	3314433	-0.0842	-0.0248	-0.3049	13.04
Maximum	4455834	3127064	3314433	0.0675	0.0752	5.4645	39.29

Table C.14 Summary of 20-centimeters Vertical Displacement Experiment at 10 Degrees Elevation Angle with Low Latency Stream.

Start date			End date			Duration (hours)	# of events
2022-01-12 07:08:31			2022-01-13 20:09:24			12	158464
	Coordinates components (m)			Displacement components (m)			Latency
	X	Y	Z	East	North	UP	Seconds
Mean	4455834	3127064	3314433	0.230621	-0.12062	0.751067	15.08206
Standard deviation	0.934523	1.03006	0.765221	0.676825	0.42063	1.372916	0.619147
Minimum	4455833	3127063	3314433	-1.7853	-1.1935	-0.3049	13.64
Maximum	4455837	3127068	3314437	2.0979	1.8218	5.4645	23.96

Table C.15 Summary of 20-centimeters Vertical Displacement Experiment at 10 Degrees Elevation Angle with Low Latency Stream.

Start date			End date			Duration (hours)	# of events
2022-04-14 21:40:34			2022-04-15 22:19:54			24	105881
	Coordinates components (m)			Displacement components (m)			Latency
	X	Y	Z	East	North	UP	Seconds
Mean	4455834	3127064	3314433	-0.01722	0.012998	0.036249	14.76666
Standard deviation	0.093981	0.078422	0.066231	0.052122	0.021642	0.127216	0.43232
Minimum	4455833	3127064	3314433	-0.168	-0.0863	-0.2194	13.79
Maximum	4455834	3127064	3314433	0.0877	0.0828	0.3033	23.32

Table C.16 Summary of 2.5-centimeters Vertical Displacement Experiment at 20 Degrees Elevation Angle with Low Latency Stream.

Start date			End date			Duration (hours)	# of events
2022-05-26 16:41:42			2022-05-27 09:52:04			24	73653
	Coordinates components (m)			Displacement components (m)			Latency
	X	Y	Z	East	North	UP	Seconds
Mean	4455834	3127064	3314434	-0.26714	0.225551	0.98772	14.50664
Standard deviation	10.98553	5.068923	6.485626	2.41567	1.455005	13.43454	0.355711
Minimum	4455706	3126998	3314361	-42.0632	-12.1581	-159.099	13.73

Maximum	4456021	3127145	3314543	19.1993	15.1209	227.0894	20.22

Table C.17 Summary of 5-centimeters Vertical Displacement Experiment at 20 Degrees Elevation Angle with Low Latency Stream.

Start date			**End date**			**Duration (hours)**	**# of events**
2022-05-27 20:05:40			2022-05-28 19:54:29			24	71712
	Coordinates components (m)			**Displacement components (m)**			**Latency**
	X	Y	Z	East	North	UP	Seconds
Mean	4455834	3127064	3314434	0.164519	-0.09456	0.868278	14.0704
Standard deviation	3.807372	2.093448	2.10172	1.364933	0.918858	4.537454	0.583749
Minimum	4455816	3127056	3314428	-16.8678	-13.8189	-18.6646	13.13
Maximum	4455902	3127092	3314473	10.8567	5.9556	82.3654	33.78

Table C.1 Summary of 10-centimeters Vertical Displacement Experiment at 20 Degrees Elevation Angle with Low Latency Stream.

Start date			**End date**			**Duration (hours)**	**# of events**
2022-05-28 19:56:45			2022-05-29 19:16:49			24	99321
	Coordinates components (m)			**Displacement components (m)**			**Latency**
	X	Y	Z	East	North	UP	Seconds
Mean	4455834	3127064	3314433	0.132406	-0.01149	0.186443	11.69356
Standard deviation	1.154719	0.766881	0.510188	0.662717	0.482178	1.228855	229.3005
Minimum	4455821	3127053	3314421	-11.3703	-9.5102	-16.1644	-43185.6
Maximum	4455848	3127072	3314441	7.1259	5.0555	16.0803	24.36

Table C.19 Summary of 15-centimeters Vertical Displacement Experiment at 20 Degrees Elevation Angle with Low Latency Stream.

Start date			**End date**			**Duration (hours)**	**# of events**
2022-05-29 19:21:05			2022-05-30 18:42:15			24	100000
	Coordinates components (m)			**Displacement components (m)**			**Latency**
	X	Y	Z	East	North	UP	Seconds
Mean	4455834	3127064	3314433	0.058414	0.072087	0.154462	15.52544

Standard deviation	2.209989	1.123966	1.344911	0.597571	0.697826	2.666849	0.383278
Minimum	4455824	3127059	3314427	-13.0323	-13.5603	-12.2753	14.62
Maximum	4455886	3127084	3314451	3.5265	6.2583	55.5203	21.06

Table C.20 Summary of 20-centimeters Vertical Displacement Experiment at 20 Degrees Elevation Angle with Low Latency Stream.

Start date			**End date**			**Duration (hours)**	**# of events**
2022-05-30 18:48:06			2022-05-31 20:22:19			24	109230
	Coordinates components (m)			**Displacement components (m)**			**Latency**
	X	Y	Z	East	North	UP	Seconds
Mean	4455840	3127069	3314439	0.513164	0.584668	9.257824	16.29189
Standard deviation	4.151763	3.065962	3.185033	1.767017	2.171701	5.379876	0.413921
Minimum	4455775	3127018	3314419	-31.7181	-6.7302	-58.6254	15.23
Maximum	4455924	3127093	3314522	20.2362	47.7223	121.8743	22.19

Table C.21 Summary of 5-centimeters Vertical Displacement Experiment at 35 Degrees Elevation Angle with Low Latency Stream.

Start date			**End date**			**Duration (hours)**	**# of events**
2022-06-01 19:21:32			2022-06-02 17:13:44			24	64932
	Coordinates components (m)			**Displacement components (m)**			**Latency**
	X	Y	Z	East	North	UP	Seconds
Mean	4455833	3127064	3314434	0.225006	0.430404	0.102917	17.88131
Standard deviation	5.954902	3.139596	4.240767	1.448775	2.178393	7.513833	1.606805
Minimum	4455782	3127041	3314404	-7.1054	-8.1726	-61.8903	13.07
Maximum	4455863	3127076	3314452	12.4112	22.5045	30.7973	72.32

Table C.22 Summary of 10-centimeters Vertical Displacement Experiment at 35 Degrees Elevation Angle with Low Latency Stream.

Start date			End date			Duration (hours)	# of events
2022-06-02 17:16:05			2022-06-03 11:43:49			24	78459
	Coordinates components (m)			Displacement components (m)			Latency
	X	Y	Z	East	North	UP	Seconds
Mean	4455834	3127064	3314433	0.107126	-0.05636	0.461612	13.98343
Standard deviation	1.342718	1.189053	1.006635	0.394334	0.710793	1.889267	0.366688
Minimum	4455791	3127041	3314385	-10.7442	-16.082	-66.2931	13.13
Maximum	4455900	3127100	3314509	6.4745	25.2916	104.1646	16.49

Table C.23 Summary of 15-centimeters Vertical Displacement Experiment at 35 Degrees Elevation Angle with Low Latency Stream.

Start date			End date			Duration (hours)	# of events
2022-06-02 17:15:59			2022-06-03 11:43:49			24	78459
	Coordinates components (m)			Displacement components (m)			Latency
	X	Y	Z	East	North	UP	Seconds
Mean	4455834	3127064	3314433	0.107126	-0.05636	0.461612	13.98343
Standard deviation	1.342718	1.189053	1.006635	0.394334	0.710793	1.889267	0.366688
Minimum	4455791	3127041	3314385	-10.7442	-16.082	-66.2931	13.13
Maximum	4455900	3127100	3314509	6.4745	25.2916	104.1646	16.49

Table C.24 Summary of 20-centimeters Vertical Displacement Experiment at 35 Degrees Elevation Angle with Low Latency Stream.

Start date			End date			Duration (hours)	# of events
2022-06-03 11:48:10			2022-06-05 20:27:24			24	129253
	Coordinates components (m)			Displacement components (m)			Latency
	X	Y	Z	East	North	UP	Seconds
Mean	4455834	3127064	3314434	-0.0667	0.024515	0.71087	14.58299
Standard deviation	10.92347	4.749082	4.175151	2.644977	3.052653	11.95798	0.419664
Minimum	4455780	3127042	3314407	-200.84	-230.223	-57.3805	13.58

Maximum	4456658	3127397	3314694	13.1252	15.0331	875.4229	19.76

Table C.25 Summary of 1-centimeter Horizontal Displacement Experiment at 10 Degrees Elevation Angle with Low Latency Stream.

Start date			**End date**			**Duration (hours)**	**# of events**
2021-12-11 09:28:35			2021-12-12 05:39:15			24	86329
	Coordinates components (m)			**Displacement components (m)**			**Latency**
	X	Y	Z	East	North	UP	Seconds
Mean	4455834	3127064	3314433	-0.06711	-0.00829	-0.16057	10.27278
Standard deviation	0.707706	0.978578	0.718171	0.411027	0.156245	1.334495	574.1009
Minimum	4455825	3127049	3314414	-10.2905	-10.4504	-18.7129	-43180.7
Maximum	4455834	3127064	3314433	0.0589	0.3347	0.2045	32.42

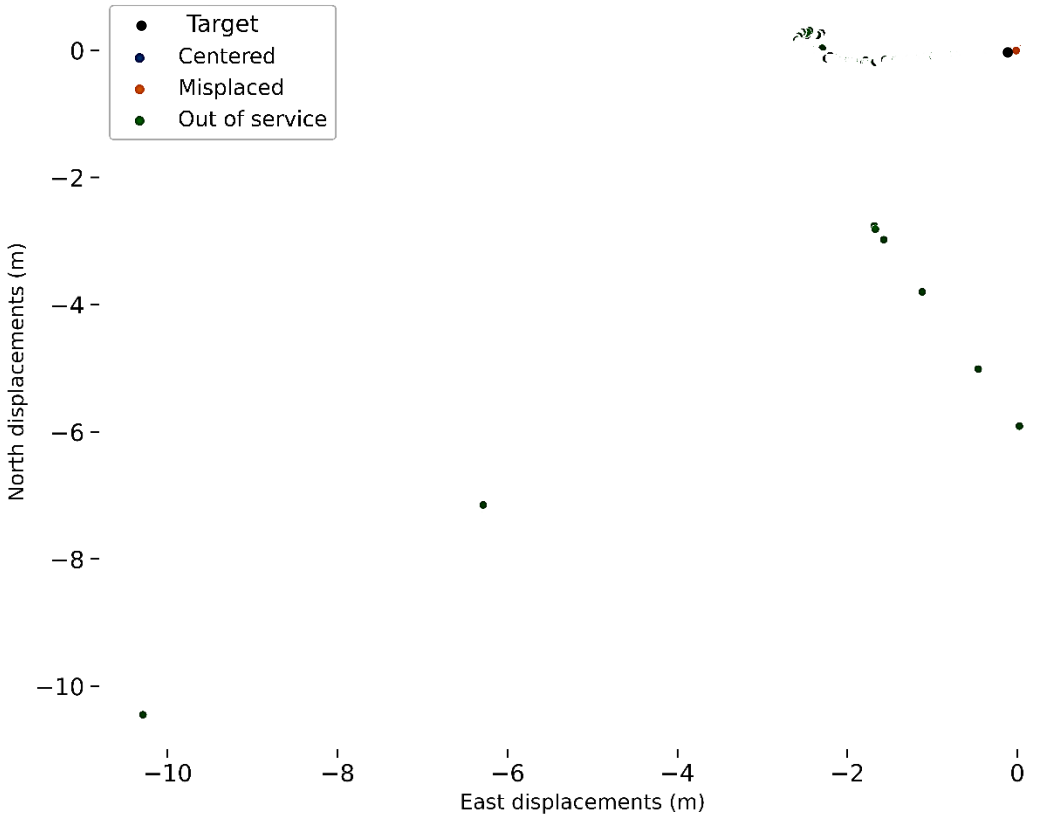

Figure C.1 Displacements scatter plot with 10 degrees elevation angle and 1 cm level of horizontal level of utilizing low latency stream displacements (Prepared by the author).

Table C.26 Summary of 2.5-centimeters Horizontal Displacement Experiment at 10 Degrees Elevation Angle with Low Latency Stream.

Start date			End date			Duration (hours)	# of events
2021-12-13 06:21:39			2021-12-14 07:37:04			12	110747
	Coordinates components (m)			Displacement components (m)			Latency
	X	Y	Z	East	North	UP	Seconds
Mean	4455834	3127064	3314433	0.143379	-0.01008	0.328474	13.80747
Standard deviation	1.045623	1.773098	0.373441	0.864627	0.730818	1.759258	0.345345
Minimum	4455833	3127064	3314433	-0.0784	-9.3509	-0.2944	13.09
Maximum	4455847	3127086	3314437	11.0111	0.8681	21.7322	26.38

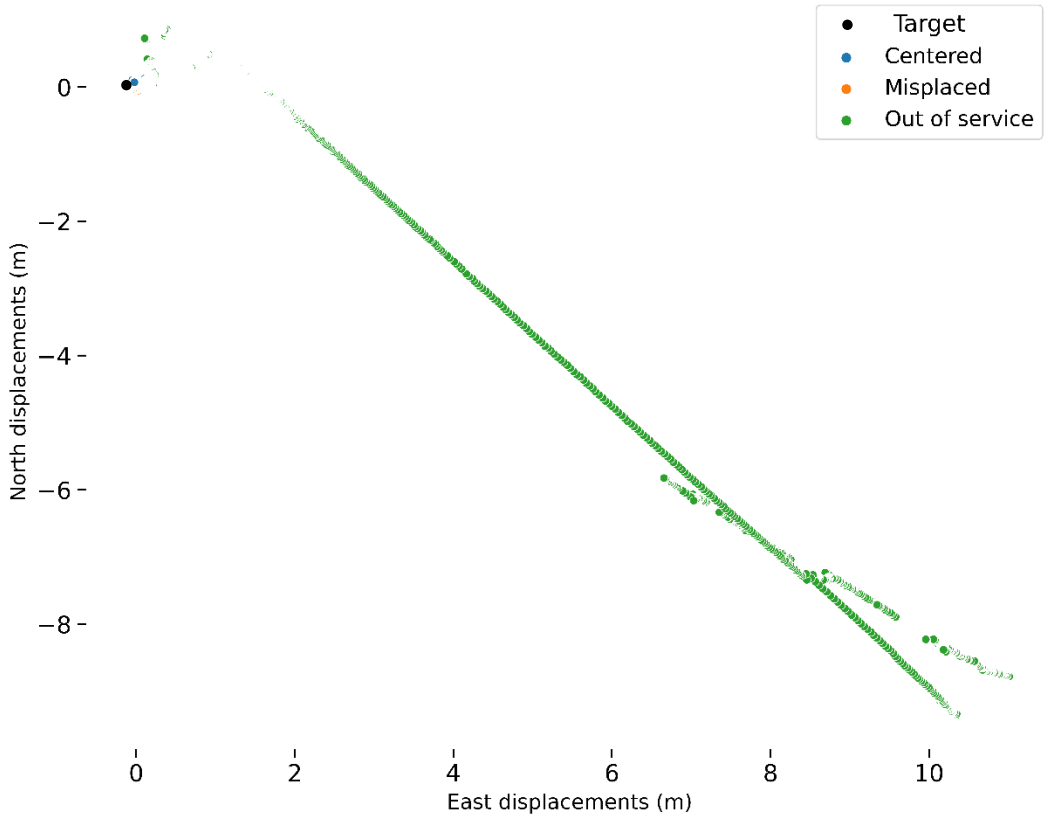

Figure C.2 Displacements scatter plot with 10 degrees elevation angle and 2.5 cm level of horizontal level of displacements utilizing low latency stream (Prepared by the author).

Table C.27 Summary of 3.75-centimeters Horizontal Displacement Experiment at 10 Degrees Elevation Angle with Low Latency Stream.

Start date			End date			Duration (hours)	# of events
2021-11-25 16:05:40			2021-11-26 19:53:14			24	118805
	Coordinates components (m)			Displacement components (m)			Latency
	X	Y	Z	East	North	UP	Seconds
Mean	4455834	3127064	3314433	0.014421	-0.00946	0.029126	17.73743
Standard deviation	0.037035	0.036134	0.029658	0.030585	0.024225	0.045107	0.420607
Minimum	4455834	3127064	3314433	-0.0612	-0.0847	-0.1027	16.78
Maximum	4455834	3127064	3314433	0.1272	0.0634	0.1825	20

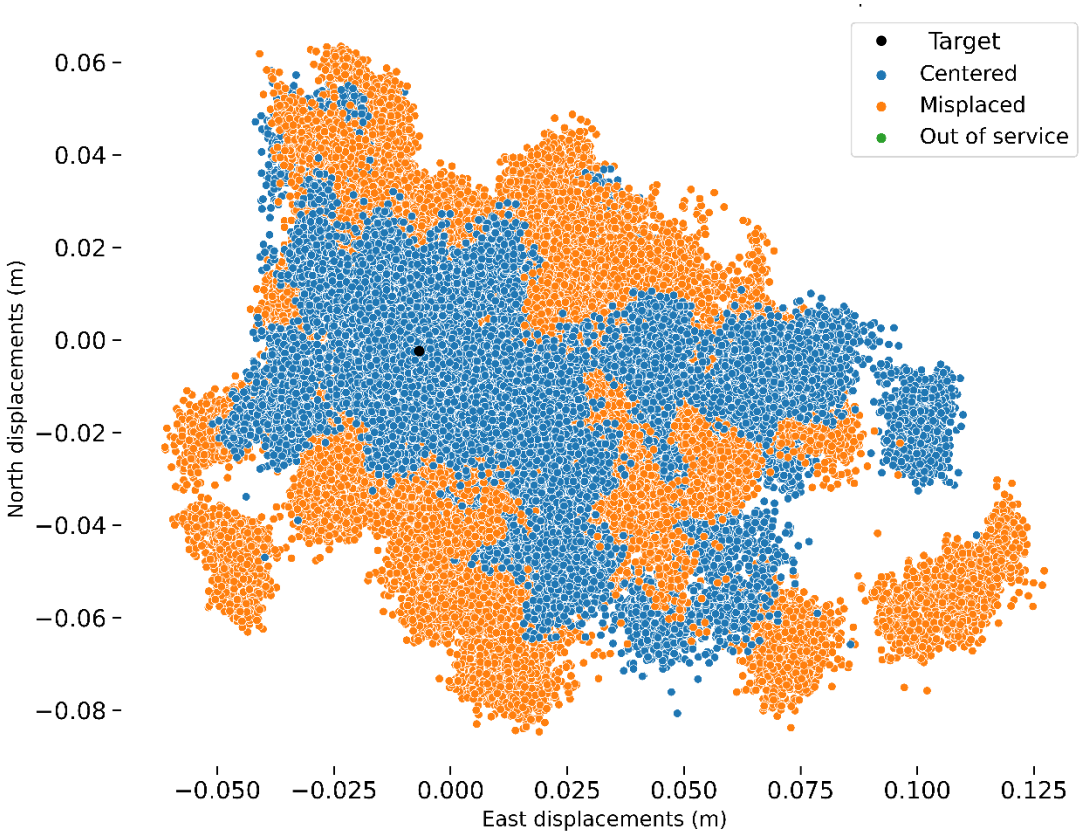

Figure C.3 Displacements scatter plot with 10 degrees elevation angle and 3.75 cm level of horizontal level of displacements utilizing low latency stream (Prepared by the author).

Table C.28 Summary of 5-centimeters Horizontal Displacement Experiment at 10 Degrees Elevation Angle with Low Latency Stream.

Start date			End date			Duration (hours)	# of events
2021-11-22 13:08:04			2021-11-23 13:09:09			24	101285
	Coordinates components (m)			Displacement components (m)			Latency
	X	Y	Z	East	North	UP	Seconds
Mean	4455834	3127064	3314433	-0.01151	-0.00934	0.034933	15.6045
Standard deviation	0.047032	0.046053	0.033577	0.039287	0.032245	0.05364	0.366666
Minimum	4455834	3127064	3314433	-0.1435	-0.1271	-0.1191	14.75
Maximum	4455834	3127064	3314433	0.1102	0.098	0.2405	19.23

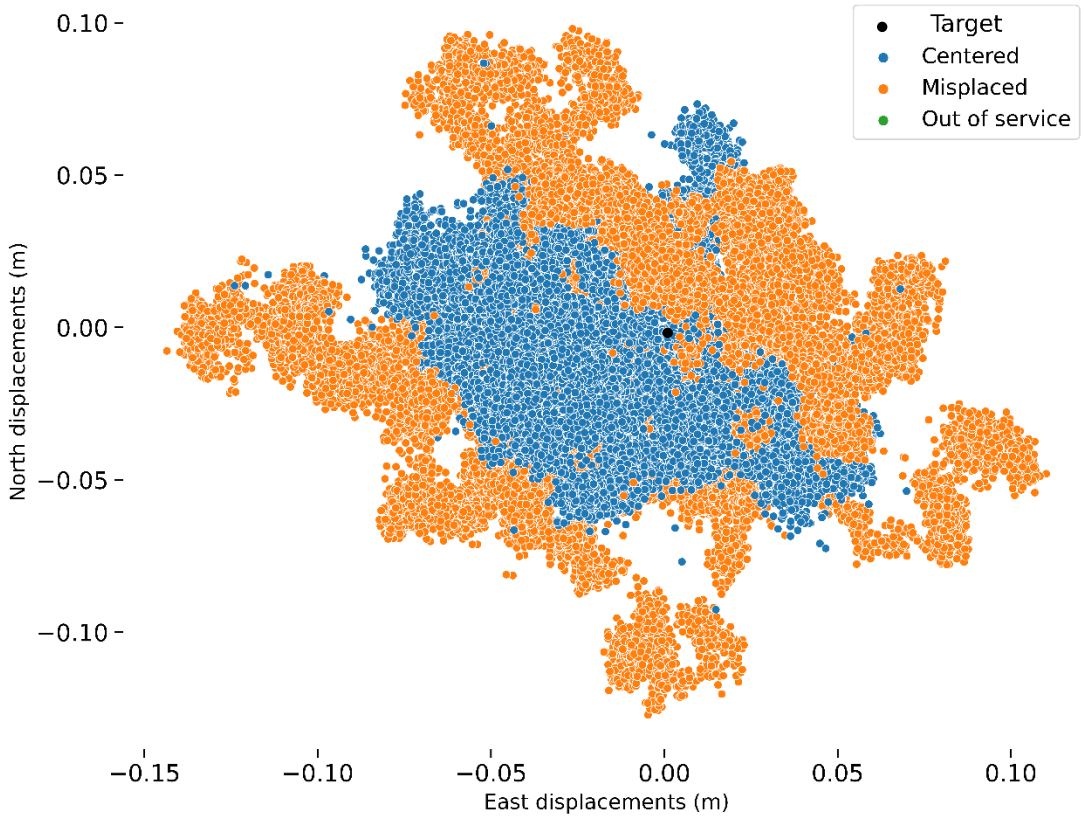

Figure C.4 Displacements scatter plot with 10 degrees elevation angle and 5 cm level of horizontal level of displacements utilizing low latency stream (Prepared by the author).

Table C.29 Summary of 10-centimeters Horizontal Displacement Experiment at 10 Degrees Elevation Angle with Low Latency Stream.

Start date			End date			Duration (hours)	# of events
2021-11-10 18:18:55			2021-11-11 18:29:19			24	101966
	Coordinates components (m)			Displacement components (m)			Latency
	X	Y	Z	East	North	UP	Seconds
Mean	4455834	3127064	3314433	0.001772	-0.00703	0.035038	14.28755
Standard deviation	0.061238	0.064737	0.050423	0.067076	0.05655	0.052785	0.411958
Minimum	4455833	3127064	3314433	-0.1949	-0.198	-0.0787	13.3
Maximum	4455834	3127064	3314433	0.1799	0.1556	0.3327	21.59

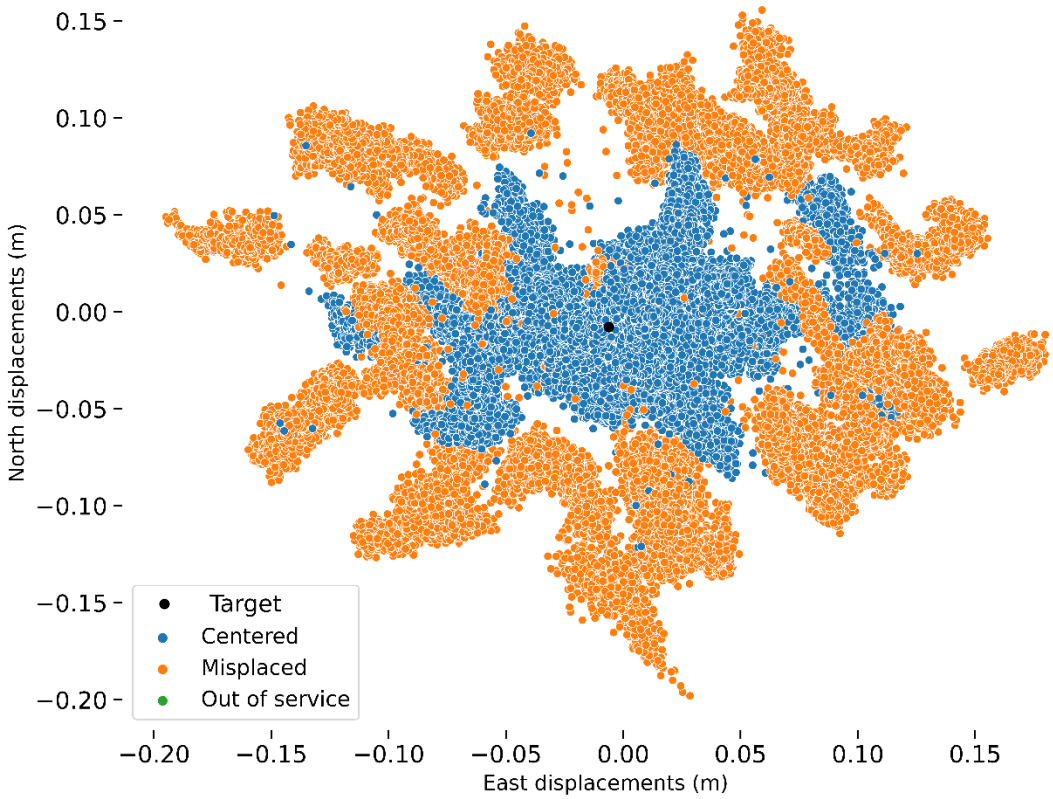

Figure C.5 Displacements scatter plot with 10 degrees elevation angle and 10 cm level of horizontal level of displacements utilizing low latency stream (Prepared by the author).

Table C.30 Summary of 15-centimeters Horizontal Displacement Experiment at 10 Degrees Elevation Angle with Low Latency Stream.

Start date			End date			Duration (hours)	# of events
2021-11-09 18:01:55			2021-11-10 18:15:59			24	102431
	Coordinates components (m)			Displacement components (m)			Latency
	X	Y	Z	East	North	UP	Seconds
Mean	4455834	3127064	3314433	0.010344	0.00049	0.024361	15.13536
Standard deviation	0.070502	0.080665	0.067658	0.091327	0.074185	0.047021	0.407814
Minimum	4455833	3127064	3314433	-0.2113	-0.181	-0.1183	14.18
Maximum	4455834	3127064	3314433	0.2375	0.1782	0.2245	16.69

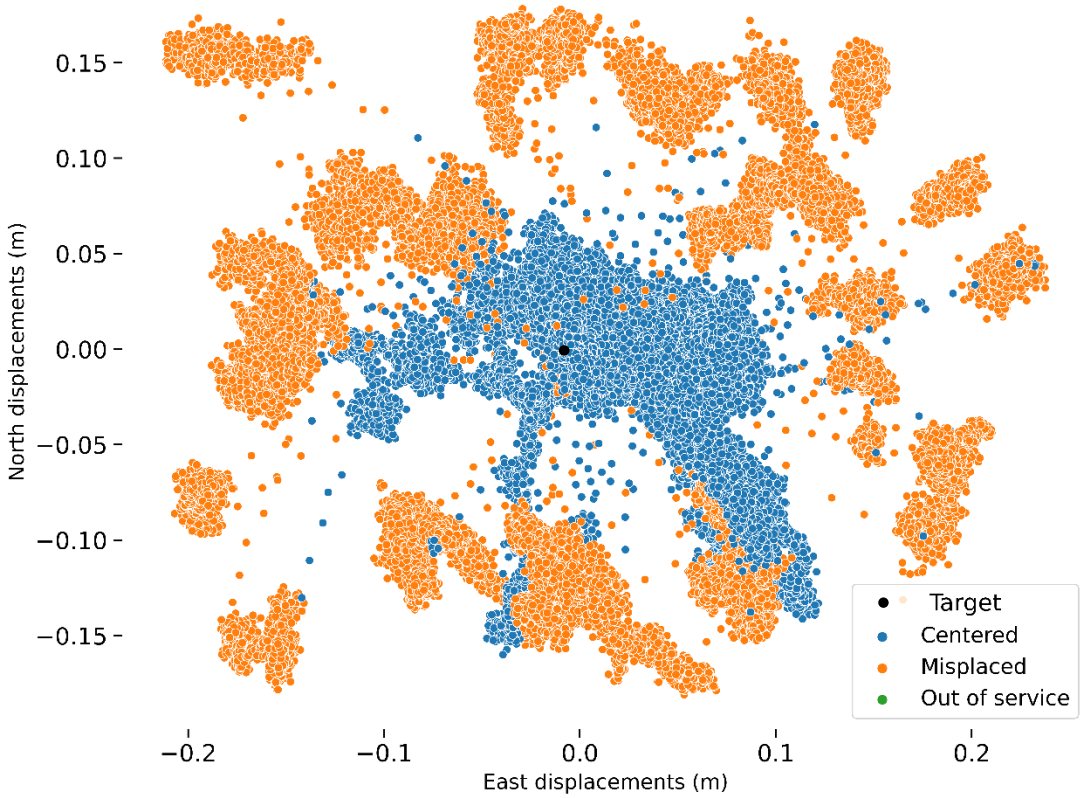

Figure C.6 Displacements scatter plot with 10 degrees elevation angle and 15 cm level of horizontal level of displacements utilizing low latency stream (Prepared by the author).

Table C.31 Summary of 20-centimeters Horizontal Displacement Experiment at 10 Degrees Elevation Angle with Low Latency Stream.

Start date			End date			Duration (hours)	# of events
2021-11-07 16:01:10			2021-11-08 15:46:59			24	99132
	Coordinates components (m)			Displacement components (m)			Latency
	X	Y	Z	East	North	UP	Seconds
Mean	4455834	3127064	3314433	0.009139	0.024356	0.033876	14.48738
Standard deviation	0.086693	0.099302	0.08685	0.114423	0.098265	0.046594	0.478253
Minimum	4455833	3127064	3314433	-0.3981	-0.2087	-0.1216	13.59
Maximum	4455834	3127064	3314433	0.3182	0.2345	0.1625	25.57

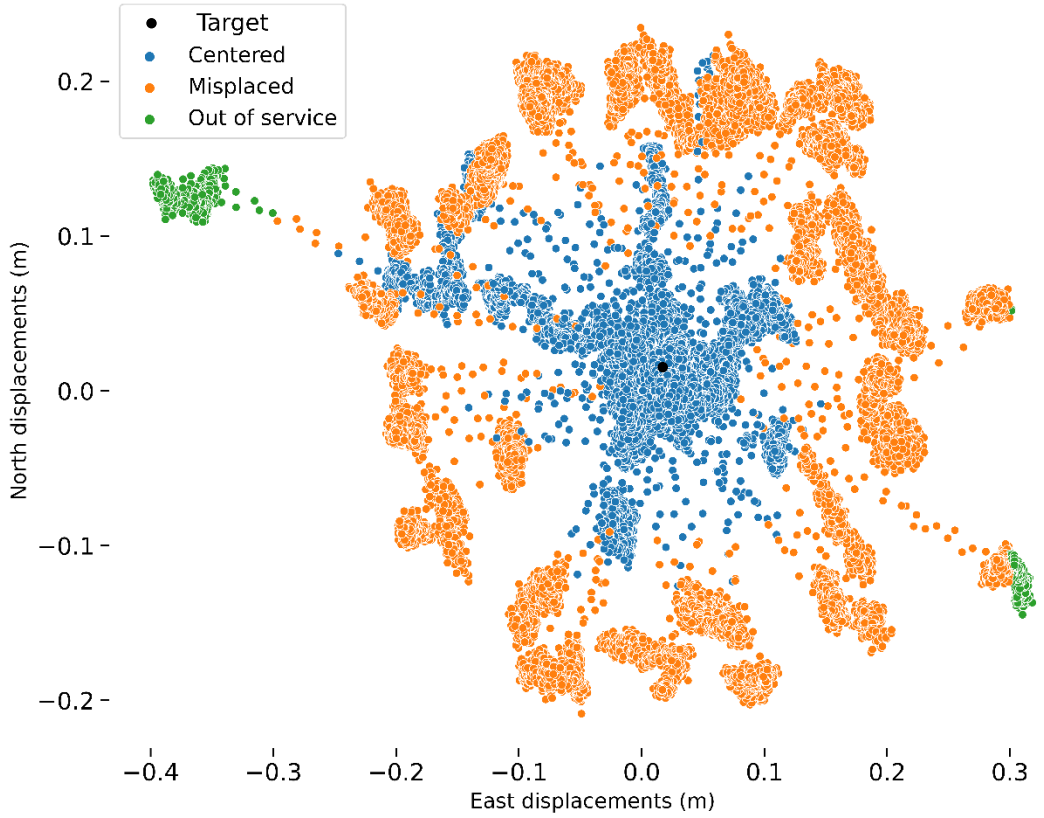

Figure C.7 Displacements scatter plot with 10 degrees elevation angle and 20 cm level of horizontal level of displacements utilizing low latency stream (Prepared by the author).

Table C.32 Summary of 2.5-centimeters Horizontal Displacement Experiment at 10 Degrees Elevation Angle with Low Latency Stream.

Start date			End date			Duration (hours)	# of events
2021-12-03 12:21:58			2021-12-04 14:09:54			12	32658
	Coordinates components (m)			Displacement components (m)			Latency
	X	Y	Z	East	North	UP	Seconds
Mean	4455834	3127064	3314433	-0.00093	0.000469	0.044786	20.96389
Standard deviation	0.030488	0.028058	0.025775	0.019475	0.019166	0.040429	0.290743
Minimum	4455834	3127064	3314433	-0.0578	-0.0605	-0.0566	19.71
Maximum	4455834	3127064	3314433	0.0467	0.0488	0.1949	22.01

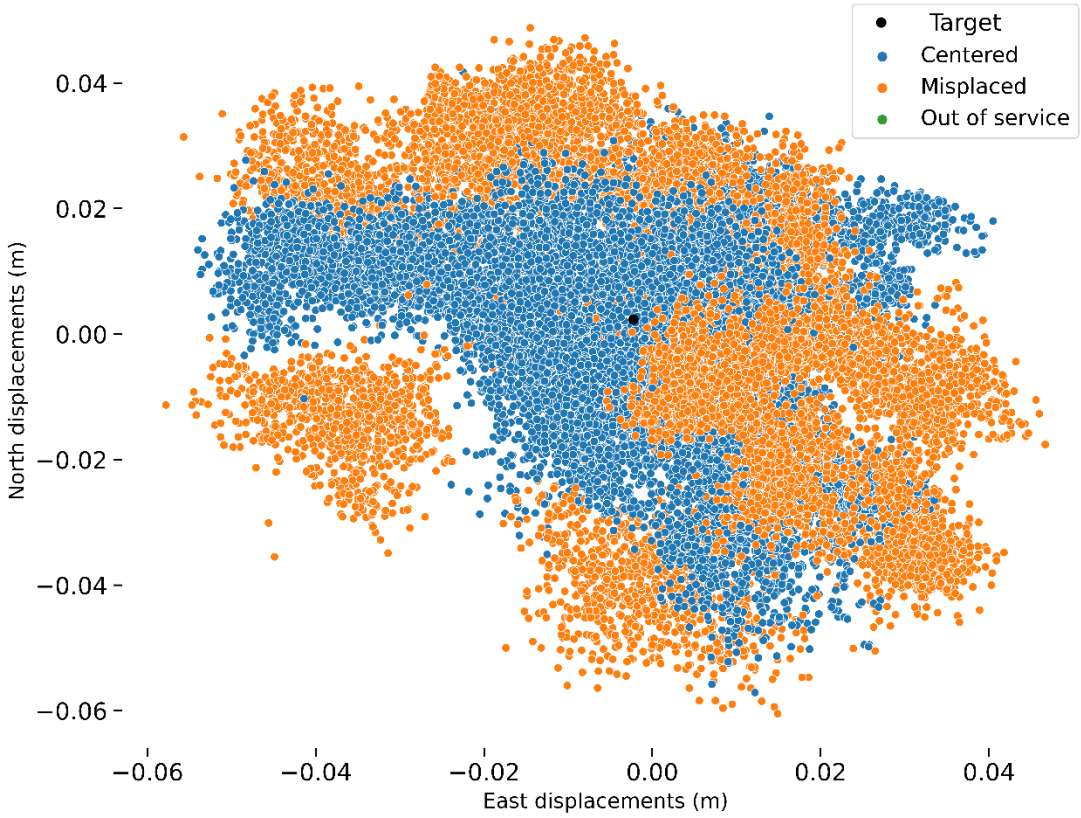

Figure C.8 Displacements scatter plot with 10 degrees elevation angle and 2.5 cm level of horizontal level of displacements utilizing low latency stream (Prepared by the author).

Table C.33 Summary of 5-centimeters 3D Displacement Experiment at 10 Degrees Elevation Angle with High Latency Stream.

Start date			End date			Duration (hours)	# of events
2022-04-25 13:34:30			2022-04-26 14:07:49			24	88240
	Coordinates components (m)			Displacement components (m)			Latency
	X	Y	Z	East	North	UP	Seconds
Mean	4455834	3127064	3314433	-0.02196	-0.02942	-0.04366	31.01398
Standard deviation	0.308418	0.319843	0.693897	0.13111	0.452082	0.676274	0.292615
Minimum	4455826	3127061	3314422	-1.2333	-7.0505	-11.9099	30.43
Maximum	4455834	3127064	3314433	1.7613	0.7608	0.6766	37

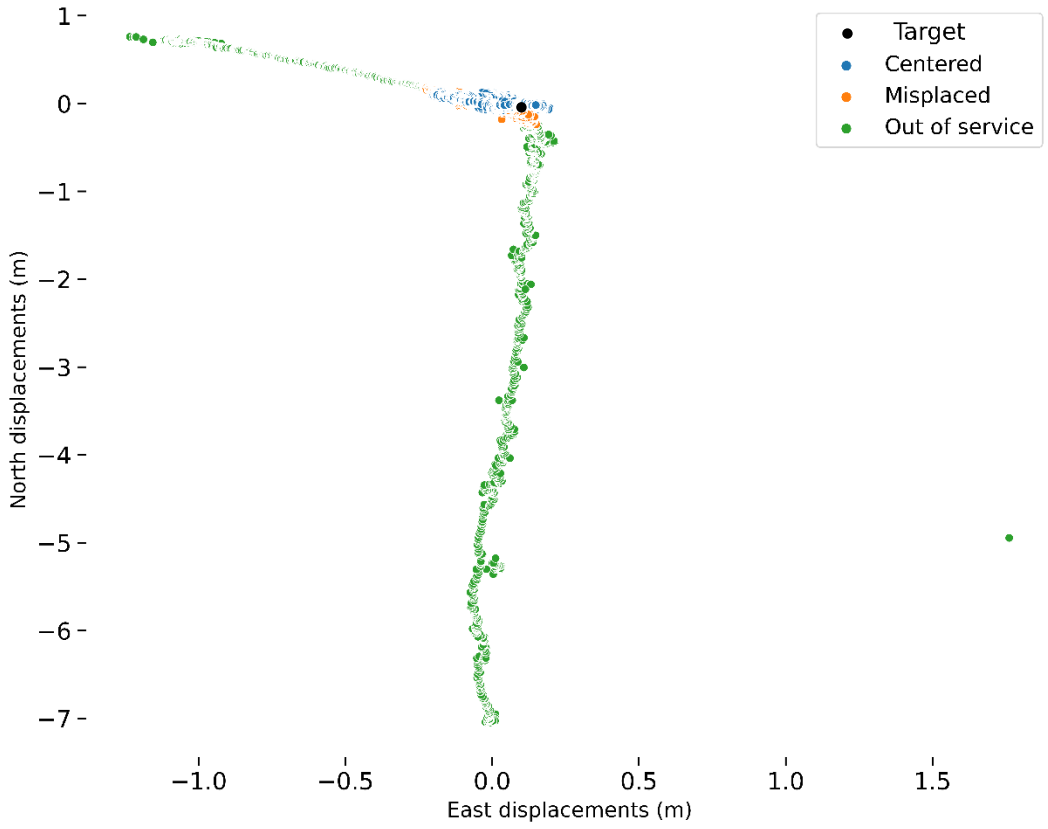

Figure C.9 Displacements scatter plot with 10 degrees elevation angle and 5 cm level of horizontal level of displacements utilizing high latency stream (Prepared by the author).

Table C.34 Summary of 10-centimeters 3D Displacement Experiment at 10 Degrees Elevation Angle with High Latency Stream.

Start date			End date			Duration (hours)	# of events
2022-04-26 14:10:14			2022-04-27 14:36:29			24	83653
	Coordinates components (m)			Displacement components (m)			Latency
	X	Y	Z	East	North	UP	Seconds
Mean	4455834	3127064	3314433	0.018351	-0.00261	0.081394	31.81533
Standard deviation	0.248318	0.172243	0.160761	0.126162	0.106918	0.299708	0.332173
Minimum	4455833	3127063	3314432	-0.5706	-0.2796	-1.5281	31.2
Maximum	4455834	3127064	3314434	0.2863	0.4008	0.548	38.67

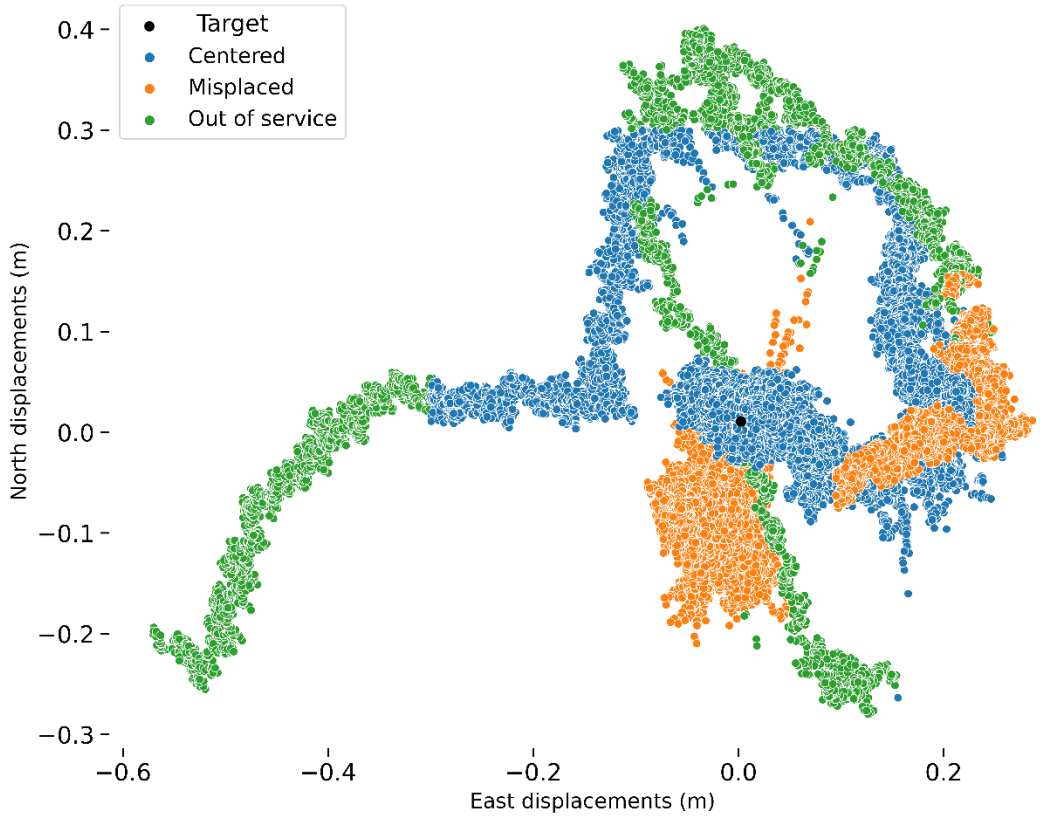

Figure C.10 Displacements scatter plot with 10 degrees elevation angle and 10 cm level of horizontal level of displacements utilizing high latency stream (Prepared by the author).

Table C.35 Summary of 15-centimeters 3D Displacement Experiment at 10 Degrees Elevation Angle with High Latency Stream.

Start date			End date			Duration (hours)	# of events
2022-04-29 14:04:09			2022-04-30 15:13:39			24	90571
	Coordinates components (m)			Displacement components (m)			Latency
	X	Y	Z	East	North	UP	Seconds
Mean	4455833	3127064	3314433	0.045046	0.06923	-0.36612	29.10894
Standard deviation	1.395828	0.759296	0.369582	0.26258	0.55865	1.510106	1.557864
Minimum	4455825	3127060	3314430	-0.346	-0.7671	-9.4335	26.37
Maximum	4455834	3127064	3314433	2.3668	2.8233	0.3718	36.19

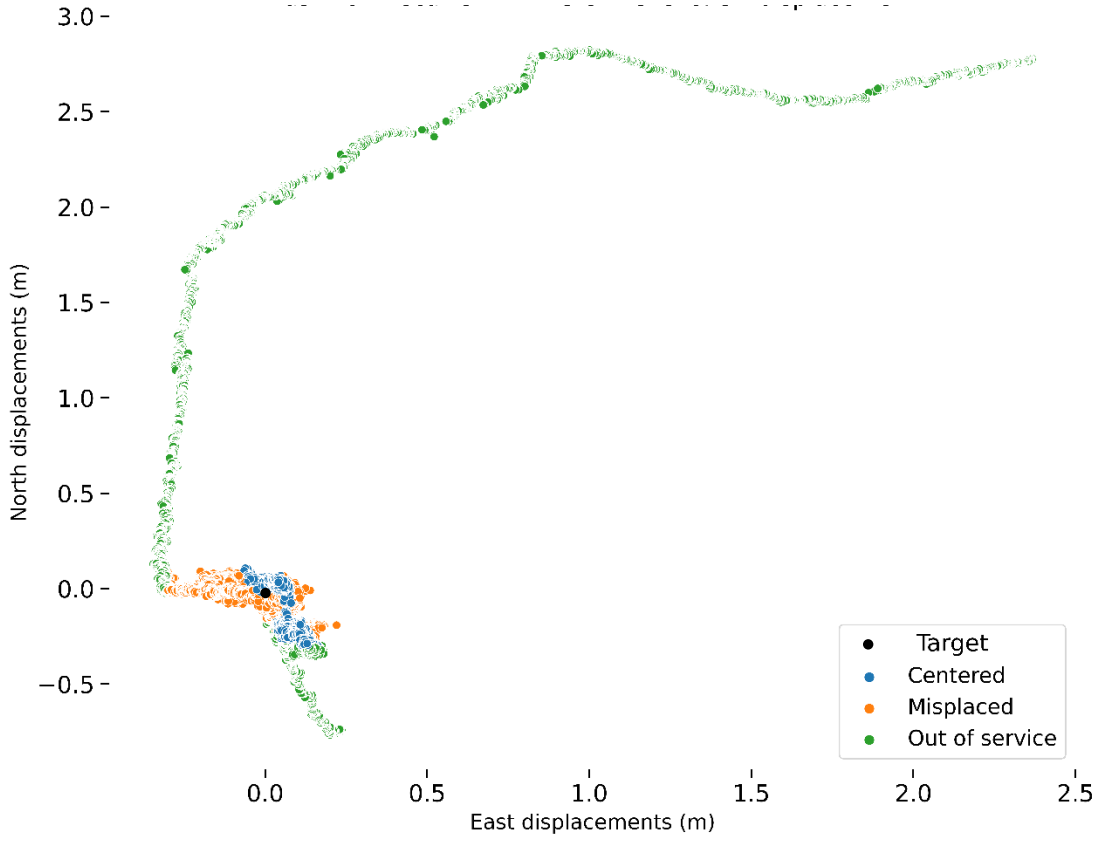

Figure C.11 Displacements scatter plot with 10 degrees elevation angle and 15 cm level of horizontal level of displacements utilizing high latency stream (Prepared by the author).

Table C.36 Summary of 20-centimeters 3D Displacement Experiment at 10 Degrees Elevation Angle with High Latency Stream.

Start date			End date			Duration (hours)	# of events
2022-04-30 15:16:37			2022-05-01 11:21:59			24	70360
	Coordinates components (m)			Displacement components (m)			Latency
	X	Y	Z	East	North	UP	Seconds
Mean	4455834	3127064	3314433	0.086744	-0.04921	0.025967	18.09761
Standard deviation	0.198527	0.104074	0.213227	0.141992	0.150701	0.229865	714.4931
Minimum	4455833	3127064	3314433	-0.4937	-0.5482	-0.3683	-43172
Maximum	4455834	3127065	3314435	0.5271	1.2406	1.8662	42.09

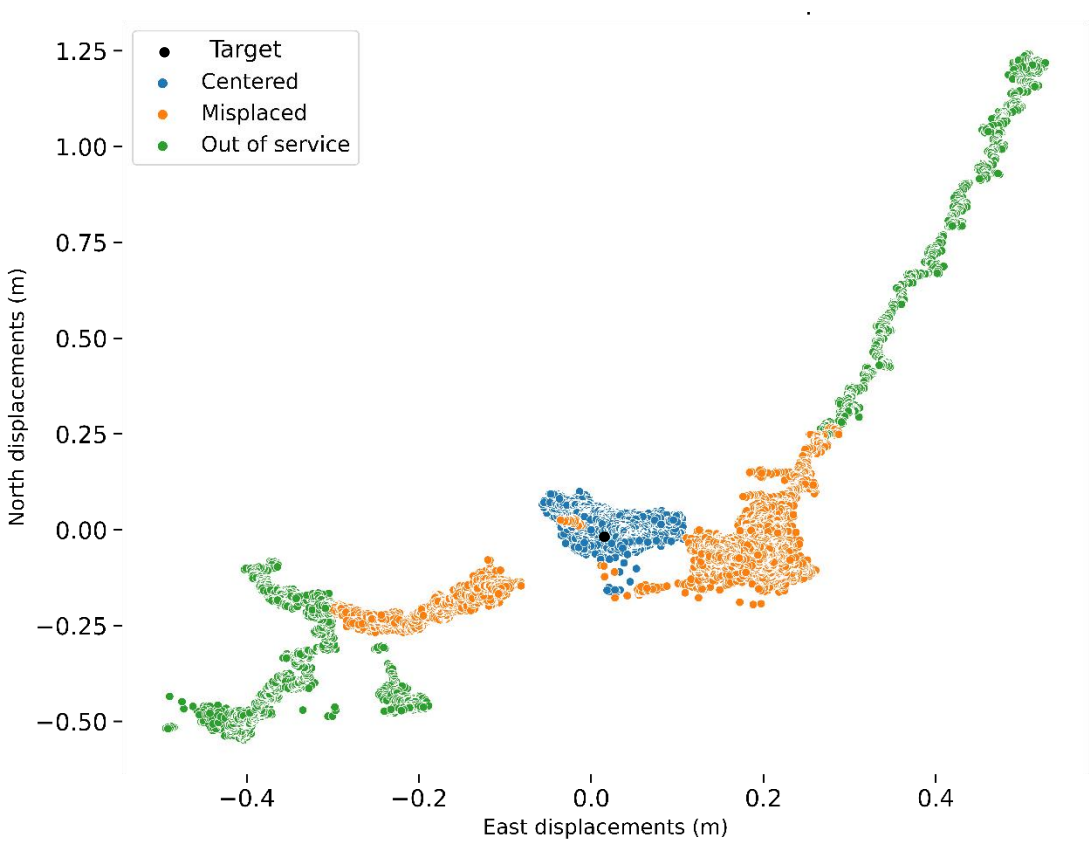

Figure C.12 Displacements scatter plot with 10 degrees elevation angle and 20 cm level of horizontal level of displacements utilizing high latency stream (Prepared by the author).

Table C.37 Summary of 5-centimeters 3D Displacement Experiment at 10 Degrees Elevation Angle with Low Latency Stream.

Start date			End date			Duration (hours)	# of events
2022-05-01 14:32:32			2022-05-02 18:31:39			24	119907
	Coordinates components (m)			Displacement components (m)			Latency
	X	Y	Z	East	North	UP	Seconds
Mean	4455834	3127064	3314433	0.056777	0.010119	0.166886	15.05893
Standard deviation	0.401216	0.55868	0.769778	0.323504	0.541513	0.817169	0.437964
Minimum	4455827	3127059	3314420	-1.424	-7.3351	-13.3442	14.02
Maximum	4455840	3127071	3314443	3.8725	5.027	10.8071	19.84

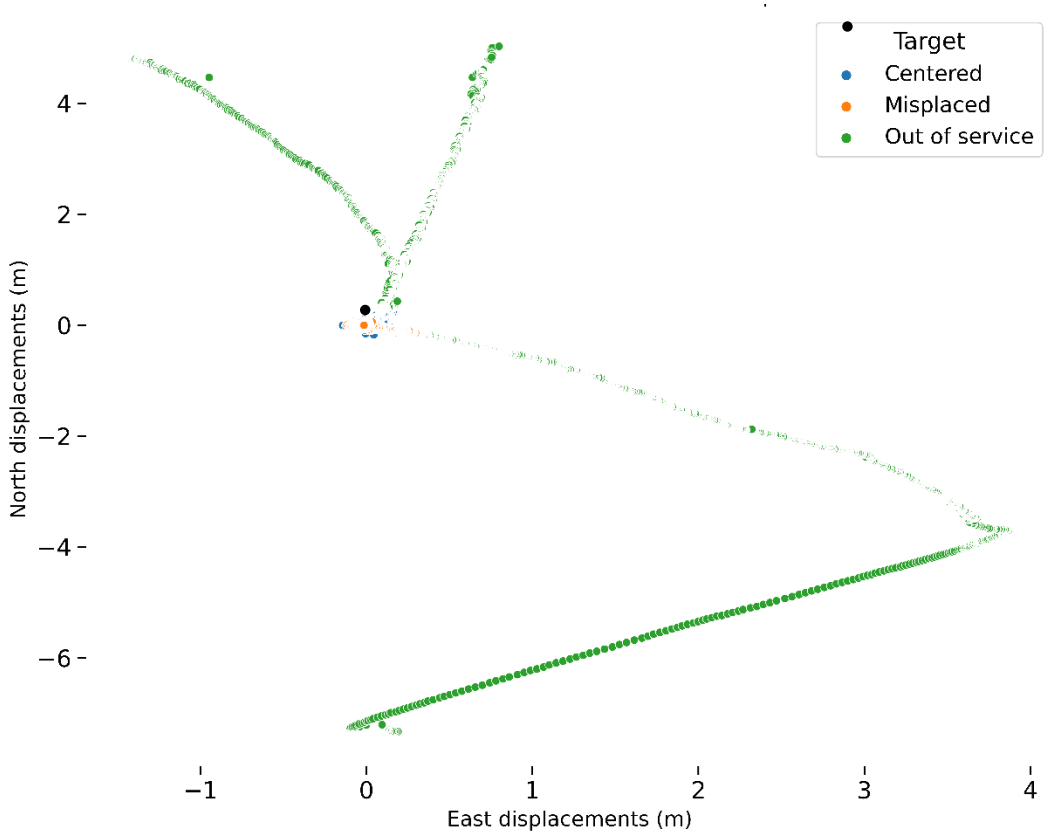

Figure C.13 Displacements scatter plot with 10 degrees elevation angle and 5 cm 3D level of displacements utilizing low latency stream (Prepared by the author).

Table C.38 Summary of 10-centimeters 3D Displacement Experiment at 10 Degrees Elevation Angle with Low Latency Stream.

Start date			End date			Duration (hours)	# of events
2022-05-03 15:49:38			2022-05-04 14:01:09			24	95159
	Coordinates components (m)			Displacement components (m)			Latency
	X	Y	Z	East	North	UP	Seconds
Mean	4455834	3127064	3314433	0.071176	-0.00791	0.160085	16.91275
Standard deviation	0.066409	0.069144	0.048734	0.048727	0.027316	0.091901	0.477276
Minimum	4455834	3127064	3314433	-0.0792	-0.2626	-0.0669	15.81
Maximum	4455834	3127064	3314433	0.1741	0.1272	0.5323	29.84

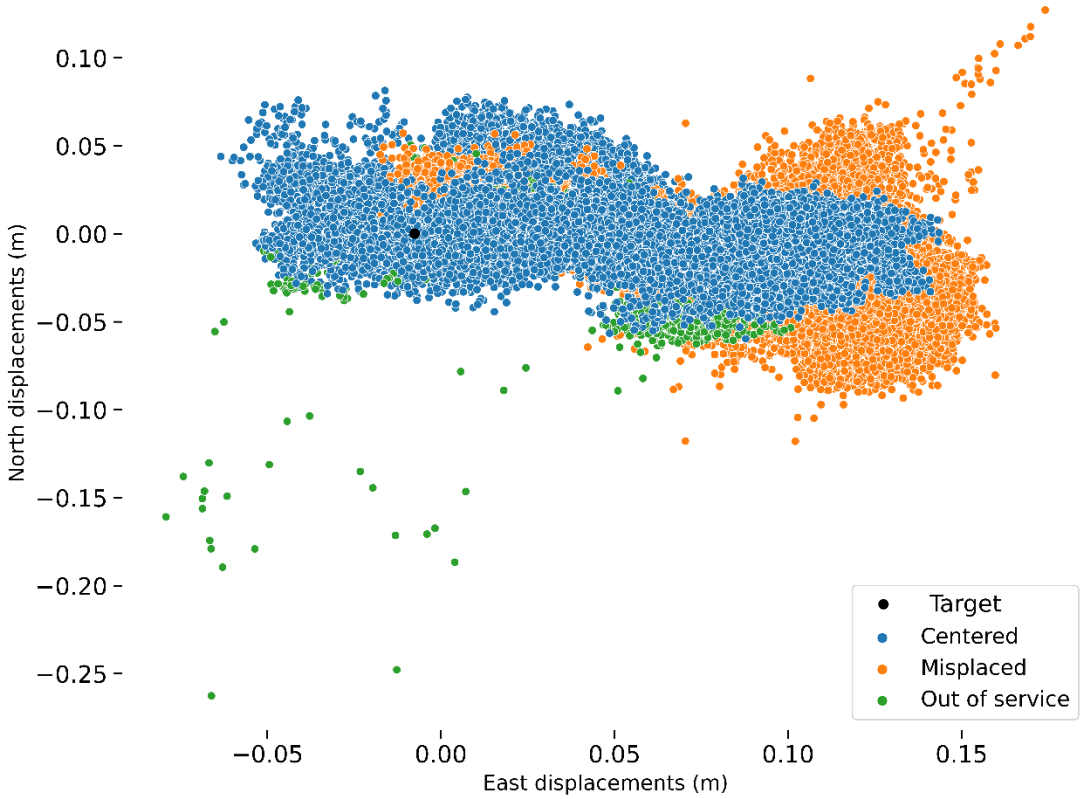

Figure C.14 Displacements scatter plot with 10 degrees elevation angle and 10 cm 3D level of displacements utilizing low latency stream (Prepared by the author).

Table C.39 Summary of 15-centimeters 3D Displacement Experiment at 10 Degrees Elevation Angle with Low Latency Stream.

Start date			End date			Duration (hours)	# of events
2022-05-04 14:02:43			2022-05-05 04:00:44			24	60023
	Coordinates components (m)			Displacement components (m)			Latency
	X	Y	Z	East	North	UP	Seconds
Mean	4455835	3127065	3314434	-0.00956	-0.19997	1.880901	17.74591
Standard deviation	2.41755	1.59551	1.561803	1.282906	0.344016	3.010852	0.374425
Minimum	4455833	3127063	3314433	-4.0596	-1.2468	-0.2881	16.88
Maximum	4455841	3127069	3314438	2.1907	4.1696	9.0074	20.63

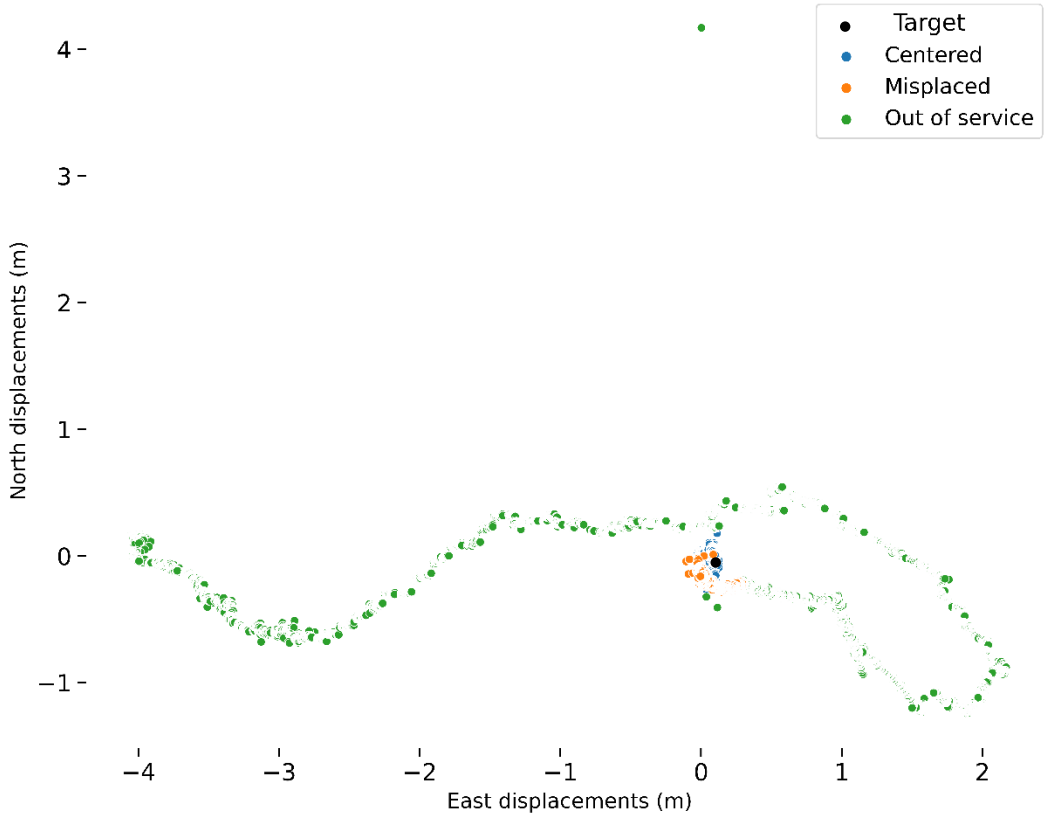

Figure C.15 Displacements scatter plot with 10 degrees elevation angle and 15 cm 3D level of displacements utilizing low latency stream (Prepared by the author).

Table C.40 Summary of 20-centimeters 3D Displacement Experiment at 10 Degrees Elevation Angle with Low Latency Stream.

Start date			End date			Duration (hours)	# of events
2022-05-05 08:57:02			2022-05-06 03:03:44			24	72139
	Coordinates components (m)			Displacement components (m)			Latency
	X	Y	Z	East	North	UP	Seconds
Mean	4455833	3127064	3314433	0.045195	-0.08962	-0.40881	17.67635
Standard deviation	1.31232	0.890442	0.522274	1.405339	0.181602	0.883111	0.456096
Minimum	4455810	3127045	3314413	-18.2733	-6.0178	-29.2972	16.65
Maximum	4455843	3127067	3314442	11.2932	3.7383	11.5518	31.44

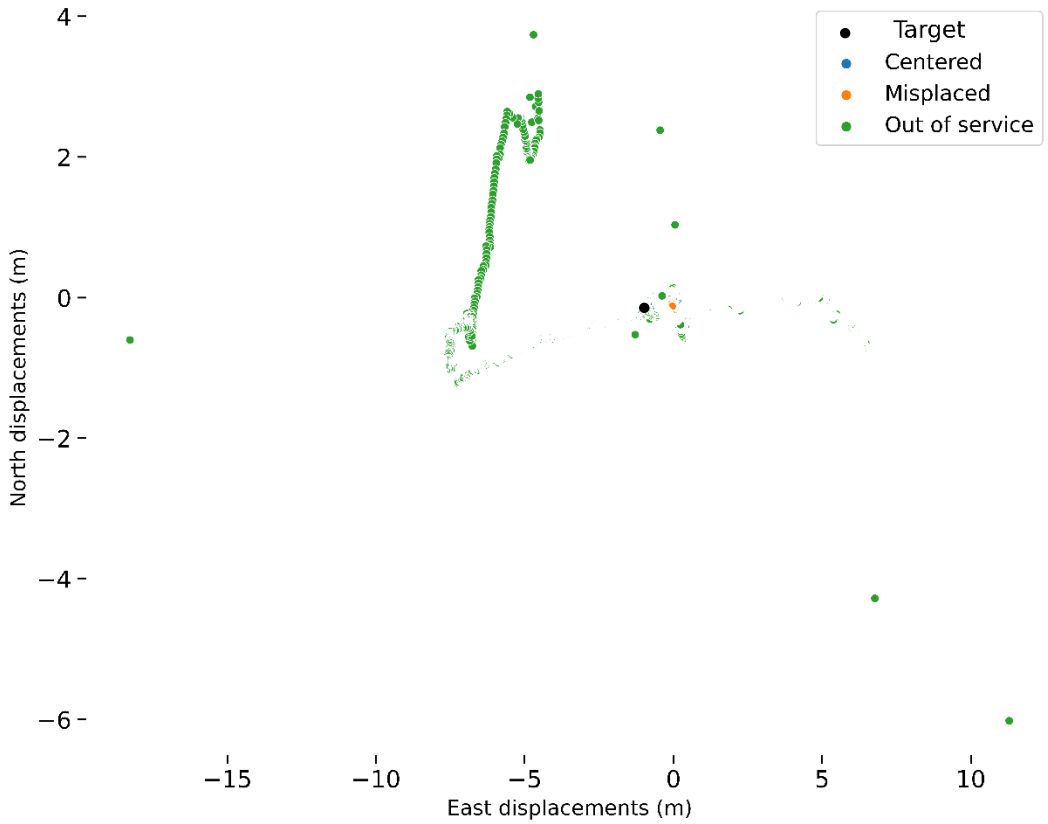

Figure C.16 Displacements scatter plot with 10 degrees elevation angle and 20 cm 3D level of displacements utilizing low latency stream (Prepared by the author).

Table C.41 Summary of 5-centimeters 3D Displacement Experiment at 20 Degrees Elevation Angle with Low Latency Stream.

Start date			End date			Duration (hours)	# of events
2022-05-06 05:52:46			2022-05-07 13:07:54			24	133805
	Coordinates components (m)			Displacement components (m)			Latency
	X	Y	Z	East	North	UP	Seconds
Mean	4455833	3127064	3314433	0.249996	0.250344	0.03682	18.5228
Standard deviation	2.343049	1.227136	1.297722	1.285896	0.842386	2.513301	0.497258
Minimum	4455817	3127057	3314426	-5.2591	-4.8471	-15.289	17.32
Maximum	4455852	3127075	3314450	9.9174	8.2146	22.5322	28.16

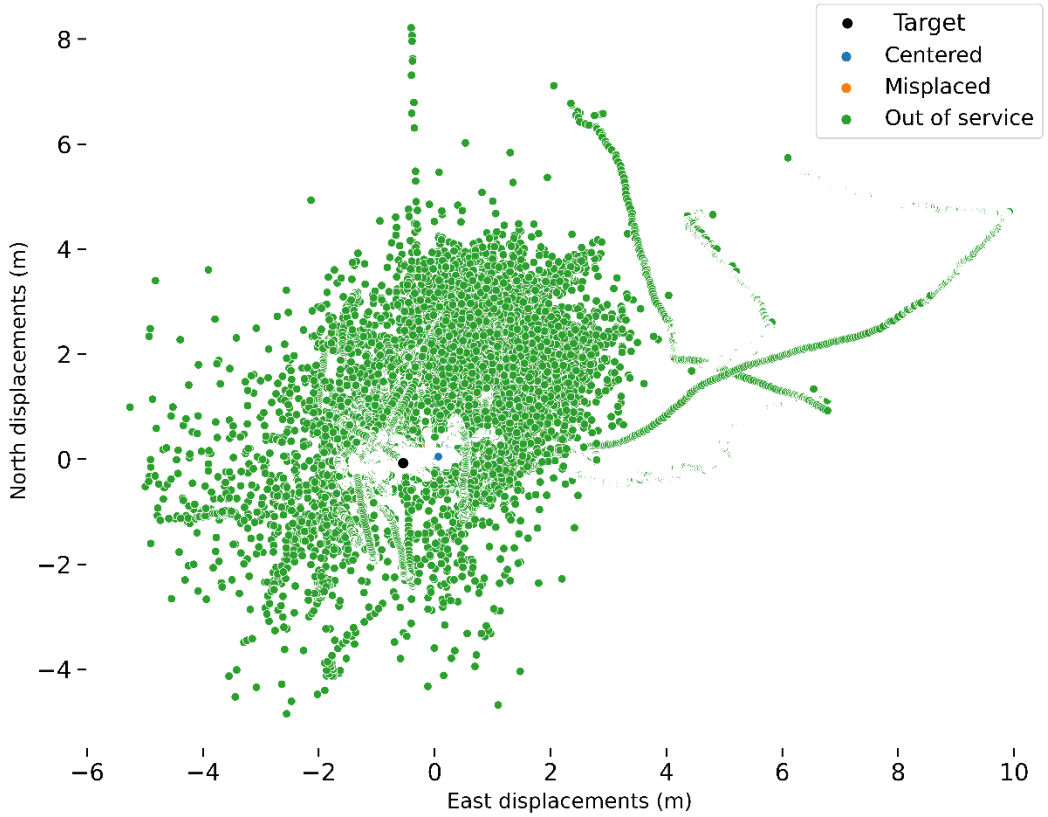

Figure C.17 Displacements scatter plot with 20 degrees elevation angle and 5 cm 3D level of displacements utilizing low latency stream (Prepared by the author).

Table C.42 Summary of 10-centimeters 3D Displacement Experiment at 20 Degrees Elevation Angle with Low Latency Stream.

Start date			End date			Duration (hours)	# of events
2022-05-07 13:10:23			2022-05-08 13:49:49			24	105561
	Coordinates components (m)			Displacement components (m)			Latency
	X	Y	Z	East	North	UP	Seconds
Mean	4455834	3127064	3314434	-0.00237	0.040684	0.57713	12.00734
Standard deviation	3.054439	1.613576	2.128646	0.827874	0.882288	3.873054	539.1399
Minimum	4455822	3127058	3314425	-10.4139	-12.1656	-12.4972	-43180.6
Maximum	4455884	3127111	3314463	9.7629	12.6535	72.6273	24.96

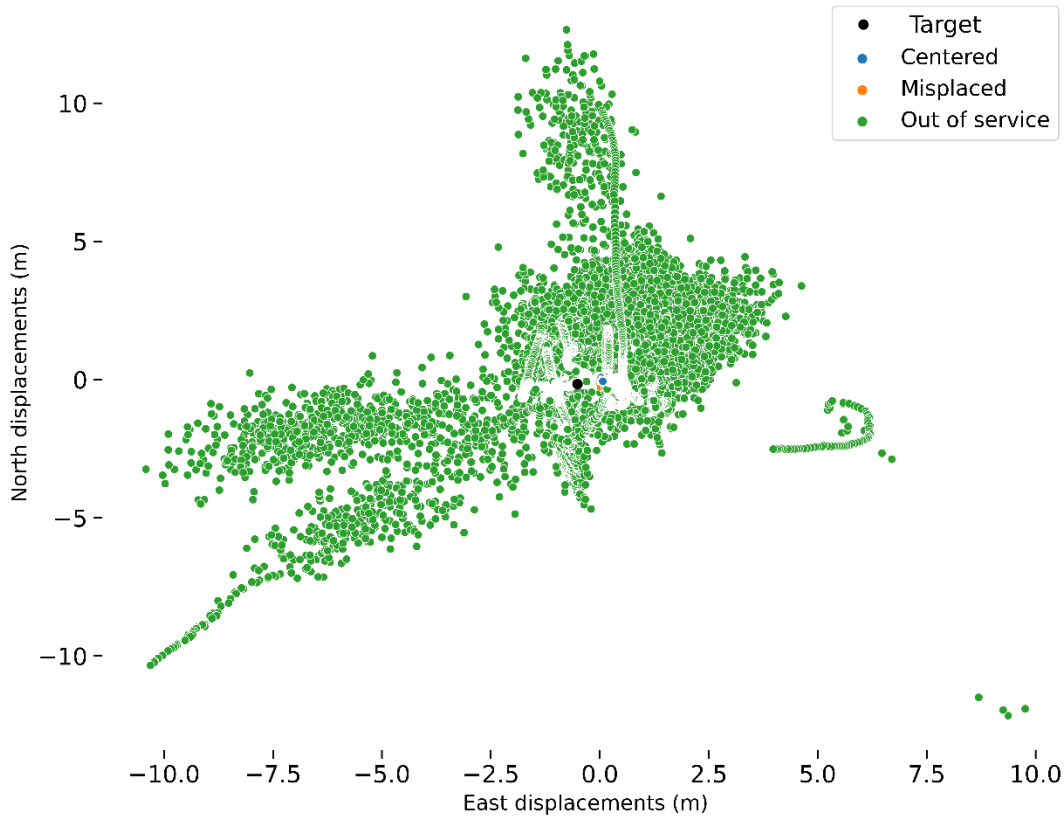

Figure C.18 Displacements scatter plot with 20 degrees elevation angle and 10 cm 3D level of displacements utilizing low latency stream (Prepared by the author).

Table C.43 Summary of 15-centimeters 3D Displacement Experiment at 20 Degrees Elevation Angle with Low Latency Stream.

Start date			End date			Duration (hours)	# of events
2022-05-07 13:10:23			2022-05-08 13:49:49			24	105947
	Coordinates components (m)			Displacement components (m)			Latency
	X	Y	Z	East	North	UP	Seconds
Mean	4455834	3127064	3314433	-0.04754	0.052134	0.301571	20.5242
Standard deviation	2.381942	1.013669	1.16064	0.680906	0.484191	2.711122	0.486316
Minimum	4455822	3127056	3314426	-12.3341	-9.7335	-14.9559	19.56
Maximum	4455883	3127084	3314460	3.0574	4.4435	58.4307	34.6

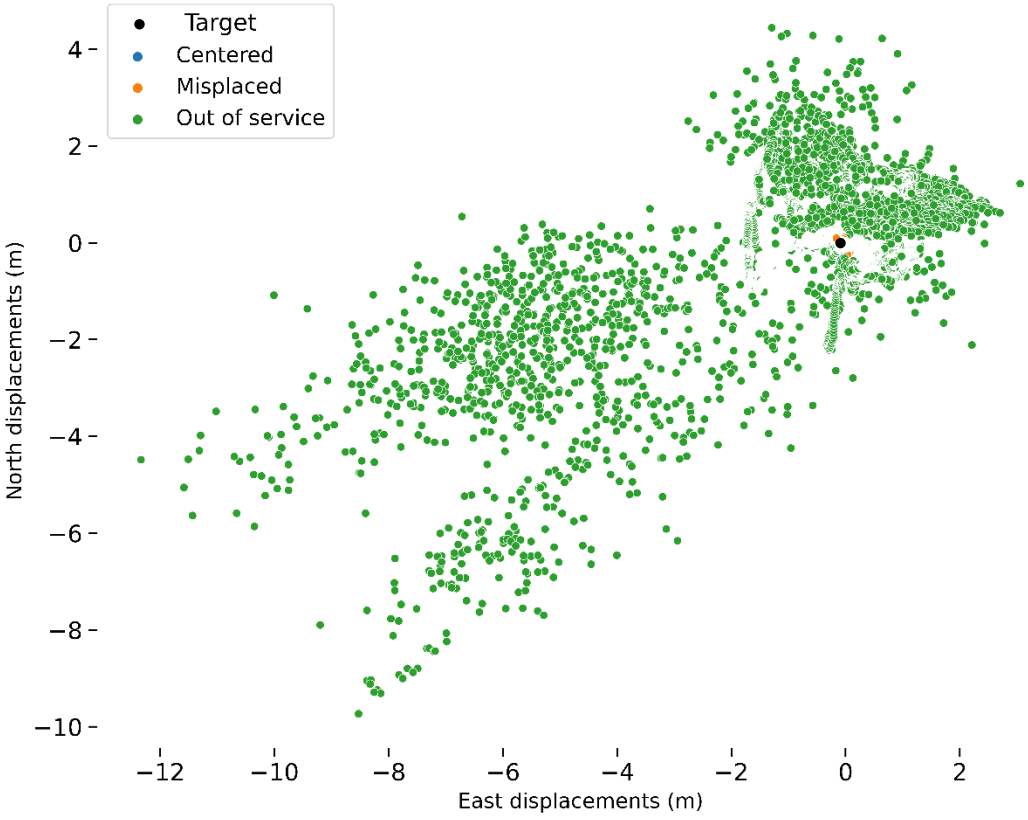

Figure C.19 Displacements scatter plot with 20 degrees elevation angle and 15 cm 3D level of displacements utilizing low latency stream (Prepared by the author).

Table C.44 Summary of 20-centimeters 3D Displacement Experiment at 20 Degrees Elevation Angle with Low Latency Stream.

Start date			End date			Duration (hours)	# of events
2022-05-07 13:10:23			2022-05-08 13:49:49			24	115827
	Coordinates components (m)			Displacement components (m)			Latency
	X	Y	Z	East	North	UP	Seconds
Mean	4455834	3127064	3314433	0.039235	0.054599	0.216087	14.12583
Standard deviation	1.528388	0.697062	0.764682	0.409612	0.462056	1.739347	0.652489
Minimum	4455821	3127058	3314426	-10.2577	-9.5391	-13.7587	13.1
Maximum	4455868	3127078	3314454	3.4988	12.2186	35.8824	29.78

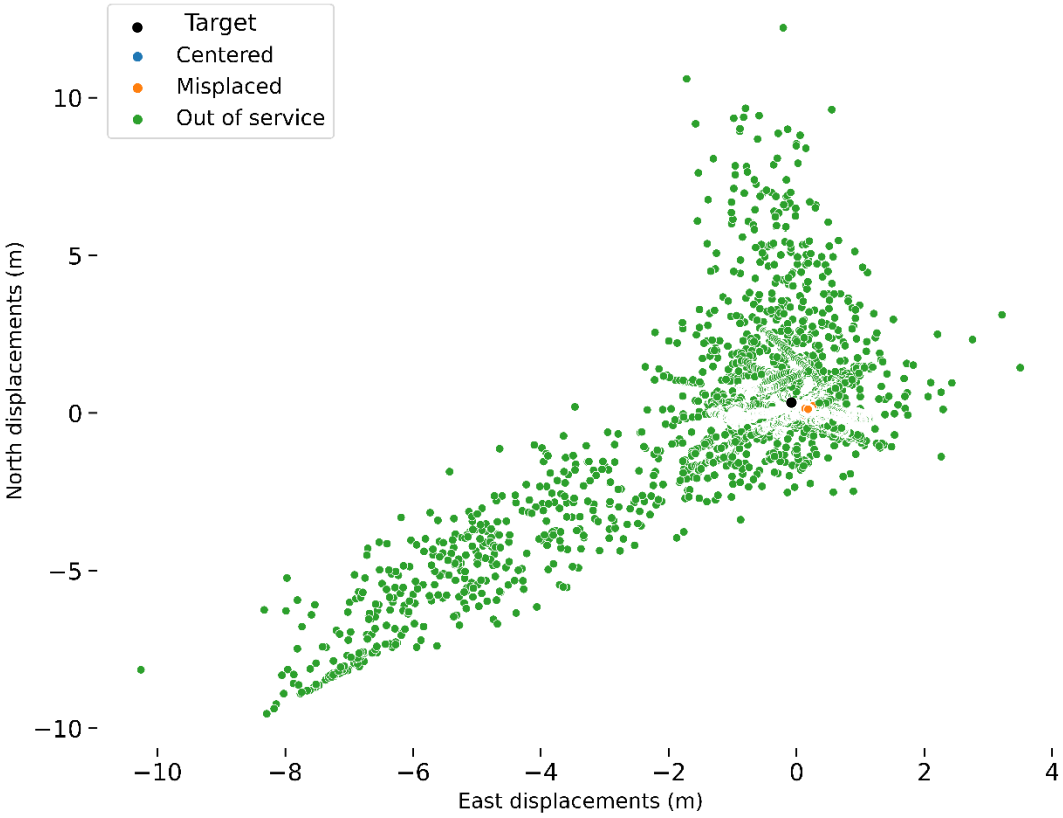

Figure C.20 Displacements scatter plot with 20 degrees elevation angle and 20 cm 3D level of displacements utilizing low latency stream (Prepared by the author).

Table C.45 Summary of 5-centimeters 3D Displacement Experiment at 30 Degrees Elevation Angle with Low Latency Stream.

Start date			End date			Duration (hours)	# of events
2022-05-10 18:06:48			2022-05-11 15:51:03			24	85679
	Coordinates components (m)			Displacement components (m)			Latency
	X	Y	Z	East	North	UP	Seconds
Mean	4455834	3127064	3314433	0.010547	0.014106	0.029608	14.94355
Standard deviation	0.094383	0.090318	0.084751	0.048875	0.039279	0.142537	0.613516
Minimum	4455832	3127062	3314431	-0.921	-0.5637	-3.039	14.05
Maximum	4455834	3127065	3314434	0.4781	0.3667	1.4374	52.91

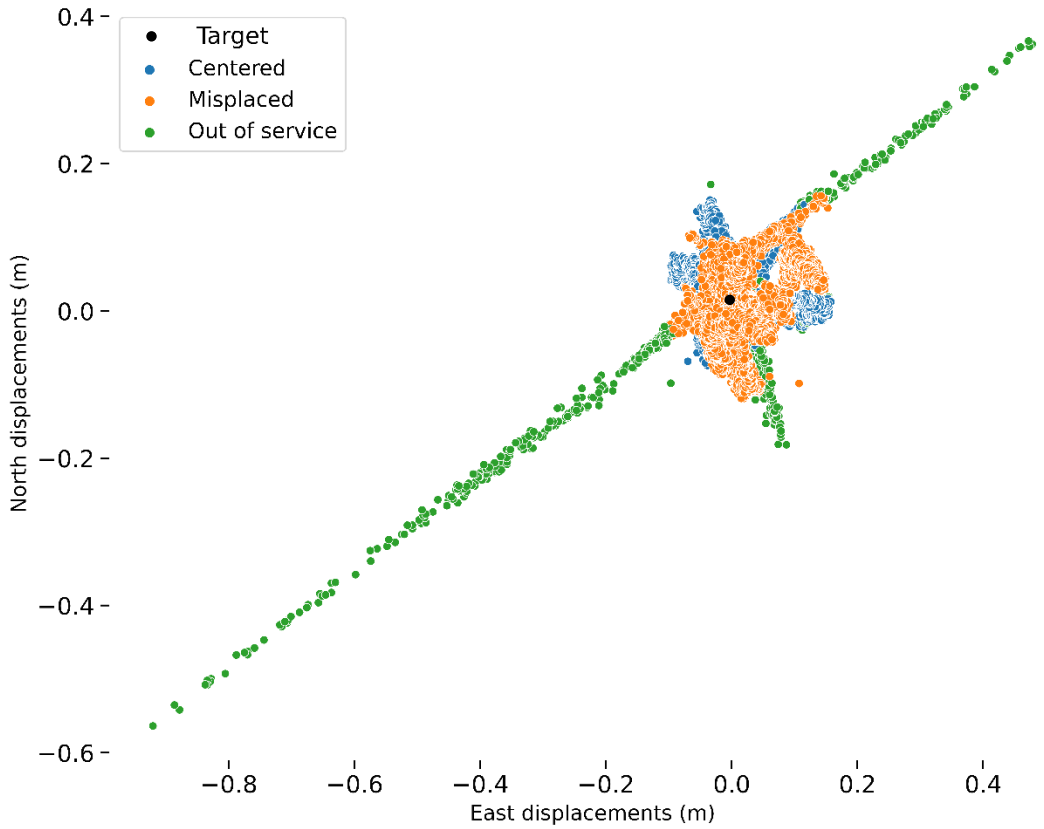

Figure C.21 Displacements scatter plot with 30 degrees elevation angle and 5 cm 3D level of displacements utilizing low latency stream (Prepared by the author).

Table C.46 Summary of 10-centimeters 3D Displacement Experiment at 30 Degrees Elevation Angle with Low Latency Stream.

Start date			End date			Duration (hours)	# of events
2022-05-12 08:03:55			2022-05-12 22:33:06			24	46615
	Coordinates components (m)			Displacement components (m)			Latency
	X	Y	Z	East	North	UP	Seconds
Mean	4455834	3127064	3314433	-0.00297	-0.03041	0.002173	30
Standard deviation	0.198377	0.111926	0.096641	0.124744	0.076592	0.199482	0
Minimum	4455832	3127063	3314433	-0.3527	-0.3105	-2.0321	30
Maximum	4455834	3127065	3314434	0.6185	0.4909	1.0948	30

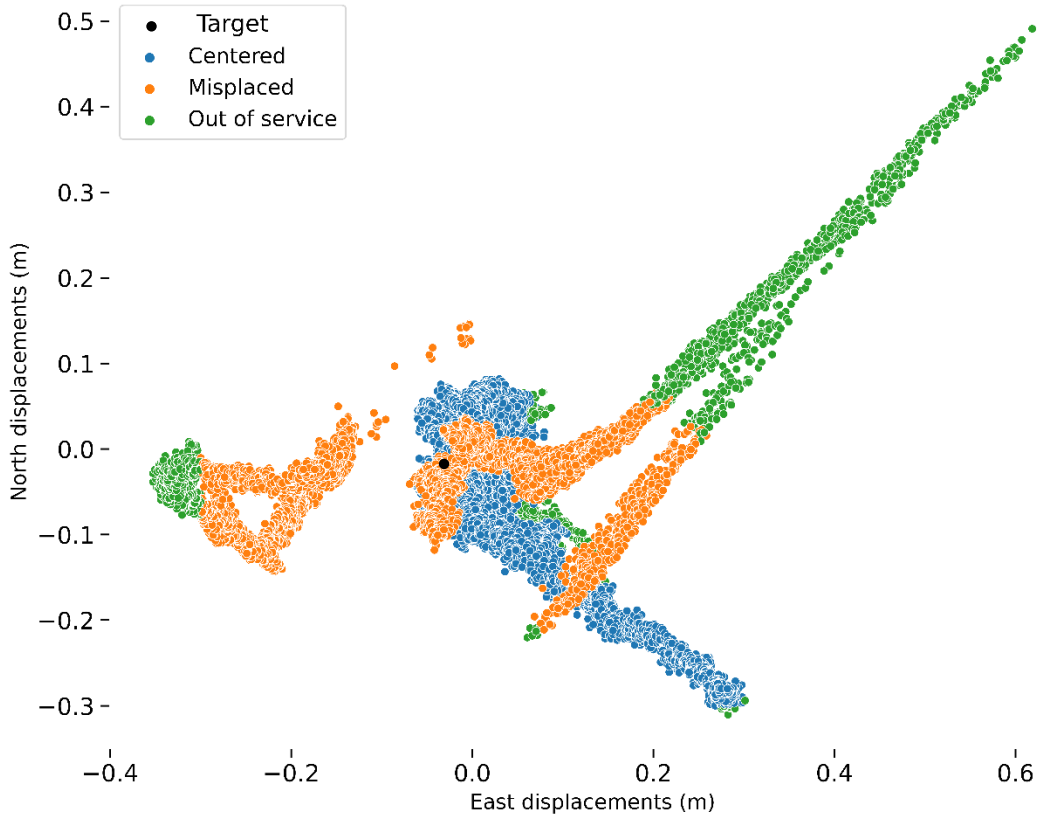

Figure C.22 Displacements scatter plot with 30 degrees elevation angle and 10 cm 3D level of displacements utilizing low latency stream (Prepared by the author).

Table C.47 Summary of 15-centimeters 3D Displacement Experiment at 30 Degrees Elevation Angle with Low Latency Stream.

Start date			End date			Duration (hours)	# of events
2022-05-14 20:03:52			2022-05-15 15:28:54			24	55220
	Coordinates components (m)			Displacement components (m)			Latency
	X	Y	Z	East	North	UP	Seconds
Mean	4455834	3127064	3314433	-0.0101	-0.02854	0.182255	14.36352
Standard deviation	0.212331	0.138151	0.124757	0.076218	0.042295	0.268582	0.709033
Minimum	4455833	3127064	3314433	-0.3466	-0.1811	-0.2477	13.34
Maximum	4455835	3127064	3314434	0.2448	0.1042	1.0391	19.37

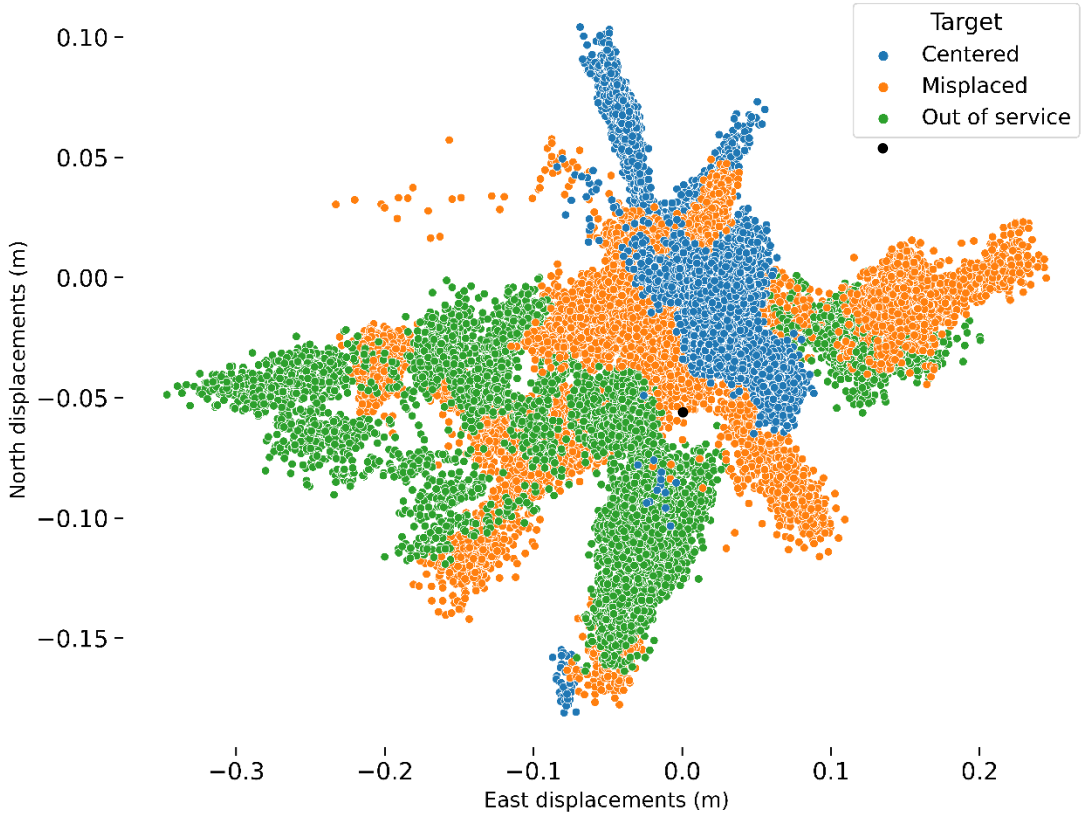

Figure C.23 Displacements scatter plot with 30 degrees elevation angle and 15 cm 3D level of displacements utilizing low latency stream (Prepared by the author).

Table C.48 Summary of 20-centimeters 3D Displacement Experiment at 30 Degrees Elevation Angle with Low Latency Stream.

Start date			End date			Duration (hours)	# of events
2022-05-25 18:54:55			2022-05-26 09:17:50			24	60415
	Coordinates components (m)			Displacement components (m)			Latency
	X	Y	Z	East	North	UP	Seconds
Mean	4455834	3127064	3314433	3.07E-05	0.018957	0.005313	13.86883
Standard deviation	0.315758	0.175269	0.347373	0.058181	0.115748	0.484053	0.33017
Minimum	4455809	3127050	3314405	-3.3789	-9.1577	-38.2733	13.17
Maximum	4455860	3127079	3314464	3.1667	10.084	41.84	15.57

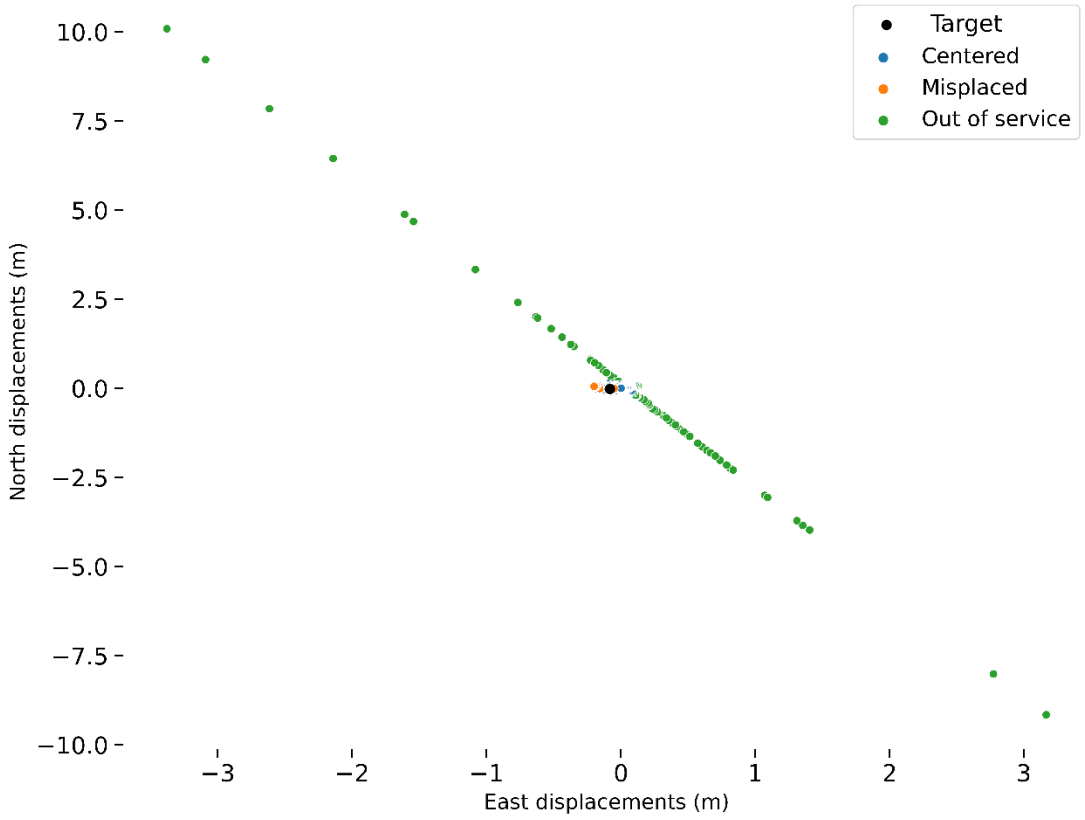

Figure C.24 Displacements scatter plot with 30 degrees elevation angle and 20 cm 3D level of displacements utilizing low latency stream (Prepared by the author).

References

Afifi, A., & El-Rabbany, A. (2016). Precise Point Positioning Model Using Triple Gnss Constellations: GPS, Galileo and BeiDou. Journal Of Applied Geodesy, 10(4), 223–232. https://doi.org/10.1515/jag-2016-0010

Afraimovich, E. L., Astafyeva, E. I., Demyanov, V. v, Edemskiy, I. K., Gavrilyuk, N. S., Ishin, A. B., Kosogorov, E. A., Leonovich, L. A., Lesyuta, O. S., & Palamartchouk, K. S. (2013). A review of GPS/GLONASS studies of the ionospheric response to natural and anthropogenic processes and phenomena. Journal of Space Weather and Space Climate, 3, A27.

Aggrey, J., & Bisnath, S. (2019a). Improving GNSS PPP Convergence: The Case of Atmospheric-Constrained, Multi-GNSS PPP-AR. SENSORS, 19(3). https://doi.org/10.3390/s19030587 Aggrey, J., & Bisnath, S. (2019b). Improving GNSS PPP convergence: The case of atmospheric-constrained, multi-GNSS PPP-AR. Sensors, 19(3), 587.

Akyol, A. A., Arikan, O., & Arikan, F. (2020). A machine learning-based detection of earthquake precursors using ionospheric data. Radio Science, 55(11), 1–21. https://doi.org/10.1029/2019RS006931

Alcántara-Ayala, I., & Oliver-Smith, A. (2019). Early Warning Systems: Lost in Translation or Late by Definition? A FORIN Approach. International Journal of Disaster Risk Science, 10(3), 317–331. https://doi.org/10.1007/s13753-019-00231-3

Alcay, S., & Atiz, O. F. (2021). Investigation of the performance of Real-Time Precise Point Positioning (RT-PPP) method using different software packages. GEOMATIK, 6(1), 77–83. https://doi.org/10.29128/geomatik.687709

Alcay, S., & Turgut, M. (2021). Evaluation of the positioning performance of multi-GNSS RT-PPP method. Arabian Journal of Geosciences, 14(3), 1–19.

Alcik, H., Ozel, O., Apaydin, N., & Erdik, M. (2009). A study on warning algorithms for Istanbul earthquake early warning system. Geophysical Research Letters, 36(5). https://doi.org/10.1029/2008GL036659

Alkan, R. M., Saka, M. H., Ozulu, İ. M., & İlçi, V. (2017). Kinematic precise point positioning using GPS and GLONASS measurements in marine environments. Measurement, 109, 36–43. https://doi.org/10.1016/j.measurement.2017.05.054

Allen, R. M., Baer, G., Clinton, J., Hamiel, Y., Hofstetter, R., Pinsky, V., Ziv, A., & Zollo, A. (2012). Earthquake early warning for Israel: Recommended implementation strategy. Isr. Geol. Surv. Rep.

Altamimi, Z., Sillard, P., & Boucher, C. (2002). ITRF2000: A new release of the International Terrestrial Reference Frame for earth science applications. Journal of Geophysical Research: Solid Earth, 107(B10), ETG-2.

Amato, A. (2020). Some reflections on tsunami early warning systems and their impact, with a look at the NEAMTWS. Bollettino Di Geofisica Teorica Ed Applicata.

Anatoly Zak. (2021). GLONASS Navigation System. http://www.russianspaceweb.com/glonass.html

Andrei, C.-O., Chen, R., Kuusniemi, H., Hernandez-Pajares, M., Juan, J. M., & Salazar, D. (2009). Ionosphere effect mitigation for single-frequency precise point positioning. Proceedings of the 22nd International Technical Meeting of the Satellite Division of The Institute of Navigation (ION GNSS 2009), 2508–2517.

Angrisano, A., Dardanelli, G., Innac, A., Pisciotta, A., Pipitone, C., & Gaglione, S. (2020). Performance Assessment of PPP Surveys with Open-Source Software Using the GNSS GPS-GLONASS-Galileo Constellations. Applied Sciences-Basel, 10(16). https://doi.org/10.3390/app10165420

Anquela Julián, A. B., Martín Furones, Á. E., Berné Valero, J. L., & Padin Devesa, J. (2013). GPS and GLONASS static and kinematic PPP results. Journal of Surveying Engineering, 139(1), 47–58.

Ashby, N. (2003). Relativity in the global positioning system. Living Reviews in Relativity, 6(1), 1–42.

Asia-Pacific Reference Frame. (2021). APREF)| Geoscience Australia. https://www.ga.gov.au/scientific-topics/positioning-navigation/geodesy/asia-pacific-reference-frame

Astudillo, J. M., Lau, L., Tang, Y. T., & Moore, T. (2018). Analysing the Zenith Tropospheric Delay Estimates in On-line Precise Point Positioning (PPP) Services and PPP Software Packages. SENSORS, 18(2). https://doi.org/10.3390/s18020580

Atiz, O. F., Alcay, S., Ogutcu, S., & Bugdayci, I. (n.d.). Comparative analysis of real-time precise point positioning method in terms of positioning and zenith tropospheric delay estimation. Survey Review. https://doi.org/10.1080/00396265.2021.2001627

Atiz, O. F., Alcay, S., Ogutcu, S., & Bugdayci, I. (2021). Comparative analysis of real-time precise point positioning method in terms of positioning and zenith tropospheric delay estimation. Survey Review, 1–13.

Awad, M., & Khanna, R. (2015). Support Vector Machines for Classification. In Efficient Learning Machines (pp. 39–66). Apress. https://doi.org/10.1007/978-1-4302-5990-9_3

Bahadur, B., & Nohutcu, M. (2019). Comparative analysis of MGEX products for post-processing multi-GNSS PPP. Measurement, 145, 361–369. https://doi.org/10.1016/j.measurement.2019.05.094

Balidakis, K., Nilsson, T., Zus, F., Glaser, S., Heinkelmann, R., Deng, Z., & Schuh, H. (2018). Estimating integrated water vapor trends from VLBI, GPS, and numerical weather models: Sensitivity to tropospheric parameterization. Journal of Geophysical Research: Atmospheres, 123(12), 6356–6372.

Banville, S., Santerre, R., Cocard, M., & Langley, R. B. (2008). Satellite and receiver phase bias calibration for undifferenced ambiguity resolution. Proceedings of the 2008 National Technical Meeting of The Institute of Navigation, 711–719.

Barker, R., Lapucha, D., & Wood, T. (2002). The Impact of High-Performance GPS on the Offshore Marine Survey, Navigation and Positioning Industry. In Offshore Technology Conference (p. 7). Offshore Technology Conference. https://doi.org/10.4043/14195-MS

Bar-Sever, Y., Gross, R., Khachikyan, R., Meyer, R., Song, T., Webb, F., Blewitt, G., Plag, H. P., Hammond, W., & Kreemer, C. (2009). GPS-aided real-time earthquake and tsunami (GREAT) alert system.

Barnes, D. E. (2019, December). 2019 Updates Earth Gravitational Model 2020. In AGU Fall Meeting Abstracts (Vol. 2019, pp. G33B-0668).

Bazlov, Y. A., Galazin, V. F., Kaplan, B. L., Maksimov, V. G., & Rogozin, V. P. (1999). Propagating PZ 90 to WGS 84 Transformation Parameters. GPS SOLUTIONS, 3(1), 13–16. https://doi.org/10.1007/PL00012773

Becker, J. S., Potter, S. H., Vinnell, L. J., Nakayachi, K., McBride, S. K., & Johnston, D. M. (2020). Earthquake early warning in Aotearoa New Zealand: a survey of public perspectives to guide warning system development. Humanities and Social Sciences Communications 2020 7:1, 7(1), 1–12. https://doi.org/10.1057/s41599-020-00613-9

Bernese GNSS Software. (2022). Bernese GNSS Software. http://www.bernese.unibe.ch/

Bernhard Hofmann-Wellenhof, H. L. E. W. (2008). GNSS — Global Navigation Satellite Systems_ GPS, GLONASS, Galileo, and more (PDFDrive).

Bertiger, W., Bar-Sever, Y., Dorsey, A., Haines, B., Harvey, N., Hemberger, D., Heflin, M., Lu, W., Miller, M., Moore, A. W., Murphy, D., Ries, P., Romans, L., Sibois, A., Sibthorpe, A., Szilagyi, B., Vallisneri, M., & Willis, P. (2020). GipsyX/RTGx, a new tool set for space geodetic operations and research. Advances in Space Research, 66(3), 469–489. https://doi.org/10.1016/j.asr.2020.04.015

Beutler, G., Rothacher, M., Schaer, S., Springer, T. A., Kouba, J., & Neilan, R. E. (1999). The International GPS Service (IGS): An interdisciplinary service in support of Earth sciences. Advances in Space Research, 23(4), 631–653.

Bevis, M., Businger, S., Herring, T. A., Rocken, C., Anthes, R. A., & Ware, R. H. (1992). GPS meteorology: Remote sensing of atmospheric water vapor using the global positioning system. Journal of Geophysical Research: Atmospheres, 97(D14), 15787–15801.

Bezcioglu, M., Yigit, C. O., & El-mowafy, A. (2019). Kinematic PPP-AR in Antarctic. April.

B.Hoffmann-Wellenhof, & H.Lichtenegg. (2001). Global positioning system, theory and practice, 5th edition. In Eos, Transactions American Geophysical Union (Fifth edit, Vol. 82, Issue 33). https://doi.org/10.1029/01eo00224

Bilal, M. A., Ji, Y., Wang, Y., Akhter, M. P., & Yaqub, M. (2022). An early warning system for earthquake prediction from seismic data using Batch Normalized Graph Convolutional Neural Network with Attention Mechanism (BNGCNNATT). Sensors, 22(17), 6482.

Bishop, C. M., & Nasrabadi, N. M. (2006). Pattern recognition and machine learning (Vol. 4, Issue 4). Springer.

Bisnath, S. (2004). Precise orbit determination of Low Earth Orbiters with a single GPS receiver-based, geometric strategy.

Bisnath, S., & Gao, Y. (2009a). Current state of precise point positioning and future prospects and limitations. In Observing our changing earth (pp. 615–623). Springer.

Bisnath, S., & Gao, Y. (2009b). Precise point positioning. GPS World, 20(4), 43–50.

Blewitt, G. (1989). Carrier phase ambiguity resolution for the Global Positioning System applied to geodetic baselines up to 2000 km. Journal of Geophysical Research: Solid Earth, 94(B8), 10187–10203.

Bock, Y., & Wdowinski, S. (2020). GNSS Geodesy in Geophysics, Natural Hazards, Climate, and the Environment. Position, Navigation, and Timing Technologies in the 21st Century, 741–820. https://doi.org/10.1002/9781119458449.CH28

Bonnet, R.-M., & Manno, V. (1994). International cooperation in space: The example of the European Space Agency (Vol. 6). Harvard University Press.

Borovcnik, M., Bentz, H.-J., & Kapadia, R. (1991). A Probabilistic Perspective. In Chance Encounters: Probability in Education. https://doi.org/10.1007/978-94-011-3532-0_2

Boucher, C., & Altamimi, Z. (2001). ITRS, PZ-90 and WGS 84: current realizations and the related transformation parameters. Journal Of Geodesy, 75(11), 613–619. https://doi.org/10.1007/s001900100208

Box, G. E. P., Jenkins, G. M., & Reinsel, G. C. (2011). Time series analysis: forecasting and control (Vol. 734). John Wiley & Sons.

Box, G. E. P., Jenkins, G. M., Reinsel, G. C., & Ljung, G. M. (2015). Time series analysis: forecasting and control. John Wiley & Sons.

Brack, A. (2017). Reliable GPS+ BDS RTK positioning with partial ambiguity resolution. GPS Solutions, 21(3), 1083–1092.

Brown, N., Keenan, R., Richter, B., & Troyer, L. (2005). Advances in ambiguity resolution for RTK applications using the new RTCM V3. 0 Master-Auxiliary messages. Proceedings of the 18th International Technical Meeting of the Satellite Division of the Institute of Navigation (ION GNSS 2005), 73–80.

Bruyninx, C., Legrand, J., Fabian, A., & Pottiaux, E. (2019). GNSS metadata and data validation in the EUREF Permanent Network. GPS Solutions, 23(4), 106. https://doi.org/10.1007/s10291-019-0880-9

Bundesamt für Kartographie und Geodäsie. (2022). BKG Ntrip Client - BNC. https://igs.bkg.bund.de/ntrip/download

Buntine, W., Niblett, T., & Uk, T. A. (1992). A Further Comparison of Splitting Rules for Decision-Tree Induction (Vol. 8).

Burkett, E. R., Given, D. D., & Jones, L. M. (2014). ShakeAlert—an earthquake early warning system for the united states west coast. US Geological Survey.

Cabinet Office, G. O. J. (2022). Service Overview | Service Overview | QZSS (Quasi-Zenith Satellite System) - Cabinet Office (Japan). https://qzss.go.jp/en/overview/index.html

Cahuasqui, J. A., Hoque, M. M., & Jakowski, N. (2022). Positioning performance of the Neustrelitz total electron content model driven by Galileo Az coefficients. GPS Solutions, 26(3). https://doi.org/10.1007/s10291-022-01278-4

Cai, C., & Gao, Y. (2013a). GLONASS-based precise point positioning and performance analysis. Advances in Space Research, 51(3), 514–524.

Cai, C., & Gao, Y. (2013b). Modeling and assessment of combined GPS/GLONASS precise point positioning. GPS Solutions, 17(2), 223–236.

Cai, C., Gong, Y., Gao, Y., & Kuang, C. (2017). An approach to speed up single-frequency PPP convergence with quad-constellation GNSS and GIM. Sensors, 17(6), 1302.

Cai, C., Liu, Z., & Luo, X. (2013). Single-frequency ionosphere-free precise point positioning using combined GPS and GLONASS observations. The Journal of Navigation, 66(3), 417–434.

Caissy, M., & Agrotis, L. (2011). Real-time working group and real-time pilot project. Int GNSS Serv Tech Rep, 2011, 183–190.

Calcaterra, S., Cesi, C., Di Maio, C., Gambino, P., Merli, K., Vallario, M., & Vassallo, R. (2012). Surface displacements of two landslides evaluated by GPS and inclinometer systems: a case study in Southern Apennines, Italy. Natural Hazards, 61(1), 257–266.

Campos, J., Johnson, K., Neeley, J., Roesch, S., Jahan, F., Niyaz, Q., & al Shamaileh, K. (2020). A Machine Learning Based Smartphone App for GPS Spoofing Detection. In N. Park, K. Sun, S. Foresti, K. Butler, & N. Saxena (Eds.), Security and Privacy in Communication Networks (pp. 235–241). Springer International Publishing.

Capilla, R. M., Berné, J. L., Martín, A., & Rodrigo, R. (2016). Simulation case study of deformations and landslides using real-time GNSS precise point positioning technique. Geomatics, Natural Hazards and Risk, 7(6), 1856–1873. https://doi.org/10.1080/19475705.2015.1137243

Capitaine, N., Guinot, B., & McCarthy, D. D. (2000). Definition of the celestial ephemeris origin and of UT1 in the international celestial reference frame. Astronomy and Astrophysics, 355, 398–405.

Capparelli, G., & Tiranti, D. (2010). Application of the MoniFLaIR early warning system for rainfall-induced landslides in Piedmont region (Italy). Landslides, 7(4), 401–410.

Cefalo, R., Manzoni, G., Noè, S., & Sluga, T. (2017). High frequency GNSS measurements for structural monitoring applications. International Conference on Computational Science and Its Applications, 169–180.

Centre National d'Etudes Spatiales. (2017). CNES/CLS Analysis Center for IGS. https://igsac-cnes.cls.fr/

Centre national d'études spatiales. (2022). The PPP-Wizard Project. http://www.ppp-wizard.net/index.html

Chadwell, C. B., & Imbsen, R. A. (2004). XTRACT: A tool for axial force-ultimate curvature interactions. In Structures 2004: Building on the past, securing the future (pp. 1–9).

Charoenphon, C., & Satirapod, C. (2022). Improving the accuracy of real-time precipitable water vapour using country-wide meteorological model with precise point positioning in Thailand. Journal Of Spatial Science, 67(2), 313–329. https://doi.org/10.1080/14498596.2020.1758969

Chen, K., Liu, Z., & Song, Y. T. (2020). Automated GNSS and teleseismic earthquake inversion (AutoQuake Inversion) for tsunami early warning: retrospective and real-time results. Pure and Applied Geophysics, 177(3), 1403–1423.

Chen, Q., Jiang, W., Meng, X., Jiang, P., Wang, K., Xie, Y., & Ye, J. (2018). Vertical deformation monitoring of the suspension bridge tower using GNSS: A case study of the fourth road bridge in the UK. Remote Sensing, 10(3), 364.

Chen, T., & Guestrin, C. (2016). Xgboost: A scalable tree boosting system. Proceedings of the 22nd Acm Sigkdd International Conference on Knowledge Discovery and Data Mining, 785–794.

Chen, T., He, T., Benesty, M., Khotilovich, V., Tang, Y., Cho, H., Chen, K., Mitchell, R., Cano, I., & Zhou, T. (2015). XGBoost: extreme gradient boosting. R Package Version 0.4-2, 1(4), 1–4.

Chen, W., Hu, C., Li, Z., Chen, Y., Ding, X., Gao, S., & Ji, S. (2004). Kinematic GPS precise point positioning for sea level monitoring with GPS buoy. Journal of Global Positioning Systems, 3(1–2), 302–307.

Cina, A., & Piras, M. (2015). Performance of low-cost GNSS receiver for landslides monitoring: test and results. Geomatics, Natural Hazards and Risk, 6(5–7), 497–514. https://doi.org/10.1080/19475705.2014.889046

Cina, A., Piras, M., & Bendea, H. I. (2013). Monitoring of landslides with mass market GPS: an alternative low-cost solution. International Archives of the Photogrammetry, Remote Sensing and Spatial Information Sciences, 5, W3.

Clarkson, K. L., Hazan, E., & Woodruff, D. P. (2012). Sublinear optimization for machine learning. In Journal of the ACM (Vol. 59, Issue 5). https://doi.org/10.1145/2371656.2371658

Cochran, E. S., Aagaard, B. T., Allen, R. M., Andrews, J., Baltay, A. S., Barbour, A. J., Bodin, P., Brooks, B. A., Chung, A., & Crowell, B. W. (2018). Research to improve ShakeAlert earthquake early warning products and their utility. US Geological Survey.

Collilieux, X., Métivier, L., Altamimi, Z., van Dam, T., & Ray, J. (2011). Quality assessment of GPS reprocessed terrestrial reference frame. GPS Solutions, 15(3), 219–231.

Collins, P., Bisnath, S., Lahaye, F., & Héroux, P. (2010). Undifferenced GPS ambiguity resolution using the decoupled clock model and ambiguity datum fixing. Navigation, 57(2), 123–135.

Colombo, O. L., Sutter, A. W., & Evans, A. G. (2004). Evaluation of precise, kinematic GPS point positioning. Proceedings of the 17th International Technical Meeting of the Satellite Division of The Institute of Navigation (ION GNSS 2004), 1423–1430.

Coltice, N., Husson, L., Faccenna, C., & Arnould, M. (2019). What drives tectonic plates? Science Advances, 5(10), eaax4295.

Combrinck, L. (2008). „Status of the African Geodetic Reference Frame (AFREF) project as at September 2008“. Augmentation Systems and Applications, 11–14.

Combrinck, L. (2010). African Geodetic Reference Frame (AFREF): Background and steps towards future implementation.

Committee, A. C. I. (2008). Building code requirements for structural concrete (ACI 318-08) and commentary.

Computers and Structures, Inc. (CSI). (2023). SAP 2000| Structural Analysis And Design. https://www.csiamerica.com/products/sap2000

Conway, E. M. (2015). Exploration and engineering: The jet propulsion laboratory and the quest for Mars. JHU Press.

Cortes, C., Vapnik, V., & Saitta, L. (1995). Support-Vector Networks Editor. In Machine Leaming (Vol. 20). Kluwer Academic Publishers.

Crane, R. K. (1977). Ionospheric scintillation. Proceedings of the IEEE, 65(2), 180–199.

Craymer, M. R., Piraszewski, M., & Henton, J. A. (2007). The North America Reference Frame (NAREF) project to densify the ITRF in North America. Proceedings of the 20th International Technical Meeting of the Satellite Division of The Institute of Navigation (ION GNSS 2007), 2145–2154.

Crozier, M. J. (2010). Landslide geomorphology: An argument for recognition, with examples from New Zealand. Geomorphology, 120(1–2), 3–15.

Dach, R., & Walser, P. (2015). Bernese GNSS Software Version 5.2.

Dal'Cól, C., Resende Filho, L. W., Pabón, R. C., Moura, R., & Pessin, G. (2022). The Impact of Ionospheric Irregularities in Autonomous Systems Operations. IGARSS 2022-2022 IEEE International Geoscience and Remote Sensing Symposium, 7681–7684.

Day, R. W. (2012). Geotechnical earthquake engineering handbook: with the 2012 International building code. McGraw-Hill Education.

De Almeida, F. G. v, Yoshizaki, H. T. Y., da Cunha, C. B., da Fonseca, E. S., & Kiyota, A. S. (2016). PPP Technical Application for Positioning in Brazil Cabotage: A Case Study. Boletim De Ciencias Geodesicas, 22(3), 526–541. https://doi.org/10.1590/S1982-21702016000300030

De Oliveira Moraes, A., Muella, M. T. A. H., de Paula, E. R., de Oliveira, C. B. A., Terra, W. P., Perrella, W. J., & Meibach-Rosa, P. R. P. (2018). Statistical evaluation of GLONASS amplitude scintillation over low latitudes in the Brazilian territory. Advances in Space Research, 61(7), 1776–1789.

De Souza, A. L. C., Jerez, G. O., & de Oliveira Camargo, P. (2022). Evaluation of amplitude and phase scintillation impact on GPS and Galileo frequencies. Copernicus Meetings.

Deng, X. (2015). Geodesy–Introduction to Geodetic Datum and Geodetic Systems. Taylor & Francis.

Department of Space, I. S. R. O. (2022). IRNSS Programme - ISRO. https://www.isro.gov.in/irnss-programme

Dick, W. R. (2011). The IERS, the Leap Second, and the public. Paper AAS, 11–667.

Dodson, A. H. (1986). Refraction and propagation delays in space geodesy. International Journal of Remote Sensing, 7(4), 515–524. https://doi.org/10.1080/01431168608954706

Doherty, P. H., Delay, S. H., Valladares, C. E., & Klobuchar, J. A. (2003). Ionospheric scintillation effects on GPS in the equatorial and auroral regions. Navigation, 50(4), 235–245.

Dong, X., Yang, L., Zhu, Q., Guo, C., Zhao, Z., & Lin, L. (2018). A Method of Retrieving Tropospheric Refractivity Above Ocean Surface using GNSS. 2018 12th International Symposium on Antennas, Propagation and EM Theory (ISAPE), 1–4. https://doi.org/10.1109/ISAPE.2018.8634353

Dousa, J. (2010). Precise near real-time GNSS analyses at Geodetic Observatory Pecny--precise orbit determination and water vapour monitoring. Acta Geodynamica et Geromaterialia, 7(1), 7–18.

Dousa, J., & Vaclavovic, P. (2014). Real-time zenith tropospheric delays in support of numerical weather prediction applications. Advances in Space Research, 53(9), 1347–1358.

Drummond, C., & Holte, R. C. (2000). Exploiting the Cost (In)sensitivity of Decision Tree Splitting Criteria. www.aaai.org

Duda, R. O., Hart, P. E., & Stork, D. G. (2000). Pattern Classification. John Wiley & Sons. Inc., New York, 5.

EBI Consulting. (2022). Magnitude, Peak Ground Velocity & Peak Ground Acceleration. https://www.ebiconsulting.com/resources_news/magnitude-peak-ground-velocity-peak-ground-acceleration/

Edberg, S. J., Evans, D. L., Graf, J. E., Hyon, J. J., Rosen, P. A., & Waliser, D. E. (2016). Studying Earth in the New Millennium: NASA Jet Propulsion Laboratory's Contributions to Earth Science and Applications Space Agencies. IEEE Geoscience and Remote Sensing Magazine, 4(1), 26–39.

El-Rabbany, Ahmed. (2002). Introduction to GPS: the global positioning system.

Elsobeiey, M., & Al-Harbi, S. (2016). Performance of real-time Precise Point Positioning using IGS real-time service. GPS Solutions, 20(3), 565–571. https://doi.org/10.1007/s10291-015-0467-z

Elsobeiey, M., & El-Rabbany, A. (2011). Impact of second-order ionospheric delay on GPS precise point positioning.

Elsobeiey, M., & El-Rabbany, A. (2012). On modelling of second-order ionospheric delay for GPS precise point positioning. The Journal of Navigation, 65(1), 59–72.

Enge, P. K. (1994). The Global Positioning System: Signals, measurements, and performance. International Journal of Wireless Information Networks, 1(2), 83–105. https://doi.org/10.1007/BF02106512

Enge, P., & Misra, P. (2011). Global Positioning System: Signals, Measurements, and Performance - Revised Second Edition (2011) (Second Edi).

Er, M., Wijngaarden, G., & Kars, H. (2010). Long-term effect of seismic activities on archaeological remains: A test study from Zakynthos, Greece. In Special Paper of the Geological Society of America (Vol. 471, pp. 145–156). https://doi.org/10.1130/2010.2471(13)

ESA. (1975). ESA Convention and Council Rules of Procedure.

ESA. (2017). NE Quick Ionospheric Model - Navipedia. https://gssc.esa.int/navipedia/index.php/NeQuick_Ionospheric_Model

ESA. (2022). GNSS Science Support Centre | GSSC. https://gssc.esa.int/#scientific-domains

European Plate Observing System. (2021). Who We Are | EPOS. https://www.epos-eu.org/about-epos/who-we-are

European Union Agency for Space Program. (2022). System | European GNSS Service Centre. https://www.gsc-europa.eu/galileo/system

European Union Agency for Space Program. (2022). Constellation Information | European GNSS Service Centre. https://www.gsc-europa.eu/system-service-status/constellation-information

Ewert, J. W., Guffanti, M., & Murray, T. L. (2005). An assessment of volcanic threat and monitoring capabilities in the United States: framework for a National Volcano Early Warning System. US Geological Survey.

Falck, C., Ramatschi, M., Bartsch, M., & Merx, A. (2010). The GNSS-based component of the German-Indonesian Tsunami Early Warning System (GITEWS): Overview, first operation results and current developments. International Geoscience and Remote Sensing Symposium (IGARSS), 134–137. https://doi.org/10.1109/IGARSS.2010.5650720

Falvey, D. A. (1974). The development of continental margins in plate tectonic theory. The APPEA Journal, 14(1), 95–106.

Farzaneh, S., Safari, A., & Parvazi, K. (2022). Precise estimation of horizontal displacement by combination of multi-GNSS (Galileo and GPS) observations via the LS-VCE method. Applied Geomatics, 14(2), 267–286.

Fawcett, T. (2006). An introduction to ROC analysis. Pattern Recognition Letters, 27(8), 861–874. https://doi.org/10.1016/j.patrec.2005.10.010

Federal Agency for Cartography and Geodesy. (2022). Networked Transport of RTCM via Internet Protocol. https://igs.bkg.bund.de/ntrip/

Feltens, J., & Schaer, S. (1998). IGS Products for the Ionosphere. Proceedings of the 1998 IGS Analysis Center Workshop Darmstadt, Germany, 3–5.

Fernandez-Hernandez, I., Vecchione, G., Díaz-Pulido, F., Jeannot, M., Valentaite, G., Blasi, R., ... & Simón, J. (2018, October). Galileo high accuracy: A program and policy perspective. In Proceedings of the 69th international astronautical congress, Bremen, Germany (pp. 1-5).

Fotopoulos, G., & Cannon, M. E. (2001). An Overview of Multi-Reference Station Methods for cm-Level Positioning. GPS Solutions, 4(3), 1–10. https://doi.org/10.1007/PL00012849

Galera Monico, J. F., Marques, H. A., Tsuchiya, I., Oyama, R. T., Silva de Queiroz, W. R., de Souza, M. C., & Wentz, J. P. (2019). Real Time PPP Applied To Airplane Flight Tests. Boletim De Ciencias Geodesicas, 25(2). https://doi.org/10.1590/s1982-21702019000200009

Gallardo, F., & Yuste, A. P. (2020). SCER Spoofing Attacks on the Galileo Open Service and Machine Learning Techniques for End-User Protection. IEEE Access, 8, 85515–85532. https://doi.org/10.1109/ACCESS.2020.2992119

Gao, G. X., Akos, D., Walter, T., & Enge, P. (2008). Understanding the GIOVE-B broadcast codes of the Galileo system. 2008 42nd Asilomar Conference on Signals, Systems and Computers, 2086–2090.

Gao, W., Meng, X. L., Gao, C. F., Pan, S. G., Zhu, Z. S., & Xia, Y. (2019). Analysis of the carrier-phase multipath in GNSS triple-frequency observation combinations. Advances In Space Research, 63(9), 2735–2744. https://doi.org/10.1016/j.asr.2018.01.019

Gao, Z., Ge, M., Shen, W., Zhang, H., & Niu, X. (2017). Ionospheric and receiver DCB-constrained multi-GNSS single-frequency PPP integrated with MEMS inertial measurements. Journal of Geodesy, 91(11), 1351–1366.

Gao, Z. Z., Ge, M. R., Shen, W. B., Li, Y., Chen, Q. J., Zhang, H. P., & Niu, X. J. (2017). Evaluation on the impact of IMU grades on BDS plus GPS PPP/INS tightly coupled integration. Advances In Space Research, 60(6), 1283–1299. https://doi.org/10.1016/j.asr.2017.06.022

Gaylord, E. H., Gaylord, C. N., & Stallmeyer, J. E. (1997). Structural engineering handbook.

Ge, M., Gendt, G., Rothacher, M. al, Shi, C., & Liu, J. (2008). Resolution of GPS carrier-phase ambiguities in precise point positioning (PPP) with daily observations. Journal of Geodesy, 82(7), 389–399.

Geertsema, M., & Highland, L. (2011). Landslides: Human Health Effects. In Encyclopedia of Environmental Health. https://doi.org/10.1016/B978-0-444-52272-6.00550-X

Geng, J., Wen, Q., Zhang, Q., Li, G., & Zhang, K. (2022). GNSS observable-specific phase biases for all-frequency PPP ambiguity resolution. Journal of Geodesy, 96(2), 1–18.

Geodetic Observatory Pecny. (2012). G-Nut Core Library. https://www.pecny.cz/Joomla25/index.php/gnss/sw

GeoNet. (2022a). About GeoNet. https://www.geonet.org.nz/about

GeoNet. (2022b). Volcanic Alert Levels. https://www.geonet.org.nz/volcano

Georg Weber, Leoš Mervart , Andrea Stürze , Axel Rülke, D., & Stöcker. (2016). BNC Help.

Geoscience Australia. (2020). Tsunami. https://www.ga.gov.au/education/classroom-resources/hazards/natural-hazards/tsunami

Geospatial Information Authority of Japan. (2021). Welcome to GSI | GSI HOME PAGE. https://www.gsi.go.jp/ENGLISH/index.html

Geospatial Information Authority of Japan. (2022). Geodetic survey | GSI HOME PAGE. https://www.gsi.go.jp/ENGLISH/page_e30030.html

German Federal Agency for Cartography and Geodesy. (2022). BKG - Bundesamt für Kartographie und Geodäsie. https://www.bkg.bund.de/DE/Home/home.html

German Research Centre for Geosciences. (2020a). IGS-Analysezentrum: GFZ. https://www.gfz-potsdam.de/sektion/geodaetische-weltraumverfahren/infrastruktur/igs-analysezentrum/

German Research Centre for Geosciences. (2020b). Profile: GFZ. https://www.gfz-potsdam.de/en/about-us/organisation/gfz-profile

Gitis, V., Derendyaev, A., & Petrov, K. (2021). Analysing the Performance of GPS Data for Earthquake Prediction. Remote Sensing, 13(9). https://doi.org/10.3390/rs13091842

Gleadall, A. (2021). Full Control G Code Designer: open-source software for unconstrained design in additive manufacturing. Additive Manufacturing, 46, 102109.

GMV Innovating Solutions S.L. (2022). MagicPPP® | GMV. https://www.gmv.com/en/products/space/magicpppr

GNS Science. (2022). About GNS Science. https://www.gns.cri.nz/

GOCA Project. (2017). GOCA. http://goca.info/

Goff, J., & Chagué-Goff, C. (2022). Tsunami. Progress in Physical Geography, 38(2), 218–240. https://doi.org/10.1177/0309133314522282

Golriz, D., Bock, Y., & Xu, X. (2021). Defining the Coseismic Phase of the Crustal Deformation Cycle With Seismogeodesy. Journal of Geophysical Research: Solid Earth, 126(10). https://doi.org/10.1029/2021JB022002

GPS Solutions. (2022). RTNet. https://www.gps-solutions.com/

Grewal, M. S., Andrews, A. P., & Bartone, C. G. (2020). Global navigation satellite systems, inertial navigation, and integration. John Wiley & Sons.

Gümüş, K., & Selbesoğlu, M. O. (2019). Evaluation of NRTK GNSS positioning methods for displacement detection by a newly designed displacement monitoring system. Measurement, 142, 131–137.

Guo, F., Li, X. X., Zhang, X. H., & Wang, J. L. (2017a). The contribution of Multi-GNSS Experiment (MGEX) to precise point positioning. Advances In Space Research, 59(11), 2714–2725. https://doi.org/10.1016/j.asr.2016.05.018

Guo, F., Li, X., Zhang, X., & Wang, J. (2017b). Assessment of precise orbit and clock products for Galileo, BeiDou, and QZSS from IGS Multi-GNSS Experiment (MGEX). GPS Solutions, 21(1), 279–290. https://doi.org/10.1007/s10291-016-0523-3

Guo, J., Xu, X., Zhao, Q., & Liu, J. (2016). Precise orbit determination for quad-constellation satellites at Wuhan University: strategy, result validation, and comparison. Journal of Geodesy, 90(2), 143–159.

Guo, Q. (2015). Precision comparison and analysis of four online free PPP services in static positioning and tropospheric delay estimation. GPS Solutions, 19(4), 537–544.

Guyon, I., Boser·, B., & Vapnik, V. (2011). Automatic Capacity Tuning of Very Large VC-dimension Classifiers.

Gwal, A. K., Choudhary, S., & Yadav, R. (2022). Study of Positional Error on Ionospheric Scintillation Over Antarctic Region and Loss due to Locking of GPS signal. In Assessing the Antarctic Environment from a Climate Change Perspective (pp. 189–205). Springer.

Hadas, T., & Bosy, J. (2014). IGS RTS precise orbits and clocks verification and quality degradation over time. GPS Solutions, 19(1), 93–105. https://doi.org/10.1007/s10291-014-0369-5

Hadas, T., & Hobiger, T. (2021). Benefits of Using Galileo for Real-Time GNSS Meteorology. IEEE Geoscience And Remote Sensing Letters, 18(10), 1756–1760. https://doi.org/10.1109/LGRS.2020.3007138

Hadas, T., Kaplon, J., Bosy, J., Sierny, J., & Wilgan, K. (2013). Near-real-time regional troposphere models for the GNSS precise point positioning technique. Measurement Science And Technology, 24(5). https://doi.org/10.1088/0957-0233/24/5/055003

Hallam, A. (1975). Alfred Wegener and the hypothesis of continental drift. Scientific American, 232(2), 88–97.

Hashemi, M., & Karimi, H. A. (2016). A Machine Learning Approach to Improve the Accuracy of GPS-Based Map-Matching Algorithms (Invited Paper). 2016 IEEE 17th International Conference on Information Reuse and Integration (IRI), 77–86. https://doi.org/10.1109/IRI.2016.18

Hastie, T., Tibshirani, R., Friedman, J. H., & Friedman, J. H. (2009a). The elements of statistical learning: data mining, inference, and prediction (Vol. 2). Springer.

Hastie, T., Tibshirani, R., Friedman, J. H., & Friedman, J. H. (2009b). The elements of statistical learning: data mining, inference, and prediction (Vol. 2). Springer.

Hein, G. W. (2020). Status, perspectives and trends of satellite navigation. Satellite Navigation, 1(1). https://doi.org/10.1186/s43020-020-00023-x

Héroux, P., Gao, Y., Kouba, J., Lahaye, F., Mireault, Y., Collins, P., Macleod, K., Tétreault, P., & Chen, K. (2004). Products and applications for Precise Point Positioning-Moving towards real-time. Proceedings of the 17th International Technical Meeting of the Satellite Division of The Institute of Navigation (ION GNSS 2004), 1832–1843.

Hesselbarth, A., & Wanninger, L. (2008). Short-term stability of GNSS satellite clocks and its effects on precise point positioning. Proceedings of the 21st International Technical Meeting of the Satellite Division of the Institute of Navigation (ION GNSS 2008), 1855–1863.

Hexagon. (2022). Precise Point Positioning (PPP) | NovAtel. https://novatel.com/an-introduction-to-gnss/chapter-5-resolving-errors/precise-point-positioning-ppp

Highland, L., & Bobrowsky, P. (2018). TXT-tool 0.001-2.1 Landslide types: descriptions, illustrations and photos. In Landslide Dynamics: ISDR-ICL Landslide Interactive Teaching Tools (pp. 1–38). Springer.

Highland, L., & Bobrowsky, P. T. (2008). The landslide handbook: a guide to understanding landslides. US Geological Survey Reston.

Hobiger, T., Ichikawa, R., Takasu, T., Koyama, Y., & Kondo, T. (2008). Ray-traced troposphere slant delays for precise point positioning. Earth, Planets and Space, 60(5), e1–e4. https://doi.org/10.1186/BF03352809

Hofleitner, A., Herring, R., & Bayen, A. (2012). Arterial travel time forecast with streaming data: A hybrid approach of flow modelling and machine learning. Transportation Research Part B: Methodological, 46(9), 1097–1122. https://doi.org/10.1016/j.trb.2012.03.006

Hofmann-Wellenhof, B., Lichtenegger, H., & Collins, J. (2012). Global positioning system: theory and practice. Springer Science & Business Media.

Hristopulos, D. T., Mertikas, S. P., Arhontakis, I., & Brownjohn, J. M. W. (2007). Using GPS for monitoring tall-building response to wind loading: Filtering of abrupt changes and low-frequency noise, variography and spectral analysis of displacements. GPS Solutions, 11(2), 85–95. https://doi.org/10.1007/s10291-006-0035-7

Hu, Y., Liu, L., Larson, K. M., Schaefer, K. M., Zhang, J., & Yao, Y. (2018). GPS interferometric reflectometry reveals cyclic elevation changes in thaw and freezing seasons in a permafrost area (Barrow, Alaska). Geophysical Research Letters, 45(11), 5581–5589.

Huang, L., Lu, Z., Li, B., Xin, G., An, W., Lv, H., Wang, N., & Zhou, X. (2016). The Performance Analysis of Multi-system Integrated Precise Point Positioning (PPP). In J. Sun, J. Liu, S. Fan, &

F. Wang (Eds.), China Satellite Navigation Conference (CSNC) 2016 Proceedings: Volume III (pp. 317–326). Springer Singapore.

Hyndman, R. J., & Athanasopoulos, G. (2018). Forecasting: principles and practice. OTexts.

IGS. (2020a). IGS RTS Contributors. http://www.igs.org/rts/contributors

IGS. (2020b). Products – International GNSS Service. https://igs.org/products/

IGS. (2020c). Real-Time Service (RTS) – International GNSS Service. https://igs.org/rts

IGS. (2020d). RTS Formats – International GNSS Service. https://igs.org/rts/formats/

IGS. (2020e). RTS Products – International GNSS Service. https://igs.org/rts/products/

IGS. (2022). IGS Components – International GNSS Service. https://igs.org/components/#wg

INTERNATIONAL GNSS SERVICE. (2020). IGS. https://igs.org/data-access/#global-dcs

International Terrestrial Frame. (2020). ITRF | Solutions. https://itrf.ign.fr/en/solutions

Jäger, R., Kälber, S., & Oswald, M. (2006). GNSS / GPS / LPS based Online Control and Alarm System (GOCA) - Mathematical Models and Technical Realisation of a System for Natural and Geotechnical Deformation Monitoring and Analysis -. Online, 0, 1–11.

Jäger, R., Kälber, S., Oswald, M., & Bertges, M. (2005). GNSS/GPS/LPS based Online Control and Alarm System (GOCA)-Mathematical models and technical realisation of a system for natural and geotechnical deformation monitoring and analysis. Proceedings of the 2005 Geodetic Deformation Monitoring: From Geophysical to Engineering Roles, IAG Symposium. Jaén, Spain, March, 17–19.

James, G., Witten, D., Hastie, T., & Tibshirani, R. (2013). An introduction to statistical learning (Vol. 112). Springer.

Janssen, V. (2009). A comparison of the VRS and MAC principles for network RTK.

Japan Meteorological Agency. (2022a). Earthquake Information. https://www.jma.go.jp/bosai/map.html#11/35.8/140.867/&elem=int&contents=earthquake_map&lang=en

Japan Meteorological Agency. (2022b). Tsunami Warnings/Advisories. https://www.jma.go.jp/bosai/map.html#5/37.979/135/&elem=warn&contents=tsunami&lang=en

Japan Meteorological Agency. (2022c). Volcanic Warnings. https://www.jma.go.jp/bosai/map.html#5/34.5/137/&contents=volcano&lang=en

Jet Propulsion Laboratory. (2020). NASA Jet Propulsion Laboratory (JPL) - Robotic Space Exploration. https://www.jpl.nasa.gov/

Jet Propulsion Laboratory. (2021). GipsyX. https://gipsy-oasis.jpl.nasa.gov/

Jet Propulsion Laboratory. (2022). Automatic Precise Positioning Service of the Global Differential GPS (GDGPS) System. https://pppx.gdgps.net//

Jiang, W., Li, Y., & Rizos, C. (2015). Locate-based precise point positioning for kinematic maritime applications. GPS SOLUTIONS, 19(1), 117–128. https://doi.org/10.1007/s10291-014-0373-9

Johnston, G., Riddell, A., & Hausler, G. (2017). The International GNSS Service. Springer Handbook of Global Navigation Satellite Systems, 967–982. https://doi.org/10.1007/978-3-319-42928-1_33

Jokinen, A., Feng, S., Milner, C., Schuster, W., Ochieng, W., Hide, C., Moore, T., & Hill, C. (2011). Precise point positioning and integrity monitoring with GPS and GLONASS. European Navigation Conference, 2011.

Jokinen, A., Feng, S., Schuster, W., Ochieng, W., Hide, C., Moore, T., & Hill, C. (2013). GLONASS aided GPS ambiguity fixed precise point positioning. The Journal of Navigation, 66(3), 399–416.

Jokinen, A., Feng, S., Schuster, W., Ochieng, W., Yang, L., Moore, T., & Hill, C. (2013). Improving ambiguity validation and integrity monitoring of Precise Point Positioning (PPP). Proceedings of the 26th International Technical Meeting of the Satellite Division of The Institute of Navigation (ION GNSS+ 2013), 1224–1233.

Kaftan, V., & Melnikov, A. (2017). Local deformation precursors of large earthquakes derived from GNSS observation data. IOP Conference Series: Earth and Environmental Science, 95(3), 032030.

Kaleev, D. v, & Saburova, V. I. (2018). Techniques and tools for analysis of navigation solution of Android N smartphones. 2018 IEEE Conference of Russian Young Researchers in Electrical and Electronic Engineering (EIConRus), 1368–1372.

Kaleev, D. v, Sergeev, N. M., Fedotovskikh, K. v, & Shiro, G. E. (2021). Modelling and Validation of Real Time Kinematic Technique in Autonomous Driving Simulator. 2021 IEEE Conference of Russian Young Researchers in Electrical and Electronic Engineering (ElConRus), 2094–2098.

Kaloop, M. R., Pijush, S., Rabah, M., Al-Ajami, H., Hu, J. W., & Zaki, A. (2022). Improving accuracy of local geoid model using machine learning approaches and residuals of GPS/levelling geoid height. Survey Review, 54(387), 505–518. https://doi.org/10.1080/00396265.2021.1970918

Kamogawa, M., Orihara, Y., Tsurudome, C., Tomida, Y., Kanaya, T., Ikeda, D., Gusman, A. R., Kakinami, Y., Liu, J.-Y., & Toyoda, A. (2016). A possible space-based tsunami early warning system using observations of the tsunami ionospheric hole. Scientific Reports, 6(1), 1–7.

Kaplan & Hegrat. (2006). Understanding GPS. In Elliott D. Kaplan Christopher J. Hegarty (Ed.), Better Corporate Reporting (Second Edi). https://doi.org/10.4324/9781351274845-10

Katsigianni, G., Loyer, S., Perosanz, F., Mercier, F., Zajdel, R., & Sośnica, K. (2019). Improving Galileo orbit determination using zero-difference ambiguity fixing in a Multi-GNSS processing. Advances in Space Research, 63(9), 2952–2963. https://doi.org/10.1016/j.asr.2018.08.035

Kavzoglu, T., & Saka, M. H. (2005). Modelling local GPS/levelling geoid undulations using artificial neural networks. Journal of Geodesy, 78(9), 520–527. https://doi.org/10.1007/s00190-004-0420-3

Kazmierski, K., Sośnica, K., & Hadas, T. (2018). Quality assessment of multi-GNSS orbits and clocks for real-time precise point positioning. Gps Solutions, 22(1), 1–12.

Kazmierski, K., Zajdel, R., & Sośnica, K. (2020). Evolution of orbit and clock quality for real-time multi-GNSS solutions. GPS Solutions, 24(4), 111. https://doi.org/10.1007/s10291-020-01026-6

Kenyeres, A., Bellet, J. G., Bruyninx, C., Caporali, A., de Doncker, F., Droscak, B., Duret, A., Franke, P., Georgiev, I., Bingley, R., Huisman, L., Jivall, L., Khoda, O., Kollo, K., Kurt, A. I., Lahtinen, S., Legrand, J., Magyar, B., Mesmaker, D., … Weber, M. (2019). Regional integration of long-

term national dense GNSS network solutions. GPS Solutions, 23(4). https://doi.org/10.1007/s10291-019-0902-7

Keras. (2023). Keras: the Python deep learning API. https://keras.io/

Khoo, V. H. S., Tor, Y. K., & Ong, G. (2010). Monitoring of High-Rise Building using Real-Time Differential GPS Monitoring of High-Rise Building using Real-Time Differential GPS. FIG Congress 2010 Facing Challenges- Building the Capaciity, April, 11–16. http://www.fig.net/pub/fig2010/papers/ts02d%5Cts02d_khoo_tor_et_al_3976.pdf

Kiliszek, D., & Kroszczyński, K. (2020). Performance of the precise point positioning method along with the development of GPS, GLONASS and Galileo systems. Measurement, 164, 108009.

Kintner, P. M., Humphreys, T., & Hinks, J. (2009). GNSS and ionospheric scintillation. Inside GNSS, 4(4), 22–30.

Kintner, P. M., Ledvina, B. M., & de Paula, E. R. (2007). GPS and ionospheric scintillations. Space Weather, 5(9).

Kim, H. S., & Lee, H. K. (2012). Elimination of clock jump effects in low-quality differential GPS measurements. Journal of Electrical Engineering & Technology, 7(4), 626-635.

Kirschenstein, M., Krasuski, K., & Cwiklak, J. (2018). Designation Of Integrated Perceptible water Vapour For Local Rural Region Using GPS Satellite Technique. Proceedings of the International Scientific Conference.

Klobuchar, J. A. (1987). Ionospheric time-delay algorithm for single-frequency GPS users. IEEE Transactions on Aerospace and Electronic Systems, 3, 325–331.

Kogure, S., Sawabe, M., & Kishimoto, M. (2006). Status of QZSS Navigation System in Japan. Proceedings of the 19th International Technical Meeting of the Satellite Division of The Institute of Navigation (ION GNSS 2006), 2092–2102.

Komac, M., Holley, R., Mahapatra, P., van der Marel, H., & Bavec, M. (2015). Coupling of GPS/GNSS and radar interferometric data for a 3D surface displacement monitoring of landslides. Landslides, 12(2), 241–257.

Kouba, J. (2009). A simplified yaw-attitude model for eclipsing GPS satellites. GPS solutions, 13, 1-12.

Kouba, J., & Héroux, P. (2001a). Precise point positioning using IGS orbit and clock products. GPS Solutions, 5(2), 12–28.

Kouba, J., & Héroux, P. (2001b). Precise Point Positioning Using IGS Orbit and Clock Products Precise Point Positioning Using IGS Orbit and Clock Products. March 2015. https://doi.org/10.1007/PL00012883

Krásná, H., Böhm, J., & Schuh, H. (2013). Tidal Love and Shida numbers estimated by geodetic VLBI. Journal of Geodynamics, 70, 21–27.

Krasuski, K. (2017). Estimation Troposphere Delay For GBAS Reference Stations. Acta Avionica, 1, 1–8.

Krasuski, K., Wierzbicki, D., & Jafernik, H. (2018). Utilization PPP method in aircraft positioning in post-processing mode. Aircraft Engineering and Aerospace Technology.

Kreemer, C., Blewitt, G., & Klein, E. C. (2014). A geodetic plate motion and Global Strain Rate Model. Geochemistry, Geophysics, Geosystems, 15(10), 3849–3889. https://doi.org/10.1002/2014GC005407

Kubo, N. (2008). Basics of GNSS. 1–5.

KUMAR, M. (1988). World Geodetic System 1984 - A Modern And Accurate Global Reference Frame. Marine Geodesy, 12(2), 117–126. https://doi.org/10.1080/15210608809379580

Kwiatkowski, D., Phillips, P. C. B., Schmidt, P., & Shin, Y. (1992). Testing the null hypothesis of stationarity against the alternative of a unit root. Journal of Econometrics, 54(1–3), 159–178.

Landau, H., Chen, X., Klose, S., Leandro, R., & Vollath, U. (2009). Trimble's RTK and DGPS solutions in comparison with precise point positioning. In Observing our Changing Earth (pp. 709–718). Springer.

Landau, H., Vollath, U., & Chen, X. (2002). Virtual reference station systems. Journal of Global Positioning Systems, 1(2), 137–143.

Langley, R. B., Banville, S., & Steigenberger, P. (2012). First results: precise positioning with Galileo prototype satellites. GPS World, 23(9), 45–49.

Latif, K., Adam, A., Yusof, Y., & Kadir, A. Z. A. (2021). A review of G code, STEP, STEP-NC, and open architecture control technologies based embedded CNC systems. The International Journal of Advanced Manufacturing Technology, 114, 2549–2566.

Laurichesse, D., Mercier, F., Berthias, J.-P., & Bijac, J. (2008). Real time zero-difference ambiguities fixing and absolute RTK. Proceedings of the 2008 National Technical Meeting of The Institute of Navigation, 747–755.

le Mével, H., Feigl, K. L., Córdova, L., DeMets, C., & Lundgren, P. (2015). Evolution of unrest at Laguna del Maule volcanic field (Chile) from InSAR and GPS measurements, 2003 to 2014. Geophysical Research Letters, 42(16), 6590–6598.

Lee, K., & Kwan, M.-P. (2018). Physical activity classification in free-living conditions using smartphone accelerometer data and exploration of predicted results. Computers, Environment and Urban Systems, 67, 124–131.

https://doi.org/10.1016/j.compenvurbsys.2017.09.012

Lehtola, V. v, Mäkelä, M., de Oliveira Marques, T., & Montloin, L. (2022). Tropospheric wet tomography and PPP: Joint estimation from GNSS crowdsourcing data. Advances in Space Research.

Leica Geosystems. (2022). Life beyond traditional RTK: Satellite based Precise Point Positioning | Leica Geosystems. https://leica-geosystems.com/products/gnss-systems/smart-antennas/leica-viva-gs16/life-beyond-traditional-rtk-satellite-based-precise-point-positioning

Li, B., Ge, H., Bu, Y., Zheng, Y., & Yuan, L. (2022). Comprehensive assessment of real-time precise products from IGS analysis centers. Satellite Navigation, 3(1), 12. https://doi.org/10.1186/s43020-022-00074-2

Li, C., Hancock, C. M., Vadakke Veettil, S., Zhao, D., Galera Monico, J. F., & Hamm, N. A. S. (2022). Distinguishing ionospheric scintillation from multipath in GNSS signals using geodetic receivers. GPS Solutions, 26(4), 1–13.

Li, J., Bao, H., Han, X., Pan, F., Pan, W., Zhang, F., & Wang, D. (2017). Real-time self-driving car navigation and obstacle avoidance using mobile 3D laser scanner and GNSS. Multimedia Tools and Applications, 76(21), 23017–23039.

Li, P., Zhang, X., Ren, X., Zuo, X., & Pan, Y. (2016). Generating GPS satellite fractional cycle bias for ambiguity-fixed precise point positioning. GPS Solutions, 20(4), 771–782. https://doi.org/10.1007/s10291-015-0483-z

Li, W., Ivan, I., Liu, Y., & Yang, L. (2021). Visual Processing and Analysis of Landslide Deformation Based on GNSS. IEEE Sensors Journal, 21(22), 25260–25266.

Li, X., Ge, M., Dai, X., Ren, X., Fritsche, M., Wickert, J., & Schuh, H. (2015). Accuracy and reliability of multi-GNSS real-time precise positioning: GPS, GLONASS, BeiDou, and Galileo. Journal of Geodesy, 89(6), 607–635.

Li, X., Liu, G., Li, X., Zhou, F., Feng, G., Yuan, Y., & Zhang, K. (2019). Galileo PPP rapid ambiguity resolution with five-frequency observations. GPS Solutions, 24(1), 24. https://doi.org/10.1007/s10291-019-0930-3

Li, X. P., & Pan, L. (2021). Precise Point Positioning with Almost Fully Deployed BDS-3, BDS-2, GPS, GLONASS, Galileo and QZSS Using Precise Products from Different Analysis Centers. REMOTE SENSING, 13(19). https://doi.org/10.3390/rs13193905

Li, X., Zhang, X., Ren, X., Fritsche, M., Wickert, J., & Schuh, H. (2015). Precise positioning with current multi-constellation global navigation satellite systems: GPS, GLONASS, Galileo and BeiDou. Scientific Reports, 5(1), 1–14.

Lim, C., Lee, Y., Cho, A., & Park, B. (2021). A Review on the Usage of RTKLIB for Precise Navigation of Unmanned Vehicles. Journal of Positioning, Navigation, and Timing, 10(4), 243–251.

Lin, C., Wu, G., Feng, X., Li, D., Yu, Z., Wang, X., Gao, Y., Guo, J., Wen, X., & Jian, W. (2021). Application of Multi-System Combination Precise Point Positioning in Landslide Monitoring. Applied Sciences, 11(18), 8378.

Lindsay, R. P. (1964). The Impact of Automation On Public Administration. Western Political Quarterly, 17(3), 78–81. https://doi.org/10.1177/106591296401700364

Liu, G., Lian, J., Liang, C., Li, G., & Hu, J. (2016). An improved complex multiple-support response spectrum method for the non-classically damped linear system with coupled damping. Bulletin of Earthquake Engineering, 14(1), 161–184.

Liu, Q., Hernández-Pajares, M., Yang, H., Monte-Moreno, E., Roma-Dollase, D., García-Rigo, A., Li, Z., Wang, N., Laurichesse, D., Blot, A., Zhao, Q., Zhang, Q., Hauschild, A., Agrotis, L., Schmitz, M., Wübbena, G., Stürze, A., Krankowski, A., Schaer, S., … Ghoddousi-Fard, R. (2021). The cooperative IGS RT-GIMs: a reliable estimation of the global ionospheric electron content distribution in real time. Earth System Science Data, 13(9), 4567–4582. https://doi.org/10.5194/essd-13-4567-2021

Liu, T., Yuan, Y., Zhang, B., Wang, N., Tan, B., & Chen, Y. (2017). Multi-GNSS precise point positioning (MGPPP) using raw observations. Journal of Geodesy, 91(3), 253–268.

Liu, W. X., Mou, W. H., & Wang, F. X. (2012). A new unequal-weighted triple-frequency first order ionosphere correction algorithm and its application in COMPASS. SCIENCE CHINA-PHYSICS MECHANICS & ASTRONOMY, 55(3), 546–552. https://doi.org/10.1007/s11433-011-4607-3

Lou, Y. D., Liu, Y., Shi, C., Yao, X. G., & Zheng, F. (2014). Precise orbit determination of BeiDou constellation based on BETS and MGEX network. SCIENTIFIC REPORTS, 4. https://doi.org/10.1038/srep04692

Lou, Y., Zheng, F., Gu, S., Wang, C., Guo, H., & Feng, Y. (2016). Multi-GNSS precise point positioning with raw single-frequency and dual-frequency measurement models. GPS Solutions, 20(4), 849–862. https://doi.org/10.1007/s10291-015-0495-8

Loyer, S., Perosanz, F., Mercier, F., Capdeville, H., & Marty, J.-C. (2012). Zero-difference GPS ambiguity resolution at CNES–CLS IGS Analysis Center. Journal of Geodesy, 86(11), 991–1003. https://doi.org/10.1007/s00190-012-0559-2

Luo, X., Lou, Y., Xiao, Q., Gu, S., Chen, B., & Liu, Z. (2018). Investigation of ionospheric scintillation effects on BDS precise point positioning at low-latitude regions. GPS Solutions, 22(3), 1–12.

Luo, X. M., Lou, Y. D., Xiao, Q. Q., Gu, S. F., Chen, B. Y., & Liu, Z. Z. (2018). Investigation of ionospheric scintillation effects on BDS precise point positioning at low-latitude regions. GPS SOLUTIONS, 22(3). https://doi.org/10.1007/s10291-018-0728-8

Lv, J., Gao, Z., Kan, J., Lan, R., Li, Y., Lou, Y., Yang, H., & Peng, J. (2022). Modeling and assessment of multi-frequency GPS/BDS-2/BDS-3 kinematic precise point positioning based on vehicle-borne data. Measurement, 189, 110453. https://doi.org/10.1016/j.measurement.2021.110453

Mader, C. L., & Gittings, M. L. (2002). Modelling the 1958 Lituya Bay mega-tsunami, II. Science of Tsunami Hazards, 20(5), 241–250.

Maglambayan, V. L. L., & Macalalad, E. P. (2022). Two-Dimensional Mapping of Ionospheric Total Electron Content over the Philippines Using Kriging Interpolation. Atmosphere, 13(10), 1626.

Malhotra, P. K. (2003). Strong-motion records for site-specific analysis. Earthquake Spectra, 19(3), 557–578.

Manesh, M. R., Kenney, J., Hu, W. C., Devabhaktuni, V. K., & Kaabouch, N. (2019). Detection of GPS Spoofing Attacks on Unmanned Aerial Systems. 2019 16th IEEE Annual Consumer Communications & Networking Conference (CCNC), 1–6. https://doi.org/10.1109/CCNC.2019.8651804

Männel, B., Brandt, A., Nischan, T., Brack, A., Sakic, P., & Bradke, M. (2020a). GFZ final product series for the International GNSS Service (IGS).

Männel, B., Brandt, A., Nischan, T., Brack, A., Sakic, P., & Bradke, M. (2020b). GFZ rapid product series for the IGS.

Maorong, G. (2022). Early-Warning and Rapid Impact Assessment with real-time GNSS in the Mediterranean: GFZ. https://www.gfz-potsdam.de/sektion/geodaetische-weltraumverfahren/projekte/ewrica

Martín, A., Hadas, T., Dimas, A., Anquela, A., & Berne, J. (2015, October). Influence of real-time products latency on kinematic PPP results. In Proceedings of the ESA 5th International Colloquium on Scientific and Fundamental Aspects of the Galileo Program, Braunschweig, Germany (pp. 27-29).

Martín, A., Anquela, A. B., Capilla, R., & Berné, J. L. (2011). PPP technique analysis based on time convergence, repeatability, IGS products, different software processing, and GPS+ GLONASS constellation. Journal of Surveying Engineering, 137(3), 99–108. https://doi.org/10.1061/(ASCE)SU.1943-5428.0000047

Martín, A., Anquela, A. B., Dimas-Pagés, A., & Cos-Gayón, F. (2015). Validation of performance of real-time kinematic PPP. A possible tool for deformation monitoring. Measurement: Journal of the International Measurement Confederation, 69, 95–108. https://doi.org/10.1016/j.measurement.2015.03.026

Martín, A., Ibáñez, S., Baixauli, C., Blanc, S., & Anquela, A. B. (2020). Multi-constellation GNSS interferometric reflectometry with mass-market sensors as a solution for soil moisture monitoring. Hydrology and Earth System Sciences, 24(7), 3573–3582. https://doi.org/10.5194/hess-24-3573-2020

Martín, A., Luján, R., & Anquela, A. B. (2020). Python software tools for GNSS interferometric reflectometry (GNSS-IR). GPS Solutions, 24(4), 1–7. https://doi.org/10.1007/s10291-020-01010-0

Martire, L., Constantinou, V., Krishnamoorthy, S., Komjathy, A., Vergados, P., Meng, X., Bar-Sever, Y., Craddock, A., & Wilson, B. (2021). Near Real-Time Tsunami Early Warning System Using GNSS Ionospheric Measurements. AGU Fall Meeting Abstracts, 2021, G45C-0415.

Masi, A., Chiauzzi, L., Braga, F., Mucciarelli, M., Vona, M., & Ditommaso, R. (2011). Peak and integral seismic parameters of L'Aquila 2009 ground motions: Observed versus code provision values. Bulletin of Earthquake Engineering, 9(1), 139–156. https://doi.org/10.1007/s10518-010-9227-1

Massachusetts Institute of Technology. (2022). GeoWeb. http://geoweb.mit.edu/

Matplotlib. (2023). Matplotlib — Visualization with Python. https://matplotlib.org/

Matplotlip. (2012). Matplotlib: Python plotting — Matplotlib 3.1.2 documentation. https://matplotlib.org/

McGuire, J. J., Smith, D. E., Frankel, A. D., Wirth, E. A., McBride, S. K., & de Groot, R. M. (2021). Expected warning times from the ShakeAlert earthquake early warning system for earthquakes in the Pacific Northwest. US Geological Survey.

Meinig, C., Stalin, S., Nakamura, A., & Milburn, H. (2005). Real-Time Deep-Ocean Tsunami Measuring, Monitoring, and Reporting System: The NOAA DART II Description and Disclosure.

Meyer, F., Bamler, R., Jakowski, N., & Fritz, T. (2006). The potential of low-frequency SAR systems for mapping ionospheric TEC distributions. IEEE Geoscience and Remote Sensing Letters, 3(4), 560–564.

Miaoyan, Z., Jun, Z., & Yong, Q. (2008). Satellite selection for multi-constellation. 2008 IEEE/ION Position, Location and Navigation Symposium, 1053–1059.

Microsoft. (2023a). Cloud Computing Services | Microsoft Azure. https://azure.microsoft.com/en-us/?OCID=AID2200086_SEM_ConnexityCSE&szredirectid=16821111425838877943710080302008005

Microsoft. (2023b). Microsoft Excel Spreadsheet Software | Microsoft 365. https://www.microsoft.com/en-us/microsoft-365/excel

Milyukov, V., Kopaev, A., Zharov, V., Mironov, A., Myasnikov, A., Kaufman, M., & Duev, D. (2010). Monitoring crustal deformations in the Northern Caucasus using a high precision long base laser strainmeter and the GPS/GLONASS network. Journal of Geodynamics, 49(3–4), 216–223.

Miura, S., Sato, T., Hasegawa, A., Suwa, Y., Tachibana, K., & Yui, S. (2004). Strain concentration zone along the volcanic front derived by GPS observations in NE Japan arc. Earth, Planets and Space, 56(12), 1347–1355.

Mongillo, M. (2011). Choosing Basis Functions and Shape Parameters for Radial Basis Function Methods.

Muafiry, I. N., Meilano, I., Heki, K., Wijaya, D. D., & Nugraha, K. A. (2022). Ionospheric Disturbances after the 2022 Hunga Tonga-Hunga Ha'apai Eruption above Indonesia from GNSS-TEC Observations. Atmosphere, 13(10), 1615.

Murphy, K. P. (2012). Machine learning: a probabilistic perspective. MIT press.

Nadarajah, N., Khodabandeh, A., Wang, K., Choudhury, M., & Teunissen, P. J. G. (2018). Multi-GNSS PPP-RTK: from large-to small-scale networks. Sensors, 18(4), 1078.

Nadarajah, N., & Teunissen, P. J. G. (2013). Instantaneous GPS/BeiDou/Galileo attitude determination: a single-frequency robustness analysis under constrained environments. Proceedings of the ION 2013 Pacific PNT Meeting, 1088–1103.

NASA. (2013). GPS-Aided and DART-Ensured Real-time (GADER) Tsunami Early Detection System. https://appliedsciences.nasa.gov/what-we-do/projects/gps-aided-and-dart-ensured-real-timegader-tsunami-early-detection-system

National Aeronautics and Space Administration. (2022). Navistar 1.

National Centers for Environmental Information (NCEI), N. (2022a). NCEI/WDS Global Historical Tsunami Database, 2100 BC to Present. https://doi.org/doi:10.7289/V5PN93H7

National Centers for Environmental Information (NCEI), N. (2022b). NCEI/WDS Global Significant Earthquake Database, 2150 BC to Present. https://doi.org/doi:10.7289/V5TD9V7K

National Centers for Environmental Information (NCEI), N. (2022c). NCEI/WDS Global Significant Volcanic Eruptions Database, 4360 BC to Present. https://doi.org/doi:10.7289/V5JW8BSH

National Coordination Office for Space-Based Positioning, N. and T. (2020). GPS.gov: New Civil Signals. https://www.gps.gov/systems/gps/modernization/civilsignals/

National Coordination Office for Space-Based Positioning, N. and T. (2021). GPS.gov: Space Segment. https://www.gps.gov/systems/gps/space/#IIIF

National Oceanic and Atmospheric Administration. (2018).

Tsunamis. https://www.noaa.gov/education/resource-collections/ocean-coasts/tsunamis

Navarro, V., Dittrich, R., Skaburskas, K., Ying, Y., Bégin, M.-E., & Perez, F. (2019). Big Data GNSS for Intermediate Frequency Recording Stations. Big Data in Space.

Nelder, J. A., & Wedderburn, R. W. M. (1972). Generalized linear models. Journal of the Royal Statistical Society: Series A (General), 135(3), 370–384.

Nelson, R. A., McCarthy, D. D., Malys, S., Levine, J., Guinot, B., Fliegel, H. F., Beard, R. L., & Bartholomew, T. R. (2001). The leap second: its history and possible future. Metrologia, 38(6), 509.

Nevada Geodetic Laboratory. (2017). NGL Global Strain Rate Map. http://geodesy.unr.edu/gsrm.php

NGS. (2022). OPUS: the Online Positioning User Service, process your GNSS data in the National Spatial Reference System. https://www.ngs.noaa.gov/OPUS/

Niell, A. E. (1996). Global mapping functions for the atmosphere delay at radio wavelengths. Journal of Geophysical Research: Solid Earth, 101(B2), 3227–3246. https://doi.org/10.1029/95jb03048

Nik, S. A., & Petovello, M. G. (2010). Implementation of a dual-frequency GLONASS and GPS L1 C/A software receiver. The Journal of Navigation, 63(2), 269–287.

Ning, Y., Han, H., & Zhang, L. (2018). Single-frequency precise point positioning enhanced with multi-GNSS observations and global ionosphere maps. Measurement Science and Technology, 30(1), 015013.

NOAA. (2022). U.S. Tsunami Warning Centers. https://tsunami.gov/

Noël, S. (2012). Rise in upper-atmospheric carbon. Nature Geoscience, 5(12), 848–849. https://doi.org/10.1038/ngeo1648

Noll, C. E. (2010). The crustal dynamics data information system: A resource to support scientific analysis using space geodesy. Advances in Space Research, 45(12), 1421-1440.

Nof, R. N., & Kurzon, I. (2021). TRUAA—Earthquake early warning system for Israel: Implementation and current status. Seismological Research Letters, 92(1), 325–341.

North American Reference Frame Densification. (2021). NAREF. http://www.naref.org/naref/

NovAtel. (2015). NovAtel CORRECT® with PPP NovAtel. https://www.novatel.com/products/novatel-correct-ppp/

NovAtel a. (2022). GPGGA Sentences . https://docs.novatel.com/OEM7/Content/Logs/GPGGA.htm

NovAtel b. (2022). GPRMC Sentences. https://docs.novatel.com/OEM7/Content/Logs/GPRMC.htm

NovAtel Inc, (2015). An Introduction to GNSS GPS, GLONASS, BeiDou, Galileo and other Global Navigation Satellite Systems NovAtel. https://www.novatel.com/assets/Documents/Books/Intro-to-GNSS.pdf%0Ahttps://www.novatel.com/an-introduction-to-gnss/

NRC. (2022). Precise Point Positioning. https://webapp.csrs-scrs.nrcan-rncan.gc.ca/geod/tools-outils/ppp.php

NumPy. (2023). NumPy. https://numpy.org/

Odijk, D., Zhang, B., & Teunissen, P. J. G. (2015). Multi-GNSS PPP and PPP-RTK: Some GPS plus BDS Results in Australia. In J. Sun, J. Liu, S. Fan, & X. Lu (Eds.), China Satellite Navigation Conference (CSNC) 2015 Proceedings, VolII (Vol. 341, pp. 613–623). https://doi.org/10.1007/978-3-662-46635-3_52

Ogutcu, S., Erkavas, Y. K., Shakor, A. Q., & Farhan, H. T. (2021). Investigating the latest contribution of BeiDou-3 FOC to GPS/GLONASS/Galileo PPP. SURVEY REVIEW. https://doi.org/10.1080/00396265.2021.2017110

OmniSTAR services. (2022). OmniSTAR. https://www.omnistar.com/about-us/

Orabi, M., Khalife, J., Abdallah, A. A., Kassas, Z. M., & Saab, S. S. (2020). A Machine Learning Approach for GPS Code Phase Estimation in Multipath Environments. 2020 IEEE/ION Position, Location and Navigation Symposium (PLANS), 1224–1229. https://doi.org/10.1109/PLANS46316.2020.9110155

Our world in Data. (2022). Natural Disasters Data Explorer. https://ourworldindata.org/explorers/natural-disasters?facet=none&Disaster+Type=Landslides&Impact=Deaths&Timespan=Decadal+average&Per+capita=false&country=~OWID_WRL

Overacker, J., Hammond, W. C., Blewitt, G., & Kreemer, C. (2022). Vertical Land Motion of the High Plains Aquifer Region of the United States: Effect of Aquifer Confinement Style, Climate Variability, and Anthropogenic Activity. Water Resources Research, 58(6). https://doi.org/10.1029/2021WR031635

Pan, L., Zhang, X., Li, X., Li, X., Lu, C., Liu, J., & Wang, Q. (2019). Satellite availability and point positioning accuracy evaluation on a global scale for integration of GPS, GLONASS, BeiDou and Galileo. Advances in Space Research, 63(9), 2696–2710. https://doi.org/10.1016/j.asr.2017.07.029

Pan, Z., Chai, H., & Kong, Y. (2017). Integrating multi-GNSS to improve the performance of precise point positioning. Advances in Space Research, 60(12), 2596–2606.

Pandas. (2023). pandas - Python Data Analysis Library. https://pandas.pydata.org/

Parolai, S., Boxberger, T., Pilz, M., Fleming, K., Haas, M., Pittore, M., Petrovic, B., Moldobekov, B., Zubovich, A., & Lauterjung, J. (2017). Assessing earthquake early warning using sparse networks in developing countries: Case study of the Kyrgyz republic. Frontiers in Earth Science, 5. https://doi.org/10.3389/feart.2017.00074

Pathy, N. B., Musa, T. A., Asillam, M. F., Aris, W. A. W., & Khamdan, S. S. (2019). Near real time ionospheric monitoring system over Malaysia using GPS Data: My-Iono Service. Journal of Physics: Conference Series, 1152(1), 012016.

Pavlis, N., Kenyon, S., Factor, J., & Holmes, S. (2008). Earth gravitational model 2008. In SEG technical program expanded abstracts 2008 (pp. 761-763). Society of Exploration Geophysicists.

Paziewski, J., Kurpinski, G., Wielgosz, P., Stolecki, L., Sieradzki, R., Seta, M., Oszczak, S., Castillo, M., & Martin-Porqueras, F. (2020). Towards Galileo plus GPS seismology: Validation of high-

rate GNSS-based system for seismic events characterisation. Measurement, 166. https://doi.org/10.1016/j.measurement.2020.108236

Pearson, K. (1920). Notes on the history of correlation. Biometrika, 13(1), 25–45.

Peck, R. B., Hanson, W. E., & Thornburn, T. H. (1991). Foundation engineering. John Wiley & Sons.

Pecoraro, G., Calvello, M., & Piciullo, L. (2019). Monitoring strategies for local landslide early warning systems. Landslides, 16(2), 213–231.

Pelc-Mieczkowska, R., & Tomaszewski, D. (2020). Space state representation product evaluation in satellite position and receiver position domain. Sensors, 20(13), 3791.

Peng, S. S. (1992). Surface subsidence engineering.

Penn State University, D. of G. (2020). Differencing | GEOG 862: GPS and GNSS for Geospatial Professionals. https://www.e-education.psu.edu/geog862/node/1727

Piccolo, D. (1990). A distance measure for classifying ARIMA models. Journal of Time Series Analysis, 11(2), 153–164.

Pirotti, F., Guarnieri, A., Masiero, A., Gregoretti, C., Degetto, M., & Vettore, A. (2015). Micro-scale landslide displacements detection using Bayesian methods applied to GNSS data. In Modern Technologies for Landslide Monitoring and Prediction (pp. 123–138). Springer.

Plotly. (2023). Plotly Python Graphing Library. https://plotly.com/python/

Prange, L., Dach, R., Lutz, S., Schaer, S., & Jäggi, A. (2015). The CODE MGEX orbit and clock solution. In IAG 150 Years (pp. 767–773). Springer.

Prasad, S. K., Towhata, I., Chandradhara, G. P., & Nanjundaswamy, P. (2004). Shaking table tests in earthquake geotechnical engineering. Current Science, 1398–1404.

Prepared, *, Cheng, P., Wen, H., Cheng, Y., Wang, H., Cheng, P., & Hanjiang, cheng, Y. (2009). China Geodetic Coordinate System 2000 * Chinese Academy of Surveying and Mapping China Geodetic Coordinate System 2000.

Python. (2023). Pickle library. https://docs.python.org/3/library/pickle.html

Pytorch. (2023). PyTorch. https://pytorch.org/

Qafisheh, M., Martín, A., Capilla, R. M., & Anquela, A. B. (2022). SVR and ARIMA models as machine learning solutions for solving the latency problem in real-time clock corrections. GPS Solutions, 26(3), 1–14. https://doi.org/10.1007/s10291-022-01270-y

Qafisheh, M. Solving the latency problem in real-time GNSS precise point positioning using open-source software. https://run.unl.pt/handle/10362/95142

Qafisheh, M., Furones, A, & Torres-Sospedra, J. (2020). Support vector regression machine learning tool to predict GNSS clock corrections in real-time PPP technique. CEUR Workshop Proceedings, 2626. http://localhost:8080/xmlui/handle/123456789/8516

Qafisheh, M., Martin, A., & Capilla, R. M. (2021, October 11). Proposed Methodology For Establishing An Early Gnss Warning System For Real-Time Deformation Monitoring. https://doi.org/10.4995/cigeo2021.2021.12691

Qi, H., Liu, Y., & Wei, D. (2014). GPS-Based Vehicle Moving State Recognition Method and Its Applications on Dynamic In-Car Navigation Systems. 2014 IEEE 12th International Conference on Dependable, Autonomic and Secure Computing, 354–360.

Qin, F., Fu, L., Wang, Y., & Mao, Y. (2021). A bagging tree-based pseudorange correction algorithm for global navigation satellite system positioning in foliage canyons. International Journal of Distributed Sensor Networks, 17(5), 15501477211016756. https://doi.org/10.1177/15501477211016757

Quan, Y., Lau, L., Roberts, G. W., Meng, X., & Zhang, C. (2018). Convolutional neural network based multipath detection method for static and kinematic GPS high precision positioning. Remote Sensing, 10(12). https://doi.org/10.3390/rs10122052

Quinlan, J. R. (1986). Induction of Decision Trees. In Machine Learning (Vol. 1).

Reduction, U. N. O. for D. R. (1901). Global assessment report on disaster risk reduction 2022: Our world at risk: Transforming governance for a resilient future. UN.

Research Institute of Geodesy, C. (2012a). Geodetic Observatory Pecny. https://www.pecny.cz/Joomla25/index.php/gnss

Research Institute of Geodesy, C. (2012b). GOP Intro. https://www.pecny.cz/

Research Institute of Geodesy, T. and C. (2020). VÚGTK, v.v.i. http://www.vugtk.cz/en/

Roberts, G. W., Tang, X., & Brown, C. J. (2019). Measurement and correlation of displacements on the Severn Suspension Bridge using GPS. Applied Geomatics, 11(2), 161–176.

Rodríguez, J. J., Kuncheva, L. I., & Alonso, C. J. (2006). Rotation forest: A New classifier ensemble method. IEEE Transactions on Pattern Analysis and Machine Intelligence, 28(10), 1619–1630. https://doi.org/10.1109/TPAMI.2006.211

Rolf Dach, P., Fridez, P., Dach, R., Andritsch, F., Arnold, D., Bertone, S., Fridez, P., Jäggi, A., Jean, Y., Maier, A., Mervart, L., Meyer, U., Orliac, E., Ortiz–Geist, E., Prange, L., Scaramuzza, S., Schaer, S., Sidorov, D., Sušnik, A., … Thaller, D. (2015). Bernese Manual.

Roman, D. R., Wang, Y. M., Saleh, J., & Li, X. (2010). Geodesy, geoids, and vertical datums: A perspective from the US National Geodetic Survey. FIG Congress, 11.

Royal Observatory of Belgium. (2021). EUREF Permanent GNSS Network. https://epncb.oma.be/

RTCM Committee, S. (2016). RTCM standard 10403.3 differential GNSS (global navigation satellite systems) services-version 3. RTCM Special Committee, 104.

RTCM Special Committee. (2016). RTCM Standard 10403.3 differential GNSS (Global Navigation Satellite Systems) Services-Version 3.

Ruhl, C. J., Melgar, D., Allen, R. M., Geng, J., Goldberg, D. E., Bock, Y., Crowell, B. W., Barrientos, S., Riquelme, S., Baez, J. C., Cabral-Cano, E., Pérez-Campos, X., Hill, E. M., Protti, M., Ganas, A., Ruiz, M., Mothes, P., Jarrín, P., Nocquet, J. M., … D'Anastasio, E. (2019). A global database of strong-motion displacement GNSS recordings and an example application to PGD scaling. Seismological Research Letters, 90(1), 271–279. https://doi.org/10.1785/0220180177

Rukundo, W. (2022). Ionospheric Electron Density and Electron Content Models for Space Weather Monitoring. In Magnetosphere and Solar Winds, Humans and Communication. IntechOpen.

Saastamoinen, J. (1972). Atmospheric correction for the troposphere and stratosphere in radio ranging satellites. The Use of Artificial Satellites for Geodesy, 15, 247–251.

Samuel, A. L. (1959). Some Studies in Machine Learning Using the Game of Checkers. IBM Journal of Research and Development, 3(3), 210–229. https://doi.org/10.1147/rd.33.0210

Sanchez, M., Pulido, J. A., Amarillo, F., & Gerner, J. L. (2008). The ESA" GNSS+" Project. Inter-satellite Ranging and Communication Links in the Frame of the GNSS Infrastructure Evolutions. Proceedings of the 21st International Technical Meeting of the Satellite Division of The Institute of Navigation (ION GNSS 2008), 2538–2546.

Sanz Subirana, J. M. J. Z. and M. H.-P. (2013). Gnss Data Processing: Vol. I.

Scaioni, M., Lu, P., Feng, T., Chen, W., Qiao, G., Wu, H., Tong, X., Wang, W., & Li, R. (2013). Analysis of spatial sensor network observations during landslide simulation experiments. European Journal of Environmental and Civil Engineering, 17(9), 802–825.

Scaioni, M., Marsella, M., Crosetto, M., Tornatore, V., & Wang, J. (2018). Geodetic and remote-sensing sensors for dam deformation monitoring. Sensors, 18(11), 3682.

Schaer, S. (1997). How to use CODE's global ionosphere maps. Astronomical Institute, University of Berne, 1–9.

Schaer, S., Beutler, G., Rothacher, M., & Springer, T. A. (1996). Daily global ionosphere maps based on GPS carrier phase data routinely produced by the CODE Analysis Center. Proceedings of the IGS Analysis Center Workshop 1996.

Scheck, M., & Bayer, U. (1999). Evolution of the Northeast German Basin—inferences from a 3D structural model and subsidence analysis. Tectonophysics, 313(1–2), 145–169.

Schmid, R., Steigenberger, P., & Gendt, G. (2007). Generation of a Consistent Absolute Phase Center Correction Model for GPS Receiver and Satellite Antennas. https://doi.org/10.1007/s00190-007-0148-y.Ralf

Schölkopf, B., Smola, A. J., & Bach, F. (2002). Learning with kernels: support vector machines, regularization, optimization, and beyond. MIT press.

Scikit-learn. (2023). scikit-learn: machine learning in Python — scikit-learn 1.2.1 documentation. https://scikit-learn.org/stable/index.html

Scripps Orbit and Permanent Array Center / California Spatial Reference Center. SOPAC Research Topics. Retrieved September 14, 2022, from

http://sopac-csrc.ucsd.edu/index.php/research-topics/

Seaborn. (2022). seaborn: statistical data visualization — seaborn 0.12.2 documentation. https://seaborn.pydata.org/

Seismosoft. (2019). Company - Seismosoft. https://seismosoft.com/company/

Sekhar, H. V., & Das, T. V. (2017). Analysing The Seismic Behaviour of Set Back Building By Using E-Tabs. International Journal of Civil Engineering and Technology, 8(1), 444–451.

ShakeAlert. (2016). ShakeAlert Earthquake Early Warning. https://www.shakealert.org/

Sheen, D.-H., Lim, I.-S., Park, J.-H., & Chi, H.-C. (2014). Magnitude scaling relationships using P waves for earthquake early warning in South Korea. Geosciences Journal, 18(1), 7–12.

Sheets, P. D., & Grayson, D. K. (2013). Volcanic activity and human ecology. Elsevier.

Shen, X., & Gao, Y. (2002). Kinematic processing analysis of carrier phase based precise point positioning. FIG XXII International Congress, Washington DC USA, Arial, 19–26.

Shi, J., & Gao, Y. (2014). A comparison of three PPP integer ambiguity resolution methods. GPS Solutions, 18(4), 519–528. https://doi.org/10.1007/s10291-013-0348-2

Sillard, P., & Boucher, C. (2001). A review of algebraic constraints in terrestrial reference frame datum definition. Journal of Geodesy, 75(2), 63–73.

SMOLA, A. J. and B. S. (2004). A tutorial on support vector regression - art%3A10.1023%2FB%3ASTCO.0000035301.49549.88.pdf. Statistics and Computing, 14, 199–222. https://doi.org/10.1023/B:STCO.0000035301.49549.88

Smola, A. J., & Schölkopf, B. (2004). A tutorial on support vector regression. Statistics and Computing, 14(3), 199–222.

Sneeuw, N., Novák, P., Crespi, M., & Sansò, F. (2012). Analysing time series of GNSS residuals by means of AR (I) MA processes. VII Hotine-Marussi Symposium on Mathematical Geodesy, International Association of Geodesy Symposia 137.

Sobolev, S. v, Babeyko, A. Y., Wang, R., Hoechner, A., Galas, R., Rothacher, M., Sein, D. v, Schröter, J., Lauterjung, J., & Subarya, C. (2007). Tsunami early warning using GPS-Shield arrays. Journal of Geophysical Research: Solid Earth, 112(B8).

Sparks, R. S. J. (2003). Forecasting volcanic eruptions. Earth and Planetary Science Letters, 210(1–2), 1–15.

Springer, T. A., Gurtner, W., Rothacher, M., & Schaer, S. (1997). EUREF activities at the CODE analysis center. Proceedings of the International Seminar on GPS in Central Europe, Penc, Hungary, May, 7–9.

Springer, T. A., & Hugentobler, U. (2001). IGS ultra rapid products for (near-) real-time applications. Physics and Chemistry of the Earth, Part A: Solid Earth and Geodesy, 26(6–8), 623–628.

Srinivasa Kumar, T., & Manneela, S. (2021). A review of the progress, challenges and future trends in tsunami early warning systems. Journal of the Geological Society of India, 97(12), 1533–1544.

Steigenberger, P., & Montenbruck, O. (2017). Galileo status: orbits, clocks, and positioning. GPS Solutions, 21(2), 319–331. https://doi.org/10.1007/s10291-016-0566-5

Štěpánek, P., Filler, V., & Buday, M. (2017). DORIS research activities at Geodetic Observatory Pecny. EGU General Assembly Conference Abstracts, 19347.

Sturze, A., Mervart, L., Sohne, W., Weber, G., & Wübbena, G. (2012). Real-time PPP using open CORS networks and RTCM standards. PPP-RTK Symposium, Frankfurt, Germany, 12–13.

Stürze, A., Mervart, L., Weber, G., Rülke, A., Wiesensarter, E., & Neumaier, P. (2016). The new version 2.12 of BKG Ntrip Client (BNC). Geophys. Res. Abstr, 18, 12012.

Subirana, J. S., Zornoza, J. J., & Pajares, M. H. (2011). GNSS signal. In Navipedia.

Sucuoğlu, H., Akkar, S., Halûk, S., & Sinan, A. (2014). Basic Earthquake Engineering. Basic Earthquake Engineering.

Sutton, R. S., & Barto, A. G. (2018). Reinforcement learning: An introduction. MIT press.

Suwarno, I., Ma'arif, A., Maharani Raharja, N., Nurjanah, A., Ikhsan, J., & Mutiarin, D. (2021). IoT-based Lava Flood Early Warning System with Rainfall Intensity Monitoring and Disaster Communication Technology. Emerging Science Journal, 4, 154–166.

Suya, R. G., Chen, Y.-T., Kwong",," Chiew Foong, & Zhang, P. (2022). BeiDou intra-system bias using different precise orbit and clock products. Measurement, 191, 110804. https://doi.org/10.1016/j.measurement.2022.110804

Suzuki, T., & Amano, Y. (2021). Nlos multipath classification of GNSS signal correlation output using machine learning. Sensors, 21(7). https://doi.org/10.3390/s21072503

Svensen, M., & Bishop, C. M. (2009). Pattern recognition and machine learning-solutions to the exercises: Web-edition. New York.

Swamynathan, M. (2019). Mastering machine learning with python in six steps: A practical implementation guide to predictive data analytics using python. Apress.

Tableau Software. (2023). Business Intelligence and Analytics Software. https://www.tableau.com/

Takács, B., Siki, Z., & Markovits-Somogyi, R. (2017). Extension of RTKLIB for the Calculation and Validation of Protection Levels. The International Archives of Photogrammetry, Remote Sensing and Spatial Information Sciences, 42, 161.

Takasu, T. (2009). RTKLIB: Open-source program package for RTK-GPS. Proceedings of the FOSS4G.

Tan, P.-N., Steinbach, M., & Kumar, V. (2016). Introduction to data mining. Pearson Education India.

Tanaka, G., Okada, M., & Mineno, H. (2015). GPS-based daily context recognition for lifelog generation using smartphone. Int. J. Adv. Comput. Sci. Appl, 6, 104–112.

Tang, H., & Xu, T. (2019). Multi-GNSS kinematic relative positioning of multiple base stations and its application in deformation monitoring. China Satellite Navigation Conference, 106–113.

Tang, X., Roberts, G. W., Li, X., & Hancock, C. M. (2017). Real-time kinematic PPP GPS for structure monitoring applied on the Severn Suspension Bridge, UK. Advances in Space Research, 60(5), 925–937. https://doi.org/10.1016/j.asr.2017.05.010

Tao, Y., Liu, C., Liu, C., Zhao, X., Hu, H., & Xin, H. (2021a). Joint time–frequency mask and convolutional neural network for real-time separation of multipath in GNSS deformation monitoring. GPS Solutions, 25(1), 1–13.

Tao, Y., Liu, C., Liu, C., Zhao, X., Hu, H., & Xin, H. (2021b). Joint time–frequency mask and convolutional neural network for real-time separation of multipath in GNSS deformation monitoring. GPS Solutions, 25(1), 25. https://doi.org/10.1007/s10291-020-01074-y

Taylor, B., Underwood, C. I., Evans, H. D. R., Ryden, K., Rodgers, D., Daly, E. J., Mandorlo, G., Falcone, M., Morris, P. A., & Prieto, R. G. (2007). Results from the Galileo GIOVE—A radiation monitors and comparison with existing radiation belt models. IEEE Transactions on Nuclear Science, 54(4), 1076–1081.

Team, G. P., Gendt, G., Altamimi, Z., Dach, R., Sohne, W., & Springer, T. (2011). GGSP Realisation and maintenance of the Galileo Terrestrial Reference Frame. Advances In Space Research, 47(2), 174–185. https://doi.org/10.1016/j.asr.2010.02.001

Tegedor, J., Øvstedal, O., & Vigen, E. (2014). Precise orbit determination and point positioning using GPS, Glonass, Galileo and BeiDou.

TensorFlow. (2023). TensorFlow. https://www.tensorflow.org/

Teresa Alonso, M., Ferigato, C., Ibanez Segura, D., Perrotta, D., Rovira-Garcia, A., & Sordini, E. (2021). Analysis of “Pre-Fit” Datasets of gLAB by Robust Statistical Techniques. STATS, 4(2), 400–418. https://doi.org/10.3390/stats4020026

TerraStar Correction Services. (2022). Home | TerraStar. https://terrastar.net/

Test and Assessment Research Center of China Satellite Navigation Office. (2022a). Constellation Status. http://www.csno-tarc.cn/en/system/constellation

Test and Assessment Research Center of China Satellite Navigation Office. (2022b). System Introduction. http://www.csno-tarc.cn/en/system/introduction

Teunissen, P. J. G. (2001). GNSS ambiguity bootstrapping: theory and application. Proceedings of International Symposium on Kinematic Systems in Geodesy, Geomatics and Navigation, 246–254.

Teunissen, P. J. G., & Khodabandeh, A. (2015). Review and principles of PPP-RTK methods. Journal of Geodesy, 89(3), 217–240.

The international disaster database. (2022). EM-DAT - The international disaster database. https://www.emdat.be/

The International GNSS Service. (2022). IGS RTS Products. http://www.igs.org/rts/products

The Multi-GNSS Experiment and Pilot Project (MGEX). (2016). IGS MGEX. http://mgex.igs.org/index.php

The Nevada Geodetic Laboratory. (2022). About NGL. http://geodesy.unr.edu/

Titov, V., Song, Y. T., Tang, L., Bernard, E. N., Bar-Sever, Y., & Wei, Y. (2017). Consistent Estimates of Tsunami Energy Show Promise for Improved Early Warning. In E. L. Geist, H. M. Fritz, A. B. Rabinovich, & Y. Tanioka (Eds.), Global Tsunami Science: Past and Future, Volume I (pp. 3863–3880). Springer International Publishing. https://doi.org/10.1007/978-3-319-55480-8_11

Tobías, G., & Navarro, P. (2015). Real-Time PPP with Galileo, paving the way to European High Accuracy Positioning.

Toka Tū Ake EQC |. (2022). The foundation from which we stand strong, together: Toka Tū Ake EQC. https://www.eqc.govt.nz/

Trimble. (2022). Trimble Business Center | Trimble Geospatial. https://geospatial.trimble.com/products-and-solutions/trimble-business-center

Trimble Positioning Services. (2022). High Precision RTX Technology | Trimble GNSS Positioning. https://positioningservices.trimble.com/services/rtx/

Tronin, A. A. (2010). Satellite remote sensing in seismology. A review. Remote Sensing, 2(1), 124–150.

Tsushima, H., & Ohta, Y. (2014). Review on near-field tsunami forecasting from offshore tsunami data and onshore GNSS data for tsunami early warning. Journal of Disaster Research, 9(3), 339–357.

Uhlemann, M., Rudenko, S., Nischan, T., & Gendt, G. (2010). GFZ results of the first IGS data reprocessing campaign. IGS Workshop, Newcastle.

UNAVCO. (2020). UNAVCO. https://www.unavco.org/

United Nations, O. for O. S. A., & UN-SPIDER Knowledge Portal. (2021). Early Warning Systems | UN-SPIDER Knowledge Portal. https://www.un-spider.org/risks-and-disasters/early-warning-systems#no-back

United States Naval Observatory. (2020). About USNO. https://maia.usno.navy.mil/index

Universitat Politècnica de Catalunya. (2021). Research group of Astronomy and Geomatics. gAGE — UPC. Universitat Politècnica de Catalunya. https://gage.upc.edu/en

University of Bern. (2022). Research: CODE - Analysis Center - Astronomical Institute. https://www.aiub.unibe.ch/research/code___analysis_center/index_eng.html

Urlichich, Y., Subbotin, V., Stupak, G., Dvorkin, V., Povalyaev, A., & Karutin, S. (2011). GLONASS modernization. Proceedings of the 24th International Technical Meeting of the Satellite Division of The Institute of Navigation (ION GNSS 2011), 3125–3128.

Urtiaga, Á. C., Berrocoso, M., Rosado, B., & Pazos, A. (2022). Detection and study of a high magnitude seismic event from GPS data: Case study of the 2011 Tohoku-Oki earthquake. Earth Sciences Research Journal, 26(2), 91–105.

Urschl, C., Gurtner, W., Hugentobler, U., Schaer, S., & Beutler, G. (2005). Validation of GNSS orbits using SLR observations. Advances in Space Research, 36(3), 412–417.

US Department of Commerce, N. N. G. S. (2022). OPUS: the Online Positioning User Service, process your GNSS data in the National Spatial Reference System.

US Department of Commerce, (2019). What We Do - NGS INFO - About Us - National Geodetic Survey.

US Department of Commerce, NOAA, N. G. S. (2020). OPUS: the Online Positioning User Service, process your GNSS data in the National Spatial Reference System. https://www.ngs.noaa.gov/OPUS/

U.S. National Geodetic Survey. (2022). NGS Coordinate Conversion and Transformation Tool (NCAT). https://geodesy.noaa.gov/NCAT/

USGS. (2020a). Liquefaction in Subsurface Layer of Sand | U.S. Geological Survey. https://www.usgs.gov/media/images/liquefaction-subsurface-layer-sand

USGS. (2020b). What is a landslide and what causes one? | U.S. Geological Survey. https://www.usgs.gov/faqs/what-landslide-and-what-causes-one

Vaclavovic, P., Dousa, J., & Gyori, G. (2013). G-Nut software library-state of development and first results. Acta Geodyn Geomater, 10(4), 431–436.

van Dierendonck, A. J., & Hua, Q. (2001). Measuring ionospheric scintillation effects from GPS signals. Proceedings of the 57th Annual Meeting of The Institute of Navigation (2001), 391–396.

Van Le, H., & Nishio, M. (2019). Structural change monitoring of a cable-stayed bridge by time-series modelling of the global thermal deformation acquired by GPS. Journal of Civil Structural Health Monitoring, 9(5), 689–701.

Vasylyev, D., Béniguel, Y., Volker, W., Kriegel, M., & Berdermann, J. (2022). Modelling of ionospheric scintillation. Journal of Space Weather and Space Climate, 12, 22.

Vereinte Nationen Office for Disaster Risk Reduction. (n.d.). Our world at risk transforming governance for a resilient future.

Veripos. (2022). Services | Veripos. https://veripos.com/services

Waldhauser, F., & Ellsworth, W. L. (2000). A Double-Difference Earthquake Location Algorithm: Method and Application to the Northern Hayward Fault, California. Bulletin of the Seismological Society of America, 90(6), 1353–1368. https://doi.org/10.1785/0120000006

Wang, A., Chen, J., Zhang, Y., Meng, L., Wang, B., & Wang, J. (2020). Evaluating the impact of CNES real-time ionospheric products on multi-GNSS single-frequency positioning using the IGS real-time service. Advances in Space Research, 66(11), 2516–2527. https://doi.org/10.1016/j.asr.2020.09.010

Wang, B., Wang, Y., Qin, K., & Xia, Q. (2018). Detecting Transportation Modes Based on LightGBM Classifier from GPS Trajectory Data. 2018 26th International Conference on Geoinformatics, 1–7. https://doi.org/10.1109/GEOINFORMATICS.2018.8557149

Wang, C.-Z., Kong, L.-W., Jiang, J., & Lai, Y.-C. (2021). Machine learning-based approach to GPS antijamming. GPS Solutions, 25(3), 115. https://doi.org/10.1007/s10291-021-01154-7

Wang, D., Xu, X., & Zhu, Y. (2018). A Novel Hybrid of a Fading Filter and an Extreme Learning Machine for GPS/INS during GPS Outages. Sensors, 18(11). https://doi.org/10.3390/s18113863

Wang, G. Q. (2013). Millimetre-accuracy GPS landslide monitoring using Precise Point Positioning with Single Receiver Phase Ambiguity (PPP-SRPA) resolution: a case study in Puerto Rico. Journal of Geodetic Science, 3(1), 22–31.

Wang, K., & Rothacher, M. (2013). Ambiguity resolution for triple-frequency geometry-free and ionosphere-free combination tested with real data. Journal Of Geodesy, 87(6), 539–553. https://doi.org/10.1007/s00190-013-0630-7

Wang, L., Li, Z., Ge, M., Neitzel, F., Wang, Z., & Yuan, H. (2018). Validation and Assessment of Multi-GNSS Real-Time Precise Point Positioning in Simulated Kinematic Mode Using IGS Real-Time Service. In Remote Sensing (Vol. 10). https://doi.org/10.3390/rs10020337

Wang, S., Wang, J., Su, C., & Ma, X. (2020). Intelligent Detection Algorithm Against UAVs' GPS Spoofing Attack. 2020 IEEE 26th International Conference on Parallel and Distributed Systems (ICPADS), 382–389. https://doi.org/10.1109/ICPADS51040.2020.00058

Wang, S., You, Z., Sun, X., & Yuan, L. (2022). A Partial Ambiguity Resolution Algorithm Based on New-Breadth-First Lattice Search in High-Dimension Situations. Sensors, 22(19), 7126.

Waskom, M. (2021). seaborn: statistical data visualization. Journal of Open-Source Software, 6(60), 3021. https://doi.org/10.21105/JOSS.03021

Watanabe, S. I., Bock, Y., Melgar, D., & Tadokoro, K. (2018). Tsunami Scenarios Based on Interseismic Models Along the Nankai Trough, Japan, From Seafloor and Onshore Geodesy. Journal of Geophysical Research: Solid Earth, 123(3), 2448–2461. https://doi.org/10.1002/2017JB014799

Weber, G., Dettmering, D., & Gebhard, H. (2005). Networked Transport of RTCM via Internet Protocol (NTRIP) BT - A Window on the Future of Geodesy (F. Sansò, Ed.; pp. 60–64). Springer Berlin Heidelberg.

Weber, G., & Mervart, L. (2007). The BKG Ntrip Client (BNC). Report on EUREF Symposium.

Weber, R., & Springer, T. A. (2001). The international GLONASS experiment: products, progress and prospects. Journal of Geodesy, 75(11), 559–568.

Wei, X., Wang, Y., & Sun, C. (2022). PerDet: Machine-Learning-Based UAV GPS Spoofing Detection Using Perception Data. Remote Sensing, 14(19). https://doi.org/10.3390/rs14194925

Wells, D. (1999). Guide To Gps Positioning.

Westwick, P. J. (2008). Into the black: JPL and the American space program, 1976-2004. Yale University Press.

Wickert, J., Reigber, C., Beyerle, G., König, R., Marquardt, C., Schmidt, T., Grunwaldt, L., Galas, R., Meehan, T. K., & Melbourne, W. G. (2001). Atmosphere sounding by GPS radio occultation: First results from CHAMP. Geophysical Research Letters, 28(17), 3263–3266.

World Metrological Organization, W. (2018). The International Network for Multi-Hazard Early Warning Systems (IN-MHEWS) | MHEWC. https://mhews.wmo.int/en/partners

Wu, Y. bin, Liu, Y., Yi, W., & Ge, H. bin. (2021). Impact of elevation mask on multi-GNSS precise point positioning performance. Earth Science Informatics, 14(3), 1111–1120.

Wu, H., Dai, Y., Wang, C., Xu, X., & Jiang, X. (2020). Identification and forewarning of GNSS deformation information based on a modified EWMA control chart. Measurement, 160, 107854.

Wu, J., Wu, S., Hajj, G., Bertiger, W., & Lichten, S. (1992). Effects of Antenna Orientation on GPS Carrier Phase. Manuscr. Geod., 18.

Wübbena, G. (2012). RTCM state space representation (SSR) overall concepts towards PPP-RTK. PPP-RTK & Open Standards Symposium, 12.

Wuhan University. (2015). IGS Data center of wuhan university. http://www.igs.gnsswhu.cn/index.php/home/index/about.html

XGBoost developers. (2022). XGBoost Documentation — XGBoost 1.7.6 documentation. https://xgboost.readthedocs.io/en/stable/

Xi, R., He, Q., & Meng, X. (2021). Bridge monitoring using multi-GNSS observations with high cutoff elevations: A case study. Measurement, 168, 108303.

Xia, F., Ye, S., Xia, P., Zhao, L., Jiang, N., Chen, D., & Hu, G. (2019). Assessing the latest performance of Galileo-only PPP and the contribution of Galileo to Multi-GNSS PPP. Advances in Space Research, 63(9), 2784–2795. https://doi.org/10.1016/j.asr.2018.06.008

Xia, P., Tong, M., Ye, S., Qian, J., & Fangxin, H. (2022). Establishing a high-precision real-time ZTD model of China with GPS and ERA5 historical data and its application in PPP. GPS Solutions, 27(1), 1–16.

Xiang, Y., Gao, Y., & Li, Y. (2020). Reducing convergence time of precise point positioning with ionospheric constraints and receiver differential code bias modelling. Journal of Geodesy, 94(1), 1–13.

Xiao, R., Shi, H., He, X., Li, Z., Jia, D., & Yang, Z. (2019). Deformation monitoring of reservoir dams using GNSS: An application to south-to-north water diversion project, China. IEEE Access, 7, 54981–54992.

Xiong, C. B., Yu, L. N., & Zhao, L. W. (2019). Analysis on the Impacts of Slant Tropospheric Delays on Precise Point Positioning. Applied Sciences-Basel, 9(22). https://doi.org/10.3390/app9224884

Xu, Q., Peng, D., Zhang, S., Zhu, X., He, C., Qi, X., Zhao, K., Xiu, D., & Ju, N. (2020). Successful implementations of a real-time and intelligent early warning system for loess landslides on the Heifangtai terrace, China. Engineering Geology, 278, 105817.

Xu, W., Yan, C., & Chen, J. (2022). Performance evaluation of BDS-2/BDS-3 combined precise time transfer with B1I/B2I/B3I/B1C/B2a five-frequency observations. GPS Solutions, 26(3). https://doi.org/10.1007/s10291-022-01262-y

Xu, X. W., & Newman, S. T. (2006). Making CNC machine tools more open, interoperable and intelligent—a review of the technologies. Computers in Industry, 57(2), 141–152.

Xu, Y., Jiang, N., Xu, G. C., Zhang, L., & Schuh, H. (2017). Fast BDS Positioning Convergence Based on the Contribution of GPS Observations. Marine Geodesy, 40(6), 404–415. https://doi.org/10.1080/01490419.2017.1323810

Xu, Z., Li, Y., Rizos, C., & Xu, X. (2010). Novel Hybrid of LS-SVM and Kalman Filter for GPS/INS Integration. The Journal of Navigation, 63(2), 289–299.

https://doi.org/DOI: 10.1017/S0373463309990361

Xue, B., Wang, H., & Yuan, Y. (2021). Performance of BeiDou-3 signal-in-space ranging errors: accuracy and distribution. GPS Solutions, 25. https://doi.org/10.1007/s10291-020-01057-z

Yaghmaei, N. (2020a). Human Cost of Disasters: An Overview of the Last 20 Years, 2000-2019. UN Office for Disaster Risk Reduction.

Yaghmaei, N. (2020b). Human Cost of Disasters: An Overview of the Last 20 Years, 2000-2019. UN Office for Disaster Risk Reduction.

Yang, H., Park, S.-C., & Lee, W.-J. (2016). Crustal deformation on the Korea peninsula based on GNSS data during 2004–2015. 2016 IEEE International Geoscience and Remote Sensing Symposium (IGARSS), 5785–5788.

Yang, S., Ben, T.-B., & Xiang, W. (2019). Build Up a Real-Time LSTM Positioning Error Prediction Model for GPS Sensors. 2019 IEEE 90th Vehicular Technology Conference (VTC2019-Fall), 1–5. https://doi.org/10.1109/VTCFall.2019.8891192

Yang, S.-S., Potirakis, S. M., Sasmal, S., & Hayakawa, M. (2020). Natural time analysis of Global Navigation Satellite System surface deformation: The case of the 2016 Kumamoto earthquakes. Entropy, 22(6), 674.

Yang, X., Liu, W., Huang, J., Xiao, W., & Wang, F. (2022). Real-time monitoring of GPS flex power based on machine learning. GPS Solutions, 26(3), 73. https://doi.org/10.1007/s10291-022-01257-9

Yang, Z., & Morton, Y. T. (2020). Low-latitude GNSS ionospheric scintillation dependence on magnetic field orientation and impacts on positioning. Journal of Geodesy, 94(6), 1–15.

Yao, Y., Peng, W., Xu, C., & Cheng, S. (2017). Enhancing real-time precise point positioning with zenith troposphere delay products and the determination of corresponding tropospheric stochastic models. Geophysical Journal International, 208(2), 1217–1230. https://doi.org/10.1093/gji/ggw451\

Yao, Y., Zhang, R., Song, W., Shi, C., & Lou, Y. (2013). An improved approach to model regional ionosphere and accelerate convergence for precise point positioning. Advances in Space Research, 52(8), 1406–1415. https://doi.org/10.1016/j.asr.2013.07.020

Ye, Q., Szeto, W. Y., & Wong, S. C. (2012). Short-term traffic speed forecasting based on data recorded at irregular intervals. IEEE Transactions on Intelligent Transportation Systems, 13(4), 1727–1737.

Yue, C., Dang, Y., Xue, S., Wang, H., Gu, S., & Xu, C. (2022). A New Optimal Subset Selection Method of Partial Ambiguity Resolution for Precise Point Positioning. Remote Sensing, 14(19), 4819.

Zaletnyik, P., Völgyesi, L., & Paláncz, B. (2008). Modelling local GPS/levelling geoid undulations using Support Vector Machines. Periodica Polytechnica Civil Engineering, 52(1), 39–43. https://doi.org/10.3311/pp.ci.2008-1.06

Zaminpardaz, S., Teunissen, P. J. G., & Khodabandeh, A. (2021). GLONASS–only FDMA+CDMA RTK: Performance and outlook. GPS Solutions, 25(3). https://doi.org/10.1007/s10291-021-01132-z

Zang, J., Wen, Y., Li, Z., Xu, C., He, K., Zhang, P., Wen, G., & Fan, S. (2022). Rapid source models of the 2021 Mw 7.4 Maduo, China, earthquake inferred from high-rate BDS3/2, GPS, Galileo and GLONASS observations. Journal of Geodesy, 96(9), 1–13.

Zedek, F., Rolland, L. M., Mikesell, T. D., Sladen, A., Delouis, B., Twardzik, C., & Coisson, P. (2021). Locating surface deformation induced by earthquakes using GPS, GLONASS and Galileo ionospheric sounding from a single station. advances in space research, 68(8), 3403–3416. https://doi.org/10.1016/j.asr.2021.06.011

Zeni, L., Damiano, E., Avolio, B., Olivares, L., Coscetta, A., Picarelli, L., & Minardo, A. (2015). Soil slope monitoring by use of a Brillouin distributed sensor. https://doi.org/10.1049/cp.2015.0156

Zhang, G., & Hsu, L.-T. (2018). Intelligent GNSS/INS integrated navigation system for a commercial UAV flight control system. Aerospace Science and Technology, 80, 368–380. https://doi.org/10.1016/j.ast.2018.07.026

Zhang, L., Yang, H., Gao, Y., Yao, Y., & Xu, C. (2018a). Evaluation and analysis of real-time precise orbits and clocks products from different IGS analysis centers. Advances in Space Research, 61(12), 2942–2954. https://doi.org/https://doi.org/10.1016/j.asr.2018.03.029

Zhang, L., Yang, H., Gao, Y., Yao, Y., & Xu, C. (2018b). Evaluation and analysis of real-time precise orbits and clocks products from different IGS analysis centers. Advances in Space Research, 61(12), 2942–2954. https://doi.org/10.1016/j.asr.2018.03.029

Zhang, X., Guo, F., & Zhou, P. (2014). Improved precise point positioning in the presence of ionospheric scintillation. GPS Solutions, 18(1), 51–60. https://doi.org/10.1007/s10291-012-0309-1

Zhao, Q., Guo, J., Li, M., Qu, L., Hu, Z., Shi, C., & Liu, J. (2013). Initial results of precise orbit and clock determination for COMPASS navigation satellite system. Journal of Geodesy, 87(5), 475–486.

Zhao, Q., Sun, B., Dai, Z., Hu, Z., Shi, C., & Liu, J. (2015). Real-time detection and repair of cycle slips in triple-frequency GNSS measurements. GPS Solutions, 19(3), 381–391.

Zhao, X., Ge, Y., Ke, F., Liu, C., & Li, F. (2020). Investigation of real-time kinematic multi-GNSS precise point positioning with the CNES products. Measurement, 166, 108231. https://doi.org/https://doi.org/10.1016/j.measurement.2020.108231

Zheng, Y., Li, Q., Chen, Y., Xie, X., & Ma, W.-Y. (2008). Understanding mobility based on GPS data. Proceedings of the 10th International Conference on Ubiquitous Computing, 312–321.

Zheng, Y., Zheng, F., Yang, C., Nie, G., & Li, S. (2022). Analyses of GLONASS and GPS+ GLONASS Precise Positioning Performance in Different Latitude Regions. Remote Sensing, 14(18), 4640.

Zhiping Liu, Q. Z. (2016). Dynamic GPS Precise Point Positioning for Deformation Monitoring Using Prior Information. January 2015. https://doi.org/10.1007/978-3-662-46632-2

Zhong, P., Ding, X., Yuan, L., Xu, Y., Kwok, K., & Chen, Y. (2010). Sidereal filtering based on single differences for mitigating GPS multipath effects on short baselines. Journal of Geodesy, 84(2), 145–158.

Zhou, F., Cao, X., Ge, Y., & Li, W. (2019). Assessment of the positioning performance and tropospheric delay retrieval with precise point positioning using products from different analysis centers. GPS Solutions, 24(1), 12. https://doi.org/10.1007/s10291-019-0925-0

Zhou, L., Perera, S., Jayawickrama, J., & Adeniyi, O. (2014). The Implication of Hyogo Framework for Action for Disaster Resilience Education. Procedia Economics and Finance, 18, 576–583. https://doi.org/10.1016/s2212-5671(14)00978-2

Zhou, Y., Lou, Y., Zhang, W., Wu, P., Bai, J., & Zhang, Z. (2022). Tropospheric Second-Order Horizontal Gradient Modelling for GNSS PPP. Remote Sensing, 14(19), 4807.

Zia, A., & Wagner, C. H. (2015). Mainstreaming early warning systems in development and planning processes: Multilevel implementation of Sendai framework in Indus and Sahel. International Journal of Disaster Risk Science, 6(2), 189–199.

Zumberge, J. F., Heflin, M. B., Jefferson, D. C., Watkins, M. M., & Webb, F. H. (1997a). Precise point positioning for the efficient and robust analysis of GPS data from large networks. Journal of Geophysical Research: Solid Earth, 102(B3), 5005–5017. https://doi.org/10.1029/96jb03860

Zumberge, J. F., Heflin, M., Jefferson, D. C., Watkins, M., & Webb, F. (1997b). Precise Point Positioning for the Efficient And Robust Analysis of GPS Data from Large Networks. Journal of Geophysical Research, 102. https://doi.org/10.1029/96JB03860

Прикладной потребительский центр Госкорпорации “Роскосмос.” (2020). About GLONASS. https://www.glonass-iac.ru/en/about_glonass/